UNIVERSITY OF CALIFORNIA

Santa Barbara

Understanding & correlating compositions, structures, & properties of conductive networks for energy conversion & storage applications

A dissertation submitted in partial satisfaction of the

requirements for the degree Doctor of Philosophy

in Chemical Engineering

by

Shona Marie Becwar

Committee in charge:

Professor Bradley Chmelka, Chair

Professor Song-I Han

Professor Michael Gordon

Professor Thuc-Quyen Nguyen

March 2022

The dissertation of Shona M Becwar is approved.

_____
Song-I Han

_____
Michael Gordon

_____
Thuc-Quyen Nguyen

_____
Bradley Chmelka, Committee Chair

March 2022

Understanding & correlating compositions, structures, & properties of conductive networks for energy conversion & storage applications

ACKNOWLEDGEMENTS

Completion of this dissertation would not have been possible without substantial support from many people, to whom I am grateful. First and foremost are my PhD advisor, Brad Chmelka, who has provided me with interesting and diverse projects have expanded my scientific interests and encouraged me to seek understandings at a fundamental chemical and materials engineering level. Brad's numerous academic partnerships and friendships have provided me with many invaluable opportunities to research and travel. Brad's enthusiasm and high expectations have pushed me to become an independent, confident, and outspoken researcher.

I additionally want to express my gratitude to my committee member Mike Gordon for always having an open door for our many passionate research discussions, for his encouragement and support, for teaching me various lab techniques, and for his part in providing me the opportunity to travel to Sweden for research. I additionally want to express my gratitude to my committee members Songi Han and Thuc-Quyen Nguyen for their valuable insights during our annual meetings and their mentorship during our one-on-one discussions.

Over the course of my PhD, I have had the opportunity to collaborate closely with numerous world-class researchers who have supported or contributed to my work and are highlighted throughout my dissertation and manuscripts. I am particularly grateful to Anders Palmqvist for welcoming me to visit his lab at Chalmers University in Sweden and his students Walter Rosas and Caroline Janson for expanding my knowledge of electrochemistry and EPR, respectively. Additionally, I am thankful for all of my SCALAR collaborators, especially Ziyang Wei, Rongli Liu, Riley Zhang, Johanna N. Weker, Xiangfeng Duan, and Philippe Sautet for their insightful

discussions and contributions to my N-carbons work. Additionally, I would like to thank the excellent staff of the NMR facility at UCSB, Jerry Hu, Jaya Nolt, and Shamon Walker.

I am grateful to the members of the Chmelka research groups for their support, encouragement, and friendship over the years. I particularly want to acknowledge the mentorship and friendships of Niels Zussblatt, Zach Berkson, Nathan Prisco, Matt Idso, and Philipp Selter who showed me how to be a successful researcher and presenter and in the Chmelka group and in their respective career paths. It has been a pleasure to work alongside the excellent company of Max Berkow, New Guy (Mike) Schmithorst, Tsatsa Battsengel, and Matt Lertola.

I would like to thank my emotional support system Sofia Martelly, Julia Fisher, and wonderful boyfriend Maxwell Berkow for their endless love, encouragement, friendship, and lunch dates. Finally, I would like to thank my loving family for their care, support, and encouragement through my PhD, and my entire life: Bruce and Julie Becwar, Alea and Garrett Becwar, Kaye Gagnon and David Richardson.

SHONA MARIE BECWAR

Doctoral Candidate in Chemical Engineering, Santa Barbara, CA, USA
smbecwar@gmail.com | 480-734-7610 | www.linkedin.com/in/ShonaBecwar

SUMMARY

Chemical engineering PhD candidate experienced in academic and industrial research in the energy field with excellent problem-solving and technical communication skills. Well-versed in chemical/material syntheses, material characterizations, macroscopic electrochemical performance optimization, and advanced atomic-level understanding.

EDUCATION

Doctor of Philosophy in Chemical Engineering **2016-current**
University of California, Santa Barbara, CA, USA grad Mar 2022
- Adviser: Brad Chmelka, PhD
- Graduate Scholars Program, Mentor for nine graduate students
- Chemical Engineering Graduate Student Association, Founding member, Social Chair
- Laboratory safety officer
- Entrepreneurial new business venture competition, Team member, Competition finalist

Bachelor of Science in Engineering in Chemical Engineering **2012-2016**
Arizona State University, Tempe, Arizona, USA GPA: 4.0
- Fulton Schools of Engineering & Barrett the Honors College
- Moeur Award for Academic Excellence, awarded by the President of the University
- Fulton Undergraduate Research Initiative Program Researcher
- Society of Women Engineers, Vice-President

RELEVANT WORK EXPERIENCE

ACADEMIC RESEARCH

Graduate Research – University of California, Santa Barbara
Department of Chemical Engineering, Santa Barbara, CA 2016 – current
Thesis: *Graphitic carbon networks for energy conversion and storage applications*
Expertise in both chemical/material synthesis and characterization methods on the atomic, mesoscopic, and macroscopic length scales on various conductive organic-based materials including heteroatom-containing graphitic carbons, polymer films, and boron clusters for electrochemical energy conversion and storage. Research emphasis on novel characterization techniques of conductive materials with dilute species, providing insight for optimization of oxygen/sulfur reduction catalysts. Knowledgeable in electrochemical performance testing and optimization. Extensive experience in technical and broad-level communication.

Undergraduate Research, Honors College Thesis Project– Arizona State University
Department of Chemical Engineering, Tempe, AZ 2014 – 2016
Thesis: *Process Design and Refinement for Bioproduction of Sustainable Butanol*
Investigated uncharacterized loss in butanol product recovery. Modified pervaporation recovery process to increase purity and minimize system losses. Presented research twice to engineering faculty, students, and public at Fulton Undergraduate Research Symposium in addition to defending the honors thesis in 2016.

INDUSTRIAL INTERNSHIPS

Engineering Operations & Technology Materials Engineering Intern – The Boeing Company
Boeing Research and Technology – Seattle, WA and Mesa, AZ 2015 – 2016
Developed research procedures, worked with lab technicians to carry out and delegate lab research, coordinated with test plane engineers, collected data and compiled findings which were presented to research executives for which I earned the **Pride at Boeing Award**.

Industrial Controls Program Manager / Technical Engineering Sales Intern
Rockwell Automation International Company, Phoenix, AZ Summer 2014
Researched, identified, and prioritized prospective accounts; summarized findings in presentation to SW district. Designed wiring lab demo cases for twelve products on the Demo Development Team and instructed wiring classes to contractor employees; labs enhanced education and skill level of students.

PUBLICATIONS

1. Kim, Zussblatt, Chung, Becwar**,** Zelenay, Chmelka. Highly Graphitic Mesoporous Fe,N-Doped Carbon Materials for Oxygen Reduction Electrochemical Catalysts. *ACS Applied Material and Interfaces.* **2018.**
2. Wei, Becwar, Chmelka, Sautet. Atomic environments of N-doped graphene probed by DFT calculations and NMR. *Journal of Physical Chemistry C.* **2021.**
3. Bashian, Zuba, Irshad, Becwar, Chmelka, Melot et al. Electrochemical Oxidative Fluorination of an Oxide Perovskite. *Chemistry of Materials*. **2021.**
4. Becwar, Chmelka, et. al. Atomic-scale understanding of the oxygen and sulfur reduction activities of mesoporous N-carbon electrocatalysts. *Submitted to Nature Materials.* **2022.**
5. Becwar, Chmelka, et. al. Correlating macroscopic compositions and structures with oxygen and sulfur reduction activities of mesoporous-Fe,N-carbon electrocatalysts. *To be submitted.* **2022.**
6. Luginbuhl. Ko, Ran, Hu, Becwar, Chmelka, Nguyen et al. Low voltage-loss organic solar cells light the way for efficient semitransparent photovoltaics. *Solar RRL*. **2022.**
7. Ready, Becwar, Chmelka, Spokoyny et. al. Synthesis and structural properties of a 2D Zn(II) dodecahydroxycloso-dodecaborate coordination polymer. *Submitted to Royal Society of Chemistry.* **2022.**

ACCOMPLISHMENTS and AWARDS

1. *Best technical presentation.* 13th Annual Clorox-Amgen Graduate Student Symposium, Santa Barbara, California. September 25, 2020.
2. *Inorganic and catalyst materials, Session Chair.* 12th Annual Amgen-Clorox Graduate Student Symposium, Santa Barbara, CA. 4 October 2019.
3. *Visiting Scholar*, funded by the Cooperative for Advanced Materials in Energy-Related Applications (CAMERA) grant, International Research Experiences for Students (IRES) program, **National Science Foundation**. Chalmers University of Technology, Gothenburg, Sweden. May & June 2019.
4. *Undergraduate Awards:* Alumni Association's Gold Circle Scholar Award, Class of 2016 Chemical Engineering Distinguished Graduate Finalist, Dean's List (2012-16), Moeur Distinguished Graduate Award for students with a 4.0 GPA, Regent High Honors Scholar, Society of Women Engineers Academic Scholarship Recipient, Tau Beta Pi Engineering Honors Society, Six Sigma Training: Green Belt/Black Belt Training Master Classes - Final Project Champions

PRESENTATIONS

1. Materials Research Society Fall Meeting, Boston, Massachusetts. *Oxygen and Sulfur Reduction Activities of Mesoporous N- & Fe,N-Carbon Electrocatalysts Correlate with Atomic-Scale Compositions and Structures*. November 30, 2021.
2. American Institute of Chemical Engineers Annual Conference, Boston, Massachusetts. *Correlating Atomic-Scale Compositions and Structures of Mesoporous N-Containing Carbon Electrocatalysts with Oxygen and Sulfur Reduction Properties*. November 8, 2021.
3. SCALAR Energy Frontiers Research Center Meeting, Santa Barbara, California. *Novel non-precious-metal carbon material electrocatalysts for LiS batteries.* September 10, 2021.
4. UCSB – Chalmers Advanced Materials for Energy and Biological Applications Conference, Virtual. *Correlating atomic-scale compositions and structures of mesoporous Fe,N-containing carbon electrocatalysts with oxygen reduction properties.* April 28 and 29, 2021.
5. SCALAR Energy Frontiers Research Center Meeting, Virtual. *Conductive and mesoporous carbon materials with heteroatom active sites for cathode catalysts materials.* March 19, 2021.
6. SCALAR Energy Frontiers Research Center DOE Review, Los Angeles, California. *Novel non-precious-metal mesoporous N- & Fe,N-carbon electrocatalysts for LiS batteries.* February 09, 2021.

7. American Institute of Chemical Engineers Annual Conference, San Francisco, California. *Compositions, Structures, and Properties of Mesoporous-Fe,N-Containing Carbon Materials for Oxygen- and Sulfur-Reduction Electrocatalysts*. November 17, 2020.
8. PRiME 2020 Electrochemical Society Joint International Meeting, Honolulu, Hawaii. *Compositions, Structures, and Properties of Mesoporous-Fe,N-Containing Carbon Materials for Oxygen- and Sulfur-Reduction Electrocatalysts.* October 6, 2020.
9. 13th Annual Clorox-Amgen Graduate Student Symposium, Santa Barbara, California. *Understanding and correlating compositions, structures, and properties of novel conductive networks for energy conversion and storage applications.* September 25, 2020.
10. UCSB Chemical Engineering Student Symposium Series, Santa Barbara, California. *Conductive and mesoporous carbon materials with heteroatom active sites for cathode catalysts materials, with an emphasis on basic NMR understandings.* April 14, 2020.
11. SCALAR Energy Frontiers Research Center Meeting, Los Angeles, California. *Conductive and mesoporous carbon materials with heteroatom active sites for cathode catalysts materials.* December 10, 2019.
12. American Institute of Chemical Engineers Annual Conference, Orlando, Florida. *Compositions, Structures, and Properties of Mesoporous-Fe,N-Containing Carbon Materials for Oxygen Reduction Electrocatalysts*. November 13, 2019.
13. SCALAR Energy Frontiers Research Center for Department of Energy Review, Santa Barbara, California. *Heteroatom-containing carbons for sulfur reduction and Insights from solid-state NMR*. October 17, 2019.
14. UCSB – Chalmers Workshop, Chalmers University of Technology, Gothenburg, Sweden. *Compositions, structures, & properties of non-precious-metal mesoporous carbon electrocatalysts.* June 18-20, 2019.
15. International Mesostructured Materials Symposium 10, Los Angeles, California. *Compositions, structures, & properties of non-precious-metal mesoporous carbon electrocatalysts for oxygen reduction*. September 11, 2018.
16. Southern California Electrochemical Energy Storage Alliance Conference, Santa Barbara, CA. *N-containing mesoporous carbon materials for improved conductivities and catalytic activities.* October 24, 2017.
17. UCSB 1st year Research Presentations Symposium, Santa Barbara, California. *N-containing mesoporous carbon materials for improved conductivities and catalytic activities.* September 26, 2017.

POSTERS

1. American Institute of Chemical Engineers Annual Conference, Boston, Massachusetts. *Understanding & Correlating Atomic-Scale Compositions & Structures of Mesoporous N-Containing Carbon Electrocatalysts with Oxygen & Sulfur Reduction Properties*. November 8, 2021.
2. Science for our Nation's Energy Future: Energy Frontiers Research Centers Energy Innovation Hubs Meeting, Virtual. *Electrocatalyst Design for Sulfur Reduction Reaction.* October 19, 2021.
3. 12th Annual Clorox-Amgen Graduate Student Symposium, Santa Barbara, California. *Understanding non-precious-metal mesoporous N-carbon electrocatalysts at an atomic level.* October 4, 2019.
4. Experimental Nuclear Magnetic Resonance Conference 2019, Pacific Grove, California. *Compositions, structures, and properties of mesoporous-Fe,N-containing carbon materials for oxygen reduction electrocatalysts*. April 8-10, 2019.
5. Materials Research Outreach Program Symposium 2019, Santa Barbara, California. *Understanding non-precious-metal N,Fe mesoporous carbon electrocatalysts at an atomic level*. January 29, 2019.
6. 10th Annual Clorox-Amgen Graduate Student Symposium, Santa Barbara, California. *Fe,N-containing mesoporous carbon materials as non-precious metal electrocatalysts for alcohol and bio-hybrid fuel cells.* October 6, 2017.

SKILLS

COMPUTER

Adobe Illustrator software, TopSpin NMR data collection and analysis software, DM Fit deconvolution software, Mathematica, HYSYS Chemical Engineering Design Software, JMP statistical software, factorial design of experiment, MATLAB, Microsoft office (word, excel, power point, publisher, outlook), connected components workbench software, employee connect, SAP enterprise portal, learning management center – training, noggin SAVO, WebEx meeting, share point, proposal works, office tools pro, quick books pro, adobe

OTHER SKILLS

Research project planning and execution, mentoring, multitasking, teaching, delegation, public speaking, nuclear magnetic resonance spectroscopy, electron paramagnetic resonance spectroscopy, X-ray diffraction, X-ray photoelectron spectroscopy, X-ray fluorescence spectroscopy, Solid-state nuclear magnetic resonance, Nitrogen sorption, electrochemical performance analyses, SixSigma Greenbelt/Blackbelt training, leadership – lab teams and community service club vice president and president positions, strong verbal and written communication skills, organization, motivation, listening, self-driven, dedicated, fast learning, team player, ethical, results oriented, strong analytical & problem solving skills, safety oriented

RELEVANT COURSEWORK

GRADUATE LEVEL

Advanced Science and Engineering of Energy Conversion, Magnetic Resonance Spectroscopy Techniques, EPR and Magnetic Resonance Methods, Electrochemistry and Electrochemical Methods, Spectroscopy of Materials, Materials Engineering Spectroscopy of Inorganic Materials, Advanced Chemical Reaction Engineering, Advanced Transport Processes-Laminar Flow and Convective Transport Processes, Advanced Topics in Equilibrium Statistical Mechanics, Advanced Theoretical Methods in Engineering, Advanced Transport Processes-Laminar Flow and Convective Transport Processes, Fundamentals and Applications of Classical Thermodynamics and Statistical Mechanics, Innovation in Engineering, Bio Reactor Design Engineering, Six Sigma Methodology/Engineering Experimentation, Air Quality Engineering

UNDERGRADUATE LEVEL

Chemical Engineering Senior Design, Principles of Chemical Engineering Design, Chemical Engineering Lab II, Process Dynamic Control, Environmental Chemistry, Chemical Reactor Design, Modern Separations, Chemical Engineering Lab I, Applied Chemical Thermodynamics, Honors Chemical Engineering Research Study, Transport Phenomena II: Heat and Mass Transfer, Transport Phenomena I: Fluids Mechanics, Elementary Physical Chemistry, Engineering Perspectives/Biological Systems, Numerical Methods for Chemical Engineers, Organic Chemistry and Lab, Modern Differential Equations with MATLAB, Structure & Properties-Materials Science, Introduction to Chemical Processing, Physics II for Engineers Electricity and Magnetism, Physics I for Engineers Mechanics and Lab, General Chemistry and Lab, Calculus for Engineers, Introduction to Engineering: Designing and Building a Recycling Machine, Business and Industrial Engineering

ABSTRACT

Understanding & correlating compositions, structures, & properties of conductive networks for energy conversion & storage applications

by

Shona M Becwar

Conjugated electrochemical materials may be the key to making large-scale energy conversion and storage devices with lower environmental impact than current industrial standards. For example, as an alternative to current expensive and non-selective precious-metal-based catalysts, N- and Fe,N-containing mesoporous carbon materials can be engineered to possess attractive properties with applications including energy conversion as fuel cell oxygen reduction reaction (ORR) catalysts,[1–8] energy storage as supercapacitor electrodes,[9–11] and water purification as water filtration membranes.[12] Additionally, lithium-sulfur (Li-S) batteries have been attracting attention due to their high theoretical capacities and energy densities, with relatively low costs.[13] However, challenges with the insulating S cathode and solubility of the S-reduction intermediates result in cell performance far below their theoretical capacities. Thus, conductive and high surface area N- and Fe,N-containing carbon materials have recently begun to be explored as SRR catalysts.[14–16] It is challenging to measure and correlate local atomic environments and their distributions with synthesis

conditions and macroscopic electrocatalytic properties in conductive and conjugated material networks due to paramagnetic and/or conductive properties, complicated distributions of disordered and ordered regions, and heterogeneous material compositions.

The objective of my thesis has been to improve understanding and viability of alternative energy conversion and storage materials. This objective encompasses many material systems. Promising systems which will be addressed in this dissertation include 1) boron clusters for solid-state redox, 2) conductive polymers in semi-transparent organic solar cells, 3) perovskites undergoing fluoride ion intercalation, and 4) the main system discussed throughout this dissertation which is mesoporous N- and Fe,N-carbons for oxygen & sulfur reduction. Key characteristics exhibited by these systems include 1) that they are comprised of extended networks with non-stoichiometric compositions, 2) that they consist of complicated heterogenous distributions of ordered and disordered structural features, and 3) their atomic-level structures are important to electron transport and electrochemical activity. In addition to conventional characterization techniques such as nitrogen sorption, X-ray photoelectron spectroscopy, Raman spectroscopy, ^{57}Fe Mössbauer spectroscopy, X-ray diffraction, solid-state NMR spectroscopy and DFT modeling calculations provide detailed atomic-level insights about the environments and distributions of nuclei which, until now, had limited use in the study of this class of materials. Specifically, solid-state nuclear magnetic resonance (NMR) spectroscopy is sensitive to atomic environments in both ordered and disordered regions of a material and can provide significantly enhanced resolution of environments which are corroborated by DFT predictions of chemical shift values. Correlating macroscopic electrochemical reduction activities with bulk and surface characterizations provides insight about material composition on many length scales enabling systematic

selection and tuning of synthesis/post-synthetic processing conditions to improve the macroscopic conductivity and electrocatalytic activities. This thesis details my contributions to the field, which relate understandings of the local atomic environments and interactions with complicated macroscopic properties and performance. Specially, allowing for more strategic synthesis and optimization strategies than have been typically employed in the past.

TABLE OF CONTENTS

1. Introduction and background ..…….....……. 1

1.1 General motivation and research objectives ……..….. 1

1.1.1 Additional background, challenges, and opportunities for heteroatom-containing mesoporous carbons as fuel cell and electrocatalysts ..……...…….. 6

1.2 Dissertation Outline ...……. 12

1.3 References ...…… 19

2. Highly Graphitic Mesoporous Fe,N-Doped Carbon Materials for Oxygen Reduction Electrochemical Catalysts ...…….. 27

2.1 Abstract ...…… 28

2.2 Introduction ……..... 29

2.3 Materials and Methods ...…… 31

2.4 Results and Discussion ……...… 37

2.5 Conclusions ……. 63

2.6 Future Directions …… 64

2.7 References …….. 65

2.8 Supporting Information …….. 75

2.8.1 Supporting Information – Tables …….. 75

2.8.2 Supporting Information – Figures …… 78

3. Atomic-scale understanding of the oxygen and sulfur reduction activities of mesoporous N-carbon electrocatalysts ……... 88

3.1 Abstract ……... 88

3.2 Introduction ……. 89

3.3 Results and Discussion …… 91

3.4 Materials and Methods ……... 108

3.5 Conclusions ……... 120

3.6 Future Directions ……... 122

3.7 Supporting Information ……. 124

3.7.1 Supporting Information – Tables …… 124

3.7.2 Supporting Information – Figures ……... 127

3.8 References ……. 155

4. Atomic environments in N-containing graphitic carbon probed by first-principles calculations and solid-state nuclear magnetic resonance …… 159

4.1 Abstract ……. 160

4.2 Introduction ……... 161

4.3 Materials and Methods ……... 164

4.4 Results and Discussion …….. 169

4.5 Conclusions ……... 182

4.6 References ……. 184

4.7 Supporting Information ……. 191

5. Correlating macroscopic compositions and structures with oxygen and sulfur reduction activities of mesoporous-Fe,N-carbon electrocatalysts ……... 201

5.1 Abstract ……. 201

5.2 Introduction ……... 203

5.3 Materials and Methods …….. 205

5.4 Results and Discussion …….. 216

5.5 Conclusions ……... 238

5.6 Future Directions ……... 239

5.7 Supporting Information …… 242

5.7.1 Supporting Information – Tables …… 242

5.7.2 Supporting Information – Figures ……... 245

5.8 References …… 264

6. Understanding and correlating complicated electronic and paramagnetic properties of conductive N- and Fe, N-carbons …… 275

6.1 Abstract …… 275

6.2 Introduction ……... 277

6.3 Special considerations for and broadening of spectra in solid-state nuclear magnetic resonance spectroscopy of conductive materials …….. 280

6.4 NMR Results, Discussion, and Future Directions …….. 292

6.5 EPR for N- and Fe,N-carbon materials ……... 303

6.6 Preliminary EPR results, predictions, and hypotheses …….. 306

6.7 Conclusions and future work …… 317

6.8 References …… 318

7. Synthesis and structural properties of a 2D Zn(II) dodecahydroxy-closo-dodecaborate coordination polymer ……... 325

7.1 Abstract …… 326

7.2 Introduction ……... 327

7.3 Materials and Methods …….. 330

7.4 Results and Discussion …….. 335

7.5 Conclusions ……... 348

7.6 Relevant Supporting Information …….. 350

7.7 References ……. 354

8. Electron donor-acceptor small molecule thin films as active layers in solar cells …… 363

8.1 Motivation and project goals …….. 363

8.2 Background, challenges, and approach …….. 364

8.3 Abstract ……. 366

8.4 Introduction ……... 367

8.5 Results and Discussion ……..… 370

8.6 Conclusions ……...… 390

8.7 Relevant Materials and Methods …… 392

8.8 References ……. 394

8.9 Relevant Supporting Information ……..… 400

9. Electrochemical Oxidative Fluorination of an Oxide Perovskite ……. 414

9.1 Abstract ……...….. 415

9.2 Introduction ……...…… 416

9.3 NMR Methods ……... 419

9.4 Results and Discussion ..…… 420

9.5 Conclusions ……... 440

9.6 References ……...…….. 442

9.7 Relevant Supporting Information …….. 452

10. Conclusions ……... 474

Appendix A: Understanding the eutectic melt and pyrolysis steps of the N-carbon synthesis, and the important role of the Zn^{2+} ion on the N moiety formation …….. 477

A.1 Understanding eutectic melt chemistry with *in situ* and *ex situ* NMR techniques ……..……. 477

A.2 Roles of divalent cations on eutectic syntheses and electrocatalytic reduction activity of mesoporous Fe,N-carbon materials ……..... 481

A.3 Future directions ……... 483

A.4 References …… 483

1. Introduction and background

1.1 General motivation and research objectives

Considering the economic and environmental challenges facing the world today, impactful future development will rely on sustainable energy technologies. Today we consume more energy than ever before in human history, over 14 times more than in the year 1900, and 30 times more than the year 1800.[17] However, the world's energy consumption is sourced primarily (over 80%) by fossil fuels including oil, coal, and gas, accounting for about 75% of global greenhouse gas emissions, driving climate change and detriment to human health.[17] Many national and international organizations have goals in place to address these issues. For instance, the United Nations Department of Economic and Social Affairs has set forth Goal Seven, which is to ensure access to affordable, reliable, sustainable, and modern energy for all. Additionally, the United States Department of Energy's Office of Energy Efficiency & Renewable Energy has a goal to accelerate the research, development, demonstration, and deployment of technologies and solutions to equitably transition America to net-zero greenhouse gas emissions economy-wide by no later than 2050. A major challenge with the global adoption and transition to renewable energy conversion and storage devices is that many of the current materials and devices do not meet their theoretical performance potentials, making them more costly than current fossil fuel alternatives.[17] Thus, it is necessary to develop technologies that can efficiently and cost effectively provide, convert, store, and utilize energy in a sustainable fashion. The processes by which we capture, store, and utilize energy (from

renewable or conventional resources) rely on materials with relevant adsorption, catalytic, or electrochemical properties that have been optimized for these applications.

Electronically active conjugated networks may be the key to making large-scale energy conversion and storage devices with lower environmental impact than current industrial materials. Conjugated carbon networks consist of connected p-orbitals that enable electron delocalization, facilitate electrical conductivity, decrease the overall energy of the system, and increase system stability. Conjugated carbon networks have diverse configurations, including cyclic, linear, and combinations of the two, that result in a variety of networks including graphene sheets of aromatic rings, and polymer carbon chains.[1] The diversity, stability, and conductivity of conjugated carbon networks makes them favorable for stable energy conversion and storage systems, including electrochemical and photovoltaic cells.

One promising application of conjugated carbon networks is as a cathode catalyst in polymer electrolyte fuel cells (PEFCs), which are energy conversion devices receiving increasing interest due to their high conversion efficiencies and low environmental impact.[2,3] Desirably, the thermodynamic efficiencies of PEFCs are not limited by the Carnot cycle, which limits the thermodynamic efficiencies of heat engines. Thus, a hydrogen fuel cell has a theoretical thermodynamic efficiency four times greater than a hydrogen burning combustion engine.[4] Electrochemical fuel cells convert chemical energy to electrical energy through the oxidation of a fuel (e.g., H_2) at the anode and reduction of oxygen at the cathode.[4,5] The oxygen reduction reaction (ORR) of protons, electrons, and oxygen to form water is typically the rate limiting step in this process and requires a catalyst at the cathode. Current cathode precious-metal (Pt)/carbon catalysts are expensive, subject to sluggish kinetics, and non-selective, causing them to degrade the membranes on which they are housed.[4,6] Alternatively,

conjugated carbon network based Fe,N-containing mesoporous carbon materials can be engineered to possess attractive properties, including energy conversion as fuel cell ORR catalysts.[4,5,7–12] Despite a variety of alternative ORR catalysts materials being proposed with performance similar to and surpassing that of conventional Pt/C catalysts,[13–16] there has been a lack of atomic level understanding regarding the material heteroatom composition–structure–function relationship with increased ORR activity, which could bolster development and systematic optimization.

Another application of conjugated carbon networks are as cathode catalysts in lithium-sulfur (Li-S) batteries, which have recently begun to attract attention for their high theoretical capacity and energy density, and relatively low costs.[37] In a Li-S battery, lithium metal is oxidized at the anode and travels through the organic either electrolyte to the sulfur cathode. At the cathode, Li^+ reacts with S_8 to form oligosulfide intermediates, which continue to react until insoluble Li_2S_2 and Li_2S products are reached in the reaction rate limiting steps. Part of the challenge with this type of cell is that the intermediates are soluble in the electrolyte, removing S from the cathode, which reduces the stability and performance of the material overtime. Additionally, S is inherently insulating, so electron transport to the reaction surface is hindered. These challenges are part of the reason that the Li-S batteries perform far below their theoretical potentials. N-containing carbon materials have only recently begun to be explored as sulfur reduction reaction (SRR) catalysts.[18,38,39] A deeper understanding of the properties and environments that may modify the reaction pathway is needed to address these challenges and develop an SRR catalyst that performs closer to the desirable theoretical LiS cell.

A key characteristic exhibited by all the conjugated material systems that I have studied is macroscopic conductivity due to their conjugated-carbon structures, enabling electron transport and utilization. Despite the broad range of applications of such materials, there has been a lack of understanding regarding composition–structure–function relationships on an atomic level, which has hindered their development and optimization. Thus, the overarching objective of my studies has been to improve understanding and viability of alternative energy conversion and storage materials. While this goal encompasses a vast field, a few specific systems are discussed in this dissertation which are united by three common themes. The first theme, being that each of the material systems are comprised of extended networks with non-stoichiometric compositions. This leads to the second theme, in that the various material systems consist of complicated heterogenous distributions of ordered and disordered structural features which we have sought to understand and to improve their viability for large scale energy conversion and storage applications. The third theme is that atomic-level structures are important to electron transport and electrochemical activity in all of the systems studied. These themes are studied and discussed for each of the types of material systems in this dissertation, which include: 1) boron clusters for solid-state redox, 2) conductive polymers in semi-transparent organic solar cells, 3) perovskites undergoing fluoride ion intercalation, and 4) mesoporous n-carbons: oxygen & sulfur reduction which is the main system discussed throughout this dissertation.

Correlating macroscopic electrochemical reduction activities with bulk and surface characterizations that provide insight about the materials composition on many length scales enables the selection and tuning of synthesis/post-synthetic processing conditions to improve the macroscopic conductivity and electrocatalytic activities. In addition to conventional

characterization techniques such as nitrogen sorption, X-ray photoelectron spectroscopy, Raman spectroscopy, ^{57}Fe Mössbauer spectroscopy, X-ray diffraction, solid-state NMR spectroscopy and DFT modeling calculations provide detailed atomic-level insights about the environments and distributions of nuclei. Specifically, solid-state nuclear magnetic resonance (NMR) spectroscopy is sensitive to atomic environments in both ordered and disordered regions of a material and can provide significantly enhanced resolution of different N-containing environments which are corroborated by DFT predictions of chemical shift values. Until now solid-state NMR spectroscopy has had limited use in the study of this class of materials due to the challenges to characterize that the materials present including paramagnetic and/or conductive properties, complicated distributions of disordered and ordered regions, and heterogeneous material compositions, many of which I have been able to use and take advantage of to study complicated conjugated electrochemical systems. This thesis shows the progress I have made towards correlating characterizations and understandings of complicated heterogenous ordered and disordered materials with electrochemical performance properties. I feel that I have also opened the door for a lot more questions to be answered in new and interesting ways. Specifically, my research allows for more strategic synthesis and optimization strategies than have been typically employed in the past. In this chapter, I introduce each thesis chapter with a brief description of their contents.

1.1.1 Additional background, challenges, and opportunities for heteroatom-containing mesoporous carbons as fuel cell and electrocatalysts

As discussed above, Li-S batteries and polymer electrolyte fuel cells are both great candidates for alternative energy conversion and storage devices. One of the main challenges hindering their more widespread application is underperformance of the cathode catalysts (in both current industrial standards and new materials) resulting in underperformance and increased costs of cell operation. Specifically, a lack of understanding of the cathode catalysts materials and their active sites means that the material cannot be efficiently and systematically optimized. Thus, development, understanding, and optimization of alternative cathode catalysts is critical. Here, I give a brief review of the development of mesoporous carbon materials, the challenges that they present in terms of their developments and application to fuel cell or battery systems, and the opportunities that that we can create to make they a more viable and desirable part of renewable and affordable alternative energy systems.

Polymer electrolyte fuel cells (PEFCs) are promising electrochemical energy conversion devices that have high theoretical thermodynamic efficiencies, high energy densities, and minimal environmental impact.[1,19,20] However, high costs associated with current cathode precious-metal (Pt) carbon catalysts hinder large-scale production.[1,3,6,21] These issues have generally been addressed by resorting to use of undesirably high Pt loadings that exacerbate their undesirably high costs. Pt-carbon catalysts also have very poor selectivity for the desired four electron reduction of oxygen to water that occurs in a fuel cell. Some groups have attempted to increase the selectivity of the polycrystalline Pt-catalyzed reactions by efficiently dispersing Pt nanoparticles, increasing lattice strain by coating metal sheets with thin Pt layers, or introducing PtX alloys (where X=Fe,Ni,Co,Cu); however, all of these techniques still

require cost prohibitive Pt (even if it is to a much lesser extent) and extensive post-synthesis processing.[26] Thus, increasing motivation to develop oxygen reduction reactions (ORR) catalysts that do not rely on precious metals (PT) that achieve comparable or greater activity, selectivity, and stability to existing materials. Porous carbon materials have shown promise as effective, stable, and non-precious-metal containing ORR electrocatlysys.[27]

Alternatively, lithium-sulfur (Li-S) batteries have begun to attract attention for their high theoretical capacity and energy density with relatively low costs.[13] Part of the challenge with this type of cell is that the intermediates are soluble in the electrolyte, removing S from the cathode, which reduces the stability and performance of the material overtime. Additionally, the S cathode is inherently insulating, so electron transport to the reaction surface is hindered. These challenges are part of the reason that the Li-S batteries perform far below their theoretical potentials. N-containing carbon materials have recently begun to be explored as sulfur reduction reaction (SRR) catalysts.[14–16]

Background provided here is in terms of ORR catalysts, as these are the systems that have driven the development of mesoporous carbon electrocatalysts. Heat treatment of almost any mixture of carbon source (e.g. peat, coconut shells), nitrogen source (e.g. ammonia, ammines, nitric acid, acetonitrile), and metal precursors will result in an ORR active carbon-based material; however, the degree of activity and stability depends on the precursor selection and synthesis.[28,29] Non-precious metal, heteroatom-containing conjugated carbon materials, including carbon nanotubes, graphene, and graphitic arrays, have been found to exhibit great ORR electrochemical activity.[30,31] Many different single- and multi-heteroatoms or dopant nuclei have been investigated and exhibit successful oxygen reduction catalysis. Specifically, Fe,N-doped porous carbon materials exhibit high oxygen reduction activity and selectivity,

making these materials promising alternatives to Pt-based precious-metal-containing catalysts.[30–35] These Fe,N-doped graphitic carbon materials, including doped carbon nanotubes,[36] graphene,[37–39] and porous carbon materials,[27] have been of particular interest due to their combined high electrical conductivities and good thermal and chemical stabilities.[40–42] High ORR activities of carbon-based heteroatom-containing materials are attributed to their high surface areas,[43] high electrical conductivities (facilitating electron transport to the reaction site),[44] and specific dopant nitrogen species (e.g., graphitic nitrogen[45,46] or pyridinic nitrogen[47–49]) that have been achieved through thoughtful selection of precursors[43,50] and optimization of synthesis conditions.[51,52] The high conductivities of doped graphene or carbon nanotubes have been, in part, attributed to the presence of a graphitizing agent, Fe, during growth, which promotes graphitic ordering.[30,53–55] These non-precious-metal,N-doped carbon materials are a desirable alternative to current catalysts; however, the synthesis of these materials are typically extensive.

Alternatively, mesoporous N- and Fe,N-containing conjugated carbon materials can be prepared by simple pyrolysis within a sacrificial template, yielding materials with uniform mesopore diameters (2-50 nm) that enable facile diffusion of reactant species to, and efficient use of, catalytic active sites.[55,56] Many conventional carbon materials, such as activated carbon (pore diameters predominantly <2 nm),[29,57] possess significantly smaller pores. Typically, synthesis of highly ORR active N- or Fe,N-doped graphitic carbon materials has required the pyrolysis of expensive nitrogen-doped graphitizable precursors, such as macrocyclic porphyrin compounds[46,47] or imidazolium ionic liquids.[41,44] However, volatilization during the pyrolysis process often results in low yields of graphitic carbon products.

Our group has developed highly-graphitic conjugated carbon frameworks with a synthesis that combines high extent of graphitization (achieved by the presence of Fe during synthesis) and inexpensive small-molecule organic precursors to exhibit high N content and high ORR catalytic activities under alkaline conditions.[55,56] Other groups have also employed various combinations of small molecules and Fe in their heteroatom-containing carbon materials. However, our N-containing and transition-metal,N-containing porous carbon materials are derived from inexpensive urea and cyclohexanehexone octahydrate. They exhibit exceptionally high N contents (up to 28 wt% N for N-containing carbon materials), large mesopore diameters, and form a eutectic melt which traps N atoms in the carbon material,[58] all highly desirable properties. Cyclohexanehexone octahydrate and urea (Ch. 3-6) are desirable precursors because these materials are already produced on an industrial scale, making scale-up of our material synthesis viable. Increased N-heteroatom content is desirable as N is the proposed ORR active sites.[56] The actual environment of the N active site environment is still up to debate in literature,[22–25] and is part of what I have investigated. In addition, the comparatively large mesopore diameters (2-50 nm)[59] are desirable as they facilitate reactant transport to interior active sites. Finally, the presence of non-precious metal (Fe) heteroatoms promote graphitization and increase conductivity.[42,56] The presence of Fe heteroatoms is linked to increased ORR activity but the role that Fe plays in ORR is also subject to debate.[24,25] The role of the Fe heteroatom in the improvement of ORR activity is another area that I have investigated using atomic level characterization techniques. Although there are many alternative ORR catalysts materials being developed,[22–25] there is a lack of atomic level understanding regarding the material N and Fe heteroatom composition–

structure–function relationships with increased ORR activity, which I believe allows for a more systematic approach to material ORR activity optimization.

My goal has been to measure and correlate atomic-level composition and structural properties of electronically active carbon materials with their desirable electrocatalytic and energy capture/storage properties. I found that the synthesis conditions, precursor compositions, and choice of templating material (e.g., salt-mixture or mesoporous-SBA-15 silica) influence the types, quantities, and distributions of Fe and N heteroatom environments, which strongly affect macroscopic oxygen reduction activities. An understanding the local electronic environments and atomic structures of these materials allow for the C, Fe, and N bonding environments which correlate with higher performance to be identified. This will enable tailoring of synthesis/post-synthesis processing conditions to increase active site concentration and thus, the optoelectronic and electrocatalytic activities. It has been challenging to measure and correlate local Fe or N heteroatom environments and their distributions in graphitic carbon materials with macroscopic electrocatalytic properties. This has been due, in part, to their paramagnetic and/or conductive characters, complicated distributions of disordered and ordered regions, and heterogeneous material compositions. In this dissertation, I report detailed new insights on the local atomic environments and distributions of N and Fe heteroatoms in high N content (~28 wt%) materials prepared with various templates that influence surface chemistry and thus the electrocatalytic properties.

Atomic-level insights are provided by solid-state ^{13}C and ^{15}N nuclear magnetic resonance (NMR) spectroscopy, and supported by nitrogen sorption, X-ray photoelectron spectroscopy, Raman spectroscopy, ^{57}Fe Mössbauer spectroscopy, X-ray diffraction, and electrocatalytic reaction analyses. Notably, low-temperature solid-state NMR measurements of materials

synthesized with ^{13}C,^{15}N-enriched precursors yield increased NMR signal sensitivity that enables powerful 2D $^{13}C\{^{15}N\}$ NMR correlation methods. The 2D $^{13}C\{^{15}N\}$ NMR spectra resolve and correlate signals from ^{15}N heteroatom sites and directly bonded ^{13}C atoms within the mesoporous carbon materials, and thus chemical shift assignments of the various atomic environments can be established in conjunction with DFT modeling. Furthermore, H atoms are present principally in pyrrolic moieties or as adsorbed water, thus surface ^{15}N and pyrrolic species can be selectively detected by 1D $^{15}N\{^{1}H\}$ cross-polarization (CP)-MAS NMR analyses of dry and water-adsorbed N-carbons. The presence of paramagnetic Fe atoms in the N-carbons presents additional characterization challenges, as Fe atoms enhance the spin-lattice relaxation rates of nearby atoms to the extent that they relax too quickly to be detected by 2D NMR. However, relaxation resolved 1D ^{15}N and ^{13}C NMR analyses can be used to understand the interaction of Fe with the various N and C environments in the carbon materials. Solid-state NMR results and analyses establish the types, atomic environments, and distributions of ^{15}N heteroatoms in the graphitic carbon materials, which, until now, have been infeasible to distinguish by scattering or other spectroscopic techniques. These analyses identify specific ^{15}N and ^{57}Fe heteroatom environments that correlate with increased reduction activity, providing useful new insights for the design of highly effective and stable electrocatalysts for applications in energy storage and conversion.

1.2 Dissertation Outline

This dissertation is divided into the following chapters, primarily focused on my main project understanding N- and Fe,N-carbon materials and their electrochemical properties (Ch 2-6). Additional chapters discuss the interesting and diverse side projects that I had to opportunity to contribute to (Ch 7-9). Due to the diversity of projects that I was able to be a part of, each chapter has been written to stand independently of the other chapters, and therefore, each possesses its own abstract, introduction, conclusions, my suggestions for future directions, and reference sections to provide proper background for the results it discusses.

Chapter 2: Highly Graphitic Mesoporous Fe,N-Doped Carbon Materials for Oxygen Reduction Electrochemical Catalysts. Highly graphitic transition-metal- and N-doped mesoporous carbon materials were synthesized from a mixture of industrial precursors (melamine and formaldehyde), and transition-metal salts pyrolyzed within the pores of a sacrificial mesostructured silica template. Synthesis conditions were tuned to enhance the extent of graphitization resulting in materials with high electrical conductivities and promising oxygen reduction reaction activities. Previously-developed surface modification techniques are applied to the materials, resulting in ORR activities that exceed those of standard Pt supported on activated carbon (Pt/C) catalysts, as measured under alkaline conditions.

My contribution to the work featured in this chapter was primarily in the electrochemical testing, general materials characterization (nitrogen sorption and XPS), and editing/writing.

The bulk of the work on this paper was done by my predecessors that are first and second author on the paper.

Chapter 3: Atomic-scale understanding of the oxygen and sulfur reduction activities of mesoporous N-carbon electrocatalysts. This chapter correlates the electrocatalytic oxygen and sulfur reduction activities of N-carbon materials (synthesized with cyclohexanehexone and urea) with differences in compositions and structures. Differences in mesopore templating agents (SBA-15 silica and a mixture of $NaCl/ZnCl_2$ salts) alter the compositions and structures achieved in the final materials. Solid-state 2D ^{15}N-^{13}C and 1D $^{15}N\{^{1}H\}$ NMR spectroscopy, in combination with X-ray scattering, Raman spectroscopy, and DFT modeling, establish the importance of isolated edge pyridinic moieties to the catalysis of both oxygen and sulfur reduction activities.

I am first author on this paper and am responsible for most of the synthesis, characterization, and electrochemical performance testing, with the exception of DFT calculations by Ziyang Wei and S-reduction testing by Rongli Liu.

Chapter 4: Atomic environments in N-containing graphitic carbon probed by first-principles calculations and solid-state nuclear magnetic resonance. This chapter is the modeling focused manuscript that parallels the experimental and performance focused manuscript for N-carbons materials discussed in chapter 3. Two-dimensional (2D) solid-state NMR experiments and chemical shift calculations for ^{15}N, ^{13}C, and ^{1}H nuclei from density functional theory (DFT) are combined to understand and assign the local atomic-scale environments of N-carbon moieties within graphitic carbon sheets. Influences from different geometries and neighboring atoms are modeled and changes in chemical shifts calculated, justifying the spectral broadening in the solid-state NMR spectra. The correlations between

calculated and experimental chemical shift values (and corresponding signal broadening), improve the understanding of the nature of heteroatom sites in N−carbon materials, and contribute to the rational design of such materials with desired electronic properties for improved electrochemical performance.

My collaborator from UCLA is the lead author on this paper as he is responsible for the DFT calculations. I worked very closely with him to discuss the hypothesized geometries and structures, group the various N-moieties, and provide experimental data for model/experimental comparisons.

Chapter 5: Correlating macroscopic compositions and structures with oxygen and sulfur reduction activities of mesoporous-Fe,N-carbon electrocatalysts. While the inclusion of Fe atoms is known to improve the reduction activities of N-carbon-based electrocatalysts, the role of the Fe atoms is debated,[24,25] as it had been challenging to resolve without advanced atomic-level characterization. These results establish that the inclusion of Fe both increases the extent of graphitization and, when coordinated with pyridinic N environments, correlates with increased reduction activity. EELS STEM imaging taken by our collaborators in Sweden establish that N, O, and Fe atoms are heterogeneously dispersed throughout the graphitic carbon matrix, while Fluorescence Detected EXAFS establishes the coordination of Fe with N, O, C, and proximate Fe atoms. ^{57}Fe Mössbauer spectroscopy directly probes Fe atoms and their interactions with between 1 and 4 proximate N species in various configurations. Finally, relaxation-resolved ^{15}N NMR spectra and resolve ^{15}N signals from ^{15}N species proximate to paramagnetic Fe heteroatoms and provide approximate ^{15}N-Fe distances, with assignments corroborated by DFT modeling. These measurements both directly and indirectly probe the local environments and confirm mutual proximities of Fe and

N heteroatoms in mesoporous-Fe,N-carbon electrocatalysts. Correlating these insights with increasing oxygen and sulfur reduction activity elucidates ideal heteroatom environments for reduction, aiding in the design of improved electrocatalysts, and demonstrates that Fe,N-carbons do not require precious metals and outperform the current industrial standard Pt/C catalysts.

I am first author on this paper and am responsible for most of the synthesis, characterization, and electrochemical performance testing. Exceptions include DFT calculations by Ziyang Wei, S-reduction testing by Rongli Liu, EXAFS done by Riley Zhang, and STEM by Tom Thersleff, and Mossbauer by Camden Hunt.

Chapter 6: Understanding and correlating complicated electronic and paramagnetic properties of conductive N- and Fe, N-carbons: While conductive Fe,N- and N-carbons are widely researched and utilized materials with many applications in energy and other fields, it is challenging to measure and correlate local Fe or N heteroatom environments and their distributions in graphitic carbons with macroscopic electrocatalytic properties. This is due in large part to the heterogeneous material compositions, high conductivity of graphitic carbons, and presence of paramagnetic centers, which can non-uniformly displace and broaden NMR signals, decrease nuclear spin-lattice relaxation times, and lead to substantial sample heating under MAS. The extent these effects have on NMR spectra are not well understood or quantified. In this chapter I review the extensive number of important factors to consider when using nuclear magnetic resonance and electron paramagnetic resonance (NMR and EPR) to understand the complicated nuclear and electronic interactions occurring in the high N-content carbon materials. I give examples from literature, I show the insights that I have contributed,

and give future work suggestions, as this is a big field with many new and complicated challenges to tackle.

Chapter 7: Synthesis and structural properties of a 2D Zn(II) dodecahydroxycloso-dodecaborate coordination polymer. This paper describes the synthesis and characterization of a 2D coordination polymer composed of a dianionicperhydroxylated boron cluster ($B_{12}(OH)_{12}^{2-}$), coordinated to Zn(II). This is the first example of a transition metal-coordinated to a $B_{12}(OH)_{12}^{2-}$-compound. The material was studied and characterized prior to and after thermal activation via XRD, FTIR, SEM, TGA, and solid-state NMR, revealing a 2D coordination polymer composed of sheets of Zn(II) ions intercalated between planes of boron clusters.

I am co-first author on this manuscript. My contribution to the work featured in this chapter is primarily a combination of 1D and 2D solid-state NMR analyses of ^{11}B and ^{1}H nuclei focused on understanding the inter and intro molecular interactions between the zinc, boron clusters, and water in the material.

Chapter 8: Electron donor-acceptor small molecule thin films as active layers in solar cells. This study summarizes several aspects that are expected to be crucial in the design of bulk heterojunction morphologies for semi-transparent solar cell applications. Specifically, we study PM2:ITIC-Th (a non-fullerene acceptor) as a model system for semi-transparent solar cells. 2D ssNMR spectroscopy analyses rationalize the different inter- and intramolecular interactions between a variety of related donor and acceptor polymer blends, consistent with the differences in their morphological features and the different optoelectronic properties. The films are among the highest-performing semitransparent OPVs reported to date.

My contribution to the work featured in this chapter is the solid-state NMR experiments and analyses.

Chapter 9: Electrochemical Oxidative Fluorination of an Oxide Perovskite. We report on the electrochemical fluorination of the A-site vacant perovskite ReO_3 using high-temperature solid-state cells as well as room-temperature liquid electrolytes. *Operando* X-ray diffraction, neutron total scattering measurements, X-ray spectroscopy, and solid-state ^{19}F NMR with magic-angle spinning were used to explore the mechanism by which fluoride ions react with the ReO_3 electrode during oxidation. This work demonstrates a practical electrolyte and cell design that can be used to evaluate the mobility of small anions like fluoride that is robust at room temperature and opens new opportunities for exploring the electrochemical fluorination of many new materials.

My contribution to the work featured in this chapter is the solid-state NMR experiments and analyses.

Chapter 10: Conclusions. This is a short section reviewing overall conclusions. More specific conclusions and future direction ideas are given in each of the chapters due to the diversity of topics covered in this thesis.

Appendix A: Understanding the eutectic melt and pyrolysis steps of the N-carbon synthesis, and the important role of the Zn^{2+} ion on the N moiety formation

To understand the qualities of the synthesized materials which enable favorable electrochemical properties, I am interested in the atomic level reactions taking place during the low temperature eutectic melt step. The goal is to identify the reactions occurring and intermediate products being formed during the eutectic melt step of the synthesis. Furthermore, the choice of templating material significantly impacts bulk heteroatom

compositions presence. The presence of the Zn ion in the salt-template seems to be key to synthesizing a material with a more favorable N moiety distribution, in this section I propose an investigation into understanding how and why it strongly affects the material produced and the electrochemical performance.

1.3 References

1. Gewirth, A. A. & Thorum, M. S. Electroreduction of dioxygen for fuel-cell applications: Materials and challenges. *Inorg. Chem.* **49**, 3557–3566 (2010).
2. Wang, X. *et al.* Nitrogen and oxygen dual-doped carbon nanohorn for electrochemical capacitors. *Carbon N. Y.* **118**, 511–516 (2017).
3. Kim, D., Zussblatt, N. P., Chung, H. T., Zelenay, P. & Chmelka, B. F. Highly-graphitic Fe,N-containing mesoporous carbon materials for oxygen reduction electrochemical catalysts. *ACS Appl. Mater. Interfaces* To Be Submitted (2017).
4. Santoro, C., Arbizzani, C., Erable, B. & Ieropoulos, I. Microbial fuel cells: From fundamentals to applications. A review. *J. Power Sources* **356**, 225–244 (2017).
5. Sebastian, D. *et al.* Insights on the extraordinary tolerance to alcohols of Fe-N-C cathode catalysts in highly performing direct alcohol fuel cells. *Nano Energy* **34**, 195–204 (2017).
6. Jahnke, J. P., Benyamin, M. S., Sumner, J. J. & Mackie, D. M. Using Reverse Osmosis Membranes to Couple Direct Ethanol Fuel Cells with Ongoing Fermentations. *Ind. Eng. Chem. Res.* **55**, 12091–12098 (2016).
7. Yang, C. J. An impending platinum crisis and its implications for the future of the automobile. *Energy Policy* **37**, 1805–1808 (2009).
8. Benyamin, M. S., Jahnke, J. P. & Mackie, D. M. Vapor-fed bio-hybrid fuel cell. *Biotechnol. Biofuels* **10**, 68 (2017).
9. Zhang, L. L. & Zhao, X. S. Carbon-based materials as supercapacitor electrodes. *Chem. Soc. Rev.* **38**, 2520–2531 (2009).

10. Ma, C. *et al.* High-surface-area and high-nitrogen-content carbon microspheres prepared by a pre-oxidation and mild KOH activation for superior supercapacitor. *Carbon N. Y.* **118**, 699–708 (2017).

11. Sellers, M. C. K., Zussblatt, N. P. & Marsh, C. P. Potassium perruthenate-treated carbon nanotube sheets for flexible supercapacitors. *Electrochem. commun.* **18**, 58–61 (2012).

12. Li, Y. *et al.* A protic salt-derived porous carbon for efficient capacitive deionization: Balance between porous structure and chemical composition. *Carbon N. Y.* **116**, 21–32 (2017).

13. Garsany, Y., Baturina, O. A. & Swider-Lyons, K. E. Impact of Sulfur Dioxide on the Oxygen Reduction Reaction at Pt/Vulcan Carbon Electrocatalysts. *J. Electrochem. Soc.* **154**, B670 (2007).

14. Peng, L. *et al.* A fundamental look at electrocatalytic sulfur reduction reaction. *Nat. Catal.* **3**, 762–770 (2020).

15. Li, L. *et al.* Stabilizing sulfur cathodes using nitrogen-doped graphene as a chemical immobilizer for Li-S batteries. *Carbon N. Y.* **108**, 120–126 (2016).

16. Bonaccorso, F. *et al.* Graphene, related two-dimensional crystals, and hybrid systems for energy conversion and storage. *Science (80-.).* **347**, (2015).

17. Ritchie, H. & Roser, M. Energy. *Our World in Data* (2020). Available at: https://ourworldindata.org/energy.

18. Atkins, R. C. & Carey, F. A. *Organic Chemistry*. (McGraw-Hill Higher Education, 2002).

19. Jacobson, M. Z., Colella, W. G. & Golden, D. M. Cleaning the Air and Improving

Health with Hydrogen Fuel-Cell Vehicles. *Science* **308**, 1901–1905 (2005).

20. Schultz, M. G., Diehl, T., Brasseur, G. P. & Zittel, W. Air pollution and climate-forcing impacts of a global hydrogen economy. *Science* **302**, 624–627 (2003).

21. Wilson, A., Kleen, G. & Papageorgopoulos, D. Fuel Cell System Cost - 2017. *DOE Hydrog. Fuel Cells Progr. Rec.* 1–12 (2017).

22. Tran, T.-N., Song, M. Y., Singh, K. P., Yang, D.-S. & Yu, J.-S. Iron–polypyrrole electrocatalyst with remarkable activity and stability for ORR in both alkaline and acidic conditions: a comprehensive assessment of catalyst preparation sequence. *J. Mater. Chem. A* **4**, 8645–8657 (2016).

23. Kramm, U. I., Lefèvre, M., Larouche, N., Schmeisser, D. & Dodelet, J. P. Correlations between mass activity and physicochemical properties of Fe/N/C catalysts for the ORR in PEM fuel cell via 57Fe Mössbauer spectroscopy and other techniques. *J. Am. Chem. Soc.* **136**, 978–985 (2014).

24. Zitolo, A. *et al.* Identification of catalytic sites for oxygen reduction in iron- and nitrogen-doped graphene materials. *Nat. Mater.* **14**, 937–942 (2015).

25. Lefèvre, M., Proietti, E., Jaouen, F. & Dodelet, J.-P. Iron-Based Catalysts with Improved Oxygen Reduction Activity in Polymer Electrolyte Fuel Cells. *Science (80-.).* **324**, 71–74 (2009).

26. Coleman, E. J., Chowdhury, M. H. & Co, A. C. Insights Into the Oxygen Reduction Reaction Activity of Pt/C and PtCu/C Catalysts. *ACS Catal.* 1245–1253 (2015). doi:10.1021/cs501762g

27. Wu, G. *et al.* Synthesis–structure–performance correlation for polyaniline–Me–C non-precious metal cathode catalysts for oxygen reduction in fuel cells. *J. Mater. Chem.* **21**,

11392 (2011).

28. Laine, J. & Yunes, S. Effects of the Preparation Method on the Pore Size Distribution of Activated Carbon from Coconut Shell. *Carbon N. Y.* **30**, 601–604 (1992).

29. Gong, K., Du, F., Xia, Z., Durstock, M. & Dai, L. Nitrogen-Doped Carbon Nanotube Arrays with High Electrocatalytic Activity for Oxygen Reduction. *Science (80-.).* **323**, 760–765 (2009).

30. Liu, J. *et al.* High-Performance Oxygen Reduction Electrocatalysts based on Cheap Carbon Black, Nitrogen, and Trace Iron. *Adv. Mater.* **25**, 6879–6883 (2013).

31. Wu, G., More, K. L., Johnston, C. M. & Zelenay, P. High-performance electrocatalysts for oxygen reduction derived from polyaniline, iron, and cobalt. *Science* **332**, 443–447 (2011).

32. Li, Q., Cao, R., Cho, J. & Wu, G. Nanocarbon electrocatalysts for oxygen reduction in alkaline media for advanced energy conversion and storage. *Adv. Energy Mater.* **4**, 1301415 (2014).

33. Tylus, U. *et al.* Elucidating Oxygen Reduction Active Sites in Pyrolyzed Metal − Nitrogen Coordinated Non-Precious-Metal Electrocatalyst Systems. *J. Phys. Chem. C* **118**, 8999−9008 (2014).

34. Zhang, M. & Dai, L. Carbon nanomaterials as metal-free catalysts in next generation fuel cells. *Nano Energy* **1**, 514–517 (2012).

35. Chung, H. T., Won, J. H. & Zelenay, P. Active and stable carbon nanotube/nanoparticle composite electrocatalyst for oxygen reduction. *Nat. Commun.* **4**, 1922 (2013).

36. Lin, Z. *et al.* Facile preparation of nitrogen-doped graphene as a metal-free catalyst for oxygen reduction reaction. *Phys. Chem. Chem. Phys.* **14**, 3381 (2012).

37. Wu, Z.-S. *et al.* 3D Nitrogen-Doped Graphene Aerogel-Supported Fe3O4 Nanoparticles as Efficient Electrocatalysts for the Oxygen Reduction Reaction. *J. Am. Chem. Soc.* **134**, 9082–9085 (2012).

38. Chung, H. T. *et al.* Direct atomic-level insight into the active sites of a high-performance PGM-free ORR catalyst. *Science (80-.).* **357**, 479–484 (2017).

39. Lee, J. S., Park, G. S., Kim, S. T., Liu, M. & Cho, J. A highly efficient electrocatalyst for the oxygen reduction reaction: N-doped ketjenblack incorporated into Fe/Fe3C-functionalized melamine foam. *Angew. Chemie - Int. Ed.* **52**, 1026–1030 (2013).

40. Nishihara, H. & Kyotani, T. Templated nanocarbons for energy storage. *Adv. Mater.* **24**, 4473–4498 (2012).

41. Paraknowitsch, B. J. P., Zhang, J., Su, D., Thomas, A. & Antonietti, M. Ionic liquids as precursors for nitrogen-doped graphitic carbon. *Adv. Mater.* **22**, 87–92 (2010).

42. Lee, K. T., Ji, X., Rault, M. & Nazar, L. F. Simple synthesis of graphitic ordered mesoporous carbon materials by a solid-state method using metal phthalocyanines. *Angew. Chemie - Int. Ed.* **48**, 5661–5665 (2009).

43. Yang, W., Fellinger, T. P. & Antonietti, M. Efficient metal-free oxygen reduction in alkaline medium on high-surface-area mesoporous nitrogen-doped carbons made from ionic liquids and nucleobases. *J. Am. Chem. Soc.* **133**, 206–209 (2011).

44. Zhang, S., Miran, M. S., Ikoma, A., Dokko, K. & Watanabe, M. Protic Ionic Liquids and Salts as Versatile Carbon Precursors. *J. Am. Chem. Soc.* **136**, 1690–1693 (2014).

45. Lai, L. *et al.* Exploration of the active center structure of nitrogen-doped graphene-based catalysts for oxygen reduction reaction. *Energy Environ. Sci.* **5**, 7936–7942 (2012).

46. Liu, R., Wu, D., Feng, X. & Müllen, K. Nitrogen-doped ordered mesoporous graphitic arrays with high electrocatalytic activity for oxygen reduction. *Angew. Chemie - Int. Ed.* **49**, 2565–2569 (2010).

47. Kundu, S. *et al.* Electrocatalytic Activity and Stability of Nitrogen-Containing Carbon Nanotubes in the Oxygen Reduction Reaction. *J. Phys. Chem. C* **113**, 14302–14310 (2009).

48. Wu, J. *et al.* Nitrogen-Doped Graphene with Pyridinic Dominance as a Highly Active and Stable Electrocatalyst for Oxygen Reduction. *ACS Appl. Mater. Interfaces* **7**, 14763–14769 (2015).

49. Guo, D. *et al.* Active sites of nitrogen-doped carbon materials for oxygen reduction reaction clarified using model catalysts. *Science* **351**, 361–365 (2016).

50. Wu, G. & Zelenay, P. Nanostructured Nonprecious Metal Catalysts for Oxygen Reduction Reaction. *Acc. Chem. Res.* **46**, 1878–1889 (2013).

51. Dorjgotov, A., Ok, J., Jeon, Y., Yoon, S. H. & Shul, Y. G. Activity and active sites of nitrogen-doped carbon nanotubes for oxygen reduction reaction. *J. Appl. Electrochem.* **43**, 387–397 (2013).

52. Gumeci, C. *et al.* Effect of pyrolysis pressure on activity of Fe–N–C catalysts for oxygen reduction. *J. Mater. Chem. A* **3**, 21494–21500 (2015).

53. Tang, Y., Allen, B. L., Kauffman, D. R. & Star, A. Electrocatalytic activity of nitrogen-doped carbon nanotube cups. *J. Am. Chem. Soc.* **131**, 13200–13201 (2009).

54. Sheng, Z. *et al.* Catalyst-Free Synthesis of Nitrogen-Doped Graphene via Thermal Annealing Graphite Oxide with Melamine and Its Excellent Electrocatalysis. *ACS Nano* **5**, 4350–4358 (2011).

55. Kim, D. *et al.* Highly Graphitic Mesoporous Fe,N-Doped Carbon Materials for Oxygen Reduction Electrochemical Catalysts. *ACS Appl. Mater. Interfaces* **10**, 25337 (2018).

56. Fechler, N. *et al.* Eutectic Syntheses of Graphitic Carbon with High Pyrazinic Nitrogen Content. *Adv. Mater.* **28**, 1287 (2016).

57. Joo, S. H. *et al.* Ordered nanoporous arrays of carbon supporting high dispersions of platinum nanoparticles. *Nature* **414**, 470–470 (2001).

58. Rouquerolt, J. *et al.* Recommendations for the Characterization of Porous Solids. *Pure Appl. Chem.* **66**, 1739–1758 (1994).

2. Highly Graphitic Mesoporous Fe,N-Doped Carbon Materials for Oxygen Reduction Electrochemical Catalysts

This chapter is adapted from a published paper. Highly graphitic transition-metal- and N-doped mesoporous carbon materials were synthesized from a mixture of industrial precursors (melamine and formaldehyde), and transition-metal salts pyrolyzed within the pores of a sacrificial mesostructured silica template. Synthesis conditions were tuned to enhance the extent of graphitization resulting in materials with high electrical conductivities and promising oxygen reduction reaction activities. Previously-developed surface modification techniques are applied to the materials, resulting in ORR activities that exceed those of standard Pt supported on activated carbon (Pt/C) catalysts, as measured under alkaline conditions.

My contribution to the work featured in this chapter was primarily in the electrochemical testing, general materials characterization (nitrogen sorption and XPS), and editing/writing. The bulk of the work on this paper was done by my predecessors that are first and second author on the paper.

Paper: *ACS Applied Materials & Interfaces* **2018** *10* (30), 25337-25349

Authors: Donghun Kim, Niels P. Zussblatt, Hoon T. Chung, Shona M. Becwar, Piotr Zelenay, and Bradley F. Chmelka

DOI: 10.1021/acsami.8b06009

2.1 Abstract

The synthesis, characterization and electrocatalytic properties of mesoporous carbon materials doped with nitrogen atoms and iron are reported and compared for the catalyzed reduction of oxygen gas at fuel cell cathodes. Mixtures of common and inexpensive organic precursors, melamine and formaldehyde were pyrolyzed in the presence of transition metal salts (*e.g.*, nitrates) within a mesoporous silica template to yield mesoporous carbon materials with greater extents of graphitization than others prepared from small molecule precursors. In particular, Fe,N-doped carbon materials possessed high surface areas (~800 m^2/g) and high electrical conductivities (~19 S/cm), which make them attractive for electrocatalyst applications. The surface compositions of the mesoporous Fe,N-doped carbon materials were post-synthetically modified by acid washing and followed by high-temperature thermal treatments, that were shown by X-ray photoelectron spectroscopy to favor the formation of graphitic and pyridinic nitrogen moieties. Such surface-modified materials exhibited high electrocatalytic oxygen-reduction activities under alkaline conditions as established by their high onset and half-wave potentials [1.04 V and 0.87 V, respectively *vs.* reversible hydrogen electrode (RHE)] and low Tafel slope (53 mV/decade). These values are superior to many similar transition-metal- and N-doped carbon materials and compare favorably with commercially available precious-metal catalysts, *e.g.*, 20 wt% Pt supported on activated carbon. The analyses indicate that inexpensive mesoporous Fe,N-doped carbon materials are promising alternatives to precious metal-containing catalysts for electrochemical reduction of oxygen in polymer electrolyte fuel cells.

2.2 Introduction

Polymer electrolyte fuel cells (PEFCs) are promising energy conversion devices that have received significant interest in recent years, due to their high conversion efficiencies, high energy densities, and low environmental impacts.[1,2] However, large-scale applications of PEFCs have been hindered by their high costs, predominantly because of the expensive precious metal platinum- and/or iridium-based catalysts that are used to promote the reduction of oxygen at the cathodes.[3,4] At near-ambient temperatures, the oxygen reduction reaction (ORR) tends to exhibit sluggish kinetics,[3] which have generally been addressed by using undesirably high loadings of Pt-based catalysts on the cathode that exacerbate the cost challenge. In addition, the effectiveness of Pt-based ORR catalysts in direct methanol or ethanol fuel cells (DMFCs or DEFCs) often suffers from fuel crossover and alcohol oxidation at the cathode, which reduces the operating voltage and overall efficiency of the fuel cell.[5,6] Thus, there is significant motivation to develop ORR catalysts that do not rely on precious metals to achieve comparable or greater activity, selectivity, or stability than existing materials.

By comparison, iron- and nitrogen-doped porous carbon materials exhibit high oxygen reduction activity and selectivity, making these materials promising alternatives to Pt-based precious metal catalysts.[7–12] Judicious selection of precursors[13–17] and optimization of synthesis conditions[18,19] have yielded high ORR activities for carbon-based materials that have been attributed to their high surface areas,[13] high electrical conductivities,[20] or specific nitrogen species (*e.g.*, graphitic nitrogen[21,22] or pyridinic nitrogen[23,24]). In particular, high-surface-area graphitic carbon materials containing Fe and N, such as Fe,N-doped carbon nanotubes,[25] graphene,[26–28] or porous carbon materials,[29] have received significant attention

because of their combined high electrical conductivities and good thermal and chemical stabilities.[30–32] High-purity nitrogen-doped graphene or carbon nanotubes, grown in the presence of iron, yield electrocatalysts with high ORR activities,[11,33,34] however their syntheses are relatively complicated. By comparison, mesoporous Fe,N-doped carbons with graphitic properties can be prepared by simple pyrolysis within a sacrificial template, yielding materials with uniform mesopore diameters (2-50 nm) that enable facile diffusion of reactant species to catalytic active sites. In contrast to many conventional carbon materials, such as activated carbon (pore diameters predominantly < 2 nm),[35] these larger mesopores facilitate more effective use of available pore surface areas.[36] Previous reports of N- or Fe,N-doped graphitic carbon materials have often relied on the pyrolysis of expensive nitrogen-doped graphitizable precursors, such as macrocyclic porphyrin compounds[22,32] or imidazolium ionic liquids.[31,37] Often, however, volatilization during the pyrolysis process results in low yields of graphitic carbon products.

Here, we report syntheses of transition-metal- and nitrogen-doped mesoporous carbon materials from inexpensive small-molecule organic precursors with improved yields and their characterization to correlate their bulk and surface compositions and structures with their macroscopic electrochemical properties. Using a combination of complementary wide-angle X-ray scattering and Raman spectroscopy analyses, we show that the relative extent of graphitic ordering, which is associated with high electrical conductivity, and thermal and chemical stability, depends strongly on the type and quantity of transition metal species present during pyrolysis. Surface compositions, including nitrogen, oxygen, and transition metal species, as well as their local bonding environments, are shown to be adjustable to improve the electrocatalytic activities of the product materials, specifically for the

technologically important oxygen reduction reaction. Following optimization of bulk and surface compositions, mesoporous Fe,N-containing carbon materials are demonstrated to possess highly graphitic carbon frameworks and exhibit a combination of relatively high surface N contents, high surface areas, high electrical conductivities, and high ORR catalytic activities and selectivities under alkaline conditions that are comparable to commercial platinum-supported-on-activated-carbon electrocatalysts.

2.3 Materials and Methods

2.3.1 Syntheses of mesoporous transition-metal- and N-doped carbon materials

Materials were prepared by pyrolyzing mixtures of an inexpensive high-N-content precursor (melamine), a cross-linking agent (formaldehyde), and transition metal (Fe, Ni, Co, or Mn) nitrate salts within a mesoporous silica (SBA-15) template, as shown schematically in Figure 2.1. Mesoporous silica (SBA-15) materials were synthesized by following previously reported protocols.[38] Briefly, 8 g of amphiphilic poly(ethyleneoxide)$_{20}$-poly(propyleneoxide)$_{70}$-poly(ethyleneoxide)$_{20}$ triblock copolymer (Pluronic^{TM} P123, Sigma-Aldrich) were dissolved in 60 mL of de-ionized water and then mixed with 240 mL of 2 M HCl (Fischer Scientific) solution and 17 g of tetraethoxysilane (TEOS, Sigma-Aldrich). After vigorously stirring for 10 min at room temperature to allow the TEOS to hydrolyze, the solution temperature was raised to 40 °C and stirred for an additional 20 h, during which time the hydrolyzed silica precursor species polymerized into a continuous network with

mesostructural order directed by the self-assembling P123 triblock copolymer species. Then, stirring was stopped and the solution temperature was raised to 90 °C for 2 days to promote further cross-linking that strengthened the silica framework. After cooling, mesostructured silica powders were recovered by vacuum-filtration and calcined in air at 550 °C for 12 h to remove the structure-directing P123 triblock copolymer species, yielding mesoporous silica powder (Figure 2.1a).

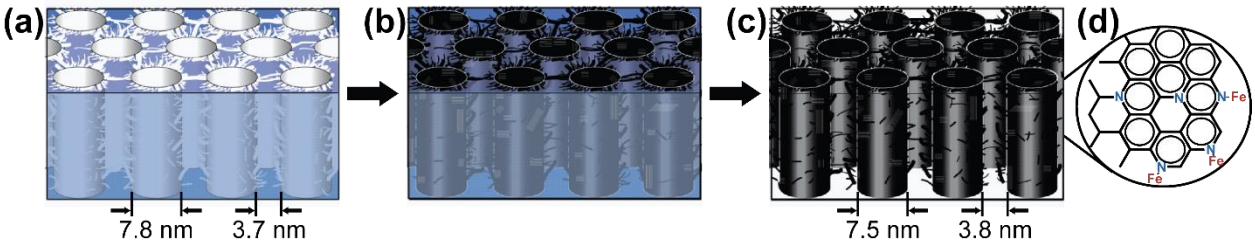

Figure 2.1. Schematic diagram of the different stages during syntheses of the mesoporous transition-metal and nitrogen-doped carbon materials with highly graphitic properties: (a) initial mesoporous silica template (blue) after calcination, (b) silica-carbon composite after precursor-infiltration and subsequent pyrolysis, and (c) mesoporous carbon (black) after removal of the silica framework. (d) A schematic diagram of different N, and Fe,N moieties within graphitic carbon.

Anhydrous $FeCl_3$ was subsequently grafted onto the pore surfaces of the mesoporous silica to promote the polymerization and graphitization[39] of melamine-formaldehyde resins. Typically, 0.36 g of anhydrous $FeCl_3$ was dissolved in 200 mL of anhydrous ethanol along with 2 g of mesoporous silica powder and stirred for 12 h. After vacuum filtering, the resulting yellow powders were dried at 90 °C for 6 h. For syntheses of mesoporous Ni-, Co-, or Mn-

doped carbon materials, equimolar anhydrous $AlCl_3$ was used instead of $FeCl_3$, to eliminate potential contributions of Fe to the ORR electrochemical activity of the non-Fe-containing materials. The roles of $AlCl_3$ and $FeCl_3$ as polymerization and graphitization agents in syntheses of mesoporous Fe,N-doped carbons were compared and shown to exhibit no significant differences in their respective ORR activities, Supporting Information, Figure S2.1.

Mesoporous Transition-metal- and nitrogen-doped carbon materials were synthesized following the general templating method reported by Ryoo, *et al.*,[40] but modified to use a melamine-formaldehyde resin. An alkaline melamine-formaldehyde solution was prepared by mixing 2.05 g of melamine into 3 mL of 0.5 M NaOH, which were subsequently mixed with 2.6 g of aqueous formaldehyde solution (37 wt% formaldehyde, Sigma-Aldrich). Immediately after mixing, this solution was stirred at 75 °C for 30 min and then cooled and neutralized with 1 M HCl aqueous solution, after which transition metal (Fe, Ni, Co, or Mn) nitrate salts at various transition metal/melamine molar ratios between 0 and 0.2 were added. Each resulting solution was combined with the $FeCl_3$- or $AlCl_3$-grafted SBA-15 silica and the mixture sonicated for 30 min within a bath sonicator. After sonication, the excess solution was removed by vacuum filtering and the recovered materials dried overnight under ambient conditions, followed by heat treatment at 120 °C for 12 h. The materials were further heat-treated at 200 °C and 350 °C for 6 h at each temperature under a N_2 atmosphere to increase the degrees of cross-linking of the melamine-formaldehyde resins to reduce volatilization of the carbon and nitrogen precursor species during subsequent pyrolysis. The mesostructured silica-resin materials were then pyrolyzed at 900 °C for 6 h under an N_2 atmosphere, yielding non-porous mesostructured silica-carbon composites, as shown schematically in Figure 2.1b.

A pyrolysis temperature of 900 °C provides a reasonable trade-off between increased graphitization versus decreased heteroatom content and/or decreased porosity that tend to occur at higher pyrolysis temperatures, which is consistent with the optimal pyrolysis temperature identified for a melamine-based Fe,N-doped carbon catalyst.[47]

The silica frameworks were subsequently dissolved in 2 M NaOH ethanol/water solution (1:1 volume ratio) with reflux for 12 h (three times). The resulting mesoporous carbon replica materials (Figure 2.1c) were acid-treated in 0.5 M H_2SO_4 solution with reflux for 12 h to remove pore-filling carbon residues and excess surface metals, followed by additional pyrolysis at 900 °C for 1 h under N_2 to remove surface oxygen species and thereby enhance oxygen reduction electrocatalytic activities. The resulting product materials were composed of graphitic carbon domains, with transition metal (*e.g.*, Fe) and N moieties present, as shown in the schematic diagram in Figure 2.1d. For comparison, conventional mesoporous carbon materials were prepared by using an identical method, except with phenol as the precursor instead of melamine.

2.3.2 Materials characterization

Thermogravimetric analyses (TGA) of the melamine-formaldehyde materials were conducted by using a METTLER TGA/sDTA851e ThermoGravimetric Analyzer under N_2 flow with a ramp rate of 10 °C/min. Residual iron contents of the mesoporous Fe,N-containing carbon materials were estimated from residual mass following high-temperature TGA measurements performed under the flow of dry air. Nitrogen sorption isotherms were acquired at 77 K with MicroMeritics Tristar 3000, and samples were dried overnight at 120 °C under flowing N_2 before the measurements. The surface areas were calculated by using the

Brunauer-Emmett-Teller (BET) method,[41] while pore volumes and size distributions were calculated by using the Barrett-Joyner-Halenda (BJH) method.[42]

X-ray diffraction (XRD) patterns were recorded with Rigaku Smartlab high-resolution diffractometer with Cu *K*α radiation operating at 40 kV and 44 mA. Small-angle XRD patterns were acquired over a 2θ range of 0.5 to 3.0° with a step size of 0.01°, and wide-angle XRD patterns were acquired over a 2θ range of 10 to 50° in increments of 0.02°. Raman spectra were obtained by using a home-built Raman spectrometer with blue wavelength excitation at 488 nm. Bulk electrical conductivities were measured by using a Solartron SI 1260 impedance analyzer. X-ray photoelectron spectroscopy (XPS) measurements were conducted on a Kratos Axis Ultra X-ray Photoelectron Spectroscopy system for approximate surface elemental analyses. Survey XPS scans were performed over the range of 800 to 100 eV with a pass energy of 160 eV in increments of 0.5 eV, while high-resolution XPS scans were conducted for C 1*s* (296-276 eV) and N 1*s* (410-390 eV) with a pass energy of 40 eV and a step-size of 0.05 eV. Surface elemental compositions were calculated from the areas of the XPS peaks by using Casa XPS 2.3.15 software (CasaSoftware Ltd., Teighnmouth, Devon, U.K.) with Gaussian distributions. Relative quantities of surface N species were estimated by deconvolution of the high-resolution XPS spectra into four peaks, corresponding to pyridinic N (398.6 ± 0.3 eV), pyrrolic or pyridonic N (400.5 ± 0.3 eV), graphitic N (401.3 ± 0.3 eV), or nitroxide (402-405 eV) moieties.[43] Images obtained by high-resolution transition electron microscopy were acquired on an FEI Tecnai G2 Sphera microscope operating at 200 kV. TEM samples were prepared by dispersing the materials in ethanol and drop-casting the solution on a carbon-coated copper grid.

2.3.3 Electrocatalytic activity evaluation

Oxygen reduction activities of mesoporous Fe,N-doped carbon catalysts were determined by conducting cyclic voltammetry and linear sweep voltammetry measurements using a CHI Electrochemical Station (Model 750b) in a conventional three-electrode configuration. A rotating-ring-disk electrode with a 5.61 mm diameter glassy carbon disk was used as a working electrode, while a graphite rod and an Ag/AgCl (3M NaCl) electrode were used as counter and reference electrodes, respectively. For tests using the rotating-disk electrode (RDE) and rotating-ring-disk electrode (RRDE), a Modulated Speed Rotator from Pine Research Instrumentation was used to control the rotation speed of the working electrode. 2 mL of a catalyst dispersion solution were prepared by mixing catalysts, deionized (milli-Q) water, and isopropanol (1:3 volume ratio) with 120 µL of 5 wt% Nafion® solution, and 20 µL of the solution were deposited onto the glassy carbon disk of the RRDE electrode to obtain catalyst loadings of 0.60 mg/cm^2 and 0.060 mg_{Pt}/cm^2 for mesoporous N-doped carbon catalysts and 20 wt% Pt on activated carbon (Pt/C), respectively. After drying, cyclic voltammograms were recorded at a scan rate of 50 mV/s in 0.1 M NaOH solution saturated with N_2 and O_2, separately. RRDE tests were conducted using a linear sweep voltammetry within an O_2-saturated 0.1 M NaOH solution at a scan rate of 5 mV/s. Identical measurements were also conducted within N_2-saturated 0.1 M NaOH solutions and subtracted from the polarization curves acquired in O_2-saturated solution to compensate capacitive currents. After the measurements, potentials were converted to the reversible hydrogen electrode (RHE) scale by measuring the potential of a 3 M Ag/AgCl reference electrode *vs.* the RHE. Four-electron selectivities of catalysts were established by using RRDE tests with a platinum-ring electrode

potential at a bias potential of 1.2 V. The amount of peroxide formed was estimated from the ring current with a collection efficiency of 37%, according to Equation 1:

$$H_2O_2\ (\%) = 200 \times \frac{\frac{I_R}{N}}{\frac{I_R}{N}+I_D}, \quad (1)$$

where I_R is the ring electrode current, N is the collection efficiency (0.37), and I_D is the disk electrode current.[44] For stability testing, RDE measurements were acquired by linear sweep voltammetry before and after 5000 cyclic voltammetry scans over a range of 0.6 V to 1.0 V *vs.* RHE in an O_2-saturated 0.1 M NaOH solution. For the methanol tolerance testing, RDE measurements were performed in O_2-saturated solutions of 0.1 M NaOH and 0.5 M MeOH, and the half-wave potential acquired from these measurements was compared with the half-wave potential acquired from otherwise identical systems, but using solutions without methanol. All electrochemical measurements were conducted at Los Alamos National Laboratory (elevation 2230 m), where the atmospheric pressure is approximately 75% of that at sea level, resulting in correspondingly lower partial pressure of oxygen.

2.4 Results and Discussion

Preparation of highly-active, high-N-content oxygen reduction catalysts requires that volatilization of the N-containing organic precursors be minimized during the pyrolysis step that is typically needed to generate conductive graphitic materials. This can be achieved by first reacting melamine with formaldehyde to form a melamine-formaldehyde resin in the mesopores of a silica template. Subsequent pyrolysis of the mesostructured melamine-formaldehyde-silica composites in the presence of a metal nitrate salt, such as $Fe(NO_3)_3$, yields mesoporous metal,N-doped carbon materials with relatively high nitrogen contents that

depend on the cross-linking of the nitrogenous organic precursor species. Use of formaldehyde as a cross-linker improves the yield and N content of the product material. In this work, yield was determined by quantifying the retained mass percentage of the organic components after thermogravimetric analysis (TGA), and near-surface N content was determined by X-ray photoelectron spectroscopy (XPS).

The TGA plot of melamine-formaldehyde resin synthesized with iron nitrate (Figure 2.2, green), shows that the material exhibits significant mass losses over different temperature regimes, as a result of the different thermal stabilities of the moieties present. Moderate mass

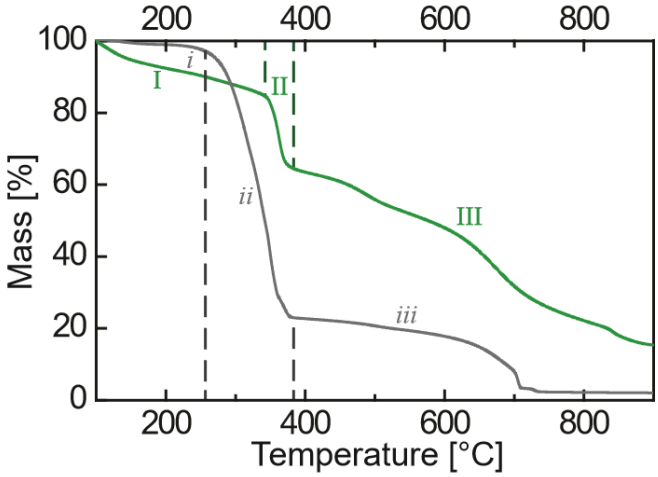

Figure 2.2. Thermogravimetric analysis plots acquired over the range 25-900 °C under nitrogen atmosphere for melamine-formaldehyde resin and $Fe(NO_3)_3$ mixture (green), and melamine and $Fe(NO_3)_3$, in grey. Distinct regions of mass loss are observed: with formaldehyde present as a cross-linker, regime I corresponds to water loss from polymer condensation or $Fe(NO_3)_3$ decomposition, regime II to decomposition of methylene cross-links, and regime III to decomposition of triazine rings. Without formaldehyde, mass loss is due decomposition of $Fe(NO_3)_3$ (*i*), amines (*ii*), and triazine rings (*iii*). The final product yields after pyrolysis at 900 °C were 15% and 2%, with and without formaldehyde, respectively.

loss was observed up to 350 °C (regime I), which is attributed to loss of water from condensation reactions that increase the extent of cross-linking of the melamine-formaldehyde resins and decomposition of iron nitrate salts.[45] Near 350 °C, the material exhibited rapid weight loss (regime II), due to the decomposition of methylene cross-links between melamine molecules, and above 400 °C (regime III), a gradual decrease in mass was observed, which has been attributed to decomposition of triazine rings.[46] XPS results (Supporting Information, Table S2.1) show that the near-surface N/C atom ratio decreased from ~0.93 before pyrolysis to ~0.04 after pyrolysis at 900 °C. This suggests that the significant loss of N from the melamine-formaldehyde resin during pyrolysis is associated with appreciable volatilization of nitrogen species from the carbonaceous networks and is accompanied by restructuring of the carbon networks. Despite the relatively low yield (~85% TGA mass loss after pyrolysis at 900 °C) and low N retention, these values are significantly higher compared to materials synthesized without the use of the formaldehyde cross-linker, in which case the volatilization of melamine results in near-complete weight loss (~98%, Figure 2.2, grey). Without formaldehyde, the mass losses are due to the decomposition of iron nitrate (< 250 °C, regime *i*),[45] amines (250-380 °C, regime *ii*), and triazine rings (above 400 °C, regime *iii*).[46] The low retained mass, ~2% after pyrolysis at 900 °C, has previously required that pyrolyzed melamine- based carbon materials be synthesized with high initial loadings of melamine,[34,47] high-surface-area substrates,[16,19,47] or in closed containers during pyrolysis.[14,16,19,34] The inclusion of a cross-linker to reduce melamine volatilization enables mesoporous materials to be synthesized with higher yield and N content (4 atom%) than previously reported (2.5 atom% N), when melamine alone has been used as a nitrogen source.[16,47] Without cross-

linking, syntheses of porous carbons have required substantially higher mass fractions of melamine precursors that are adsorbed and pyrolyzed on high-surface area carbon substrates[24,47] or the use of closed containers during pyrolysis.[14,16,19] In addition, compared to polymeric nitrogen-containing precursors (e.g., melamine-based resins[29]), the use of small-molecule melamine precursors enables the preparation of porous N-carbon materials by templating.

Because of the possibility for large loss of mass during pyrolysis, mesostructural ordering of carbonaceous materials can be difficult to achieve. After removal of the mesoporous SBA-15 silica template by dissolution at high pH, the mesoporous nitrogen-doped carbon materials exhibit short-range, but not long-range, mesostructural order, as revealed by a combination of scattering and sorption analyses. The small-angle X-ray scattering (SAXS) pattern of mesoporous N-doped carbon material (Supporting Information, Figure S2.2) shows no distinct reflections and thus no detectable long-range mesostructural order. This is consistent with restructuring of the carbonaceous network as a combined result of the complicated chemistry and longer-range interactions that occur during decomposition of the melamine-formaldehyde resin, volatilization of some pyrolysis products, and silica removal. By comparison, sorption measurements and high-resolution transmission electron microscopy (TEM) images reveal significant short-range mesostructural order. Specifically, N_2 sorption measurements (Supporting Information, Figure S2.3) revealed Type-IV isotherms, indicative of the presence of uniform mesopores,[48] as observed in previously-synthesized mesoporous carbons, such as CMK-3.[49] Brunauer-Emmett-Teller (BET)[41] and Barrett-Joyner-Halenda (BJH)[42] sorption analyses were used to determine the specific surface area (800 m^2/g), specific pore volume (0.66 cm^3/g), and established a narrow pore-size distribution centered about 3.8

nm (Figure 2.3a). This mean mesopore size corresponds well with the wall thickness of the mesoporous silica templates used to prepare the mesoporous N-doped carbon materials. High surface areas and large pore volumes indicate that mesoporosity is maintained after removal of silica framework. This is corroborated by the high-resolution TEM images of the Fe,N-doped carbon material in Figure 2.3b, which shows mesopores with dimensions of 3-4 nm between carbonaceous features approximately twice this size. However, the high extents of mesostructural order appear to be confined to local regions, as they are not evidenced by the SAXS patterns. Nevertheless, the large surface areas, large pore volumes, and uniform mesopore dimensions of the N-doped carbon materials are expected to yield beneficial catalytic properties.

Both short- and long-range graphitic order are present in the melamine-formaldehyde-derived transition-metal- and N-doped mesoporous carbon materials, the extents to which depend strongly on the transition metal species used. In the presence of transition metal oxides, the decomposition of the melamine-formaldehyde resin and restructuring of the carbonaceous network at high pyrolysis temperatures (> 350 °C) results in materials with increased graphitic properties, compared to materials prepared in the absence of metal species.[50] This is evident in wide-angle X-ray scattering (WAXS) patterns shown in Figure 2.4a for mesoporous Fe,N-, Ni,N-, Co,N-, and Mn,N-doped carbon materials prepared identically, except for the use of the different respective metal nitrate salts. All show reflections at 26.2°, corresponding to a *d*-spacing of 0.34 nm, which is assigned to the (002) plane of graphitic carbon layers.[51] The mesoporous Fe,N- and Ni,N-carbon materials show sharper (002) reflections, consistent with previous reports that found iron and nickel species to be superior graphitization catalysts for other organic precursors, such as phthalocyanines.[32]

By comparison, those formed from Co- or Mn-containing salts exhibit (002) reflections that are significantly less intense. Broad reflections are also observed at lower scattering angles (centered at ca. 20°), which indicate the presence of less-ordered carbon[51] with somewhat larger *d*-spacing (*ca.* 0.4 nm). This is consistent with the greater intensities of this reflection

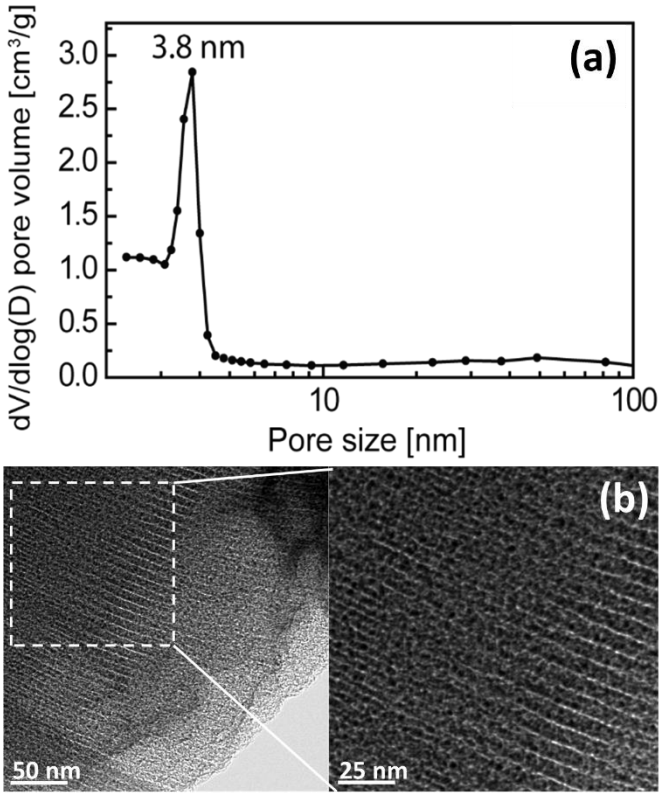

Figure 2.3. (a) BJH pore-size distribution and (b) representative TEM images of an mesoporous Fe,N-doped carbon material synthesized from melamine-formaldehyde resin with iron nitrate (0.05 iron nitrate-to-melamine mole ratio). The mean pore size of 3.8 nm established in (a) is consistent with the mesopore dimensions (parallel light regions) shown in (b). The wide-angle X-ray diffraction pattern of this material is shown in Figure 2.5b.

relative to the sharper reflection at 26.2° for the less-ordered Mn,N-, Co,N- and Ni,N-analogues, compared to the Fe,N-carbon materials. All of the mesoporous N-doped carbon materials yield a weaker second reflection at 43.5° that is assigned to the superposition of the (100) and (101) graphitic planes.[51] Additionally, the mesoporous Fe,N-carbon material exhibits a reflection at 44.5°, likely from metallic α-Fe,[52] which indicates some iron ions were reduced during high-temperature pyrolysis with carbon materials.

Whereas WAXS is sensitive to long-range atomic structural order, the positions, relative intensities, and widths of Raman spectroscopy bands are sensitive to locally ordered, as well as disordered, graphitic moieties in mesoporous metal- and nitrogen-doped carbon materials. For example, in the range of 1000-2000 cm^{-1}, Raman spectra of single-crystal graphite exhibit only a narrow band centered at 1575 cm^{-1}, associated with a characteristic lattice-vibration mode of graphite.[53] By comparison, mesoporous Fe,N-, Ni,N-, Co,N-, and Mn,N-doped carbon materials show broad Raman bands (Figure 2.4b) with two intensity maxima at approximately 1350 and 1580 cm^{-1}. Each of these spectra can be deconvoluted into four Lorentzian-shaped bands centered at 1200, 1350, 1450, and 1580 cm^{-1}. The bands centered at 1350 cm^{-1} and 1450 cm^{-1} are associated with relatively disordered graphitic structures that have been attributed to the lattice vibrations of graphite near crystalline domain edges[53] or distorted (*e.g.*, heteroatom-doped) graphitic lattices,[54] respectively. These bands are consistent with the high surface areas of the materials, which are expected to have significant relative fractions of carbon moieties at the edges of crystalline domains or near nitrogen atoms in the graphitic lattices. The broad band centered at 1200 cm^{-1}, by comparison, is attributed to a stretching vibration of polyene-like structures.[55] The dominant peaks centered at 1350 and1580 cm^{-1} are designated as *D* and *G* Raman bands, respectively, and their intensity ratio

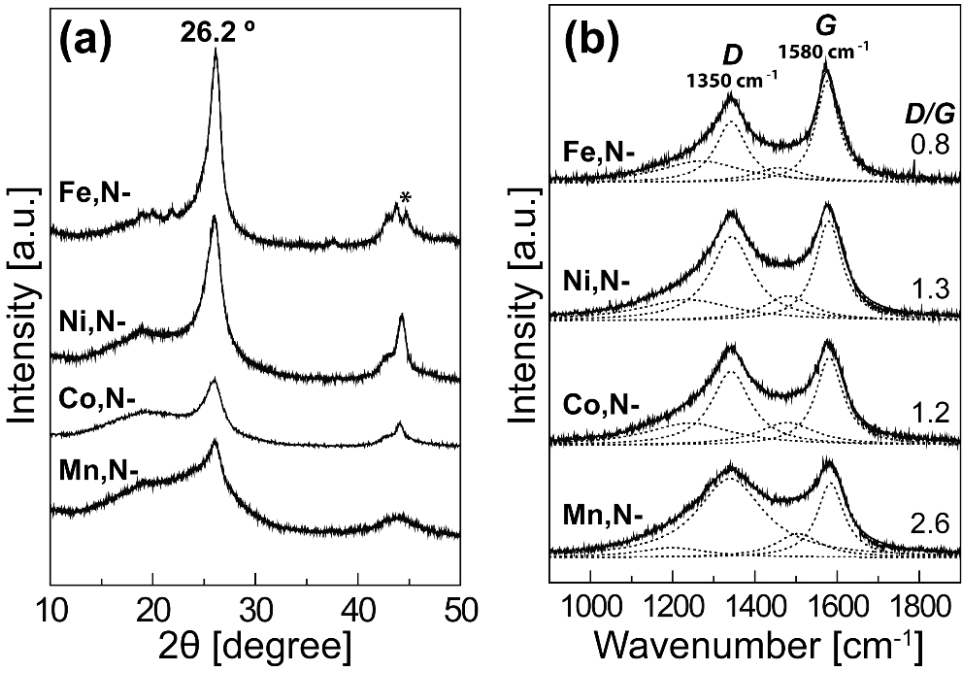

Figure 2.4. (a) Wide-angle X-ray scattering (WAXS) patterns and (b) Raman spectra of mesoporous Fe,N-, Ni,N-, Co,N-, and Mn,N-doped carbon materials prepared under identical conditions, except for the transition metal nitrate salt used. The molar ratio of metal nitrate salt to melamine for all materials was 0.10. The WAXS reflections at 26.2° and the Raman bands at 1580 cm^{-1} indicate the highly graphitic properties of the mesoporous Fe,N- and Ni,N-doped carbon materials. A reflection from α-Fe is indicated by the asterisk.

(*D/G*) is considered to be inversely correlated with the degree of graphitization.[53,55] Accordingly, the Raman spectra of mesoporous Fe,N-, Ni,N-, Co,N-, and Mn,N-doped carbon materials yield *D/G* intensity ratios of 0.8, 1.3, 1.2, and 2.6, respectively, which correspond reasonably well with the relative extents of graphitization (Fe>Ni>Co>Mn) observed in the WAXS results. Additionally, the narrowness of the Raman *D* band has been proposed as another indication of graphitic properties.[56] The full-width-at-half-maximum values were

measured to be 92, 124, 115, and 197 cm^{-1} for the mesoporous Fe,N-, Ni,N-, Co,N-, and Mn,N-doped carbon materials, respectively, consistent with their corresponding *D/G* intensity ratios. Thus, both the Raman and WAXS analyses support the beneficial role of iron nitrate in syntheses of mesoporous Fe,N-doped carbon materials with high extents of graphitization. Furthermore, polarization curves for the mesoporous Fe,N-, Ni,N-, Co,N-, and Mn,N-doped carbon materials (Supporting Information, Figure S2.4) establish that the Fe,N-doped carbon exhibited greater ORR activity.

Iron is a known graphitizing agent,[32] so the extent of graphitic order depends on the relative quantity of transition metal used and choice of organic precursor species. mesoporous Fe,N-doped carbon materials were synthesized with different quantities of iron nitrate (initial iron nitrate/melamine molar ratios of 0.02, 0.05, 0.10, 0.20), and their graphitic properties were examined by WAXS. As shown in Figure 2.5a, the relative intensities of the reflections at 26.2° are higher for materials prepared with higher molar ratios of iron nitrate, which indicate higher degrees of graphitic ordering over the range of molar ratios tested. Additionally, these melamine-formaldehyde-derived mesoporous N-doped carbon materials synthesized with transition metal salts exhibit higher graphitic properties than if other precursors are used. Figure 2.5b compares the WAXS pattern of a melamine-formaldehyde-derived mesoporous carbon prepared with iron nitrate, with those of materials prepared under otherwise identical synthesis conditions, but using phenol-formaldehyde resins[57] without and with the iron nitrate

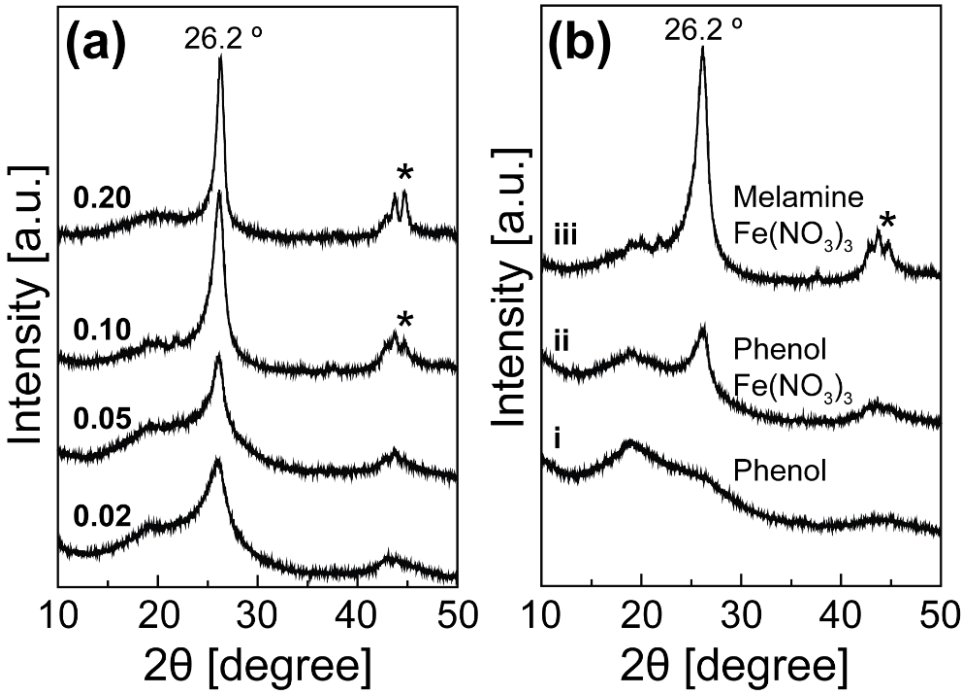

Figure 2.5. Wide-angle X-ray scattering patterns of mesoporous carbon materials prepared under identical conditions by using (a) melamine-formaldehyde resin and $Fe(NO_3)_3$, but with different molar ratios (0.02, 0.05, 0.10, and 0.20) of iron nitrate to melamine, and (b) different precursors: (i) phenol-formaldehyde resin without $Fe(NO_3)_3$, (ii) phenol-formaldehyde resin with $Fe(NO_3)_3$, and (iii) melamine-formaldehyde resin with $Fe(NO_3)_3$. A reflection from α-Fe is indicated by the asterisk.

salt. The WAXS pattern of the phenol-formaldehyde-derived mesoporous carbon without iron salt (i) shows only a single broad reflection below 20° and no clear evidence of graphitic ordering. By comparison, when iron nitrate was used, the resulting mesoporous carbon material (ii) exhibited a weak reflection at ~26° that was much less intense than those for melamine-formaldehyde-derived mesoporous carbon materials (iii). The superior graphitic properties of melamine-resin-derived mesoporous carbons suggest that intermediate species

formed during pyrolysis of melamine-formaldehyde resin enable restructuring of the carbonaceous network at high temperature, which results in carbon moieties with greater extents of both local and long-range crystalline order. While pyrolysis of several similar small-molecule organic precursors with iron or nickel salts have been previously shown to yield materials with graphitic properties,[50] the melamine-formaldehyde-resin-derived mesoporous carbon materials prepared with iron nitrate appear to exhibit greater extents of graphitization.

The bulk electrical conductivities of these mesoporous transition-metal- and N-doped carbon materials are relatively high and correlate with the degree of graphitization achieved for the different transition metal nitrates used. Conventional mesoporous carbon materials prepared from phenol-formaldehyde resin[57] are non-graphitic (as shown in Figure 2.5b,i), and are therefore expected to have low bulk electrical conductivities due to their high porosities and absence of conductive graphitic domains. Bulk conductivities were determined from impedance measurements for all samples and are tabulated in Supporting Information, Table S2.2. As expected, the conductivity of the mesoporous carbon material prepared from phenol-formaldehyde was relatively low at 4.6 S/cm. For comparison, graphite powder exhibited a value of 98 S/cm, due to the presence of large crystalline graphitic domains without significant porosity. In contrast, mesoporous transition-metal- and N-doped carbon materials prepared from melamine-formaldehyde exhibited higher bulk electrical conductivities, in spite of their nitrogen contents that have often been reported to reduce electron conductivities.[58] While the mesoporous Mn,N-doped carbon with relatively poor graphitic properties exhibited only slightly higher conductivity (7 S/cm) than conventional mesoporous carbon materials, the more graphitic mesoporous Fe,N- and Ni,N-doped carbon materials manifested significantly higher bulk electrical conductivities of 19 and 17 S/cm, respectively. Although the

mesoporous Fe,N-doped carbon material was less conductive than non-porous graphite (without nitrogen), its conductivity was more than 4 times greater than conventional mesoporous carbon materials, which is advantageous for use as an electrocatalyst.

Post-synthesis acid leaching and heat treatment have been demonstrated to increase the oxygen reduction activities of other N-containing carbon materials[20,59,66] and were used similarly here for the mesoporous Fe,N-doped carbon material. Oxygen reduction activities of otherwise identical mesoporous Fe,N-doped carbons, except for their different post-synthesis treatments, were evaluated by rotating ring-disk electrode (RRDE) tests in a 0.1 M NaOH electrolyte solution. Polarization curves were measured under alkaline conditions for the (i) as-synthesized mesoporous carbon catalysts, (ii) after acid treatment, and (iii) after acid treatment and additional pyrolysis (900 °C for 1 h under flowing N_2 gas), and the results are shown in Figure 2.6a and Table 2.1. As can be seen from the polarization curves in Figure 2.6a generally shifting to greater absolute current (indicating higher catalytic rates) at higher potentials (indicating smaller required overpotentials), each post-synthesis treatment results in improved electrocatalytic activities. Additionally, peroxide yields (i.e., fraction of O_2 reduced to hydrogen peroxide, rather than water) were calculated from the RRDE ring current by using Equation 1, and are plotted as a function of the applied potential in Figure 2.6b. In addition to resulting in higher electrocatalytic activities, the post-synthesis treatments reduce the generation of peroxides, which improves catalyst efficiency for the four-electron reduction of O_2 to water and thus fuel conversion efficiency.[60] A summary of the electrochemical measurement results, including onset potentials, half-wave potentials, Tafel slopes, and exchange current densities, are provided in Table 2.1.

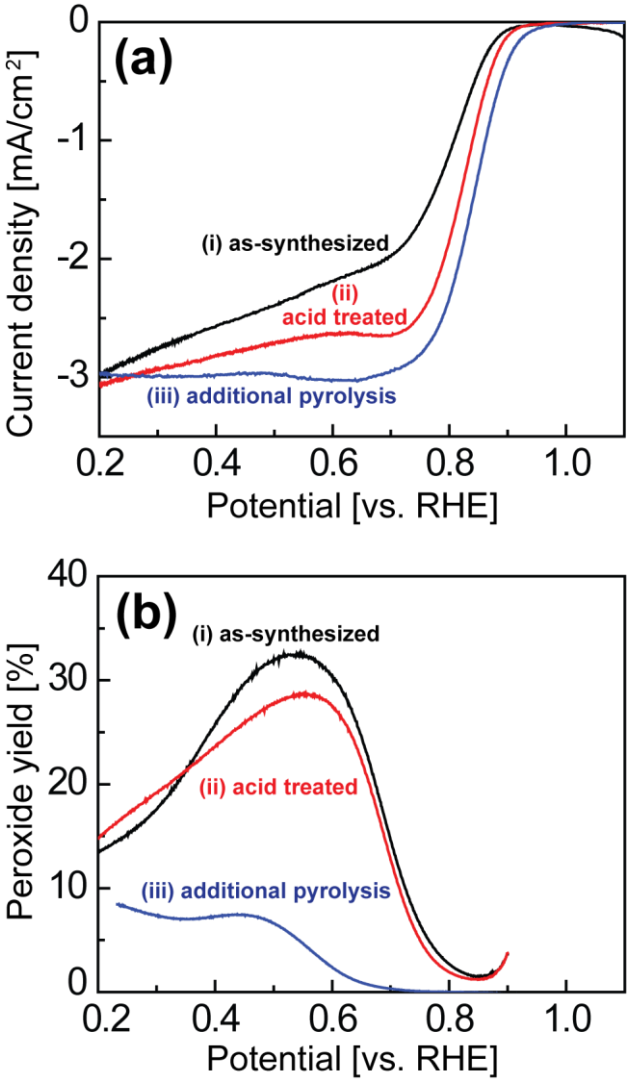

Figure 2.6. (a) Polarization curves and (b) peroxide yields of mesoporous Fe,N-doped carbon catalysts synthesized using an iron nitrate-to-melamine molar ratio of 0.10 followed by (i) pyrolysis and then alkaline washed to remove the mesoporous silica template (as-synthesized), (ii) after pyrolysis, alkaline washing, and an additional acid treatment, and (iii) after pyrolysis, alkaline washing, acid treatment and an additional second pyrolysis step. These materials were identical to those used in Table 2.1, and Supporting Information Tables S2.3, and S2.4.

Table 2.1. Electrochemical analyses of the kinetics of oxygen reduction for mesoporous Fe,N-doped carbon catalysts synthesized with an iron nitrate-to-melamine molar ratio of 0.10, but with different post-synthesis treatments

Treatments	*Onset potential (V vs. RHE)*	*Half-wave potential (V vs. RHE)*	*Tafel slope[a] (mV/decade)*	*Exchange current density[a] (10^{-5} A/m^2)*
As-synthesized	0.95	0.76	76	4.6
Acid treatment	0.96	0.82	60	0.46
Additional pyrolysis	1.02	0.84	60	1.2

[a] Tafel slopes and exchange current densities were calculated from mass-transport-corrected kinetic current densities.

As-synthesized mesoporous Fe,N-doped carbon catalysts prepared with alkaline treatment to remove silica templates exhibit a high onset potential of 0.95 V versus RHE, which establishes high ORR activity. However, the reduction current increases slowly as the potential is decreased (Figure 2.6a,i), resulting in relatively low half-wave potential of 0.76 V, and high Tafel slope of 76 mV/decade (Table 2.1). As a result, a saturated current-density plateau in the low potential region (i.e., limiting current density), is not clearly observed. In addition, the Pt ring current reveals that this catalyst produces a significant quantity of peroxide (32.6% at 0.54 V), indicating significant contributions from the two-electron oxygen reduction process. The two-electron process, which generates peroxides, is less favorable than the four-electron reduction to water, because peroxide lowers the fuel conversion efficiency, and can negatively affect the fuel cell membrane and electrode stability.[60] By comparison, following acid treatment to leach-out pore-filling carbonaceous materials, the half-wave potential increases to 0.82 V, consistent with a lower Tafel slope of 60 mV/decade (Table

2.1), while the onset potential and peroxide yield are not significantly altered. The decreased value of the Tafel slope after acid treatment indicates that acid leaching removes less-active surface species from the catalysts and/or improves accessibility to active species. However, the catalyst still produces a large quantity of peroxide (maximum peroxide yield of 28% at 0.57 V *vs.* RHE) *via* the two-electron reduction process. Finally, additional pyrolysis of the acid-treated catalyst significantly improves ORR activities, as established by the higher onset potential (1.02 V), half-wave potential (0.84 V), and four-electron selectivity (maximum peroxide yield reduced to 9% at ~0.20 V *vs.* RHE), implying that the additional pyrolysis step increased the number of active sites in mesoporous Fe,N-doped carbon catalysts. This is also supported by increased exchange current density with comparable Tafel slope, compared to the catalyst with acid treatment only. Based on these results, the acid and heat treatments significantly improve the oxygen reduction activities of the mesoporous Fe,N-doped carbon catalysts.

Increased ORR activities of the mesoporous Fe,N-doped carbon catalysts after post-synthesis treatments can be correlated with increased surface nitrogen and decreased surface oxygen contents. Approximate surface elemental compositions of the mesoporous Fe,N-doped carbon catalysts before and after post-synthesis treatments were estimated and compared by survey X-ray photoelectron spectroscopy (XPS) analyses, and the results are tabulated in Supporting Information, Table S2.3. Initially, because of the high nitrogen content of melamine-based resin, the melamine-formaldehyde-silica composite with iron nitrate contained *ca.* 30 atom% surface N species. By comparison, after the first pyrolysis at 900 °C, the surface nitrogen content decreased significantly to 5 atom%, reflecting the low thermal stability of these nitrogen species at high temperatures. As-synthesized mesoporous Fe,N-

doped carbon prepared following alkaline dissolution of the silica frameworks show *ca.* 4 atom% surface N, 0.7 atom% surface Fe, and 14 atom% surface O contents. The relatively high oxygen content of the material is attributed to surface oxidation during exposure to the alkaline dissolution solution, which offsets the loss of surface oxygen from removal of the silica. Post-synthesis acid treatment of the material leads to lower surface iron content (from 0.7% to 0.1%), consistent with dissolution and removal of Fe species, without other significant changes in surface composition. In conjunction with the electrochemical tests shown in Figure 2.6, this suggests that acid treatment exposes surface species that are active for oxygen reduction. Finally, the XPS analysis reveals that the second pyrolysis step at 900 °C, which results in significantly higher ORR activities, further decreases surface oxygen content to ~3 atom%. Thus, mesoporous Fe,N-doped carbon catalysts prepared under optimized post-synthesis treatment conditions exhibit surface elemental compositions of ~4 atom% nitrogen and ~3 atom% oxygen, which are similar to other highly active N-doped carbon-based ORR catalysts.[61]

Complementing the survey XPS estimates of near-surface elemental compositions, high-resolution nitrogen XPS enables the identification of different types of surface nitrogen sites. This specifically includes distinguishing between pyridinic and graphitic nitrogen species that are thought to be associated with ORR active sites.[21,23,62,63] High-resolution N 1*s* XPS spectra were acquired for mesoporous Fe,N-doped carbon materials after the various synthesis steps shown in Figure 2.7: (a) with no post-synthesis treatment, (b) after acid treatment, and (c) following acid treatment and additional pyrolysis for 1 h at 900 °C. The quantities of each nitrogen species were estimated by deconvoluting the nitrogen XPS spectra into four peaks: pyridinic and Fe-bonded nitrogen (398.6 eV), pyrrolic and pyridonic nitrogen (400.5 eV),

graphitic nitrogen (401.3 eV), and nitrogen oxide (402-405 eV),[43] the results of which are summarized in Supporting Information, Table S2.4. The low concentrations of surface nitrogen

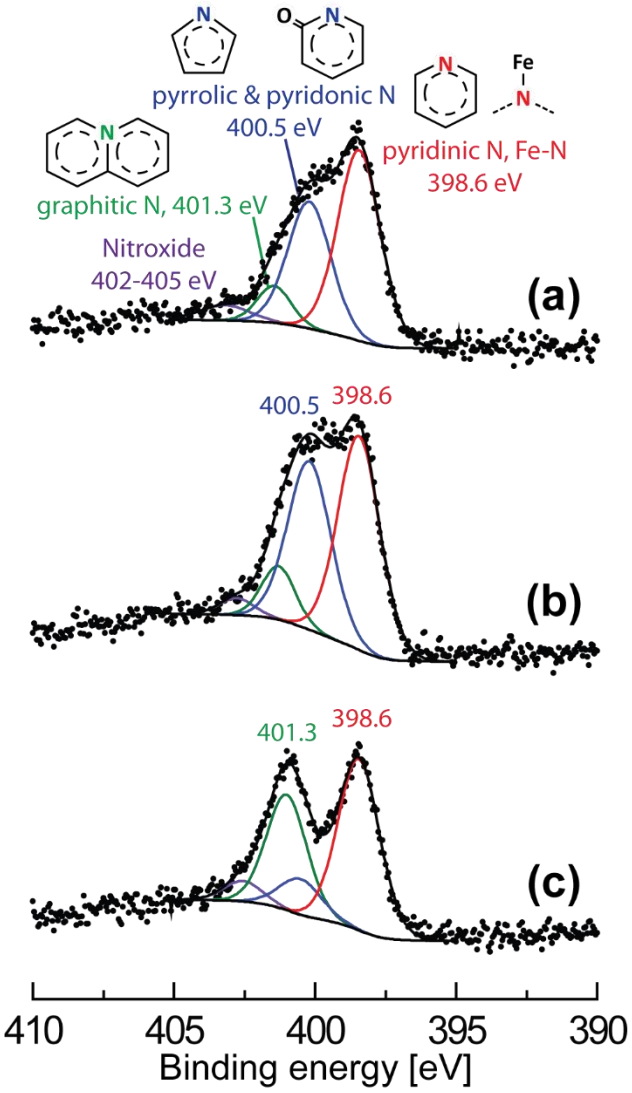

Figure 2.7. High-resolution X-ray photoelectron spectroscopy (XPS) spectra of mesoporous Fe,N-doped carbon catalysts synthesized with an iron nitrate-to-melamine molar ratio of 0.1, and (a) no post-synthesis treatment, (b) after acid treatment, and (c) after acid treatment and additional pyrolysis for 1 h at 900 °C. These materials were identical to those used in Figure 2.6, Table 2.1, and Supporting Information Tables S2.3 and S2.4.

species limit the sensitivity and resolution of the spectra, resulting in overlap of peaks associated with pyridinic and Fe-bonded nitrogen, as well as those for the pyrrolic and pyridonic nitrogen moieties, which cannot be distinguished from each other. After alkaline dissolution of the silica template, as-synthesized mesoporous Fe,N-doped carbon catalysts, the materials contain *ca*. 50 atom% pyridinic or Fe-bonded nitrogen, 35 atom% pyrrolic and/or pyridonic nitrogen, and small amounts of graphitic nitrogen and nitroxide (Figure 2.7a). Following acid treatment (Figure 2.7b), the relative percentages of the pyrrolic and/or pyridonic nitrogen species increased, while those of pyridinic or Fe-bonded nitrogen decreased, consistent with acid dissolution of surface iron species. However, after the additional pyrolysis step, the relative percentages of pyrrolic and/or pyridonic nitrogen species significantly decreased and an increase of the percentage of graphitic nitrogen species was observed (Figure 2.7c). In combination with the electrochemical measurement results, this suggests that graphitic nitrogen species are associated with higher ORR activity than pyrrolic/pyridonic nitrogen species, consistent with several prior findings.[23,63] As the second pyrolysis step reduces the surface oxygen contents significantly, the XPS peak around 400.5 eV can be assigned mainly to pyridonic nitrogen species, which contain oxygen, with a smaller contribution from pyrrolic moieties, which do not. Collectively, the electrochemical measurements and the high-resolution XPS analysis indicate that influencing the distributions of surface nitrogen species present an opportunity to increase the number of ORR active sites and thus to improve ORR activities.

Besides the types of nitrogen moieties present, the oxygen reduction activities also depend on the amount of Fe species in mesoporous Fe,N-doped carbon materials, for which there

appears to be an optimal value. As discussed previously (Figure 2.5a), additional iron species are favorable for increasing graphitic properties. However, the amount of iron species that improve ORR activity is generally very low (typically < 1.0 atom%),[47,64,65] with excess resulting in iron particles within the graphitic carbon layers. Although surface iron species can be dissolved by acid treatment, encapsulated particles are not readily removed, resulting in potentially considerable amounts of Fe residues[7,52] and a decrease in gravimetric densities of active sites in the catalysts. mesoporous Fe,N-doped carbon catalysts were prepared with differing iron nitrate-to-melamine molar ratios (0, 0.02, 0.05, 0.10, and 0.20), and their oxygen reduction activities were evaluated by rotating disk electrode tests. As shown in Figure 2.8a, the mesoporous N-doped carbon catalyst prepared without iron nitrate exhibited a slowly increasing reduction current with decreasing potential. By comparison, a small quantity of iron nitrate added to the synthesis resulted in a catalyst with higher onset and half-wave potentials. The reduction currents of mesoporous Fe,N-doped carbon catalysts increased at higher molar ratios of iron-nitrate-to-melamine, resulting in a maximum onset potential and a maximum half-wave potential observed for the catalysts prepared with 0.05 and 0.10 iron-nitrate-to-melamine ratios, respectively. Iron is known to be beneficial for high ORR activity,[66] for which the optimum iron content has been reported to be very low (e.g., 0.05 wt%).[47] Therefore, the greater ORR activities observed here for increasing iron-nitrate-to-melamine molar ratios (up to 0.10) suggests that the extent of graphitization is important, as corroborated by the WAXS and Raman results in Figures 2.4 and 2.5.

The incorporation of additional iron nitrate, which promotes a higher extent of graphitization, however, eventually led to decreased specific ORR electrocatalytic activity (per mass of catalyst). This is attributed to excess quantities of iron in the carbon frameworks that increase

the bulk density of the resulting materials, though do not significantly contribute to increased ORR activity. Based on the TGA results, the catalyst prepared with a 0.20 molar ratio of iron nitrate/melamine is estimated to possess 22 wt% Fe (Supporting Information, Figure S2.5), resulting in higher bulk densities of the catalysts. A high extent of graphitization, however, tends to be associated with a decreased heteroatom loading or lower porosity, which requires a tradeoff between these properties to obtain high ORR activity. Figure 2.8b separately plots the onset and half-wave potentials measured for the materials prepared with different amounts of iron nitrate. Optimal molar ratios of Fe nitrate/melamine were found to be 0.10 and 0.05 for the highest onset and half-wave potentials, respectively. These results indicate the desirability of optimizing the amount of Fe incorporated into the mesoporous Fe,N-doped carbon materials to obtain high ORR activity. Highly-graphitic mesoporous Fe,N-doped carbon materials prepared under optimized synthesis conditions exhibited high ORR activities under alkaline conditions, that were comparable to commercial carbon-supported 20 wt% Pt/C. Oxygen reduction activities were evaluated by using linear sweep voltammetry in an O_2-saturated 0.1 M NaOH solution with a RDE rotation rate of 900 rpm, as shown in Figure 2.9a. An optimized mesoporous Fe,N-doped carbon catalyst showed excellent ORR activity with a high onset potential of 1.04 V versus RHE, which is almost identical to Pt/C catalysts. Magnified polarization curves of the high potential region (shown in Supporting Information, Figure S2.6) more clearly demonstrate the nearly identical onset potentials. This onset potential value is greater than reported for most transition metal oxide catalysts (*e.g.*, Ni-doped Co_3O_4 nanowire arrays on graphene foam, for which an onset potential of ~0.97 V vs. RHE has been measured) or N-doped porous carbon materials.[67] It is also close to the values reported for nanostructured N-doped carbon materials, such as carbon nanotube-graphene

complexes (1.05 V),[61] carbon nanotube/Fe_3C nanoparticle hybrids (1.07 V),[64] and Fe,N-doped carbon

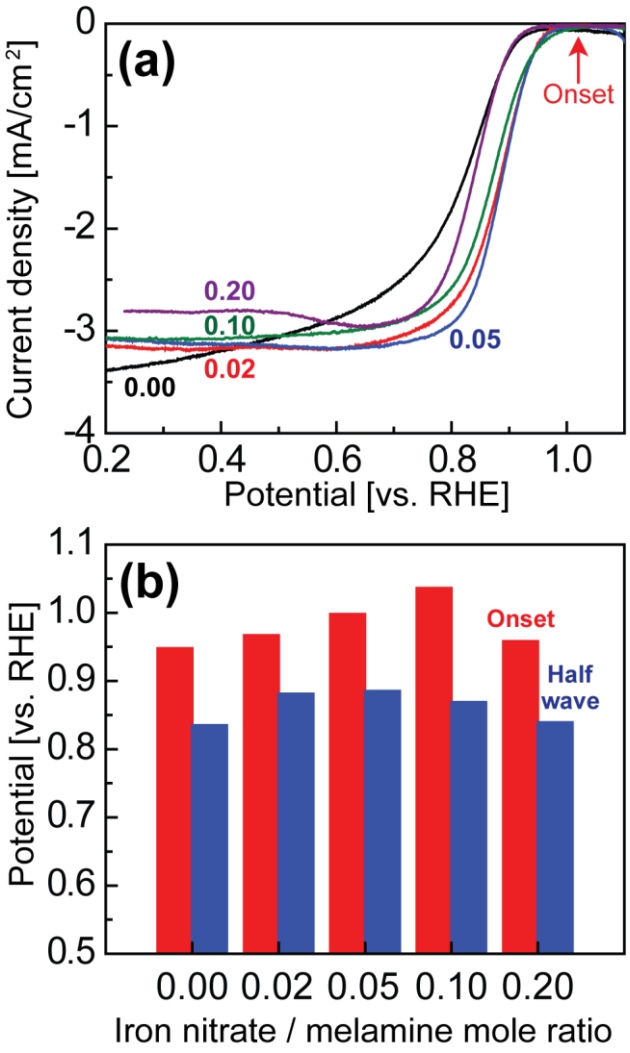

Figure 2.8. (a) Polarization curves and (b) onset and half-wave potentials of mesoporous Fe,N-doped carbon catalysts prepared under identical conditions including post-synthesis acid treatment and additional pyrolysis, except with different $Fe(NO_3)_3$:melamine molar ratios of 0, 0.02, 0.05, 0.10, and 0.20.

nanofibers on expanded graphite (1.07 V),[65] indicating that the ORR activities of mesoporous Fe,N-doped carbon materials prepared by pyrolysis of inexpensive melamine-formaldehyde can be comparable to high-purity nanostructured carbons. Additionally, the mesoporous Fe,N-doped carbon catalyst showed a half-wave potential of 0.87 V, which is higher than that of the Pt/C catalyst (0.85 V) and is comparable to other Fe,N-doped carbon catalysts fabricated from conducting polymer[20] or macrocyclic compounds[66,68] (Table S2.5). These excellent electrocatalytic activities likely result from a combination of the high mesoporosity and highly graphitic properties of the material, which provide accessible ORR active sites and high electrical conductivity, respectively.

Mesoporous Fe,N-doped carbon also compares favorably to Pt/C catalysts on the basis of Tafel slopes, which were calculated to evaluate their relative electrochemical activities for oxygen reduction. The onset and half-wave potentials are dependent on catalyst loading and the associated density of active sites, as higher catalyst loadings yield increased exchange current densities. However, comparable catalyst loadings cannot be easily determined, as the active sites of Fe,N-doped carbon catalysts are still under debate. Nevertheless, Tafel slopes, which are independent of catalyst loading, can establish relative electrocatalytic activities. Specifically, Tafel slopes of the mesoporous Fe,N-doped catalysts synthesized with an iron nitrate-to-melamine ratio of 0.05 were determined from the slope of *iR*-loss-corrected overpotential, plotted as a function of logarithmic mass-transport-corrected kinetic current density, and compared with those of commercial Pt/C catalysts. As shown in Figure 2.9b, the 20 wt% Pt/C catalyst exhibits a Tafel slope of 67 mV/decade, consistent with literature

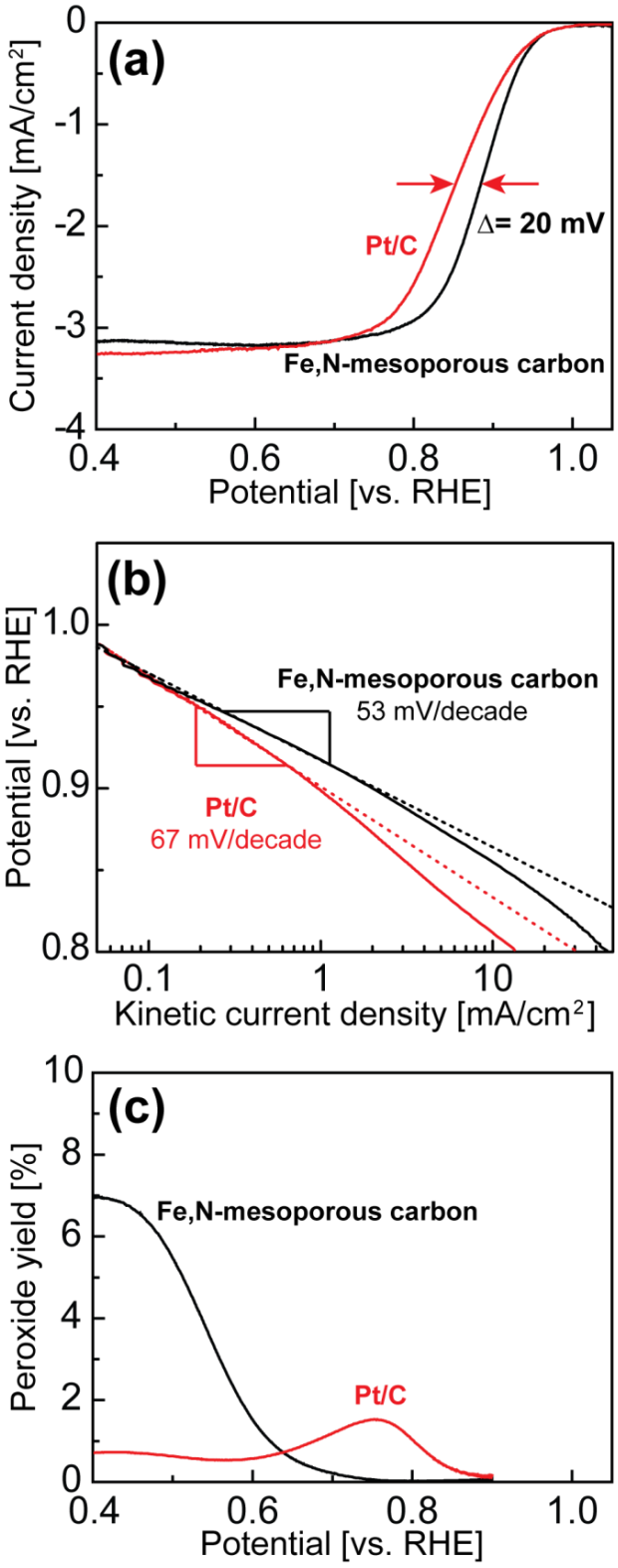

Figure 2.9. (a) Polarization curves, (b) mass-transport- and *iR*-loss-corrected Tafel plots, and (c) peroxide yields for Pt/C and for a mesoporous Fe,N-doped carbon catalyst synthesized

with an iron nitrate-to-melamine molar ratio of 0.05 and post-synthesis acid and heat treatments. The data were acquired under alkaline conditions (0.1 M NaOH) by linear sweep voltammetry with a rotating ring disk electrode operating at 900 rpm.

values.[44] By comparison, the mesoporous Fe,N-doped carbon catalyst yields a lower Tafel slope of 53 mV/decade, which is consistent with their higher half-wave potentials, while their onset-potentials are comparable. The low Tafel slope value, in combination with high onset and half-wave potentials, establish the fast ORR kinetics of the mesoporous Fe,N-doped carbon catalysts.

The mesoporous Fe,N-doped carbon catalyst was also found to generate less partially-reduced peroxide species than the Pt/C catalyst, which contributes to higher energy conversion efficiencies and stabilities of the catalysts. Figure 2.9c compares the peroxide yields of mesoporous Fe,N-doped carbon and Pt/C catalysts, as acquired from RRDE measurements and calculated by using Equation 1. The commercially available 20 wt% Pt/C catalyst exhibited a low peroxide yield over the entire potential region, with a maximum of 1.5% at 0.75 V versus RHE. By comparison, mesoporous Fe,N-doped carbon catalyst generated a negligible amount of peroxide at potentials higher than 0.8 V *vs.* RHE, though the amount of peroxide produced was relatively high in the range 0.7–0.8 V. While the mesoporous Fe,N-doped carbon catalyst generated less peroxide than the Pt/C catalyst at potentials higher than ~0.63 V, the peroxide yield increased to ~7% at 0.4 V. This trend is consistent with the small decrease observed in the limiting current of the Fe,N-doped carbon catalyst at potentials below 0.6 V (Figure 2.9a). The low peroxide yield at high potential is desirable, as Fe,N-doped carbon catalysts often suffer from poor stability of their oxygen reduction activity at high

potentials. The peroxide generated from the partial reduction of oxygen has been suggested to oxidize the catalysts or to generate more reactive radicals by coupling with Fe^{2+} ions (e.g., Fenton's reagent), resulting in catalyst degradation.[69] It should be noted that due to the high porosity of the Fe,N-doped carbon, the thickness of its catalyst layer was greater than for Pt/C, so the lower apparent peroxide generation may be due to a combination of higher intrinsic selectivity against peroxide production, greater opportunity for the partially-reduced peroxide to be fully reduced to water before exiting the catalyst layer, or a higher probability of being decomposed via a non-electrochemical disproportionation reaction. Nevertheless, the low apparent production of peroxide species by the mesoporous Fe,N-doped carbon catalyst at high potentials results in improved electrocatalytic stability, which was evaluated by comparing oxygen reduction activities before and after potential cycling. As shown in Supporting Information, Figure S2.7, after 5000 cyclic voltammetry scans, the commercially available Pt/C catalysts manifested a 34 mV decrease in the half-wave potential, whereas the mesoporous Fe,N-doped carbon catalysts exhibited a much lower 16 mV decrease in half-wave potential. The smaller decrease in half-wave potential for the mesoporous Fe,N-doped carbon reflects its higher catalytic stability compared to Pt/C, which can be attributed to the low apparent peroxide formation, as well as the highly graphitic property of the mesoporous Fe,N-doped carbon catalysts.

Mesoporous Fe,N-doped carbon catalysts also exhibited excellent alcohol tolerance versus platinum catalyst alternatives. For example, methanol in direct methanol fuel cells (DMFCs) diffuses from the anode to the cathode and is oxidized on Pt-based cathode catalysts, reducing the power output of DMFCs, especially at high voltages.[70] Therefore, high methanol rejection is desirable for ion-conduction membranes, which typically increase the cost of these fuel

cells. The effects of methanol presence were examined for Pt/C and mesoporous Fe,N-doped carbon catalysts by acquiring polarization curves under 0.1 M NaOH without and with 0.5 M methanol, as shown in Supporting Information, Figures S2.8a,b, respectively. Pt/C catalysts are well known for catalyzing methanol oxidation at the potentials typical of the DMFC cathode operation, and show a significant (~360 mV) decrease in their half-wave potentials in the presence of methanol. By comparison, mesoporous Fe,N-doped carbon catalysts show almost identical polarization curves with and without 0.5 M methanol (~10 mV decrease in half-wave potential), significantly reducing the potentially detrimental effect of methanol fuel crossover. The high oxygen reduction activity, stability, and selectivity of melamine-formaldehyde-derived mesoporous Fe,N-doped carbon catalysts prepared by pyrolysis and additional treatments suggest that they can reduce the cost of PEFCs by both replacing expensive Pt catalysts and also lowering requirements for fuel cell membranes.

2.5 Conclusions

The synthesis, characterization, and electrocatalytic properties of mesoporous Fe and N-doped carbon materials are reported and compared for the catalyzed reduction of oxygen gas at fuel cell cathodes. Melamine, an inexpensive organic precursor with high N content, formaldehyde, and transition-metal salts (iron or nickel nitrate salts) were pyrolyzed within a mesoporous silica template to yield mesoporous carbon materials. The transition-metal-doped carbons showed high mesoporosities with narrow pore-size distributions (centered at 3.8 nm), which are expected to lead to lower mass transport resistance within the pores and improve accessibility to surface active species. Incorporation of Fe or Ni nitrate salts during synthesis resulted in higher extents of graphitization compared to other materials prepared by pyrolysis of small molecules. The highly graphitic properties, which include high thermal and chemical stabilities, as well as high electrical conductivity, proved favorable for electrode materials. Specifically, after optimizing surface compositions and Fe loadings, mesoporous Fe,N-doped carbon materials showed high oxygen reduction electrocatalytic activity under alkaline conditions with onset and half-wave potentials that are comparable to those of Pt/C catalysts. XPS analyses revealed that the catalysts prepared under optimized synthesis conditions have ~3 atom% surface oxygen and ~4 atom% surface nitrogen species, with most of the nitrogen atoms present in pyridinic or graphitic nitrogen moieties, which were correlated with ORR active sites. Correlation of ORR activity with the relative populations of these nitrogenous moieties provided insights into catalytically active sites of N-doped carbon materials. The favorable oxygen reduction properties of mesoporous Fe,N-doped carbon catalysts make them attractive in diverse electrochemical applications.

2.6 Future Directions

The understanding from this material and studies provided us valuable information on how material synthesis and modification processes correlate with increased reduction properties. Although highly effective catalyst materials, the Fe-doped melamine-formaldehyde-derived mesoporous carbons were generally unsuitable for examination by NMR methods due to their high conductivities and relatively low (2-4 atom%) nitrogen contents. Therefore, the Fe-doped melamine-formaldehyde-derived mesoporous carbons were not the most conducive material to study and advance my area of expertise, which is to provide atomic-level understanding to iterate and optimize this alternative energy conversion system. For these reasons, we took all the valuable knowledge that we learned from this system type and moved to another N-carbon system which was discussed in chapters 3, 4, and 5. Thus, as a future direction I suggest studying the cyclohexanehexone-urea derived N-carbon systems as we my primary system of focus.

2.7 References

(1) Jacobson, M. Z.; Colella, W. G.; Golden, D. M. Cleaning the Air and Improving Health with Hydrogen Fuel-Cell Vehicles. *Science* **2005**, *308*, 1901–1905.

(2) Schultz, M. G.; Diehl, T.; Brasseur, G. P.; Zittel, W. Air Pollution and Climate-Forcing Impacts of a Global Hydrogen Economy. *Science* **2003**, *302*, 624–627.

(3) Gewirth, A. A.; Thorum, M. S. Electroreduction of Dioxygen for Fuel-Cell Applications: Materials and Challenges. *Inorg. Chem.* **2010**, *49*, 3557–3566.

(4) Strickler, A. L.; Jackson, A.; Jaramillo, T. F. Active and Stable Ir@Pt Core–Shell Catalysts for Electrochemical Oxygen Reduction. *ACS Energy Lett.* **2017**, *2*, 244–249.

(5) Wang, J.-T.; Wasmus, S.; Savinell, R. F. Real-Time Mass Spectrometric Study of the Methanol Crossover in a Direct Methanol Fuel Cell. *J. Electrochem. Soc.* **1996**, *143*, 1233–1239.

(6) Gurau, B.; Smotkin, E. S. Methanol Crossover in Direct Methanol Fuel Cells: A Link between Power and Energy Density. *J. Power Sources* **2002**, *112*, 339–352.

(7) Wu, G.; More, K. L.; Johnston, C. M.; Zelenay, P. High-Performance Electrocatalysts for Oxygen Reduction Derived from Polyaniline, Iron, and Cobalt. *Science* **2011**, *332*, 443–447.

(8) Li, Q.; Cao, R.; Cho, J.; Wu, G. Nanocarbon Electrocatalysts for Oxygen Reduction in Alkaline Media for Advanced Energy Conversion and Storage. *Adv. Energy Mater.* **2014**, *4*, 1301415.

(9) Tylus, U.; Jia, Q.; Strickland, K.; Ramaswamy, N.; Serov, A.; Atanassov, P.; Mukerjee, S. Elucidating Oxygen Reduction Active Sites in Pyrolyzed Metal−Nitrogen Coordinated Non-Precious-Metal Electrocatalyst Systems. *J. Phys. Chem. C* **2014**, *118*, 8999−9008.

(10) Zhang, M.; Dai, L. Carbon Nanomaterials as Metal-Free Catalysts in Next Generation Fuel Cells. *Nano Energy* **2012**, *1*, 514–517.

(11) Gong, K.; Du, F.; Xia, Z.; Durstock, M.; Dai, L. Nitrogen-Doped Carbon Nanotube Arrays with High Electrocatalytic Activity for Oxygen Reduction. *Science* **2009**, *323*, 760–764.

(12) Sebastián, D.; Serov, A.; Matanovic, I.; Artyushkova, K.; Atanassov, P.; Aricò, A. S.; Baglio, V. Insights on the Extraordinary Tolerance to Alcohols of Fe-N-C Cathode Catalysts in Highly Performing Direct Alcohol Fuel Cells. *Nano Energy* **2017**, *34*, 195–204.

(13) Yang, W.; Fellinger, T.-P.; Antonietti, M. Efficient Metal-Free Oxygen Reduction in Alkaline Medium on High-Surface-Area Mesoporous Nitrogen-Doped Carbons Made from Ionic Liquids and Nucleobases. *J. Am. Chem. Soc.* **2011**, *133*, 206–209.

(14) Nallathambi, V.; Leonard, N.; Kothandaraman, R.; Barton, S. C. Nitrogen Precursor Effects in Iron-Nitrogen-Carbon Oxygen Reduction Catalysts. *Electrochem. Solid-State Lett.* **2011**, *14*, B55–B58.

(15) Wu, G.; Zelenay, P. Nanostructured Nonprecious Metal Catalysts for Oxygen Reduction Reaction. *Acc. Chem. Res.* **2013**, *46*, 1878–1889.

(16) Ganesan, S.; Leonard, N.; Barton, S. C. Impact of Transition Metal on Nitrogen Retention and Activity of Iron–Nitrogen–Carbon Oxygen Reduction Catalysts. *Phys. Chem. Chem. Phys.* **2014**, *16*, 4576–4585.

(17) Dombrovskis, J. K.; Palmqvist, A. E. C. One-Pot Synthesis of Transition Metal Ion-Chelating Ordered Mesoporous Carbon/Carbon Nanotube Composites for Active and Durable Fuel Cell Catalysts. *J. Power Sources* **2017**, *357*, 87–96.

(18) Dorjgotov, A.; Ok, J.; Jeon, Y.; Yoon, S. H.; Shul, Y. G. Activity and Active Sites of Nitrogen-Doped Carbon Nanotubes for Oxygen Reduction Reaction. *J. Appl. Electrochem.* **2013**, *43*, 387–397.

(19) Gumeci, C.; Leonard, N.; Liu, Y.; McKinney, S.; Halevi, B.; Barton, S. C. Effect of Pyrolysis Pressure on Activity of Fe–N–C Catalysts for Oxygen Reduction. *J. Mater. Chem. A* **2015**, *3*, 21494–21500.

(20) Tran, T.-N.; Song, M. Y.; Singh, K. P.; Yang, D.-S.; Yu, J.-S. Iron–polypyrrole Electrocatalyst with Remarkable Activity and Stability for ORR in Both Alkaline and Acidic Conditions: A Comprehensive Assessment of Catalyst Preparation Sequence. *J. Mater. Chem. A* **2016**, *4*, 8645–8657.

(21) Lai, L.; Potts, J. R.; Zhan, D.; Wang, L.; Poh, C. K.; Tang, C.; Gong, H.; Shen, Z.; Lin, J.; Ruoff, R. S. Exploration of the Active Center Structure of Nitrogen-Doped Graphene-Based Catalysts for Oxygen Reduction Reaction. *Energy Environ. Sci.* **2012**, *5*, 7936–7942.

(22) Liu, R.; Wu, D.; Feng, X.; Müllen, K. Nitrogen-Doped Ordered Mesoporous Graphitic

Arrays with High Electrocatalytic Activity for Oxygen Reduction. *Angew. Chemie - Int. Ed.* **2010**, *49*, 2565–2569.

(23) Kundu, S.; Nagaiah, T. C.; Xia, W.; Wang, Y.; Dommele, S. Van; Bitter, J. H.; Santa, M.; Grundmeier, G.; Bron, M.; Schuhmann, W.; Muhler, M. Electrocatalytic Activity and Stability of Nitrogen-Containing Carbon Nanotubes in the Oxygen Reduction Reaction. *J. Phys. Chem. C* **2009**, *113*, 14302–14310.

(24) Wu, J.; Ma, L.; Yadav, R. M.; Yang, Y.; Zhang, X.; Vajtai, R.; Lou, J.; Ajayan, P. M. Nitrogen-Doped Graphene with Pyridinic Dominance as a Highly Active and Stable Electrocatalyst for Oxygen Reduction. *ACS Appl. Mater. Interfaces* **2015**, *7*, 14763–14769.

(25) Chung, H. T.; Won, J. H.; Zelenay, P. Active and Stable Carbon Nanotube/Nanoparticle Composite Electrocatalyst for Oxygen Reduction. *Nat. Commun.* **2013**, *4*, 1922.

(26) Wu, Z.; Yang, S.; Sun, Y.; Parvez, K.; Feng, X.; Müllen, K. 3D Nitrogen-Doped Graphene Aerogel-Supported Fe_3O_4 Nanoparticles as Efficient Electrocatalysts for the Oxygen Reduction Reaction. *J. Am. Chem. Soc.* **2012**, *134*, 9082–9085.

(27) Lin, Z.; Song, M.; Ding, Y.; Liu, Y.; Liu, M.; Wong, C. Facile Preparation of Nitrogen-Doped Graphene as a Metal-Free Catalyst for Oxygen Reduction Reaction. *Phys. Chem. Chem. Phys.* **2012**, *14*, 3381–3387.

(28) Chung, H. T.; Cullen, D. A.; Higgins, D.; Sneed, B. T.; Holby, E. F.; More, K. L.; Zelenay, P. Direct Atomic-Level Insight into the Active Sites of a High-Performance PGM-Free ORR Catalyst. *Science* **2017**, *357*, 479–484.

(29) Lee, J. S.; Park, G. S.; Kim, S. T.; Liu, M.; Cho, J. A Highly Efficient Electrocatalyst for the Oxygen Reduction Reaction: N-Doped Ketjenblack Incorporated into Fe/Fe_3C-Functionalized Melamine Foam. *Angew. Chemie - Int. Ed.* **2013**, *52*, 1026–1030.

(30) Nishihara, H.; Kyotani, T. Templated Nanocarbons for Energy Storage. *Adv. Mater.* **2012**, *24*, 4473–4498.

(31) Paraknowitsch, B. J. P.; Zhang, J.; Su, D.; Thomas, A.; Antonietti, M. Ionic Liquids as Precursors for Nitrogen-Doped Graphitic Carbon. *Adv. Mater.* **2010**, *22*, 87–92.

(32) Lee, K.; Ji, X.; Rault, M.; Nazar, L. F. Simple Synthesis of Graphitic Ordered Mesoporous Carbon Materials by a Solid-State Method Using Metal Phthalocyanines. *Angew. Chemie - Int. Ed.* **2009**, *48*, 5661–5665.

(33) Tang, Y.; Allen, B. L.; Kauffman, D. R.; Star, A. Electrocatalytic Activity of Nitrogen-Doped Carbon Nanotube Cups. *J. Am. Chem. Soc.* **2009**, *131*, 13200–13201.

(34) Sheng, Z.; Shao, L.; Chen, J.; Bao, W.; Wang, F.; Xia, X. Catalyst-Free Synthesis of Nitrogen-Doped Graphene via Thermal Annealing Graphite Oxide with Melamine and Its Excellent Electrocatalysis. *ACS Nano* **2011**, *5*, 4350–4358.

(35) Joo, S. H.; Choi, S. J.; Oh, I.; Kwak, J.; Liu, Z.; Terasaki, O.; Ryoo, R. Ordered Nanoporous Arrays of Carbon Supporting High Dispersions of Platinum Nanoparticles. *Nature* **2001**, *412*, 169–172.

(36) Gu, D.; Li, W.; Wang, F.; Bongard, H.; Spliethoff, B.; Schmidt, W.; Weidenthaler, C.; Xia, Y.; Zhao, D.; Schüth, F. Controllable Synthesis of Mesoporous Peapod-like Co_3O_4@Carbon Nanotube Arrays for High-Performance Lithium-Ion Batteries.

Angew. Chemie - Int. Ed. **2015**, *54*, 7060–7064.

(37) Zhang, S.; Miran, M. S.; Ikoma, A.; Dokko, K.; Watanabe, M. Protic Ionic Liquids and Salts as Versatile Carbon Precursors. *J. Am. Chem. Soc.* **2014**, *136*, 1690–1693.

(38) Zhao, D.; Huo, Q.; Feng, J.; Chmelka, B. F.; Stucky, G. D. Nonionic Triblock and Star Diblock Copolymer and Oligomeric Surfactant Syntheses of Highly Ordered, Hydrothermally Stable, Mesoporous Silica Structures. *J. Am. Chem. Soc.* **1998**, *120*, 6024–6036.

(39) Jang, J.; Oh, J. H.; Stucky, G. D. Fabrication of Ultrafine Conducting Polymer and Graphite Nanoparticles. *Angew. Chemie - Int. Ed.* **2002**, *41*, 4016–4019.

(40) Ryoo, R.; Joo, S. H.; Jun, S. Synthesis of Highly Ordered Carbon Molecular Sieves via Template-Mediated Structural Transformation. *J. Phys. Chem. B* **1999**, *103*, 7743–7746.

(41) Brunauer, S.; Emmett, P. H.; Teller, E. Adsorption of Gases in Multimolecular Layers. *J. Am. Chem. Soc.* **1938**, *60*, 309–319.

(42) Barrett, E. P.; Joyner, L. G.; Halenda, P. P. The Determination of Pore Volume and Area Distributions in Porous Substances. I. Computations from Nitrogen Isotherms. *J. Am. Chem. Soc.* **1951**, *73*, 373–380.

(43) Bagreev, A.; Menendez, J. A.; Dukhno, I.; Tarasenko, Y.; Bandosz, T. J. Bituminous Coal-Based Activated Carbons Modified with Nitrogen as Adsorbents of Hydrogen Sulfide. *Carbon* **2004**, *42*, 469–476.

(44) Paulus, U. A.; Schmidt, T. J.; Gasteiger, H. A.; Behm, R. J. Oxygen Reduction on a

High-Surface Area Pt/Vulcan Carbon Catalyst: A Thin-Film Rotating Ring-Disk Electrode Study. *J. Electroanal. Chem.* **2001**, *495*, 134–145.

(45) Keely, W. M.; Maynor, H. W. Thermal Studies of Nickel, Cobalt, Iron and Copper Oxides and Nitrates. *J. Chem. Eng. Data* **1963**, *8*, 297–300.

(46) Manley, T. R.; Higgs, D. A. Thermal Stability of Melamine Formaldehyde Resins. *J. Polym. Sci. Polym. Symp.* **1973**, *42*, 1377–1382.

(47) Liu, J.; Sun, X.; Song, P.; Zhang, Y.; Xing, W.; Xu, W. High-Performance Oxygen Reduction Electrocatalysts Based on Cheap Carbon Black, Nitrogen, and Trace Iron. *Adv. Mater.* **2013**, *25*, 6879–6883.

(48) Sing, K. S. W.; Everett, D. H.; Haul, R. A. W.; Moscou, L.; Pierotti, R. A.; Rouquérol, J.; Siemieniewska, T. Reporting Physisorption Data for Gas/Solid Systems with Special Reference to the Determination of Surface Area and Porosity. *Pure Appl. Chem.* **1985**, *57*, 603–619.

(49) Jun, S.; Joo, S. H.; Ryoo, R.; Kruk, M.; Jaroniec, M.; Liu, Z.; Ohsuna, T.; Terasaki, O. Synthesis of New, Nanoporous Carbon with Hexagonally Ordered Mesostructure. *J. Am. Chem. Soc.* **2000**, *122*, 10712–10713.

(50) Zhu, J.; Xu, Y.; Zhang, Y.; Feng, T.; Wang, J.; Mao, S.; Xiong, L. Porous and High Electronic Conductivity Nitrogen-Doped Nano-Sheet Carbon Derived from Polypyrrole for High-Power Supercapacitors. *Carbon* **2016**, *107*, 638–645.

(51) Gao, W.; Wan, Y.; Dou, Y.; Zhao, D. Synthesis of Partially Graphitic Ordered Mesoporous Carbons with High Surface Areas. *Adv. Energy Mater.* **2011**, *1*, 115–123.

(52) Chen, W.; Pan, X.; Bao, X. Tuning of Redox Properties of Iron and Iron Oxides via Encapsulation within Carbon Nanotubes. *J. Am. Chem. Soc.* **2007**, *129*, 7421–7426.

(53) Tuinstra, F.; Koenig, L. Raman Spectrum of Graphite. *J. Chem. Phys.* **1970**, *53*, 1126–1130.

(54) Ramm, M.; Ata, M.; Brzezinka, K.; Gross, T.; Unger, W. Studies of Amorphous Carbon Using X-Ray Photoelectron Spectroscopy, near-Edge X-Ray-Absorption Fine Structure and Raman Spectroscopy. *Thin Solid Films* **1999**, *354*, 106–110.

(55) Dippel, B.; Jander, H.; Heintzenberg, J. NIR FT Raman Spectroscopic Study of Flame Soot. *Phys. Chem. Chem. Phys.* **1999**, *1*, 4707–4712.

(56) Sadezky, A.; Muckenhuber, H.; Grothe, H.; Niessner, R.; Pöschl, U. Raman Microspectroscopy of Soot and Related Carbonaceous Materials: Spectral Analysis and Structural Information. *Carbon* **2005**, *43*, 1731–1742.

(57) Lee, J.; Yoon, S.; Hyeon, T.; Oh, S. M.; Kim, K. B. Synthesis of a New Mesoporous Carbon and Its Application to Electrochemical Double-Layer Capacitors. *Chem. Commun.* **1999**, 2177–2178.

(58) Wei, D.; Liu, Y.; Wang, Y.; Zhang, H.; Huang, L.; Yu, G. Synthesis of N-Doped Graphene by Chemical Vapor Deposition and Its Electrical Properties. *Nano Lett.* **2009**, *9*, 1752–1758.

(59) Ferrandon, M.; Kropf, A. J.; Myers, D. J.; Artyushkova, K.; Kramm, U.; Bogdano, P.; Wu, G.; Johnston, C. M.; Zelenay, P. Multitechnique Characterization of a Polyaniline − Iron − Carbon Oxygen Reduction Catalyst. *J. Phys. Chem. C* **2012**, *116*, 16001–

16013.

(60) Othman, R.; Dicks, A. L.; Zhu, Z. Non Precious Metal Catalysts for the PEM Fuel Cell Cathode. *Int. J. Hydrogen Energy* **2012**, *37*, 357–372.

(61) Li, Y.; Zhou, W.; Wang, H.; Xie, L.; Liang, Y.; Wei, F.; Idrobo, J.-C.; Pennycook, S. J.; Dai, H. An Oxygen Reduction Electrocatalyst Based on Carbon Nanotube–graphene Complexes. *Nat. Nanotechnol.* **2012**, *7*, 394–400.

(62) Faubert, G.; Côté, R.; Dodelet, J.-P.; Lefèvre, M.; Bertrand, P. Oxygen Reduction Catalysts for Polymer Electrolyte Fuel Cells from the Pyrolysis of Fe^{II} Acetate Adsorbed on 3,4,9,10-Perylenetetracarboxylic Dianhydride. *Electrochim. Acta* **1999**, *44*, 2589–2603.

(63) Ikeda, T.; Boero, M.; Huang, S. F.; Terakura, K.; Oshima, M.; Ozaki, J. Carbon Alloy Catalysts: Active Sites for Oxygen Reduction Reaction. *J. Phys. Chem. C* **2008**, *112*, 14706–14709.

(64) Yang, W.; Liu, X.; Yue, X.; Jia, J.; Guo, S. Bamboo-like Carbon nanotube/Fe_3C Nanoparticle Hybrids and Their Highly Efficient Catalysis for Oxygen Reduction. *J. Am. Chem. Soc.* **2015**, *137*, 1436–1439.

(65) Buan, M. E. M.; Muthuswamy, N.; Walmsley, J. C.; Chen, D.; Rønning, M. Nitrogen-Doped Carbon Nanofibers on Expanded Graphite as Oxygen Reduction Electrocatalysts. *Carbon* **2016**, *101*, 191–202.

(66) Yang, D.-S.; Song, M. Y.; Singh, K. P.; Yu, J.-S. The Role of Iron in the Preparation and Oxygen Reduction Reaction Activity of Nitrogen-Doped Carbon. *Chem. Commun.*

2015, *51*, 2450–2453.

(67) Qian, Y.; Du, P.; Wu, P.; Cai, C.; Gervasio, D. F. Chemical Nature of Catalytic Active Sites for the Oxygen Reduction Reaction on Nitrogen-Doped Carbon-Supported Non-Noble Metal Catalysts. *J. Phys. Chem. C* **2016**, *120*, 9884–9896.

(68) Osmieri, L.; Monteverde Videla, A. H. A.; Armandi, M.; Specchia, S. Influence of Different Transition Metals on the Properties of Me–N–C (Me = Fe, Co, Cu, Zn) Catalysts Synthesized Using SBA-15 as Tubular Nano-Silica Reactor for Oxygen Reduction Reaction. *Int. J. Hydrogen Energy* **2016**, *41*, 22570–22588.

(69) Banham, D.; Ye, S.; Pei, K.; Ozaki, J.-I.; Kishimoto, T.; Imashiro, Y. A Review of the Stability and Durability of Non-Precious Metal Catalysts for the Oxygen Reduction Reaction in Proton Exchange Membrane Fuel Cells. *J. Power Sources* **2015**, *285*, 334–348.

(70) Chu, Y. H.; Shul, Y. G. Alcohol Crossover Behavior in Direct Alcohol Fuel Cells (DAFCs) System. *Fuel Cells* **2012**, *12*, 109–115.

2.8 Supporting Information

2.8.1 Supporting Information – Tables

Table S2.1. Near-surface elemental compositions of cross-linked and pyrolyzed melamine-formaldehyde resin measured by integrating the peaks of survey X-ray photoelectron spectra

Materials	*Near-surface composition (atom %)*			*N/C ratio*
	C	N	O	
Melamine-formaldehyde resin	46	43	12	0.93
Pyrolyzed (900 °C)	90	4	6	0.04

Table S2.2. Electrical conductivity of mesoporous carbon materials prepared from different precursors

Carbon materials	*Apparent conductivity* [a] *(S/cm)*
Conventional mesoporous carbon[b]	4.6
Mn,N-doped mesoporous carbon[c]	7
Co,N-doped mesoporous carbon[c]	10
Ni,N-doped mesoporous carbon[c]	17
Fe,N-doped mesoporous carbon[c]	19
Graphite powder[d]	98

[a] Electrical conductivities were measured with an impedance analyzer, while the samples were pressed at 70 MPa.

[b] Conventional mesoporous carbon material synthesized with phenol-formaldehyde resin, according to the process of Lee, et al., *Chem. Commun.* **1999**, 2177.

[c] Synthesized with a transition metal/melamine mole ratio of 0.1.

[d] Commercially available graphite powder (non-porous, Sigma-Aldrich); this value is lower than the conductivity of single crystal graphite (3×10^5 S/cm along to the basal planes and 3×10^2 S/cm normal to the basal planes), due to contact resistances between particles.

Table S2.3. Near-surface elemental compositions of Fe,N-doped mesoporous carbon catalysts synthesized with an iron nitrate-to-melamine molar ratio of 0.10 after different post-synthesis treatments.[a]

Treatments	*Near-surface composition* [b] *(atom %)*				
	C	N	O	Fe	Si
Precursor composite materials	47	31	18	0.2	3
Pyrolysis (900 °C, 6 h)	76	5	13	0.3	6
As-synthesized mesoporous carbon	81	4	14	0.7	0.7
Acid treatment (0.5 M H_2SO_4)	82	4	14	0.1	0.6
Additional pyrolysis (900 °C, 1 h)	93	4	3	0.2	0.1

[a] The effects of the different post-synthesis treatments on material performance are shown in Figure 2.6 and Table 2.1.

[b] Near-surface compositions were measured by integrating the peaks of survey X-ray photoelectron spectra.

Table S2.4. Relative amounts of different types of nitrogen-species in Fe,N-doped mesoporous carbon catalysts synthesized with an iron nitrate-to-melamine molar ratio of 0.10, after different post-synthesis treatments.[a]

Treatments	*Relative amounts* [b] *(atom %)*			
	nitroxide (402-405 eV)	graphitic N (401.3 eV)	pyrrolic N + pyridonic N (400.5 eV)	pyridinic N (398.6 eV)
As-synthesized mesoporous carbon	5	8	35	52
Acid treatment (0.5 M H_2SO_4)	3	10	39	48
Additional pyrolysis (900 °C, 1 h)	6	33	10	51

[a] The effects of the different post-synthesis treatments on material performance are shown in Figure 2.6 and Table 2.1.

[b] Relative amounts of nitrogen species were measured by deconvoluting the high-resolution nitrogen X-ray photoelectron spectra shown in Figure 2.7.

Table S2.5. Comparisons of alkaline ORR performance parameters of the Fe,N-doped mesoporous carbon material presented here with other recent reports.

Reference	*Solution*	*ORR catalyst*	*Onset Potential*	*Half-Wave Potential*	*Tafel Slope*
			[V *vs.* RHE]	[V *vs.* RHE]	mV/decade
Kim *et al.* (this paper)	0.1 M NaOH	Fe,N-doped mesoporous carbon	1.04	0.87	53
		20 wt% Pt/C Catalyst	1.04	0.85	67
Osmieri *et al.*, *Int. J. Hydrog. Energy* **2016**, *41*, 22570	0.1 M KOH	Fe-N-C	0.98	0.87	63.2
		20 wt% Pt/C (QuinTech)	1.00	0.89	67.5/116
Tran, et al., *J. Mater. Chem. A* **2016**, *4*, 8645	0.1 M KOH	FePPyC-900	0.96	0.88	95
		Tanaka 20 wt% Pt/C	0.96	0.84	106
Yang, et al., *Chem. Commun.* **2015**, *51*, 2450	0.1 M KOH	N-OMC(FePc)	1.01	0.91	61
		Pt/C catalyst	1.04	0.96	68

2.8.2 Supporting Information – Figures

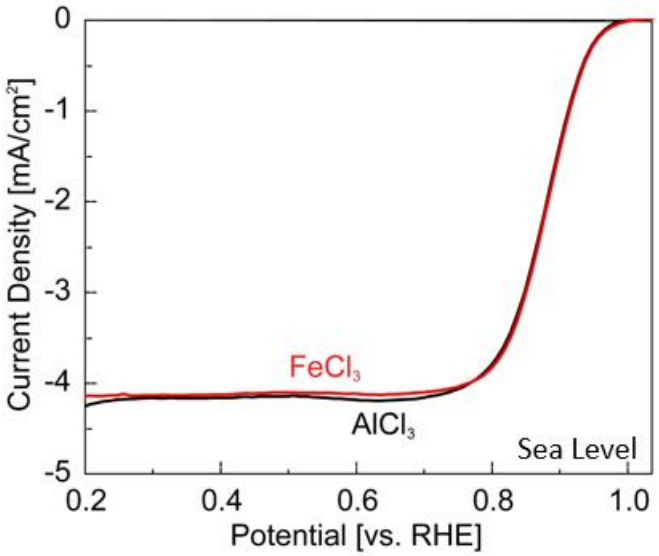

Figure S2.1. Polarization curves of Fe,N-doped mesoporous carbon materials prepared by grafting mesoporous silica with $FeCl_3$ (red) or with $AlCl_3$ (black), showing plots of the current density measured as a function of applied potential (*vs*. RHE). Negligible differences are observed for the $FeCl_3$- versus $AlCl_3$-grafted materials. Note: these data were acquired at sea level at UCSB and exhibit moderately higher limiting currents, compared to data acquired at Los Alamos National Laboratory at 2230 m, where the partial pressure of oxygen is lower.

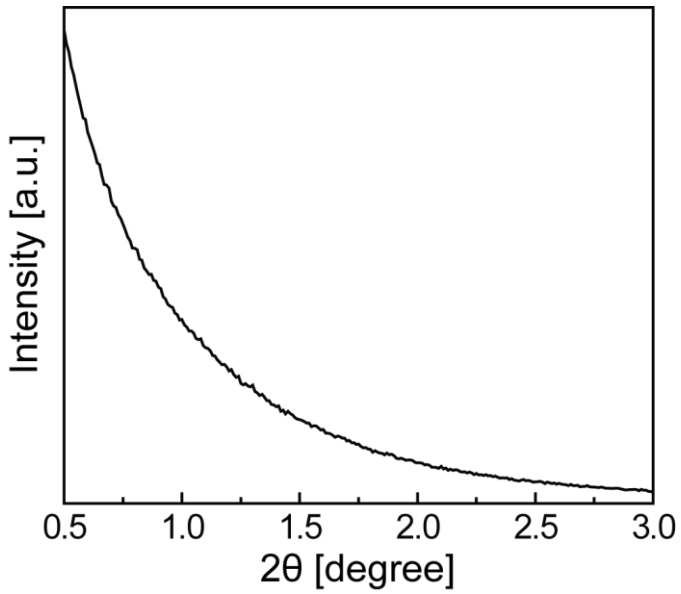

Figure S2.2. Small-angle X-ray scattering pattern of the Fe,N-doped mesoporous carbon material synthesized from melamine-formaldehyde resin with iron nitrate (0.05 iron nitrate-to-melamine mole ratio). No distinct reflections are observed, establishing that the material does not have a long-range mesoscopic order. The sample is the same as used in Figure 2.3. The relationship between the complicated resin-decomposition chemistry during pyrolysis and whether and how the replica mesoporous carbon posts may be connected to maintain mesostructural order and mechanical integrity, especially after dissolution of the mesoporous silica template, are unknown and difficult to characterize.

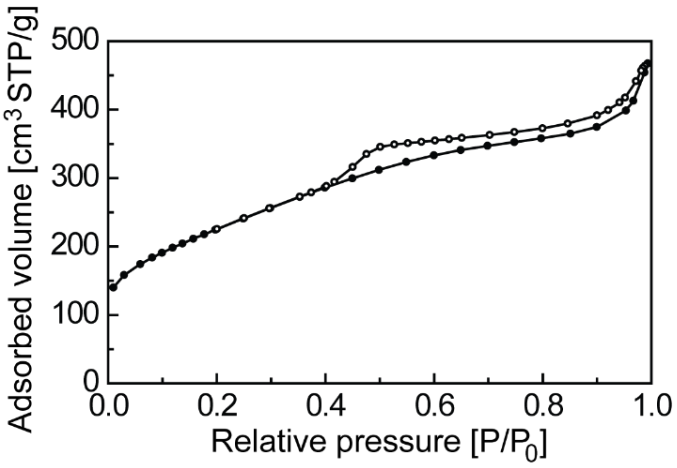

Figure S2.3. Nitrogen sorption isotherm at 77 K for the Fe,N-doped mesoporous carbon material whose SAXS pattern is shown in Figure S2.1, which exhibits Type IV behavior with H_2 hysteresis that indicates the presence of both mesoporosity and microporosity, as described in Sing, et al., *Pure Appl. Chem.* **1985**, *57*, 603. This material was synthesized with an iron nitrate-to-melamine mole ratio of 0.05.

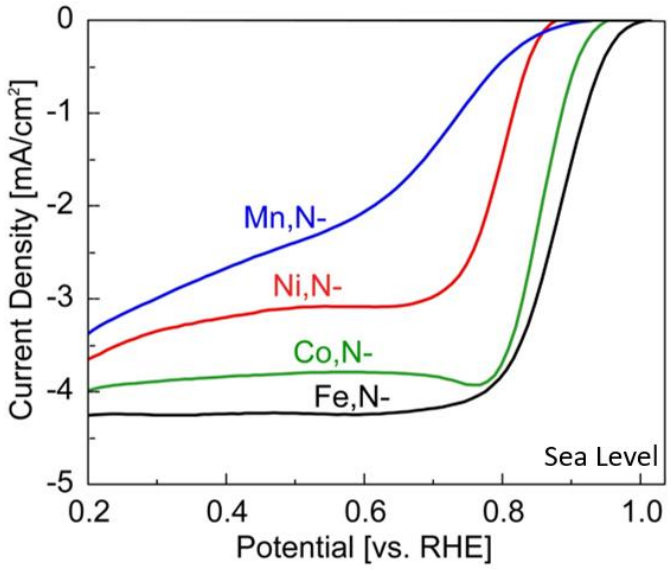

Figure S2.4. Polarization curves acquired from linear sweep voltammetry measurements of Mn,N-, Ni,N-, Co,N-, and Fe,N-doped mesoporous carbon catalysts synthesized with a 0.05 molar ratio of metal nitrate-to-melamine, showing plots of the current densities of the respective materials as functions of the applied potential (*vs.* RHE). The Fe,N-doped mesoporous carbon catalyst exhibits the largest limiting current, greatest onset potential, and greatest half-wave potential, indicating superior electrochemical ORR activity. Note: These data were acquired at sea level at UCSB and exhibit moderately higher limiting currents, compared to data acquired at Los Alamos National Laboratory at 2230 m where the partial pressure of oxygen is lower.

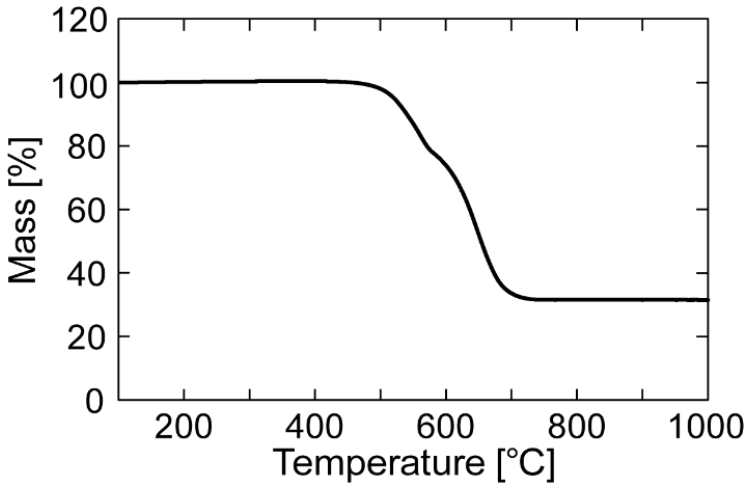

Figure S2.5. Thermogravimetric analysis plot acquired under dry air for Fe,N-doped mesoporous carbon prepared with an initial Fe/melamine mole ratio of 0.20. During heating, two regions of mass loss are observed at ca. 500 °C and 600 °C, which are attributed to combustion of disordered and graphitic carbon, respectively, consistent with the results of Fuertes, et al., *J. Mater. Chem.* **2005**, *15*, 1079. Following heating to 1000 °C, the remaining material was measured to be 32% of the initial sample mass and attributed to Fe_2O_3, based on results reported by Maldonado, et al., *J. Phys. Chem. B* **2005**, *109*, 4707 and Wu, et al., *J. Am. Chem. Soc.* **2012**, *134*, 9082. This suggests the initial material was 22% iron by mass.

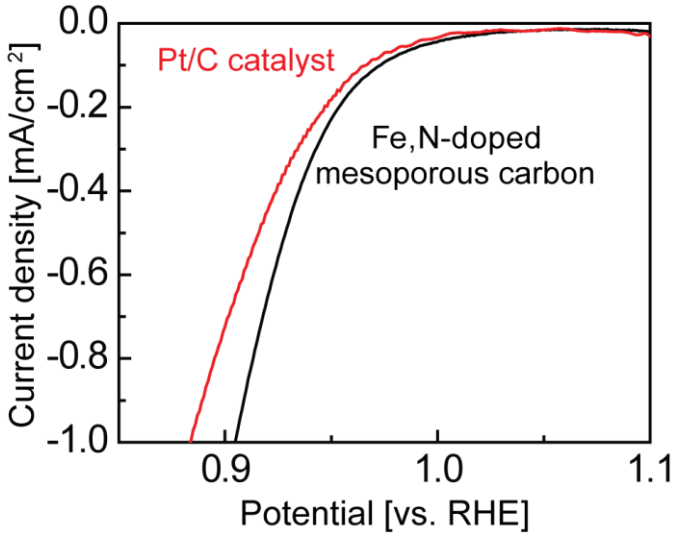

Figure S2.6. High potential region of polarization curves of Fe,N-doped mesoporous carbon and Pt/C catalysts measured at 900 rpm in a 0.1 M NaOH solution. The Fe,N-doped mesoporous carbon catalyst, synthesized with an iron nitrate-to-melamine molar ratio of 0.10, exhibited high oxygen reduction activity, which is established by its high onset potential.

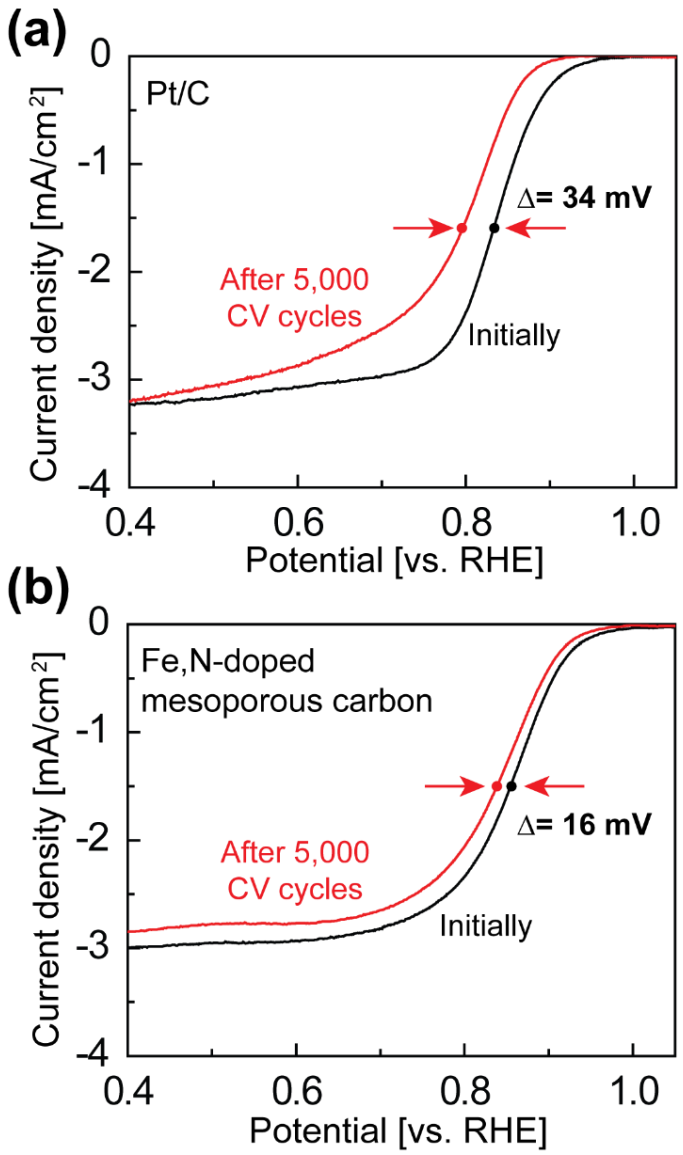

Figure S2.7. Polarization curves acquired from linear sweep voltammetry for (a) Pt/C catalyst and (b) Fe,N-doped mesoporous carbon catalyst synthesized with an iron nitrate-to-melamine molar ratio of 0.10 and with post-synthesis acid and heat treatments before and after 5000 cyclic voltammetry scans between 0.6 and 1.0 V versus RHE. The decrease in half-wave potential for the Pt/C catalyst has been attributed to agglomeration of the Pt nanoparticles, consistent with observations by Borup, et al., *Chem. Rev.* **2007**, *107*, 3904. The small decrease in half-wave potential for the Fe,N-doped mesoporous carbon compares favorably with other

non-precious metal catalysts as reported in Ren, et al., *ACS Appl. Mater. Interfaces* **2016**, *8*, 4118.

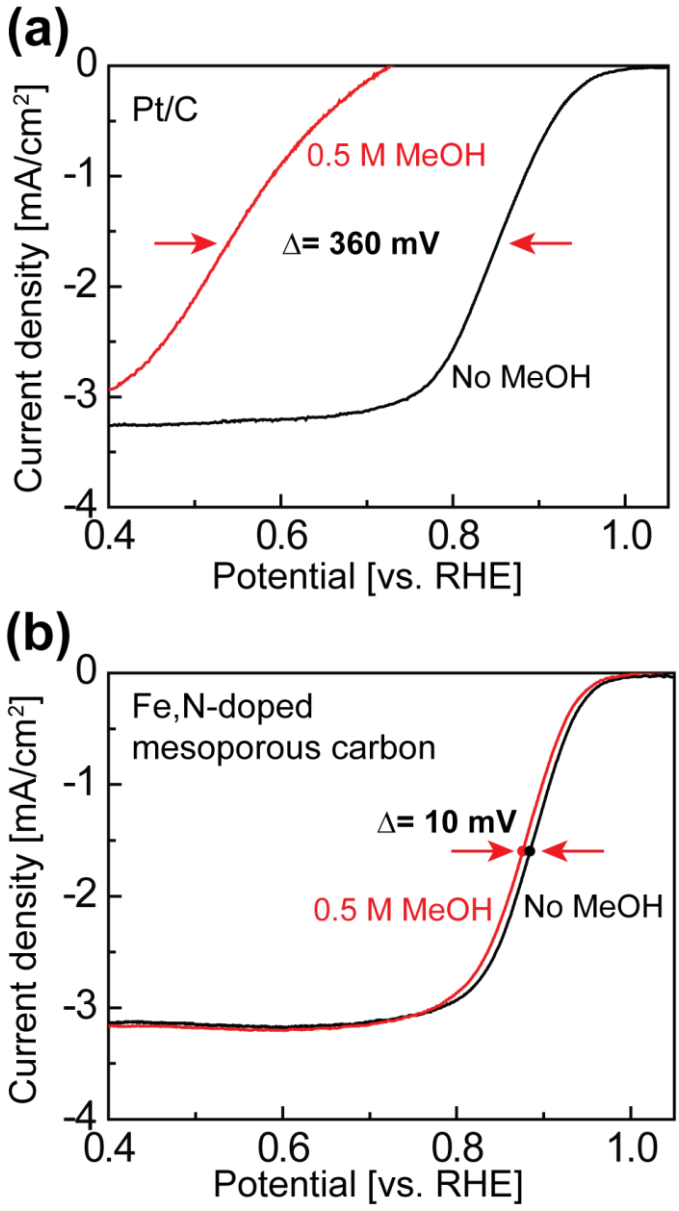

Figure S2.8. Polarization curves acquired from linear sweep voltammetry for (a) a Pt/C catalyst and (b) Fe,N-doped mesoporous carbon catalyst synthesized with an iron nitrate-to-melamine molar ratio of 0.05 and with post-synthesis acid and heat treatments without and

with 0.5 M methanol. Conventional platinum catalysts are versatile in that they show electrochemical activities for many reactions other than oxygen reduction, but often exhibit poor selectivity for specific reactions, such as the ORR, as a consequence. N- and Fe,N-doped carbon catalysts exhibit high ORR selectivity, which is expected to be beneficial to alcohol-based fuel cells. The addition of methanol was associated with a large (360 mV) decrease in half-wave potential of the Pt/C catalyst. By contrast, the negligible 10 mV change observed for the Fe,N-doped carbon catalyst demonstrates its higher selectivity for the ORR in the presence of methanol fuel crossover.

3. Atomic-scale understanding of the oxygen and sulfur reduction activities of mesoporous N-carbon electrocatalysts

This chapter is adapted from a manuscript submitted to *Nature Materials*. I am first author on this paper and am responsible for most of the synthesis, characterization, and electrochemical performance testing, with the exception of DFT calculations by Ziyang Wei and S-reduction testing by Rongli Liu.

Authors: Shona M. Becwar, Zachariah J. Berkson, Niels P. Zussblatt, Ziyang Wei, Nina Fechler, Philipp Selter, Lele Peng, Rongli Liu, Walter Rosas Arbelaez, Anders E. C. Palmqvist, Xiangfeng Duan, Philippe Sautet, and Bradley F. Chmelka

Journal: *Nature Materials*, under review

3.1 Abstract

Mesoporous-N-carbons exhibit high oxygen and sulfur reduction activities that are comparable to or surpass those of activated-carbon-supported-Pt electrocatalysts. Favorable properties include high nitrogen contents (>10 mol%), high fractions of N moieties at surface sites, 3-nm mesopores to promote diffusion, and electron conductivity to surface N environments where reactions occur. The types, quantities, and distributions of N-heteroatom environments (especially those at surface sites) are shown to strongly influence macroscopic

reduction activities. Specifically, solid-state 2D ^{15}N-^{13}C and 1D $^{15}N\{^{1}H\}$ NMR spectroscopy, in combination with X-ray scattering, Raman spectroscopy, and DFT modeling, establish the importance of edge pyridinic moieties, the populations of which depend on synthesis conditions and compositions, including judicious selection of template species that affects the distribution of surface N sites. The analyses correlate the atomic-scale compositions, mesoscale structures, and macroscopic O_2 and sulfur reduction properties of mesoporous N-carbons as promising non-precious-metal cathode electrocatalysts for fuel cells and batteries.

3.2 Introduction

Carbon materials containing nitrogen (N) heteroatoms have received significant attention as inexpensive and environmentally-benign materials for catalytic and electrochemical applications, such as electrodes,[1] electrocatalysts,[2–6] and catalyst supports.[7–10] These materials have been proposed as replacements for costly Pt-based oxygen-reduction (OR) catalysts as cathodes of fuel cells[2,11–14] or metal-air batteries,[15,16] and have recently been shown to catalyze sulfur-reduction (SR) in Li-S batteries.[16–19] Platinum-carbon (Pt/C) catalysts exhibit sluggish and nonselective kinetics for OR,[20] which are often offset by the use of high Pt loadings (20-40 wt%) that significantly increase the costs of electrochemical devices and limit their adoption.[5,20,21] Even though N-carbons exhibit favorable OR and SR properties, they have yet to be widely adopted, due in part to their typically low quantities of active sites (associated with nitrogen contents <4 mol%) and often diffusion-limited kinetics (associated with the sub-nanometer pore dimensions of most activated carbons).

Achieving high-performing N-carbon electrocatalysts requires a combination of material properties that include high electrical conductivities, low molecular diffusion resistances, and

accessible and catalytically active surface moieties.[22] High extents of graphitization tend to increase conductivity, while high nitrogen contents increase the number of active sites. However, the presence of heteroatoms, such as N, often lowers the extent of graphitization.[23] Similarly, high mesopore surface areas increase the number of accessible reaction sites and facilitate diffusion of reactant and product species, but diminish electrical conductivity. These factors must be balanced to provide sufficient electron and reactant transport to surface reaction sites for effective electrocatalytic reduction. Mesoporous N-carbons with both high electrical conductivities (2.0 S/cm) and high N contents (up to 28 wt%) have been reported,[24] however little is known about the atomic-level origins of their electrochemical properties, including OR or SR activities. This has been due to their non-stoichiometric compositions, lack of long-range order, electrical conductivities, and complicated distributions of surface species,[25] which have made them challenging to characterize.

Till now, scattering and spectroscopy techniques have provided insufficient resolution to determine the types, relative quantities, or local structures of heteroatoms in conductive carbon materials. This accounts, in part, for the diversity of nitrogen-containing moieties (e.g., pyrrolic,[26] pyridinic,[27,28] or graphitic[29]) that have been proposed to account for the oxygen and sulfur[18] reduction activities of N-carbon catalysts. By comparison, solid-state nuclear magnetic resonance (NMR) spectroscopy is sensitive to atomic environments in both ordered and disordered regions of a material and can provide significantly enhanced resolution of different N-containing environments. While two-dimensional (2D) NMR has been used to identify local structures of N atoms in diamagnetic solids, e.g., polymers[30] and carbon nitrides[31], electrically conductive N-carbon materials present significant challenges with respect to both sensitivity and resolution.[32] Here, we overcome such challenges to resolve,

identify, and quantify bulk and surface compositions and structures of high N-content mesoporous carbon electrocatalysts, the distributions of which are correlated with their macroscopic OR and SR properties. 2D NMR, in combination with density functional theory (DFT) shielding calculations, enable distinct types of N moieties to be distinguished, among which edge pyridinic species are determined to be important for OR and SR performance.

3.3 Results and Discussion

The reduction activities and stabilities of mesoporous N-carbons depend dramatically on their surface compositions, which are influenced by materials synthesis conditions, in particular the interactions of precursor species with templating agents during pyrolysis. For example, mesoporous N-carbons can be prepared through high-temperature (1073 K) pyrolysis of cyclohexanehexone-octahydrate and urea precursors in the presence of a mesopore templating agent, such as a eutectic mixture of structure-directing $ZnCl_2$-NaCl salts or hexagonal mesoporous SBA–15 silica (Supplementary Figure S3.1).[24] Under otherwise identical synthesis conditions, except for different templating agents, mesoporous N-carbons are obtained with similar bulk compositions and porosities. Specifically, these two templating agents yield N-carbon materials with similar mesopore dimensions (3-4 nm diameter) and mesopore size distributions, as determined by nitrogen sorption (Supplementary Figure S3.2, Table S3.1). The mesopores are large enough to mitigate mass transport limitations associated with the sub-nanometer pore dimensions of conventional activated-carbons.[33–36] The mesoporous silica- and salt-templated N-carbons exhibit similar and modest extents of long-range graphitic order, as evident from their wide- and small-angle X-ray scattering patterns

(Supplementary Figure S3.3a,b) and Raman spectra (Supplementary Figure S3.3c). X-ray photoelectron spectroscopy (XPS) results (Supplementary Figure S3.4, Tables S3.2 and S3.3) establish that the mesoporous N-carbons synthesized using the salt- or mesoporous silica-templates have near-surface N contents of 16 mol% and 22 mol%, respectively (compared to their corresponding bulk N contents of 19 mol% and 28 mol%, respectively, as measured by X-ray fluorescence, Table S3.4). These values are 4-5 times higher than are typical for porous N-carbons and are desirable because surface N moieties are thought to be closely associated with electrocatalytic reduction sites.[32,36]

Template-dependent oxygen and sulfur reduction properties

Despite their similar bulk compositions and mesoscale structures, mesoporous N-carbons prepared with the different mesoporous silica or $ZnCl_2$-NaCl salt templates under otherwise identical conditions exhibit surprisingly different electrocatalytic reduction properties and stabilities. For example, **Figure 3.1a** shows the oxygen reduction polarization curves acquired under acidic conditions for the salt- (green) and silica-templated (purple) N-carbons, which are compared to a standard 20 wt% Pt/C catalyst. The salt-templated N-carbon exhibits a high onset potential of 0.93 V and a large limiting current of 3.8 mA/cm^2 (**Table 3.1**), manifesting a plateau in current density that indicates the potential region in which the catalyst material is performing optimally. The performance of the mesoporous salt-templated N-carbon approaches that of a 20 wt% Pt/C electrode, which exhibits an onset potential of 0.98 V and a similar limiting current. By comparison, the mesoporous silica-templated N-carbon exhibits a significantly lower current density than the salt-templated N-carbon at all potentials examined

and the absence of a limiting current-density plateau. We note the silica-templated N-carbon has a somewhat higher surface N content (22 mol%) and a lower surface area (1100 m^2/g), compared to the salt-templated N-carbon (16 mol%, 1800 m^2/g), properties which are expected to have offsetting influences on overall OR activity and are not different enough to account for the large differences in OR performance. Similar results are obtained for OR by the same catalysts under alkaline conditions, as manifested by polarization curves shown in

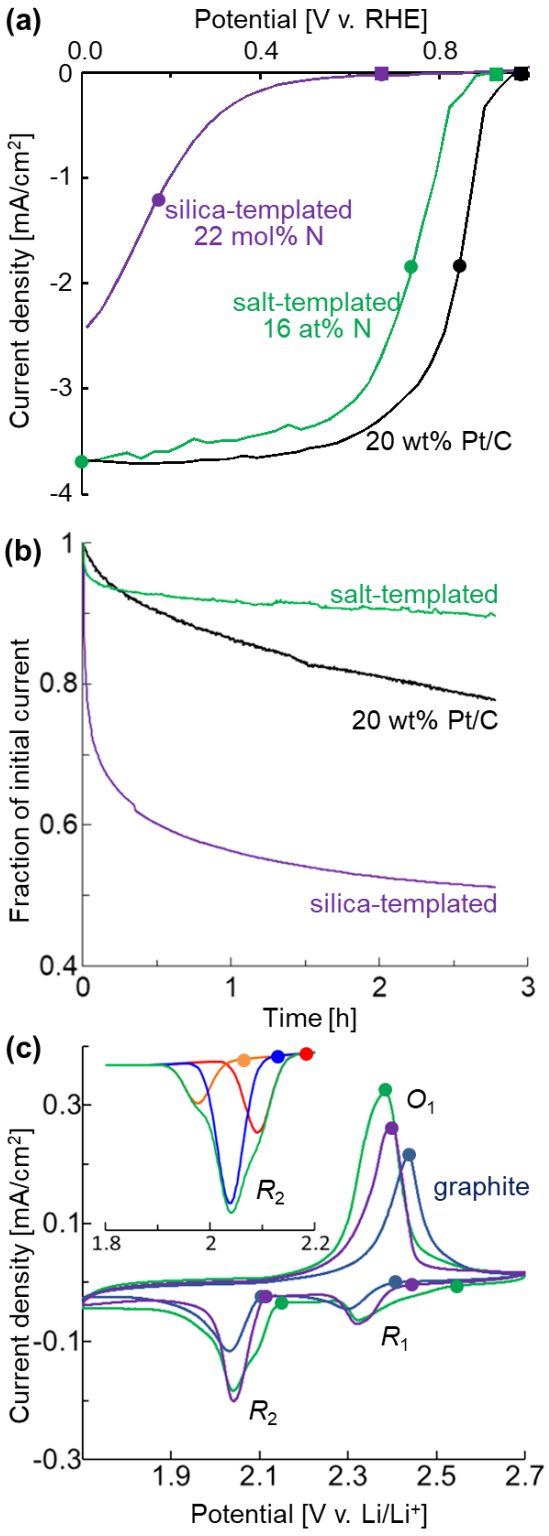

Figure 3.1. Electrocatalytic activity and stability of mesoporous N-carbons. (a) Polarization and (b) stability curves for the electrocatalytic reduction of oxygen under acidic conditions

(0.1 M $HClO_4$) and (c) reduction of sulfur by otherwise identical cyclohexanehexone-urea-derived mesoporous N-carbons pyrolyzed at 1073 K using mesoporous SBA-15 silica (purple) or a $ZnCl_2$-NaCl mixture (green) as templating agents. Oxygen reduction performances in (a,b) are compared to a 20 wt% Pt/C catalysts (black), with the respective onset potentials indicated by the colored squares and the half-wave potentials by colored circles. The sulfur reduction properties in (c) are compared to a standard graphitic carbon (blue), with the various oxidation (O_1) and reduction (R_1,R_2) peaks labeled by colored dots; deconvoluted contributions to of the R_2 peak(s) observed for the salt-templated N-carbon are shown in the upper left inset of (c) with the respective deconvolution onset potentials indicated by the colored dots. Currents were normalized by the geometric electrode area. Stability curves were collected by holding the potential at 0.4 V. Oxygen reduction data were collected using a rotating disk electrode, while sulfur reduction data were collected via cyclic voltammetry in a coin cell.

Table 3.1. Onset potentials, half-wave potentials, and limiting current density values obtained from Figure 3.1a for oxygen reduction by salt- and silica-templated mesoporous N-carbons and 20 wt% Pt/C electrocatalysts.

	Onset Potential	**Half-wave Potential**	**Limiting current density**
Porous carbons	V	V	mA/cm^2
Salt-templated	0.93	0.8	3.8
Silica-templated	0.60	0.7	–
20 wt% Pt/C	0.98	0.9	3.8

Figures S3.5 and S3.6 of the Supplementary Information. Furthermore, the composition of the $ZnCl_2$-NaCl salt template can be optimized to improve the reduction performances of these materials. As shown in Figure S3.5, the best ORR performance was observed for an optimum template composition of 65 mol% $ZnCl_2$ and 35 mol% NaCl, and this optimized composition has been used unless otherwise specified.

Interestingly, the salt-templated mesoporous N-carbon also exhibits superior stability for catalyzing the reduction of oxygen. Normalized plots of current density (assessed by holding the applied potential constant at an intermediate value) as functions of time are shown in **Figure 3.1b** for the silica- and salt-templated N-carbons, and for 20 wt% Pt/C. The materials exhibit dramatically different extents of performance loss compared to their respective initial values, with the salt-templated N-carbon manifesting significantly greater temporal stability under the conditions examined. Specifically, the salt-templated N-carbon retained 90% of its initial activity after 3 h, compared to 78% for 20 wt% Pt/C, and 51% for the silica-templated N-carbon, manifesting superior robustness against poisoning and higher selectivity towards the four-electron oxygen reduction reaction, compared to Pt/C catalysts.[2,11,12] The high and stable OR activity of the salt-templated N-carbon suggests that it may also be effective in catalyzing other reduction reactions.

In fact, similar relative behaviors are observed for the mesoporous salt- and silica-templated N-carbons as sulfur reduction catalysts. Whereas Pt/C materials are widely used as ORR catalysts, they tend to be poisoned by sulfur, which renders them unsuitable for use as a SRR catalysts.[37] By comparison, N-containing carbon materials are significantly less prone to deactivation by sulfur, though their efficacy as SRR catalysts has only recently begun to be explored.[18,38,39] **Figure 3.1c** shows cyclic voltammetry curves in coin cells for these salt-

(green) and silica-templated (purple) N-carbons, compared to a standard graphitic carbon (blue), where lower potentials for oxidation reactions are desirable. The oxidation peak of the salt-templated N-carbon is 2.38 V, a lower potential than either the silica-templated N-carbon (2.40 V) or the graphitic carbon (2.44 V). For the reduction peaks, higher onset potentials are desirable, and the two reduction peaks R_1 and R_2 are correlated with the reduction of S_8 into polysulfide intermediates and of polysulfides into Li_2S_2/Li_2S, respectively.[18] The salt-templated N-carbons exhibits a higher R_1 onset potential (2.54 V) than either the silica-templated N-carbon (2.42 V) or the graphitic carbon (2.40 V). The salt-templated N-carbon displays the highest potential, with a first partially resolved R_2 reduction peak at 2.19 V, followed by additional partially resolved reductive peaks at 2.13 V and 1.96 V (Figure 3.1c, inset), suggesting the presence of multiple reduction sites or mechanisms.[18,40] The silica-templated N-carbon and the graphitic carbon both exhibit a single R_2 peak at 2.12 V and 2.11 V, respectively, suggesting that there may be only one major active site or reduction mechanism responsible for these signals in both types of templated materials. The salt-templated N-carbon exhibits the smallest peak separation distances between R_1-O_1 and R_2-O_1 (Supplementary Table S3.5), which manifests faster sulfur reduction kinetics, and higher peak intensities that indicate more efficient utilization of sulfur species in the electrodes.[18,19] The superior reduction activities and stabilities of the salt-templated N-carbon suggest that it has a different and more catalytically effective distribution of surface N-carbon moieties, compared to the silica-templated material. However, conventional measurements provide few insights on the compositional or structural differences that might account for the superior performance and stability of the salt-templated N-carbon.

Nitrogen moieties and distributions in mesoporous N-carbons

The electrocatalytic properties of high-N-content-carbons likely originate from the specific types of surface N sites, the local structures and distributions of which are expected to depend on interfacial interactions with the templating agents that are used to induce mesoporosity. Whereas XPS is sensitive to near-surface species (<10 nm penetration depth),[41,42] solid-state NMR techniques can detect, resolve, correlate, and quantify different types and distributions of ^{15}N and ^{13}C moieties in bulk and surface environments of mesoporous N-carbons. Previous solid-state NMR analyses of N-containing carbons have primarily relied on conventional 1D magic-angle spinning (MAS) ^{15}N and ^{13}C NMR spectra, which generally yield partially resolved signals that have often been assigned based on comparisons to solution-state measurements, DFT calculations, and scattering based techniques.[30,42–46] Such analyses are complicated by the broad distributions of N heteroatoms within the semi-crystalline and electrically conductive graphitic sheets, which severely limit spectral resolution.

By comparison, 2D NMR spectra yield enhanced resolution by correlating signals in a 2D frequency map that can be assigned to distinct local atomic environments.[30–32] Specifically, 2D ^{13}C-^{15}N dipolar-mediated Heteronuclear Multi-Quantum Correlation (HMQC) MAS NMR spectra in Figure 3.2a,b of the salt- and silica-templated N-carbons reveal distributions of correlated ^{15}N and ^{13}C signal intensities associated with at least four different types of ^{15}N-^{13}C environments: graphitic, pyrrolic, isolated edge pyridinic and paired or defect pyridinic (see extended discussion in Supporting Information). In conjunction with DFT modeling, the correlated signals can be assigned to distinct local bonding environments of ^{15}N and ^{13}C

species, based on their calculated nuclear shieldings which manifest different isotropic chemical shifts. Nuclear shieldings were calculated and converted to ^{15}N and ^{13}C isotropic chemical shifts, ranges of which are reported in Table 3.2 for eleven graphitic, two pyrrolic, and eleven pyridinic structures using different periodic cells (Supplementary Figures S3.8-S3.11). In particular, there are three types of pyridinic nitrogen sites: those that are isolated from other N heteroatoms at the edges of graphitic sheets (yellow),[47,48] those near other pyridinic moieties (including "paired" pyrimidinic, pyrazinic, or other diazinic species) or those associated with interior pyridinic defect sites (red).[46,49] In the latter case, the presence of two or more nearby (within 3 bond distances) N moieties results in lower electron density, as manifested by the displacement of NMR signals to higher frequency (i.e., higher chemical shift values). DFT-calculated pairs of ^{15}N and ^{13}C isotropic chemical shifts for the distinct N-carbon moieties are shown as colored points in the experimental 2D ^{13}C-^{15}N correlation spectra of Figure 3.2a,b for graphitic N (blue), pyrrolic (purple), isolated edge (yellow) and paired or defect (red) pyridinic moieties. The calculated chemical-shift ranges are compared in Table 3.2 to the distributions of NMR signal intensity observed in the 2D ^{13}C-^{15}N NMR spectra (Figure 3.2a,b) in the two mesoporous N-carbons. The DFT analyses thus enable confident assignments of the correlated ^{15}N and ^{13}C NMR signals and their distributions to distinct types of graphitic, pyrrolic, isolated edge pyridinic, and paired or defect pyridinic N moieties.

The correlated 2D ^{13}C-^{15}N NMR signals observed for the different mesoporous N-carbons are similar, though with important differences that manifest their different surface chemistries and resulting oxygen- and sulfur-reduction properties. The 2D ^{13}C-^{15}N NMR spectra of the salt- and silica-templated mesoporous N-carbons (Figure 3.2a,b) show broad distributions of

correlated intensities that are assigned to ^{15}N atoms within graphitic sheets (blue regions) and pyrrolic environments (purple, present in small quantities compared to the other N moieties). Notably, the salt-templated N-carbon exhibits significantly stronger correlated signal intensity associated with isolated edge pyridinic moieties (Figure 3.2a, yellow) than the silica-templated N-carbon (Figure 3.2b), indicating that they are more prevalent in the salt-templated N-carbon. In addition, the salt-templated N-carbon shows strong resolved ^{15}N intensity (Figure 3.2a, red) that corresponds to paired or defect pyridinic species, which are unresolved in the silica-templated N-carbon. Correlated intensity is also observed at the boundaries of these chemical shift ranges (green regions), which correspond to commingled pyridinic and graphitic moieties that are in close proximity to one another (within three bond distances, Supplementary Figure S3.12). Several of the modeled structures (Supplementary Figure S3.8) yield DFT-calculated ^{15}N and ^{13}C shieldings that do not coincide with experimentally observed signal intensity in Figure 3.2a,b, indicating that they are not present or exist in small fractions that are below the sensitivity limit of the measurements (<1%). Schematic diagrams in Figure 3.2a,b show the different types of N-carbon moieties present in the mesoporous N-carbons as established by the 2D ^{13}C-^{15}N NMR spectra in Figure 3.2a,b and by DFT modeling.

Based on the improved resolution provided by the 2D ^{13}C-^{15}N NMR spectra (Figure 3.2a,b), the broad and overlapping ^{15}N signals detected in the quantitative 1D direct-excitation ^{15}N MAS NMR spectra (Figure 3.2c,d) can be confidently deconvolved to establish the relative populations of the different N moieties present in the salt- and silica-templated mesoporous N-carbons. The positions and linewidths of the deconvolved signals correspond to the intensity distributions observed in the 2D correlation spectra of Figure 3.2. Whereas the

two N-carbons have similar relative fractions of graphitic (39%), pyridinic (56%), and pyrrolic (5%) environments, they exhibit significantly different relative quantities of isolated edge and

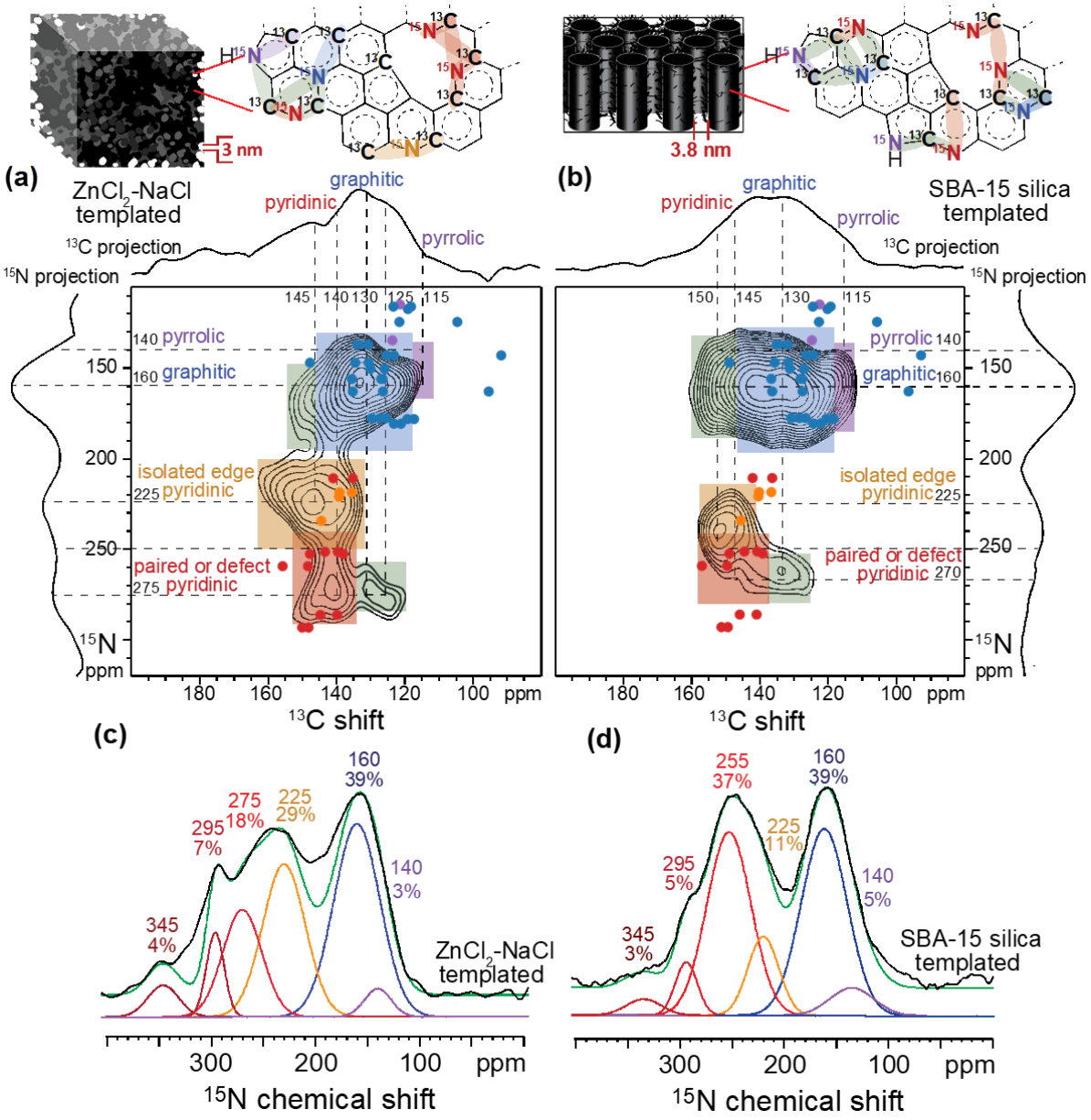

Figure 3.2. Resolving and quantifying ^{15}N species in high-N-content mesoporous carbons. Solid-state 2D ^{13}C-^{15}N HMQC NMR correlation spectra acquired at 9.4 T, 95 K, and 8 kHz MAS of **(a)** $ZnCl_2$-NaCl salt-templated and **(b)** SBA-15 silica-templated mesoporous N-carbons, showing their significantly different distributions of N-carbon

moieties. The 2D spectra were acquired with recoupling times of 0.6 ms, which probes dipole-dipole-coupled ^{13}C-^{15}N moieties within distances of approximately 0.4 nm (three bonds or less, see Supplementary Figure S3.12). The colored points represent calculated ^{13}C and ^{15}N shieldings from DFT for nuclei in N-carbon moieties and their local environments up to three bond distances, as described in the text. 1D ^{13}C and ^{15}N projections are shown along the horizontal and vertical axes, respectively. The purple, blue, yellow, and red shaded regions indicate correlated signals arising, respectively, from pyrrolic, graphitic, isolated edge pyridinic, and paired or defect pyridinic moieties present in the high-N-content mesoporous carbons, as depicted in the schematic diagrams above the 2D spectra. The green shaded regions indicate correlated signals arising from nearby or commingled N-containing moieties. Quantitative 1D single-pulse ^{15}N MAS NMR spectra of the same **(c)** salt- and **(d)** silica-templated materials as in **(a)** and **(b)** and acquired under the same conditions. Signal positions and linewidths determined by the 2D spectra were used to deconvolve, fit, and quantify the integrated signal intensities of the 1D spectra.

Table 3.2. Ranges of isotropic ^{15}N and ^{13}C chemical shifts associated with different mesoporous N-carbon moieties, as calculated from DFT modeling and consistent with experimental NMR results in Figure 3.2.[a]

	δ_{iso} ^{15}N (ppm)		
N-carbon moiety	DFT modeling	Experiment Salt-templated	Experiment, Silica-templated
graphitic	125 – 185	130– 190	130 – 190
pyrrolic	110 – 150	135 – 170	135 – 170
isolated edge pyridinic	225	225	225
paired/defect pyridinic	200 – 300	240 – 290	240 – 280
	δ_{iso} ^{13}C (ppm)		
N-carbon moiety	DFT modeling	Experiment, Salt-templated	Experiment, Silica-templated
graphitic	90 – 150	120 – 145	120 – 145
pyrrolic	120	110 – 120	110–120
isolated edge pyridinic	145	145	145
paired/defect pyridinic	135 – 160	135 – 155	135 – 155

[a] Specific N-carbon modeled moieties and structures are shown in Figures S3.8-S3.11. Isotropic ^{15}N and ^{13}C chemical shifts are referenced to polycrystalline glycine.

paired/defect pyridinic moieties.[1] Most interestingly, the salt-templated N-carbon has a significantly larger faction of isolated edge pyridinic N sites (29% vs. 11%) than the silica-templated N-carbon, which manifests their importance to the superior reduction activities observed in Figure 3.1. Interestingly, the quantitative 1D direct-excitation ^{15}N MAS NMR spectra also reveal additional signals at 295 ppm and 345 ppm for both the salt- and silica-

[1] Analyses of 1D ^{15}N MAS spectra establish the presence of minor Knight-shifted ^{15}N signals that account for about 0.2% of the total ^{15}N signal intensity for both materials (Supplementary Figure S14).

templated materials that are not present in the respective 2D NMR spectra. Separate T_1 -filtered 1D ^{15}N MAS NMR spectra establish that the ^{15}N moieties associated with these signals undergo rapid nuclear spin-lattice relaxation (T_1 ~ 100 ms, Supplementary Figure S13), which are infeasible to detect by 2D NMR and which are consistent with their being in conductive local environments. Such environments have been shown to cause chemical shift displacements and non-Gaussian chemical shift distributions, including in carbon-based conductive materials.[50–53] The fast-relaxing ^{15}N signals at 295 and 345 ppm are displaced to higher frequencies for both the silica- and salt-templated mesoporous N-carbon materials and account for 8% and 11% of the N moieties, respectively. DFT calculations of local chemical shieldings indicate that these signals are likely associated with paired or defect pyridinic moieties. When the onset and half-wave potentials for oxygen reduction and the sulfur reduction potentials are normalized to the fractional N contents of each moiety in the differently templated N-carbon materials (Supplementary Figure S14), consistent results emerge: higher percentages of isolated pyridinic N moieties, and to a lesser extent the fast-relaxing pyridinic ^{15}N moieties, correlate with the higher oxygen reduction and sulfur reduction performances of the salt-templated N-carbon material, manifesting the importance of the pyridinic N moieties to the ORR and SRR properties.

The compositional differences of the salt- and silica-templated mesoporous N-carbons likely arise from differences in surface interactions during pyrolysis. The $ZnCl_2$-NaCl-template forms a low-melting eutectic at 1073 K,[35] such that the Zn^{2+} cations appear to promote the formation of pyridinic N-carbon moieties at the surfaces of the mesoporous salt template during synthesis (see Tables S3.2 and S3.3 in the Supplementary Information). By comparison, during pyrolysis under otherwise identical conditions, the mesoporous silica

template is expected to interact relatively weakly with the nascent N-carbon network. These different interactions likely account for the significantly larger percentages of edge pyridinic moieties in the salt-templated N-carbons, compared to the silica-templated material.

N-surface moieties and adsorption sites in mesoporous N-carbons

Among the different N heteroatom moieties that are established by 2D NMR to be present in the mesoporous N-carbons, accessible surface species are most important for the reduction activities measured in Figure 3.1. After pyrolysis, the graphitic N-carbons are composed predominantly of C, N, and O, and a small fraction of H atoms (Supplementary Tables S3.2, S3). H atoms are present principally in pyrrolic moieties or as adsorbed water, the latter of which is expected to be associated with hydrophilic N moieties on the mesopore surfaces. Such surface ^{15}N and pyrrolic species can be selectively detected by 1D $^{15}N\{^{1}H\}$ cross-polarization (CP)-MAS NMR analyses, which exploit dipolar interactions between proximate (<1 nm) ^{15}N and ^{1}H nuclei to enhance ^{15}N signal intensity. Nitrogen sites at the mesopore surfaces can be distinguished from bulk N moieties by analyzing dry and water-adsorbed N-carbons synthesized using the different templates. This is clearly shown in Figure 3.3, where the 1D $^{15}N\{^{1}H\}$ CP-MAS NMR spectrum of the mesoporous salt-templated N-carbon with approximately 10 wt% adsorbed water (blue) exhibits significantly greater intensity in the spectral regions associated with the pyridinic moieties, compared to the same material, except dry. Both spectra show strong ^{15}N intensity centered at 140 ppm (purple region) from pyrrolic N-moieties[43] that are directly bonded and therefore strongly dipole-dipole-coupled to H atoms, which yield enhanced ^{15}N signals from the dilute (ca. 2%) pyrrolic species (Figure 3.2c). More

importantly, the hydrated material yields a partially resolved ^{15}N signal centered at 225 ppm (yellow region) from isolated edge pyridinic N-moieties (Figure 3.2a,c), which is significantly

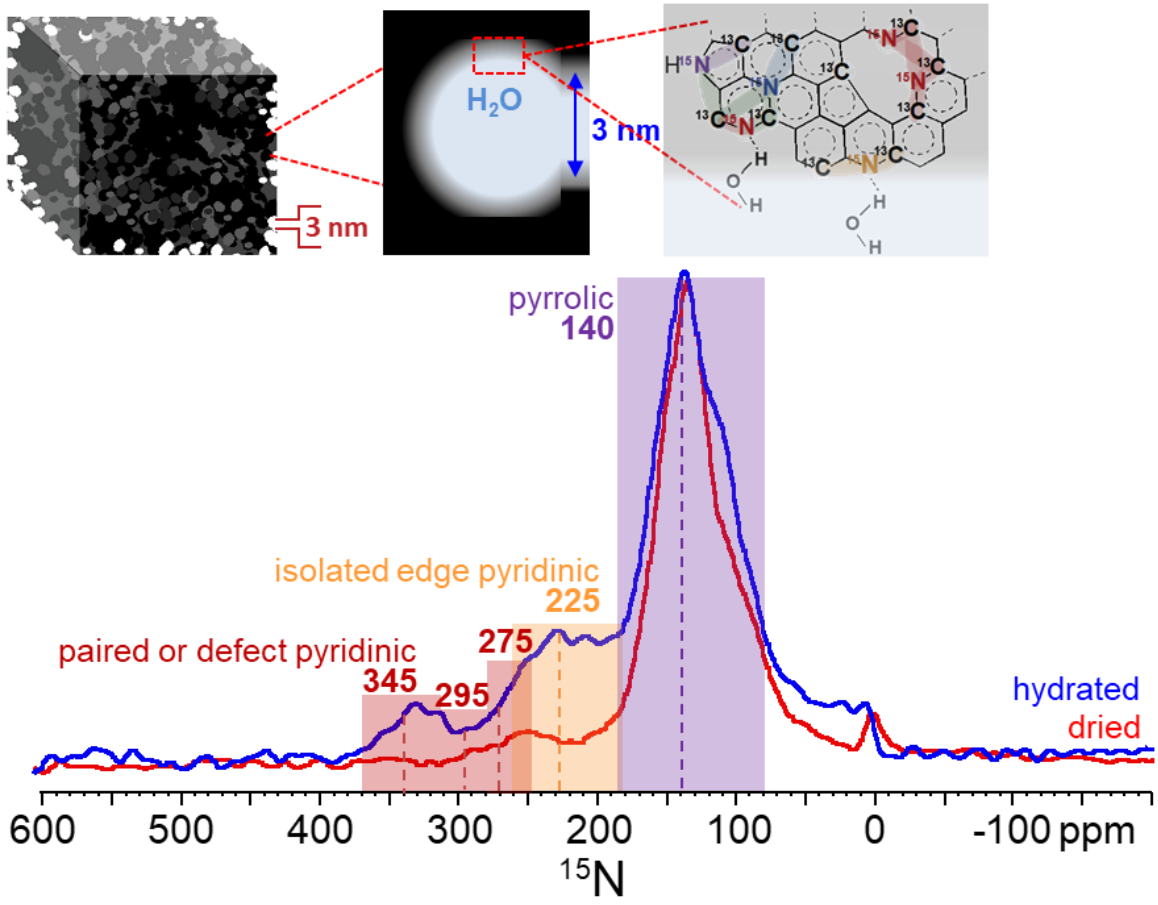

Figure 3.3. Detection of surface ^{15}N species in mesoporous N-carbons. Solid-state 1D $^{15}N\{^{1}H\}$ CP-MAS NMR spectrum acquired at 9.4 T, 97 K, 8 kHz MAS, and a 2 ms contact time for mesoporous N-carbon templated by a $ZnCl_2$-NaCl salt mixture: dehydrated (red) or with 10 wt% adsorbed water (blue). The colored bands indicate spectral regions that correspond to the different ^{15}N-carbon moieties identified in Figure 3.2a: paired pyridinic (red), isolated edge pyridinic (yellow), graphitic (blue), and pyrrolic (purple) that are near dipolar-coupled ^{1}H atoms.

more intense than in the spectrum of the otherwise identical dry material. Pyridinic species do not have directly bonded H atoms, so the observed increase in $^{15}N\{^{1}H\}$ CP-MAS intensity manifests strong interactions with adsorbed water, consistent with the accessibility of these isolated pyridinic moieties at the edges of graphitic sheets on mesopore surfaces. Weaker ^{15}N intensity is also observed in the range 250–360 ppm (red region) from paired pyridinic moieties the signals of which are also enhanced in the presence of adsorbed water. 1D $^{13}C\{^{1}H\}$ CP-MAS NMR spectra of the salt-templated N-carbon without and with adsorbed water (Supplementary Figure S3.16) similarly show enhanced signals from ^{13}C species in pyridinic and pyrrolic environments, consistent with the 1D$^{15}N\{^{1}H\}$ CP-MAS analyses. By comparison, 1D $^{15}N\{^{1}H\}$ CP-MAS NMR spectra of the silica-templated N-carbon without and with adsorbed water (Supplementary Figure S3.17) exhibit minimal differences between the hydrated and dried spectra, consistent with low fractional quantities of pyridinic moieties on the surfaces of the poorer performing catalyst. Thus, compared to the silica-templated N-carbon, both paired and isolated edge pyridinic-N species are more prevalent on the surfaces of the salt-templated analog, the latter especially so, manifesting their important contributions to the superior oxygen- and sulfur-reduction activities of the salt-templated mesoporous N-carbon.

3.4 Materials and Methods

Materials syntheses

Mesostructured silica (SBA-15) was prepared according to a previously reported procedure.[54] Briefly, 8.0 g of poly(ethyleneoxide)$_{20}$-poly(propylene-oxide)$_{70}$-poly(ethyleneoxide)$_{20}$ triblock copolymer (Pluronic® P123, Sigma-Aldrich) were dissolved in 60 ml of deionized water. To this solution was added 17 g of tetraethoxysilane and 240 ml of 3 M HCl, and the combined solution was stirred vigorously at room temperature for 10 min. The solution was then stirred for 20 h at 313 K, placed in a 363 K oven without stirring for 2 days, vacuum-filtered, and then calcined in air at 823 K to remove the structure-directing surfactant species to obtain the mesoporous silica powder.

Mesoporous N-carbon materials were synthesized from urea and cyclohexanehexone as described previously.[55] Briefly, urea (99%, Sigma-Aldrich) and cyclohexanehexone octahydrate (97%, Sigma-Aldrich) were mixed in a 3:1 stoichiometric ratio, such that the total numbers of carbonyl groups on the cyclohexanehexone octahydrate molecules and amine groups on the urea molecules were equal (see Fig. S1). The mixture of urea and cyclohexanehexone octahydrate was heated to 341 K to form the eutectic melt, and then to 363 K to promote cross-linking. The cross-linked solid was then pyrolyzed by heating at a ramp rate of 2.5 K/min to 1073 K under flowing N_2 gas and held at the target temperature for 60 min. Mesoporosity was introduced according to the templating method originally reported by Ryoo, *et al*.,[33,56] modified for use with the eutectic precursor melt.

In this method, previously prepared SBA-15 mesoporous silica powder was mixed into the urea and cyclohexanehexone octahydrate mixture (in a ratio 0.85 g SBA-15 per gram of mixture) after it had been heated to form a eutectic melt, but before subsequent heating to

promote cross-linking. The composite silica and cross-linked organic material was then pyrolyzed, as described above, after which the silica was selectively dissolved from the composite at room temperature by stirring in 2 M NaOH for 24 h, which was prepared from 98.9% NaOH pellets (Fisher, <0.001% Fe) in deionized water, followed by washing while stirring in 0.5 M H_2SO_4 for 12 h, which was prepared by dilution of 95+% sulfuric acid in deionized water (VWR Chemicals), and finally washed in dry ethanol for 20 min. These steps resulted in mesoporous N-containing carbon materials with a mesoporous graphitic structure that lacks significant long-range order, as evidenced by wide-angle X-ray scattering (WAXS), small-angle X-ray scattering (SAXS), and BET sorption analyses (Table S3.1, Figures S3.2 and S3.3).

Alternatively, mesoporous N-containing carbon materials were prepared by using a "salt-templating" method, where a mixture of sodium chloride and zinc chloride salts served as the sacrificial templating material.[35] After the organic precursors were heated to form a eutectic melt at 341 K (before significant cross-linking occurs at 363 K), a physical mixture of ground 65 mol% $ZnCl_2$ (98+%, Acros Organics) and 35 mol% NaCl (Macron Fine Chemicals) was added in a 1:3 mass ratio of organic precursors to salts. Following pyrolysis under the same conditions as used for the silica-templated materials, the composite products were ground into a powder, and the salts removed by washing in deionized water. For consistency, the salt-templated material was also washed while stirring in 2 M NaOH, then in 0.5 M H_2SO_4, and finally in dry ethanol, as described above for the silica-templated N-carbon. The resulting salt-templated mesoporous N-carbons contained negligible contents of templating species (< 0.4 mol% Si, Zn, Na, or Cl) and the impurity Fe contents were very low (0.01 mol% Fe in the

bulk materials), as determined by the XPS, XRF, and the associated discussion of the results in Tables S3.2, S3.3, and S3.4 of the Supplementary Information.

Following the removal of either template material, the resultant mesoporous high-N-content carbon products were dried in a vacuum oven at 323 K. Versions of the materials were also prepared by using ^{13}C,^{15}N-enriched urea (99% ^{13}C, 99% ^{15}N, Sigma Aldrich) under otherwise identical conditions to improve ^{13}C and ^{15}N signal sensitivity for solid-state nuclear magnetic resonance (NMR) spectroscopy.

Electrocatalytic activity and stability tests

Oxygen Reduction

Oxygen reduction activities of the porous high-N-content carbon materials were determined by conducting staircase voltammetry (SV) measurements with a BioLogic VSP potentiostat. A three-electrode configuration was used with a rotating-disk electrode with a 5.61 mm diameter glassy carbon disk used as the working electrode, and with a graphite rod and a Ag/AgCl (3 M NaCl) electrode as the counter and reference electrodes, respectively. Catalyst inks for alkaline fuel cell conditions were prepared by dispersing 7.4 mg of high-N-content carbon materials into a mixture composed of 250 μL of milli-Q-water, 750 μL of isopropanol, and 60 μL of 5 wt% Nafion^{TM} solution. The suspension was sonicated for 60 min to form a homogeneous ink, and then 20 μL of catalyst ink were deposited drop-wise onto a glassy carbon electrode and dried at 40 °C to yield a catalyst loading of 712 μg/cm^2. To evaluate ORR performance under alkaline conditions, staircase voltammetry tests were conducted within an O_2-saturated 0.1 M KOH solution. Catalyst inks for acidic fuel cell

conditions were prepared by dispersing 7.4 mg of high-N-content carbon into a mixture composed of 250 μL of milli-Q-water, 750 μL of isopropanol, and 240 mg of 5 wt% Nafion^{TM} solution. The suspension was sonicated for 60 min to form a homogeneous ink, and then catalyst ink was deposited dropwise onto the glassy carbon electrode and dried at 40 °C to yield a catalyst loading of 780 mg/cm^2. To evaluate ORR performance under acidic conditions, staircase voltammetry tests were conducted within an O_2-saturated 0.1 M $HClO_4$ solution. For both sets of conditions, five cyclic voltammetry cycles were ran to activate the electrocatalyst prior to SV testing. The steady-state ORR polarization curves were collected by using staircase voltammetry with a potential step of 0.01 V and a holding time at each potential of 10 s. During the tests, the working electrode was rotated at a rate of 900 rpm using a Modulated Speed Rotator (Pine Research Instrumentation) to promote mixing of the electrolyte and reduce concentration gradients in the bulk fluid in contact with the catalyst layer. Following the measurements, the oxygen reduction currents were scaled by the area of the glassy carbon electrode to obtain current densities, and the potentials were converted to the reversible hydrogen electrode (RHE) scale. Stability tests were conducted using the same synthesis and set-up under acidic conditions. A constant and intermediate potential (0.4 V) was applied while the current produced was measured over a 3-h time period.

Sulfur Reduction

The electrolyte (referred to as "blank electrolyte") was made by combining 1 M lithium bis(trifluoromethane-sulfonyl) imide (Sigma-Aldrich) and 0.2 M lithium nitrate (Sigma-Aldrich) in a mixed dimethoxyethane (Sigma-Aldrich) and 1,3-dioxolane (Sigma-Aldrich) solution (1:1 by volume). The Li_2S_6 catholyte (0.1 M) was prepared by reacting sublimed sulfur (Sigma-Aldrich) with Li_2S (Sigma-Aldrich) in stoichiometric proportions in the blank

electrolyte. The mixture was vigorously stirred at 50 °C in an argon-filled glove box overnight to produce a brownish-red Li_2S_6 catholyte solution. Sulfur-reduction performance was evaluated by conducting cyclic voltammetry measurements of the mesoporous nitrogen-containing carbon materials in CR2032 coin cells that were assembled in an argon-filled glovebox. The cathode slurry was prepared by mixing nitrogen-carbon or graphite, carbon black, and polyvinylidene fluoride binder at a mass ratio of 8:1:1 in N-methyl-2-pyrrolidone. The slurry mixture was drop cast onto a carbon-coated aluminum foil with a diameter of 1.3 cm. The loading of the nitrogen-carbon material was 1 mg/cm^2. Afterwards, the Li_2S_6 catholyte was used as a sulfur source and drop-cast on the cathode. The mass loading of the sulfur was 0.15 mg/cm^2 to ensure maximum utilization of sulfur. The sulfur cathodes were then directly assembled into a CR2032 coin cell with lithium foil, a Celgard 2500 separator, and blank electrolyte. Cyclic voltammetry curves were recorded over the voltage range of 1.7 V–2.7 V at a scanning rate of 0.1 mV/s.

X-ray analyses

Graphitic ordering in the mesoporous N-carbon materials was assessed by using wide-angle powder X-ray diffraction (XRD) using a Rigaku Smartlab high-resolution diffractometer with Cu K_α radiation operating at 40 kV and 44 mA. Wide-angle XRD patterns were recorded over a 2θ range of 10° to 70° in increments of 0.05°. Small-angle X-ray scattering analyses were conducted to assess the extents of long-range mesostructural order in the mesoporous N-carbon materials. Wide-angle XRD patterns were recorded over a 2θ range of 0° to 3° in increments of 0.01°.

Near-surface elemental compositions were determined by X-ray photoelectron spectroscopy (XPS) using a Kratos Axis Ultra XPS system to acquire survey scans over a range of 0 to 1200 eV with a step size of 0.5 eV and a pass energy of 160 eV. Quantitative characterization of different near-surface nitrogenous species was accomplished using high-resolution N *1s* XPS, scanning a range of 390 to 410 eV with a step size of 0.05 eV and a pass energy of 20 eV. Spectra were processed by using CasaXPS software, and each high-resolution N *1s* spectrum was deconvoluted into multiple Gaussian lineshapes, based on the binding energies of electrons associated with nitrogen atoms in various functional groups.[25] Bulk elemental compositions were measured by X-ray fluorescence (XRF) using a Rigaku ZSX Primus IV instrument with a wavelength dispersive sequential diffractometer and were collected with ZSX Guidance software. A rhodium source was used and operated at 3.5 kW for all elements. Results were obtained through semi-quantitative methods, and theoretically calculated using the fundamental-parameter method and ZXS Guidance's internal sensitivity library.

Raman spectroscopy

Raman measurements were also conducted to assess graphitic ordering of the mesoporous N-carbons using a Horiba Jobin Yvon T64000 confocal microscope 100X operating in single mono mode with a 1800 groove/mm grating, a liquid-nitrogen-cooled CCD detector, 488 nm excitation, and 20 s acquisition time. Raman data were processed with linear baseline subtraction and deconvoluted into Lorentzian line shapes.

Solid-state NMR spectroscopy

Solid-state ^{13}C and ^{15}N magic-angle-spinning (MAS) NMR spectroscopy were used to analyze the local environments of ^{13}C and ^{15}N moieties in the N-carbon materials synthesized from a 1:3 molar ratio of cyclohexanehexone octahydrate and uniformly ^{13}C,^{15}N-enriched urea. All solid-state NMR spectra were acquired on a Bruker AVANCE II HD 400 DNP-NMR spectrometer with a 9.4 T superconducting magnet operating at Larmor frequencies of 400.20, 100.64, and 40.56 MHz for ^{1}H, ^{13}C, and ^{15}N nuclei, respectively, and equipped with a variable-temperature 3.2 mm HXY MAS probehead. The experiments were conducted at low temperature (95 K) with 100 kHz SPINAL-64[57] ^{1}H decoupling during the acquisition periods, using zirconia rotors, Kel-F® caps, and under 8 kHz MAS conditions. Low-temperature conditions were used to improve NMR signal sensitivity for the 2D NMR measurements and to mitigate the influences of rapid nuclear spin-lattice and spin-spin relaxation effects. Chemical shifts were observed to vary with temperature, so all experiments were conducted under the same temperature and MAS conditions for consistency. Chemical shifts were referenced using uniformly ^{13}C,^{15}N-enriched glycine powder at room temperature as a secondary standard, with ^{13}C chemical shifts referenced to the carboxyl carbon atom at 172.7 ppm (tetramethylsilane at 0 ppm) and ^{15}N chemical shifts referenced to 33.4 ppm (liquid NH_3 at 0 ppm).[58] The N-carbon materials were diluted with KBr at a sample:KBr ratio of 1:3 w/w before being loaded into the MAS rotor. The KBr served as both an internal temperature probe[59] and to reduce undesirable sample heating that may arise from rapid rotation of conductive samples in the high magnetic field required for the NMR measurements.[60] The temperature of the MAS gas stream nearest to the stator was measured to be 95 K, and the

actual sample temperature was estimated from ^{79}Br T_1 relaxation measurements[61] to be *ca*. 99 K.

Compared to 1D NMR, two-dimensional (2D) NMR techniques yield enhanced spectral resolution by exploiting through-space dipole-dipole interactions over sub-nanometer distances to correlate the isotropic chemical shifts of dipole-dipole-coupled spin pairs, such as ^{13}C and ^{15}N nuclei in mesoporous N-carbons. The 2D NMR spectra resolve and correlate signals from ^{15}N sites and their ^{13}C nearest neighbors on 2D frequency maps that are generally presented as 2D contour plots, allowing the local structures of the heteroatom sites to be determined. The high N contents and isotopic enrichment with ^{15}N and ^{13}C enable 2D NMR spectra to be acquired with a remarkable combination of sensitivity and resolution. Specifically, solid-state 2D ^{13}C-^{15}N *H*eteronuclear *M*ultiple *Q*uantum *C*oherence (HMQC) experiments were conducted using the $SR4_1^2$ pulse sequence, according to Hu et al.,[62] employing recoupling over 12 rotor periods (corresponding to 1.5 ms), to recouple dipole-dipole-coupled ^{13}C and ^{15}N spins. The 2D dipolar-mediated ^{13}C-^{15}N HMQC NMR spectra[63] in Figure 3.2 were acquired using 1024 transients, with 32 t_1 increments in the indirect dimension in STATES-TPPI acquisition mode. Recycle delays of 10 s (corresponding to 1.3T_1) for highest signal sensitivity. Heteronuclear ^{13}C-^{15}N dipole-dipole couplings scale with the cube of the distance separating the two nuclear spins,[64,65] making these measurements sensitive principally to ^{13}C and ^{15}N nuclei that are directly bonded, physically interacting, or to a lesser extent by weak next-nearest neighbor interactions. The latter contributes negligibly to the overall measured signal intensity as consequence of the short ^{13}C-^{15}N recoupling times used here (0.6 ms, 2–3 bond distances),[66] which preferentially detect dipolar-coupled nuclei over short distances as corroborated by buildup-curves (Supplementary Figure S3.11) that

were simulated by using the SIMPSON[67,68] simulation package version 4.1.1. Recoupling was implemented by using the $SR4_1^2$ supercycle sequence for the experimental conditions enumerated above, with powder averaging accounted for by using the REPULSION scheme[69] and with 678 combinations of α and β angles and 26 γ angles were used. The recoupling efficiency was normalized with respect to the result of a standard spin-echo experiment. For the recoupling efficiency versus distance calculations, a two-spin system (^{13}C, ^{15}N) was simulated without chemical shift anisotropy (CSA) interactions, with the offsets chosen to be representative of experimentally encountered values.

Quantitative one-dimensional (1D) solid-state spin-echo ^{15}N NMR experiments in Figure 3.2 were used to quantify the integrated intensities of signals, the positions and linewidths of which are manifested in the 2D ^{13}C-^{15}N spectra. A recycle delay of 20 s ($5T_1$) was used to ensure full spin-lattice relaxation of the ^{15}N nuclei in the SBA-15-silica- and $ZnCl_2$-NaCl salt-templated materials and were acquired with 2000 scans. Fast MAS spin-echo ^{15}N NMR experiments (Supplementary Figure S3.12) were acquired with very short delay times of 30 ms and about 10^6 scans.

1D $^{15}N\{^1H\}$ CP-MAS spectra with and without the presence of adsorbed water (Figures 3.3, Supplementary Figure S3.14) were acquired to identify surface N-moieties and corroborate the assignment of pyrrolic N. These experiments were acquired with a contact time of 2000 μs, 10^5 scans, and recycle delay of 1 s. 1D $^{13}C\{^1H\}$ CP-MAS spectra (Supplementary Figure S3.13) were acquired with a 2000 μs contact time and 5000 scans. In the case of the CP measurements where water was used to probe the material surface, KBr salt could no longer be used to dilute the conductivity of the N-carbons. Instead, the materials were diluted with SBA-15 silica at a sample:silica ratio of 1:3 w/w. Water was also mixed in

with the silica and N-carbon mixture in a ratio of about 1:3 w/w to create the hydrated materials. The samples were then dried in a vacuum oven at 120 ˚C.

Density Functional Theory (DFT) Modeling[2]

The 2D ^{13}C-^{15}N NMR spectra in Figure 3.2 of the manuscript were analyzed in conjunction with DFT modeling to assign the correlated signals to distinct N-carbon moieties and structures (Supplementary Figure S3.7), determining the local bonding environments of the ^{15}N and ^{13}C species. DFT calculations yield the electronic shieldings of nuclei in distinct atomic environments, which are manifested as differences in isotropic ^{15}N and ^{13}C chemical shifts ($\delta_{cs,iso}$). Such shielding calculations were conducted using a linear-response method, where a one-electron wavefunction is developed on a basis set of plane waves and electron-nuclei interactions are treated with the PAW approach.[70,71]

General calculation method

Density-functional theory[72] (DFT) calculations were performed by my collaborator and co-author Ziyang Wei. DFT calculations were performed using the Vienna Ab initio Simulation Package[70] (VASP) and the Perdew–Burke-Ernzerhof[73] (PBE) functional at the generalized gradient approximation (GGA) level. The dDsC dispersion correction[74,75] was

[2] J. Towns, T. Cockerill, M. Dahan, I. Foster, K. Gaither, A. Grimshaw, V. Hazlewood, S. Lathrop, D. Lifka, G. D. Peterson, R. Roskies, J. R. Scott, N. Wilkins-Diehr, "XSEDE: Accelerating Scientific Discovery", *Computing in Science & Engineering*, 16. 62-74 (2014). doi:10.1109/MCSE.2014.80

applied. All calculations were spin-polarized. Gaussian smearing was applied with sigma equal to 0.1. For geometry optimizations, a cutoff energy as 500 eV was used. The energy convergence criterion was 10^{-6} eV and forces were optimized to 0.02 eV/Å with 3*3*1 *k*-points used for the terrace model, 1*3*1 for the armchair model, and 3*1*1 for the zigzag model.

For the NMR shift calculations, the linear response method[71,76] provided in VASP was used, with the cutoff energy set to be 600 eV. 5*5*1 *k*-points were used for the terrace model, 1*7*1 for the armchair model, and 7*1*1 for the zigzag model. An energy convergence criterion of 10^{-10} eV was used, unless convergence problem occurred, in which case the criterion was lowered to at most 10^{-7} eV. An example for graphitic ^{15}N NMR is shown in Supplementary Figure S3.9, where the chemical shift difference due to lower energy convergence criterion was below 0.01 ppm, which can be considered negligible compared to other sources of uncertainty. LNMR_SYM_RED was used to discard symmetry operations that were not consistent with the way *k*-space derivatives were calculated in the linear response calculations of chemical shifts. NLSPLINE was used to construct the PAW projectors in reciprocal space using a spline interpolation so that they were *k*-differentiable. Default values were used for the step size (0.001) for the finite difference *k*-space derivative and the order (1) of the finite difference stencil.

Computational chemical shift reference

The calculated results from VASP were compared with the experimental NMR measurements by using:

$$\delta_i = \delta_{\text{calculated},i} - \delta_{\text{calculated},i,\text{ref}} + \delta_{\text{exp},\,i,\text{ref}},$$

where δ_i are the ^{13}C or ^{15}N isotropic chemical shifts that correspond to the positions of the colored dots in Figure 3.2, $\delta_{calculated,i}$ are the chemical shift values calculated for each specified model nitrogen-carbon motif in Figure 3.2, $\delta_{calculated,i,ref}$ are the ^{13}C or ^{15}N isotropic chemical shift values calculated for solid crystalline α-glycine used as a reference, and $\delta_{exp,i,ref}$ are the experimentally measured ^{13}C or ^{15}N isotropic chemical shifts for α-glycine of 172.7 ppm for ^{13}C and 33.4 ppm for ^{15}N.

3.5 Conclusions

Mesoporous carbon materials were synthesized by the pyrolysis of molecular precursors in the presence of sacrificial $ZnCl_2$-NaCl salt or mesoporous silica templates. Favorable properties of these materials include high nitrogen contents (>10 mol%), high fractions of N moieties at surface sites, 3-nm mesopores to promote diffusion, and electron conductivity to surface N environments where reactions occur. The non-precious-metal-containing materials exhibit high oxygen and sulfur reduction activities that are comparable to conventional 20 wt% Pt supported on activated carbon or graphite, respectively, with superior stabilities. The types, quantities, and distributions of N-heteroatom environments (especially those at surface sites) are shown to strongly influence macroscopic reduction activities. Specifically, differences in the macroscopic OR and SR properties of the salt- and silica-templated N-carbons are accounted for by clear differences in the distributions of N heteroatoms among different moieties, especially edge pyridinic sites. The quantitative distributions of surface pyridinic species are established by solid-state 2D ^{13}C-^{15}N and 1D $^{15}N\{^{1}H\}$ NMR, in conjunction with DFT, XPS, Raman spectroscopy, X-ray diffraction, and electron microscopy analyses. Specifically, surface pyridinic N moieties are shown to be present in higher fractional quantities and at accessible mesopore surface sites in the salt-templated mesoporous N-carbon, compared to the silica-templated analog, and likely account for the differences in their macroscopic reduction activities. The different surface compositions arise from interactions of nitrogenous carbon moieties as they form during pyrolysis with the different template surfaces. This manifests the important role of template surface chemistry in mediating the surface compositions and structures, as well as the mesoscale porosity of N-carbon electrocatalysts, which presents opportunities for optimizing macroscopic OR and SR

properties. The new atomic-level insights into the types of N-carbon moieties that are important in oxygen and sulfur reduction catalysts are expected to aid the development of non-precious-metal electrocatalysts and provide criteria for the rational design of novel heteroatom-containing carbon materials.

3.6 Future Directions

An area that could be further explored is understanding the reactions and mechanism occurring during the low temperature eutectic melt and pyrolysis steps of the N-carbon synthesis, and how the steps can be varied to increase the formation of desirable N moieties. Correlating varied pyrolysis temperatures and $NaCl/ZnCl_2$ ratio conditions with the oxygen reduction properties under alkaline conditions has been done (**Chapter 3**) with the goal of identifying the types and distributions of N-moieties formed in the most desirable materials. However, I propose synthesizing N-carbon materials with varied eutectic and pyrolysis temperatures and times, measuring their reduction performance, and correlating that with the relative fractions of N-moieties formed as determined by quantitative solid-state ^{15}N NMR (**Chapter 3 Figure 3.2c,d**). This would allow for direct comparison of the N-moieties and distributions to the low temperature eutectic melt and pyrolysis time and temperature synthesis conditions.

Along the same lines, compared to silica-templating, salt-templating of the N-carbons is shown to increase both the oxygen- and sulfur-reduction performances by increasing the fraction of isolated pyridinic N moieties formed. We hypothesize that the differences in N environment distributions are caused by the differences in carbon-template interactions that occur during the high temperature pyrolysis step of the reaction, as the silica template is only expected to have weak non-ionic interactions with the graphitizing carbons, but the salt template is expected to have strong electrostatic interactions, specifically between the Zn ion and N. Correlating a varied $NaCl/ZnCl_2$ ratio with the oxygen reduction properties has been done (**Chapter 3 Figure S3.5**). However, understanding the reactions that occur during pyrolysis to promote the formation of the desirable environments would be very interesting

and a valuable contribution to the field. I suggest solid-state ^{67}Zn and ^{23}Na NMR studies at a high magnetic field of the salt-templated material, post-pyrolysis and pre-washing, so that the template materials are still in the graphitized N-carbon. Correlating this data for materials synthesized at a variety of $NaCl/ZnCl_2$ ratios with the types and distributions of N-moieties formed and with reduction performance should elucidate the types of environments formed during pyrolysis that result in higher insolated pyridinic N environments and higher reduction performances.

Furthermore, *in situ* increasing temperature ^{1}H NMR can be used to help elucidate the reactions and reaction mechanisms being formed during the low temperature eutectic melt step of the reaction, and possibly some pyrolysis depending on the probe tolerance for temperature. Specifically, comparing the *in situ* NMR of silica- and salt-templating (or varied salt template ratios) synthesis steps would be very insightful. ^{15}N and ^{13}C *in situ* NMR will be challenging as the very low signal to noise ratio achieved with these nuclei, means that many scans are required therefore affecting the time held at each temperature step. Preliminary ^{1}H and ^{15}N in situ NMR experiments examining the very slow melt of cyclohexanehexone and $^{15}N,^{13}C$-enriched urea combined in an NMR rotor and inserted into the magnet being held at 80˚C were taken as a function of reaction time are shown in **Appendix A**. **Chapter three** has laid the groundwork for the above investigations that would not only show how to optimize a material (as is common in the literature), but would provide an in-depth understanding of the conditions and environments necessary for optimization that could be applied much more broadly than our specific cyclohexanehexone-urea derived N-carbon materials.

3.7 Supporting Information

3.7.1 Supporting Information - Tables

Table S3.1. BET surface areas and pore size distributions of the mesoporous N-carbon materials

Material	*Surface area*	*Pore diameters*
	m^2/g	*nm*
SBA-15 silica templated	1100	1-2, 3-4
$ZnCl_2$-NaCl templated	1800	1-1.5, 2.5-4

Near-surface versus bulk nitrogen compositions of high-N-content carbons

Identifying and quantifying the different types and distributions of nitrogen moieties present in the N-carbon materials is crucial to understanding the relationship between electrical conductivity and heteroatom content (N atoms) of the electrocatalyst materials, as well as how synthesis conditions affect these characteristics. The overall near-surface and bulk nitrogen contents of the mesoporous N-carbon materials templated by $ZnCl_2$-NaCl and SBA-15 silica are high, compared to conventionally prepared N-carbon materials. XPS analyses yield near-surface nitrogen compositions of 16 and 22 mol% (Tables S3.2 and S3.3) for the salt- and silica-templated N-carbons, respectively, compared to bulk nitrogen compositions of 28 and 19 mol% (Table S3.4), as determined from XRF analyses.

Trace amounts (<0.4 mol%) of the templating materials (Zn, Na Si, Cl) and Fe impurities (0.1 mol% or less) were detected within the product mesoporous N-carbon materials. The trace Zn contents are the same within experimental uncertainty between the two materials and in similar types of local environments (as evidenced by EXAFS) and therefore are unlikely to account for the differences in reduction performance. The differences in the even lower trace

Fe contents between the materials also do not correlate with increased reduction performance. The elemental compositions show that the mesoporous N-containing carbon materials can be prepared with little to no retention of the templating materials after their removal.

Local atomic N environments are challenging to resolve and quantify by conventional techniques, such as XPS. Whereas XPS probes near-surface (<10 nm) species, solid-state NMR measures all NMR-active nuclei in the bulk sample. For example, among the nitrogenous moieties that are present in the salt- and silica-templated N-carbon materials, the relative populations of near-surface graphitic N (11 and 17 mol%, respectively) estimated by XPS are lower than those measured (42 and 41%) by deconvolution of the quantitative direct-excitation ^{15}N MAS NMR spectra in Figure 3.2c,d of the manuscript. In combination, these results indicate the predominantly non-surface locations of graphitic N moieties. This is corroborated by the surface-sensitive 1D ^{15}N{^{1}H} CP-MAS NMR spectra (Figure 3.3), which show substantially less intensity associated with the graphitic N moieties, compared to the pyridinic and pyrrolic moieties.

Table S3.2. Near-surface elemental compositions of high-N-content carbons obtained by X-ray photoelectron spectroscopy (XPS)[a]

Material	*Near-surface elemental composition [mol%]*							
	C	N	O	Zn	Fe	Na	Si	Cl
SBA-15 silica templated	69	22	8	0.21	0.12	-	-	-
$ZnCl_2$-NaCl templated	72	16	11	0.22	-	-	-	-

[a] Near-surface compositions were estimated by integrating the peaks of survey X-ray photoelectron spectra. Mean values are shown for multiple measurements and materials

syntheses, which were reproducible to within ca. ±1 mol% for C and N and within ca. 0.05 mol% for Zn and Fe.

Table S3.3. Relative populations of different near-surface N moieties in high-N-content carbons from XPS[a]

Material	*Bulk elemental composition [mol%]*							
	C	N	O	Zn	Fe	Na	Si	Cl
SBA-15 silica templated	63	28	9	0.09	0.01	0.36	0.23	0.11
$ZnCl_2$-NaCl templated	62	19	19	0.07	0.01	0.25	0.06	0.06

[a] Estimated by deconvolution of the high-resolution N *1s* XPS spectra in Figure S3.4.

Table S3.4. Bulk elemental compositions of high-N-content carbons determined by X-ray fluorescence (XRF)

Material	*Bulk elemental composition [mol%]*							
	C	N	O	Zn	Fe	Na	Si	Cl
SBA-15 silica templated	63	28	9	0.09	0.01	0.36	0.23	0.11
$ZnCl_2$-NaCl templated	62	19	19	0.07	0.01	0.25	0.06	0.06

Table S3.5. S-reduction separation distances between the oxidative (*O*) and reductive (*R*) peaks of the high-N-content carbons compared to a graphitic carbon standard

Peak separation	*salt-templated mV*	*silica-templated mV*	*graphitic carbon (without N) mV*
$\boldsymbol{R_2}$-$\boldsymbol{O_1}$	342	350	406
$\boldsymbol{R_1}$-$\boldsymbol{O_1}$	57	78	138

3.7.2 Supporting Information – Figures

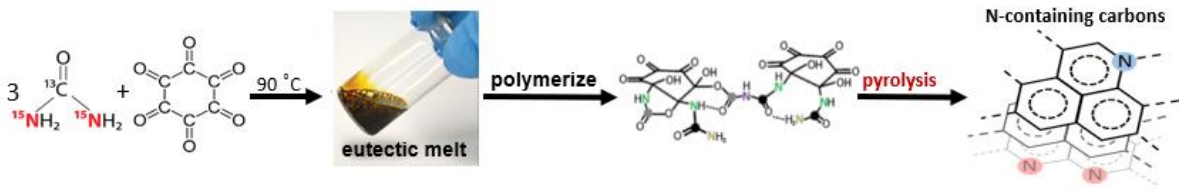

Figure S3.1. Synthesis of nitrogen-containing mesoporous carbon electrocatalyst materials. The reactant mixture (cyclohexanehexone and urea) is combined at room temperature and heated to 363 K under air to form a eutectic melt. The mesoporous templating agent (SBA-15 mesoporous silica or $ZnCl_2$-NaCl salt mixture) is then combined with the eutectic melt and subsequently pyrolyzed in a nitrogen atmosphere at 1073 K to form the mesoporous N-containing carbon materials. The photo of the eutectic melt is from Fechler, *et al.*[24]

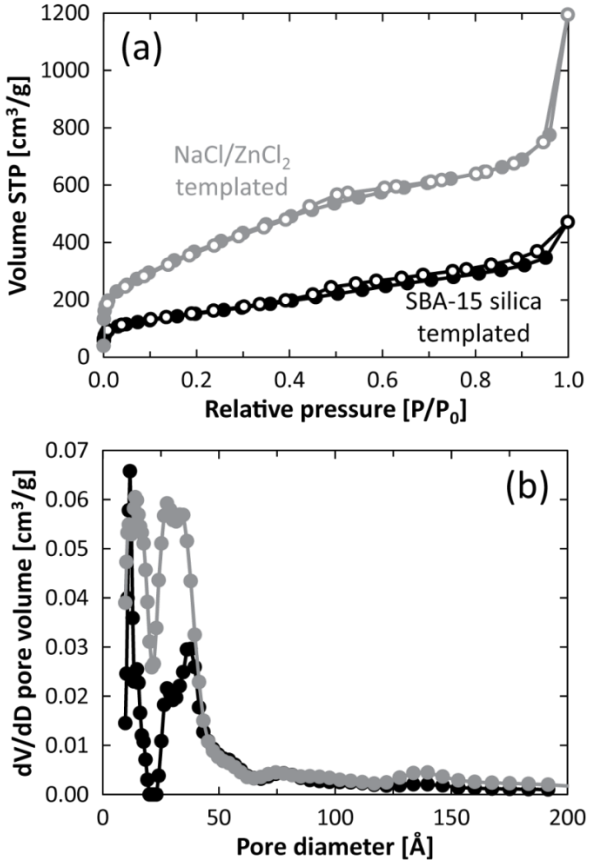

Figure S3.2. (a) Nitrogen sorption isotherms at 77 K and (b) pore-size distributions for the SBA-15 silica-templated (black) and $ZnCl_2$-NaCl-templated (grey) mesoporous high-N-content carbon materials, which were prepared by condensation of a 1:3 molar ratio of cyclohexanehexone octahydrate to urea at 1073 K. The pore-size distributions were calculated using the non-local-density functional theory (NLDFT) method[77] and indicate that the porous materials prepared by either templating method possess similar approximately bimodal distributions of pores with diameters in the ranges of 1.0-1.5 nm and 2.5-4.0 nm. Brunauer-Emmett-Teller (BET) analyses[78] yielded estimated specific surface areas of the SBA-15 and $ZnCl_2$-NaCl-templated materials of 1100 m^2/g and 1800 m^2/g, respectively, as shown in Supplementary Table S3.1.[55]

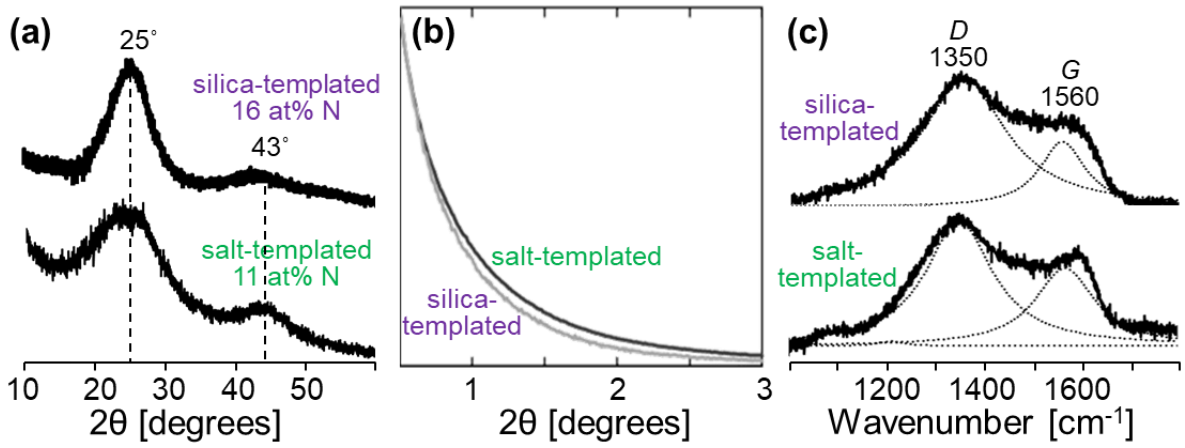

Figure S3.3. Extent of graphitization of mesoporous N-carbons. (a) Wide-angle XRD patterns, (b) small-angle XRD patterns, and (c) Raman spectra acquired at 298 K of cyclohexanehexone-urea-derived mesoporous N-carbons pyrolyzed at 1073 K using mesoporous SBA-15 silica (purple) or a $ZnCl_2$-NaCl mixture (green) as templating agents. Corresponding TEM images of the N-carbons can be found in Supplementary Figure S3.7.

Extended Discussion of X-ray diffraction and Raman analyses

A small extent of periodic long-range order is evident in the wide-angle X-ray scattering (WAXS) patterns in Supplementary Figure S3.3a of mesoporous silica- and salt-templated N-carbons. Each pattern exhibits broad reflections at 25° 2θ (0.34 nm *d*-spacing) that are indexable to the (*002*) stacking plane of graphite, along with weaker broad scattering intensities at 43° 2θ (0.21 nm *d*-spacing) that correspond to overlapping reflections associated with the (*100*) and (*101*) planes of graphite.[79] The breadths of the WAXS reflections, and absence of reflections in SAXS patterns (Supplementary Figure S3.3b), manifest relatively poor long-range ordering of the graphitic sheets in the mesoporous N-carbons, as would be expected in such heteroatom-containing-carbons. An estimate of the relative extents of

graphitic order in the materials is provided by Raman spectroscopy, which is sensitive to both ordered and disordered graphitic domains. The Raman spectra in Supplementary Figure S3.3c show broad intensity in the range 1000–1700 cm^{-1} that can be deconvoluted into Lorentzian-shaped bands centered at 1560 cm^{-1} (*G*) and 1350 cm^{-1} (*D*), which are associated with bond vibrations in locally distorted graphitic lattices, specifically heteroatom or edge/surface environments[80,81] and stretching vibrations in polyene-type structures, respectively.[82] The integrated intensity ratios (*D/G*) of these dominant Raman bands are both approximately 3.2 for the salt- and silica-templated N-carbons, with a low value manifesting a higher extent of graphitic ordering,[31,33] and thus bulk electrical conductivities.[34] These values are similar to those reported in the literature for other high-heteroatom-content (≥15 wt% N, O, and/or S combined) carbons.[83,84] A possible low-intensity band at ca. 1080 cm^{-1} is thought to correspond to α-carbon,[85,86] and accounts for less than ca. 1% of the overall spectral intensity in the silica- and salt-templated materials. The similarities of the D/G ratios for the silica- and salt-templated N-carbons here suggest that differences in extent of graphitization cannot account for the large difference in reduction performance manifested in Figure 3.1.

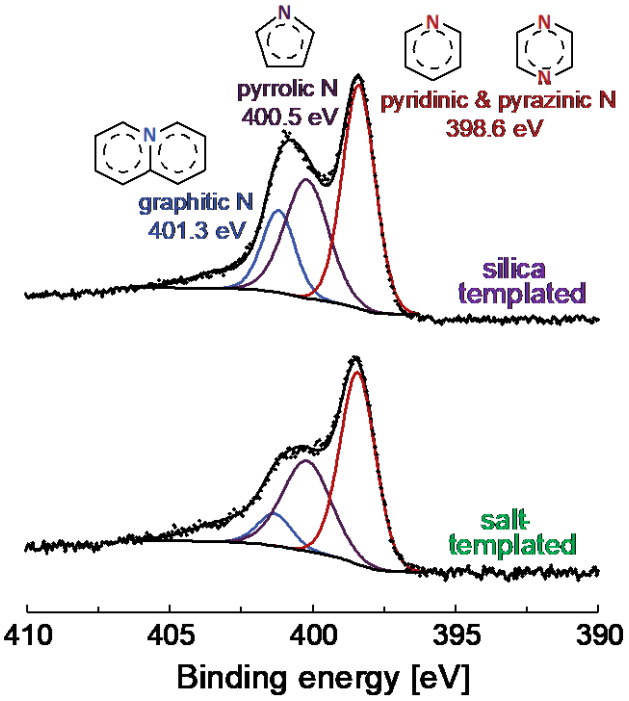

Figure S3.4. High-resolution N *1s* X-ray photoelectron spectra of N-containing carbon materials prepared by the pyrolysis of a 1:3 molar ratio of cyclohexanehexone-octahydrate and urea at 1073 K under identical conditions except for the mesopore templates used: (top) SBA-15 silica versus (bottom) a $ZnCl_2$-NaCl (65:35 molar ratio) salt mixture.

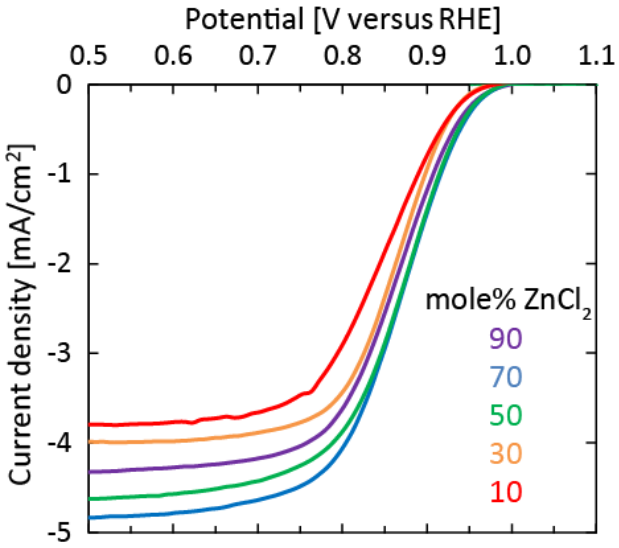

Figure S3.5. Polarization curves associated with the electrocatalytic oxygen reduction activities acquired under alkaline conditions at room temperature for mesoporous N-carbons synthesized with different $ZnCl_2$:NaCl salt-template molar ratios ranging from 10-90 mol% $ZnCl_2$ (with the balance NaCl). Under these conditions, the best ORR performance was observed for an optimum template composition of 65 mol% $ZnCl_2$ and 35 mol% NaCl, and this optimized composition has been used unless otherwise specified. The current data were normalized by the electrode area to show potential as a function of current density. Data were collected at 900 RPM by staircase voltammetry with the materials deposited on a rotating-disk electrode. Changing the composition of the templating material, while keeping all other synthesis parameters the same, affects the final compositions of the mesoporous N-carbon materials and their oxygen and sulfur reduction performances.

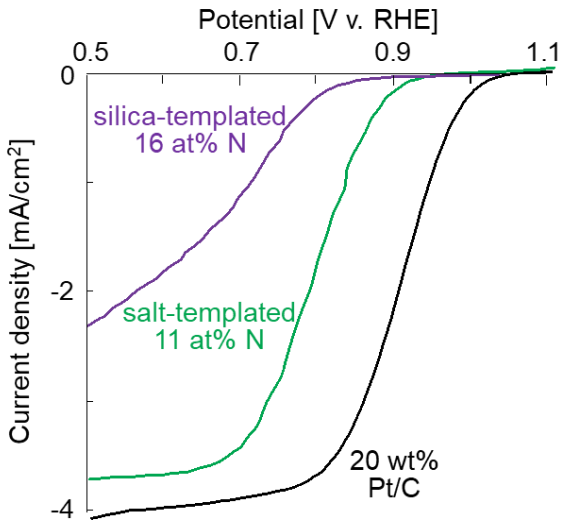

Figure S3.6. Electrocatalytic activity of mesoporous N-carbons under alkaline conditions. Polarization curves for the electrocatalytic reduction of oxygen by cyclohexanehexone-urea-derived mesoporous N-carbons pyrolyzed at 1073 K using mesoporous SBA-15 silica (purple) or a $ZnCl_2$-NaCl (65:35 molar ratio) salt mixture (green) as templating agents. Material performances are compared to a 20 wt% Pt/C catalyst (black). Current data were normalized by the geometric electrode area to show potential as a function of current density. Data were collected at 900 RPM by staircase voltammetry with the materials deposited on a rotating-disk electrode.

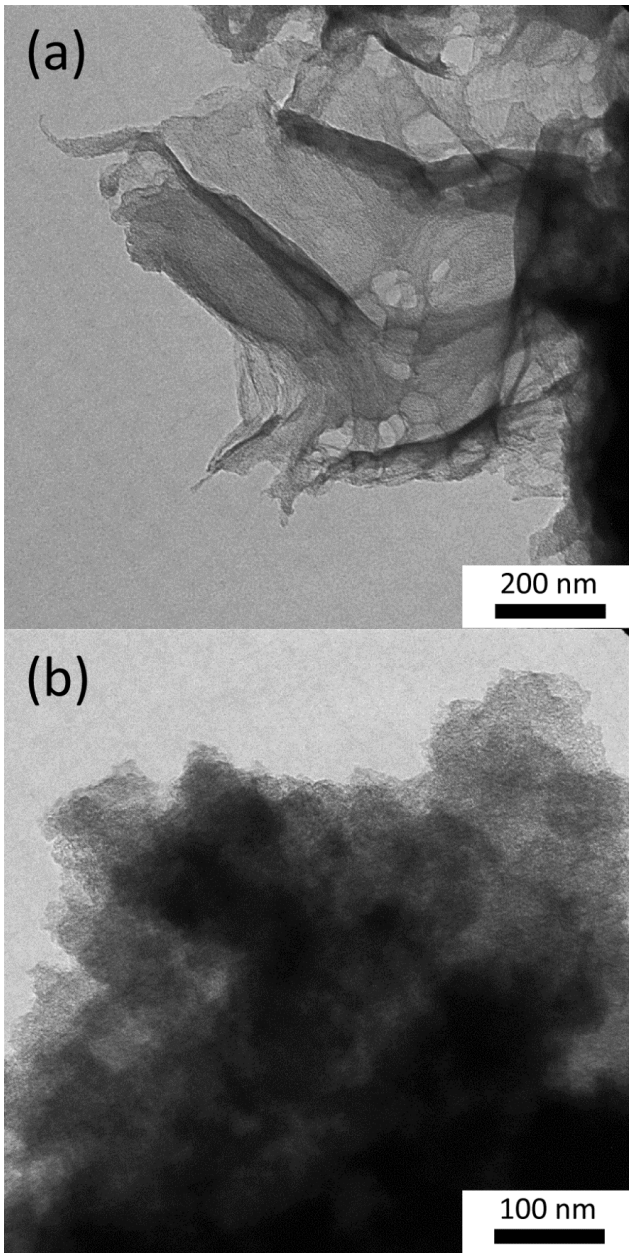

Figure S3.7. Transmission electron microscopy images of cyclohexanehexone-octahydrate- and urea-derived N-containing carbon materials prepared by pyrolyzing a 1:3 molar ratio of cyclohexanehexone-octahydrate and urea at 1073 K in which mesoporosity was introduced by templating with (a) hexagonal SBA-15 mesoporous silica or (b) a $ZnCl_2$-NaCl (65:35 molar ratio) salt mixture. Representative TEM images of the mesoporous materials show that neither

the $ZnCl_2$-NaCl-templated nor the SBA-15-templated material exhibit substantial degrees of mesoscopic order.

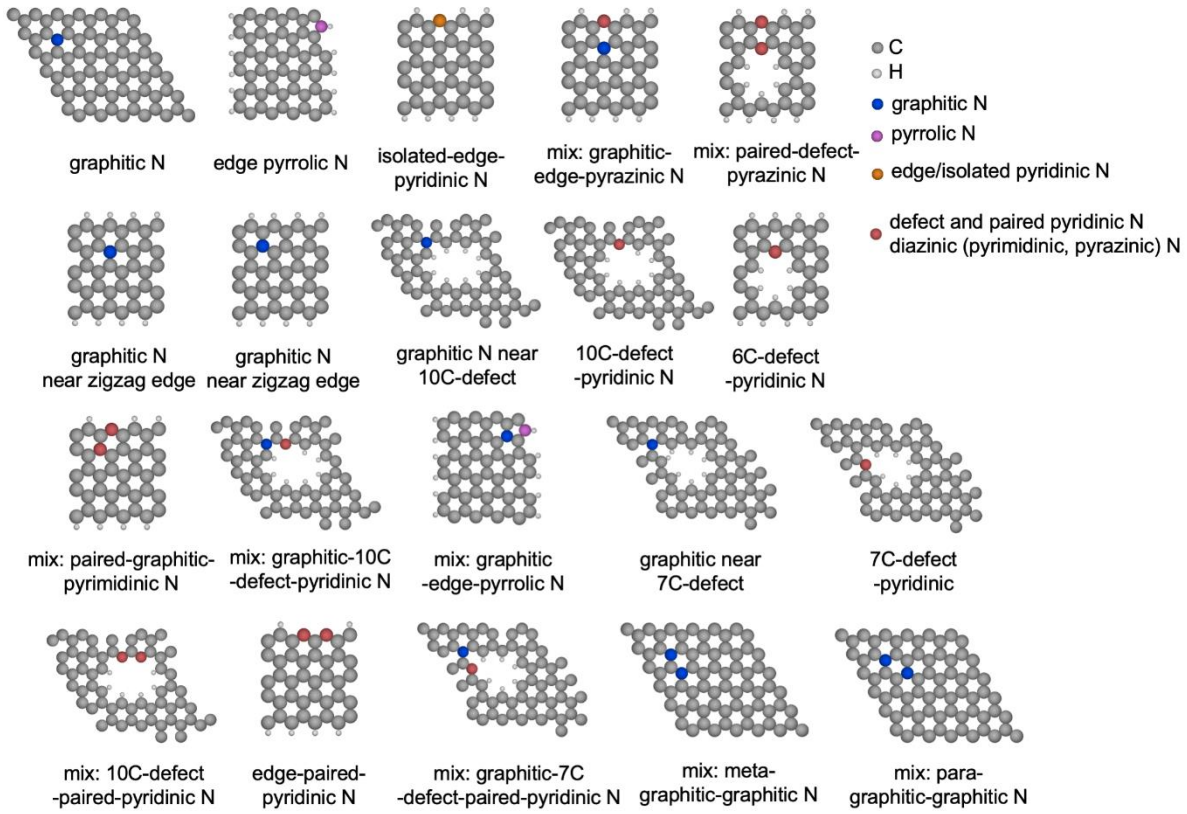

Figure S3.8. Schematic diagrams of nitrogen-carbon structural motifs used to calculate ^{15}N and ^{13}C isotropic chemical shielding values by DFT. Carbon atoms are shown in grey, hydrogen atoms are white, and the different types of N-carbon moieties are shown in different colors: graphitic N as blue, pyrrolic N as purple, isolated pyridinic edge N as yellow, and defect and paired pyridinic N (this includes diazinic species: pyrimidinic, pyrazinic N) as red.

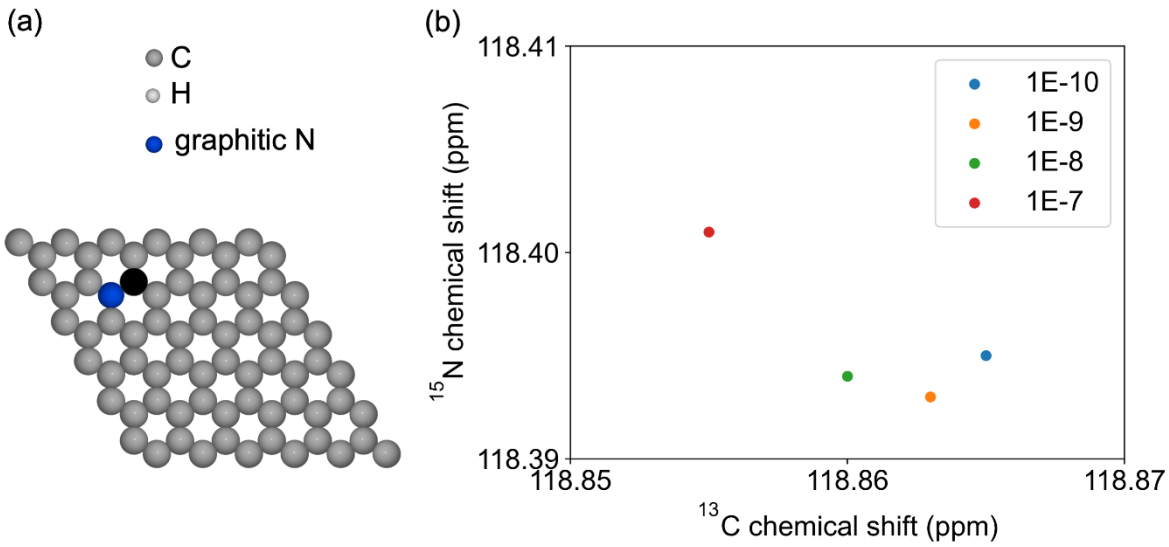

Figure S3.9. (a) Schematic diagram of a representative structural motif, e.g., graphitic N, used to calculate ^{15}N and ^{13}C nuclear shieldings from which DFT-predicted isotropic chemical shift values were determined. The N atom is shown in blue, other carbon atoms in shades of grey, and hydrogen atoms in white. The black circle indicates a C atom that is a first N neighbor. (b) ^{15}N and ^{13}C isotropic chemical shifts calculated for graphitic N using different DFT energy convergence criteria for the respective nuclear shieldings: 10^{-10} (blue), 10^{-9} (orange), 10^{-8} (green), 10^{-7} (red) eV. The figure demonstrates that varying the convergence criteria has a negligible effect on the final calculated chemical shift values (<0.01 ppm).

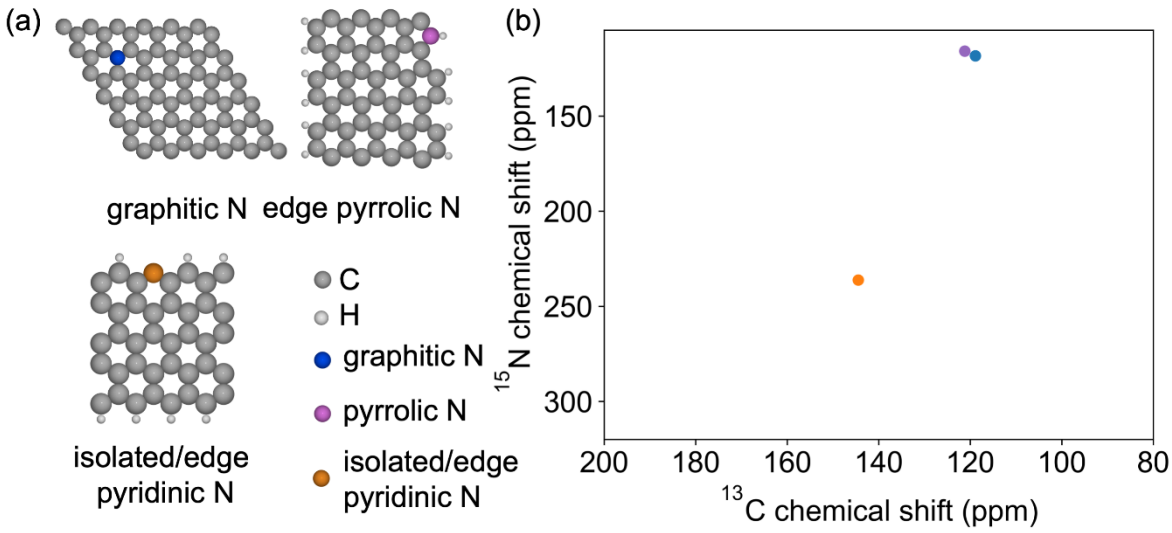

Figure S3.10. (a) Representative schematic diagrams of the N-carbon structures with isolated N heteroatoms used in the DFT calculations of ^{15}N and ^{13}C nuclear shieldings from which (b) ^{15}N and ^{13}C isotropic chemical shifts were determined. The vacuum in *z*-axis was set to 20 Å. For surface pyrrolic or side pyridinic N (see Supplementary Figure S3.8), the planar vacuum was set to 15 Å. DFT calculations suggest that the ^{15}N pyrrolic signal will be displaced +20 ppm in the presence of adsorbed water molecules.

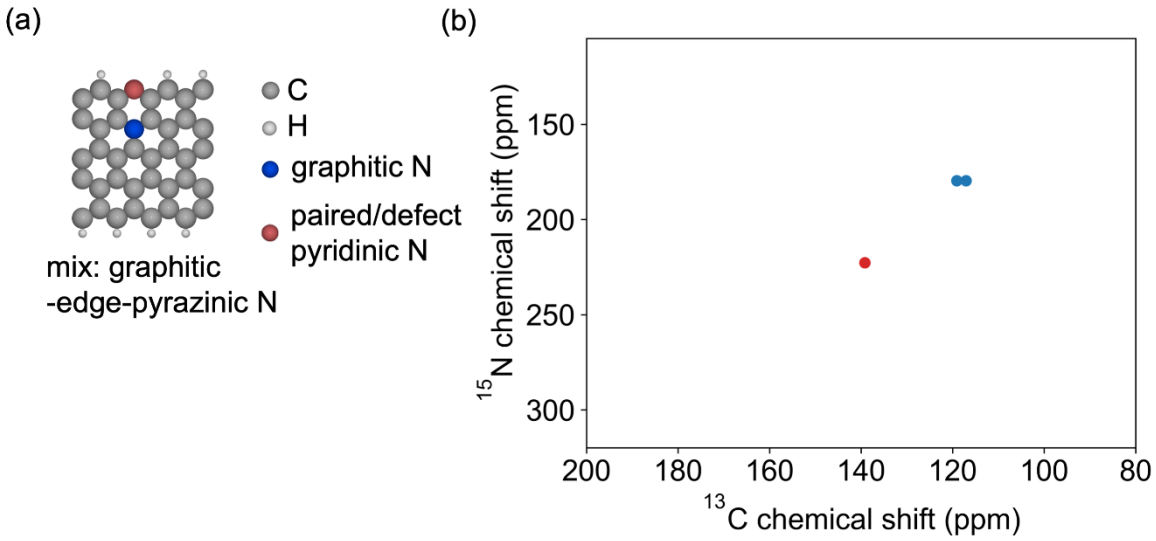

Figure S3.11. (a) Representative schematic diagram of an N-carbon structure with near-neighbor N heteroatoms used in the DFT calculations of ^{15}N and ^{13}C nuclear shieldings from which (b) ^{15}N and ^{13}C isotropic chemical shifts were determined. The vacuum in *z*-axis was set to 20 Å. A variety of first and second near-neighbors results in a distribution of local bonding environments that account for the broadening observed in the experimental 2D NMR spectra.

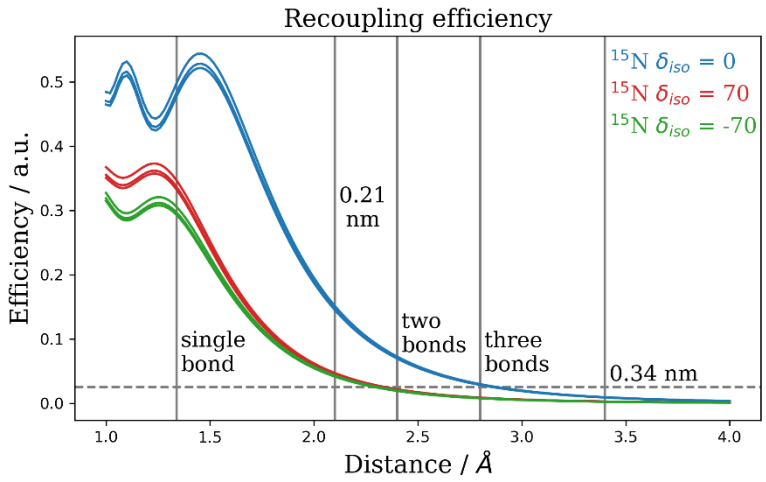

Figure S3.12. Recoupling efficiency of the SR4$_1^2$ recoupling pulse sequence versus the internuclear ^{13}C-^{15}N distance; the dashed line is a guide to the eye and corresponds to 2.5%

efficiency. Vertical grey lines represent typical values for ^{13}C-^{15}N bond lengths, and their corresponding *d*-spacings in X-ray diffraction patterns. Nine sets of simulations are shown, with three ^{13}C offsets (45 ppm, 65 ppm, 95 ppm) and three ^{15}N offsets (-70 ppm, 0 ppm, 70 ppm); recoupling occurred on the ^{15}N channel. RF fields were set to the experimental conditions described in the main manuscript.

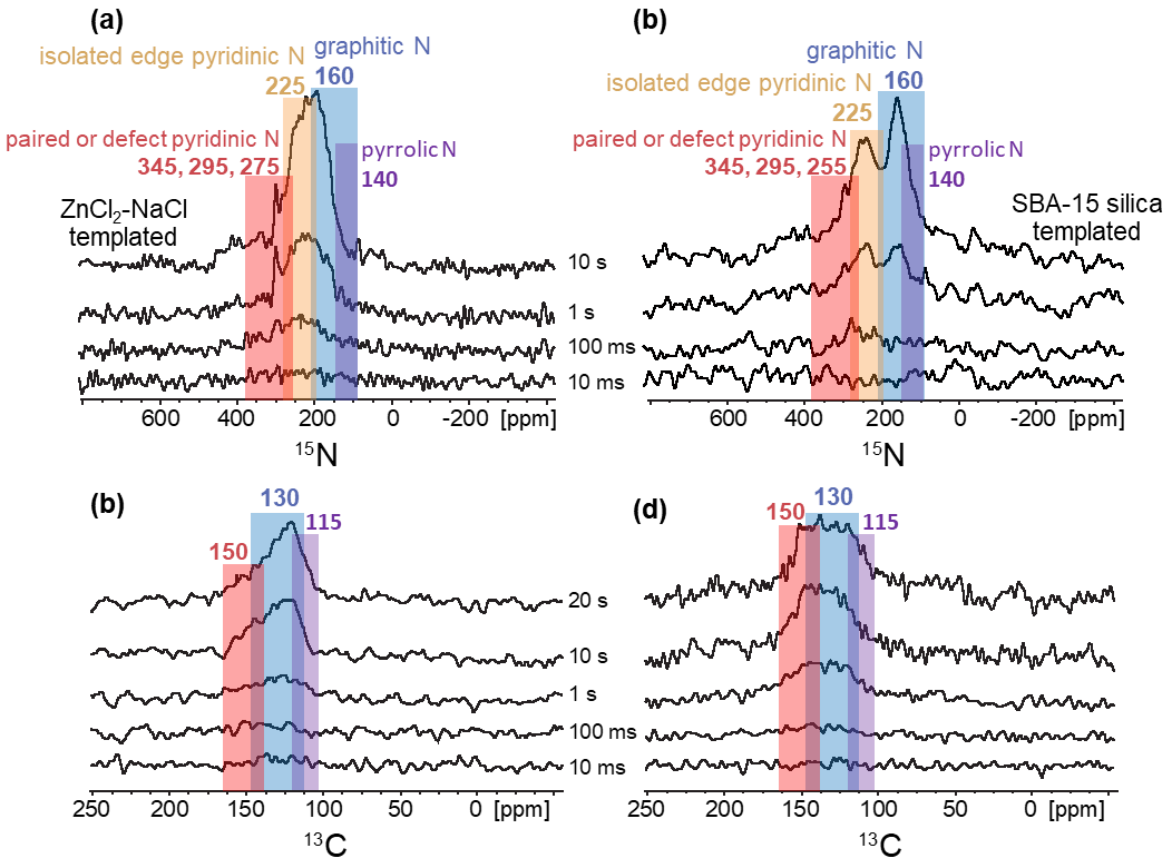

Figure S3.13. T_1-filtered 1D ^{15}N and ^{13}C NMR spectra acquired with recycle delays from 10 ms to 10 s for ^{15}N and 10 ms to 20 s for ^{13}C for the same (a,b) mesoporous salt-templated and (c,d) mesoporous silica-templated N-carbon materials as used in Figure 2 of the main manuscript. The ^{15}N and ^{13}C signals have been assigned, based on the 2D NMR spectra and DFT-calculated shieldings in Figure 2, to various N moieties: pyrrolic (purple), graphitic (blue), isolated edge pyridinic (yellow), and paired/defect pyridinic (red). The fastest-relaxing N-carbon moieties are associated with the pyridinic groups, as evidenced by their ^{15}N signals which are first to appear at 225-275 ppm for recycle delay times > 10 ms, followed closely by graphitic ^{15}N and ^{13}C moieties, which indicate interactions of their nuclear spins with conduction electrons. All experiments were conducted at 95 K on a 400 MHz spectrometer at 8 kHz MAS.

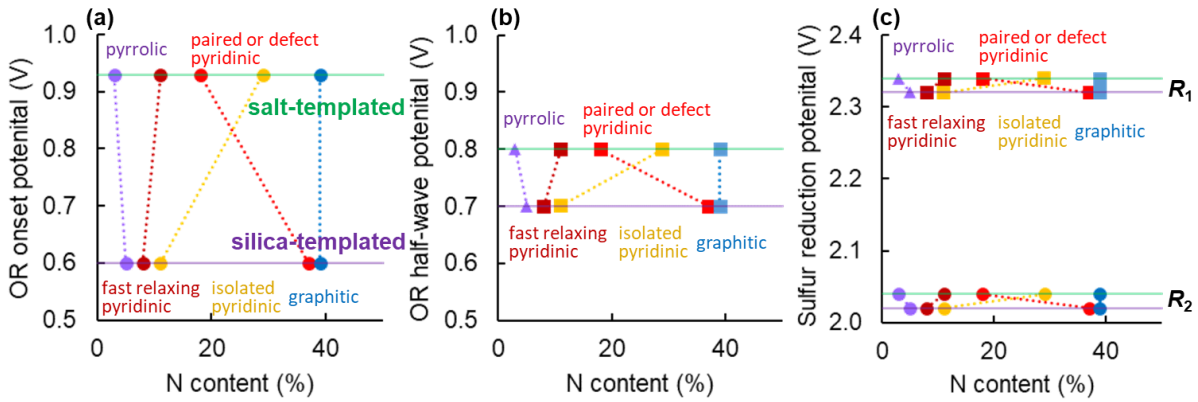

Figure S3.14. (a) Onset and (b) half-wave oxygen reduction potentials from Figure 3.1a and Table 1 of the main manuscript, and (c) sulfur reduction potentials R_1 and R_2 from Figure 3.1c, measured for the mesoporous salt- and silica-templated N-carbon materials (green and purple lines, respectively). Fractional N contents of each type of N-carbon moiety were determined from the quantitative 1D ^{15}N NMR spectra in Figure 3.2c,d. For each of the different measures of electrochemical performance, consistent results are obtained: the pyrrolic N contents (purple) and the graphitic N contents (blue) are approximately the same in the differently templated materials and therefore cannot account for the much higher onset and half-wave oxygen reduction potentials or the higher sulfur reduction potentials of the salt-templated N-carbon material. By comparison, higher percentages of isolated pyridinic N moieties (yellow), and to a lesser extent the fast-relaxing pyridinic ^{15}N moieties (corresponding to ^{15}N signals at 345 ppm and 295 ppm, maroon) in the salt-templated N-carbon, correlate with both higher oxygen reduction and sulfur reduction performances, manifesting the importance of these pyridinic N moieties on ORR and SRR properties. Interestingly, the onset and half-wave oxygen reduction potentials appear to vary inversely with the percentage of paired or defect pyridinic N moieties (red), which represent a significantly lower fraction of the overall N moieties in the salt-templated N-carbon compared to the silica-templated material.

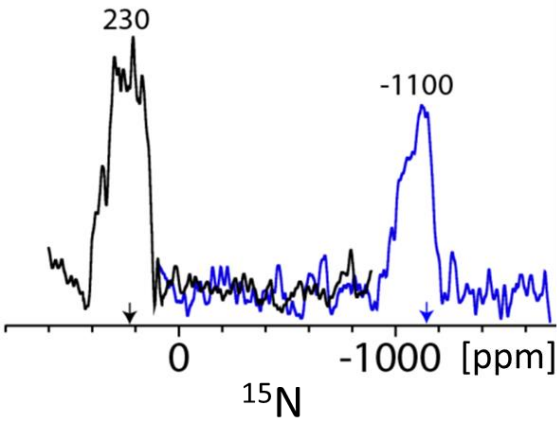

Figure S3.15. Solid-state ^{15}N Hahn-echo MAS NMR spectra of the salt-templated N-carbon acquired at 45 kHz MAS (1.3 mm rotor), 11.7 T at two different spectrometer frequencies centered at 225 ppm (black) and -1170 ppm (blue), as indicated by the respective colored arrows. The experiment was conducted at room temperature, but due to resistive heating the sample temperature was measured to be approximately 336 K. based on the T_1 value of ^{79}Br in polycrystalline KBr, which was added to the MAS rotor as a diluent to reduce the effects of electrical conductivity on the NMR experiments and which also served as a convenient internal temperature reference. The signal at 230 ppm is associated with the same diamagnetic species discussed in the main text. The signal at -1100 ppm is likely a Knight-shifted signal(s) that arises from ^{15}N-carbon nuclei within the bulk of the conductive graphitic materials, that are coupled to conduction electrons.[87] Very short recycle delays (30 ms) and a high number of scans (1.1×10^6) were used to detect fast-relaxing species (-1100 ppm), thus the relative intensities of the signals shown are not quantitative; separate quantitative analyses indicate that the signal at -1100 ppm accounts for only about 0.2% of the total ^{15}N signal intensity.

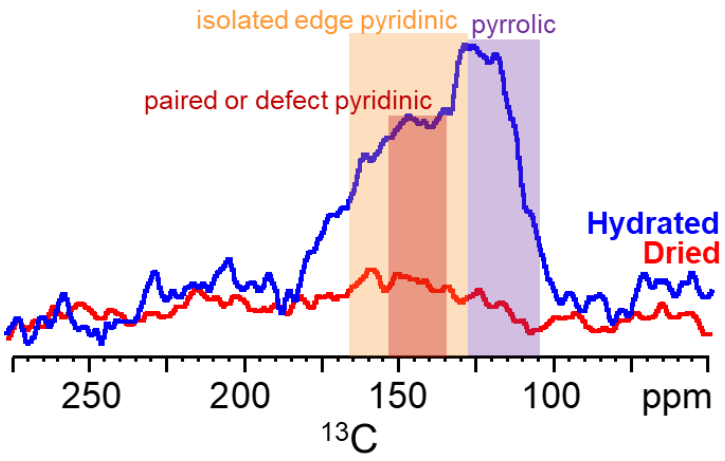

Figure S3.16. Detection of surface ^{13}C species in salt-templated mesoporous N-carbons. Solid-state 1D $^{13}C\{^{1}H\}$ CP-MAS NMR spectra acquired at 9.4 T, 97 K, and 8 kHz MAS of mesoporous N-carbons templated by a $ZnCl_2$-NaCl (65:35 molar ratio) mixture: dry (red) or with adsorbed water (blue). The colored bands indicate spectral regions that correspond to the different ^{15}N-carbon moieties identified in Figure 3.2a: paired or defect pyridinic (red), isolated edge pyridinic (yellow), and pyrrolic (purple) that are near dipolar-coupled ^{1}H nuclei.

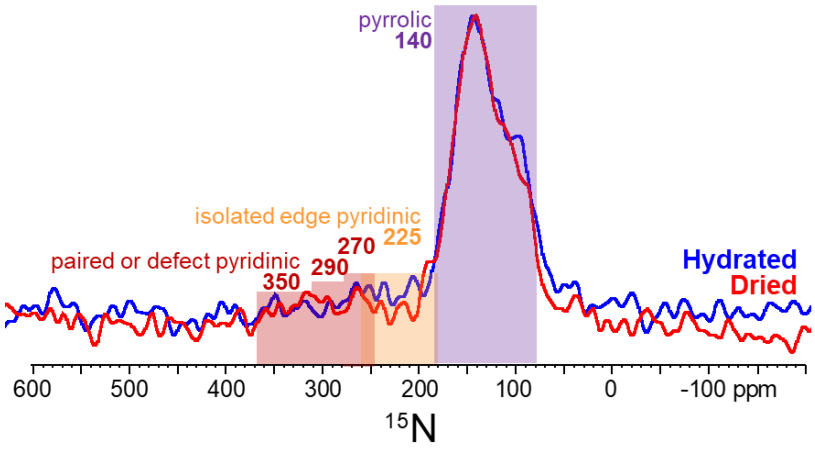

Figure S3.17. Detection of surface ^{15}N species in silica-templated mesoporous N-carbons. Solid-state 1D $^{15}N\{^{1}H\}$ CP-MAS NMR spectra acquired at 9.4 T, 97 K, and 8 kHz MAS of mesoporous N-carbons templated by SBA-15 silica: dry (red) or with adsorbed water (blue). The colored bands indicate spectral regions that correspond to the different ^{15}N-carbon moieties identified in Figure 3.2b: paired or defect pyridinic (red), isolated edge pyridinic (yellow), graphitic (blue), and pyrrolic (purple) that are near dipolar-coupled ^{1}H atoms. There is not a significant difference in between the hydrated and dried samples curves. Thus, even though the silica-templated mesoporous N-carbon material has a higher overall N content, the most important edge pyridinic environments are present in low fractional quantities on the surface and appear to be located in sites that are inaccessible to adsorbing water, accounting for the lower oxygen and sulfur reduction performances compared to the salt-templated N-carbon electrocatalyst.

Extended discussion of solid-state 2D NMR analyses

The 2D ^{13}C-^{15}N NMR spectra of can be analyzed, in conjunction with DFT modeling, to assign the correlated signals to distinct N-carbon moieties and structures (Supplementary Figure S3.7), thereby identifying the local bonding environments of the ^{15}N and ^{13}C species and their distributions. DFT calculations yield the electronic shieldings of nuclei in distinct atomic environments, which are manifested as differences in isotropic ^{15}N and ^{13}C chemical shifts ($\delta_{cs,iso}$). The DFT analyses and resulting nuclear shieldings enable confident assignments of the correlated ^{15}N and ^{13}C signals in the experimental 2D ^{13}C-^{15}N correlation spectra and provide insights on the distributions of local bonding environments that account for the broad lineshapes. The calculated shieldings of ^{15}N and ^{13}C nuclei in different mesoporous N-carbon moieties are shown in Table 3.2. For example, ^{15}N and ^{13}C atoms in graphitic environments are calculated to have isotropic chemical shifts in the ranges of 110–190 ppm and 90–150 ppm, respectively (Figure 3.2, blue points).[49] Atoms in pyrrolic environments are predicted to exhibit isotropic ^{15}N and ^{13}C chemical shifts of 110–150 ppm and 110-125 ppm, respectively (Figure 3.2, purple points). Similarly, pyridinic moieties that are isolated from other N heteroatoms at the edges of graphitic sheets are calculated to have ^{15}N and ^{13}C isotropic chemical shifts of 215-240 ppm and 130-145 ppm, respectively (Figure 3.2, yellow points).[47] The presence of two or more nearby (within 3 bond distances) N moieties results in lower electron density, as manifested by the displacement of NMR signals to higher frequency (*i.e.*, higher chemical shift values). For example, paired pyridinic moieties (includes diazinic species: pyrimidinic, pyrazinic) or those associated with interior pyridinic defect sites are calculated to have isotropic ^{15}N and ^{13}C chemical shifts of 210–300 ppm and 135–160 ppm (red points), respectively.[46,49] The DFT analyses thus enable the correlated ^{15}N and ^{13}C NMR

signals in the N-carbons to be confidently assigned to distinct types of graphitic, pyrrolic, isolated edge pyridinic, and paired or defect pyridinic N moieties.

Using the DFT insights, the distinct distributions of 2D NMR signal intensity observed in Figure 3.2 for the different mesoporous N-carbons can be assigned and related to both their different surface chemistries, as well as to their resulting oxygen- and sulfur-reduction properties. For example, the 2D ^{13}C-^{15}N NMR spectrum in Figure 3.2a of the salt-templated mesoporous N-carbon shows broad distributions of correlated intensities in the ranges of 130–190 ppm in the ^{15}N dimension and 120–145 ppm in the ^{13}C dimension (blue region), which are assigned to ^{15}N atoms within graphitic sheets based on DFT calculations and literature.[31,46] Similarly, correlated signals at 135–170 ppm in the ^{15}N dimension and 110–120 ppm in the ^{13}C dimension (purple region) are assigned to ^{15}N atoms in pyrrolic[30,31,43] environments, which are present in very small quantities compared to the other N environments (see below). Correlated signals centered at 225 ppm in the ^{15}N dimension and 145 ppm in the ^{13}C dimension (yellow region) arise from surface and edge pyridinic[43] ^{15}N moieties that are relatively isolated. Correlated intensities in the range of 240–290 ppm in the ^{15}N dimension and 135–155 ppm in the ^{13}C dimension (red region) are assigned to molecularly proximate ("paired") and internal defect pyridinic ^{15}N moieties.[30,31,46,49] In addition, correlated intensity is observed at the boundaries of these chemical shift ranges (green regions), which establish that subsets of the pyridinic and graphitic species are in close proximity to one another (within three bond distances, Supplementary Figure S3.11), manifesting commingled species. These include paired or defect pyridinic ^{15}N signals at 255–280 ppm correlated with graphitic ^{13}C signals at 120–135 ppm (lower green region) and graphitic ^{15}N signals at 150–190 ppm correlated with pyridinic ^{13}C signals at 145–160 ppm (upper green region). Several of the modeled structures

(Supplementary Figure S3.7) yield DFT-calculated ^{15}N and ^{13}C shieldings that do not coincide with experimentally observed signal intensity in Figure 3.2a, indicating that they are not present or exist in small fractions that are below the sensitivity limit of the measurements (<1%).

For the mesoporous N-carbons prepared under identical conditions except with SBA-15 silica as a mesostructure-directing template, similar types of N-containing moieties are present, as manifested in the 2D ^{13}C-^{15}N NMR spectrum (Figure 3.2b), although with significantly different distributions and relative populations. The salt-templated N-carbon exhibits significantly stronger correlated signal intensity in the isolated edge pyridinic region (centered at 225 ppm in the ^{15}N dimension and 145 ppm in the ^{13}C dimension, yellow region) than the silica-templated N-carbon, suggesting that the salt-templated N-carbon has a larger ratio of these environments. Additionally, the salt-templated N-carbon shows well resolved ^{15}N intensity at higher frequency associated with paired or defect pyridinic shift values (240-280 ppm in ^{15}N dimension, red), from which isolated edge pyridinic moieties are unresolved in the silica-templated material. We note that the relatively weak ^{15}N signals at ~300 ppm in the 1D ^{15}N MAS NMR spectra (Fig. 2c,d) are not observed in the 2D ^{13}C-^{15}N NMR spectra (Fig. 2a,b), likely due to broadening of weak correlated 2D intensity that manifests a broad distribution of local environments. In conclusion, the 2D ^{13}C-^{15}N NMR spectra of the salt- and silica-templated mesoporous N-carbons exhibit clear differences in the distributions of ^{15}N-carbon species, which are attributed to their different interactions with the template surfaces during pyrolysis.

3.8 References

1. Xu, Y. *et al.* Holey graphene frameworks for highly efficient capacitive energy storage. *Nat. Commun.* **5**, (2014).
2. Gong, K., Du, F., Xia, Z., Durstock, M. & Dai, L. Nitrogen-Doped Carbon Nanotube Arrays with High Electrocatalytic Activity for Oxygen Reduction. *Science.*. **323**, 760–764 (2009).
3. Zhao, Y., Nakamura, R., Kamiya, K., Nakanishi, S. & Hashimoto, K. Nitrogen-doped carbon nanomaterials as non-metal electrocatalysts for water oxidation. *Nat. Commun.* **4**, 1–7 (2013).
4. Liang, H. W., Zhuang, X., Brüller, S., Feng, X. & Müllen, K. Hierarchically porous carbons with optimized nitrogen doping as highly active electrocatalysts for oxygen reduction. *Nat. Commun.* **5**, 4973 (2014).
5. She, Z. W. *et al.* Combining theory and experiment in electrocatalysis: Insights into materials design. *Science* **355**, (2017).
6. Lu, Z. *et al.* High-efficiency oxygen reduction to hydrogen peroxide catalysed by oxidized carbon materials. *Nat. Catal.* **1**, 156–162 (2018).
7. Joo, S. H. *et al.* Ordered nanoporous arrays of carbon supporting high dispersions of platinum nanoparticles. *Nature* **412**, 169–172 (2001).
8. Lefèvre, M., Proietti, E., Jaouen, F. & Dodelet, J.-P. Iron-Based Catalysts with Improved Oxygen Reduction Activity in Polymer Electrolyte Fuel Cells. *Science (80-.).* **324**, 71–74 (2009).

9. He, L., Weniger, F., Neumann, H. & Beller, M. Synthesis, Characterization, and Application of Metal Nanoparticles Supported on Nitrogen-Doped Carbon: Catalysis beyond Electrochemistry. *Angew. Chemie - Int. Ed.* **55**, 12582–12594 (2016).

10. Sahoo, B. *et al.* A Biomass-Derived Non-Noble Cobalt Catalyst for Selective Hydrodehalogenation of Alkyl and (Hetero)Aryl Halides. *Angew. Chemie - Int. Ed.* **56**, 11242–11247 (2017).

11. Yang, W., Fellinger, T. P. & Antonietti, M. Efficient metal-free oxygen reduction in alkaline medium on high-surface-area mesoporous nitrogen-doped carbons made from ionic liquids and nucleobases. *J. Am. Chem. Soc.* **133**, 206–209 (2011).

12. Li, Y. *et al.* An oxygen reduction electrocatalyst based on carbon nanotube-graphene complexes. *Nat. Nanotechnol.* **7**, 394–400 (2012).

13. Chung, H. T., Won, J. H. & Zelenay, P. Active and stable carbon nanotube/nanoparticle composite electrocatalyst for oxygen reduction. *Nat. Commun.* **4**, 1922 (2013).

14. Chung, H. T. *et al.* Direct atomic-level insight into the active sites of a high-performance PGM-free ORR catalyst. *Science.* **357**, 479–484 (2017).

15. Dong, Q. & Wang, D. Catalysts in metal-air batteries. *MRS Commun.* **8**, 372–386 (2018).

16. Zhang, J., Zhao, Z., Xia, Z. & Dai, L. A metal-free bifunctional electrocatalyst for oxygen reduction and oxygen evolution reactions. *Nat. Nanotechnol.* **10**, 444–452 (2015).

17. Lei, T. *et al.* Inhibiting Polysulfide Shuttling with a Graphene Composite Separator for Highly Robust Lithium-Sulfur Batteries. *Joule* **2**, 2091–2104 (2018).

18. Peng, L. *et al.* A fundamental look at electrocatalytic sulfur reduction reaction. *Nat. Catal.* **3**, 762–770 (2020).

19. Zhong, Y. *et al.* Popcorn Inspired Porous Macrocellular Carbon: Rapid Puffing Fabrication from Rice and Its Applications in Lithium–Sulfur Batteries. *Adv. Energy Mater.* **8**, 1–8 (2018).

20. Othman, R., Dicks, A. L. & Zhu, Z. Non precious metal catalysts for the PEM fuel cell cathode. *Int. J. Hydrogen Energy* **37**, 357–372 (2012).

21. Hu, Z. & Srinivasan, M. P. Preparation of high-surface-area activated carbon from coconut shell fibers. *Microporous Mesoporous Mater.* **27**, 11–18 (1999).

22. Guo, C. Z., Liao, W. L., Sun, L. T. & Chen, C. G. Synthesis of non-noble nitrogen-containing catalysts for cathodic oxygen reduction reaction: A critical review. *Int. J. Electrochem. Sci.* **10**, 2467–2477 (2015).

23. Wang, X., He, Z., Shi, Y. & Li, B. Nitrogen-Doped Ordered Mesoporous Carbon as Metal-Free Catalyst for Power Generation in Single Chamber Microbial Fuel Cells. *J. Electrochem. Soc.* **164**, F620–F627 (2017).

24. Fechler, N. *et al.* Eutectic Syntheses of Graphitic Carbon with High Pyrazinic Nitrogen Content. *Adv. Mater.* **28**, 1287 (2016).

25. Dorjgotov, A., Ok, J., Jeon, Y., Yoon, S. H. & Shul, Y. G. Activity and active sites of nitrogen-doped carbon nanotubes for oxygen reduction reaction. *J. Appl. Electrochem.* **43**, 387–397 (2013).

26. Ding, W. *et al.* Space-confinement-induced synthesis of pyridinic- and pyrrolic-nitrogen-doped graphene for the catalysis of oxygen reduction. *Angew. Chemie - Int. Ed.* **52**, 11755–11759 (2013).

27. Guo, D. *et al.* Active sites of nitrogen-doped carbon materials for oxygen reduction reaction clarified using model catalysts. *Science* **351**, 361–365 (2016).

28. Wu, J. *et al.* Nitrogen-Doped Graphene with Pyridinic Dominance as a Highly Active and Stable Electrocatalyst for Oxygen Reduction. *ACS Appl. Mater. Interfaces* **7**, 14763–14769 (2015).

29. Lai, L. *et al.* Exploration of the active center structure of nitrogen-doped graphene-based catalysts for oxygen reduction reaction. *Energy Environ. Sci.* **5**, 7936–7942 (2012).

30. Baccile, N. *et al.* Structural Insights on Nitrogen-Containing Hydrothermal Carbon Using Solid-State Magic Angle Spinning ^{13}C and ^{15}N Nuclear Magnetic Resonance. *J. Phys. Chem. C* **115**, 8976–8982 (2011).

31. Hu, Y. *et al.* Synthesis of ^{13}C-,^{15}N-Labeled Graphitic Carbon Nitrides and NMR-Based Evidence of Hydrogen-Bonding Assisted Two-Dimensional Assembly. *Chem. Mater.* **29**, 5080–5089 (2017).

32. Szewczyk, I. *et al.* Electrochemical Denitrification and Oxidative Dehydrogenation of Ethylbenzene over N-doped Mesoporous Carbon: Atomic Level Understanding of Catalytic Activity by 15N NMR Spectroscopy. *Chem. Mater.* **32**, 7263–7273 (2020).

33. Ryoo, R., Joo, S. H. & Jun, S. Synthesis of Highly Ordered Carbon Molecular Sieves via Template-Mediated Structural Transformation. *J. Phys. Chem. B* **103**, 7743–7746 (1999).

34. Wu, Z. *et al.* Synthesis of Ordered Mesoporous Carbon Materials with Semi-Graphitized Walls via Direct In-situ Silica-Confined Thermal Decomposition of CH_4 and Their Hydrogen Storage Properties. *Top. Catal.* **52**, 12–26 (2009).

35. Fechler, N., Fellinger, T. P. & Antonietti, M. 'Salt Templating': A simple and sustainable pathway toward highly porous functional carbons from ionic liquids. *Adv. Mater.* **25**, 75–79 (2013).

36. Kim, D. *et al.* Highly Graphitic Mesoporous Fe,N-Doped Carbon Materials for Oxygen Reduction Electrochemical Catalysts. *ACS Appl. Mater. Interfaces* **10**, 25337 (2018).

37. Garsany, Y., Baturina, O. A. & Swider-Lyons, K. E. Impact of Sulfur Dioxide on the Oxygen Reduction Reaction at Pt/Vulcan Carbon Electrocatalysts. *J. Electrochem. Soc.* **154**, B670 (2007).

38. Li, L. *et al.* Stabilizing sulfur cathodes using nitrogen-doped graphene as a chemical immobilizer for Li-S batteries. *Carbon N. Y.* **108**, 120–126 (2016).

39. Bonaccorso, F. *et al.* Graphene, related two-dimensional crystals, and hybrid systems for energy conversion and storage. *Science.* **347**, (2015).

40. Wild, M. *et al.* Lithium sulfur batteries, a mechanistic review. *Energy Environ. Sci.* **8**, 3477–3494 (2015).

41. Jansen, R. J. J. & van Bekkum, H. XPS of nitrogen-containing functional groups on activated carbon. *Carbon N. Y.* **33**, 1021–1027 (1995).

42. Zhao, L. *et al.* Sustainable nitrogen-doped carbonaceous materials from biomass derivatives. *Carbon N. Y.* **48**, 3778–3787 (2010).

43. Kuroki, S., Nabae, Y., Chokai, M., Kakimoto, M. A. & Miyata, S. Oxygen reduction activity of pyrolyzed polypyrroles studied by ^{15}N solid-state NMR and XPS with principal component analysis. *Carbon N. Y.* **50**, 153–162 (2012).

44. Falco, C., Sevilla, M., White, R. J., Rothe, R. & Titirici, M. M. Renewable nitrogen-doped hydrothermal carbons derived from microalgae. *ChemSusChem* **5**, 1834–1840 (2012).

45. Carrasco, P. M. *et al.* Structure-conductivity relationships in chemical polypyrroles of low, medium and high conductivity. *Synth. Met.* **156**, 420–425 (2006).

46. Gammon, W. J., Hoatson, G. L., Holloway, B. C., Vold, R. L. & Reilly, A. C. Bonding in hard and elastic amorphous carbon nitride films investigated using ^{15}N, ^{13}C, and ^{1}H NMR spectroscopy. *Phys. Rev. B* **68**, 195401 (2003).

47. Wang, X., Hou, Z., Ikeda, T. & Terakura, K. NMR chemical shifts of ^{15}N-bearing graphene. *J. Phys. Chem. C* **118**, 13929–13935 (2014).

48. Huo, J. *et al.* Improved hydrothermal stability of Pd nanoparticles on nitrogen-doped carbon supports. *Catal. Sci. Technol.* **8**, 3548–3561 (2018).

49. Martin, G. J., Martin, M. L. & Gouesnard, J.-P. *^{15}N-NMR Spectroscopy*. (Springer-Verlag, 1981).

50. Pell, A. J., Pintacuda, G. & Grey, C. P. Paramagnetic NMR in solution and the solid state. *Prog. Nucl. Magn. Reson. Spectrosc.* **111**, 1–271 (2019).

51. Yesinowski, J. P., Berkson, Z. J., Cadars, S., Purdy, A. P. & Chmelka, B. F. Spatially correlated distributions of local metallic properties in bulk and nanocrystalline GaN. *Phys. Rev. B* **95**, (2017).

52. Saito, R., Tsukada, M., Kobayashi, K. & Kamimura, H. Nuclear magnetic resonance in higher-stage graphite intercalation compounds. *Phys. Rev. B* **35**, 2963–2971 (1987).

53. Kume, K., Maniwa, Y., Suematsu, H., Iye, Y. & Tanuma, S. High resolution ^{13}C NMR in HOPG intercalation compounds. *Synth. Met.* **8**, 69–75 (1983).

54. Zhao, D. *et al.* Triblock copolymer syntheses of mesoporous silica with periodic 50 to 300 angstrom pores. *Science* **279**, 548–52 (1998).

55. Fechler, N. *et al.* Eutectic Syntheses of Graphitic Carbon with High Pyrazinic Nitrogen Content. *Adv. Mater.* **28**, 1287–1294 (2016).

56. Jun, S. *et al.* Synthesis of new, nanoporous carbon with hexagonally ordered mesostructure. *J. Am. Chem. Soc.* **122**, 10712–10713 (2000).

57. Fung, B. M., Khitrin, A. K. & Ermolaev, K. An Improved Broadband Decoupling Sequence for Liquid Crystals and Solids. *J. Magn. Reson.* **142**, 97–101 (2000).

58. Bertani, P., Raya, J. & Bechinger, B. ^{15}N chemical shift referencing in solid state NMR. *Solid State Nucl. Magn. Reson.* **61**–**62**, 15–18 (2014).

59. Thurber, K. R. & Tycko, R. Measurement of sample temperatures under magic-angle spinning from the chemical shift and spin-lattice relaxation rate of ^{79}Br in KBr powder. *J. Magn. Reson.* **196**, 84–87 (2009).

60. Yesinowski, J. P., Ladouceur, H. D. D., Purdy, A. P. P. & Miller, J. B. B. Electrical and ionic conductivity effects on magic-angle spinning nuclear magnetic resonance parameters of CuI. *J. Chem. Phys.* **133**, 234509 (2010).

61. Thurber, K. R. & Tycko, R. Measurement of sample temperatures under magic-angle spinning from the chemical shift and spin-lattice relaxation rate of ^{79}Br in KBr powder. *J. Magn. Reson.* **196**, 84–87 (2009).

62. Hu, B., Trébosc, J. & Amoureux, J. P. Comparison of several hetero-nuclear dipolar recoupling NMR methods to be used in MAS HMQC/HSQC. *J. Magn. Reson.* **192**, 112–122 (2008).

63. Lesage, A., Sakellariou, D., Steuernagel, S. & Emsley, L. Carbon — Proton Chemical Shift Correlation in Solid-State NMR by Through-Bond Multiple-Quantum Spectroscopy. *J. Am. Chem. Soc.* **120**, 13194–13201 (1998).

64. Weingarth, M. & Baldus, M. Introduction to Biological Macromolecules. in *Illustrated Medical Biochemistry* Chapter 1 (Jaypee Brothers Medical Publishers (P) Ltd., 2005). doi:10.5005/jp/books/10375_3

65. Levitt, M. H. *Spin Dynamics: Basics of Nuclear Magnetic Resonance*. (John Wiley & Sons, 2008).

66. Kobayashi, T., Singappuli-Arachchige, D., Wang, Z., Slowing, I. I. & Pruski, M. Spatial distribution of organic functional groups supported on mesoporous silica nanoparticles: a study by conventional and DNP-enhanced ^{29}Si solid-state NMR. *Phys. Chem. Chem. Phys.* **19**, 1781–1789 (2017).

67. Bak, M., Rasmussen, J. T. & Nielsen, N. C. SIMPSON: A General Simulation Program for Solid-State NMR Spectroscopy. *J. Magn. Reson.* **147**, 296–330 (2000).

68. Tošner, Z. *et al.* Computer-intensive simulation of solid-state NMR experiments using SIMPSON. *J. Magn. Reson.* **246**, 79–93 (2014).

69. Bak, M. & Nielsen, N. C. Repulsion, A Novel Approach to Efficient Powder Averaging in Solid-State NMR. *J. Magn. Reson.* **125**, 132–139 (1997).

70. Kresse, G. & Hafner, J. Ab initio molecular dynamics for liquid metals. *Phys. Rev. B* **47**, 558–561 (1993).

71. Yates, J. R., Pickard, C. J. & Mauri, F. Calculation of NMR chemical shifts for extended systems using ultrasoft pseudopotentials. *Phys. Rev. B - Condens. Matter Mater. Phys.* **76**, 1–11 (2007).

72. Kohn, W. & Sham, L. J. Self-consistent equations including exchange and correlation effects. *Phys. Rev.* **140**, A1133 (1965).

73. Perdew, J. P., Burke, K. & Ernzerhof, M. Perdew, Burke, Ernzerhof - 1997 - Generalized Gradient Approximation Made Simple(2). *Phys. Rev. Lett.* **77**, 3865–3868 (1996).

74. Steinmann, S. N. & Corminboeuf, C. Comprehensive benchmarking of a density-dependent dispersion correction. *J. Chem. Theory Comput.* **7**, 3567–3577 (2011).

75. Steinmann, S. N. & Corminboeuf, C. A generalized-gradient approximation exchange hole model for dispersion coefficients. *J. Chem. Phys.* **134**, (2011).

76. Pickard, C. J. & Mauri, F. All-electron magnetic response with pseudopotentials: NMR chemical shifts. *Phys. Rev. B - Condens. Matter Mater. Phys.* **63**, 2451011–2451013 (2001).

77. Ravikovitch, P. I., Haller, G. L. & Neimark, A. V. Density functional theory model for calculating pore size distributions: pore structure of nanoporous catalysts. *Adv. Colloid Interface Sci.* **76**–**77**, 203–226 (1998).

78. Brunauer, S., Emmett, P. H. & Teller, E. Adsorption of Gases in Multimolecular Layers. *J. Am. Chem. Soc.* **60**, 309–319 (1938).

79. Gierszal, K. P., Jaroniec, M., Kim, T.-W., Kim, J. & Ryoo, R. High temperature treatment of ordered mesoporous carbons prepared by using various carbon precursors and ordered mesoporous silica templates. *New J. Chem.* **32**, 981 (2008).

80. Tuinstra, F. & Koenig, L. Raman Spectrum of Graphite. *J. Chem. Phys.* **53**, 1126–1130 (1970).

81. Herrmann, I., Kramm, U. I., Radnik, J., Fiechter, S. & Bogdanoff, P. Influence of Sulfur on the Pyrolysis of CoTMPP as Electrocatalyst for the Oxygen Reduction Reaction. *J. Electrochem. Soc.* **156**, B1283–B1292 (2009).

82. Dippel, B., Jander, H. & Heintzenberg, J. NIR FT Raman spectroscopic study of flame soot. *Phys. Chem. Chem. Phys.* **1**, 4707–4712 (1999).

83. Wu, M. *et al.* Fe/N/S-composited hierarchically porous carbons with optimized surface functionality, composition and nanoarchitecture as electrocatalysts for oxygen reduction reaction. *J. Catal.* **352**, 208–217 (2017).

84. Zhu, J. *et al.* Porous and high electronic conductivity nitrogen-doped nano-sheet carbon derived from polypyrrole for high-power supercapacitors. *Carbon N. Y.* **107**, 638–645 (2016).

85. Milenov, T. & Avramova, I. Deposition of graphene by sublimation of pyrolytic carbon. *Opt. Quantum Electron.* **47**, 851–863 (2015).

86. Ferrari, A. C. & Robertson, J. Interpretation of Raman spectra of disordered and amorphous carbon. *Phys. Rev. B* **61**, (2000).

87. Knight, W. D. Nuclear Magnetic Resonance Shift in Metals. *Phys. Rev.* **76**, 1259–1260 (1949).

4. Atomic environments in N-containing graphitic carbon probed by first-principles calculations and solid-state nuclear magnetic resonance

This chapter is adapted from a published paper. My collaborator from UCLA is the lead author on this paper as he is responsible for the DFT calculations. I worked very closely with him to discuss the hypothesized geometries and structures, group the various N-moieties, and provide experimental data for model/experimental comparisons.

Paper: *J. Phys. Chem. C* **2021**, 125, 16, 8779–8787

DOI: 10.1021/acs.jpcc.1c00511

Authors: Ziyang Wei, Shona M. Becwar, Bradley F. Chmelka, and Philippe Sautet

The detailed experimental insights obtained from the 2D $^{13}C\{^{15}N\}$ NMR spectra (Chapter 3) of local N and C bonding environments are analyzed in conjunction with important DFT modeling to assign the correlated signals to distinct N-carbon moieties and structures. DFT calculations yield the electronic shieldings of nuclei in distinct atomic environments, which are manifested as differences in isotropic ^{15}N and ^{13}C chemical shifts ($\delta_{cs,iso}$). It was found that variations in bonding environments manifest as differences in predicted chemical shieldings (thus chemical shifts) which agree with the broad distributions of signals detected by NMR. This has not been shown before for these types of materials. The differences in chemical shift

values between graphitic, pyridinic, pyrrolic N-moieties were found to be largely accounted for by differences in electronegativity. The smaller differences in distributions of local ^{13}C and ^{15}N environments are primarily accounted for by surface effects and influences of proximate N atoms. The DFT analyses thus enable the correlated ^{15}N and ^{13}C NMR signals in the N-carbons to be confidently assigned to distinct types of graphitic, pyrrolic, isolated edge pyridinic, and paired or defect pyridinic N moieties.

My collaborator from UCLA, Ziyang Wei, is the lead author on this paper as he is responsible for the DFT calculations and the majority of the writing in this manuscript. I worked very closely with him to discuss the hypothesized geometries and structures, group the various N-moieties, and provide experimental data, analyses, and discussion for model/experimental comparisons.

4.1 Abstract

To understand the nature and structure of N-doping centers in carbon materials, we combine two-dimensional (2D) solid-state NMR experiments and chemical shift calculations for ^{15}N, ^{13}C, and ^{1}H nuclei from density functional theory (DFT). Calculated chemical shift values agree with experimental signal locations found in the 2D ^{13}C–^{15}N NMR spectra. The chemical shift values of graphitic/pyridinic/pyrrolic N-moieties are differentiated by comparing the electronegativities of the various environments. Interestingly, the shift

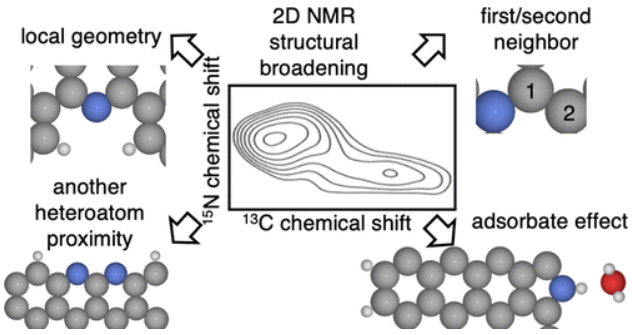

calculations also account for the spectral broadening detected in the experimental spectra. Four main factors were found to account for NMR signal broadening which include: (1) the standalone N/C geometry, (2) the effect of a second N atom nearby, (3) differences in a first or second neighbor C atom, and (4) the influence of proximate residual water, which is important to understanding the electrocatalytic environments. As expected, there is a correlation between the charge of the probed atom and its chemical shift such that the smaller the charge (i.e., higher electron density), the more shielded the nucleus is, and thus the smaller the associated chemical shift. The correlations between calculated and experimental chemical shift values (and corresponding signal broadening), improve the understanding of the nature of heteroatom sites in N−carbon materials, and contribute to the rational design of such materials with desired electronic properties for improved electrochemical performance.

4.2 Introduction

Nitrogen-containing carbons have emerged as an important class of materials due to their attractive electronic properties with applications as electrodes,[1,2] electrocatalysts,[3,4] and catalyst supports.[5] Typical N-doping of graphene, however, provides a mix of different local N structures, where the simplest species[6] are pyrrolic, pyridinic, and graphitic nitrogen. Materials with high extents of doping are desired and present a large range of lateral assembly and interactions among these three basic types of N centers. To establish tentative performance−structure relations, numerous experimental efforts have been made to detect the local environments of N-doped graphene including Raman spectroscopy,[7] X-ray photoelectron spectroscopy[1,8] (XPS), scanning tunneling microscopy[7,9] (STM), and NMR[10]

spectroscopy. However, Raman spectroscopy can provide only limited insights into the detailed local structure of N atoms since distributions of various local moieties are present, which limit the resolution. XPS, in principle, is sensitive to the local bonding near surfaces, but the slight differences in binding energies are hard to accurately simulate and interpret, especially since the resolution is low.[1,8] STM provides high-resolution images of local structures, but the sampling of the various sites is challenging. Two-dimensional (2D) solid-state nuclear magnetic resonance (ssNMR) is desirable as this spectroscopy technique is able to achieve high resolution on the atomic-scale,[11] and is particularly amenable to complementary analyses with first-principles calculations. Although solid-state NMR has been utilized to determine the local structures of different periodic carbon materials,[10,12] theoretical predictions of NMR spectral features from ab initio calculations are generally scarce, limiting the accuracy in the interpretation of the spectra in terms of local structures. Such predictions had been limited to finite systems until Mauri et al. extended the theory to periodic systems.[13] Mauri et al. later made improvements to account for the translational invariance when the projector-augmented wave (PAW) method is used; this is known as the gauge including the projector-augmented wave (GIPAW) approach.[14,15] The GIPAW method has been utilized in various systems to represent the influences of structural variations on NMR signals.[16−19] Periodic models are important to represent the variations in NMR chemical shifts, especially for systems with delocalized wave functions. Thonhauser et al. investigated both finite and periodic carbon systems and showed that a relatively large finite system, coronene, is still different from a periodic model.[20] Results of Özcan et al.[21] also showed in the case of graphene that for cluster models, five to six concentric hexagonal shells, i.e., 150−216 C atoms in the model, are needed to achieve converged ^{13}C chemical shifts on center

C atoms at the level of 5 ppm, in line with the results of Vahä kangas et al.[22] The results of Skachkov et al.[23] and de Souza et al.[24] are achieved using periodic graphene models, although the reported ^{13}C chemical shifts are different from the value reported by Thonhasuer (roughly by 10 ppm). Instead, the results of Skachkov et al.[23] and de Souza et al.[24] match better with the value obtained by Casabianca[25] using a cluster model. Moreover, none of these studies investigated the effect of N-heteroatoms. For the N-doped graphene system, to the best of our knowledge, the only relevant work has been done by Zhang et al. using cluster models[26] and there is no study done using periodic models. In this work, density functional theory (DFT)-based first-principles calculations are performed on periodic N-doped graphene models to simulate a 2D ^{13}C–^{15}N heteronuclear multiple quantum coherence (HMQC) spectrum, to understand the relationship between local structure and ^{13}C or ^{15}N chemical shifts. Results are compared to experimental 2D NMR spectra and allow a more detailed interpretation of it. Various local structures with a mix of multiple basic N species are modeled to provide insights into the structure-related broadening, which can be further decomposed into (1) standalone geometry effects and (2) influences of additional proximate N atoms. The influence of a small amount of adsorbed water is modeled by adding explicitly water molecules to reflect the experimental measurement condition. To better understand the link between the local structure and chemical shift, the relationships between local structure, atomic charge, and chemical shifts are discussed, enabling a more detailed understanding of the influence of N-doping motifs on the electronic structure. These results open the rational design of N-doped carbon materials with desired electronic properties to improve electrochemical performance.

4.3 Materials and Methods

4.3.1 Modeling

The Vienna Ab initio Simulation Package[27] (VASP) was used for calculations. The Perdew−Burke−Ernzerhof[28] (PBE) exchange−correlation functional at the generalized gradient approximation (GGA) level is used. The density-dependent dispersion correction (dDsC)[29,30] van der Waals correction was applied for all structures. Three different sets of graphene structures were used: a hexagonal terrace model which consists of 72 C atoms (6 × 6 supercell), an armchair edge model which consists of 66 C atoms and 12 H atoms (before substitution with N), and a zigzag edge model consisting of 40 C atoms and 8 H atoms. The vacuum in the z-axis was set to 20 Å. For the armchair/zigzag ribbon model, the in-plane vacuum between the ribbons was at least 15 Å. For geometry optimizations, a Monkhorst−Pack 3 × 3 × 1 k-point mesh was used for the terrace model, 1 × 3 × 1 for armchair, and 3 × 1 × 1 for zigzag. For NMR calculation, a 5 × 5 × 1 k-point mesh was used for the terrace model, 1 × 7 × 1 for armchair, and 7 × 1 × 1 for zigzag. The test for the convergence of the chemical shifts in non-doped models with respect to the k-points mesh is shown in the Supporting Information (SI), Table S4.1, and convergence to the level of 1−2 ppm was achieved.

All of the calculations were developed on a basis set of plane waves. A Gaussian smearing with a sigma value of 0.1 eV was used through all calculations. For energy calculations, a cutoff energy for the plane-wave basis set at 500 eV and an electronic step convergence criterion of 10^{-6} eV were used. For geometry optimizations, forces were optimized to 0.02 eV/Å. For NMR calculations, a cutoff energy for the plane-wave basis set at 600 eV and an electronic step convergence criterion of 10^{-10} eV were set for most cases due to the

requirement of such calculations. For some models (a full list can be found in the SI, Section 2) that do not converge under this criterion, the electronic step convergence criterion may be loosened to at most 10^{-7} eV and it has been tested on the graphitic N system that the influence on the calculated NMR chemical shifts is only up to 0.01 ppm, as shown in the SI, Figure S4.1. The variation of the chemical shifts of non-doped models with respect to the cutoff energy is shown in the SI, Table S4.2, and convergence to the level of 1 ppm was achieved for a value of 600 eV. The accurate precision setting was always used. Default values are used for the order of the stencils used to calculate the magnetic susceptibility and the step size for the finite-difference k-space derivative, corresponding to equations 38, 40, and 47 in the work of Yates et al.[15] VASP outputs the chemical shift tensor following the convention $\delta_{11} > \delta_{22} > \delta_{33}$ and the isotropic shift is calculated as[31]

$$\delta_{\text{iso}} = \frac{\delta_{11} + \delta_{22} + \delta_{33}}{3} \tag{4.1}$$

The output values without core contribution were used as this will only lead to a negligible difference of smaller than 0.001 ppm, as shown in the SI, Table S4.3. We used the values without the G=0 contribution since the G=0 contribution is not a bulk property and is affected by the surface currents that appear on the surface of the sample.[14] VASP assumes a spherical shape for the G=0 contribution,[14] which may not be the case for the N-doped graphene sample. More details can be found in the SI, Section 5. The conversion to a value that is amenable to experimental measurement and comparison was done via[20,23,24]

$$\delta = \delta_{\text{system,calcd}} - \delta_{\text{ref,calcd}} + \delta_{\text{ref,exp}} \quad (4.2)$$

4.3.2 Experimental solid-state NMR

The reference system here is chosen as α glycine for ^{13}C, ^{15}N, and ^{1}H. The experimental values used are 33.4 ppm for $\delta_{ref,exp,N}$ 172.7 ppm for $\delta_{ref,exp,C}$, and 3.54 ppm for $\delta_{ref,exp,H}$. It is worth mentioning that the $\delta_{ref,exp,H}$ is an average chemical shift value of three H atoms in the NH_3 group of glycine.[19] Note that the reference values for the ^{13}C, ^{15}N, and ^{1}H isotropic chemical shifts are consistent relative to commonly used standards: tetramethylsilane (TMS) as 0 ppm for ^{13}C and ^{1}H and liquid ammonia as 0 ppm[32] for ^{15}N. The CHARGEMOL package is used to calculate the Density Derived Electrostatic and Chemical (DDEC6) charge[33,34] based on VASP charge density. For the construction of 2D ^{13}C–^{15}N spectra, we consider the first neighbor C−N pairs since the experimental dipole-mediated 2D NMR spectrum depicts signal intensity that is proportional to r^{-3} , where r is the distance between the two nuclei.[35,36] For pristine graphene, the second neighbor distance in the network is 1.73 times the first neighbor distance. This ratio is maintained after geometry optimizations in graphitic N and pyridinic N models, whereas in pyrrolic N models, the ratio is found to be 1.54. As the result, the 2D NMR signal intensity from a second neighbor will be only roughly one-fifth compared to the signal strength arising from a first neighbor in graphitic or pyridinic N models and one-fourth in pyrrolic N models. Experimentally, a mesoporous N-carbon material containing 16 atom % N was synthesized by pyrolyzing a 1:3 molar ratio of cyclohexanehexone octahydrate (97%, Sigma-Aldrich) and uniformly ^{13}C,^{15}N-enriched urea (99 atom % ^{13}C, 99 atom % ^{15}N,

Sigma-Aldrich), in the presence of an SBA-15 silica template, according to the procedure of Fechler et al.[37] Isotopic enrichment with ^{13}C and ^{15}N enabled solid-state 2D NMR characterization of the N-carbons. ^{13}C and ^{15}N chemical shifts were referenced to their respective values in uniformly ^{13}C,^{15}N-enriched glycine powder, using the same values as mentioned in the computational settings. The carbon materials were diluted with KBr at a sample:KBr ratio of 1:3 w/w before being loaded into the MAS rotor. The KBr served as both an internal temperature probe[38] and to reduce undesirable sample heating that may arise from rapid rotation of conductive samples in the high magnetic field required for the NMR measurements.[39] Solid-state two-dimensional (2D) ^{13}C–^{15}N heteronuclear multiple quantum coherence (HMQC) experiments were used to correlate ^{13}C and ^{15}N isotropic chemical shifts of ^{13}C and ^{15}N nuclei that are dipole−dipole-coupled through space. A schematic diagram of the 2D NMR pulse sequence is provided as the SI, Figure S4.2a. Briefly, the solid-state dipolar-mediated ^{13}C-^{15}N HQMC NMR spectrum was acquired using the $SR4_1^2$ sequence to filter polarization transfer from ^{13}C to ^{15}N (for indirect detection) and back to the ^{13}C (for direct detection). These experiments were performed with 100 kHz ^{1}H decoupling, using zirconia rotors, Vespel caps, and under 8 kHz MAS on a Bruker AVANCE II HD 400 DNP-NMR spectrometer with a 9.4 T superconducting magnet operating at 400.20, 100.64, and 40.56 MHz for ^{1}H, ^{13}C, and ^{15}N nuclei, respectively, and equipped with a variable-temperature 3.2 mm HXY MAS probehead. $SR4_1^2$ was used as the dipolar recoupling scheme according to Hu et al.[40] Heteronuclear ^{13}C-^{15}N dipole−dipole couplings scale with respect to the cube of the distance separating two nuclear spins,[35,36] making these measurements sensitive principally to ^{13}C and ^{15}N nuclei that are covalently bonded directly, or to a lesser extent, by weak next-nearest neighbor interactions. The latter contribute negligibly to the overall

measured signal intensity as a consequence of the short ^{13}C-^{15}N recoupling times used here (0.6 ms, sensitive out to 2−3 bond distances),[41] but preferentially detect dipolar-coupled nuclei over shorter (1−2 bond) distances. The 2D dipole-mediated ^{13}C–^{15}N HMQC NMR spectrum[42] was acquired using 1024 transients, with 32 t_1 increments in the indirect dimension in STATES-TPPI acquisition mode. Recycle times of 10 s (corresponding to 1.3 T_1 of ^{15}N nuclei) were used for maximum signal sensitivity. Low-temperature conditions were used to improve NMR signal sensitivity through enhanced polarization from the Boltzmann distribution and to mitigate the influences of rapid nuclear spin relaxation effects. The temperature measured in the MAS gas stream nearest to the stator was 95 K, and the actual sample temperature was estimated from ^{79}Br T_1 relaxation measurements to be ca. 99 K. Similarly, 2D ^{15}N–^{1}H heteronuclear correlation (HETCOR)-MAS experiments were used to correlate ^{1}H and ^{15}N isotropic chemical shifts of ^{1}H and ^{15}N nuclear spin pairs that are dipole−dipole-coupled through space over sub-nanometer distances and corroborate the assignment of pyrrolic N. A schematic diagram of the 2D NMR pulse sequence is provided as the SI, Figure S4.2b. Specifically, following a 90-degree pulse, ^{1}H polarization was allowed to evolve for incremented durations (for indirect detection), after which a shaped pulse was used to transfer ^{1}H polarization to dipole−dipole-coupled ^{15}N nuclei for direct detection. The N-doped material was exposed to atmospheric conditions for 1 week, and surface adsorbed water accounted for 0.5 mass % of the sample. These experiments were performed using zirconia rotors, Vespel caps, and under 10 kHz MAS on a 500 MHz Bruker AVANCE NMR spectrometer with an 11.7 T superconducting magnet operating at 500.24 and 50.69 MHz for ^{1}H and ^{15}N nuclei, respectively, and equipped with a 4 mm HXY MAS probehead. The spectrum was acquired at room temperature, with a contact time of 3000 μs, and 4000 scans.

4.4 Results and Discussion

DFT calculations are first performed on non-doped graphene systems to investigate ^{13}C chemical shifts and validate the computational parameters. The structures of the three basic models without N-doping are shown in **Figure 4.1**, and some characteristic structures with N doping are shown in **Figure 4.2**. The numbers on the C atoms correspond to those of **Table 4.1**.

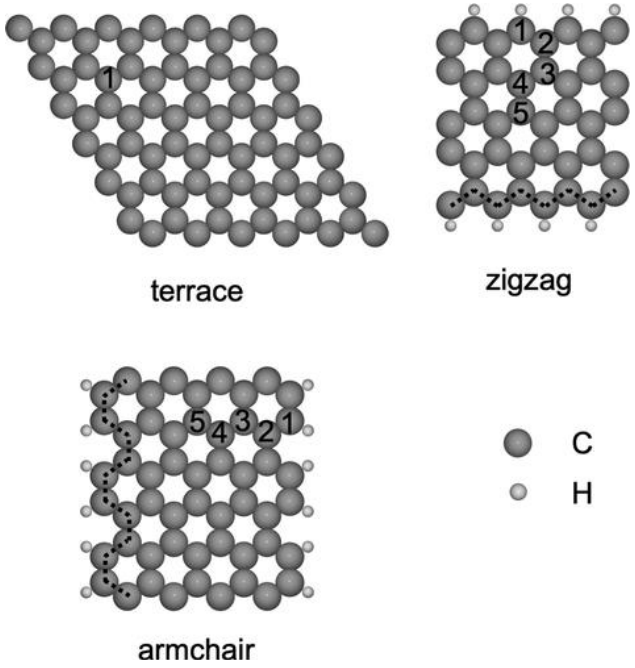

Figure 4.1. Atomic structures of the three basic unit cell models used in this study. The terrace model is 2D, while the armchair and the zigzag ribbons are one-dimensional (1D). One or two long repeat vectors are added to generate a three-dimensional (3D) structure for the plane-wave calculation. Atom numbers correspond to the values shown in Table 4.1, with atoms depicted as follows: gray: C; white: H. The dotted lines indicate the armchair and zigzag edges.

The graphene terrace atom is calculated to have a ^{13}C isotropic chemical shift of 119.2 ppm, which matches the experimental range between 117 and 123 ppm in the literature.[43–46] Also, compared with other computational results, our result generally matches the 118.0 ppm value reported by Thonhauser et al.[20] but is roughly 7 ppm lower than the values reported by Skachkov et al.,[23] 127.1 ppm, and de Souza et al.,[24] 127.6 ppm. Thonhauser used Quantum Espresso with benzene as the reference molecule and Skachkov used ADF-BAND with TMS as the reference molecule. The reference difference may lead to this 7 ppm difference. However, the difference between Thonhauser and de Souza is unexplained as they both use Quantum Espresso with benzene as the reference molecule. The center C atoms in our zigzag and armchair models are calculated to have a ^{13}C chemical shift value of 108.6 and 111.3 ppm, which is slightly smaller than the ^{13}C chemical shift in the terrace model by 10 and 8 ppm, respectively. Further increasing the thickness of both models cannot improve the match, as shown in the SI, Table S4.4, and the thicknesses of both models are used through this work: 9 for the armchair model and 5 for the zigzag model. We have checked the influence of multilayer stacking by comparing graphene and graphite: ^{13}C isotropic chemical shift values change from 119.2 to 120.3 and 123.7 ppm for inequivalent sites in graphite. The values match well with experimental results,[47,48] around 119 ppm, and the trend matches the results of de Souza.[24] We focus on single-layer models in this study since the effects will be smaller than 5 ppm.

Table 4.1. ^{13}C Isotropic Chemical Shifts of Different C Atoms in Terrace, Zigzag, and Armchair Models[a]

model	*atom*	*^{13}C chemical shift (ppm)*
terrace	1	119.2
zigzag	1	117.0
zigzag	2	124.4
zigzag	3	111.6
zigzag	4	110.8
zigzag	5	108.6
armchair	1	110.0
armchair	2	116.6
armchair	3	112.5
armchair	4	110.2
armchair	5	111.3

[a]Labeled atoms are shown in Figure 4.1.

The agreement of theoretically predicted chemical shifts with experimental data for the non-doped systems validate the general modeling approach. Thus, N-doped systems are calculated with the aforementioned settings. We first investigate different structure models with one N atom: a graphitic N atom in a graphene terrace model (Figure 4.2 structure 1), a pyrrolic N atom at an armchair edge (Figure 4.2 structure 4), and a pyridinic N atom at a zigzag edge (Figure 4.2 structure 2) and other inner defect edges (Figure 4.3 structures 1, 2, 3, and 4). Subsequently, the influence of introducing a second N atom is taken into account by considering various models with graphitic−graphitic, pyridinic−graphitic, pyrrolic−graphitic, and pyridinic−pyridinic N pairs. Pyrrolic−pyrrolic and pyrrolic−pyridinic N pairs are not taken into account since these pairs are separated by larger distances than the 2−3 bond distances that are possible to probe via HMQC solid-state NMR.[41] The simulated 2D $^{13}C–^{15}N$ results are shown in **Figure 4.2**. For each inequivalent C atom as a first neighbor of N atoms, a C−N data point is added using the simulated ^{13}C and ^{15}N chemical shift.

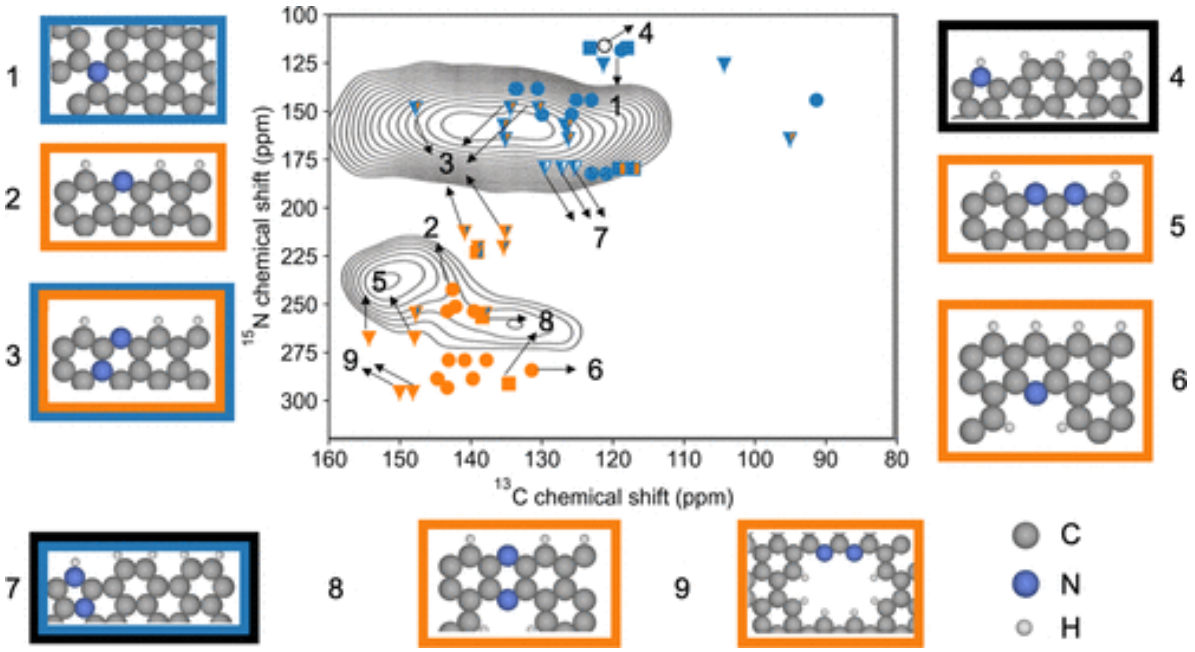

Figure 4.2. Simulated $^{13}C–^{15}N$ correlation NMR chemical shifts, together with the experimental 2D $^{13}C–^{15}N$ intensity for a $^{13}C,^{15}N$-enriched mesoporous N-carbon material containing 16 atom % N. Points are simulated results, and contour lines indicate experimental signal. The point styles indicate other nearby N atoms. Filled circles: atoms without other N atoms nearby, triangles:atoms with another N atom as a second neighbor, and squares: atoms with another N atom as a third neighbor. The color indicates the type of the local N structure: blue for graphitic N atoms, orange for pyridinic N atoms, and white for pyrrolic N atoms (with a black outline when necessary). For triangles and squares, the left half indicates the type for the probed N atom and the right half indicates the type for the neighbor N atom.

Because both the number of equivalent C atoms and the ratio of different modeling structures are not taken into account, the point density in a certain region cannot be quantitatively linked with the experimental signal intensity. The symbol type indicates the presence and distance

(in the term of bonds) of other nearby N atoms. Circles stand for N atoms without other N atoms within three bond distances. Triangles represent N atoms with a nearby N as second neighbor and squares represent N atoms with a third neighbor N. The color indicates the type of the local N structure: blue represents graphitic N atoms, which are bonded to three C atoms. Orange represents pyridinic N atoms, which are bonded to 2 C atoms. White represents pyrrolic N atoms, which are bonded to 2 C atoms and 1 H atom. For triangles and squares, the left half indicates the type of the probed N atom and the right half indicates the type of neighbor N atom. The match between the calculated and experimental chemical shifts will be investigated in the next step.

In general, the calculated ^{13}C and ^{15}N isotropic chemical shifts match well with the experimental data (as shown in **Figure 4.2**) and explain the observed signal broadening. A perfect match is not necessary, since some local structures probed in the calculations might not be present in large enough quantities in the experimental sample to provide a detectable signal. The spectrum can be separated into two general regions. The upper region containing both pyrrolic N and graphitic N shows ^{15}N and ^{13}C chemical shifts in the ranges of 120−200 and 110−160 ppm, respectively. The lower region containing various pyridinic structures shows intensity spanning the ranges of 220−280 and 120−160 ppm for ^{15}N and ^{13}C isotropic chemical shifts, respectively. Comparison with previous ^{13}C and ^{15}N NMR chemical shift assignments of the various N-moieties in carbonaceous materials and graphitic carbon nitrides shows agreement with our assignments.[49−53] ^{15}N chemical shifts exhibit clear trends with respect to local N environments: pyrrolic N atoms have the lowest ^{15}N isotropic chemical shifts, followed by graphitic, and pyridinic N with the highest ^{15}N isotropic chemical shifts. This trend also holds for ^{13}C isotropic chemical shifts, although there are overlaps between

different types of N environments. This can be understood by incorporating the influence of the bonding environment: the pyrrolic and graphitic N atoms have three neighbors, whereas pyridinic N has two neighbors, which leads to a decrease in the electron density at the nuclei on pyridinic N atoms and the adjacent C atoms. The relatively smaller difference between pyrrolic and graphitic N atoms stems from the electronegativity difference between C (2.55) and H (2.20): pyrrolic N and C atoms have a slightly larger electron density and hence smaller chemical shift. A more detailed understanding can be achieved by decomposing the structure-related broadening into two aspects: the geometric effect for the N atom itself and the neighbor effect influenced by the proximity of other N atoms. The neighboring effect follows a general trend: a graphitic N neighbor decreases the ^{15}N isotropic chemical shifts of pyridinic N environments, and a pyridinic N neighbor increases the ^{15}N isotropic chemical shifts of graphitic and pyridinic N environments. This is consistent with the fact that the electron-rich graphitic N atom transfers some electronic density to its less rich pyridinic neighbor. Although graphitic N has a larger ^{15}N chemical shift than pyrrolic N (118.4 > 115.3 ppm), a graphitic N neighbor decreases the ^{15}N isotropic chemical shift of pyrrolic N nuclei, and a pyrrolic N neighbor increases the ^{15}N isotropic chemical shift of graphitic N nuclei. The influence of a graphitic N neighbor on an adjacent graphitic moiety is small: with a second or third graphitic N neighbor, the ^{15}N chemical shift changes from 118.4 to 125.6 or 117.2 ppm, respectively. The influence of a pyridinic N neighbor on a pyridinic N center is complicated and no simple trend is found. The effect of pyridinic or pyrrolic N neighbors on a pyrrolic moiety is not investigated since they cannot act as close neighbors within a distance of three bonds. All of the possible combinations of N-moieties are explored and the calculated ^{15}N and ^{13}C chemical shifts explain a large part of the observed broadening of the spectrum in both dimensions. The

influence of the morphology on the ^{13}C and ^{15}N isotropic chemical shifts of the graphene edges, straight or curved at vacancy islands, can be quantified by the Menger curvature c, which is the reciprocal of the radius of the circle that passes through three points.[54] This descriptor captures the local curvatures of the signaling C/N atoms. The center N atom and two most adjacent edge C atoms give three 2D positions: x_1, x_2, and x_3. The Menger curvature is defined by

$$c(x_1, x_2, x_3) = \frac{4A}{\|x_1 - x_2\| \, \|x_2 - x_3\| \, \|x_3 - x_1\|} \tag{4.3}$$

where A denotes the area of the triangle spanned by x_1, x_2, and x_3. The symbol ‖‖ denotes the L^2 norm in the 2D space. Thus, the ^{15}N isotropic chemical shifts can be correlated with the curvatures, which are a descriptor of the local geometry. This relationship in different N-doped graphene systems is shown in **Figure 4.3**. The idea of local curvature is validated via the data point of the N-doped 6 C defected terrace model: **Figure 4.3b**, structure 2, and the data point of the N-doped 10 C defected terrace model: **Figure 4.3b**, structure 3. Although globally

these two structures are very different, the local curvatures of these two N atoms are rather similar and the ^{15}N chemical shifts are very close. The 6 and 10 C defected terrace models are created by removing 6 and 10 C atoms from the pristine terrace model, saturating dangling bonds with H atoms and substituting one edge C−H pair with a N atom. The local geometry effect correlates the extent of defect curvature with ^{15}N chemical shifts. Specifically,

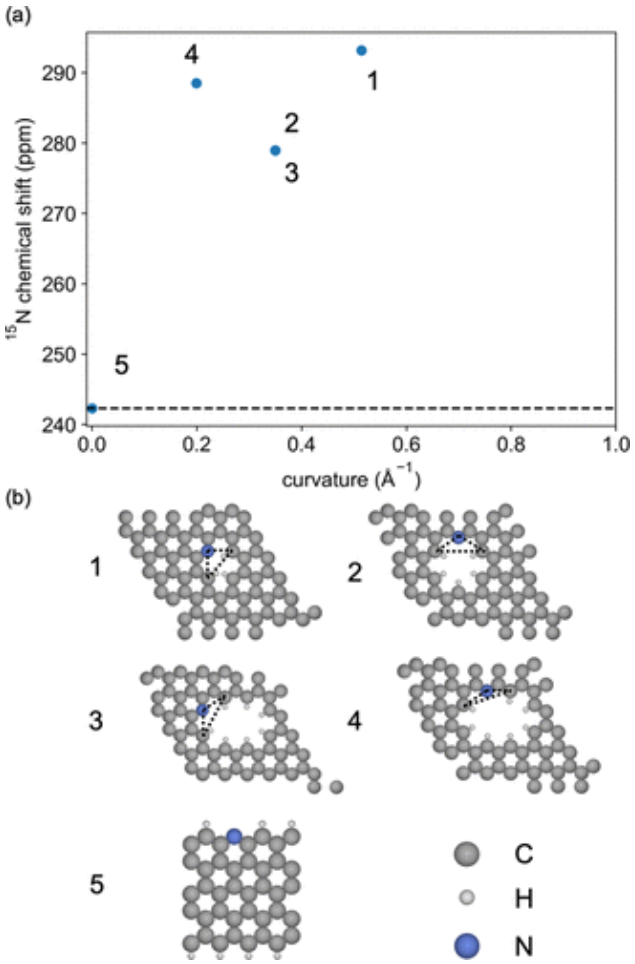

Figure 4.3. (a) Relationship between the curvature and ^{15}N isotropic chemical shift. The dotted line indicates the ^{15}N isotropic chemical shift at the limit of zero curvature, i.e., simple edge pyridinic N at the zigzag edge, structure 5 in (b). This is also structure 2 in Figure 4.2. (b) Underlying structures associated with the data points appearing in (a). The models are listed in order of decreasing curvature with atoms depicted as follows: gray: C, white: H, and blue: N. The dotted lines indicate the N atom and the two most adjacent edge C atoms used to calculate the Menger curvature.

environments with increased local curvature are found to have increasing chemical shifts (**Figure 4.3**). This is similar to the relationship between surface curvature and ^{13}C chemical

shifts in carbon nanotube systems.[25] NMR detects differences in electronic shielding which is manifested as differences in isotropic chemical shifts and which can intuitively be connected to atomic charge.[55] In **Figure 4.4**, the relationship between the DDEC6 charge of the signal

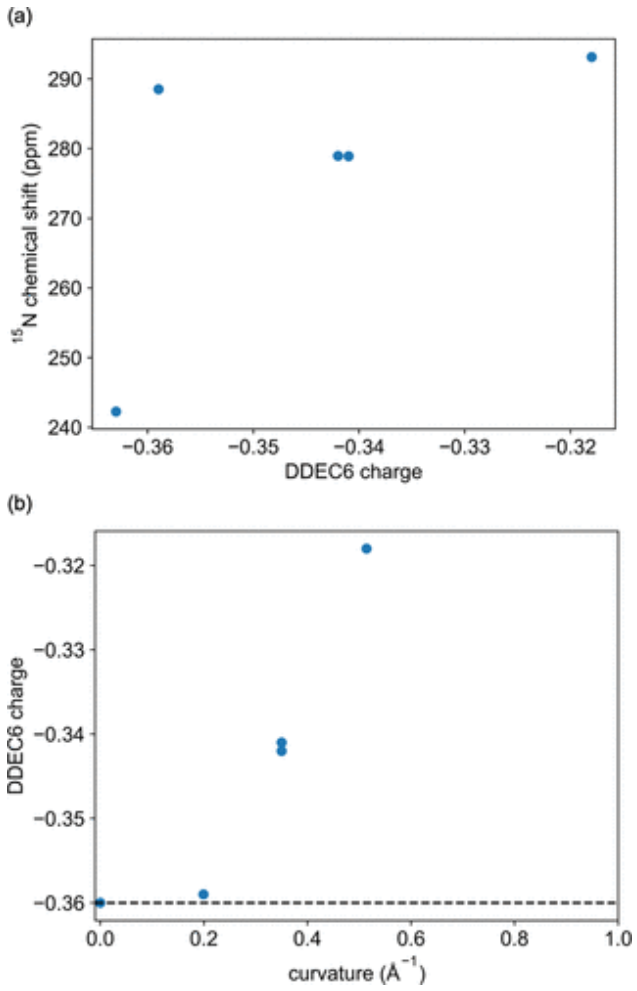

Figure 4.4. Relationship between (a) atomic charge and chemical shift and (b) charge and curvature of the models shown in Figure 4.3 (b). Negative values denote an accumulation of electron density (negative charge); positive values indicate electron density depletion (positive charge).

atom and the curvatures is shown. The data points generally follow a trend: the smaller the charge, i.e., the higher the electron density, the more shielded the nucleus and hence the smaller the chemical shift. For N-doped systems, the larger the curvature, the more positive the charge, meaning that the curvature hinders N atoms taking electrons from neighbor C atoms.

Now that the atomic charge descriptor has been established, both the ^{15}N and ^{13}C chemical shifts of the 2D NMR spectrum (**Figure 4.2**) can be analyzed and correlated using this descriptor. **Figure 4.5** shows the relationship between atomic charges and chemical shifts for N and C atoms, in panels (a) and (b), respectively. Once again, both ^{13}C and ^{15}N chemical shifts follow a general trend: within each type, more negative charge (higher electron density) corresponds to more shielding (thus, smaller chemical shifts). The calculated charge refers to the density enclosed in a finite volume assigned for each atom, and the trend between different types is not necessarily identical with that of the previous discussion concerning the density at the nuclei based on electronegativities.

Interestingly, unlike the ^{13}C chemical shifts in **Figure 4.5b** following a single-scaling relation, different N species give different offsets. Differences in first neighbors of the center N atoms explain the differences in offsets: 2 C atoms for pyridinic N centers, 3 C atoms for graphitic N centers, and 2 C atoms with 1 H atom for pyrrolic N centers. It is also worth mentioning that the second C neighbors, although not shown in **Figure 4.2**, show generally negative charge, whereas first neighbor C atoms show generally positive charge. As N has a greater electronegativity (3.04) than C (2.55), the electron density is transferred from the first neighbor to N, creating a depletion zone around the N atom. The second neighbor C atom

experiences increased electron density, forming a charge ripple. This also contributes to the broadening of ^{13}C chemical shifts.

Experimentally, water is used to probe the presence of N species on the material surface. Thus, modeling this effect is crucial for understanding experimental results under such operating conditions. The interaction between surface adsorbed water and surface N atoms

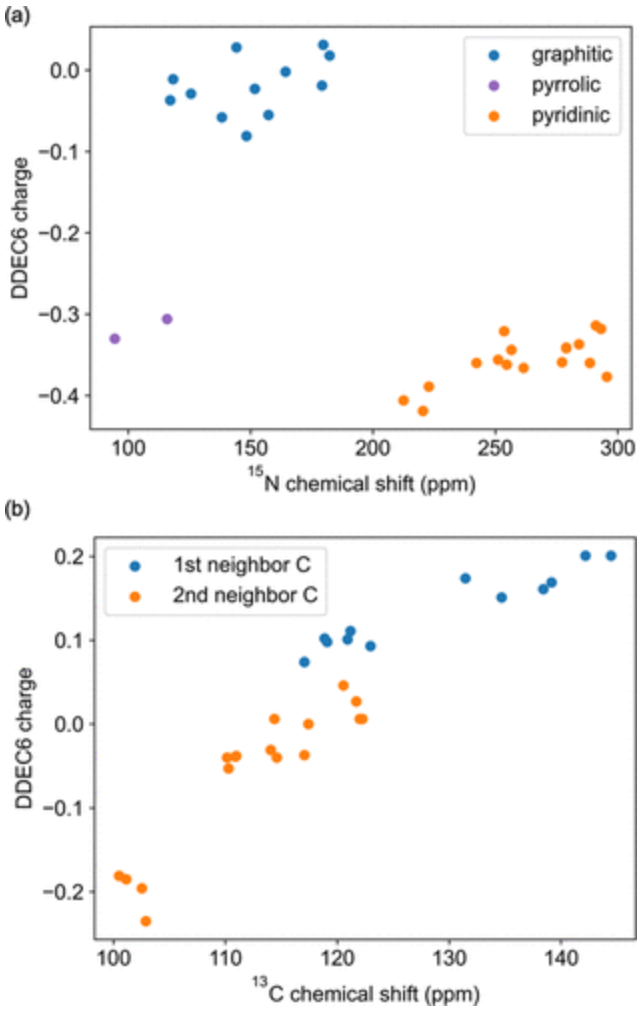

Figure 4.5. Relationship between charge and chemical shift of (a) N atoms and (b) C atoms as the first and second neighbor of N atoms from the models utilized in this study. Negative values denote an accumulation of electron density (negative charge); positive values indicate electron density depletion (positive charge).

varies strongly with respect to the type of N atom, see the SI, Figure S4.4 for structures. For a pyrrolic N atom, the O atom from water forms a hydrogen bond with the H atom from the pyrrolic NH group. Since O has a greater electronegativity (3.44) than N (3.04) and H (2.20), the electron density is transferred from NH to O. Thus, the N and H nuclei are both effectively deshielded and accordingly exhibit larger ^{15}N and ^{1}H isotropic chemical shifts, as shown in **Figure 4.6**. To test the convergence of this effect with the number of water molecules, up to four water molecules are added to the pyrrolic N model, and the influence after three molecules added is small (**see Figure 4.6**).

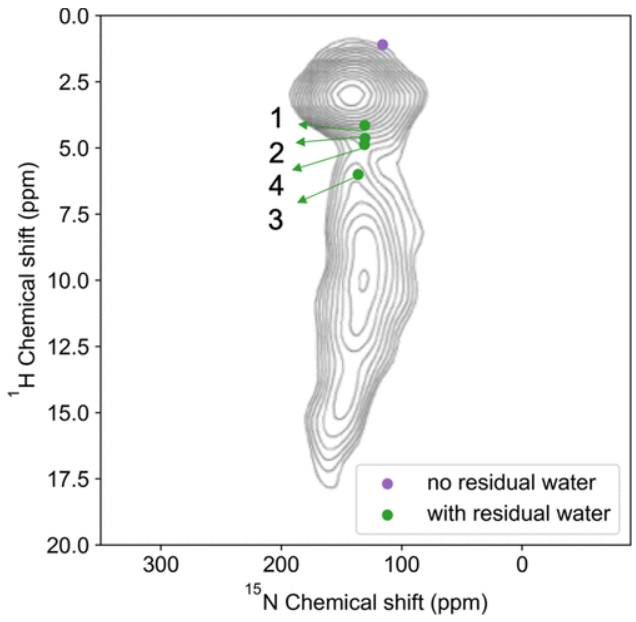

Figure 4.6. Simulated and experimental 2D ^{15}N–^{1}H NMR correlation for a 16 atom % N mesoporous N-carbon material. The points are simulated results and contour lines indicate experimental signal intensity. The data points shown are from the pyrrolic N model with 0, 1, 2, 3, and 4 water molecules. Numbers next to scatters indicate the numbers of water molecules in the models.

Residual water has an effect on the other two types of N atoms, but this is not directly reflected in the 2D $^{15}N-^{1}H$ NMR spectrum of **Figure 4.6** since there is no first neighbor H of pyridinic N or graphitic N. For pyridinic N, interactions with adsorbed water result in greater shielding of the pyridinic ^{15}N nucleus and corresponding deshielding of the ^{1}H nucleus in water. It is also found that the O atom, instead of the H atom, will interact with the graphitic N atom. As a result, graphitic N is deshielded, but this is not reflected on the 2D $^{15}N-^{1}H$ spectrum since the distance from the water H atom to the graphitic N atom is large. For the 2D $^{13}C-^{15}N$ spectra, the overall result of water coordination is that the ^{15}N chemical shift of pyrrolic N will be shifted toward larger values with a magnitude of 15−20 ppm, graphitic N will be shifted toward larger values with a magnitude of about 6 ppm, and pyridinic N will be shifted toward smaller values with a magnitude of about 25 ppm. Detailed values are listed in the **SI, Table S4.5**. If we consider the Gibbs free energy change of water on graphitic/pyrrolic/ pyridinic moieties, as shown in the **SI, Table S4.6**, we find that water adsorption is favorable on pyrrolic and pyridinic N sites. This explains why in **Figure 4.2**, where water adsorption is not included, the pyrrolic structure (4) appears with an underestimated chemical shift compared to the experimental data, and why some pyridinic group chemical shifts are overestimated. Correction for the influence of water significantly improves the agreement. The influence of residual water on the ^{15}N and ^{1}H isotropic chemical shifts can also be reflected on the atomic charge, see the **SI, Figure S4.5**. This influence is relevant for applications since it indicates that the electronic properties will be altered when the materials are in electrocatalytic conditions.

4.5 Conclusions

DFT calculations are used in this work to predict and explain the chemical shifts of ^{15}N, ^{13}C, and ^{1}H atoms in N-doped graphene systems. A number of different models are investigated: non-doped models (terrace, zigzag edge, and armchair edge), single N-doped models (graphitic, pyridinic, and pyrrolic N), and N pair models (graphitic−graphitic, pyridinic−pyridinic, pyrrolic−graphitic, and pyridinic−pyridinic). Comparisons of predicted chemical shifts with experimental 2D $^{13}C–^{15}N$ spectra show good agreement, especially when the influence of water adsorption is included. The major difference between the chemical shifts of graphitic/pyridinic/pyrrolic N-moieties is understood by comparing the electronegativities of the various environments.

Furthermore, for each type of environment, the general concept of signal broadening is decomposed into four different factors, the influences of which are discussed in detail. The first factor is the standalone N/C geometry, where a larger curvature of the graphene edge is found to give a more positive chemical shift. The second factor is the effect of a second N atom nearby: a graphitic N atom close to a pyridinic N decreases the chemical shift, while a pyridinic N close to a graphitic N increases the chemical shift. The trends of other types of moiety mixing are more complicated, but the overall signal broadening matches the experimental spectrum well. The third factor is that for each specific structure, the second neighbor C atom experiences a lower chemical shift. The fourth factor is the influence of residual water, which is important to understand the aqueous environment in oxygen reduction reaction or hydrogen evolution reaction. The introduction of this factor matches with the experimental 2D $^{15}N–^{1}H$ spectrum and provides better agreement with the experimental $^{13}C–^{15}N$ spectrum. With the free energy taken into account, water adsorption on pyrrolic and

pyridinic N sites is found to be more stable and to induce a positive or negative deviation in the chemical shift, respectively. An intuitive correlation between the charge of the probed atom and the chemical shift is confirmed: the smaller the charge, i.e., the higher the electron density, the more shielded the nucleus is, and hence the smaller the chemical shift. The relationship between charge and chemical shifts is discussed, enabling a more detailed understanding of the electronic influence of N-doping. These results can be used for the rational design of N-containing carbon materials with desirable electronic properties to improve electrochemical performance. They can also lead to a determination of the nature of active sites in these electrocatalysts by comparison of several N-doped carbon materials.

4.6 References

(1) Reddy, A. L. M.; Srivastava, A.; Gowda, S. R.; Gullapalli, H.; Dubey, M.; Ajayan, P. M. Synthesis Of Nitrogen-Doped Graphene Films For Lithium Battery Application. *ACS Nano* **2010**, *4*, 6337−6342.

(2) Xu, Y.; Lin, Z.; Zhong, X.; Huang, X.; Weiss, N. O.; Huang, Y.; Duan, X. Holey graphene frameworks for highly efficient capacitive energy storage. *Nat. Commun.* **2014**, *5*, No. 4554.

(3) Gong, K.; Du, F.; Xia, Z.; Durstock, M.; Dai, L. Nitrogen-Doped Carbon Nanotube Arrays with High Electrocatalytic Activity for Oxygen Reduction. *Science* **2009**, *323*, 760−764.

(4) Zhao, Y.; Nakamura, R.; Kamiya, K.; Nakanishi, S.; Hashimoto, K. Nitrogen-doped carbon nanomaterials as non-metal electrocatalysts for water oxidation. *Nat. Commun.* **2013**, *4*, No. 2390.

(5) Lefévre, M.; Proietti, E.; Jaouen, F.; Dodelet, J.-P. Iron-Based Catalysts with Improved Oxygen Reduction Activity in Polymer Electrolyte Fuel Cells. *Science* **2009**, *324*, 71−74.

(6) Wang, H.; Maiyalagan, T.; Wang, X. Review on Recent Progress in Nitrogen-Doped Graphene: Synthesis, Characterization, and Its Potential Applications. *ACS Catal.* **2012**, *2*, 781−794.

(7) Deng, D.; Pan, X.; Yu, L.; Cui, Y.; Jiang, Y.; Qi, J.; Li, W.-X.; Fu, Q.; Ma, X.; Xue, Q.; Sun, G.; et al. Toward N-Doped Graphene via Solvothermal Synthesis. *Chem. Mater.* **2011**, *23*, 1188−1193.

(8) Li, X.; Wang, H.; Robinson, J. T.; Sanchez, H.; Diankov, G.; Dai, H. Simultaneous Nitrogen Doping and Reduction of Graphene Oxide. *J. Am. Chem. Soc.* **2009**, *131*, 15939−15944.

(9) Zhao, L.; et al. Visualizing Individual Nitrogen Dopants in Monolayer Graphene. *Science* **2011**, *333*, 999−1003.

(10) Baccile, N.; Laurent, G.; Coelho, C.; Babonneau, F.; Zhao, L.; Titirici, M.-M. Structural Insights on Nitrogen-Containing Hydrothermal Carbon Using Solid-State Magic Angle Spinning ^{13}C and ^{15}N Nuclear Magnetic Resonance. *J. Phys. Chem. C* **2011**, *115*, 8976−8982.

(11) Chmelka, B. F. Materializing opportunities for NMR of solids. *J. Magn. Reson.* **2019**, *306*, 91−97.

(12) Thomas, H. R.; Day, S. P.; Woodruff, W. E.; Vallés, C.; Young, R. J.; Kinloch, I. A.; Morley, G. W.; Hanna, J. V.; Wilson, N. R.; Rourke, J. P. Deoxygenation of Graphene Oxide: Reduction or Cleaning? *Chem. Mater.* **2013**, *25*, 3580−3588.

(13) Mauri, F.; Louie, S. G. Magnetic Susceptibility of Insulators from First Principles. *Phys. Rev. Lett.* **1996**, *76*, 4246−4249.

(14) Pickard, C. J.; Mauri, F. All-electron magnetic response with pseudopotentials: NMR chemical shifts. *Phys. Rev. B* **2001**, *63*, No. 245101.

(15) Yates, J. R.; Pickard, C. J.; Mauri, F. Calculation of NMR chemical shifts for extended systems using ultrasoft pseudopotentials. *Phys. Rev. B* **2007**, *76*, No. 024401.

(16) Profeta, M.; Mauri, F.; Pickard, C. J. Accurate First Principles Prediction of ^{17}O NMR Parameters in SiO_2: Assignment of the Zeolite Ferrierite Spectrum. *J. Am. Chem. Soc.* **2003**, *125*, 541−548.

(17) D'Anna, V.; Norsic, S.; Gajan, D.; Sanders, K.; Pell, A.; Lesage, A.; Monteil, V.; Copéret, C.; Pintacuda, G.; Sautet, P. Structural Characterization of the EtOH-$TiCl_4$-$MgCl_2$ Ziegler-Natta Precatalyst. *J. Phys. Chem. C* **2016**, *120*, 18075−18087.

(18) Kerber, R. N.; Kerber, T.; Rozanska, X.; Delbecq, F.; Sautet, P. Grafting trimethylaluminum and its halogen derivatives on silica: General trends for 27Al SS-NMR response from first principles calculations. *Phys. Chem. Chem. Phys.* **2015**, *17*, 26937-26945.

(19) Stievano, L.; Tielens, F.; Lopes, I.; Folliet, N.; Gervais, C.; Costa, D.; Lambert, J.-F. Density Functional Theory Modeling and Calculation of NMR Parameters: An ab Initio Study of the Polymorphs of Bulk Glycine. *Cryst. Growth Des.* **2010**, *10*, 3657−3667.

(20) Thonhauser, T.; Ceresoli, D.; Marzari, N. NMR shifts for polycyclic aromatic hydrocarbons from first-principles. *Int. J. Quantum Chem.* **2009**, *109*, 3336−3342.

(21) Özcan, N.; Vähäkangas, J.; Lantto, P.; Vaara, J. Characteristic Spectral Patterns in the ^{13}C Nuclear Magnetic Resonance Spectra of Hexagonal and Crenellated Graphene Fragments. *Chem. Phys. Chem.* **2014**, *15*, 1799−1808.

(22) Vähäkangas, J.; Ikäläinen, S.; Lantto, P.; Vaara, J. Nuclear magnetic resonance predictions for graphenes: Concentric finite models and extrapolation to large systems. *Phys. Chem. Chem. Phys.* **2013**, *15*, No. 4634.

(23) Skachkov, D.; Krykunov, M.; Kadantsev, E.; Ziegler, T. The Calculation of NMR Chemical Shifts in Periodic Systems Based on Gauge Including Atomic Orbitals and Density Functional Theory. *J. Chem. Theory Comput.* **2010**, *6*, 1650−1659.

(24) de Souza, F. A.; Ambrozio, A. R.; Souza, E. S.; Cipriano, D. F.; Scopel, W. L.; Freitas, J. C. NMR Spectral Parameters in Graphene, Graphite, and Related Materials: Ab Initio Calculations and Experimental Results. *J. Phys. Chem. C* **2016**, *120*, 27707−27716.

(25) Casabianca, L. B. Effect of Curvature on Carbon Chemical Shielding in Extended Carbon Systems. *J. Phys. Chem. A* **2016**, *120*, 7011−7019.

(26) Zhang, Y.; Hao, J.; Li, J.; Hao, C. Theoretical study of triiodide reduction reaction on nitrogen-doped graphene for dye-sensitized solar cells. *Theor. Chem. Acc.* **2016**, *135*, No. 23.

(27) Kresse, G.; Hafner, J. Ab initio molecular dynamics for liquid metals. *Phys. Rev. B* **1993**, *47*, No. 558.

(28) Perdew, J. P.; Burke, K.; Ernzerhof, M. Generalized Gradient Approximation Made Simple. *Phys. Rev. Lett.* **1996**, *77*, 3865−3868.

(29) Steinmann, S. N.; Corminboeuf, C. A generalized-gradient approximation exchange hole model for dispersion coefficients. *J. Chem. Phys.* **2011**, *134*, No. 044117.

(30) Steinmann, S. N.; Corminboeuf, C. Comprehensive Benchmarking of a Density-Dependent Dispersion Correction. *J. Chem. Theory Comput.* **2011**, *7*, 3567−3577.

(31) Mason, J. Conventions for the reporting of nuclear magnetic shielding (or shift) tensors suggested by participants in the NATO ARW on NMR shielding constants at the University of Maryland, College Park, July 1992. *Solid State Nucl. Magn. Reson.* **1993**, *2*, 285− 288.

(32) Bertani, P.; Raya, J.; Bechinger, B. ^{15}N chemical shift referencing in solid state NMR. *Solid State Nucl. Magn. Reson.* **2014**, *61-62*, 15−18.

(33) Manz, T. A.; Limas, N. G. Introducing DDEC6 atomic population analysis: Part 1. Charge partitioning theory and methodology. *RSC Adv.* **2016**, *6*, 47771−47801.

(34) Limas, N. G.; Manz, T. A. Introducing DDEC6 atomic population analysis: Part 2. Computed results for a wide range of periodic and nonperiodic materials. *RSC Adv.* **2016**, *6*, 45727−45747.

(35) Separovic, F.; Naito, A. Advances in Biological Solid-State NMR: Proteins and Membrane-Active Peptides; *Royal Society of Chemistry* **2014.**

(36) Levitt, M. H. *Spin Dynamics: Basics of Nuclear Magnetic Resonance;* John Wiley & Sons **2013**.

(37) Fechler, N.; Zussblatt, N. P.; Rothe, R.; Schlögl, R.; Willinger, M.- G.; Chmelka, B. F.; Antonietti, M. Eutectic Syntheses of Graphitic Carbon with High Pyrazinic Nitrogen Content. *Adv. Mater.* **2015**, *28*, 1287−1294.

(38) Thurber, K. R.; Tycko, R. Measurement of sample temperatures under magic-angle spinning from the chemical shift and spin-lattice relaxation rate of ^{79}Br in KBr powder. *J. Magn. Reson.* **2009**, *196*, 84−87.

(39) Yesinowski, J. P.; Ladouceur, H. D.; Purdy, A. P.; Miller, J. B. Electrical and ionic conductivity effects on magic-angle spinning nuclear magnetic resonance parameters of CuI. *J. Chem. Phys.* **2010**, *133*, No. 234509

(40) Hu, B.; Trébosc, J.; Amoureux, J.-P. Comparison of several hetero-nuclear dipolar recoupling NMR methods to be used in MAS HMQC/HSQC. *J. Magn. Reson.* **2008**, *192*, 112−122.

(41) Kobayashi, T.; Singappuli-Arachchige, D.; Wang, Z.; Slowing, I. I.; Pruski, M. Spatial distribution of organic functional groups supported on mesoporous silica nanoparticles:

A study by conventional and DNP-enhanced ^{29}Si solid-state NMR. *Phys. Chem. Chem. Phys.* **2017**, *19*, 1781−1789.

(42) Lesage, A.; Sakellariou, D.; Steuernagel, S.; Emsley, L. Carbon-Proton Chemical Shift Correlation in Solid-State NMR by Through-Bond Multiple-Quantum Spectroscopy. *J. Am. Chem. Soc.* **1998**, *120*, 13194−13201.

(43) Si, Y.; Samulski, E. T. Synthesis of Water-Soluble Graphene. Nano Lett. 2008, 8, 1679−1682. (44) Gao, W.; Alemany, L. B.; Ci, L.; Ajayan, P. M. New insights into the structure and reduction of graphite oxide. *Nat. Chem.* **2009**, *1*, 403− 408.

(45) Marcano, D. C.; Kosynkin, D. V.; Berlin, J. M.; Sinitskii, A.; Sun, Z.; Slesarev, A.; Alemany, L. B.; Lu, W.; Tour, J. M. Improved Synthesis of Graphene Oxide. *ACS Nano* **2010**, *4*, 4806−4814.

(46) Stankovich, S.; Dikin, D. A.; Piner, R. D.; Kohlhaas, K. A.; Kleinhammes, A.; Jia, Y.; Wu, Y.; Nguyen, S. T.; Ruoff, R. S. Synthesis of graphene-based nanosheets via chemical reduction of exfoliated graphite oxide. *Carbon* **2007**, *45*, 1558−1565.

(47) Resing, H.; Weber, D.; Anderson, M.; Miller, G.; Moran, M.; Poranski, C., Jr; Mattix, L. NMR Shift Tensors for Polyacetylene and Graphite. *Polym. Prepr.* **1982**, *23*, No. 101.

(48) Darmstadt, H.; Roy, C.; Kaliaguine, S.; Xu, G.; Auger, M.; Tuel, A.; Ramaswamy, V. Solid state ^{13}C-NMR spectroscopy and XRD studies of commercial and pyrolytic carbon blacks. *Carbon* **2000**, *38*, 1279−1287.

(49) Kuroki, S.; Nabae, Y.; Chokai, M.; Kakimoto, M.-a.; Miyata, S. Oxygen reduction activity of pyrolyzed polypyrroles studied by ^{15}N solid-state NMR and XPS with principal component analysis. *Carbon* **2012**, *50*, 153−162.

(50) Gammon, W.; Hoatson, G.; Holloway, B.; Vold, R.; Reilly, A. Bonding in hard and elastic amorphous carbon nitride films investigated using ^{15}N, ^{13}C, and ^{1}H NMR spectroscopy. *Phys. Rev. B* **2003**, *68*, No. 195401.

(51) Huo, J.; Duan, P.; Pham, H. N.; Chan, Y. J.; Datye, A. K.; Schmidt-Rohr, K.; Shanks, B. H. Improved hydrothermal stability of Pd nanoparticles on nitrogen-doped carbon supports. *Catal. Sci. Technol.* **2018**, *8*, 3548−3561.

(52) Hu, Y.; Shim, Y.; Oh, J.; Park, S.; Park, S.; Ishii, Y. Synthesis of ^{13}C-,^{15}N-Labeled Graphitic Carbon Nitrides and NMR-Based Evidence of Hydrogen-Bonding Assisted Two-Dimensional Assembly. *Chem. Mater.* **2017**, *29*, 5080−5089.

(53) Wang, X.; Hou, Z.; Ikeda, T.; Terakura, K. NMR Chemical Shifts of ^{15}N-Bearing Graphene. *J. Phys. Chem. C* **2014**, *118*, 13929−13935.

(54) Leger, J. Menger Curvature and Rectifiability. *Ann. Math.* **1999**, *149*, 831−869.

(55) Farnum, D. Advances in Physical Organic Chemistry; *Elsevier*, **1975**; *11*, 123−175.

(56) Towns, J.; Cockerill, T.; Dahan, M.; Foster, I.; Gaither, K.; Grimshaw, A.; Hazlewood, V.; Lathrop, S.; Lifka, D.; Peterson, G. D.; Roskies, R.; Scott, J. R.; Wilkins-Diehr, N. XSEDE: Accelerating Scientific Discovery. *Comput. Sci. Eng.* **2014**, *16*, 62−74.

4.7 Supporting information

Table S4.1. Convergence of chemical shift values with respect to k-point mesh

model	*k-point mesh*	*^{13}C chemical shift (ppm)*
terrace	3*3*1	121.1
terrace	4*4*1	120.2
terrace	5*5*1	119.2
zigzag	5*1*1	108.3
zigzag	6*1*1	110.2
zigzag	7*1*1	108.6
armchair	1*5*1	110.2
armchair	1*6*1	111.0
armchair	1*7*1	111.3

*Our current k-points mesh ensures convergence at a level of 1-2 ppm.

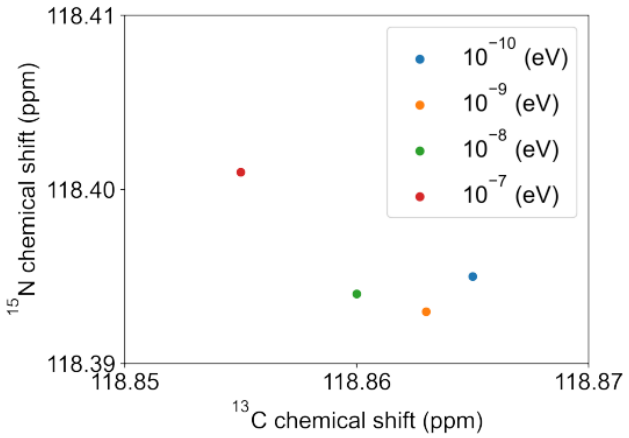

Figure S4.1: Chemical shift values with respect to electronic convergence criteria of graphitic N model.

The convergence of ^{13}C and ^{15}N chemical shift values with respect to electronic convergence criteria is tested on a graphitic N model. Electronic structure convergence criteria (EDIFF values) of 10^{-7}, 10^{-8}, 10^{-9}, and 10^{-10} eV are tested. The first neighbor N-C pair values

are shown here. The ^{13}C and ^{15}N chemical shift reference specie used here, alpha-glycine, is always calculated using EDIFF=10^{-10} eV.

It can be concluded that the EDIFF=10^{-7} eV setting will have a convergence at 0.02 ppm level. Models calculated with 10^{-8} eV: zigzag edge pyridinic N model, non-doped zigzag edge model, pyrazinic N model-1, pyrazinic N model-2, defected zigzag edge pyridinic N model-1, defected zigzag edge pyridinic N model-2, para graphitic N-graphitic N model, meta graphitic N-graphitic N model Models calculated with 10^{-7} eV: zigzag edge graphitic N model.

Table S4.2. Convergence of chemical shift values with respect to cutoff energy

Cutoff Energy (eV)	*^{15}N Chemical Shift (ppm)*	*First Neighbor ^{13}C Chemical Shift (ppm)*
600	118.4	118.9
700	117.0	118.2

The cutoff energy of the reference species, alpha-glycine, are also calculated using changing cutoff energy (ENCUT setting in VASP). It can be concluded that our cutoff energy ensures S-4 convergence at lower than 1 ppm level.

Table S4.3. Influence of including or excluding the core contribution on chemical shift values

Model	*^{15}N Chemical Shift without core contribution (ppm)*	*^{15}N Chemical Shift with core contribution (ppm)*
graphitic N	118.3954	118.3954
pyrrolic N	242.3040	242.3044
pyridinic N	115.9484	115.9484

The influence of including or excluding the core contribution on ^{15}N chemical shift values is tested on graphitic N model, pyrrolic N model and pyridinic N model. 4 decimal points are shown in order to show the differences. It can be concluded that including core contribution will lead to a difference at 0.0001 ppm level.

This part corresponds to equations 61, 62 and 63 in the work of Pickard *et al*.[S1] The bare induced field in reciprocal space is calculated as:

$$\mathbf{B}_{bare}^{(0)}(\mathbf{G}) = \frac{4\pi}{c}\frac{i\mathbf{G}\times\mathbf{j}_{bare}^{(0)}(\mathbf{G})}{G^2} \tag{1}$$

However, this equation cannot be applied at **G=0**. Following the convention of Mauri,[S2] a spherical sample is assumed and then this contribution is calculated as:

$$\mathbf{B}_{in}^{(1)}(\mathbf{G}) = \frac{8\pi}{3}\overleftrightarrow{\chi}\mathbf{B} \tag{2}$$

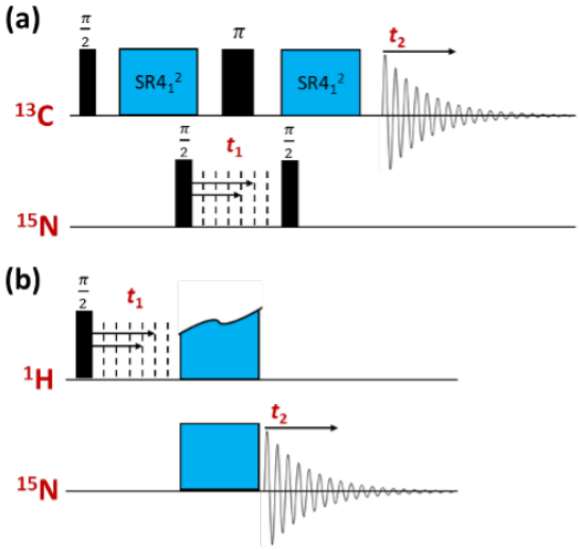

Figure S4.2. Schematic diagrams of the 2D solid-state NMR pulse sequences of (a) the dipolar-mediated ^{13}C-^{15}N HQMC-MAS NMR experiment used to acquire the spectrum in **Figure 4.2**, and (b) the ^{15}N-^{1}H HETCOR-MAS NMR experiment used to acquire the spectrum in **Figure 4.6**.

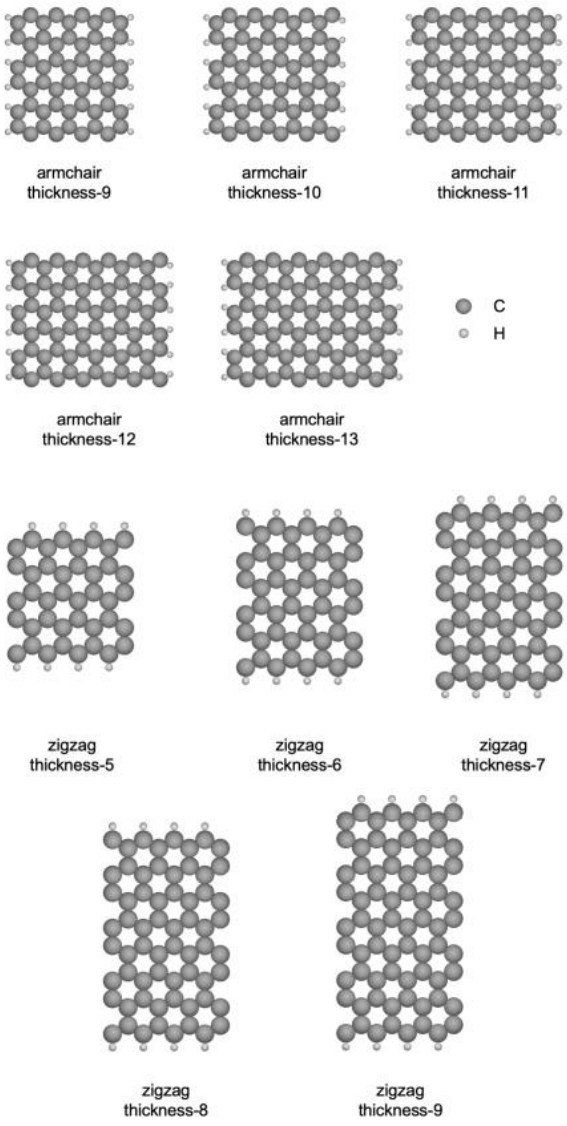

Figure S4.3: Structures of armchair and zigzag models with different thicknesses.

Table S4.4. Convergence of ^{13}C chemical shift values of center C atom in armchair and zigzag models with respect to model thickness

model	*thickness*	*^{13}C chemical shift (ppm)*
armchair	9	111.3
armchair	10	109.3
armchair	11	114.4
armchair	12	109.7
armchair	13	109.5
zigzag	5	108.6
zigzag	6	109.5
zigzag	7	112.3
zigzag	8	110.7
zigzag	9	108.6

For armchair models, it can be observed that the model with a thickness of 11 has the largest ^{13}C chemical shift value of center C atom, reaching 114.4, whereas other thicker models has a value of 109. We choose to use the model with a thickness as 9, ensuring that the error bar of ^{13}C chemical shift value will be in the range of 2-3 ppm. For zigzag models, it can be observed that the model with a thickness of 8 has the largest ^{13}C chemical shift value of center C atom, reaching 110.7, whereas other thicker models has a value of 109. We choose to use the model with a thickness as 5, ensuring that the error bar of ^{13}C chemical shift value will be in the range of 2-3 ppm.

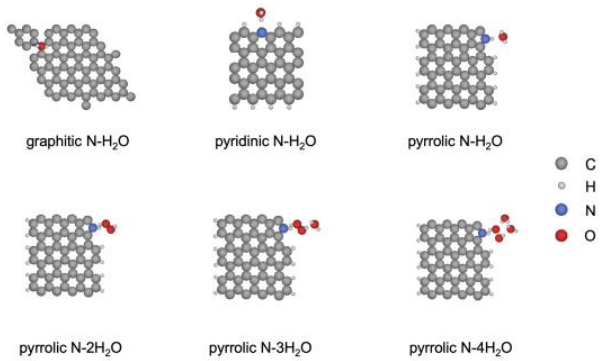

Figure S4.4: structures of models with adsorbed H2O. color scheme: grey: C, white: H, blue: N, red: O.

Table S4.5. Influence of water adsorption on ^{15}N chemical shifts

model	*^{15}N chemical shift (ppm)*
graphitic N	118.4
graphitic N-H_2O	124.6
pyridinic N	242.3
pyridinic N-H_2O	217.9
pyrrolic N	115.9
pyrrolic N-H_2O	131.0
pyrrolic N-2H_2O	131.2
pyrrolic N-3H_2O	136.5
pyrrolic N-4H_2O	130.6

Table S4.6. Adsorption free energies of H_2O molecules in graphitic N, pyridinic N, and pyrrolic N models. All the values are in unit of eV. For water molecule, the C_v term includes $C_{v,trans}$ and $C_{v,rot}$.

Energy term (eV)	*H_2O*	graphitic N-H_2O	pyridinic N-H_2O	pyrrolic N-H_2O	pyrrolic N-2H_2O	pyrrolic N-3H_2O	pyrrolic N-4H_2O
E		-0.189	-0.428	-0.275	-0.732	-1.021	-1.361
ZPE	0.564	0.589	0.638	0.607	1.275	1.909	2.579
Cv	0.078	0.057	0.065	0.043	0.145	0.193	0.267
TS	0.588	0.120	0.130	0.078	0.305	0.387	0.533
G		-0.011	-0.206	-0.051	-0.313	-0.350	-0.440

We investigated more structures related to pyrrolic N model because the experimental 2D ^{1}H-^{15}N NMR spectra give direct information on the pyrrolic species, as it has a N-H bond. Temperature is considered to be room temperature, 300 K. The gas phase free energy can be calculated:

$$G_{gas} = U + pV - TS$$
$$= E_{ele} + ZPE + \int_0^T C_t\, dT + \int_0^T C_r\, dT + \int_0^T C_{vib}\, dT + pV - TS$$
$$= E_{ele} + ZPE + nk_BT + \int_0^T C_{vib}\, dT - TS$$

where G is the Gibbs free energy, U is the internal energy, p is the pressure, V the volume, T is the temperature, S is the entropy, that can be decomposed into its translational, rotational and vibrational components (St , Sr, Svib), E_{ele} is the electronic energy, ZPE stands for the zero point energy, C_t , C_r, C_{vib} are translational, rotational and vibrational heat capacities, n takes care for the translational and vibrational heat capacity and pV term (4 for non-linear molecules, and 3.5 for linear molecules), k_B is the Boltzmann constant.

Here we consider the real residual water on surface to be much larger than those in the models, and Gibbs free energy of water to be closer to the case of aqueous environment.

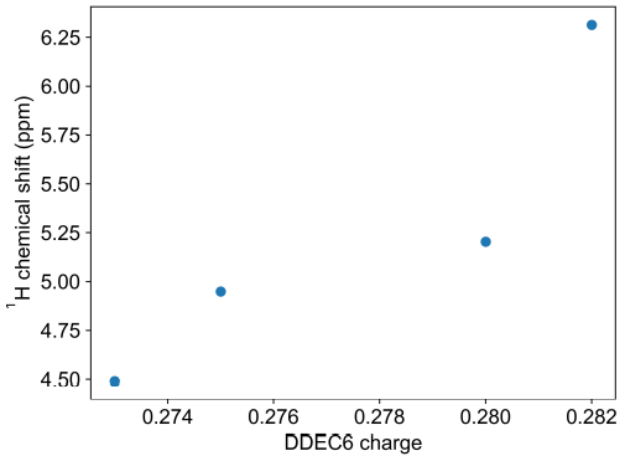

Figure S4.5: Relationship between ^{1}H chemical shift values and DDEC6 charge on H atom in side pyrrolic N-H_2O models

Supporting Information References

(S1) Pickard, C. J.; Mauri, F. All-electron magnetic response with pseudopotentials: NMR chemical shifts. *Phys. Rev. B* **2001**, *63*, 245101.

(S2) Mauri, F.; Louie, S. G. Magnetic susceptibility of insulators from first principles. *Phys. Rev. Lett.* **1996**, *76*, 4246.

(S3) Wertz, D. H. Relationship between the gas-phase entropies of molecules and their entropies of solvation in water and 1-octanol. *J. Am. Chem. Soc.* **1980**, *102*, 5316–5322.

(S4) Liang, Y.; Liu, S.; Xia, Y.; Li, Y.; Yu, Z.-X. Mechanism, regioselectivity, and the kinetics of phosphine-catalyzed [3+2] cycloaddition reactions of allenoates and electron deficient alkenes. *Chem. Eur. J.* **2008**, *14*, 4361.

(S5) Wang, P.; Steinmann, S. N.; Fu, G.; Michel, C.; Sautet, P. Key role of anionic doping for H_2 production from formic acid on Pd (111). *ACS Catal.* **2017**, *7*, 1955–1959.

5. Correlating macroscopic compositions and structures with oxygen and sulfur reduction activities of mesoporous-Fe,N-carbon electrocatalysts

This chapter is adapted from a not yet submitted manuscript. I am first author on this paper and am responsible for most of the synthesis, characterization, and electrochemical performance testing. Exceptions include DFT calculations by Ziyang Wei, S-reduction testing by Rongli Liu, EXAFS done by Riley Zhang, and STEM by Tom Thersleff, and Mossbauer by Camden Hunt.

Authors: Shona M. Becwar, Ziyang Wei, Rongli Liu, Pu Zhang, Walter Rosas, Zachariah J. Berkson, Niels P. Zussblatt, Gabriel Menard, Anders Palmqvist, Johanna Nelson Weker, Xiangfeng Duan, Thomas Thersleff, Philippe Sautet, and Bradley F. Chmelka

5.1 Abstract

Mesoporous N- and Fe,N-carbons exhibit high and stable activities for oxygen and sulfur reduction that are comparable to or surpass those of standard Pt-activated-carbon and graphite electrocatalysts. Favorable properties include high nitrogen contents (>15 atom%), high fractions of N moieties at surface sites, 3-nm mesopores to promote diffusion, and electron conductivity to surface N environments where the reduction reactions occur. The types,

quantities, and distributions of N-heteroatom environments, especially those at surface sites, are shown to strongly influence macroscopic reduction activities.[1] N- and Fe,N-mesoporous carbons synthesized using different mesopore templates (e.g., salt versus silica) are explored to understand the atomic level differences that correlate with increased reduction (sulfur reduction for Li-S batteries, and oxygen reduction for fuel cells) activity, and how they can be optimized. Compared to 20 wt% Pt supported on activated carbon, the salt-templated mesoporous Fe,N-carbon exhibits the highest reduction activity, exceeding even that of the commercial Pt-carbon catalyst. We have previously used 2D ^{13}C-^{15}N NMR spectra to resolve signals from four distinct types of N-heteroatom environments: pyrrolic, graphitic, edge/isolated pyridinic, and pyrazinic/pyridinic moieties.[1] The inclusion of Fe-heteroatoms significantly improves carbon-based electrocatalyst reduction activity, however, the atomic-level origins of such properties are more complicated and have thus remained elusive. Nevertheless, direct probing of the Fe sites with ^{57}Fe Mössbauer spectroscopy and the N sites with solid-state ^{15}N NMR and spin-lattice relaxation-time analyses, resolve signals from ^{15}N species that are proximate to paramagnetic Fe-heteroatoms allowing ^{15}N-Fe distances to be estimated. XRD, XPS, XRF, Raman spectroscopy, STEM, and EXAFS are used to characterize the materials amongst many length scales and corroborate the hypotheses. Understanding the roles of the Fe and N carbon-moieties in electrocatalytic reduction yields new design criteria for syntheses of high performance non-precious-metal electrocatalysts with diverse fuel cell and battery applications.

5.2 Introduction

High N contents, high electrical conductivities, and high surface areas of Fe,N-carbons make them attractive as replacements for costly Pt-based oxygen-reduction electrocatalysts for oxygen-reduction (OR) in fuel cells[1–6] and for sulfur-reduction electrocatalysts (SR) in Li-S batteries,[1,7–10] However, much remains unknown regarding the specific moieties that catalyze the reductions. For example, in different N-carbons, pyrrolic nitrogen,[11] pyridinic nitrogen,[1,11–13] and/or graphitic nitrogen[14,15] species have been proposed as reduction active sites. In the high performing carbon-based electrocatalyst materials prepared with both Fe- and N-containing precursors, the role of Fe has also been widely debated, with some proposing that Fe atoms serve as catalysts for the formation of active nitrogen moieties,[16] or that Fe-containing moieties such as $Fe_2N_xC_y$[17] or porphyrinic planar FeN_4[18,19] species serve as electrocatalytic active sites. Overall, the disorder in heteroatom-containing carbons has left the types and structures of the reduction active sites open to debate. Elucidating the types of heteroatom species in such materials is challenging, in part because scattering techniques such as wide-angle X-ray scattering and Raman spectroscopy provide limited insights into bonding environments of Fe and N heteroatoms, which tend to occupy distributions of local environments. X-ray absorption spectroscopy (XAS), is sensitive to the valence electron environment of transition metal ions, and has proven valuable in elucidating different Fe moieties in Fe,N-carbons when paired with density functional theory calculations.[18] X-ray photoelectron spectroscopy (XPS), in principle, is sensitive to differences in the types of Fe and N environments that are present in N-carbons, but the small differences in binding energy associated with different nitrogen-containing moieties limit spectral resolution and reduce the confidence of assignments.[20]

By contrast, solid-state nuclear magnetic resonance (ssNMR) spectroscopy and analyses are capable of distinguishing and quantifying molecular environments within complicated heterogeneous materials,[21–23] including materials with electrical conductivity,[24–26] and porous carbons.[27] For N-containing carbons prepared by high-temperature condensation, one-dimensional (1D) solid-state NMR has previously been used to monitor differences resulting from high-temperature syntheses and to identify potential ORR active sites,[28–31] but the generally low nitrogen contents and broad distributions of ^{15}N environments have resulted in low sensitivity and low resolution, even with isotopic enrichment in ^{15}N. Recently, solid state ^{15}N NMR has been used to establish the types, quantities, and distributions of N-heteroatom environments, for N-carbons prepared with various mesopore templating agents, concluding that the mesopore templating agent used strongly influences the types of N-environments formed, and that a salt-template over a silica-template results in greatly enhanced macroscopic OR and SR activities.[1] The challenge of characterizing Fe,N-carbon with solid-state NMR is significantly increased by the presence of unpaired Fe electrons, in which paramagnetic broadening greatly influences sensitivity and resolution of sites near Fe.[32] Therefore, the crucial Fe and N species have not been probed due to challenges with Fe. However, we have found that differences in the relaxation times of nuclei near unpaired Fe electrons can be used to gain insights into the N species closest to paramagnetic Fe.

Here, we report the local environments of Fe and N active sites in high-surface-area mesoporous Fe,N- and N-carbons with high heteroatom contents elucidated by combined EELS STEM, extended X-ray absorption fine structure (EXAFS) spectroscopy, Mössbauer spectroscopy, and solid-state 1D ^{15}N NMR spectroscopy. The combined analyses elucidate the macroscopic electrocatalytic properties of the material. In the mesoporous Fe,N-carbons,

electrocatalytic activity correlates both to the presence specific N moieties and their proximity to Fe moieties, showing overall reduction activity may be improved by preparation of materials with a range of catalytically-active sites.

5.3 Materials and Methods

Materials syntheses

Mesostructured silica (SBA-15) was prepared according to a previously reported procedure.[33] Briefly, 8.0 g of poly(ethyleneoxide)$_{20}$-poly(propylene-oxide)$_{70}$-poly(ethyleneoxide)$_{20}$ triblock copolymer (Pluronic® P123, Sigma-Aldrich) were dissolved in 60 ml of deionized water. To this solution was added 17 g of tetraethoxysilane and 240 ml of 3 M HCl, and the combined solution was stirred vigorously at room temperature for 10 min. The solution was then stirred for 20 h at 313 K, placed in a 363 K oven without stirring for 2 days, vacuum-filtered, and then calcined in air at 823 K to remove the structure-directing surfactant species to obtain the mesoporous silica powder.

Mesoporous Fe,N- and N-carbon materials were synthesized from urea and cyclohexanehexone as described previously.[1,34] Briefly, urea (99%, Sigma-Aldrich) and cyclohexanehexone octahydrate (97%, Sigma-Aldrich) were mixed in a 3:1 stoichiometric ratio, such that the total numbers of carbonyl groups on the cyclohexanehexone octahydrate molecules and amine groups on the urea molecules were equal (see Fig. S1). In the case of the Fe-containing material, anhydrous $FeCl_2$ was added at this step as well. The mixture of urea and cyclohexanehexone octahydrate was heated to 341 K to form the eutectic melt, and then

to 363 K to promote cross-linking. The cross-linked solid was then pyrolyzed by heating at a ramp rate of 2.5 K/min to 1073 K under flowing N_2 gas and held at the target temperature for 60 min. Mesoporosity was introduced according to the templating method originally reported by Ryoo, *et al*.,[35,36] modified for use with the eutectic precursor melt.

In this method, previously prepared SBA-15 mesoporous silica powder was mixed into the urea and cyclohexanehexone octahydrate mixture (in a ratio 0.85 g SBA-15 per gram of mixture) after it had been heated to form a eutectic melt, but before subsequent heating to promote cross-linking. The composite silica and cross-linked organic material were then pyrolyzed, as described above. The silica was selectively dissolved from the composite at room temperature by stirring in 2 M NaOH for two consecutive 12 h washes, filtration, and drying cycles., NaOH was prepared from 98.9% NaOH pellets (Fisher, <0.001% Fe) in deionized water. Following washing, the material was stirred in 0.5 M H_2SO_4 for 12 h, which was prepared by dilution of 95+% sulfuric acid in deionized water (VWR chemicals). Finally, the material was washed in dry ethanol for 20 min. These steps resulted in mesoporous N-containing carbon materials with a mesoporous template, as evidenced by the TEM image in **Figure S5.7a**, and the nitrogen sorption data in **Table S5.1**.

Alternatively, mesoporous N-containing carbon materials were prepared by using a "salt-templating" method, where a mixture of sodium chloride and zinc chloride salts served as the sacrificial templating material.[37] After the organic precursors were heated to form a eutectic melt at 341 K (before significant cross-linking occurs at 363 K), a physical mixture of ground 65 mol% $ZnCl_2$ (97+%, Acros Organics) and 35 mol% NaCl (Macron Fine Chemicals) was added in a 1:3 mass ratio of organic precursors to salts. Following pyrolysis under the same conditions as used for the silica-templated materials, the composite products were ground into

a powder, and the salts removed by washing in deionized water. For consistency, the salt-templated material was also washed while stirring in 2 M NaOH, then in 0.5 M H_2SO_4, and finally in dry ethanol, as described above for the silica-templated N-carbon. These steps resulted in mesoporous N-containing carbon materials with a mesoporous template, as evidenced by the TEM image in **Figure S5.7b**, and the nitrogen sorption data in **Table S5.1**. The salt-templated mesoporous N-carbons contain negligible contents of templating materials, such as Fe and Zn, as determined by the XPS, XRF, and the associated discussion of the results in **Tables S5.2 and S5.3**.

Following the removal of either template material, the resultant mesoporous high-N-content carbon products were dried in a vacuum oven at 323 K. Versions of the materials were also prepared by using ^{13}C,^{15}N-enriched urea (99% ^{13}C, 99% ^{15}N, Sigma Aldrich) under otherwise identical conditions to improve ^{13}C and ^{15}N signal sensitivity for solid-state nuclear magnetic resonance (NMR) spectroscopy.

Electrocatalytic activity and stability tests

Oxygen Reduction

Oxygen reduction activities of the porous high-N-content carbon materials were determined by conducting staircase voltammetry (SV) measurements with a BioLogic VSP potentiostat, as reported previously.[1] A three-electrode configuration was used with a rotating-disk electrode with a 5.61 mm diameter glassy carbon disk used as the working electrode, and with a graphite rod and a Ag/AgCl (3 M NaCl) electrode as the counter and reference electrodes, respectively. Catalyst inks for alkaline fuel cell conditions were prepared by

dispersing 7.4 mg of high-N-content carbon materials into a mixture composed of 250 μL of milli-Q-water, 750 μL of isopropanol, and 60 μL of 5 wt% Nafion^{TM} solution. The suspension was sonicated for 60 min to form a homogeneous ink, and then 20 μL of catalyst ink were deposited drop-wise onto a glassy carbon electrode and dried at 40 °C to yield a catalyst loading of 712 μg/cm^2. To evaluate ORR performance under alkaline conditions, staircase voltammetry tests were conducted within an O_2-saturated 0.1 M KOH solution. Catalyst inks for acidic fuel cell conditions were prepared by dispersing 7.4 mg of high-N-content carbon into a mixture composed of 250 μL of milli-Q-water, 750 μL of isopropanol, and 240 mg of 5 wt% Nafion^{TM} solution. The suspension was sonicated for 60 min to form a homogeneous ink, and then catalyst ink was deposited dropwise onto the glassy carbon electrode and dried at 40 °C to yield a catalyst loading of 780 mg/cm^2. To evaluate ORR performance under acidic conditions, staircase voltammetry tests were conducted within an O_2-saturated 0.1 M $HClO_4$ solution. For both sets of conditions, five cyclic voltammetry cycles were ran to activate the electrocatalyst prior to SV testing. The steady-state ORR polarization curves were collected by using staircase voltammetry with a potential step of 0.01 V and a holding time at each potential of 10 s. During the tests, the working electrode was rotated at a rate of 900 rpm using a Modulated Speed Rotator (Pine Research Instrumentation) to promote mixing of the electrolyte and reduce concentration gradients in the bulk fluid in contact with the catalyst layer. Following the measurements, the oxygen reduction currents were scaled by the area of the glassy carbon electrode to obtain current densities, and the potentials were converted to the reversible hydrogen electrode (RHE) scale. Stability tests were conducted using the same synthesis and set-up under acidic conditions. A constant and intermediate potential (0.4 V) was applied while the current produced was measured over a 3-h time period.

To be added: Fuel cell measurements, waiting on collaborator.

Sulfur Reduction

Sulfur reduction testing was done according to previous reporting.[1] The electrolyte (referred to as "blank electrolyte") was made by combining 1 M lithium bis(trifluoromethane-sulfonyl) imide (Sigma-Aldrich) and 0.2 M lithium nitrate (Sigma-Aldrich) in a mixed dimethoxyethane (Sigma-Aldrich) and 1,3-dioxolane (Sigma-Aldrich) solution (1:1 by volume). The Li_2S_6 catholyte (0.1 M) was prepared by reacting sublimed sulfur (Sigma-Aldrich) with Li_2S (Sigma-Aldrich) in stoichiometric proportions in the blank electrolyte. The mixture was vigorously stirred at 50 °C in an argon-filled glove box overnight to produce a brownish-red Li_2S_6 catholyte solution. Sulfur-reduction performance was evaluated by conducting cyclic voltammetry measurements of the mesoporous nitrogen-containing carbon materials in CR2032 coin cells that were assembled in an argon-filled glovebox. The cathode slurry was prepared by mixing nitrogen-carbon or graphite, carbon black, and polyvinylidene fluoride binder at a mass ratio of 8:1:1 in N-methyl-2-pyrrolidone. The slurry mixture was drop cast onto a carbon-coated aluminum foil with a diameter of 1.3 cm. The loading of the nitrogen-carbon material was 1 mg/cm^2. Afterwards, the Li_2S_6 catholyte was used re d dvas a sulfur source and drop-cast on the cathode. The mass loading of the sulfur was 0.15 mg/cm^2 to ensure maximum utilization of sulfur. The sulfur cathodes were then directly assembled into a CR2032 coin cell with lithium foil, a Celgard 2500 separator, and blank electrolyte. Cyclic voltammetry curves were recorded over the voltage range of 1.7 V–2.7 V at a scanning rate of 0.1 mV/s.

EELS STEM

To be added, waiting for collaborator.

X-ray Absorption Spectroscopy

XAS measurements were conducted at beamline 4–1, Stanford Synchrotron Radiation Lightsource. Fe K-edge in a fluorescence geometry with a 30-element Canberra germanium detector was used. A metal Fe reference foil, placed after the sample holder, for simultaneous energy calibration. XAS was collected up to a wavenumber, k, of 15.2 $Å^{-1}$. Data processing and analysis were conducted with ATHENA and ARTEMIS, part of the IFEFFIT software suite.[38] All spectra were calibrated, normalized, and background-subtracted per the protocols outlined in the ATHENA documentation.[39] EXAFS data were fit to the DFT calculated models (**Figure S5.8**) with a k window of 3–12.1 $Å^{-1}$, and single scattering pathways. Using the S_0^2 value calculated from the Fe reference foil at the beamline, a calibration factor was used to obtain the coordination number from the fitted parameters.

Mössbauer spectroscopy

^{57}Fe Mössbauer measurements were acquired in the Ménard lab by Camden Hunt. Measurements were performed on a MS6 Mössbauer Spectroscopy System from SEE CO with a ^{57}Co(Rh) source. Measurements were taken at 298 K under a nitrogen atmosphere using 50 mg of sample in HDPE sample cups. Run time for each measurement was 24 h. The isomer shift and Doppler velocity were calibrated against iron foil.

X-ray analyses

Graphitic ordering in the mesoporous N-carbon materials was assessed by using wide-angle powder X-ray diffraction (XRD) using a Rigaku Smartlab high-resolution diffractometer with Cu K_α radiation operating at 40 kV and 44 mA. Wide-angle XRD patterns were recorded over a 2θ range of 10° to 70° in increments of 0.05°. Small-angle X-ray scattering analyses were conducted to assess the extents of long-range mesostructural order in the mesoporous N-carbon materials. Small-angle XRD patterns were recorded over a 2θ range of 0° to 3° in increments of 0.01°.

Near-surface elemental compositions were determined by X-ray photoelectron spectroscopy (XPS) using a Kratos Axis Ultra XPS system to acquire survey scans over a range of 0 to 1200 eV with a step size of 0.5 eV and a pass energy of 160 eV. Quantitative characterization of different near-surface nitrogenous species was accomplished using high-resolution N *1s* XPS, scanning a range of 390 to 410 eV with a step size of 0.05 eV and a pass energy of 20 eV. Spectra were processed by using CasaXPS software, and each high-resolution N *1s* spectrum was deconvoluted into multiple Gaussian lineshapes, based on the binding energies of electrons associated with nitrogen atoms in various functional groups.[20] Bulk elemental compositions were measured by X-ray fluorescence (XRF) using a Rigaku ZSX Primus IV instrument with a wavelength dispersive sequential diffractometer and were collected with ZSX Guidance software. A rhodium source was used and operated at 3.5 kW for all elements. Results were obtained through semi-quantitative methods, and theoretically calculated using the fundamental-parameter method and ZXS Guidance's internal sensitivity library.

Raman spectroscopy

Raman measurements were also conducted to assess graphitic ordering of the mesoporous N-carbons using a Horiba Jobin Yvon T64000 confocal microscope 100X operating in single mono mode with a 1800 groove/mm grating, a liquid-nitrogen-cooled CCD detector, 488 nm excitation, and 20 s acquisition time. Raman data were processed with linear baseline subtraction and deconvoluted into Lorentzian line shapes.

Solid-state NMR spectroscopy

Solid-state ^{13}C and ^{15}N magic-angle-spinning (MAS) NMR spectroscopy were used to analyze the local environments of ^{13}C and ^{15}N moieties in the N-carbon materials synthesized from a 1:3 molar ratio of cyclohexanehexone octahydrate and uniformly ^{13}C,^{15}N-enriched urea. All solid-state NMR spectra were acquired on a Bruker AVANCE II HD 400 DNP-NMR spectrometer with a 9.4 T superconducting magnet operating at Larmor frequencies of 400.20, 100.64, and 40.56 MHz for ^{1}H, ^{13}C, and ^{15}N nuclei, respectively, and equipped with a variable-temperature 3.2 mm HXY MAS probehead. The experiments were conducted at low temperature (95 K) with 100 kHz SPINAL-64[40] ^{1}H decoupling during the acquisition periods, using zirconia rotors, Kel-F® caps, and under 8 kHz MAS conditions. Low-temperature conditions were used to improve NMR signal sensitivity for the 2D NMR measurements and to mitigate the influences of rapid nuclear spin-lattice and spin-spin relaxation effects. Chemical shifts were observed to vary with temperature, so all experiments were conducted under the same temperature and MAS conditions for consistency. Chemical shifts were referenced using uniformly ^{13}C,^{15}N-enriched glycine powder at room temperature as a secondary standard, with ^{13}C chemical shifts referenced to the carboxyl carbon atom at

172.7 ppm (tetramethylsilane at 0 ppm) and ^{15}N chemical shifts referenced to 33.4 ppm (liquid NH_3 at 0 ppm).[41] The N-carbon materials were diluted with KBr at a sample:KBr ratio of 1:3 w/w before being loaded into the MAS rotor. The KBr served as both an internal temperature probe[42] and to reduce undesirable sample heating that may arise from rapid rotation of conductive samples in the high magnetic field required for the NMR measurements.[43] The temperature of the MAS gas stream nearest to the stator was measured to be 95 K, and the actual sample temperature was estimated from ^{79}Br T_1 relaxation measurements[44] to be *ca*. 99 K. The high N contents and isotopic enrichment with ^{15}N and ^{13}C enable NMR spectra to be acquired with a remarkable combination of sensitivity and resolution. One-dimensional (1D) solid-state spin-echo ^{15}N NMR experiments of the salt-templated Fe,N- and N-containing carbons in **Figure 5.5** were acquired with 10,000 scans at varied relaxation times increasing from 10 ms to 10 s.

Extended discussion

The spectra show overlapping ^{15}N signals with partially-resolved maxima at 300 ppm assigned to pyridinic N atoms found in pyridinic moieties (including "paired" pyrimidinic, pyrazinic, or other diazinic species) or associated with interior pyridinic defect sites (red).[45–47] Signals centered at 230 ppm are assigned to N atoms that are isolated from other N heteroatoms at the edges of graphitic sheets (yellow).[1,48] Finally, signals centered at 160 ppm assigned to graphitic N environments (blue) and a small fraction of signal at 140 ppm assigned to pyrrolic N species (purple).[1]

Density Functional Theory (DFT) Modeling

NMR Calculations

The ^{15}N NMR spectra were analyzed in conjunction with DFT modeling to assign the correlated signals to distinct N-carbon moieties and structures (**Figure S5.8**), determining the local bonding environments of the ^{15}N species. DFT calculations yield the electronic shieldings of nuclei in distinct atomic environments, which are manifested as differences in isotropic ^{15}N chemical shifts ($\delta_{cs,iso}$). Such shielding calculations were conducted using a linear-response method, where a one-electron wavefunction is developed on a basis set of plane waves and electron-nuclei interactions are treated with the PAW approach.[49,50]

General calculation method

Density-functional theory[51] (DFT) calculations were performed using the Vienna Ab initio Simulation Package[49] (VASP) and the Perdew–Burke-Ernzerhof[52] (PBE) functional at the generalized gradient approximation (GGA) level. The dDsC dispersion correction[53,54] was applied. All calculations were spin-polarized. Gaussian smearing was applied with sigma equal to 0.1. For geometry optimizations, a cutoff energy as 500 eV was used. The energy convergence criterion was 10^{-6} eV and forces were optimized to 0.02 eV/Å with 3*3*1 *k*-points used for the terrace model, 1*3*1 for the armchair model, and 3*1*1 for the zigzag model.

Different spin states of the system have been tested and the spin density was found to be mainly localized on the Fe atom. The most stable spin states were used for both geometry optimization and NMR calculations.

For the nuclear shielding calculations, the linear response method[50,55] provided in VASP was used, with the cutoff energy set to be 600 eV. 5*5*1 *k*-points were used for the terrace model, 1*7*1 for the armchair model, and 7*1*1 for the zigzag model. An energy convergence criterion of 10^{-6} eV was used. LNMR_SYM_RED was used to discard symmetry operations that were not consistent with the way *k*-space derivatives were calculated in the linear response calculations of chemical shifts. NLSPLINE was used to construct the PAW projectors in reciprocal space using a spline interpolation so that they were *k*-differentiable. Default values were used for the step size (0.001) for the finite difference *k*-space derivative and the order (1) of the finite difference stencil.

Computational chemical shift reference

The calculated results from VASP were compared with the experimental NMR measurements by using:

$$\delta_i = \delta_{\text{calculated},i} - \delta_{\text{calculated},i,\text{ref}} + \delta_{\text{exp},\,i,\text{ref}} \quad ,$$

where δ_i are the reported ^{15}N isotropic chemical shift, $\delta_{\text{calculated},i}$ is the calculated chemical shift value calculated for different model Fe-N-C as shown in Fig. SX, $\delta_{\text{calculated},i,\text{ref}}$ is the ^{15}N isotropic chemical shift value calculated for solid a-glycine and $\delta_{\text{exp},i,\text{ref}}$ is the experimentally measured ^{15}N isotropic chemical shift for a-glycine of 33.4 ppm for ^{15}N.

5.4 Results and Discussion

While Pt-carbon (Pt/C) catalysts demonstrate desirably high oxygen reduction reaction catalysis performance, their stability is notoriously poor as the Pt-catalysts sites are quickly poisoned or oxidized, so a non-precious-metal substitute to Pt/C-catalyst with higher performance, selectivity, and stability than Pt/C is very desirable. Previously, it has been shown that the surface chemistry resulting from the interaction between the mesoporogens and carbon material during high temperature pyrolysis affects both the overall N content (which does not correlate with increased reduction activity) and the specific N moieties concentrations which do correlate with increased reduction activity.[1] Additionally, it was shown that the same N environments important to the catalysis of oxygen reduction in fuel cells appear to be important to the catalysis of sulfur-reduction in Li-S batteries,[1,7] exemplifying the diversity of mesoporous N-carbons. Here, mesoporous N- and Fe,N-carbons are prepared through high-temperature (1073 K) pyrolysis of cyclohexanehexone-octahydrate and urea precursors in the presence of a mesopore templating agent, such as a eutectic mixture of structure-directing $ZnCl_2$-NaCl salts or hexagonal mesoporous SBA–15 silica[56] (**Figure S5.1**). The presence of Fe is incorporated during initial synthesis steps with $FeCl_2$. The goal is to understand how the surface chemistry of mesoporogens and incorporation of various N and Fe heteroatoms affects the material performance, and eventually elucidate the active site. We have found that the presence of Fe-heteroatoms is important to both the synthesis as Fe encourages increase in extent of graphitization (see **Figure S5.2**), thus conductivity, allowing electrons to move to the reaction site, and the reduction performance of the materials as Fe is a part of a highly effective Fe-N active site. The higher surface area and more tortuous pore structure (3-4 nm diameter) of the mesopore-templated carbons than conventional activated-

carbons allow better reactant/product transport though solution to the reaction site **(see Table S5.1).**[35,37,57,58] Desirably, the mesoporous silica- and salt-templated N-carbons exhibit similar modest extents of periodic long-range order and graphitic order, which is increased with the incorporation of the Fe graphitizing agent, as evident in their wide- and small-angle X-ray scattering and Raman spectroscopy patterns, respectably (**Figure S5.2**). X-ray photoelectron spectroscopy (XPS, **Table S5.2**) results establish that the high near surface N-contents of the mesoporous N-carbons synthesized using the salt- or mesoporous silica-templates (16 mol% and 22 mol%, respectively) are decreased by the presence of the graphitizing Fe (16-12 mol% N, for 0.03-0.1 mol% Fe). Similarly, the bulk N contents (19 mol%, 28 mol% for the salt-,silica-templates, respectively) are decreased by Fe incorporation (19-17 mol% N, for 0.03-0.1 mol% Fe), as measured by X-ray fluorescence (XRF, **Table S5.3**). Importantly, these N contents are still 3-4 times higher than are typical for porous N-carbons, which is desirable as the presence of specific surface N moieties have been shown to be closely associated with electrocatalytic reduction sites,[1,59,58] and Fe-N sites, as shown below.

Oxygen- and sulfur-reduction properties dependance of templated mesoporous N-carbons

While their bulk compositions and mesoscale structures are similar, mesoporous N-carbons prepared under identical conditions with the exception of different mesopore templates (silica or $ZnCl_2$-NaCl salt) and Fe-heteroatom inclusion exhibit surprisingly different electrocatalytic reduction properties and stabilities. For instance, high oxygen reduction activity is assessed with polarization curves acquired by measuring current as a function of the difference in potential (from the RHE at 1000 mV) with the most desirable

performance achieving high current densities at low potential differences. Figure 5.1a shows polarization curves for silica-templated N-carbons (purple), and salt-templated N- and Fe,N-carbons (green, orange), compared with a 20 wt% Pt-carbon-standard (black). The OR activities (summarized in Table 5.1) of the mesoporous N-carbons are significantly higher when a $ZnCl_2$/NaCl salt mixture is used to produce mesoporosity (onset potential of 0.93 V v. RHE, limiting current density of 3.8 mA/cm^2), compared to mesoporous silica (onset potential of 0.60 V v. RHE, no limiting current achieved). Additionally, the incorporation of a small amount (0.1 wt%) of Fe (optimized Fe-content in Figure S5.3) in the mesoporous N-carbon greatly improves oxygen reduction reactivity (onset potential of 0.95 V v. RHE, limiting current density of 5.0 mA/cm^2) (see Figure S5.4a for silica-templated Fe,N-carbons). Thus, this highest performing carbon material is that of the salt-templated Fe,N-carbon with its oxygen reduction activity even surpassing that of the commercial 20 wt% Pt-C (onset potential of 0.98 V v. RHE, limiting current density of 3.8 mA/cm^2).

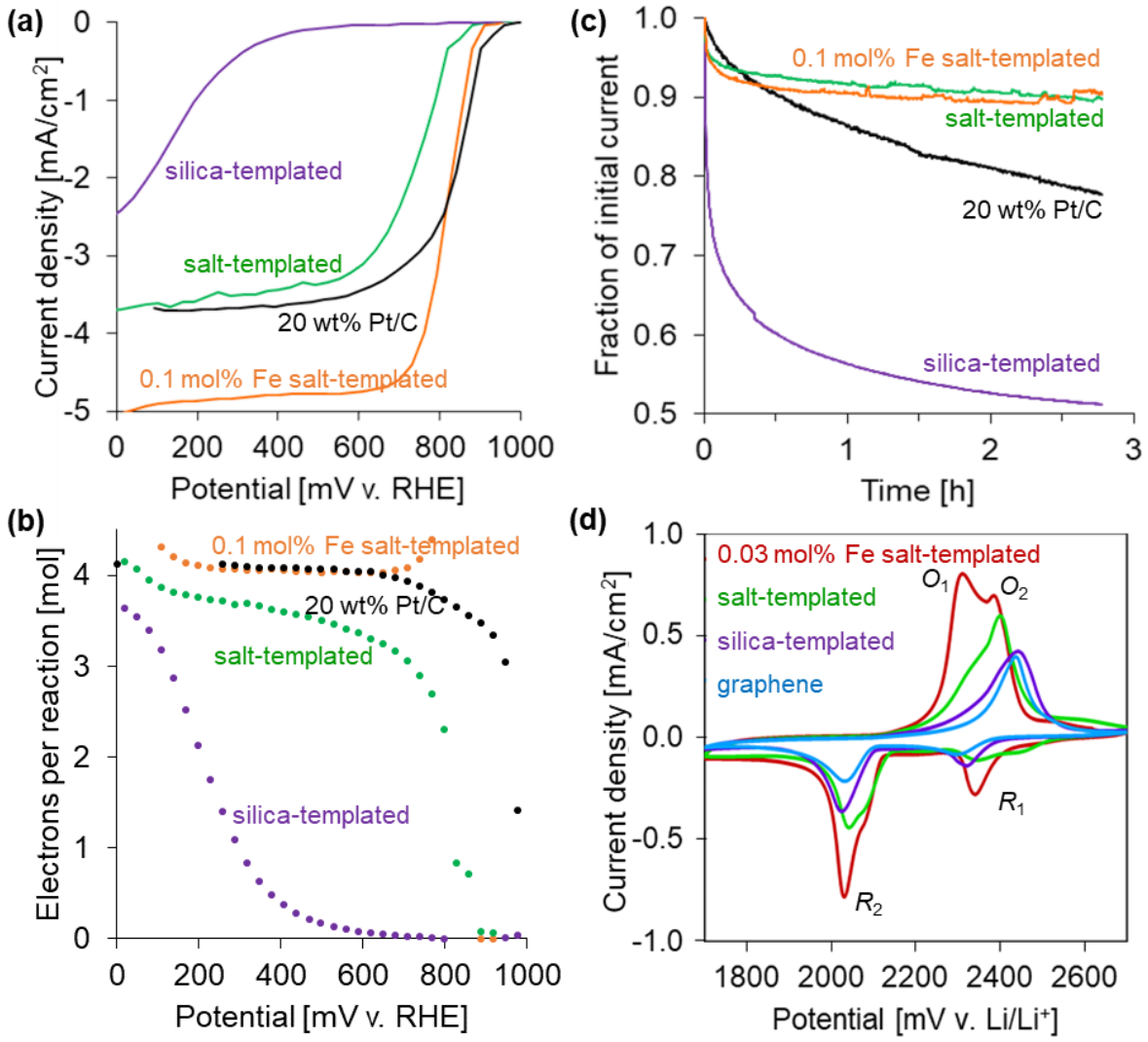

Figure 5.1. Electrocatalytic activity, electron consumption, and stability of mesoporous N- and Fe,N-carbons. Electrocatalytic activity and stability curves for the electrocatalytic reduction of (a,b,c) oxygen under acidic conditions (0.1 M $HClO_4$) and (d) sulfur by cyclohexanehexone-urea-derived mesoporous N-carbons pyrolyzed at 1073 K using mesoporous SBA-15 silica (purple) or a $ZnCl_2$-NaCl mixture (green, orange, red) as templating agents. Oxygen reduction performances are compared to a 20 wt% Pt/C catalyst (black), while sulfur reduction performances are compared to graphite (blue). (b) Theoretical number of moles of electron consumed during oxygen reduction as a function of potential, calculated according to the Koutecký-Levich equations. (c) Stability testing of the best

performing salt-templated Fe,N-carbon showing the fraction of the initially detected current as a function of time, when a constant potential of 400 mV was applied. (d) The various oxidation (O_1, O_2) and reduction (R_1, R_2) peaks are labeled on the S-reduction curve. Currents were normalized by the geometric electrode area. All ORR experiments were conducted with a rotating disk electrode at room temperature in a 0.1 M KOH electrolyte solution. (a) and (c) were conducted at 900 RPM. Sulfur reduction data were collected via cyclic voltammetry in a coin cell. The salt- and silica-templated non-Fe-containing N-carbon data shown above was originally presented by Becwar *et al*.,[1] but reproduced with permission here for the sake of comparison with the superior performance of the Fe,N-carbon.

Table 5.1 Onset potentials, half-wave potentials, and limiting current values for oxygen reduction by salt- and silica-templated mesoporous Fe,N- and N-carbons and 20 wt% Pt/C electrocatalysts.

	Onset potential	***Half-wave potential***	***Limiting current density***
	V	*V*	*mA/cm²*
SBA-15 silica templated	0.60	0.7	-
$ZnCl_2$-NaCl templated, no Fe	0.93	0.8	3.8
$ZnCl_2$-NaCl templated, 0.03 mol% Fe	0.98	0.9	3.8
$ZnCl_2$-NaCl templated, 0.1 mol% Fe	0.95	0.8	5.0

In addition to high OR activity, reaction selectivity is also an important factor of a good catalyst. An ideal catalyst is selective in achieving the desirable four-electron reduction of O_2 to produce water, rather than the most common and undesirable side reaction which is the two-electron reduction of O_2 to form corrosive peroxides.[60,61] The selectivity and effectiveness of the active sites is assessed by calculating the theoretical number of electrons transferred

during OR over all potentials. This data is obtained by measuring current density at different rotation speeds and calculated according to the Koutecký-Levich equations, with an ideal catalyst achieving a majority of four-electron reactions even at high potentials (small potential differences).[60] For instance, **Figure 5.1b** shows the theoretical number of electrons transferred during the OR of silica-templated N-carbons (purple) and salt-templated N- and Fe,N-carbons (green, orange) as a function of potential, compared with a 20 wt% Pt-carbon-standard (black). The use of the salt-template over the silica-template increases the tendency of four electron reactions, but still not achieving primarily four electron reductions at most potentials. However, both the salt- and silica-templated Fe-containing materials (see **Figure S5.4b** for silica-templated Fe,N-carbons) show a majority of four-electron reduction reactions (desired) occurring over most potentials, indicating that the incorporation of Fe is the most important factor the site-specific activity, and is likely is part of the active site. While the Pt-carbon catalyst also desirably achieves a majority of four-electron reactions over most potentials, we know form the literature that the Pt sites are quickly poisoned,[2,3,6] and material stability a major concern.

The use of a salt-template and incorporation of Fe-heteroatoms both appear to increase the stability of an ORR catalyst over time, exceeding that of current Pt/C catalysts. Pt-carbon catalysts are plagued by poor stability due to active site poisoning, exacerbating the high costs of the Pt active sites. Normalized plots of current density (assessed by holding the applied potential constant at an intermediate value) as a function of time are shown in **Figure 5.1c** for the silica- and salt-templated Fe,N- and N-carbons, compared to a 20 wt% Pt/C, with the most desirable performance maintaining a high fraction of the initial current density over time. Both the salt-templated N- and Fe,N-carbons achieve stability (90% of initial current after 3 h)

higher than that of the 20 wt% Pt-carbon (78% after 3 h), while the silica-templated N-carbon has poor long term stability (51% after 3 h). As opposed to the reacting electrons per potential curves, here it is clear that the mesopore templating agent is the important factor in achieving higher long-term stability. Specifically, compositional differences of the salt- and silica-templated mesoporous N-carbons likely arise from differences in surface interactions during pyrolysis. The $ZnCl_2$-NaCl-template forms a low-melting eutectic at 1073 K,[37] such that the Zn^{2+} cations appear to promote the formation of pyridinic N-carbon moieties at the surfaces of the mesoporous salt template during synthesis, whereas the silica template is expected to interact relatively weakly with the nascent N-carbon network[1] (see **Table S5.2** for extended discussion on elemental composition and how Zn content is only important to synthesis, not performance). The high and stable OR activity of the salt-templated Fe,N-carbon suggests that it may also be effective in catalyzing other reduction reactions.

The significance of non-precious-metal electrocatalysts stems beyond that of oxygen reduction to many other areas including the catalytic reduction of sulfur in Li-S batteries, overcoming the electrical conductivity challenges of inherently insulating S_8 and decreasing the rate limiting activation energies of traditional and non-doped graphenes.[1,9] Similar relative behaviors are observed for the mesoporous salt- and silica-templated N-carbons as sulfur reduction catalysts to that of the reduction of oxygen. **Figure 5.1d** shows cyclic voltammetry curves in coin cells for these salt- (green, red) and silica-templated (purple) N-carbons, compared to a standard graphite (blue). The optimized Fe content for S-reduction in the salt-templated-Fe,N-carbon is only 0.03 mol% Fe (shown in red, optimization shown in **Figure S5.5**), although the Fe content is lower than the optimized amount for OR, the important point being shown is how the inclusion of Fe increases reduction performance. Here, lower

potentials for oxidation reactions are desirable. The oxidation peak (O_2) of the salt-templated Fe,N-carbon is 2.38 V, a slightly lower potential than the salt-templated N-carbon (2.40 V), the silica-templated N-carbon (2.44 V), and the graphite (2.44 V) (see also **Table 5.2**). Interestingly, the Fe,N-carbon has a distinct much lower potential (2.31 V, O_1) extra peak, indicating that the presence of Fe is important to the types of surface environments where the oxidation reactions are occurring. For the reduction peaks, higher onset potentials are desirable, and the two reduction peaks R_1 and R_2 are correlated with the reduction of S_8 into polysulfide intermediates and of polysulfides into Li_2S_2/Li_2S, respectively.[9] The salt-templated N- and Fe,N-carbons exhibit higher R_1 onset potentials (2.55 V and 2.52 V, respectively) than either the silica-templated N-carbon (2.44 V) or the graphite (2.41 V). The salt-templated Fe,N and N-carbons display the highest R_2 onset potential, with a first partially resolved R_2 reduction onset potential of 2.16 V (Fe,N), 2.17 V (N), followed by additional partially resolved reductive peaks starting from 2.11 V (Fe,N), 2.12 V (N) and 2.05 V (Fe,N), 2.06 V (N), suggesting the presence of multiple reduction sites or mechanisms.[9,62] Inclusion of Fe into the carbon particularly intensifies the second partially resolved peak. However, the silica-templated N-carbon and the graphite both only exhibit a single R_2 peak starting from 2.12, 2.13 V, respectively, suggesting that there may be only one major active site or reduction mechanism responsible for these signals in both types of templated materials. Thus, both synthesis with a salt-template and the presence of Fe-heteroatoms are crucial to optimized SR performance. The role of Fe must then be beyond that of a graphitizing agent, thus a part of the SR active site and a way to trap soluble intermediates thereby mitigating sulfur losses.

Table 5.2. Peak position and onset potential values for sulfur reduction by salt- and silica-templated mesoporous Fe,N- and N-carbons and standard graphite as electrocatalysts.

	Peak position [V]			
	R_1	R_2	O_1	O_2
SBA-15 silica templated	2.32	2.02		2.44
$ZnCl_2$-NaCl templated, no Fe	2.34	2.04		2.40
$ZnCl_2$-NaCl templated, 0.03 mol% Fe	2.34	2.03	2.31	2.38
graphite	2.30	2.03		2.44
	Onset potential [V]			
	R_1	R_2		O_2
SBA-15 silica templated, no Fe	2.44	2.12		2.12
$ZnCl_2$-NaCl templated, no Fe	2.55	2.16		2.12
$ZnCl_2$-NaCl templated, 0.03 mol% Fe	2.52	2.13		2.18
graphite	2.41	2.12		2.13

Both the incorporation of Fe-heteroatoms and the use of a salt-template are crucial in contributing to crucial to optimized SR and OR performance of N-carbons. While each provide distinct advantages, both are required to achieve the best material performance, even higher than that of a standard 20 wt% Pt-carbon catalyst for OR and a graphene for SR. Interestingly, the best performing material actually has the lowest overall N content, suggesting that whatever N moieties are in this material and a part of the active sites are much more highly performing than the others. The material performance and stability measured in a scalable full-fuel-cell is in agreement with the half-cell findings. In a full-cell, the salt-templated Fe,N-carbon was the highest performing OR material with cycling stability that far exceeded that of the Pt/C catalyst (**Figure S5.6**). With the importance of both the templating material and Fe-heteroatom content established, the role that these influences play in developing and acting as part of the active site is investigated on a variety of length scales.

Heteroatom dispersion imaging - STEM/EELS

Electrochemical activity measurements reveal the importance of Fe heteroatoms to macroscopic reduction activity of the N-carbons, however, correlating performance activity with information about the material compositions on the nano or atomic scales is crucial to understanding the active sites. Aberration-corrected scanning transmission electron microscopy (STEM) can spatially resolve such features, and when combined with electron energy-loss spectroscopy (EELS) and energy dispersive X-ray (EDX) spectroscopy, information about local chemistry and elemental compositions can be deduced, respectively. EELS STEM imaging has been used to establish the proximity of Fe and N atoms at the edges of carbon nanotubes-graphene complexes, but with low resolution and no information about bonding between the speices.[3] Such images are challenging to acquire for graphitic carbon materials since electron radiation sources are highly ionizing hence, can easily lead to beam damage at high acceleration voltages. In this study, we investigate the local chemistry and composition of N-carbons using simultaneously acquired *Z*-contrast STEM, EELS, and EDX hyperspectral datacubes from an aberration-corrected TEM operated below the knock-on threshold of Carbon.

The salt-templated 0.1 mol% Fe,N-carbon is imaged by *Z*-contrast HAADF HR-STEM which shows that graphitic carbons material in white on a dark background (Figure 5.2a,b). The insets denote the regions scanned for EDX and EELS, used to generate the color composite image showing the distribution of Fe (red), O (green), and N (purple) throughout the graphitic carbon sheets with a resolution of about 2 nm. This map was generated by fitting inelastic electron scattering cross sections for carbon, nitrogen, oxygen, and iron to experimentally acquired EELS data from the hyperspectral datacube in this region. The

individual elemental dispersion maps (Figure 5.2c-f) indicate that oxygen and nitrogen are fairly uniformly distributed and strongly correlated with the carbon network, thus integrated and dispersed through the carbon, as expected in a pyrolyzed graphitic carbon. Fe atoms are fairly homogeneously dispersed through the carbon matrix as detected by specialized SEM techniques, on a scale that is smaller than visible on the EDS maps. This is consistent with Fe atoms being coordinated to N and C atoms on the atomic scale throughout the matrix. The two brighter regions of Fe overlap contain both Fe and oxygen heteroatoms, suggesting the presence of some iron-oxide inclusions (about 2 nm). However, the lack of significant large and brightly colored Fe regions indicates a lack of Fe clusters which are undesirable as Fe clusters are known to initially aid in reduction activity, but are quickly poisoned, thus are non-ideal active sites. To ensure that sites like iron-oxide sites do not affect the reduction performance testing, CV activation cycles are ran prior to reduction performance testing. Importantly, the HR-STEM reveals that Fe atoms are present and well dispersed throughout the carbon networks and are proximate to N-heteroatoms on the atomic scale, supporting the hypothesis that N and Fe atoms are proximate and play important roles in the active sites. However, no bonding information can be inferred from STEM, so further atomic-scale characterizations are necessary before conclusions can be drawn.

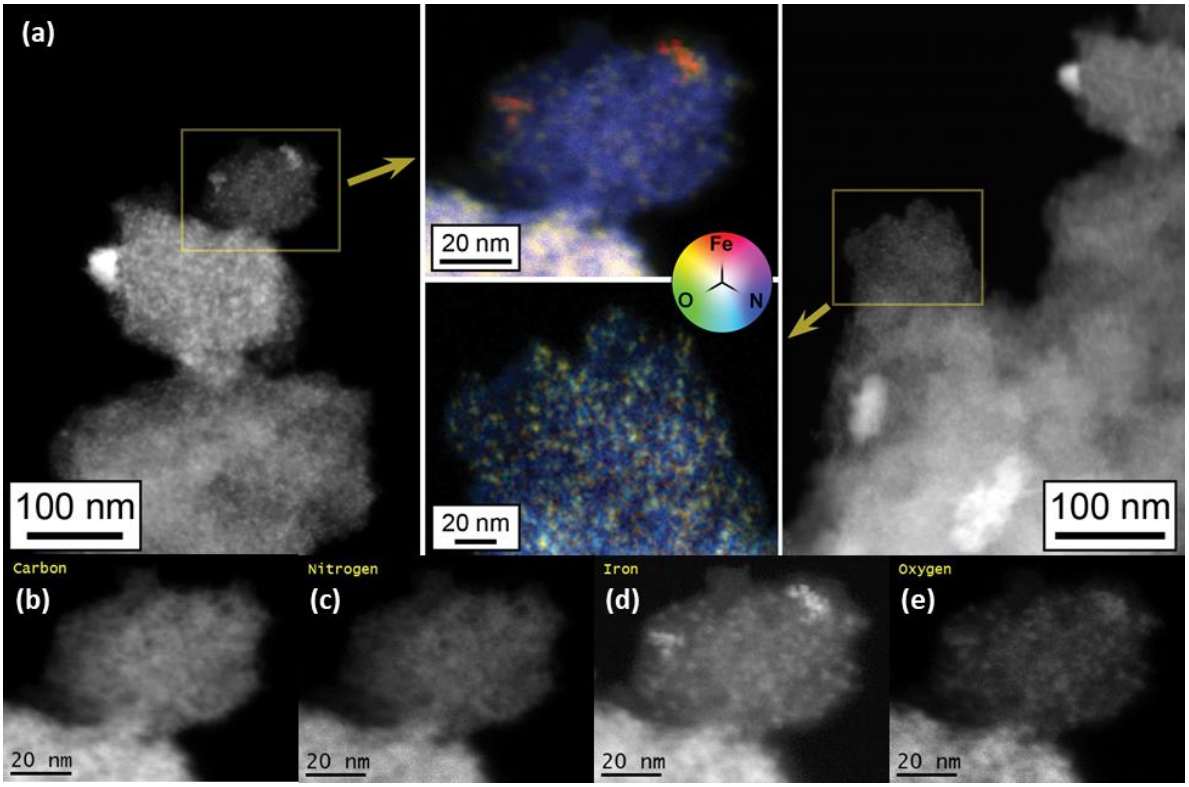

Figure 5.2. Images of the nanoscale distributions of nuclei in the salt-templated Fe,N-carbons as probed by STEM EDS. (a) Composite EELS STEM image showing iron in red, oxygen in green, and nitrogen in blue. Element specific STEM images for (b) carbon, (c) nitrogen, (d) iron, and (d) oxygen. Spectra were collected at 60 kV.

Local Fe and N compositions and structures

To determine the roles of Fe and N-heteroatoms in Fe,N-carbons, the compositions and structures of the atomic-level environments need to be elucidated and understood. Information on the local environments of ^{15}N heteroatoms, and their proximity to Fe, in salt-templated N- and Fe,N-carbons is accessed directly by solid-state ^{15}N NMR spectroscopy. Solid-state NMR analyses of Fe-containing carbons are exceptionally rare due to the complicating influences

of paramagnetic Fe species on proximate ^{13}C or ^{15}N species,[63] which introduce unpaired electrons into the material that couple with nearby nuclear spins. Nevertheless, local compositions and structures of Fe heteroatoms with respect to surrounding atoms are interrogated using EXAFS at the Fe K-edge and ^{57}Fe Mössbauer spectroscopy.

The average coordination and radial distance of nearest neighbor atoms in proximity to Fe heteroatoms are elucidated with fluorescence detected EXAFS spectroscopy at the Fe *K*-edge. For example, the Fe-*K*-edge EXAFS of the 0.1 mol% Fe salt-templated N-carbon is shown in **Figure 5.3**. The experimental data (orange) is fit (black dash) using the DFT modeling (**Figure S5.8**) data of the Fe-N-C moiety structures in a graphitic carbon matrix. EXAFS data confirm that the model is a good model of this material system. The presence of Fe-N bonds in the model and EXAFS, is of particular interest as these heteroatoms are expected to be linked to the active site. **Table 5.3** shows the fit parameters of the EXAFS data including the radial distances of each Fe-X bonds. The Fe-N1 radial distance is approximately 1.9 Å with a coordination number of 2.5, as expected for moieties at the edges of graphitic sheets. This agrees with the Fe-C2 radial distance, which is approximately 3.42 Å (or two bond distances from Fe) with a coordination number of 4.9, this low coordination to the next nearest neighbors could be due to Fe-N sites at the edges of graphitic sheets, where there are fewer C atoms to interact with than in the middle of a carbon sheet. Finally, the Fe-C1 radial distance is approximately 2.1 Å with a much higher coordination number of 9.8, as expected for an Fe-C moieties within the carbon sheets more so than at the edges. The EXAFS analyses both agrees with these proximities suggested as possible by the STEM data, and provides the additional information about which species are specifically bonded to Fe heteroatoms. From the EXAFS, we start to get an understanding of the Fe-N-C environments present on an atomic

scale from the perspective of the Fe heteroatoms, but more information on the specific N and Fe moieties present is needed to correlate them with catalytic effectiveness.

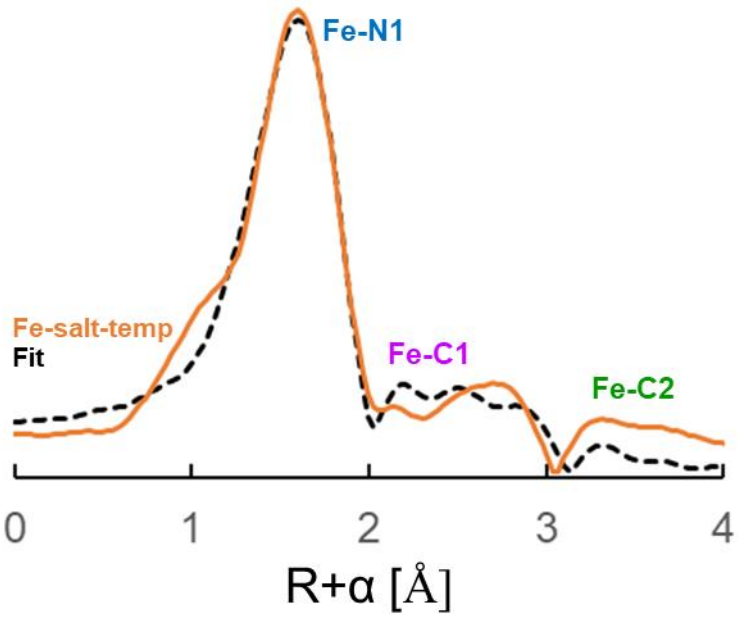

Figure 5.3. Radial distribution function for the Fe-*K*-edge EXAFS (orange) and curvefit (black dash) in R-space (FT magnitude) showing Fe-bonding distances for different Fe moieties as determined from the Fe-*K*-edge of fluorescence-detected EXAFS spectrum for the salt-templated Fe,N-carbon; Fe-N1 (blue), Fe-C1 (pink), and Fe-C2 (green). The data are k3-weighted and not phase-corrected. Imaginary space data can be seen in Figure S5.7.

Table 5.3. Fit parameters[a] for Fe-*K*-edge EXAFS of the 0.1 mol% Fe salt-templated N-carbon material.

Path[b]	*Coordination number*	σ^2 *[Å^2]*	*Radial distance [Å]*
Fe – N1	2.5(9)	0.005(2)	1.91(7)
Fe – C1	9.8(4)	0.006(9)	2.06(2)
Fe – C2	4.9(7)	0.006(9)	3.42(8)

[a] S_0^2 was fixed as 0.65 by fitting the Fe foil placed after the sample. ΔE0 was refined as a global fit parameter, returning a value of (8 ± 2) eV. Data ranges: $3 \leq k \leq 12.1$ Å^{-1}, $1 \leq R \leq 3.5$ Å. The number of variable parameters is 10, out of a total of 14.3 independent data points. R factor for this fit is 0.1%.

[b] The paths for Fe - N1, Fe – C1, and Fe – C2 are from the crystal structures of Fe (zigzag, 2n, iso-1).

The identities and relative quantities of Fe moieties in the salt-templated Fe,N-carbon are directly established by ^{57}Fe Mössbauer spectroscopy, which is highly sensitive to small changes in the chemical environment of ^{57}Fe nuclei based on the emission and absorption of gamma rays in solids. The ^{57}Fe Mössbauer spectrum of the salt-templated Fe,N-carbon (**Figure 5.4**) is deconvoluted into three doublets arising from three distinct ^{57}Fe environments, which are assigned on the basis of their isotropic shifts and quadrupolar splitting parameters (**Table S5.4**). Specifically, the majority (84%) of detected ^{57}Fe species are in the form of Fe_xN species (red). Generally, x has been assigned to values 1, 2, and 4,[18,64,65] however, in depth studies of such species have also specifically assigned this signal to x=1 (i.e., FeN coordination).[66,67] Weaker doublet signals are attributed square-planar porphyrin-like to $Fe^{II}N_2C_2$ moieties (green, 6%) and N-$Fe^{II}N_{2+2}$/C moieties (yellow, 10%).[18,64,65,68–70] A small presence of Fe_2O_3 is possible as the small sextet could in low intensity and be broadened, thus not distinguishable. The presence of metallic Fe however, is very unlikely due to the lack of

a prominent sextet, regardless of temperature. It is important to remember that these quantities are from the perspective of the Fe atoms, if we consider them from the perspective of the N quantities, there approximately 53% Fe_xN-like species, 32% N-$Fe^{II}N_{2+2}$/C-like species, and 15% $Fe^{II}N_2C_2$-like species. The presence of Fe species coordinated with one or more N and C atoms, as detected by Mössbauer spectroscopy, not only supports the EELS STEM data suggesting the nanoscale proximities of Fe and N species, but corroborates the Fe-N and Fe-N bonding environments detected by EXAFS.

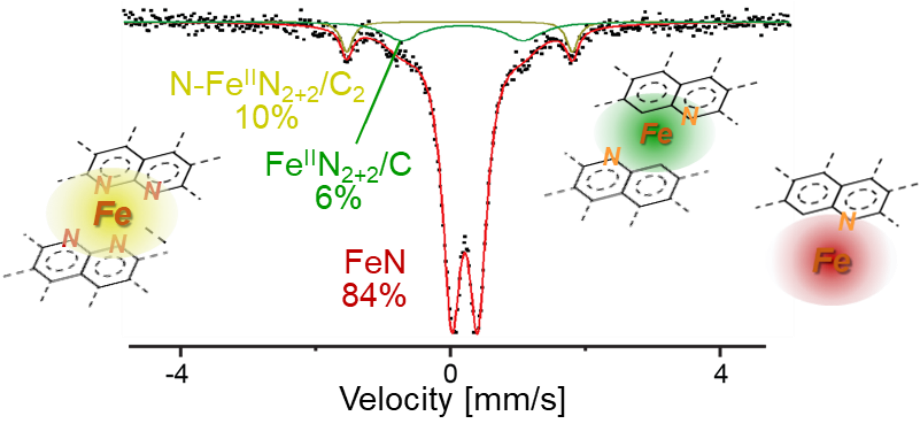

Figure 5.4. ^{57}Fe Mössbauer spectrum (black points) of the salt-templated Fe,N-carbon. The spectrum is deconvoluted into three sets of doublets. each corresponding to a different Fe environment. The three Fe environments and their relative abundance are assigned as follows: i) Fe,N moieties (red; 84%)[66,67]; ii) $Fe^{II}N_2C_2$ moieties (yellow, 10%), and; iii) N-$Fe^{II}N_{2+2}$/C moieties (green, 6%).[18,64,65,68–70] The ^{57}Fe Mössbauer spectrum was acquired at 298 K.

N interactions with Fe species

The use of a mesopore-inducing salt-template and the presence of Fe-heteroatoms result in proximate Fe and N environments that likely contribute to the increase in reduction performance, selectivity, and stability of the salt-templated Fe,N-carbon. While the Mössbauer and EXAFS data corroborate assignments based on Fe bond vibrations, directly probing the N environments should further support and these data while providing details about the N bonding environments. Information on the local environments of ^{15}N heteroatoms, and their proximity to Fe, in salt-templated N- and Fe,N-carbons is accessed directly by solid-state ^{15}N NMR spectroscopy. We have previously deconvolved the relative populations of the different N moieties present in the salt- and silica-templated mesoporous N-carbons and established the importance of pyridinic moieties on reduction performance of N-carbon materials, assigning ^{15}N shifts centered at 300 ppm, 225 ppm, 160 ppm, and 140 ppm to paired or defect pyridinic, isolated edge pyridinic, graphitic, and pyrrolic environments, respectively.[1] Here the goal is understanding interactions of the N moieties with the Fe environments. However, solid-state NMR analyses of Fe-containing carbons are exceptionally rare due to the complicating influences of paramagnetic Fe species on proximate (1-2 bonds) ^{13}C or ^{15}N species, which introduce unpaired electrons into the material that couple with nearby nuclear spins. Such electron-nuclear couplings may substantially broaden and/or displace the ^{15}N NMR signals associated with ^{15}N-environments near unpaired electrons.[71–73] Some articles suggest that the Fe,N active site are Fe-hemes, Fe-porphyrin, or ferricyanides which are reasonable conclusions drawn from the characterization techniques used up until this point.[74,75] However, the ^{15}N chemical shifts of such species have been widely studied in

the context of biology, to be between 700 and 1100 ppm.[76–78] The N-carbons exhibit no such signals representative of these species (**Figure S5.10**).

Nevertheless, the mesoporous salt-templated Fe,N-carbon contains many N-environments that are near paramagnetic Fe species, in addition to those found in the non-Fe-containing equivalent, which are expected to contribute to the increased reduction activity of the material. Relaxation-resolved NMR measurements exploit the very rapid spin-lattice (T_1) relaxation of nuclear spins experiencing paramagnetic interactions, which are often orders-of-magnitude shorter than the diamagnetic analogue,[71,79–81] thus can be used to gain insights on the N-species closest to the paramagnetic Fe. Specifically, relaxation-resolved 1D ^{15}N NMR spectra of the salt-templated Fe,N- and N-carbons (**Figure 5.5b,c**) reveal the broad and overlapping ^{15}N signals that increase in intensity at different rates as the relaxation times increase to elucidate the types of N-moieties proximate to Fe atoms.

The ^{15}N NMR spectra were analyzed in conjunction with DFT modeling to assign the correlated signals to distinct N-carbon moieties and structures (**Figure S5.8**), determining the local bonding environments of the ^{15}N species. DFT calculations yield the electronic shieldings of nuclei in distinct atomic environments, which are manifested as differences in isotropic ^{15}N chemical shifts ($\delta_{cs,iso}$). Such shielding calculations were conducted using a linear-response method, where a one-electron wavefunction is developed on a basis set of plane waves and electron-nuclei interactions are treated with the PAW approach.[49,50] Nuclear shieldings were calculated and converted to ^{15}N chemical shifts for terrace, armchair, and zigzag configurations of between 1 and 4 N atoms coordinated with Fe atoms within or at the edges of graphitic sheets. DFT-calculated ^{15}N chemical shifts for the distinct N-carbon moieties are shown as colored bars in **Figure 5.5a** above the experimental relaxation-resolved

1D ^{15}N NMR spectra of the salt-templated Fe,N-carbons **Figure 5.5c**. Schematics of the basic DFT models for terrace (graphitic, blue), armchair (staggered pyridinic, red), and zigzag (stacked pyridinic, yellow) showing the carbons of the graphitic sheet (grey), the directly affected N or C atoms (blue), and Fe atoms (orange) also in **Figure 5.5a**, while a more extensive view of the modeled schematics can be found in **Figure S5.8**.

While the N-carbon spectra at longer relaxation times appear fairly similar, there are important differences between the spectra at shorter times. The relaxation-resolved 1D ^{15}N NMR spectrum acquired with a very short relaxation delay (0.01 s) selectively enhances and resolves a narrow (20 ppm FWHM) ^{15}N signal at 300 ppm (red) only present in the Fe-containing carbons, indicating that fast-relaxing paramagnetic Fe species are near the paired or defect pyridinic N nuclei, enhancing their relaxation rates. Shift position and analyses of this ^{15}N T_1 relaxation rate data indicate that Fe and paired or defect pyridinic N are within 1 to 2 bond distances or 2 to 4 Å of each other (**Figure S5.9 and associated extended discussion**). DFT chemical shift predictions corroborate this finding, suggesting that a ^{15}N signal around 300 ppm is due to Fe interacting with up to four paired pyridinic N atoms at the edge of a graphitic sheet in an armchair configuration, similar to the $Fe^{II}N_{2+2}C_2$ (green) and N-$Fe^{II}N_{2+2}$/C (yellow) environments suggested by the Mössbauer spectroscopy. Additionally, the relaxation-resolved 1D ^{15}N NMR spectra of both the Fe,N- and N-carbon species exhibit signal at short times, first evident around 100 ms. Shift position and analyses of this ^{15}N T_1 relaxation rate data indicate that both the pair or defect pyridinic signals centered at 275 and 300 ppm aas well as isolated pyridinic N signals centered at 225 ppm were found to have both fast (indicating proximity to fast-relaxing unpaired or conduction band electrons) and slow (diamagnetic relaxation not influenced unpaired/conduction band electrons) relaxing

components, indicating that a fraction of the pyridinic N species are interacting with likely conduction band electrons (**Figure S5.9 and associated extended discussion**). DFT chemical shift predictions again corroborate this finding, suggesting that the isolated edge pyridinic ^{15}N signal around 225 ppm is interacting Fe atoms at the edge of a graphitic sheet in an armchair configuration, similar to the Fe,N environments suggested by the Mössbauer spectroscopy.

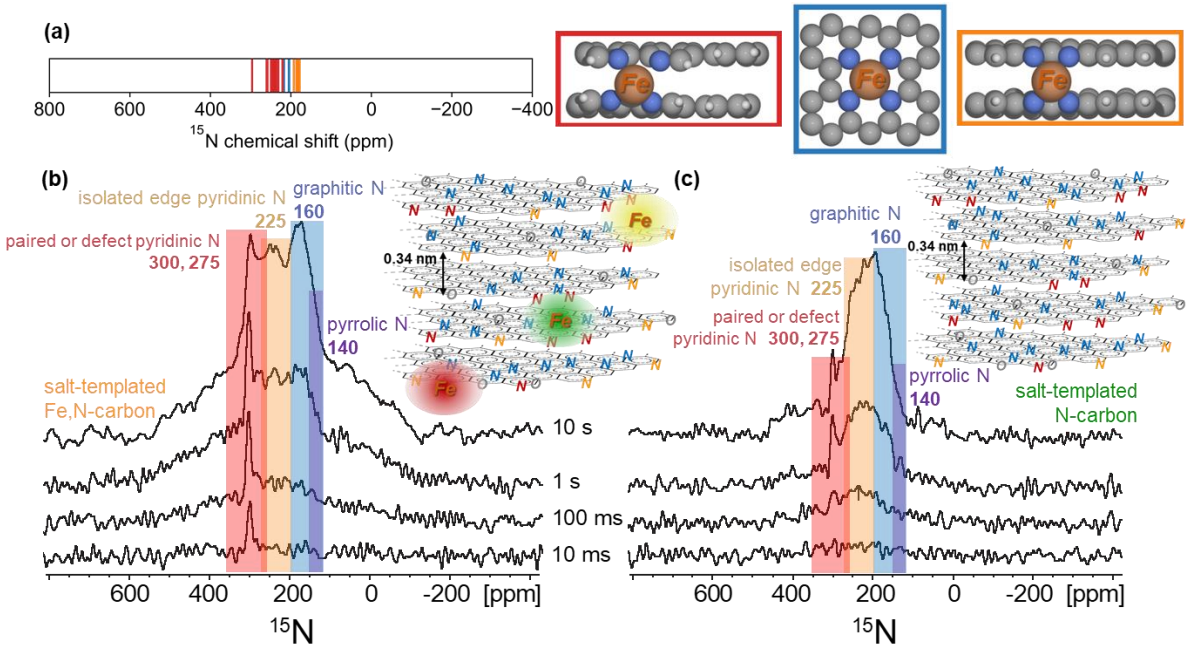

Figure 5.5. (a) Calculated ^{15}N shieldings from DFT for nuclei in Fe,N-carbon moieties and their local environment, as pictured in the schematic and described in the text. Relaxation-resolved 1D ^{15}N NMR spectra of the salt-templated (b) Fe,N- and (c) N-carbons. The T_1 filtered spectra are shown for relaxation times increasing from 10 ms to 10 s. Signals are assigned to various N moieties including pyrrolic (purple), graphitic (blue), isolated edge pyridinic (yellow), and paired/defect pyridinic (red) N-C moieties.[47] The presence of paired/defect pyridinic signal intensity at times as low as 10 ms in the Fe-containing species,

and not until 100 ms in the non-Fe containing N-carbons, indicates the presence of paramagnetically influenced nuclear relaxation in the Fe,N-carbon. All experiments were conducted at low temperatures (95 K) on a 400 MHz spectrometer at 8 kHz MAS. Representative schematics of the various Fe- and N-moieties is shown at the top right of each of the spectra, where the colors of the Fe species coordinate with the Mössbauer being sheets FeN (red), N-$Fe^{II}N_{2+2}$/C (yellow), and $Fe^{II}N_2C_2$ (green).

The presence of fast relaxing pyridinic N and to a lesser extent or further distance C species is corroborated by relaxation resolved ^{13}C NMR (Figure S5.10), and agrees with both the EXAFS distance and coordination numbers and Mössbauer Fe environment assignments. Schematics of the proposed Fe,N- and N- atomic-level structural environments are shown at the top right of the respective spectra (Figure 5.5b,c) with the N species colored according to their NMR assignments and the Fe species by their Mössbauer assignments. Novel insights from relaxation resolved ^{15}N NMR and DFT modeling suggest that the majority of Fe atoms seem to be incorporated on the edges between graphic sheets, proximate to primarily paired or defect pyridinic N species.

Finally, a broad feature spanning -100 to 500 ppm only becomes visible and increases uniformly in intensity at longer delay times, indicating that the signal comes from a distribution of similar types of species. Because the signal only appears at longer delay times, and because the Fe,N-carbons achieve higher extents of graphitization than the N-carbon materials, this signal is likely due to graphic N in conductive regions which significantly broadens NMR signals. Thus, the N environments responsible for these signals are expected

to be deep within the graphitic sheets, while the important reactions happen on the material surfaces, supporting the above hypotheses. These novel insights from relaxation resolved ^{15}N NMR analyses and DFT calculations, along with Mössbauer spectroscopy, EXAFS, and STEM indicate that the majority Fe atoms coordinate with pyridinic N species between the edges of graphic sheets, indicating a correlation between these species and increased electrochemical performance.

5.5 Conclusions

The importance of the presence of Fe and the use of a mesopore salt-template to electrochemical oxygen and sulfur reduction performance data were demonstrated on a macroscopic scale, however, an understanding of the atomic scale environments was required to understand the electrochemical active sites. The dispersion of Fe particles throughout N-carbons, and proximity of Fe to N and O heteroatoms was demonstrated on the nanoscale with composite EELS STEM images, and bonding between Fe atoms with N, C, O, and Fe was confirmed with fluorescence detected EXAFS. Fe was found to coordinate with one, two and four different N atoms on the edges of the graphitic carbon planes, as probed from the perspective of the Fe particles using ^{57}Fe Mössbauer spectroscopy. Finally, novel insights coordinating Fe with pyrazinic and pyridinic N environments on the edges of graphitic sheets were directly probed from the prospective of N atoms by relaxation resolved solid-state ^{15}N NMR spectroscopy and corroborated by DFT modeling, taking advantage of the paramagnetic relaxation of Fe. The high SR and OR performance of the mesoporous salt-templated Fe,N-carbons is therefore explained by the diversity of Fe and N heteroatom sites, and specifically Fe with pyrazinic and pyridinic N environments. Both Fe and pyrazinic/pyridinic N are act as an SR active site and a way to trap soluble intermediates thereby mitigating sulfur losses, and as an OR active site that catalyzes S-reduction more than the N-site alone. These insights into the types of nitrogen sites in reduction catalysts are expected to aid in the further development of non-precious-metal-containing catalysts, by providing new criteria for the rational design of new heteroatom-containing carbon materials.

5.6 Future Directions

There are a lot of directions that this project has the potential to take from understanding more about the synthesis, to optimization of performance, and furthering NMR techniques and understanding. From the perspective of the material synthesis, a lot of the same things I suggested for the future directions in Chapter 3 apply here. These include a very methodical optimization of the eutectic melt conditions, the salt-templating ratios, the temperature and atmosphere conditions, for every specific performance system. However, insights from in situ NMR of the eutectic melt and pyrolysis, as well as zinc NMR of the pyrolyzed but unwashed carbon materials, will be the most interesting directions that take advantage of the Chmelka group expertise. Additionally, the inclusion of sulfur-heteroatoms in carbon materials has been suggested from preliminary experiments from our collaborators to also contribute to increased S-reduction potential. This would be a major project, but finding either a small sulfur- and nitrogen-containing compound (or much more likely a sulfur-containing compound to include in the cyclohexanehexone-urea synthesis), optimizing the material for S-reduction, and characterizing it across all length scales to achieve an understanding of the types of N-, S- or NS-moieties and catalytic active sites that form would truly be insightful to the emerging field of S-reduction catalysis for LiS batteries.

From the perspective of material performance and optimization, there are a few important directions to consider. One of these directions is optimization of the material for the specific application. For example, the 0.1 mol% M Fe salt-templated N-carbon was found to be the ideal material for catalyzing oxygen reduction in alkaline conditions, whereas the 0.03 mol% Fe salt-templated N-carbon was found to be optimal for sulfur reduction. However, factors including the salt ratio, Fe content, and post synthetic washing or modifications all have strong

effects on the final material performance properties and need to be optimized for each case considered. This however, again will be a very long and tedious optimization process to be done thoroughly. Then, what will be interesting to and make use of the Chmelka lab expertise, will be to see how the synthesis of these different materials affects the final material N-moiety distributions (Chapter 2-5) and paramagnetic or Knight shifted interactions that arise from differing amounts of overall heteroatom contents (Chapter 6).

This leads to the final direction that I wanted to highlight here which is the development of standard NMR or other spectroscopic techniques and practices that make the atomic-level characterization and understandings of such complicated conductive systems more generalizable, understandable, and accessible to more researchers in this and related fields. Our unique ability to understand the materials from their conception (as we do the synthesis of them) gives us a real advantage that, combined with strong NMR and physics knowledge, allows for development of such techniques. As a starting point, I suggest having collaborators synthesize their well characterized N-carbon-like materials with nuclear enrichment and measuring their materials in ways similar to those outlined in Chapters 3-5. My hypothesis is that these materials will have similar NMR spectra that can be similarly interpreted and compared with the data and the previous chapters, providing insight into the generalizability of the current techniques. From there I think it is very important to consider all of the influences that the electrons in the material have on the characterization and performance of the material. Many of these important considerations have been laid out in Chapter 6. I hypothesize that a combination of various NMR and EPR techniques will allow for the best understanding of nuclear-nuclear, electron-nuclear, and electron-electron interactions within the materials, with the end goal of a deep atomic-level understanding of the material active

sites. One technique that would be really interesting is a combination of NMR and EPR, which is HYSCORE, which should provide understanding of the interactions between the various nuclear environments we have already assigned, and lone electrons. My experiences with the NMR magnet have also lead my to believe that the Fe-containing carbons may also have some extent of magnetic properties which I suggest to probe by SQUID magnetometry, a technique available to us at UCSB through the MRL. Thus, I believe that there are a lot of directions that this project could evolve from here, but seeking to understand the interactions between the various nuclear environments we have already assigned and nearby electrons would be an important path of the expertise of the Chmelka group.

5.7 Supporting Information

5.7.1 Supporting Information – Tables

Table S5.1. BET surface areas of the mesoporous N-carbon materials

Material	*Surface area*	*Pore diameters*
	m^2/g	*nm*
SBA-15 silica templated	1100	1-2, 3-4
$ZnCl_2$-NaCl templated	1800	1-1.5, 2.5-4
$ZnCl_2$-NaCl templated, 0.03 mol% Fe		
$ZnCl_2$-NaCl templated, 0.1 mol% Fe		

Near-surface versus bulk nitrogen compositions of high-N-content carbons

Identifying and quantifying the different types and distributions of nitrogen moieties present in the Fe,N- and N-carbon materials is crucial to understanding the relationship between electrical conductivity and heteroatom content (N atoms) of the electrocatalyst materials, as well as how synthesis conditions affect these characteristics. The overall near-surface and bulk nitrogen contents of the mesoporous Fe,N- and N-carbon materials templated by $ZnCl_2$-NaCl and SBA-15 silica are high, compared to conventionally prepared N-carbon materials. XPS analyses yield near-surface nitrogen compositions of 16 and 22 mol% (Tables S5.2 and S5.3) for the salt- and silica-templated N-carbons, respectively, compared to bulk nitrogen compositions of 28 and 19 mol% (Table S5.4), as determined from XRF analyses.

Trace amounts (<0.4 mol%) of the templating materials (Zn, Na Si, Cl) and Fe impurities (0.1 mol% or less) were detected within the product mesoporous N-carbon materials. The trace Zn contents are the same within experimental uncertainty between the two materials and in similar types of local environments (as evidenced by EXAFS) and therefore are unlikely to account for the differences in reduction performance. The differences in the even lower trace

Fe contents between the materials also do not correlate with increased reduction performance. The elemental compositions show that the mesoporous N-containing carbon materials can be prepared with little to no retention of the templating materials after their removal.

Local atomic N environments are challenging to resolve and quantify by conventional techniques, such as XPS. Whereas XPS probes near-surface (<10 nm) species, solid-state NMR measures all NMR-active nuclei in the bulk sample. For example, among the nitrogenous moieties that are present in the salt- and silica-templated N-carbon materials, the relative populations of near-surface graphitic N (16 and 22 mol%, respectively) estimated by XPS are lower than those measured (42 and 41%) by deconvolution of the quantitative direct-excitation ^{15}N MAS NMR spectra in **Figure 5.2c,d** of the manuscript. In combination, these results indicate the predominantly non-surface locations of graphitic N moieties.

Table S5.2. Near-surface elemental compositions of high-N-content carbons obtained by X-ray photoelectron spectroscopy (XPS)[a]

	XPS near-surface elemental composition [mol%]							
	C	N	O	Zn	Fe	Na	Si	Cl
SBA-15 silica templated	69	22	8	0.21	0.02	-	-	-
$ZnCl_2$-NaCl templated, no Fe	72	16	11	0.22	0.00	-	-	-
$ZnCl_2$-NaCl templated, 0.01 mol% Fe	69	16	12	0.14	0.06	-	-	-
$ZnCl_2$-NaCl templated, 0.1 mol% Fe	76	12	12	0.13	0.13	-	-	-

[a] Near-surface compositions were estimated by integrating the peaks of survey X-ray photoelectron spectra. Mean values are shown for multiple measurements and materials syntheses, which were reproducible to within ca. ±1 mol% for C and N and within ca. 0.05 mol% for Zn and Fe.

Table S5.3. Bulk elemental compositions of high-N-content carbons determined by X-ray fluorescence (XRF)

	XRF bulk elemental composition [mol%]							
	C	N	O	Zn	Fe	Na	Si	Cl
SBA-15 silica templated	63	28	9	0.09	0.01	0.4	0.23	0.11
$ZnCl_2$-NaCl templated, no Fe	62	19	19	0.07	0.01	0.3	0.06	0.06
$ZnCl_2$-NaCl templated, 0.03 mol% Fe	65	19	15	0.05	0.03	0.1	0.05	0.10
$ZnCl_2$-NaCl templated, 0.1 mol% Fe	67	17	15	0.05	0.10	0.2	0.09	0.05

[a] Near-surface compositions were estimated by integrating the peaks of survey X-ray photoelectron spectra.

Table S5.4. Mössbauer spectroscopy values of the integrated intensities, isomeric chemical shift (δ), quadrupole splitting values (|ΔEQ|), and references corresponding to the assigned environments.

Species	*Integrated intensity*	*δ*	*$\|\Delta E_Q\|$*	*References*
	%	mm/s	mm/s	
Fe_xN	84	0.25	0.39	[18,64,65]
FeN				[66,67]
$N\text{-}Fe^{II}N_{2\text{-}2}/C$	6	0.22	1.80	[18,64,68]
$Fe^{II}N_2C_2$	10	0.17	3.36	[82,83]

Table S5.5. Near-surface elemental compositions of high-N-content carbon materials estimated by integrating the peaks of survey X-ray photoelectron spectra.

Material	*Near-Surface elemental composition [atom%]*			
	pyridinic/pyrazinic N	graphitic N	pyrrolic N	nitroxide
No template	46	18	27	10
SBA-15 silica templated	45	16	32	7
$ZnCl_2$-NaCl templated, no Fe	34	23	33	10
$ZnCl_2$-NaCl templated, 0.1 mol% Fe	22	35	36	7

5.7.2 Supporting Information – Figures

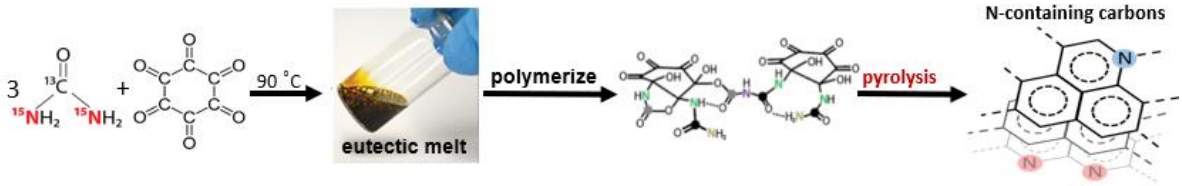

Figure S5.1. Synthesis of Fe,N- or N-containing mesoporous carbon electrocatalyst materials. The reactant mixture (cyclohexanehexone and urea) is combined at room temperature and heated to 363 K under air to form a eutectic melt. The reactant $FeCl_2$ can also be added at this stage to produce the Fe-containing sample. The mesoporous templating agent (SBA-15 mesoporous silica or $ZnCl_2$-NaCl salt mixture) is then combined with the eutectic melt and subsequently pyrolyzed in a nitrogen atmosphere at 1073 K to form the mesoporous Fe,N- and N-containing carbon materials. The photo of the eutectic melt is from Fechler, *et al.*[56]

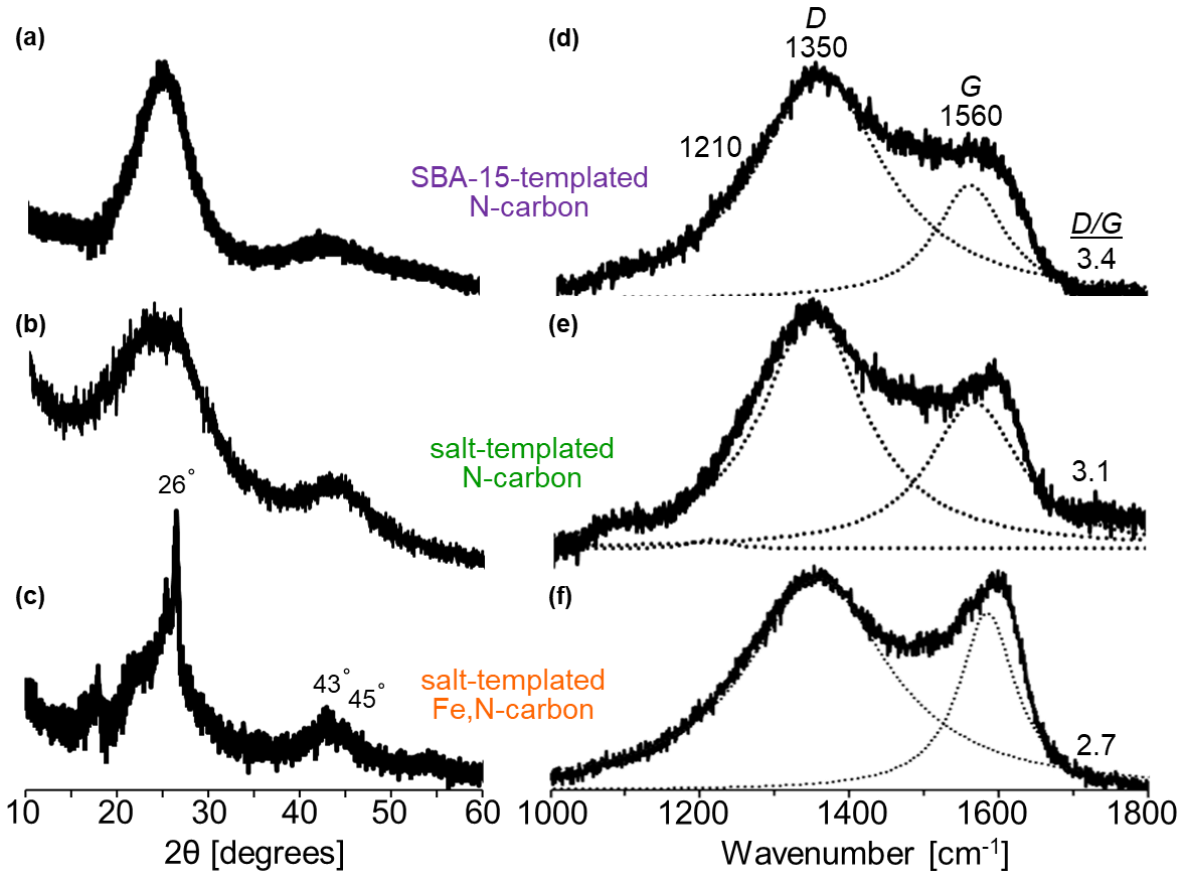

Figure S5.2. Extents of graphitization of mesoporous N- and Fe,N-carbons. Wide-angle XRD patterns of cyclohexanehexone-urea-derived carbons pyrolyzed at 1073 K using SBA-15 mesoporous silica (a) or a NaCl-$ZnCl_2$ mixture to template mesoporosity of (b) N-, and (c) 0.1 mol% Fe,N-carbons. The WAXS patterns exhibit a broad reflection at 26° 2θ (0.34 nm *d*-spacing) that is indexable to the (*002*) stacking of aromatic moieties of graphitic carbon materials. A second weaker reflection at 43° 2θ (0.21 nm *d*-spacing) corresponds to the superposition of the (*100*) and (*101*) graphitic planes. [84] Raman spectra of silica-templated (d) or salt-templated (e) N-, and (f) Fe,N-carbons. Broad regions of intensity at 1000-1700 cm^{-1} can be deconvoluted into Lorentzian-shaped bands centered at 1570 cm^{-1} (*G*) and 1350 cm^{-1} (*D*) which are attributed respectively to the bond vibrations in locally distorted graphitic lattices associated with heteroatom or edge/surface environments[85,86] and stretching vibrations

in polyene-type structures.[87] The integrated intensity ratios (*D/G*) of the dominant Raman bands are an approximate measure of the relative extents of graphitic ordering within the materials, where lower values suggest a higher extent of graphitic ordering, desirable for bulk conductivity.[85,87] The *D/G* ratios are decreasing, indicating increasing extent of graphitization, with increasing oxygen-reduction performance.

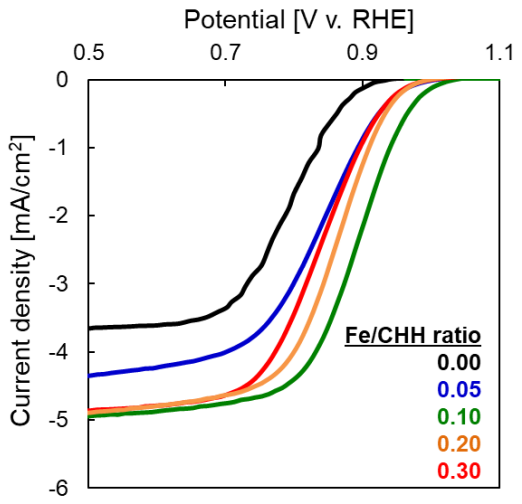

Figure S5.3. Current-potential polarization curves showing the optimization of Fe-heteroatom content. Polarization curves for the electrocatalytic reduction of oxygen (O_2) by cyclohexanehexone-urea-derived carbons pyrolyzed at 1073 K using a NaCl-$ZnCl_2$ mixture to template mesoporosity and various molar ratios of $FeCl_2$ tetrahydrate to cyclohexanehexone-octahydrate to determine the optimized Fe content. Curves were collected by staircase voltammetry with the materials deposited on a rotating disk electrode measured in a 0.1 M KOH solution saturated with O_2 gas, and currents normalized by the geometric electrode area, rotating at 900 RPM. The optimal performance of the ratio 0.1 M Fe/CHH was chosen for all future experiments.

Polarization curves collected in O_2-saturated 0.1 M KOH for materials prepared by pyrolysis of cyclohexanehexone, urea, and $FeCl_2$ salt, where the Fe-to-cyclohexanehexone molar ratio (Fe/CHH ratio) is varied between 0.00 and 0.30.

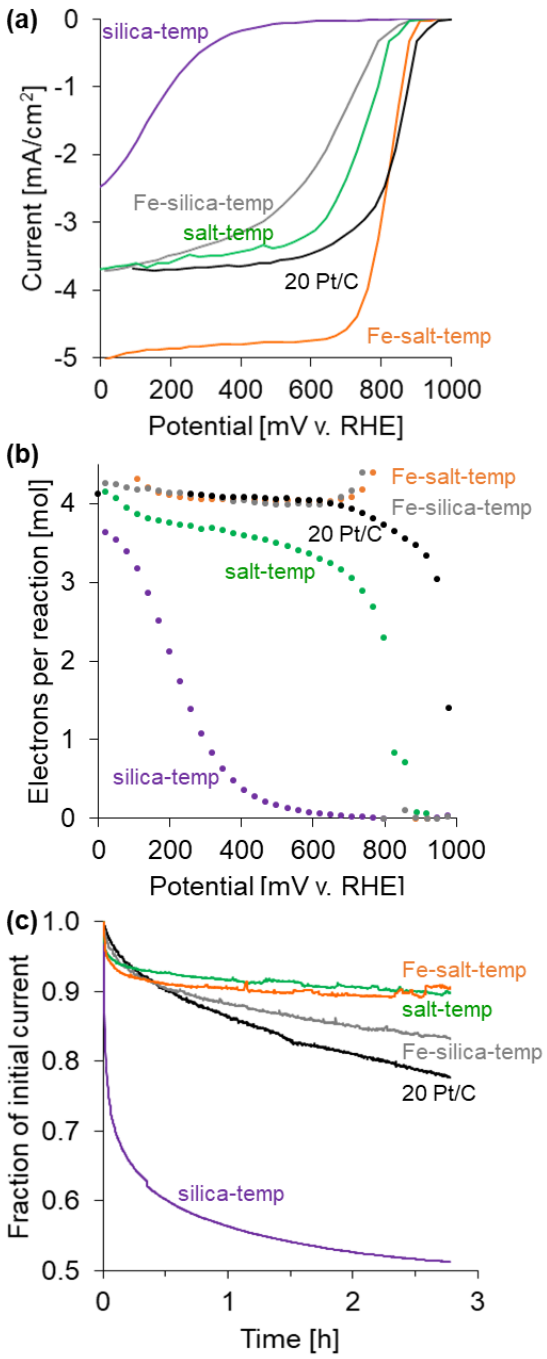

Figure S5.4. Oxygen reduction reaction activity, electron consumption, and stability of mesoporous Fe,N- and N-carbons showing superior electrocatalytic performance of salt-templated Fe,N-carbons. The difference between this figure and **Figure 5.1** is that this also includes data for the silica-templated Fe,N-carbons in grey. **(a)** Polarization curves for the

electrocatalytic reduction of oxygen by silica-templated N- and Fe,N-carbons (purple, grey), salt-templated N- and 0.1 mol% Fe,N-carbons (green, orange) compared with a 20 wt% Pt-carbon-standard (black) catalysts. **(b)** Theoretical number of moles of electron consumed during oxygen reduction as a function of potential, calculated according to the Koutecký-Levich equations. **(c)** Stability testing of the best performing salt-templated Fe,N-carbon showing the fraction of the initially detected current as a function of time when a constant potential of 400 mV was applied. All experiments were conducted with a rotating disk electrode at room temperature in a 0.1 M KOH electrolyte solution. **(a)** and **(c)** were conducted at 900 RPM.

Here, the performance and stability data are evaluated for a half-cell cell by rotating ring disk electrode (RRDE) collected under alkaline conditions (0.1 M KOH) with oxygen saturation of the electrolyte. Material performance, selectivity, and stability curves indicate the importance of both salt-templating and the presence of Fe-heteroatoms in the N-carbons are important to the best performing material and active sites.

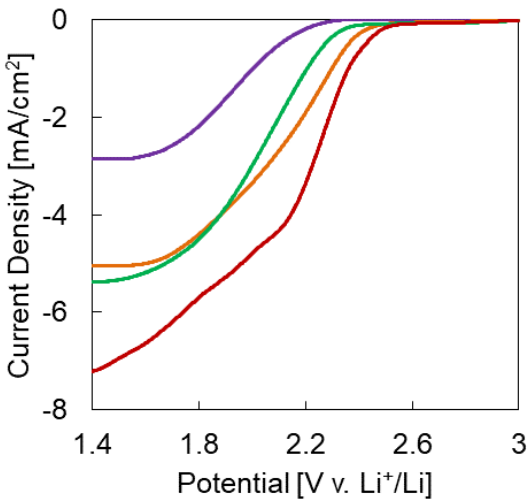

Figure S5.5. Sulfur reduction reaction activity of silica and salt-templated Fe,N- and N-carbons. Polarization curves for the electrocatalytic reduction of sulfur by silica- and salt-templated N-carbons (purple, green). The SR activity of the 0.1 mol% Fe salt-templated Fe,N-carbon discussed throughout this paper is shown in orange. The activity of the SR optimized 0.03 mol% Fe salt-templated Fe,N-carbons is shown in maroon. Experiments were conducted with a rotating disk electrode at room temperature in a 0.1 M KOH electrolyte solution at 900 RPM.

Extended discussion of Figure S5.5

The significance of non-precious-metal electrocatalysts stems beyond that of oxygen reduction to many other areas including the catalytic reduction of sulfur in LiS batteries, overcoming the conductivity challenges of inherently insulating S_8 and decreasing the rate limiting activation energies of traditional and non-doped graphenes.[1,9] Here, similar relative behaviors are observed for the mesoporous salt- and silica-templated N-carbons as sulfur reduction catalysts to that of the reduction of oxygen. **Figure S5.5** shows sulfur reduction curves measured via rotating disk electrode for the salt- (green) and silica-templated (purple)

N-carbons, where higher onset potentials and current densities are desirable. As with the OR performance, the SR performance of the salt-templated N-carbons is significantly higher than that of the silica-templated N-carbons. The SR activity of salt-templated Fe,N-carbons optimized for OR is shown in orange, which does not exhibit a significant difference from the SR performance of the salt-templated N-carbon. However, it was found that the optimal Fe-content for OR is different than for SR (0.1 mol% Fe compared to 0.03 mol% Fe). The SR-optimized salt-templated 0.03 mol% Fe,N-carbon activity curve is shown in red, with both a higher onset potential and current density than all other materials. Thus again, both synthesis with a salt-template and presence of Fe-heteroatoms are crucial to optimized SR performance. The roles of Fe and pyrazinic/pyridinic N are hypothesized to act as an SR active site and a way to trap soluble intermediates thereby mitigating sulfur losses. However, because the optimized Fe-content is different for SR than for OR activity, an investigation of the material composition, performances, and active sites will be the subject of a future manuscript. The significance of showing the SRR performance here is to show that that use of a salt-template and the presence of Fe-heteroatoms are applicable and crucial to optimized SR and OR performance.

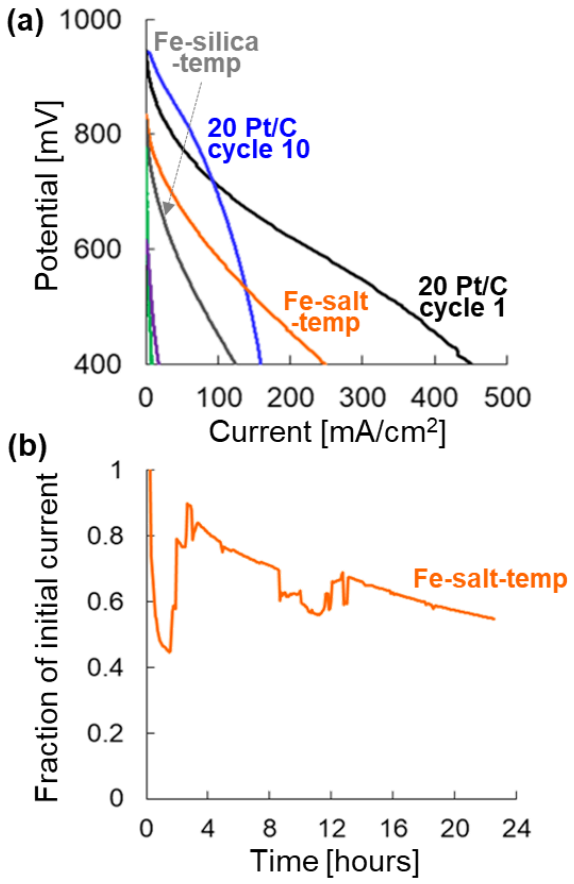

Figure S5.6. Fe,N-carbon performance and stability in an polymer electrolyte membrane fuel cell. (a) Polarization curves for the electrocatalytic reduction of oxygen by salt-templated (orange) and SBA-15-templated (grey) Fe,N-carbons compared with a standard Pt/C catalyst on cycle one (black) and cycle 10 (blue). **(b)** Stability testing of the best performing salt-templated Fe,N-carbon showing the fraction of the initially detected current as a function of time. The cell was operated at 80˚C with the anode fueled by H_2 gas and cathode by air at 100% relative humidity, both fuels were heated to 80˚C prior to entering the cell.

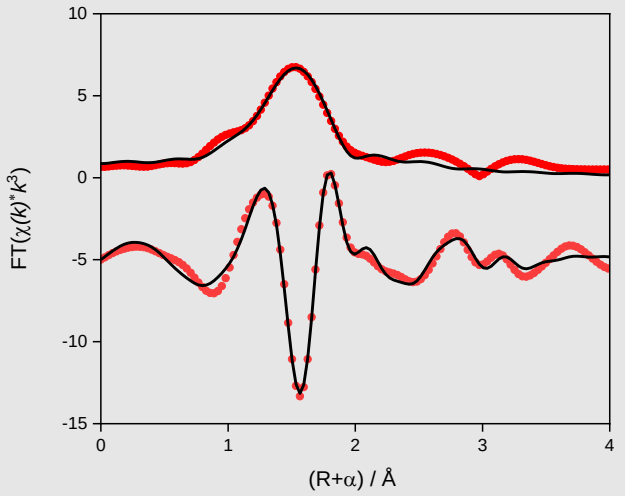

Figure S5.7. Fe K-edge EXAFS (points) and curvefit (solid line) for the salt-templated Fe,N-carbon shown in R-space (FT magnitude and imaginary components). The data are k3-weighted and not phase-corrected.

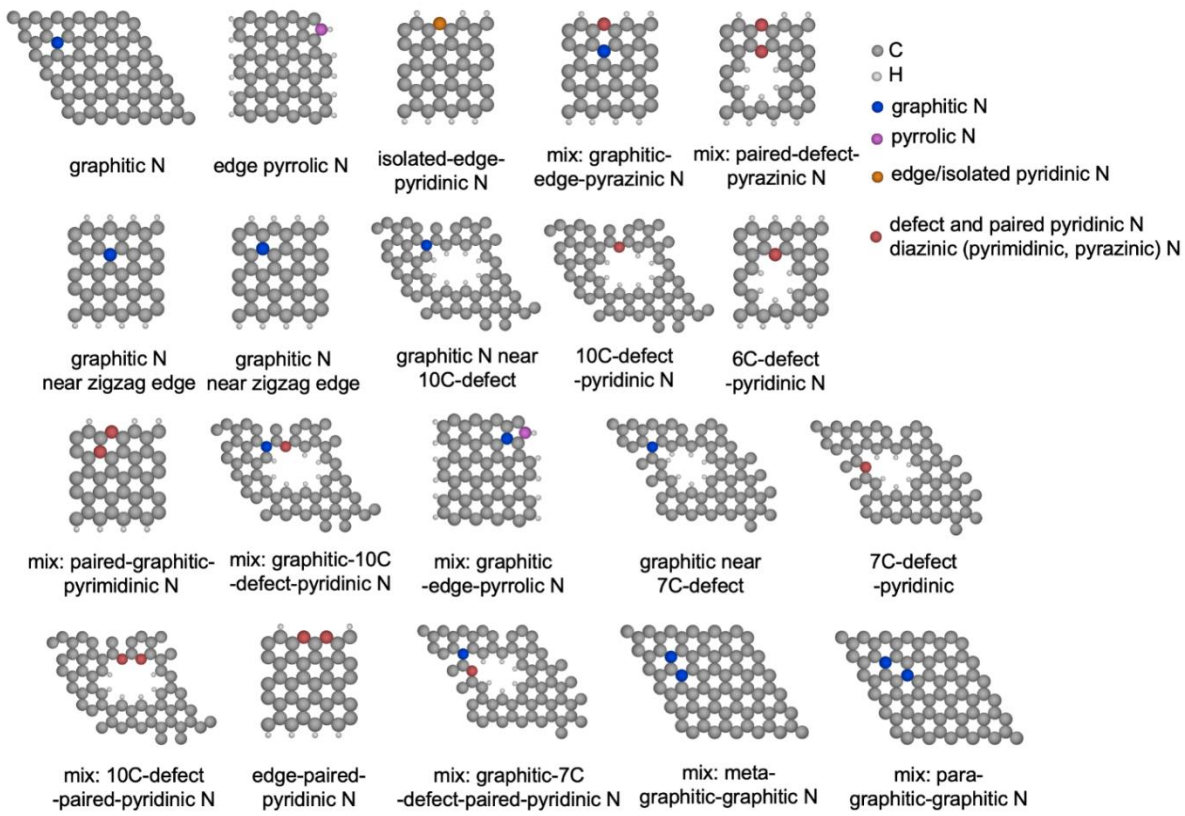

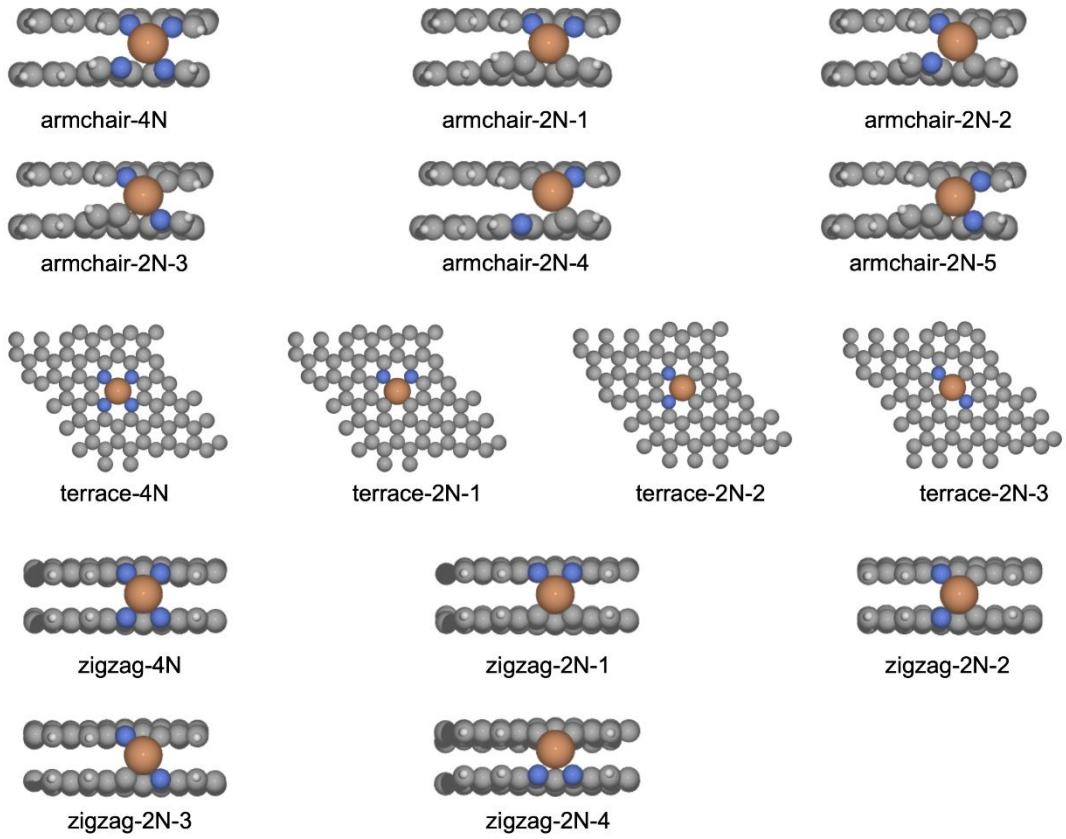

Figure S5.8. Schematic diagrams of N- and Fe,N-carbon structural motifs used to calculate ^{15}N and ^{13}C isotropic chemical shielding values by DFT. Carbon atoms are shown in grey, hydrogen atoms are white, and the different types of N-carbon moieties are shown in different colors: graphitic N as blue, pyrrolic N as purple, isolated pyridinic edge N as yellow, and defect and paired pyridinic N (this includes diazinic species: pyrimidinic, pyrazinic N) as red.

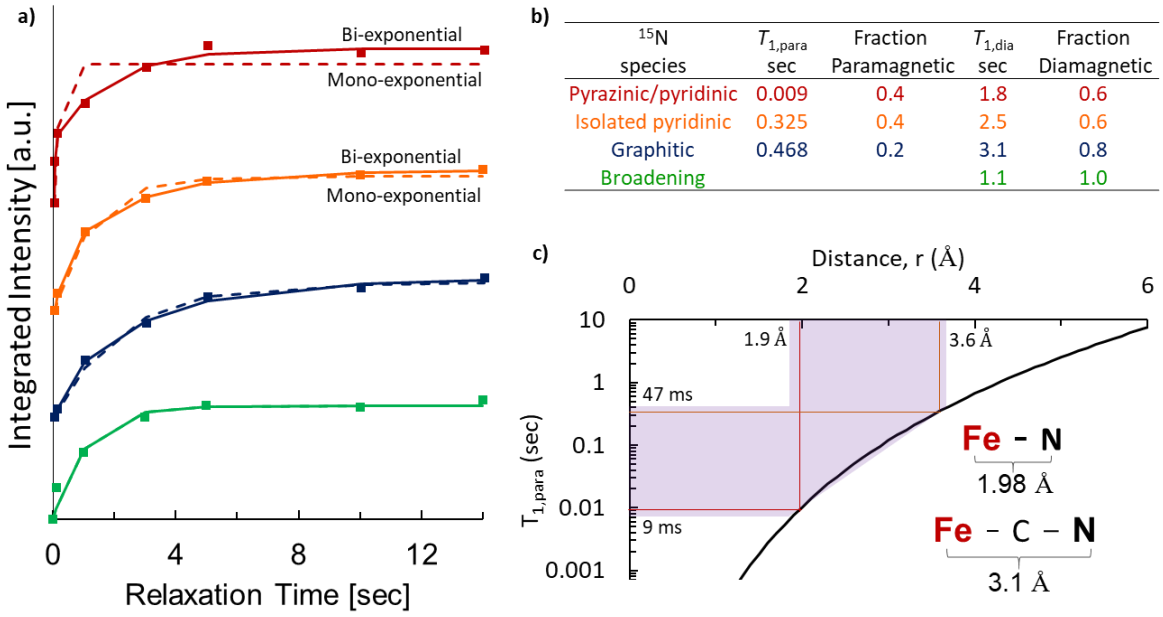

^{15}N species	$T_{1,para}$ sec	Fraction Paramagnetic	$T_{1,dia}$ sec	Fraction Diamagnetic
Pyrazinic/pyridinic	0.009	0.4	1.8	0.6
Isolated pyridinic	0.325	0.4	2.5	0.6
Graphitic	0.468	0.2	3.1	0.8
Broadening			1.1	1.0

Figure S5.9. Spin-lattice relaxation time processing to consider paramagnetic effects of Iron. Spin-lattice relaxation times of paired or defect pyrazinic ^{15}N (red), isolated edge pyridinic ^{15}N (yellow), graphitic ^{15}N (blue), and paramagnetic broadening (green). **(a)** Plot of integrated intensity of each ^{15}N species as a function of relaxation delay time with bi-exponential curve fits as solid lines and mono-exponential curves fits as dashed lines. **(b)** Bi-exponential curve fitting parameters of each species showing the diamagnetic and paramagnetic spin-lattice relaxation values and the respective approximate amount of species influenced by the paramagnetic species. **(c)** Solomon equation plotted for electron-^{15}N spin pairs, overlaid with the experimentally determined paramagnetic spin-lattice relaxation values and their corresponding electon-^{15}N atomic distances. **(c inset)** Approximate bond distances of species consistent with these calculations.[18,88]

Figure S5.9 Extended Discussion

The spin-lattice relaxation constant is measured by collecting a series of 1D ^{15}N NMR spectra with varied relaxation times. At small relaxation delay times, only very quickly

relaxing species, for instance the species affected by the paramagnetic effects of Fe, produce NMR signal intensity, providing information about the proximity of Fe to other species. Theoretically, the intensity of the magnetization of each signal will build to maximum values by the Bloch equation:[63]

$$M(\tau) = M_0\left(1 - e^{\left(\frac{-\tau}{T_1}\right)}\right)$$

Here, M is the magnetization in the direction of the magnetic field, M_0 is the magnitude of magnetization vector, τ is the relaxation delay time, and T_1 is the spin-lattice relaxation value.

The mesoporous salt-templated Fe,N-carbon material contains different types of ^{15}N environments that are near and far from paramagnetic Fe species. In **Figure S5.9,** the solid-state Hahn-echo ^{15}N T_1-filtered MAS NMR spectra show increasing signal intensity with increasing relaxation delay times. The spectra show ^{15}N signals with partially-resolved maxima at 300, 225, and 160 ppm, which are assigned respectively to pyridinic/pyrazinic, isolated pyridinic, and graphitic ^{15}N environments on the basis of their shift positions.[1] Interestingly, for the relaxation-resolved 1D ^{15}N NMR spectrum with a very short relaxation delay of only 0.010 s, there is distinct narrow (20 ppm FWHM) ^{15}N signal at 300 ppm, indicating that this material is in close molecular proximity to the Fe heteroatom sites. This signal is assigned based on shift position, analyses of the ^{15}N T_1 relaxation times, DFT calculations, and comparison to theoretical equations. The T_1-filtered ^{13}C MAS NMR spectra of the salt-templated Fe,N-containing carbon materials can also be found in **Figure S5.10**.

T_1 values are affected by many factors, but three major contributors are the diamagnetic interactions, paramagnetic interactions as in the Fe-heteroatom containing material, and metallic (Korringa) interactions. The relationship between each of these contributors and the overall T_1 value are shown by this relationship:

$$\frac{1}{T_1(r,T)} = \frac{1}{T_{1,para}(r)} + \frac{1}{T_{1,dia}} + \frac{1}{T_{1,K}(T)}$$

Here, $T_1(r,T)$ is the overall spin-lattice relaxation value as influenced by internuclear distance (r) and temperature (T), $T_{1,para}(r)$ is the paramagnetic contribution, $T_{1,dia}$ is the diamagnetic contribution, and $T_{1,K}(T)$ is the Korringa contribution. Spin-lattice diffusion interactions (diamagnetic) are present in all NMR sensitive systems and characterize the relaxation of nuclei not affected by additional interactions such as paramagnetic or Korringa. Korringa interactions are characteristic of metallic-like behavior of the material and are sensitive to temperature. Paramagnetic interactions arise from the presence of unpaired electrons in the material coupled with nearby nuclear spins. Such interactions significantly decrease the spin-lattice relaxation time for affected nuclei. However, these electron-nuclear couplings exponentially decay (inversely proportional to r^6) with increasing distance from the paramagnetic source, thus the interactions are very localized. Due to the very fast times associated with paramagnetic interactions, I expect paramagnetic contributions dominate the overall T_1 value for very short times and provide information about the influence of fast relaxing Fe species on nearby nuclei, thus I focus on this interaction.

To characterize the T_1 values associated with each of the ^{15}N environments, each of the time-resolved spectra were deconvoluted. The integrated intensities at each time point are then plotted as a function of relaxation time, where the leveling off of integrated intensity indicates return of the nuclear spin magnetization to equilibrium. Each of these data sets were fit with mono-exponential curves as shown by the dashed lines and color-coordinated according to the same three environments in Figure S5.9a. However, I hypothesize that T_1 values of moieties near Fe will be shorter than T_1 values of moieties not affected by Fe, so more than one T_1 value is required to characterize each moiety. The isolated edge pyridinic ^{15}N species (yellow)

and especially the paired or defect pyridinic ^{15}N signal (red), were fitted with a much more appropriate bi-exponential fit (solid line). The bi-exponential fit allows for T_1 values affected (paramagnetic, short times) and not affected (diamagnetic, long times) by Fe-heteroatoms to be accounted for, and gives a rough estimate of the fractions of the signal associated with each.

The fitting of exponential curves to T_1 filtered data, in **Figure S5.9a**, shows that a bi-exponential fit is a significant improvement to that of the mono-exponential for the ^{15}N paired or defect pyridinic, and moderate improvement for the ^{15}N isolated edge pyridinic species. This suggests that the paired or defect pyridinic ^{15}N species are most affected by the presence of the Fe heteroatoms due to the significantly improved fit of the bi-exponential curve. Bi-exponential fits of the ^{15}N graphitic species and broad 160 ppm signals show negligible improvement and thus, are not likely close to Fe species. The table in **Figure S5.9b**, lists the T_1 values and relative fraction of species in each component as estimated by the constants ($M_{0,para}$, $M_{0,dia}$) associated with the equation for a bi-exponential fit:

$$M(\tau) = M_{0,para}\left(1 - e^{\left(\frac{-\tau}{T_{1,para}}\right)}\right) + M_{0,dia}\left(a - e^{\left(\frac{-\tau}{T_{1,dia}}\right)}\right)$$

Here, $M(\tau)$ is the magnetization in the direction of the magnetic field as a function of allotted relaxation time (τ), $M_{0,para}$ is the magnitude of what I have assumed to be paramagnetic relaxation dominated magnetization vector, $M_{0,dia}$ is the magnitude of the slower relaxing magnetization, $T_{1,para}$ is the fast relaxing spin-lattice relaxation value, and $T_{1,dia}$ is the more slowly relaxing spin-lattice relaxation value.

The atomic distances between an electron-nuclear pairs can be predicted from nuclear spin-lattice relaxation times by the Solomon equation. The equation uses nuclei specific

information to predict T_1 relaxation times as a function of internuclear distance between dipole-dipole coupled nuclei:[63,79]

$$\frac{1}{T_{1,para}(r)} = \frac{3}{10}\left(\frac{\mu_0}{4\pi}\right)^2 \frac{\gamma_e^2 \gamma_n^2 g^2 \hbar^2}{r^6}\left[\frac{\tau}{1+(\omega_n)^2\tau^2}\right]$$

Where r is the distance between the paramagnetic center and a ^{15}N nucleus, μ_0 is the permittivity of free space, γ_e is the gyromagnetic ratio of the electron, γ_n is the gyromagnetic ratio of ^{15}N, g is the electron g-factor, $\hbar$ is plank's constant, τ is the electron spin-lattice relaxation constant, and ω_n is the Lamour frequency of ^{15}N.[63,79] Previous experiments by our group have found the electron spin-lattice relaxation constant (τ) to be about 300 μs at 95 K. The Solomon equation does not account for spin-diffusion, but I expect that it is weak in this material. **Figure S5.9c** plots the ^{15}N paramagnetic spin-lattice relaxation values as a function of electron-^{15}N electronuclear distance predicted by the Solomon equation. Increasing spin-lattice relaxation time is proportional to increasing interatomic distance to the sixth power, thus ^{15}N environments with the shortest relaxation times are closest to paramagnetic centers. This graph is overlaid with the experimentally determined paramagnetic ^{15}N spin-lattice relaxation values (**Figure S5.9b**) and their corresponding electon-^{15}N atomic distances. The experimentally determined paramagnetic spin-lattice relaxations values (purple shaded region) predict ^{15}N-Fe distances of 2 to 4 Å (1 to 2 bond lengths), which are consistent with typical ^{15}N-Fe bond lengths of 2 Å,[18,88] and typical -^{15}N-C-Fe bond lengths of about 3.1 Å.[89] This combination of T_1-filtered measurements and ^{15}N-ernichment allows me to approximate the distances of ^{15}N species from paramagnetic Fe for the first time in Fe,N-containing carbon materials.

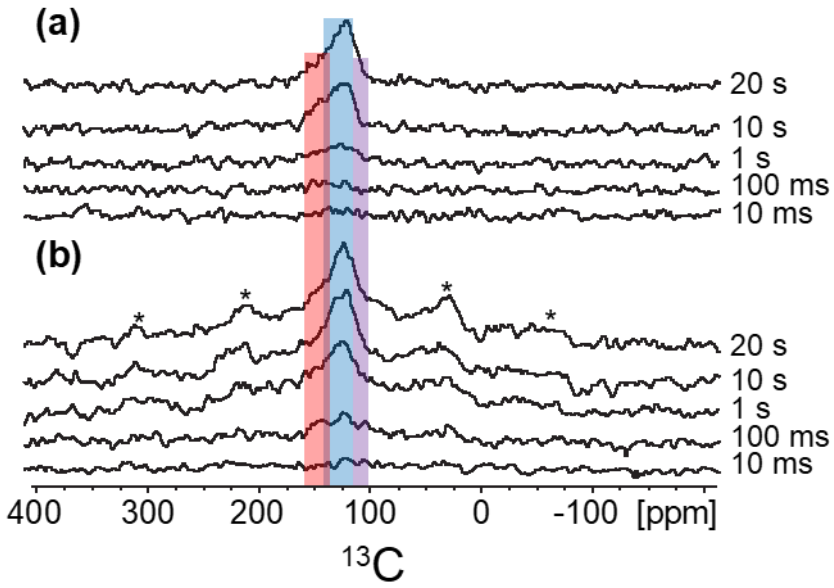

Figure S5.10. Direct probing of ^{13}C environments in the salt-templated N- and Fe,N-carbons. T_1 filtered 1D ^{13}C NMR spectra of the salt-templated **(a)** N- and **(b)** Fe,N-carbons are shown. The T_1 filtered spectra are shown for relaxation times increasing from 10 ms to 20 s. Signals are assigned to various C moieties including pyrrolic (115 ppm, purple), graphitic (130 ppm, blue), and pyrazinic/pyridinic (145 and 150 ppm, red) N-C moieties.[1] The presence of pyrazinic/pyridinic and graphitic signal intensity at times as low as 100 ms in the Fe-containing species, and not until 1 s in the non-Fe containing N-carbons, indicates the presence of paramagnetically influenced nuclear relaxation in the Fe,N-carbon. All experiments were conducted at low temperatures (95 K) on a 400 MHz spectrometer at 8 kHz MAS.

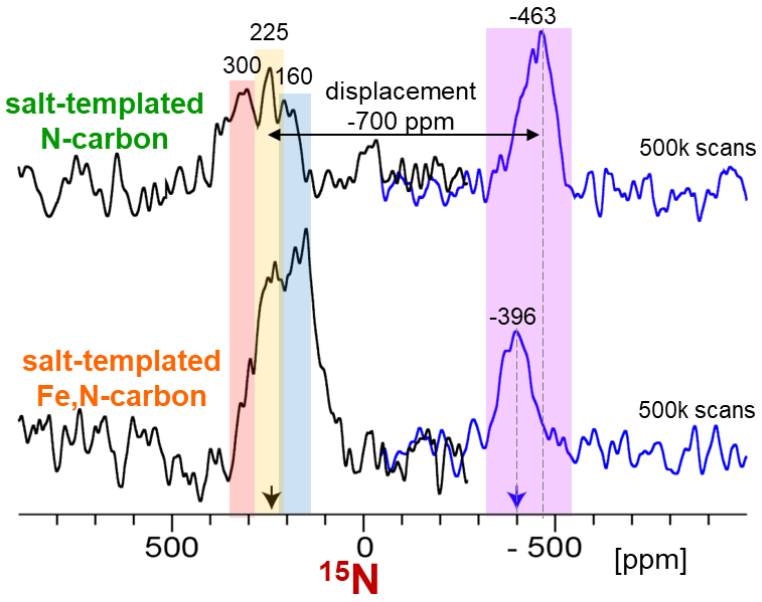

Figure S5.11. Solid-state ^{15}N Hahn-echo MAS NMR spectra of the salt-templated N-(top) and 0.1 mol% Fe,N-carbons acquired at 55 kHz MAS (1.3 mm rotor), 11.7 T at two different spectrometer frequencies centered at 225 ppm (black) and -400 ppm (blue), as indicated by the respective colored arrows. The experiment was conducted at room temperature, but due to resistive heating the sample temperature was measured to be approximately 336 K, based on the T_1 value of ^{79}Br in polycrystalline KBr, which was added to the MAS rotor as a diluent to reduce the effects of electrical conductivity on the NMR experiments and which also served as a convenient internal temperature reference. The signals at 300, 225, and 160 ppm are associated with the pyridinic and graphitic species as discussed in the main text. The presence of these signals in a fast-relaxing experiment suggests that some fraction of each of the species is affected by the presence of unpaired/conduction band electrons. The increased intensity of the same signals in the Fe-containing material suggests additional interaction with either conduction band or unpaired electrons, as expected by the increased extent of reaction and presence of Fe atoms in these materials, compared to the N-carbon.

The significantly displaced signal -463 ppm in the salt-templated N-carbon material is likely a Knight-shifted signal(s) that arises from ^{15}N-carbon nuclei within the bulk of the conductive graphitic materials, that are coupled to conduction electrons.[90] Very short recycle delays (10 ms) and a high number of scans ($5x10^6$) were used to detect fast-relaxing species (-463 ppm), thus the relative intensities of the signals shown are not quantitative. Separate quantitative analyses indicate that the signal at -463 ppm accounts for only about 0.2% of the total ^{15}N signal intensity. The salt-templated 0.1 mol% Fe,N-carbon material still has a large but slightly less displaced signal centered around -396 ppm. Again, the Fe-containing material is expected to have additional interaction with either conduction band or unpaired electrons, thus the difference in extent of electronic interaction is expected, compared to the N-carbon.

5.8 References

1. Becwar, S. M. *et al.* Atomic-scale understanding of the oxygen and sulfur reduction activities of mesoporous N-carbon electrocatalysts. *Nat. Mater*. to be submitted (2022).
2. Yang, W., Fellinger, T. P. & Antonietti, M. Efficient metal-free oxygen reduction in alkaline medium on high-surface-area mesoporous nitrogen-doped carbons made from ionic liquids and nucleobases. *J. Am. Chem. Soc.* **133**, 206–209 (2011).
3. Li, Y. *et al.* An oxygen reduction electrocatalyst based on carbon nanotube-graphene complexes. *Nat. Nanotechnol.* **7**, 394–400 (2012).
4. Chung, H. T., Won, J. H. & Zelenay, P. Active and stable carbon nanotube/nanoparticle composite electrocatalyst for oxygen reduction. *Nat. Commun.* **4**, 1922 (2013).
5. Chung, H. T. *et al.* Direct atomic-level insight into the active sites of a high-performance PGM-free ORR catalyst. *Science (80-.).* **357**, 479–484 (2017).
6. Gong, K., Du, F., Xia, Z., Durstock, M. & Dai, L. Nitrogen-Doped Carbon Nanotube Arrays with High Electrocatalytic Activity for Oxygen Reduction. *Science (80-.).* **323**, 760–765 (2009).
7. Lei, T. *et al.* Inhibiting Polysulfide Shuttling with a Graphene Composite Separator for Highly Robust Lithium-Sulfur Batteries. *Joule* **2**, 2091–2104 (2018).
8. Zhang, J., Zhao, Z., Xia, Z. & Dai, L. A metal-free bifunctional electrocatalyst for oxygen reduction and oxygen evolution reactions. *Nat. Nanotechnol.* **10**, 444–452 (2015).
9. Peng, L. *et al.* A fundamental look at electrocatalytic sulfur reduction reaction. *Nat. Catal.* **3**, 762–770 (2020).
10. Zhong, Y. *et al.* Popcorn Inspired Porous Macrocellular Carbon: Rapid Puffing

Fabrication from Rice and Its Applications in Lithium–Sulfur Batteries. *Adv. Energy Mater.* **8**, 1–8 (2018).

11. Ding, W. *et al.* Space-confinement-induced synthesis of pyridinic- and pyrrolic-nitrogen-doped graphene for the catalysis of oxygen reduction. *Angew. Chemie - Int. Ed.* **52**, 11755–11759 (2013).
12. Wu, J. *et al.* Nitrogen-Doped Graphene with Pyridinic Dominance as a Highly Active and Stable Electrocatalyst for Oxygen Reduction. *ACS Appl. Mater. Interfaces* **7**, 14763–14769 (2015).
13. Guo, D. *et al.* Active sites of nitrogen-doped carbon materials for oxygen reduction reaction clarified using model catalysts. *Science* **351**, 361–365 (2016).
14. Liu, G., Li, X., Ganesan, P. & Popov, B. N. Studies of oxygen reduction reaction active sites and stability of nitrogen-modified carbon composite catalysts for PEM fuel cells. *Electrochim. Acta* **55**, 2853–2858 (2010).
15. Lai, L. *et al.* Exploration of the active center structure of nitrogen-doped graphene-based catalysts for oxygen reduction reaction. *Energy Environ. Sci.* **5**, 7936–7942 (2012).
16. Subramanian, N. P. *et al.* Nitrogen-modified carbon-based catalysts for oxygen reduction reaction in polymer electrolyte membrane fuel cells. *J. Power Sources* **188**, 38–44 (2009).
17. Tributsch, H., Koslowski, U. I. & Dorbandt, I. Experimental and theoretical modeling of Fe-, Co-, Cu-, Mn-based electrocatalysts for oxygen reduction. *Electrochim. Acta* **53**, 2198–2209 (2008).
18. Zitolo, A. *et al.* Identification of catalytic sites for oxygen reduction in iron- and

nitrogen-doped graphene materials. *Nat. Mater.* **14**, 937–942 (2015).

19. Chung, H. T. *et al.* Direct atomic-level insight into the active sites of a high-performance PGM-free ORR catalyst. *Science (80-.).* **357**, 479–484 (2017).

20. Dorjgotov, A., Ok, J., Jeon, Y., Yoon, S. H. & Shul, Y. G. Activity and active sites of nitrogen-doped carbon nanotubes for oxygen reduction reaction. *J. Appl. Electrochem.* **43**, 387–397 (2013).

21. Zujovic, Z., Webber, A. L., Travas-Sejdic, J. & Brown, S. P. Self-Assembled Oligoanilinic Nanosheets: Molecular Structure Revealed by Solid-State NMR Spectroscopy. *Macromolecules* **48**, 8838–8843 (2015).

22. Mao, K., Kennedy, G. J., Althaus, S. M. & Pruski, M. Determination of the average aromatic cluster size of fossil fuels by solid-state NMR at high magnetic field. *Energy and Fuels* **27**, 760–763 (2013).

23. Wang, Z. *et al.* Quantitative atomic-scale structure characterization of ordered mesoporous carbon materials by solid state NMR. *Carbon N. Y.* **131**, 102–110 (2018).

24. Leskes, M. *et al.* Surface-Sensitive NMR Detection of the Solid Electrolyte Interphase Layer on Reduced Graphene Oxide. *J. Phys. Chem. Lett.* **8**, 1078–1085 (2017).

25. Halat, D. M. *et al.* Probing Oxide-Ion Mobility in the Mixed Ionic-Electronic Conductor La2NiO4+δby Solid-State17O MAS NMR Spectroscopy. *J. Am. Chem. Soc.* **138**, 11958–11969 (2016).

26. Yesinowski, J. P., Berkson, Z. J., Cadars, S., Purdy, A. P. & Chmelka, B. F. Spatially correlated distributions of local metallic properties in bulk and nanocrystalline GaN. *Phys. Rev. B* **95**, (2017).

27. Pham, H. N. *et al.* Carbon Overcoating of Supported Metal Catalysts for Improved

Hydrothermal Stability. *ACS Catal.* **5**, 4546–4555 (2015).

28. Kuroki, S., Nabae, Y., Chokai, M., Kakimoto, M. A. & Miyata, S. Oxygen reduction activity of pyrolyzed polypyrroles studied by 15N solid-state NMR and XPS with principal component analysis. *Carbon N. Y.* **50**, 153–162 (2012).
29. Baccile, N. *et al.* Structural Insights on Nitrogen-Containing Hydrothermal Carbon Using Solid-State Magic Angle Spinning 13C and 15N Nuclear Magnetic Resonance. *J. Phys. Chem. C* **115**, 8976–8982 (2011).
30. Zhao, L. *et al.* Sustainable nitrogen-doped carbonaceous materials from biomass derivatives. *Carbon N. Y.* **48**, 3778–3787 (2010).
31. Falco, C., Sevilla, M., White, R. J., Rothe, R. & Titirici, M. M. Renewable nitrogen-doped hydrothermal carbons derived from microalgae. *ChemSusChem* **5**, 1834–1840 (2012).
32. Carrasco, P. M. *et al.* Structure-conductivity relationships in chemical polypyrroles of low, medium and high conductivity. *Synth. Met.* **156**, 420–425 (2006).
33. Zhao, D. *et al.* Triblock copolymer syntheses of mesoporous silica with periodic 50 to 300 angstrom pores. *Science* **279**, 548–52 (1998).
34. Fechler, N. *et al.* Eutectic Syntheses of Graphitic Carbon with High Pyrazinic Nitrogen Content. *Adv. Mater.* **28**, 1287–1294 (2016).
35. Ryoo, R., Joo, S. H. & Jun, S. Synthesis of Highly Ordered Carbon Molecular Sieves via Template-Mediated Structural Transformation. *J. Phys. Chem. B* **103**, 7743–7746 (1999).
36. Jun, S. *et al.* Synthesis of new, nanoporous carbon with hexagonally ordered mesostructure. *J. Am. Chem. Soc.* **122**, 10712–10713 (2000).

37. Fechler, N., Fellinger, T. P. & Antonietti, M. ‘Salt Templating’: A simple and sustainable pathway toward highly porous functional carbons from ionic liquids. *Adv. Mater.* **25**, 75–79 (2013).

38. Ravel, B. & Newville, M. ATHENA, ARTEMIS, HEPHAESTUS: Data analysis for X-ray absorption spectroscopy using IFEFFIT. *J. Synchrotron Radiat.* **12**, 537–541 (2005).

39. Ravel, B. ATHENA: XAS Data Processing. (2015). Available at: https://bruceravel.github.io/demeter/documents/Athena/index.html. (Accessed: 1st April 2015)

40. Fung, B. M., Khitrin, A. K. & Ermolaev, K. An Improved Broadband Decoupling Sequence for Liquid Crystals and Solids. *J. Magn. Reson.* **142**, 97–101 (2000).

41. Bertani, P., Raya, J. & Bechinger, B. 15N chemical shift referencing in solid state NMR. *Solid State Nucl. Magn. Reson.* **61**–**62**, 15–18 (2014).

42. Thurber, K. R. & Tycko, R. Measurement of sample temperatures under magic-angle spinning from the chemical shift and spin-lattice relaxation rate of 79 Br in KBr powder. *J. Magn. Reson.* **196**, 84–87 (2009).

43. Yesinowski, J. P., Ladouceur, H. D. D., Purdy, A. P. P. & Miller, J. B. B. Electrical and ionic conductivity effects on magic-angle spinning nuclear magnetic resonance parameters of CuI. *J. Chem. Phys.* **133**, 234509 (2010).

44. Thurber, K. R. & Tycko, R. Measurement of sample temperatures under magic-angle spinning from the chemical shift and spin-lattice relaxation rate of 79Br in KBr powder. *J. Magn. Reson.* **196**, 84–87 (2009).

45. Martin, G. J., Martin, M. L. & Gouesnard, J.-P. *15N-NMR Spectroscopy*. (Springer-

Verlag, 1981).

46. Gammon, W. J., Hoatson, G. L., Holloway, B. C., Vold, R. L. & Reilly, A. C. Bonding in hard and elastic amorphous carbon nitride films investigated using 15N, 13C, and 1H NMR spectroscopy. *Phys. Rev. B* **68**, 195401 (2003).

47. Becwar, S. M., Berkson, Z. J., Selter, P., Zussblatt, N. P. & Chmelka, B. F. Understanding and correlating complicated electronic and paramagnetic properties of conductive N- and Fe, N-carbons. *J. Magn. Reson.* manuscript in preparation (2022).

48. Wang, X., Hou, Z., Ikeda, T. & Terakura, K. NMR chemical shifts of 15N-bearing graphene. *J. Phys. Chem. C* **118**, 13929–13935 (2014).

49. Kresse, G. & Hafner, J. Ab initio molecular dynamics for liquid metals. *Phys. Rev. B* **47**, 558–561 (1993).

50. Yates, J. R., Pickard, C. J. & Mauri, F. Calculation of NMR chemical shifts for extended systems using ultrasoft pseudopotentials. *Phys. Rev. B - Condens. Matter Mater. Phys.* **76**, 1–11 (2007).

51. Kohn, W. & Sham, L. J. Self-consistent equations including exchange and correlation effects. *Phys. Rev.* **140**, A1133 (1965).

52. Perdew, J. P., Burke, K. & Ernzerhof, M. Perdew, Burke, Ernzerhof - 1997 - Generalized Gradient Approximation Made Simple(2). *Phys. Rev. Lett.* **77**, 3865–3868 (1996).

53. Steinmann, S. N. & Corminboeuf, C. Comprehensive benchmarking of a density-dependent dispersion correction. *J. Chem. Theory Comput.* **7**, 3567–3577 (2011).

54. Steinmann, S. N. & Corminboeuf, C. A generalized-gradient approximation exchange hole model for dispersion coefficients. *J. Chem. Phys.* **134**, (2011).

55. Pickard, C. J. & Mauri, F. All-electron magnetic response with pseudopotentials: NMR chemical shifts. *Phys. Rev. B - Condens. Matter Mater. Phys.* **63**, 2451011–2451013 (2001).

56. Fechler, N. *et al.* Eutectic Syntheses of Graphitic Carbon with High Pyrazinic Nitrogen Content. *Adv. Mater.* **28**, 1287 (2016).

57. Wu, Z. *et al.* Synthesis of Ordered Mesoporous Carbon Materials with Semi-Graphitized Walls via Direct In-situ Silica-Confined Thermal Decomposition of CH4 and Their Hydrogen Storage Properties. *Top. Catal.* **52**, 12–26 (2009).

58. Kim, D. *et al.* Highly Graphitic Mesoporous Fe,N-Doped Carbon Materials for Oxygen Reduction Electrochemical Catalysts. *ACS Appl. Mater. Interfaces* **10**, 25337 (2018).

59. Szewczyk, I. *et al.* Electrochemical Denitrification and Oxidative Dehydrogenation of Ethylbenzene over N-doped Mesoporous Carbon: Atomic Level Understanding of Catalytic Activity by 15N NMR Spectroscopy. *Chem. Mater.* **32**, 7263–7273 (2020).

60. Janson, C. & Palmqvist, A. E. C. Influence of Precursor Functional Groups on the Formation and Performance of Iron-Coordinating Ordered Mesoporous Carbons as Fuel Cell Catalysts. *J. Phys. Chem. C* **121**, 21827 (2017).

61. Othman, R., Dicks, A. L. & Zhu, Z. Non precious metal catalysts for the PEM fuel cell cathode. *Int. J. Hydrogen Energy* **37**, 357–372 (2012).

62. Wild, M. *et al.* Lithium sulfur batteries, a mechanistic review. *Energy Environ. Sci.* **8**, 3477–3494 (2015).

63. Levitt, M. H. *Spin Dynamics: Basics of Nuclear Magnetic Resonance*. (John Wiley & Sons, 2008).

64. Kramm, U. I., Lefèvre, M., Larouche, N., Schmeisser, D. & Dodelet, J. P. Correlations

between mass activity and physicochemical properties of Fe/N/C catalysts for the ORR in PEM fuel cell via 57Fe Mössbauer spectroscopy and other techniques. *J. Am. Chem. Soc.* **136**, 978–985 (2014).

65. Wang, M. *et al.* The role of iron nitrides in the Fe–N–C catalysis system towards the oxygen reduction reaction. *Nanoscale* **9**, 7641–7649 (2017).

66. Rissanen, L. *et al.* The production of the new cubic FeN phase by reactive magnetron sputtering. *Appl. Surf. Sci.* **138**–**139**, 261–265 (1999).

67. Borsa, D. M. & Boerma, D. O. Phase identification of iron nitrides and iron oxy-nitrides with Mössbauer spectroscopy. *Hyperfine Interact.* **151**–**152**, 31–48 (2003).

68. Ferrandon, M. *et al.* Multitechnique Characterization of a Polyaniline − Iron − Carbon Oxygen Reduction Catalyst. *J. Phys. Chem. C* **116**, 16001–16013 (2012).

69. Koslowski, U. I., Abs-Wurmbach, I., Fiechter, S. & Bogdanoff, P. Nature of the catalytic centers of porphyrin-based electrocatalysts for the ORR: A correlation of kinetic current density with the site density of Fe-N4 centers. *J. Phys. Chem. C* **112**, 15356–15366 (2008).

70. Strickland, K. *et al.* Highly active oxygen reduction non-platinum group metal electrocatalyst without direct metal-nitrogen coordination. *Nat. Commun.* **6**, 1–8 (2015).

71. Pell, A. J., Pintacuda, G. & Grey, C. P. Paramagnetic NMR in solution and the solid state. *Prog. Nucl. Magn. Reson. Spectrosc.* **111**, 1–271 (2019).

72. Mcconnell, H. M. & Robertson, R. E. Isotropic nuclear resonance shifts. *J. Chem. Phys.* **29**, 1361–1365 (1958).

73. Mcconnell, H. M. & Robertson, R. E. Comments on 'Theory of isotropic hyperfine

interactions in π-electron radicals'. *J. Chem. Phys.* **28**, 991–992 (1958).

74. Xiao, H. *et al.* Fe-N-carbon black for the oxygen reduction reaction in sulfuric acid. *Carbon N. Y.* **57**, 443–451 (2013).

75. Wu, G. & Zelenay, P. Nanostructured Nonprecious Metal Catalysts for Oxygen Reduction Reaction. *Acc. Chem. Res.* **46**, 1878–1889 (2013).

76. Fujii, H. & Yoshida, T. 13C and15N NMR studies of iron-bound cyanides of heme proteins and related model complexes: Sensitive probe for detecting hydrogen-bonding interactions at the proximal and distal sides. *Inorg. Chem.* **45**, 6816–6827 (2006).

77. Aviles, G. & Chang*, C. K. 15N NMR of Sterically Distorted Cyanomet Haems. *Chem. Commun.* 31–32 (1992).

78. Behere, D. V., Gonzalez-Vergara, E. & Goff, H. M. of hemoprotein prosthetic-group environment and. *Biochim. Biophys. Acta* **832**, 319–325 (1985).

79. Solomon, I. Relaxation Processes in a System of Two Spins. *Phys. Rev.* **99**, 559–566 (1955).

80. Bloembergen, N. Proton relaxation times in paramagnetic solutions. *J. Chem. Phys.* **27**, 572–573 (1957).

81. Kowalewski, J., Nordenskiöld, L., Benetis, N. & Westlund, P. O. Theory of nuclear spin relaxation in paramagnetic systems in solution. *Prog. Nucl. Magn. Reson. Spectrosc.* **17**, 141–185 (1985).

82. Shen, H. *et al.* Atomically FeN2 moieties dispersed on mesoporous carbon: A new atomic catalyst for efficient oxygen reduction catalysis. *Nano Energy* **35**, 9–16 (2017).

83. Shang, R., Steinmann, S. N., Xu, B.-Q. & Sautet, P. Mononuclear Fe in N-doped carbon: computational elucidation of active sites for electrochemical oxygen reduction

and oxygen evolution reactions. *Catal. Sci. &Technology* 1006–1014 (2020). doi:10.1039/c9cy01935a

84. Gierszal, K. P., Jaroniec, M., Kim, T.-W., Kim, J. & Ryoo, R. High temperature treatment of ordered mesoporous carbons prepared by using various carbon precursors and ordered mesoporous silica templates. *New J. Chem.* **32**, 981 (2008).

85. Tuinstra, F. & Koenig, L. Raman Spectrum of Graphite. *J. Chem. Phys.* **53**, 1126–1130 (1970).

86. Herrmann, I., Kramm, U. I., Radnik, J., Fiechter, S. & Bogdanoff, P. Influence of Sulfur on the Pyrolysis of CoTMPP as Electrocatalyst for the Oxygen Reduction Reaction. *J. Electrochem. Soc.* **156**, B1283–B1292 (2009).

87. Dippel, B., Jander, H. & Heintzenberg, J. NIR FT Raman spectroscopic study of flame soot. *Phys. Chem. Chem. Phys.* **1**, 4707–4712 (1999).

88. Suzuki, N. *et al.* Novel Iron Porphyrin-Alkanethiolate Complex with Intramolecular NH,,,S Hydrogen Bond: Synthesis, Spectroscopy, and Reactivity. *J. Am. Chem. Soc.* **121**, 11571–11572 (1999).

89. Willans, M. J., Wasylishen, R. E. & McDonald, R. Polymorphism of potassium ferrocyanide trihydrate as studied by solid-state multinuclear NMR spectroscopy and X-ray diffraction. *Inorg. Chem.* **48**, 4342–4353 (2009).

90. Knight, W. D. Nuclear Magnetic Resonance Shift in Metals. *Phys. Rev.* **76**, 1259–1260 (1949).

6. Understanding and correlating complicated electronic and paramagnetic properties of conductive N- and Fe, N-carbons

This chapter is meant to be a review and methodology discussion pertaining to understanding and correlating complicated electronic and paramagnetic properties of conductive and mesoporous N- and Fe, N-carbons. I have provided a thorough background for the specific and extensive special considerations that must be accounted for when attempting to use solid-state EPR or solid-state NMR for characterizations of complicated heterogeneous and conductive materials. I show the work that I have done towards understanding the electron-nuclear interactions and overcoming these specific challenges with the mesoporous N and Fe-N carbon materials discussed in Ch 2-5 of this thesis. I also discuss future work suggestion, give my hypotheses of the outcomes of such experiments, and provide examples from literature to support my hypotheses.

6.1 Abstract

While conductive Fe,N- and N-carbons are widely researched and utilized materials with many applications in energy and other fields, it is challenging to measure and correlate local Fe or N heteroatom environments and their distributions in graphitic carbons with

macroscopic electrocatalytic properties. This is due, in large part, to the heterogeneous material compositions, high conductivity of graphitic carbons, and presence of paramagnetic centers, which can non-uniformly displace and broaden NMR signals, decrease nuclear spin-lattice relaxation times, and lead to substantial sample heating under MAS.[1] The special challenges and considerations that need to be accounted for to characterize such materials by solid-state NMR and EPR techniques effectively are consolidated as background in this chapter. The extent these effects have on NMR spectra is not well understood or quantified. Modeling groups are still working to be able to understand, quantify, and predict such effects. Partly due to the facts that the effects of conductivity and paramagnetic species vary widely with the types of materials being studied, experimental temperature, and dilution, to name a few. Nevertheless, solid-state Hahn-echo ^{15}N and ^{13}C T_1-filtered MAS NMR spectra show increasing signal intensity with increasing relaxation delay times in both the mesoporous Fe,N- and N-carbons, indicative of proximity to conduction band electrons. Additionally, narrow and fast relaxing solid-state Hahn-echo ^{15}N signals specifically in the Fe,N-carbon materials indicate proximity of Fe atoms to pyridinic N species. Detailed analyses of the relaxation resolved species allow for prediction of distances between the Fe, N, and C atoms which provides valuable information about the types of environments present. Additionally, spin-echo ^{15}N NMR spectra acquired under fast MAS (>40 kHz) and variable temperature (325 – 400 K) conditions reveal a small fraction of ^{15}N signals that are significantly displaced by interactions with conduction band electrons in the mesoporous N-carbons. These significantly displaced ^{15}N shifts and T_1 relaxation times (between 9 and 330 ms) both exhibit significant temperature dependences (~140 ppm/K), which is consistent with strong paramagnetic contact interactions. Finally, CW EPR spectra of the various Fe,N- and N-

carbon silica- and salt-templated materials elucidate differences in the electronic environments caused by the templating agent or presence of Fe heteroatoms. However, additional EPR experiments, which are outlined below, are necessary to gain understanding of the interactions between unpaired or conduction band electron with nearby heteroatom species, and how these environments correlate with increased electrochemical activity. In this chapter I review the extensive number of important factors to consider when using magnetic resonance spectroscopy techniques to understand the complicated nuclear and electronic interactions occurring in the high N-content carbon materials, in addition to the solid-state NMR and EPR analyses I have already conducted of the mesoporous graphitic Fe,N- and N-carbons which provide evidence for interactions of both paramagnetic and conduction band electrons with N heteroatom sites.

6.2 Introduction

Mesoporous-N-carbons prepared by high-temperature pyrolysis of urea and cyclohexanehexone precursors (Figure 6.1) exhibit high and accessible surface areas, high electrical conductivities, and high electrocatalytic activities which can be used as a fuel cell cathode to catalyze the four-electron oxygen reduction reaction (ORR), as well as the sulfur reduction reaction (SRR).[2] These materials are templated with either a salt- or silica-mesopore inducing templates to increase surface area. Disorder, electrical conductivity, and nonstoichiometric distributions in heteroatom-containing carbon materials make characterization challenging. Wide-angle X-ray scattering and Raman spectroscopy provide

limited insights into bonding environments of N heteroatoms, but do confirm the presence of graphitic carbon sheets with short range order and significant edge/heteroatom defects.

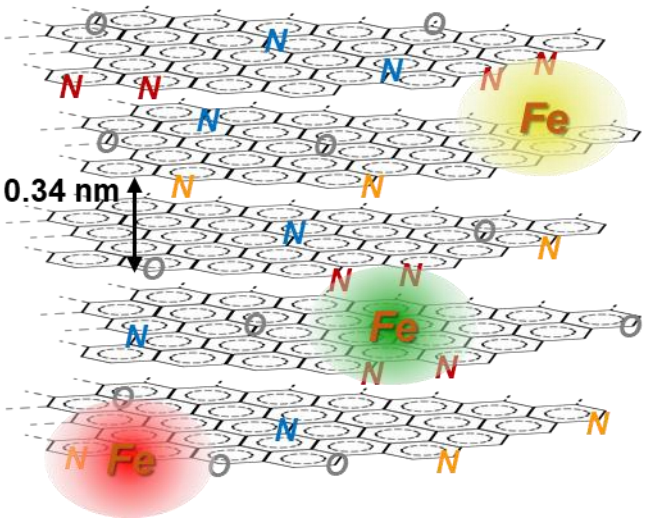

Figure 6.1. Proposed structure of graphitic Fe,N-heteroatom containing carbon materials with 0.34 nm d-spacing as measured by WAXS at the edge of a carbon sheet.

N sites that are responsible for catalyzing the reduction reactions are of particular interest as electrons are required for the reaction, however, the correlation between N-sites and nearby conduction band or unpaired electrons is unknown, due to the complicated interactions that need to be both understood and accounted for when considering methods to characterize such complicated conductive N-carbon materials. X-ray photoelectron spectroscopy (XPS) is in principle sensitive to differences in the types of N environments that are present in N-containing carbon materials, but the lack of ability account for surface/bulk heterogeneity does not provide a complete picture of such complicated materials, and the small differences in binding energy associated with different nitrogen-containing moieties are challenging to resolve.

NMR spectroscopy is a powerful atomic-scale characterization technique used to probe the local magnetic fields of atomic nuclei which provides detailed information about the electronic structure of the nuclei in the material, and about their surrounding environments. While NMR is able to resolve the nitrogen-carbon environments present in these materials,[2,3] the electron-nuclear interactions have yet to be understood. This is because the influence of unpaired electrons in conductive samples poses many special considerations to NMR spectroscopy as an environmental characterization technique that are still being investigated.[4–6] These include homogeneous and inhomogeneous broadening, bulk magnetic susceptibility, paramagnetic susceptibility influences, Knight shifts and the Korringa relation, and heating challenges with DNP, all of which are reviewed below. These special considerations have added a lot of challenges and understanding to the field, but there is a lot of room for improvement and streamlining of these techniques before NMR spectroscopy can be more easily accessible and applied to the characterization of complicated conductive materials. Thus, the goal of this manuscript is to increase understanding between conduction band/unpaired electron environments of N-carbons and electron-nuclear interaction involving paramagnetic species in Fe,N-carbons and the effects that these environments have on solid-state NMR and EPR spectroscopy techniques and spectra.

6.3 Special considerations for and broadening of spectra in solid-state nuclear magnetic resonance spectroscopy of conductive materials

6.3.1 Homogeneous and inhomogeneous spectral broadening

The T_2 relaxation rate gives important information allowing for the differentiation between molecular species by NMR,[7] but can also be an important source of broadening in the case of almost all samples, not just conductive samples. The two common sources that are usually first investigated when broadening occurs are inhomogeneous and homogeneous broadening: 1) inhomogeneous broadening which is due to fluctuating microscopic magnetic fields, and 2) homogenous broadening which is due to variation in macroscopic magnetic fields over volume of the sample due to instrument imperfections and susceptibility effects.[7] A lot of the challenges that are faced with broadening of conductive or paramagnetic samples also stem from the very important relaxation rate. Conductivity and paramagnetic electrons from proximate species can influence the rate at which the species relax, as well as the local magnetic field strength felt by each nuclei, causing a distribution of relaxation rates, and thus broadening of the spectra and displacement of the chemical shifts, which will be discussed in the sections below.

6.3.2 Aromaticity and ring-current shifts

Aromatic systems are generally known to have approximately equal bond length, characteristic ultra-violet absorptions, and strong spin delocalization resulting in ring-current shifts in NMR.[7,8] Similarly, there is an effect known as the sphere-current which is observed

in three-dimensional fullerenes.[9] Ampère's law suggests that since the electrons in a conductive system are free to circulate, rather than being localized in bonds as they would be in most non-aromatic molecules, they respond much more strongly to the magnetic field.[10] A magnetic field is directed perpendicular to the plane of the aromatic system, a ring current is induced in the delocalized π-electrons of the aromatic ring.[11] Therefore, a ring current creates its own magnetic field, which in terms of the Maxwell's equations is called the induced magnetic field (B^{ind}). The induced magnetic field varies over the molecule and can be calculated using the Bio-Savart's law [Equation 6.1]:[11–13]

$$\boldsymbol{B}^{\mathrm{ind}}(\boldsymbol{R}) = \frac{\mu_0}{4\pi}\int \frac{\boldsymbol{j}(\boldsymbol{r}) \times (\boldsymbol{r}-\boldsymbol{R})}{|\boldsymbol{r}-\boldsymbol{R}|^3}\,\mathrm{d}\boldsymbol{r} \qquad [6.1]$$

Which relates a position in the molecules field (R) the to induced current density of the molecule ($j(r)$).[11–13] Externally, the aromatic molecule is experiencing a different magnetic field (B^{ind}) than the external magnetic field (B^{ext}), which can be related by the NMR shielding tensor [Equation 6.2]:[11–13]

$$\boldsymbol{B}^{\mathrm{ind}}(\boldsymbol{R}) = -\boldsymbol{\sigma}(\boldsymbol{R})\boldsymbol{B}^{\mathrm{ext}} \qquad [6.2]$$

Therefore, it is very important to account for the differences in chemical shift that will be cause by the presence of ring-current shifts in aromatic materials. In refence in my work on graphitic and conductive carbon materials, which consist of an extended network of aromatic rings, ring-current shifts are expected to be present and play a role on the chemical shifts measured my NMR spectroscopy techniques. Additionally, the sphere-current found in 3D systems may be found in the Boron cluster systems I have studied.

6.3.3 Broadening by non-uniform heating of conductive samples

The use of magic-angle spinning (MAS) NMR in high magnetic fields is one of the most useful techniques to solid-state NMR investigations as it mimics the orientational averaging achieved by solutions in solid-state samples. The averaging causes the signal to narrow and generally achieve the isotropic chemical shift value, and sometimes spinning sidebands which occur at multiples of the spinning speed and can be used to determine the chemical shift anisotropy of the nuclei.[7] However, the process of spinning can affect the materials and the measurement system. In complicated conductive samples, this is an important consideration.[14–16] Conductive samples are known to pose some limitations on the performance of ssNMR spectroscopy, including limited radio- frequency (RF) penetration depth and thus limited and highly inhomogeneous excitation across the sample, and RF heating and shortening of nuclear relaxation times.[17] Additionally, eddy currents are loops of electrical current induced within conductors by a changing magnetic field. When the conductive samples are being spun by MAS, eddy currents can lead to unwanted heating effects that should be accounted for when planning the experiments.[15,16] When spinning conductive samples, more drive pressure is required to spin than with a non-conducting counterpart, something I have observed in spinning graphitic carbon materials. The higher pressures required to spin samples with higher effective electrical conductivities indicate the presence of a "braking effect," which arise from the rotation induced currents.[16]

It is important to consider that heating due to spinning a conductive sample can affect both the material integrity in the temperature surpasses that at which it will start to react or degrade, and that the change in temperature can affect the chemical shift. For instance, this is clearly displayed by the figures from Yesinowski et al. that show how spinning the same electrically

conductive ^{207}Pb sample at varied MAS speeds, dramatically affects the chemical shift. With higher the spinning speeds, the lack of uniformity in the sample temperature is amplified, causing the signals to broaden (by up to 100 ppm in shift and 50 ppm in width) as is shown in Figure 6.2b. However, there is also a benefit to the observation in that it is an easy way to test if the materials are experiencing bulk magnetic susceptibility and heating effects. Additionally, the use of eddy current heating has been proposed as an option to vary the issues

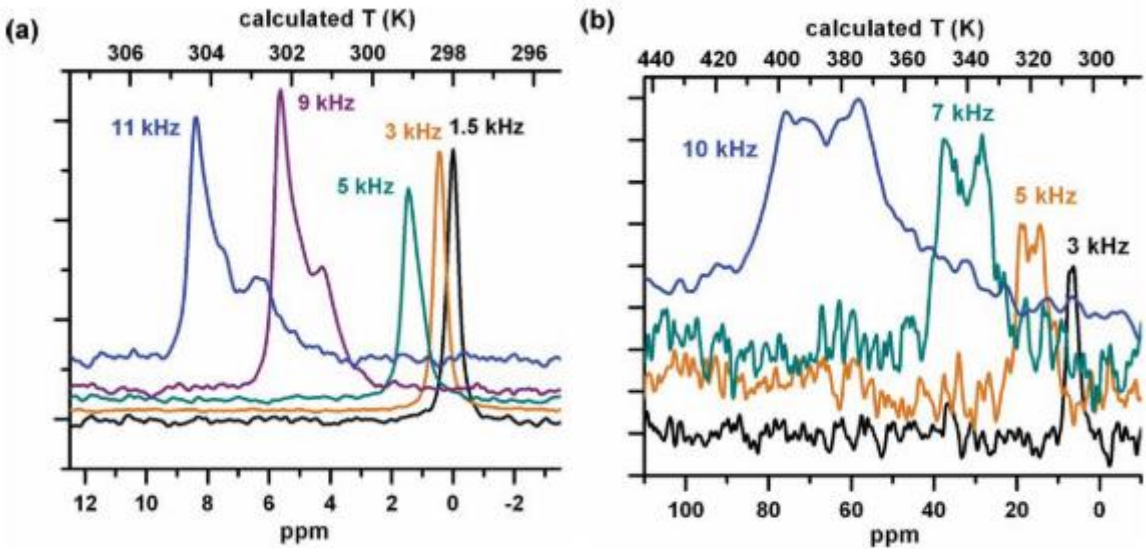

Figure 6.2. ^{207}Pb solid-state NMR spectra at different spinning speeds comparing the differences in chemical shift measured between (a) diluted thermometric CuI and (b) non-diluted thermometric CuI. The lower axis is ^{207}Pb chemical shift, the upper axis is corresponding calculated temperature. In (a) only modest frictional heating effects from sample spinning are seen, whereas in (b) resistive heating by induced currents in the near-bulk CuI produces a large nonuniform temperature increase in the sample. This figure is from Yesinowski et al..[16]

temperature of a sample in an NMR rotor.[15,16] Importantly though, it was found that with signal loss due to skin depth issues and rotation drag can be mitigated by simply diluting the conductive samples with non-conductive and inert matrixes.[16,18,19] This is shown in Figure 6.2a where the same sample as in Figure 6.2b has been diluted which dramatically decreased the issues with temperature uniformity and increase. There is still some variation in chemical shift and broadening of the signal, but it is decreased by an order of magnitude. Thus, while spinning conductive samples can cause dramatic broadening and chemical shift displacement due to thermal heating, the effect can be largely measured and mitigated by the incorporation of non-conductive and inert matrixes into the NMR rotors.

6.3.4 Paramagnetic effects

Many conductive systems have molecules or materials with paramagnetic centers, which are atoms or ions possessing at least one unpaired electron, meaning they are also considered paramagnetic systems.[4] Most NMR measurements are conducted on diamagnetic materials, but NMR of paramagnetic materials gives rise to special effects which manifest as wide chemical shift ranges and broadened signals.[4] Specifically, the important property of these systems are the hyperfine interaction between unpaired electrons and the NMR active observed nucleus, which cause paramagnetic shifts and shift anisotropy (SA), paramagnetic relaxation enhancements (PRE), and additional sources of substantial broadening due to bulk magnetic susceptibility effects. Paramagnetic nuclei influence those around them, leading to shorter relaxation times (T_1) of the observed nuclei. This is challenging in that a distribution

of these centers can lead to non-uniform relaxation times and diminishes the resolution of an NMR spectrum to the extent that coupling is rarely resolved.[4] However, this also allows for the rate of spectral acquisition can be high and the ability to selectively detect nuclei that are proximate to paramagnetic species.

There have been many explanations for the interaction of paramagnetic nuclei and electrons with other species in the materials and how this affects the corresponding NMR spectra from various field of research. The first and seemingly most commonly used is the Solomon–Bloembergen–Morgan theory (1955), which site a combination of molecular dynamics, fast chemical exchange, and electronic relaxation as the effect of stochastic fluctuations in the hyperfine interaction, and thus the source of the nuclear relaxation.[4,20–22] Shortly after (1958), McConnell introduced and understanding of paramagnetic shifts from d-block metal ions, where he identified two important contributions to the isotropic shift: 1) contact shift - due to through-bond transfer of the unpaired electron spin onto the nucleus, and 2) the pseudo-contact shift (PCS) - from the through-space spin-dipolar coupling between the unpaired electrons and the nucleus.[23,24]

Because the paramagnetic effect is so complicated and often intertwined with other affects such as bulk magnetic susceptibility, Knight shift, conductivity, it is very important to be able to model and understand these complicated effects.[4] An important step among this massive effort has been the observation is that the contact shifts can be broken down into a sum of contributions from the metal ions that transfer unpaired electronic spin density onto the nucleus, known as ‘path- way contributions’.[25] This idea has allowed for the analysis of the contact shifts of complex battery materials which contain multiple types of metal ions.[26–29] Finally, paramagnetic effects are only subject to temperature in that their spin relaxation rate

generally increases with decreasing temperature, and sometimes a shift of a few ppm. The presence of paramagnetic centers and relaxations significantly complicate the NMR spectra, over diamagnetic systems, but are beginning to be understood and reproducible.

6.3.5. Knight shifts and the Korringa relation

Knight shifts are deviations in the NMR frequency shifts of paramagnetic materials or metals from the same atom in a nonmetallic environment. The Knight shift is due to the conduction electrons in metals which impose an additional field to be observed by the nuclei, due to the spin orientations of the conduction electrons in the presence of an external field.[7] These small differences in the net magnetic field felt by the nuclei manifest as a shift (Knight shift) that can be observed in the nuclear magnetic resonance.

As a brief history, Walter Knight's paper in 1949 was the first observation of what are now known as Knight shifts.[30] Interestingly, the idea of a chemical shift was not fully realized and published until a year later in 1950 by Proctor and Yu,[31] who cited Knight's paper, showing how this discovery really helped advance the field of NMR studies and understanding. In his paper, Knight found that there were displacements in the chemical shifts (then just known as resonance frequencies) of the same nuclei when comparing spectra of their metallic and salt forms. This displacement is now known as the Knight shift.[30] The first paper showing experimental evidence of Knight shifts in solid-state NMR seems to be from E. Andrew in a 1981 paper where he discusses how M.A.S. of metals removes the anisotropy of the isotropic Knight shift so that it can be easily measured, specifically in aluminum and copper metals. This was followed up shortly by Saito et al. and Kume et al. who showed what I believe to be the first theoretical (calculated) and experimental evidence of ^{13}C Knight shifts

in the solid-state NMR of carbon materials, which in this case were highly oriented pyrolytic graphite (HOPG) compounds.[32,33]

Because of their similarities, there is a lot of confusion between Knight shifts and paramagnetic effects. The Knight shift is due to the conduction electrons in metals which impose an additional field to be observed by the nuclei, due to the spin orientations of the conduction electrons in the presence of an external field.[7] These small differences in the net magnetic field felt by the nuclei manifest as a shift (Knight shift) that can be observed in the nuclear magnetic resonance. As previously discussed, the isotropic chemical shifts of paramagnetic materials can be largely affected by the pseudocontact shift term which results from the anisotropy of the magnetic field caused by the paramagnetic center. Paramagnetic effects give rise to a wide chemical shift range and broadened signals.[7] The similarities between the two make the effects challenging to discern even now. However, Knight shifts and paramagnetic effects do have a distinguishing element, which is temperature dependence. This is manifested in the Knight-Korringa relation which was published in 1950. Korringa showed that the spin relaxation rate (T_1), times the square of the magnetic resonance field shift (the Knight shift) obtained from an NMR experiment is equal to a constant (κ), times the temperature (T),[4,34,35] or:

$$K^2 T_1 T = S = \left(\frac{\hbar}{4\pi k_B}\right)\left(\frac{g\mu_B}{\hbar\gamma_B}\right)^2 \qquad [6.3]$$

This relationship has been used and successful in many systems. One such example is from Cho, Berkson et al. where they show the $T_{1,K}^{-1}$ values of solid-state ^{19}F NMR spectra of F:In_2O_3 doped metal oxide nanocrystals (3% InF_3) at the peak maximum of the Knight shift

distribution (K = 100 ppm) as a function of temperature.[36] The slope is then then equal to K^2/S, and clearly fits quite well with the experimental data shown in Figure 6.3.

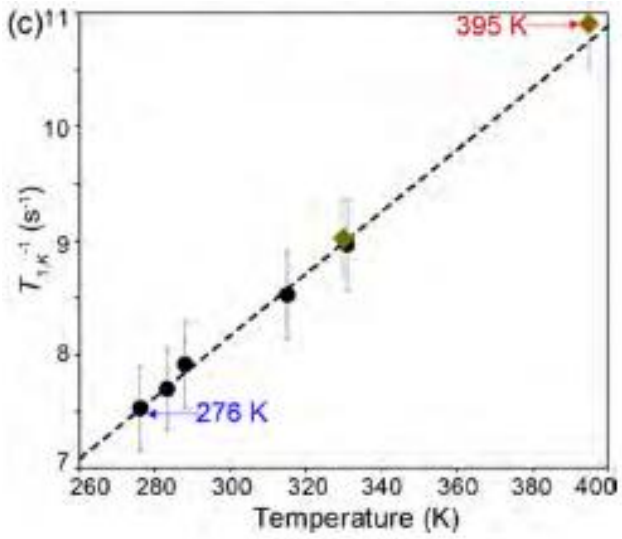

Figure 6.3. Plot of the $T_{1,K}^{-1}$ values of solid-state ^{19}F NMR spectra of F:In_2O_3 doped metal oxide nanocrystals (3% InF3) diluted in a 1:1 ratio by mass with KBr at the peak maximum of the Knight shift distribution (K = 100 ppm) as a function of temperature. Black circles and brown diamonds indicate $T_{1,K}^{-1}$ values measured under MAS conditions of 25 and 35 kHz, respectively. The dashed line indicates theoretical values obtained from the Knight−Korringa equation [Equation 6.3]. This figure is from Cho, Berkson et al..[36]

It should be noted however, that even in simple metallic systems it has been shown that the experimental T_1 values are greater than the values predicted. This is because of the neglect of effects such as electron–electron interactions, and other relaxation mechanisms. Identifying the Knight shift among so many other complicated interactions in conductive materials is still a challenge that we are investigating today.

6.3.6 DNP and heating of conductive samples

Heating challenges are a very important consideration because the material environments, mobility, and reactivity are all affected by the sample temperature, not to mention the reproducibility of the experiment. DNP (dynamic nuclear polarization) NMR is a special type of NMR where massive signal enhancements can be achieved by transferring spin polarization from electrons (which are much more highly susceptible to alignment in the magnetic field) to nuclei, thereby aligning the nuclear spins to the extent that electron spins are aligned. This technique is especially powerful for systems with nuclear enrichment is not possible, or where signals are very weak.[4,7,17] The majority of DNP NMR studies have focused on insulating samples such as organic solids and non-conductive inorganic materials. However, many technologically relevant materials are electrically conductive, such as energy storage (batteries and supercapacitors) and energy conversion (fuel cells, photo and electrocatalysts) systems, which require mobile electrons for their performance.[17] In these conductive systems, the free electrons provide significant challenges to DNP NMR, as it uses electron polarization. Therefore, DNP NMR of conductive carbon systems and the additional phenomena related to the interaction of the conduction (or delocalized) electrons with the μw irradiation are crucial, and relatively unknown. A good investigation/overview of DNP NMR of conductive samples was conducted by Leskes and coworkers.[17]

As previously discussed, heating due to bulk magnetic susceptibility, or the resistance to spinning that can be caused by a conductive material being in the presence of a strong magnetic field can cause significant sample heating. However, exposing conductive samples to microwave can also cause significant samples heating. The first published DNP NMR

experiments of samples with conduction electrons were of lithium metals by Overhauser DNP, reporting sample heating.[37,38] Low field DNP NMR of coal revealed that dielectric losses led to reduced effective μw power, and significant cooling measures were required to avoid sample heating.[39]

The interesting thing is that the heating competes with the signal enhancement expected by DNP, thus in some cases of using DNP on conductive samples, low or negative signal enhancement is actually experienced.[17] DNP NMR used to characterize the solid electrolyte interphase formed on reduced graphene oxide anodes achieved low signal enhancements of about 70 for the solvent protons and limited to the outer surface layer of the interphases.[40] Leskes and coworkers conducted a very useful investigation into the effect of electrical conductivity of conductive-carbon-samples on the DNP efficacy in conductive carbons which are important to energy storage and conversion. They found that the presence of conductive carbons decrease signal enhancement, and that the more conductive the samples, the less enhancement it has. This was done by measuring the ^{1}H signal enhancement of samples starting with an inert mixture of KBr and TEKPol radicals, which achieve a signal enhancement of 25, compared to the non-microwaved sample as shown in Figure 6.4. Carbon black was then added into the samples in different ratios, and the signal enhancement quicky dropped from 7, to 5, to 1 with increasing amounts of carbon black. It is proposed that the decrease in enhancements are due to reactivity of the carbons with the nitroxide radicals, a change in the glass forming properties of the radicals' solution, or an effect related to the conductive nature of the carbon powders. This experiment confirms that the presence of a conductive carbon material in an otherwise polarizable samples, makes the enhancements and therefore benefits of DNP NMR experiments invalid in this case.

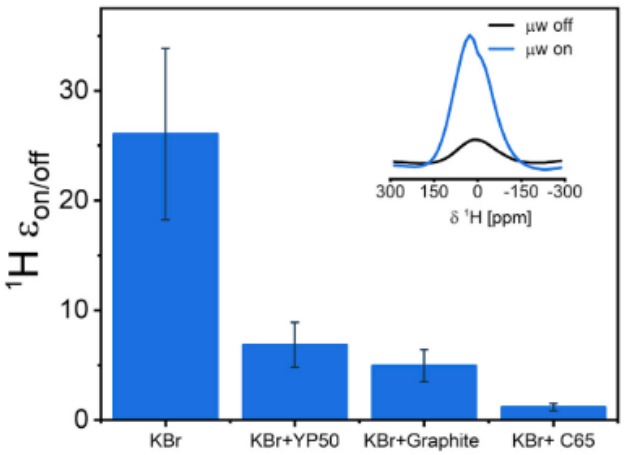

Figure 6.4. Comparison of the ^{1}H enhancement achieved in static DNP-NMR from samples of KBr wetted with TEKPol TCE solution with and without carbon additives: YP-50, graphite and C65. Insert: the μw on and off spectra from a sample mixed with YP-50. Experiments were conducted at 10 K using a polarization time of 60 seconds. This figure is from Leskes and coworkers.[17]

Two processes, the decay of nuclear polarization and the heat dissipation between μw pulses, have an opposite effect on the efficiency of DNP using pulses.[17] This is a big limitation to the use of DNP NMR for any conductive samples. Pulsed DNP limits the exposure of the samples to microwave to only short bursts, allowing for some electronic excitation. M. Leskes and coworkers found pulsed DNP to be a somewhat effective solution to the heating issue, and have achieved positive signal enhancement for very specific carbon systems of moderate conductivity by this method, compared to typical NMR techniques.[17] This seems like a promising technique that may allow for pulsed DNP signal enhancement to provide effective characterization of conductive materials, but is very system specific. I think a lot more

research needs to be done before we can reliably and safely use pulsed DNP NMR as a good technique to characterize conductive carbon materials.

6.4 NMR Results, Discussion, and Future Directions

Previously, 1D ^{15}N cross-polarization $^{15}N\{^{1}H\}$, and dipolar-mediated 2D $^{13}C\{^{15}N\}$ NMR (Figure 6.5) spectroscopy techniques have been employed to differentiate bulk/surface N-heteroatom distributions, and confidently resolve/correlate specific N-heteroatom environments with increased oxygen and sulfur reduction performance (thus catalytic active sites). These techniques have distinguished pyrrolic, graphitic, edge/isolated pyridinic, and paired or defect pyridinic N and C environments with ^{15}N chemical shifts between 150 and 400 ppm, (purple, blue, yellow, and red in Figure 6.5b).[2] Characterizations of the nuclear environments are necessary to understand and characterize the different N and C moieties present in N-carbon materials.

Paramagnetic and Knight shifts, caused by interaction of nuclei with unpaired/**conduction** band electrons, are expected even in non-Fe-containing N-carbons.[41] These shifts will manifest 1) in the material as significantly shortened relaxation rates (T_1), and 2) typically, in the spectrum by displacement and broadening of signals, as was observed. Paramagnetic shifts, caused by interaction of nuclei with unpaired electrons, can cause significant broadening and displacement of NMR signals.[41] Time resolved ^{15}N MAS NMR (Figure 6.5) was used to elucidate very fast relaxing components of the Fe,N-carbons in the typical ^{15}N signal range. ^{15}N NMR signal that could be distinguished by its fast T_1 relaxation rate, presumably due to interaction with unpaired electrons. Some components the pyrrolic and

pyridinic N-heteroatom environments (red and yellow) are faster relaxing as they show up at very short echo times in the Fe,N-carbons (more than in the N-carbon materials), suggesting proximity to pyrrolic and pyridinic N-species to Fe heteroatoms causing fast relaxation and possible small paramagnetic shifts.

More specifically, the spin-lattice relaxation constant is measured by collecting a series of 1D ^{15}N NMR spectra with varied relaxation times. At small relaxation delay times, only very quickly relaxing species, for instance the species affected by the paramagnetic effects of Fe, produce NMR signal intensity, providing information about the proximity of Fe to other species. Theoretically, the intensity of the magnetization of each signal will build to maximum values by the Bloch equation:[7]

$$M(\tau) = M_0\left(1 - e^{\left(\frac{-\tau}{T_1}\right)}\right) \qquad [6.4]$$

Here, M is the magnetization in the direction of the magnetic field, M_0 is the magnitude of magnetization vector, τ is the relaxation delay time, and T_1 is the spin-lattice relaxation value.

The mesoporous salt-templated Fe,N-carbon material contains different types of ^{15}N environments that are near and far from paramagnetic Fe species. In Figure 6.5**,** the solid-state Hahn-echo ^{15}N T_1-filtered MAS NMR spectra show increasing signal intensity with increasing relaxation delay times. The spectra show ^{15}N signals with partially-resolved maxima at 300, 225, 160, and 140 ppm, which are assigned respectively to paired or defect pyridinic (red), isolated pyridinic (yellow), graphitic (blue), and pyrrolic (purple) ^{15}N environments on the basis of their shift positions.[2] Interestingly, for the relaxation-resolved 1D ^{15}N NMR spectrum with a very short relaxation delay of only 0.010 s, there is distinct narrow (20 ppm FWHM) ^{15}N signal at 300 ppm, indicating that this material is in close molecular proximity to the Fe heteroatom sites. This signal is assigned based on shift position, analyses of the ^{15}N T_1

relaxation times, DFT calculations, and comparison to theoretical equations. Additionally, in both the N- and Fe,N-carbon materials, signal intensity begins to appear as early as 100 ms, with more intensity appearing early in the Fe,N-carbon materials, suggesting that a larger fraction of these species are influenced by unpaired or conduction band environment.

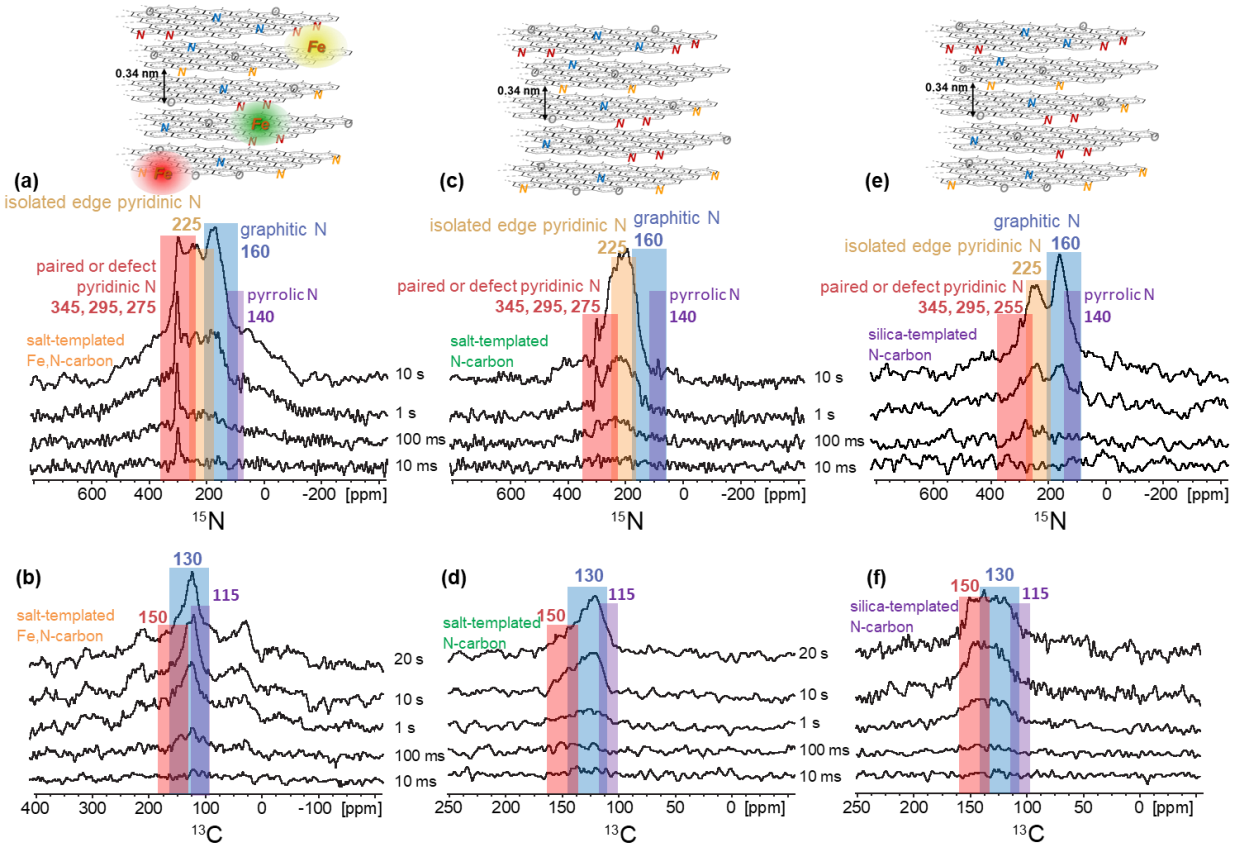

Figure 6.5. Relaxation-resolved 1D ^{15}N and ^{13}C NMR spectra of the **(a,b)** salt-templated Fe,N-carbons, **(c,d)** salt-templated N-carbons, and silica-templated N-carbons **(e,f)**, respectively. The T_1 filtered spectra are shown for relaxation times increasing from 10 ms to 10 s for ^{15}N and 10 ms to 20 s for ^{13}C. Signals are assigned to various N moieties including pyrrolic (purple), graphitic (blue), isolated edge pyridinic (yellow), and paired/defect pyridinic (red) N-C moieties.[3] The presence of paired or defect pyridinic signal intensity at

times as low as 10 ms in the Fe-containing species, and not until 100 ms in the non-Fe containing N-carbons, indicates the presence of paramagnetically influenced nuclear relaxation in the Fe,N-carbon. All experiments were conducted at low temperatures (95 K) on a 400 MHz spectrometer at 8 kHz MAS. Representative schematics of the various Fe- and N-moieties is shown at the top right of each of the spectra, where the colors of the Fe species coordinate with N-$Fe^{II}N_{2+2}$/C (green) and $Fe^{II}N_2C_2$ (yellow).

The T_1-filtered ^{13}C MAS NMR spectra of the salt-templated Fe,N-containing carbon materials can also be found in **Figure 6.5c,b**. Again, the signal assignments are based on previous assignments with ^{13}C chemical shift signals centered around 140, 130, and 115 ppm for pyridinic (red), graphitic (blue), and pyrrolic (purple) species, respectively. In both the N- and Fe,N-carbon materials, signal intensity begins to appear as early as 100 ms, with more intensity appearing early in the Fe,N-carbon materials, suggesting that a larger fraction of these species are influenced by unpaired or conduction band environment.

T_1 values are affected by many factors, but three major contributors are the diamagnetic interactions, paramagnetic interactions as in the Fe-heteroatom containing material, and metallic (Korringa) interactions. The relationship between each of these contributors and the overall T_1 value are shown by this relationship:

$$\frac{1}{T_1(r,T)} = \frac{1}{T_{1,para}(r)} + \frac{1}{T_{1,dia}} + \frac{1}{T_{1,K}(T)} \quad [6.5]$$

Here, $T_1(r,T)$ is the overall spin-lattice relaxation value as influenced by internuclear distance (r) and temperature (T), $T_{1,para}(r)$ is the paramagnetic contribution, $T_{1,dia}$ is the diamagnetic contribution, and $T_{1,K}(T)$ is the Korringa contribution. Spin-lattice diffusion

interactions (diamagnetic) are present in all NMR sensitive systems and characterize the relaxation of nuclei not affected by additional interactions such as paramagnetic or Korringa. Korringa interactions are characteristic of metallic-like behavior of the material and are sensitive to temperature. Paramagnetic interactions arise from the presence of unpaired electrons in the material coupled with nearby nuclear spins. Such interactions significantly decrease the spin-lattice relaxation time for affected nuclei. However, these electron-nuclear couplings exponentially decay (inversely proportional to r^6) with increasing distance from the paramagnetic source, thus the interactions are very localized. Due to the very fast times associated with paramagnetic interactions, I expect paramagnetic contributions dominate the overall T_1 value for very short times and provide information about the influence of fast relaxing Fe species on nearby nuclei, thus I focus on this interaction.

To characterize the T_1 values associated with each of the ^{15}N environments, each of the time-resolved spectra were deconvoluted. The integrated intensities at each time point are then plotted as a function of relaxation time, where the leveling off of integrated intensity indicates return of the nuclear spin magnetization to equilibrium. Each of these data sets were fit with mono-exponential curves as shown by the dashed lines and color-coordinated according to the same three environments in Figure S6.6a. However, I hypothesize that T_1 values of moieties near Fe will be shorter than T_1 values of moieties not affected by Fe, so more than one T_1 value is required to characterize each moiety. The isolated edge pyridinic ^{15}N species (yellow) and especially the paired or defect pyridinic ^{15}N signal (red), were fitted with a much more appropriate bi-exponential fit (solid line). The bi-exponential fit allows for T_1 values affected (paramagnetic, short times) and not affected (diamagnetic, long times) by Fe-heteroatoms to be accounted for and gives a rough estimate of the fractions of the signal associated with each.

The fitting of exponential curves to T_1 filtered data, in Figure 6.6, shows that a bi-exponential fit is a significant improvement to that of the mono-exponential for the ^{15}N paired or defect pyridinic, and moderate improvement for the ^{15}N isolated edge pyridinic species. This suggests that the paired or defect pyridinic ^{15}N species are most affected by the presence of the Fe heteroatoms due to the significantly improved fit of the bi-exponential curve. Bi-exponential fits of the ^{15}N graphitic species and broad 160 ppm signals show negligible

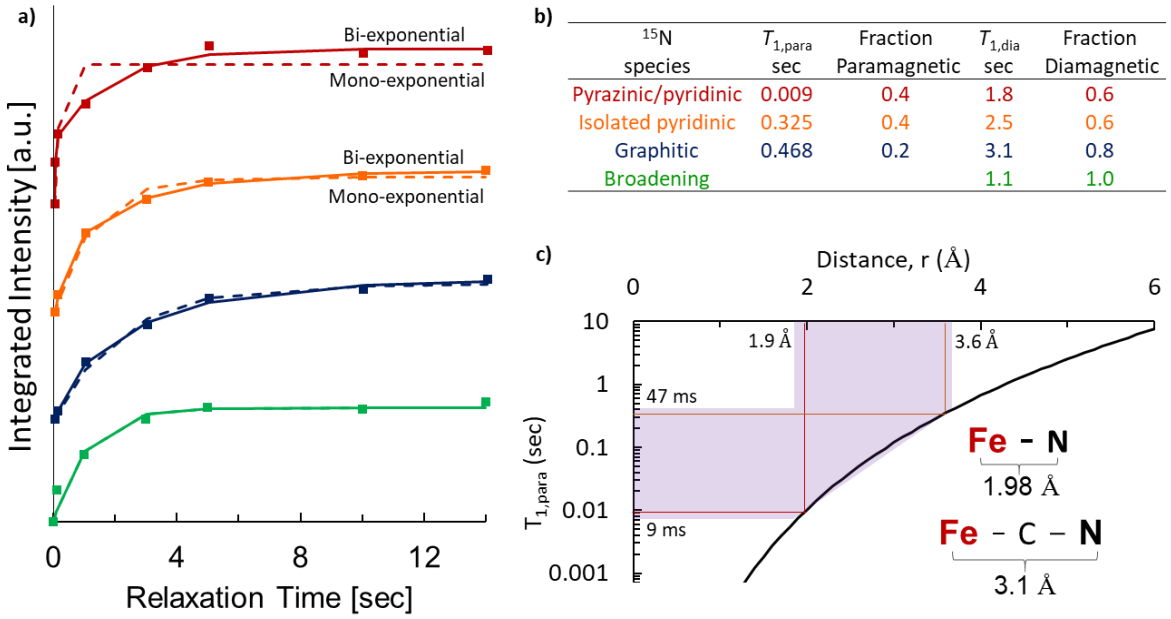

^{15}N species	$T_{1,para}$ sec	Fraction Paramagnetic	$T_{1,dia}$ sec	Fraction Diamagnetic
Pyrazinic/pyridinic	0.009	0.4	1.8	0.6
Isolated pyridinic	0.325	0.4	2.5	0.6
Graphitic	0.468	0.2	3.1	0.8
Broadening			1.1	1.0

Figure 6.6. Spin-lattice relaxation time processing to consider paramagnetic effects of Iron. Spin-lattice relaxation times of paired or defect pyrazinic ^{15}N (red), isolated edge pyridinic ^{15}N (yellow), graphitic ^{15}N (blue), and paramagnetic broadening (green). (a) Plot of integrated intensity of each ^{15}N species as a function of relaxation delay time with bi-exponential curve fits as solid lines and mono-exponential curves fits as dashed lines. (b) Bi-exponential curve fitting parameters of each species showing the diamagnetic and paramagnetic spin-lattice relaxation values and the respective approximate amount of species influenced by the

paramagnetic species. (c) Solomon equation plotted for electron-^{15}N spin pairs, overlaid with the experimentally determined paramagnetic spin-lattice relaxation values and their corresponding electon-^{15}N atomic distances. (c inset) Approximate bond distances of species consistent with these calculations.[42,43]

improvement and thus, are not likely close to Fe species. The table in Figure 6.6b, lists the T_1 values and relative fraction of species in each component as estimated by the constants ($M_{0,para}$, $M_{0,dia}$) associated with the equation for a bi-exponential fit:

$$M(\tau) = M_{0,para}\left(1 - e^{\left(\frac{-\tau}{T_{1,para}}\right)}\right) + M_{0,dia}\left(a - e^{\left(\frac{-\tau}{T_{1,dia}}\right)}\right) \qquad [6.6]$$

Here, $M(\tau)$ is the magnetization in the direction of the magnetic field as a function of allotted relaxation time (τ), $M_{0,para}$ is the magnitude of what I have assumed to be paramagnetic relaxation dominated magnetization vector, $M_{0,dia}$ is the magnitude of the slower relaxing magnetization, $T_{1,para}$ is the fast relaxing spin-lattice relaxation value, and $T_{1,dia}$ is the more slowly relaxing spin-lattice relaxation value.

The atomic distances between an electron-nuclear pairs can be predicted from nuclear spin-lattice relaxation times by the Solomon equation. The equation uses nuclei specific information to predict T_1 relaxation times as a function of internuclear distance between dipole-dipole coupled nuclei:[7,20]

$$\frac{1}{T_{1,para}(r)} = \frac{3}{10}\left(\frac{\mu_0}{4\pi}\right)^2 \frac{\gamma_e^2\gamma_n^2 g^2 \hbar^2}{r^6}\left[\frac{\tau}{1+(\omega_n)^2\tau^2}\right] \qquad [6.7]$$

Where r is the distance between the paramagnetic center and a ^{15}N nucleus, μ_0 is the permittivity of free space, γ_e is the gyromagnetic ratio of the electron, γ_n is the gyromagnetic

ratio of ^{15}N, g is the electron g-factor, $\hbar$ is plank's constant, τ is the electron spin-lattice relaxation constant, and ω_n is the Lamour frequency of ^{15}N.[7,20] Previous experiments by our group have found the electron spin-lattice relaxation constant (τ) to be about 300 μs at 95 K. The Solomon equation does not account for spin-diffusion, but I expect that it is weak in this material. Figure 6.6c plots the ^{15}N paramagnetic spin-lattice relaxation values as a function of electron-^{15}N electronuclear distance predicted by the Solomon equation. Increasing spin-lattice relaxation time is proportional to increasing interatomic distance to the sixth power, thus ^{15}N environments with the shortest relaxation times are closest to paramagnetic centers. This graph is overlaid with the experimentally determined paramagnetic ^{15}N spin-lattice relaxation values (**Figure 6.6b**) and their corresponding electon-^{15}N atomic distances. The experimentally determined paramagnetic spin-lattice relaxations values (purple shaded region) predict ^{15}N-Fe distances of 2 to 4 Å (1 to 2 bond lengths), which are consistent with typical ^{15}N-Fe bond lengths of 2 Å,[42,43] and typical -^{15}N-C-Fe bond lengths of about 3.1 Å.[44] This combination of T_1-filtered measurements and ^{15}N-ernichment allows me to approximate the distances of ^{15}N species from paramagnetic Fe for the first time in Fe,N-containing carbon materials.

Paramagnetic and Knight shifts, caused by interaction of nuclei with unpaired/**conduction** band electrons, are expected even in non-Fe-containing N-carbons.[41] These shifts will manifest 1) in the material as significantly shortened relaxation rates (T_1), and 2) typically, in the spectrum by displacement and broadening of signals. Knight shifts in NMR are caused by interaction of nuclei with **conduction** band electrons.[41] The electrical conductivity of graphitic carbon materials suggests that there is an availability of conduction band electrons in graphitic carbon materials to couple with and influence nuclei to produce Knight shifted signals.

Through spin counting and fast MAS ^{15}N NMR techniques, it was determined that not all signals are seen at typical ^{15}N NMR shift values (150 - 400 ppm).

Each NMR experiment is conducted with a central frequency and can interact with nearby frequencies. However, I suspected that a knight or paramagnetic shift that was associated with this non-Fe-containing conductive N-carbon could be far enough away from the central frequency that it was not being detected by my original experiment. Thus, I conducted the same ^{15}N Hahn-echo fast MAS NMR spectra, moved the central frequency of the experiment, retuned the instrument, and repeated the experiment. An echo experiment was necessary to suppress background in all of these experiments. However, the fast MAS is very important to the success of the experiment. This I because an echo experiment introduces additional time components into the relaxation process which is depended on the spinning speed of the rotor. If a signal is very fast relaxing due to paramagnetic or conductive influence, it may relax too quickly and not bee seen by a slower spinning rotor to the point that the signals relax too quickly to be detected at room temperature and standard 10 kHz MAS NMR.

Solid-state ^{15}N Hahn-echo fast MAS NMR spectra of the salt-templated N- and Fe,N-carbons (Figure 6.7) reveal additional ^{15}N signal that is significantly displaced from the 150-400 ppm range. As expected, signal intensity is present at 300, 225, and 160 ppm which is associated with the same diamagnetic and paramagnetic species as discussed in Chapters 3 and 5. Similar displacements were found in both the Fe- and non-Fe-containing samples, indicating that the shifts are due to the N-carbon material itself (not just paramagnetic Fe), likely interaction with conduction band electrons, suggestive of a Knight shift. The signal around -400 ppm is likely a Knight-shifted signal(s) that arises from ^{15}N-carbon nuclei within the bulk of the conductive graphitic materials, that are coupled to conduction electrons.[30] Very

short recycle delays (10 ms) and a high number of scans ($5x10^6$) were used to detect fast-relaxing species (-400 ppm), thus the relative intensities of the signals shown are not quantitative; separate quantitative analyses indicate that the signal at -400 ppm accounts for only about 0.2% of the total ^{15}N signal intensity.

Fast relaxing and significantly displaced ^{15}N signals in both the Fe,N- and N-carbon materials (Figure 6.7) with shift between -390 and -470 ppm. However, as discussed above, an important distinction between paramagnetic and knight shifted signals is their dependence on temperature. My goal is to understand and characterize the environments of these fast-relaxing ^{15}N species and how they interact with nearby electrons. Due to the very complicated nature of the materials, I chose to work further on the more simple salt-templated non-Fe-containing N-carbons, and understand the nature of the significantly displaced signal. Thus,

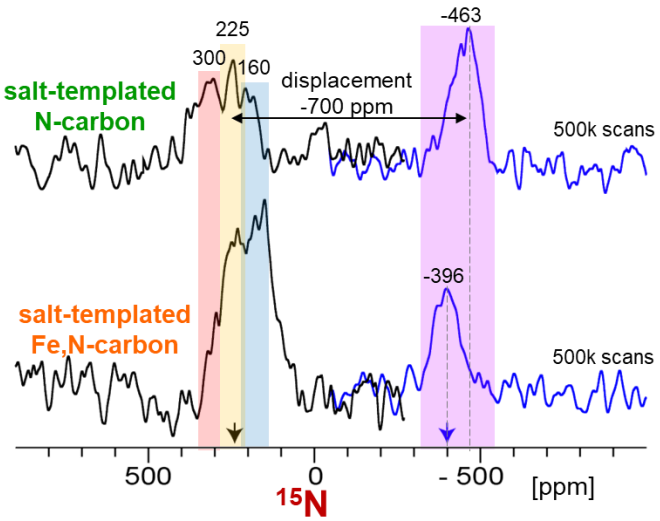

Figure 6.7. Solid-state ^{15}N Hahn-echo MAS NMR spectra of the salt-templated N-(top) and 0.1 mol% Fe,N-carbons acquired at 55 kHz MAS (1.3 mm rotor), 11.7 T at two different spectrometer frequencies centered at 225 ppm (black) and -400 ppm (blue), as indicated by the respective colored arrows. The experiment was conducted at room temperature, but due

to resistive heating the sample temperature was measured to be approximately 336 K, based on the T_1 value of ^{79}Br in polycrystalline KBr, which was added to the MAS rotor as a diluent to reduce the effects of electrical conductivity on the NMR experiments and which also served as a convenient internal temperature reference.

temperature dependent (336 K to 327 K) fast MAS spin-echo ^{15}N NMR experiment were conducted on the salt-templated N-carbon material (Figure 6.8a). The displaced signals are extremely dependent on temperature and fast relaxing, the the displaced signal around -1100 ppm at 336 K but all the way to -2350 ppm at 327 K. With a very small difference in temperature (measured by ^{79}Br relaxation), the signal shifted so significantly that it had to be measured at a different central frequency. The ^{15}N chemical shift values are then plotted as a function of temperature and found to have a very strong temperature dependence of 140 ppm/K, this has not been reported for any similar materials. The spin-lattice relaxation rates of the of displaced signals are plotted and also extremely temperature dependent (-1.9ms/K). The very strong chemical shift dependence on temperature suggests that this significantly displaced signal are experiencing Knight shift behavior. While these results are fascinating, they are preliminary. Similar experiments need to be conducted on the Fe,N salt-templated carbons as a start. However, it is clear that the presence of unpaired or conduction band electrons are impacting the NMR chemical shifts and need to be understood before confident conclusions can be made.

6.5 EPR for N- and Fe,N-carbon materials

Characterizations of the nuclear environments are necessary to understand and characterize the different N and C moieties present in N-carbon materials. My goal remains to understand and characterize the environments of these fast relaxing ^{15}N species and how they interact with nearby electrons. While NMR enables understanding of these complicated electron-nuclear interactions from the perspective of the NMR active nuclei, EPR enables new insights by directly probing electron-nuclear interactions from the perspective of the electrons. Unpaired electrons are expected to interact with near-by nitrogen and iron environments, as first detected by the fast relaxing ^{15}N species in ^{15}N NMR. To probe the interaction between unpaired elections and nearby nuclei, I have outlined the use of low temperature and pulsed EPR techniques (ESEEM) here. In the N-carbon materials there should be EPR signal from ^{14}N (S=1), or ^{15}N (S=1/2) when that sample is ^{15}N-enriched. In the Fe,N-carbon materials, there should be additional signal due to the presence of paramagnetic Fe. All samples will have conduction band electrons, which should interact with the EPR active nuclei. The following EPR techniques should be able to elucidate the molecular and electronic structures of paramagnetic species in my graphitic carbon materials.

6.5.1 Continuous-Wave EPR and variable atmospheres

Before advanced EPR techniques can be explored, the simplest experiment (CW room temperature EPR) is required to confirm that signal can be achieved in these samples. The advantages of CW EPR include simplicity and high signal to noise ratios achieved.[16] However, the challenges with CW EPR can include significant signal overlap and broadening[45] which is why more techniques are explored. In the case of the N- and Fe,N-

carbons, the materials are hypothesized to interact with the water and oxygen in air.[46] The presence of oxygen could create additional interactions with EPR active oxygen species which could alter the results. Thus, for CW experiments I propose to conduct them both with atmospheric conditions and dehydrated in a nitrogen atmosphere. I expect that the inert atmosphere sample may have less broad signal intensity.

6.5.2 Low/Variable Temperature CW EPR

To study the effects of temperature on g-value and linewidth, as well as investigate the presence of a Curie temperature and metal-to-insulator-like transition,[45,47] I will conduct variable temperature EPR. Linewidths of the spectra and g-values are typically influenced by temperature while in the insulator regime (below about 70 K Curie transition), and independent of temperature in the metal regieme.[47] With low temperature, atomic scale motion is reduced and linewidths are expected to broaden. However, low temperature EPR is also used to increase signal intensity, taking advantage of the effect of temperature on the Boltzmann distribution of spins. Decreasing the temperature will likely increase the T_1 value, which is already quite slow for EPR of metal containing materials and can increase the experimental time. These factors are competing, so to see if the advantages outweigh the disadvantages of low temperature, I suggest variable temperature experiments. This will again be a simple CW EPR experimental set-up. I will use liquid nitrogen (or helium of possible), to cool samples down while a probe heater will be used to regulate temperature.

6.5.3 Pulsed EPR for Echo Detection

Only samples with inhomogeneously broadened spins, caused by physical differences in spin distributions, will have signals that can be detected by EPR echo sequences.[16] The graphitic N- and Fe,N-carbons are known to have a variety of different N- and Fe,N-bonding environments, as shown by NMR, so I expect that there will be echo detected signal specifically between the ^{14}N or ^{15}N species and nearby unpaired and conduction band electrons. Echo detection experiments move signal away from the instrument deadtime which is useful for signal detection of fast relaxing species. The carbon materials contain fast relaxing nuclear species (for the NMR timescale) which are presumably caused by fast-relaxing unpaired electrons nearby, thus it is likely that this feature of echo detection experiments will be useful to my measurements. I will likely start with *the primary two-pulse echo* sequence as it is fast and will indicate the presence of echo detected species. I with the use the *stimulated three-pulse echo* sequence to 1) confirm the presence of echo signals, and 2) stretch out the time of the fast-relaxing FID. Once the presence of echo signals is confirmed, I can move on to ESEEM experiments.

6.5.3 ESEEM – estimating paramagnetic/N centers

To characterize the interactions between paramagnetic centers and nearby nuclei, I will think that ESEEM experiments will be critical. The ESEEM technique observes nuclear modulation from which hyperfine couplings between paramagnetic centers and nearby nuclei can be discerned. For a nucleus to be detected in the ESEEM spectra, it must be near a paramagnetic center. In the carbon materials there is a variety of EPR active nuclei that include a small amount of ^{1}H, up to 25% ^{13}C enrichment, up to 100% ^{14}N and ^{15}N enrichment, and a

small amount Fe with ^{57}Fe at natural abundance. I propose to start with 2p-ESEEM (two-pulse electron spin echo envelope modulation) experiments with a simple pi/2-pi-echo pulse sequence. This is done by applying a pi/2 pulse on spins which are aligned in a magnetic field, and allowing the precession of spins to begin for some time (τ) in which different spins will relax at different rates (dephasing). Then, a pi pulse is applied which flips the spins by 180 degrees and the same time (τ) will pass before detection of the FID begins. Because the same amount of time passes, but the spins are going the opposite direction, the fastest spins and slower spins will meet backup after the time (τ) has passed, essentially undoing the dephasing that passed after the first pulse. Thus, the spins relaxing at difference rates will all have been collected and measured simultaneously. The challenge with 2p-ESEEM that may arise is poor resolution due to the variety of paramagnetic nuclei present. In this case I suggest using a 3p-ESEEM experiment which should help mitigate this issue.[15] In this experiment the electrons are aligned with the magnetic field and a pi/2 pulse is applied and allowed to relax for a time (τ) while dephasing occurs. A second pulse is then applied and allowed to relax for τ plus an amount of time T which is varied throughout the experiment. Finally, a third pi/2 pulse is applied, the time τ is allowed to pass, and then the echo FID is detected.

6.6 Preliminary EPR results, predictions, and hypotheses

The results that I have for EPR data are all rather preliminary. This is why I have proposed and suggested many experiments based on the background that I have provided. In this section I show preliminary results, and provide additional hypotheses supported by experimental data, literature data, simulated data or calculations.

6.6.1 Materials

I have found that using different mesopore templating agents results in varied N-heteroatom contents, distributions and types of N environments, conductivity, and ORR activity (as discussed in Ch 3 and 5). For all of these material variations, the performance is increased with the incorporation of Fe-heteroatoms. Thus, the materials I examine are salt- or silica-templated, Fe,N- or N-carbons. Varying the sample enrichments gives me a preliminary answer as to which species are coupled to the unpaired electron species. Between both enriched and non-enriched samples, I expect to achieve the same g-values with different splittings by varying the enrichment of samples. For instance, if there is interaction between electrons and C nuclei, we may not see signal in a non-enriched sample as ^{12}C is a S=0 nucleus. However, when I use ^{13}C-enriched samples which are S=1/2, we may see a new signal arising. Finally, the N- and Fe,N-carbons are used to catalyze the oxygen reduction reaction (ORR), so when exposed to air, I suspect that there could be interaction with some type of oxygen radical, thus I will test both with atmospheric conditions and dehydrated in a nitrogen atmosphere.

6.6.2 Continuous-Wave EPR and variable atmospheres

The simplest EPR experiment (CW room temperature EPR) is measured first and is required to check if signal can be achieved. The electrical conductivity of graphitic carbon materials suggests that there is an availability of electrons in graphitic carbon materials to couple with nuclei and produce EPR signal. Previous literature also suggests the viability of EPR for graphitic carbon materials. EPR was first applied for the study of graphene in 2009 by L.Ćirić et. al..[47] They measured CW EPR spectra that composed of a single signal with a

g-value of 2.004, which they attribute to interactions between paramagnetic defects and conduction band electrons in the graphene.[47] Many studies follow with similar results of a single narrow signal with g-values between graphene quantum dots with a g-value of 2.0029[48] and graphene sheets with g-values between 2.0015 and 2.0097[45], among many others. However, these samples had little to no N in most cases, where as my material is a graphitic carbon with a significant enough amount of N to see electron-nitrogen correlations. Investigations of graphitic carbon nitrides have found that there are two overlapping g-values suggesting an axial symmetry, like CW EPR experiments by Liu et al. (Figure 6.8).[49] In this paper the two g-values are 2.0034 and 2.0028. The g-value of 2.0034 was attributed to unpaired electrons on sp^2-carbon atoms within the π-conjugated aromatic rings, and the shoulder with a g-value of 2.0028 was attributed to C-N groups.[49] There are a handful of literature examples of basic CW EPR of N-containing carbon materials with narrow signals.

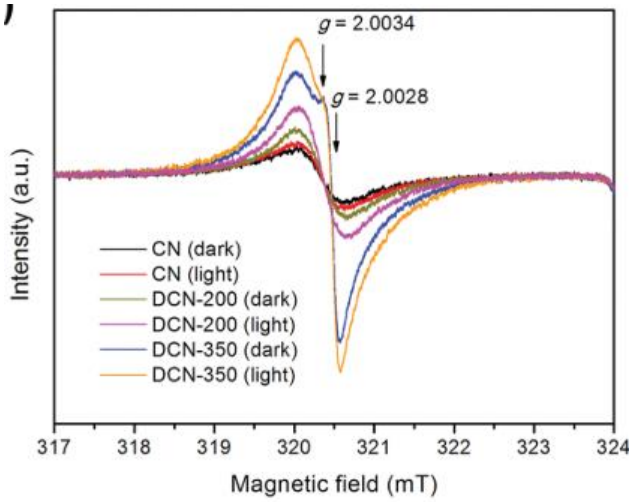

Figure 6.8. This figure is from Liu et al. of room-temperature EPR spectra for CN measured with and without the light irradiation. Two g-values are assigned. This figure is taken from Zhang et. al., 2012.[49]

and g-values around 2.003 G to 3400 G.[49–54] Because my materials contain a significant amount (5-25 wt%[2]) of ^{14}N (S=1) within the graphitic carbon, I hypothesize that there is likely more than one g-value or signal.

CW EPR in atmospheric and under a nitrogen atmosphere are used to look for EPR signal and examine the presence/effect of paramagnetic species present. The CW EPR experiment for my Fe,N- and N-carbons at room temperature prepared in an inert nitrogen atmosphere (a) and in standard atmosphere (b) can be seen in Figure 6.9 for the salt- or silica-templated, Fe,N- or N-carbons of varied enrichments as indicated, as previously discussed. Between the standard atmosphere and inert nitrogen atmosphere samples of the respective samples distinguished by color. When comparing the signals of similar samples under air and nitrogen atmospheres, there does not seem to be a significant change in EPR signal shape. Thus, oxygen

from the air is likely not adsorbing onto the material surface in significant quantities, and the EPR signals achieved are achieved from internal species.

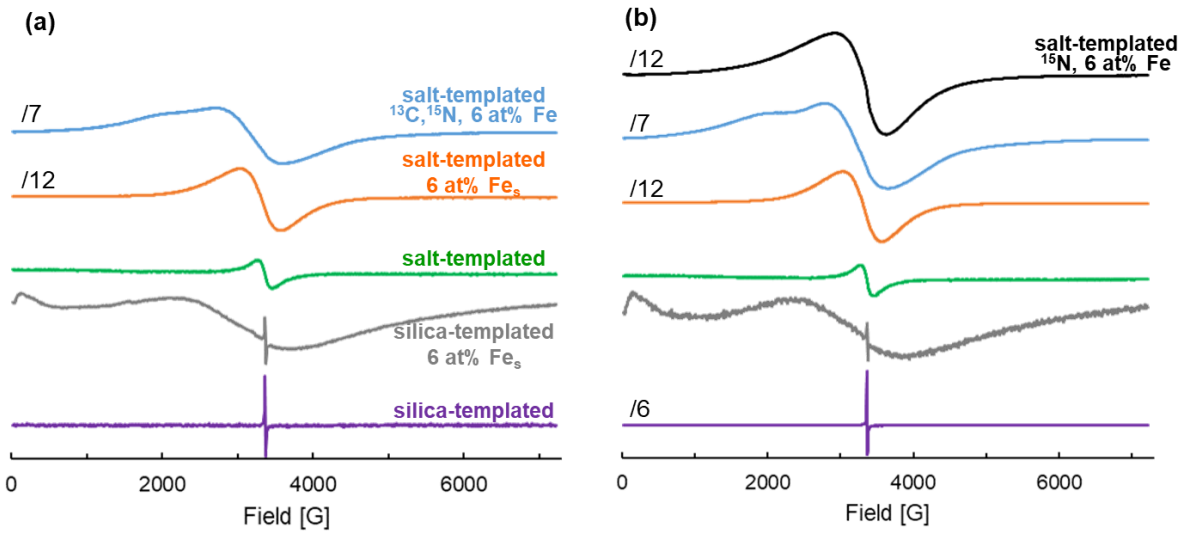

Figure 6.9. CW EPR experiment for samples at room temperature prepared in an inert nitrogen atmosphere (a) and in standard atmosphere (b) of the salt- or silica-templated N-carbons (green and purple), the salt- or silica-templated Fe,N-carbons (grey and orange), or the salt-templated Fe,N-carbons with ^{13}C,^{15}N- and ^{15}N-enrichments (blue and black).

Now that I have discussed the variations in CW EPR spectra between the heteroatom contents of the carbon materials, I will comment on the differences between the preparation methods or templates. The silica-templated sample appears to most closely match with previous literature investigations of a single narrow signal, as I discussed at the beginning of this section. Moving from the silica-templated N-carbon, signal broadening is notable when comparing the salt-templated samples, and significant when comparing with Fe-containing

samples. The silica-templated material is less conductive and has a more narrow signal than the more highly conductive salt-templated material, suggesting that changing the conductivity of the material has affected nuclear-electron interactions (with the conduction band). Additionally, all Fe-containing materials have much more broad background signals than the non-Fe-containing materials, likely due to the introduction of unpaired electron spins. Generally, there appears to be a single signal with g-value around 2.042. However, (especially in the salt-templated Fe-containing samples) there could be multiple g-values that are currently broad and overlapping with similar g-values, as has previously been observed by Liu et al..[49] Importantly, the presence of EPR ^{13}C-enriched-nuclei (as opposed to non-EPR-active ^{12}C-nuclei) does appear to affect the signal, possibly introducing an additional signal with a similar g-value. This is suggestive that Non-Lorentzian lineshapes are attributed to unresolved interactions with paramagnetic nuclei.[55] Because the signals are so broad, CW EPR spectra do not seem well resolved enough to draw conclusions about the symmetry of the material. Decreasing temperature can decreased broad lines. Using an echo spectrum should mitigate homogeneous broadening and show more narrow signals, both of which I discuss in the upcoming sections.[15]

6.6.3 Low/Variable Temperature CW EPR

For graphitic carbon materials low/variable temperature EPR tends to exhibit specific patterns. C´iric et. al. found, and Barbon et. al. confirmed, for graphitic carbon materials a linear dependence between temperature and spin susceptibility below the Curie temperature, at which the material undergoes a metal-to-insulator-like transition.[45,47] The existence of such

a transition was suggested by variable temperature magnetic susceptibility[56] and electrical conductivity measurements[57] conducted on other N-containing carbon materials.

Linewidths of the spectra and g-values are found to be influenced by temperature, following different trends above and below the about 70 K Curie transition, as demonstrated by Ciric et. al. (Figure 6.10).[47] The linewidth has temperature independent contributions from conduction band electrons and dipolar broadening starting around 70 K from localized spins. Below 70 K, the g-value decreases with decreasing temperature. Above the 70 K Curie transition, the g-factor is essentially independent of temperature. At temperatures above 70 K, the electrons are delocalized thus the material is conductive and electrons freely throughout (like a metal). Because the electrons are delocalized the temperature does not affect the linewidths and g-factors. At temperatures below 70 K the electrons are no longer free to conduct as they have begun to localize (insulator-like regime). However, the extent to which they are localized (electron mobility) is dictated by temperature, thus, as temperature decreases the mobility decreases and is manifested by changes in linewidth and g-factor. Because the N-carbon materials are also graphitic carbon, I expect to encounter a metal-to-insulator-like transition at a Curie temperature, likely around a similar temperature value. This is my hypothesis and supporting literature arguments, however, experiments must be run on the N-carbon materials to observe such relationships.

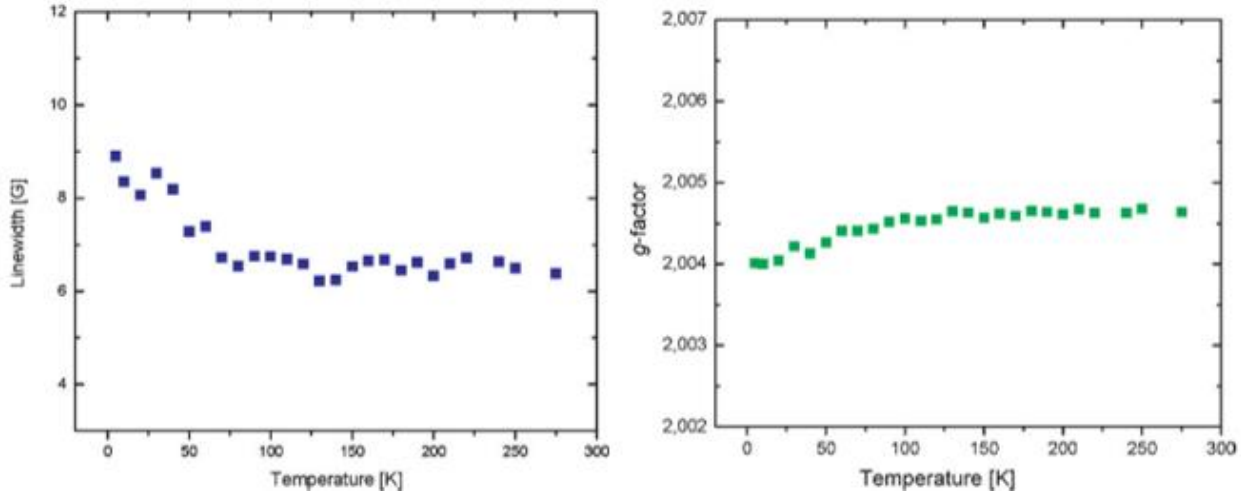

Figure 6.10. Temperature dependence of (a) signal linewidth, and (b) g-value of a graphitic carbon material as measured by CW EPR. The metal-to-insulator transition at the Curie value is observed around 70 K. These measurements are from Ciric et. al..[47]

6.6.4 Pulsed EPR for Echo Detection

Pulsed EPR with echo detection should 1) confirm the presence of echo signals indicating that advanced ESEEM techniques may be possible, and 2) stretch out the time of the fast-relaxing FID. In an echo experiment, only inhomogeneously broadened signals remain which should increase the signal resolution of the experiment if I have multiple overlapping signals, which I have assumed due to the broad and poorly resolved signals I have measured (Figure 6.9). Additionally, as discussed extensively above, the solid-state NMR data suggests that there are a variety of N-carbon environments, again suggesting that there should be multiple signals distinguishable via pulsed EPR techniques. A good example of this in literature is an EDEPR experiment by Barbon et al. (Figure 6.11). Here an integrated CW experiment is compared to an EDEPR experiment, in which the resolution is significantly increased as two

signals of different widths are evident. I expect similarly increased resolution and a number of signals to be resolved in my samples with this type of experiment. Because there are multiple species in my experiments as established by NMR, there should be multiple signals resolved by ERP. If I observe resolved signal intensity, I can attempt fitting the spectrum with EasySpin modeling.

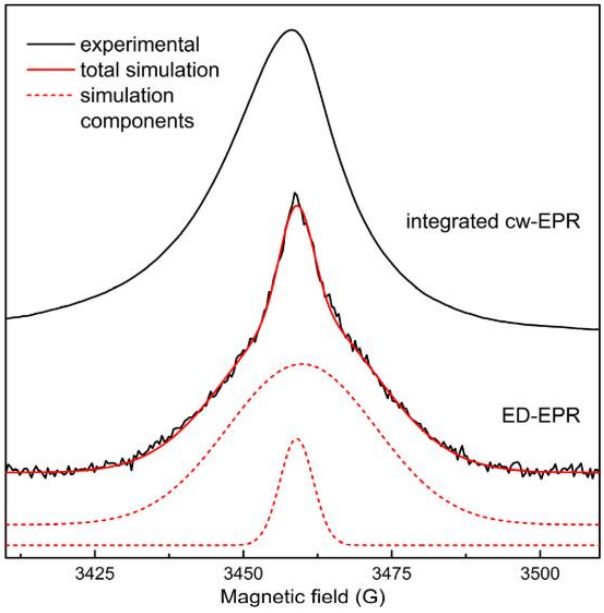

Figure 6.11. Integrated cw-EPR spectrum (top) and EDEPR spectrum (second, black) of a graphitic carbons sample 80 K. For the EDEPR, the tau was 200 ns. The simulation of the EDEPR spectrum (red) is sum of two Gaussian components is shown with the two separated components (dashed red lines). This figure is from Barbon et al., 2017.[45]

6.6.3 Pulsed EPR – ESEEM

Once the ability to detect and echo spectra has been confirmed, techniques like ESEEM can be used to characterize and understand the interactions between the unpaired electrons and the paramagnetic nuclei. Barbon et al. conducted ESEEM EPR experiments on graphitic carbon materials with ^{1}H and ^{13}C nuclear spins, which with 0.34 T magnetic field should yield signal intensity around 14.5 MHz and 3.6 MHz, respectively (Figure 6.12). The presence of these signals indicates the proximity of unpaired electrons to each of these respective nuclei. In my material I expect electron proximity to ^{1}H and ^{13}C nuclei, as well as proximity to ^{14}N or ^{15}N nuclei, depending on the sample, thus an additional signal with a slightly lower frequency than the ^{13}C signal. However, there should be very few ^{1}H's present in the sample, thus the signal at 14.5 MHz will be significantly less intense than in my spectra. This ESEEM EPR technique should be able to elucidate which species are near enough to paramagnetic centers to be affect by the unpaired electron. I will correlate my NMR and EPR results with

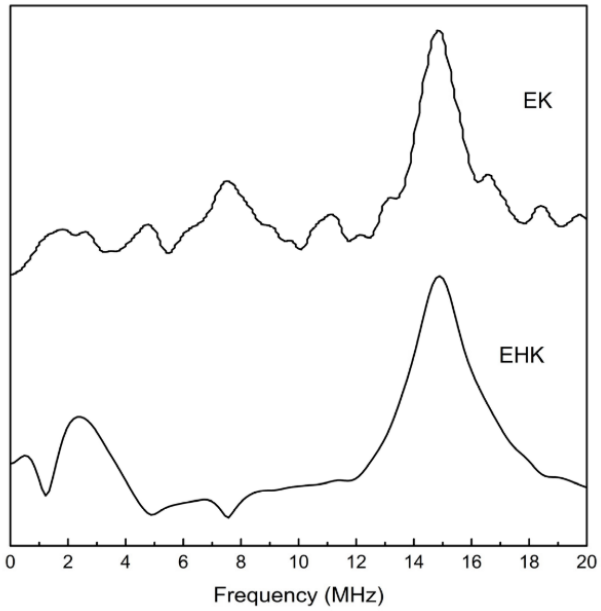

Figure 6.12: 2p-ESEEM spectra of samples EH and EHK recorded at 80 K and at a magnetic field of 3460 G. At this field the nuclear frequencies of protons and 13C are respectively 14.7 MHz and 3.7 MHz. This figure is from Barbon et al., 2017.[45]

ORR activity to determine the electron-nuclear environments likely functioning as ORR active sites. This could lead to additional advances EPR techniques like HYSCOR, which would also allow me to estimate distances between the unpaired electron and nuclei (which I have done by NMR and my collaborator has done by DFT) and would be exciting to confirm by EPR.

6.7 Conclusions and Future Work

Solid-state NMR experiments and analyses elucidate the N-environments present in the N- and Fe,N-carbon material, which are correlated with increased electrochemical activity. NMR of N- and Fe,N-heteroatom containing graphitic carbon materials suggest the presence of paramagnetic and knight shifted species due to electron-nuclear interaction, which cause NMR shift displacements and EPR signal. While NMR can be used to characterize the nuclear environments formed, EPR can correlate the various N,(and other)-heteroatom moieties with nearby unpaired or conduction band electrons. Preliminary EPR experiments and analyses indicate that differences in heteroatom presence, porogen material, and even ^{13}C- and ^{15}N-enrichment all affect the EPR spectra. The EPR experiments that I have outlined above should elucidate the interactions between these unpaired and conduction band electrons and EPR active nuclei. These interactions are important to understanding the material as both active N sites and conductivity (electron presence) are crucial components to catalyzing the reduction reaction. Finally, I propose to conduct variable temperature SQUID measurements to correlate the changing of magnetic moment with the variable temperature NMR (chemical shift) and EPR (conductivity) interactions. These results should enable not only identification of the types, atomic environments, and distributions of ^{15}N heteroatoms in mesoporous Fe,N- and N-carbons, but also an understanding of how the conductivity and paramagnetic properties of the materials affect their macroscopic performance and atomic level characterization.

6.8 References

1. Griffin, J. M., Forse, A. C. & Grey, C. P. Solid-state NMR studies of supercapacitors. *Solid State Nucl. Magn. Reson.* **74**–**75**, 16–35 (2016).
2. Becwar, S. M. *et al.* Atomic-scale understanding of the oxygen and sulfur reduction activities of mesoporous N-carbon electrocatalysts. *Nat. Mater*. to be submitted (2022).
3. Becwar, S. M. *et al.* Correlating macroscopic compositions and structures with oxygen and sulfur reduction activities of mesoporous-Fe,N-carbon electrocatalysts. *J. Am. Chem. Soc.* to be submittied (2022).
4. Pell, A. J., Pintacuda, G. & Grey, C. P. Paramagnetic NMR in solution and the solid state. *Prog. Nucl. Magn. Reson. Spectrosc.* **111**, 1–271 (2019).
5. Mineo, H. & Fujimura, Y. Quantum Design of Pi-Electron Ring Currents in Polycyclic Aromatic Hydrocarbons: Parallel and Antiparallel Ring Currents in Naphthalene. *J. Phys. Chem. Lett.* 2019–2025 (2017).
6. Forse, A. C., Griffin, J. M., Presser, V., Gogotsi, Y. & Grey, C. P. Ring Current Effects: Factors Affecting the NMR Chemical Shift of Molecules Adsorbed on Porous Carbons. *J. Phys. Chem. C* **118**, 7508–7514 (2014).
7. Levitt, M. H. *Spin Dynamics: Basics of Nuclear Magnetic Resonance*. (John Wiley & Sons, 2008).
8. Gomes, J. A. N. F. & Mallion, R. B. Aromaticity and ring currents. *Chem. Rev.* **101**, 1349–1383 (2001).
9. Johansson, M. P., Jusélius, J. & Sundholm, D. Sphere currents of buckminsterfullerene. *Angew. Chemie - Int. Ed.* **44**, 1843–1846 (2005).
10. Assis, A. K. T. & Chaib, J. P. M. C. *Ampère's Electrodynamics*. (C. Roy Keys Inc.,

2015).

11. Merino, G., Heine, T. & Seifert, G. The induced magnetic field in cyclic molecules. *Chem. - A Eur. J.* **10**, 4367–4371 (2004).

12. Jameson, C. J. & Buckingham, A. D. Molecular electronic property density functions: The nuclear magnetic shielding density. *J. Chem. Phys.* **73**, 5684–5692 (1980).

13. Bieger, W., Seifert, G., Eschrig, H. & Grossmann, G. LCAO Xα calculations of nuclear magnetic shielding in molecules. *Chem. Phys. Lett.* **115**, 275–280 (1985).

14. Dvinskikh, S. V., Castro, V. & Sandström, D. Heating caused by radiofrequency irradiation and sample rotation in 13C magic angle spinning NMR studies of lipid membranes. *Magn. Reson. Chem.* **42**, 875–881 (2004).

15. Aubert, G., Jacquinot, J. F. & Sakellariou, D. Eddy current effects in plain and hollow cylinders spinning inside homogeneous magnetic fields: Application to magnetic resonance. *J. Chem. Phys.* **137**, (2012).

16. Yesinowski, J. P., Ladouceur, H. D. D., Purdy, A. P. P. & Miller, J. B. B. Electrical and ionic conductivity effects on magic-angle spinning nuclear magnetic resonance parameters of CuI. *J. Chem. Phys.* **133**, 234509 (2010).

17. Svirinovsky-Arbeli, A. *et al.* The effects of sample conductivity on the efficacy of dynamic nuclear polarization for sensitivity enhancement in solid state NMR spectroscopy. *Solid State Nucl. Magn. Reson.* **99**, 7–14 (2019).

18. Goddard, Y. A., Vold, R. L., Cross, J., Espe, M. P. & Hoatson, G. L. Observation of a deuteron nuclear magnetic resonance Knight shift in conductive polyaniline. *J. Chem. Phys.* **122**, (2005).

19. Bastow, T., Forwood, C., Gibson, M. & Smith, M. Local site symmetry and electronic

structure of trialuminide and related intermetallic alloys probed by solid-state NMR. *Phys. Rev. B - Condens. Matter Mater. Phys.* **58**, 2988–2997 (1998).

20. Solomon, I. Relaxation Processes in a System of Two Spins. *Phys. Rev.* **99**, 559–566 (1955).

21. Bloembergen, N. Proton relaxation times in paramagnetic solutions. *J. Chem. Phys.* **27**, 572–573 (1957).

22. Kowalewski, J., Nordenskiöld, L., Benetis, N. & Westlund, P. O. Theory of nuclear spin relaxation in paramagnetic systems in solution. *Prog. Nucl. Magn. Reson. Spectrosc.* **17**, 141–185 (1985).

23. Mcconnell, H. M. & Robertson, R. E. Isotropic nuclear resonance shifts. *J. Chem. Phys.* **29**, 1361–1365 (1958).

24. Mcconnell, H. M. & Robertson, R. E. Comments on 'Theory of isotropic hyperfine interactions in π-electron radicals'. *J. Chem. Phys.* **28**, 991–992 (1958).

25. Grey, C. P. & Dupré, N. NMR studies of cathode materials for lithium-ion rechargeable batteries. *Chem. Rev.* **104**, 4493–4512 (2004).

26. Clément, R. J. *et al.* Spin-transfer pathways in paramagnetic lithium transition-metal phosphates from combined broadband isotropic solid-state MAS NMR spectroscopy and DFT calculations. *J. Am. Chem. Soc.* **134**, 17178–17185 (2012).

27. Kim, J. *et al.* Linking local environments and hyperfine shifts: A combined experimental and theoretical 31P and 7Li solid-state NMR study of paramagnetic Fe(III) phosphates. *J. Am. Chem. Soc.* **132**, 16825–16840 (2010).

28. Strobridge, F. C. *et al.* Characterising local environments in high energy density Li-ion battery cathodes: A combined NMR and first principles study of LiFexCo1-xPO4. *J.*

Mater. Chem. A **2**, 11948–11957 (2014).

29. Xu, X. *et al.* Identifying the Critical Role of Li Substitution in P2-Nax[LiyNizMn1-y-z]O2 (0 < x, y, z < 1) Intercalation Cathode Materials for High Energy Na-ion Batteries. *Chem. Mater.* 1260–1269 (2014).

30. Knight, W. D. Nuclear Magnetic Resonance Shift in Metals. *Phys. Rev.* **76**, 1259–1260 (1949).

31. Proctor, W. G. & Yu, F. C. The dependence of a nuclear magnetic resonance frequency upon chemical compound. *Physical Review* **77**, 717 (1950).

32. Saito, R., Tsukada, M., Kobayashi, K. & Kamimura, H. Nuclear magnetic resonance in higher-stage graphite intercalation compounds. *Phys. Rev. B* **35**, 2963–2971 (1987).

33. Kume, K., Maniwa, Y., Suematsu, H., Iye, Y. & Tanuma, S. High resolution 13C NMR in HOPG intercalation compounds. *Synth. Met.* **8**, 69–75 (1983).

34. Korringa, J. Nuclear magnetic relaxation and resonnance line shift in metals. *Physica* **16**, 601–610 (1950).

35. Ansermet, J. P., Slichter, C. P. & Sinfelt, J. H. Solid state NMR techniques for the study of surface phenomena. *Prog. Nucl. Magn. Reson. Spectrosc.* **22**, 401–421 (1990).

36. Cho, S. H. *et al.* Syntheses of Colloidal F:In2O3 Cubes: Fluorine-Induced Faceting and Infrared Plasmonic Response. *Chem. Mater.* **31**, 2661–2676 (2019).

37. Overhauser, A. W. Polarization of nuclei in metals. *Phys. Rev.* **92**, 411–415 (1953).

38. Sagane, R. & Dudziak, W. The dependence of the 33-Mev Pi+ production cross section on atomic number. *Phys. Rev.* **92**, 212 (1953).

39. Wind, R. A., Duijvestijn, M. J., van der Lugt, C., Manenschijn, A. & Vriend, J. Applications of dynamic nuclear polarization in 13C NMR in solids. *Prog. Nucl. Magn.*

Reson. Spectrosc. **17**, 33–67 (1985).

40. Leskes, M. *et al.* Surface-Sensitive NMR Detection of the Solid Electrolyte Interphase Layer on Reduced Graphene Oxide. *J. Phys. Chem. Lett.* **8**, 1078–1085 (2017).

41. Yesinowski, J. P., Berkson, Z. J., Cadars, S., Purdy, A. P. & Chmelka, B. F. Spatially correlated distributions of local metallic properties in bulk and nanocrystalline GaN. *Phys. Rev. B* **95**, (2017).

42. Zitolo, A. *et al.* Identification of catalytic sites for oxygen reduction in iron- and nitrogen-doped graphene materials. *Nat. Mater.* **14**, 937–942 (2015).

43. Suzuki, N. *et al.* Novel Iron Porphyrin-Alkanethiolate Complex with Intramolecular NH,,,S Hydrogen Bond: Synthesis, Spectroscopy, and Reactivity. *J. Am. Chem. Soc.* **121**, 11571–11572 (1999).

44. Willans, M. J., Wasylishen, R. E. & McDonald, R. Polymorphism of potassium ferrocyanide trihydrate as studied by solid-state multinuclear NMR spectroscopy and X-ray diffraction. *Inorg. Chem.* **48**, 4342–4353 (2009).

45. Barbon, A. & Tampieri, F. Identification of slow relaxing spin components by pulse EPR techniques in graphene-related materials. *AIMS Mater. Sci.* **4**, 147–157 (2017).

46. Fechler, N. *et al.* Eutectic Syntheses of Graphitic Carbon with High Pyrazinic Nitrogen Content. *Adv. Mater.* **28**, 1287 (2016).

47. Ćirić, L. *et al.* Towards electron spin resonance of mechanically exfoliated graphene. *Phys. Status Solidi Basic Res.* **246**, 2558–2561 (2009).

48. Li, Q., Noffke, B. W., Liu, Y. & Li, L. S. Understanding fundamental processes in carbon materials with well-defined colloidal graphene quantum dots. *Curr. Opin. Colloid Interface Sci.* **20**, 346–353 (2015).

49. Liu, G. *et al.* In Situ Bond Modulation of Graphitic Carbon Nitride to Construct p–n Homojunctions for Enhanced Photocatalytic Hydrogen Production. *Adv. Funct. Mater.* **26**, 6822–6829 (2016).

50. Arčon, D. *et al.* Origin of magnetic moments in carbon nanofoam. *Phys. Rev. B - Condens. Matter Mater. Phys.* **74**, 1–9 (2006).

51. Shenderova, O. A. *et al.* Nitrogen control in nanodiamond produced by detonation shock-wave-assisted synthesis. *J. Phys. Chem. C* **115**, 14014–14024 (2011).

52. Kausteklis, J. *et al.* Electron paramagnetic resonance study of nanostructured graphite. *Phys. Rev. B - Condens. Matter Mater. Phys.* **84**, (2011).

53. Janson, C. & Palmqvist, A. E. C. Improved Oxygen Reduction Activity of Transition Metal-Chelating Ordered Mesoporous Carbon Fuel Cell Catalysts by Milder Template Removal. *Catal. Letters* **149**, 1297–1304 (2019).

54. Janson, C. & Palmqvist, A. E. C. Influence of Precursor Functional Groups on the Formation and Performance of Iron-Coordinating Ordered Mesoporous Carbons as Fuel Cell Catalysts. *J. Phys. Chem. C* **121**, 21827 (2017).

55. Tampieri, F., Silvestrini, S., Riccò, R., Maggini, M. & Barbon, A. A comparative electron paramagnetic resonance study of expanded graphites and graphene. *J. Mater. Chem. C* **2**, 8105–8112 (2014).

56. Błoński, P. *et al.* Doping with Graphitic Nitrogen Triggers Ferromagnetism in Graphene. *J. Am. Chem. Soc.* **139**, 3171–3180 (2017).

57. Wang, H. *et al.* Synthesis of single-crystal-like nanoporous carbon membranes and their application in overall water splitting. *Nat. Commun.* **8**, 13592 (2017).

7. Synthesis and structural properties of a 2D Zn(II) dodecahydroxycloso-dodecaborate coordination polymer

This chapter is adapted from a submitted manuscript. This paper describes the synthesis and characterization of a 2D coordination polymer composed of a dianionicperhydroxylated boron cluster ($B_{12}(OH)_{12}^{2-}$), coordinated to Zn(II). This is the first example of a transition metal-coordinated to a $B_{12}(OH)_{12}^{2-}$-compound. The material was studied and characterized prior to and after thermal activation via XRD, FTIR, SEM, TGA, and solid-state NMR, revealing a 2D coordination polymer composed of sheets of Zn(II) ions intercalated between planes of boron clusters. My contribution to the work featured in this chapter was primarily a combination of 1D and 2D solid-state NMR analyses of ^{11}B and ^{1}H nuclei focused on understanding the inter and intro molecular interactions between the zinc, boron clusters, and water in the material. My collaborator and I are co-first authors on this manuscript.

Paper: Synthesis and structural properties of a 2D Zn(II) dodecahydroxycloso-dodecaborate coordination polymer

Authors: Austin D. Ready[†], Shona M. Becwar[†], Dahee Junga, Emily Schueller, Kierstyn P. Andersona, Rebecca Kubena, Ram Seshadric, Bradley F. Chmelka, Alexander M. Spokoyny

7.1 Abstract

In this work, we discuss the synthesis and characterization of a 2D coordination polymer composed of a dianionic perhydroxylated boron cluster, $[B_{12}(OH)_{12}^{2-}]$, coordinated to Zn(II)—the first example of a transition metal-coordinated $[B_{12}(OH)_{12}]^{2-}$ compound. This material was synthesized via cation exchange from the starting cesium salt and then subjected to rigorous characterizion prior to and after thermal activation. Numerous techniques, including XRD, FTIR, SEM, TGA, and solid-state NMR, revealed a 2D coordination polymer composed of sheets of Zn(II) ions intercalated between planes of boron clusters. The as-synthesized material was then evacuated of solvent via thermal treatment, and atomic-level changes from this transformation were elucidated through a combination of 1D and 2D solid-state NMR analyses of ^{11}B and ^{1}H nuclei on the cluster, suggesting the full removal of coordinated solvent molecules. Evidence also suggests that $[B_{12}(OH)_{12}^{2-}]$ can adjust its coordination to Zn(II) in the solid-state through hemilability of its numerous -OH ligands.

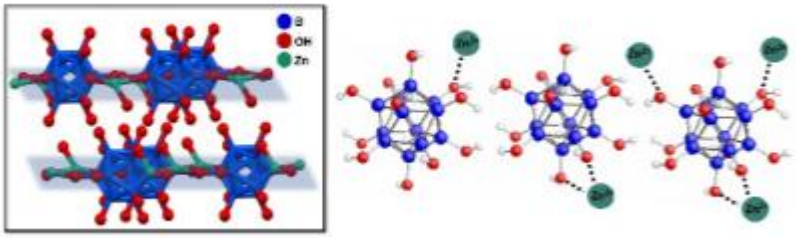

7.2 Introduction

Coordination polymers are an exciting class of materials featuring a high degree of chemical tunability due to the enormous variety of molecular building blocks available.[1-3] Among these, boron rich clusters have been recently introduced as promising scaffolds for the construction of various types of coordination networks.[4-31] In general, polyhedral boron clusters (Scheme 1) are highly appealing as building blocks for structured materials due to their symmetry, chemical tunability, and thermal/chemical robustness arising from a three-dimensional delocalization of electron density.[4-10,32,33]

Notably, Stang et al. explored the use of carboranes (Scheme 1)— neutral twelve-membered boron clusters in which two vertices have been replaced with carbon atoms—as linkers to form metalcoordinated networks,[11,17] among other early examples of using carborane clusters to form coordination polymers.[29,31] Compared to purely boron-containing clusters, the presence of two carbon atoms in carboranes engenders an inherent directionality to the cluster through disruption of the symmetrical electronic environment. Shortly thereafter, Hupp, Mirkin, and co-workers reported the syntheses of Zn(II) and Co(II) carborane-containing MOFs.[12,13,25] Additionally, Planas et al. published a series of papers[14,15,23,26,27] investigating a number of carborane-based MOFs and coordination polymers. These works showcased the ability of boron clusters which are functionalized with various substituents (Scheme 1) to be used as hybrid building blocks for the formation of coordination polymer networks. Of particular interest is the coordination ability of purely boron-containing clusters such as dianionic dodecaborate—$[B_{12}H_{12}]^{2-}$. In 1964, Muetterties demonstrated that due to the highly delocalized bonding in dodecaborate, the dicesium salt ($Cs_2B_{12}H_{12}$) can withstand temperatures up to 650°C without significant thermal decomposition, as well as exposure to

strong acids and bases.[34] Furthermore, $[B_{12}H_{12}]^{2-}$ is also amenable to functionalization, as evident by the variety of perhalogenated derivatives ($[B_{12}X_{12}]^{2-}$; X= F, Cl, Br, I) synthesized by Knoth, Muetterties, and others in subsequent years.[35-37] These halogenated clusters and their derivatives have since been studied due to their ability to act as highly inert, weakly coordinating anions.[38-48] A notable example from Strauss et al. showed a thorough solid-state characterization of $Na_2B_{12}X_{12}$ compounds (X = F, Cl) and the corresponding hydrates.[49] By comparing the Na—O bond valence contributions of the hydrates, the authors were able to rank these halogenated derivatives with respect to dodecaborate in terms of relative coordinating ability towards Na^+ ions in the solid state ($B_{12}Cl_{12}^{2-} \ll B_{12}H_{12}^{2-} < B_{12}F_{12}^{2-}$).

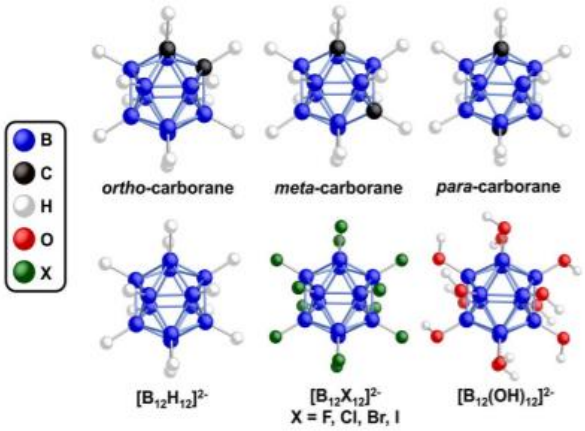

Scheme 1. Icosahedral boron clusters studied thus far as metal-coordinating moieties.

Recently, Xing and Duttwyler used an electrophilic metal ion in combination with an unfunctionalized $[B_{12}H_{12}]^{2-}$ building block to create the first porous boron cluster-containing network where the coordination is driven purely by direct cage-metal interactions.[30] Notably, the authors observed a linear B—H···M interaction (M = Cu(II)), a previously unrecognized bonding motif for a metal dodecaborate complex, as the boron cluster typically coordinates to

metal centers with two or three B-H units.[50-53] We hypothesized that a perhydroxylated dodecaborate cluster,[21,22,54] where instead of -H groups the icosahedral boron cluster core features twelve -OH groups (i.e. $[B_{12}(OH)_{12}]^{2-}$) could be an interesting building block with which to create a coordination polymer. For example, we previously reported[19] the synthesis of a hybrid metal oxide system, wherein $[B_{12}(OH)_{12}]^{2-}$ was used as a starting material to form a cross-linked network featuring B—O—Ti linkages connecting an amorphous array of TiO_2 nanoparticles. We later expanded this chemistry to synthesize a boron-rich hybrid tungsten oxide material.[18] Additionally, the synthesis and crystallographic characterization of a number of alkali metal $M_2[B_{12}(OH)_{12}]$ compounds has been reported[16,20-22,24,28,54] (M = Li, Na, K, Rb, Cs). Despite research on Zn(II)-boron cluster coordination compounds,[55] however, to date there remain no reports of the synthesis and characterization of a crystalline, perhydroxylated dodecaborate coordination polymer with a cation other than a monovalent alkali metal.

Herein, we present the synthesis and characterization of $ZnB_{12}(OH)_{12}$, a 2D coordination polymer composed of planes of divalent Zn(II) ions coordinated by $[B_{12}(OH)_{12}]^{2-}$ units, the first example of a transition metal-coordinated $[B_{12}(OH)_{12}]^{2-}$ compound. We report a facile synthesis as well as a thorough investigation of the change in chemical environment of the cluster upon high temperature solvent removal, as determined via XRD refinement and ^{1}H-^{11}B and ^{1}H-^{1}H solid-state 2D NMR studies of the as-synthesized and activated materials.

7.3 Materials and Methods

7.3.1 Synthesis of $ZnB_{12}(OH)_{12}$

$Cs_2[B_{12}(OH)_{12}]$ (120 mg, 0.20 mmol) was added to a 20 mL reaction tube. MilliQ water (3.0 mL) was added. The suspension was heated to 95 °C until all $Cs_2[B_{12}(OH)_{12}]$ was dissolved. A solution of $Zn(NO_3)_2 \cdot 6\ H_2O$ (714 mg, 2.4 mmol) in MilliQ water (3.0 mL) was prepared at room temperature and added dropwise to the homogenous $Cs_2[B_{12}(OH)_{12}]$ solution. Upon addition, a crystalline white precipitate formed immediately (Figure 7.2). The suspension was stirred at 95 °C for two days. After completion, the suspension was cooled to room temperature, and was centrifuged (2000 rpm, 10 minutes) to separate the solids. The top aqueous solution was decanted. Another portion of MilliQ water (15.0 mL) was added. The suspension was stirred in an ice-water bath for 5 min, and centrifuged (2000 rpm, 5 minutes) to separate the solids. This washing step was repeated another two times to remove soluble impurities. The resulting white powder was dried in vacuo with a lyophilizer for one day to yield the final product (65 mg, 0.162 mmol, 81%). The material was activated by heating in vacuo at 220°C for 24 hours.

7.3.2 Synthesis X-ray crystallography and structure determination

XRD patterns (Figure 7.2b and Figure 7.3b) were collected on a ground sample of $ZnB_{12}(OH)_{12}$ from 5 to 120° (2θ) on an Empyrean diffractometer with Cu-Kα radiation (λ = 1.54 Å). The powder pattern was indexed using the EXPO2014 software with the N-TREOR09 indexing algorithm to obtain a unit cell with *P*–1 symmetry. This unit cell was put into TOPAS, along with the diffraction data, and a Pawley fit was performed to obtain refined

cell, background, profile (peak shape), and sample displacement parameters. Note that coordinated solvent molecules which are present in the as-synthesized material were omitted for all of the XRD refinement procedures discussed herein. These parameters were fixed and information about the atoms was imported into TOPAS. The boron clusters were fixed in shape as rigid bodies with the -OH groups replaced by -F atoms for simplicity because they have the same X-ray scattering power. The clusters were allowed to rotate and translate, as well as the zinc ions. A simulated annealing algorithm was implemented in TOPAS which varied the atom positions in order to minimize the least squared error from the XRD pattern. When the cell parameters were also allowed to vary the cell relaxed into monoclinic symmetry. FINDSYM was used on the resulting structure to obtain the new space group, which was monoclinic C2/m. Simulated annealing was performed on the new monoclinic structure to obtain the best fit to the XRD pattern. Finally, a Rietveld refinement was performed in order to obtain atomic displacement parameters and statistical information about the quality of the fit.

7.3.3 Solid-state NMR spectroscopy

Solid-state ^{1}H and ^{11}B magic-angle-spinning (MAS) NMR spectroscopy were used to analyze the local environments of ^{1}H and ^{11}B in the as-synthesized and activated boron clusters. All solid-state NMR spectra were acquired on a Bruker AVANCE II HD 800 NMR spectrometer with an 18.8 T superconducting magnet operating at Larmor frequencies of 800.24 and 256.75 MHz for ^{1}H and ^{11}B nuclei, respectively, and equipped with a fast MAS 1.3 mm HX probe head. The experiments were conducted using zirconia rotors with Kel-F® caps at 25 kHz MAS and at room temperature, which was maintained by cooling. ^{1}H chemical

shifts were referenced to TKS as a secondary standard (^{1}H chemical shift of 0.25 ppm), and ^{11}B signals were referenced to borax powder ($Na_2B_4O_7$) as a secondary standard (^{11}B shift of 2.26 ppm).[56] The materials were diluted with KBr at a sample:KBr ratio of 1:1 w/w before being loaded into the MAS rotor. The KBr served as both an internal temperature probe[57] and to reduce undesirable sample heating that may arise from rapid rotation of conductive samples in the high magnetic field required for the NMR measurements.[58] Compared to 1D NMR, two-dimensional (2D) NMR techniques yield enhanced spectral resolution by exploiting through-space dipole-dipole interactions over subnanometer distances to correlate the NMR signals of dipole-dipole-coupled spin pairs, such as ^{1}H and ^{11}B nuclei in the boron clusters.

Solid-state 2D $^{11}B\{^{1}H\}$ Heteronuclear Correlation (HETCOR) NMR spectroscopy experiments were acquired using 32 transients, with a recycle delay of 1–5 s, 0.5 ms contact time, and 256 scans in the indirect dimension. Heteronuclear ^{1}H-^{11}B dipole-dipole couplings scale with the cube of the distance separating the two nuclear spins,[59,60] so that the short contact times used were sensitive principally to ^{1}H and ^{11}B nuclei that are directly bonded, physically interacting, or, to a lesser extent, by weaker next-nearest neighbor interactions.

Solid-state 2D $^{1}H\{^{1}H\}$ double-quantum–single-quantum (DQ-SQ) NMR spectra were acquired using a Hahn-echo sequence to remove the ^{1}H background of the NMR probehead. For DQ excitation, the Back-to-Back (BaBa) scheme[61,62] was used under MAS conditions of 25 kHz, with XY16 phase cycling63 to remove background signals. A zfilter delay of 10 rotor periods was used before acquisition to remove spurious magnetization. The acquisition of the indirect dimension was rotor-synchronized, with 64 data points recorded using the States-TPPI method. Recycle delays were in the range of 1–5 s, as determined from saturation recovery measurements.

Solid-state 1D ^{1}H and ^{11}B Hahn-echo NMR experiments were conducted to quantify the integrated intensities of signals, the positions and linewidths of which are manifested in the 2D spectra. For the ^{1}H spectra, recycle delays of 20 s ($5T_1$) were used to ensure full spin-lattice relaxation of the ^{1}H signals and were acquired with 64 scans and a 0.8 ms echo delay. For the ^{11}B spectra, a recycle delay of 4 s ($>5T_1$) was used to ensure full spin-lattice relaxation of the ^{11}B signals and were acquired with 124 scans and a 0.8 ms echo delay.

7.3.4 Scanning Electron Microscopy

SEM images were captured with a JEOL JSM-6700F FE-SEM. The LEI detector was used with an accelerating voltage of 5.0 kV, emission current of 10 μA, and a probe current of 8 μA.

7.3.5 Infrared Spectroscopy

IR spectra were measured on a Jasco FT/IR-4100. A background spectrum was measured and automatically subtracted prior to sample measurements. 64 scans were used on a typical measurement.

7.3.6 Thermogravimetric Analysis

Thermogravimetric analysis was carried out on a PerkinElmer Pyris Diamond TG/DTA. Samples were heated in alumina oxide trays from 25 °C to 650 °C at a rate of 20 °C/min under a constant flow of argon (200 mL/min).

7.3.7 Density Functional Theory

Calculations were performed using SCM ADF software. XYZ coordinates for $[B_{12}(OH)_{12}]^{2-}$ determined by refinement of the powder pattern were imported, and the structure was subsequently modified within the software to create a monodentate, bidentate, and fully bound cluster. To reduce the computation time and complexity, Zn(II) ions were replaced by electron-withdrawing $-CF_3$ or $-CF_2$ groups for the monodentate and bidentate interactions, respectively. Consequently, the clusters were calculated in their 2- charge state. Geometry pre-optimizations were performed, followed by full geometry optimizations at the GGA:PBE-D3(BJ) theory level with a DZP basis set and scalar relativistic effects considered. Electron densities were approximated by visualizing the Mulliken charges from the optimized geometries.

7.4 Results and Discussion

7.4.1 Synthesis

$ZnB_{12}(OH)_{12}$ was synthesized via cation exchange of the starting material $Cs_2[B_{12}(OH)_{12}]$ (Figure 7.1a) by leveraging the effect that the counterion of the boron cluster has on the solubility of the material. The cesium-coordinated cluster is soluble in hot aqueous solution, while the final zinc-coordinated cluster is insoluble in water. The material was recovered after centrifugation and subjected to lyophilization. The resulting solid white powder still contains water molecules in the crystal lattice, as evident by various characterization methods (see below).

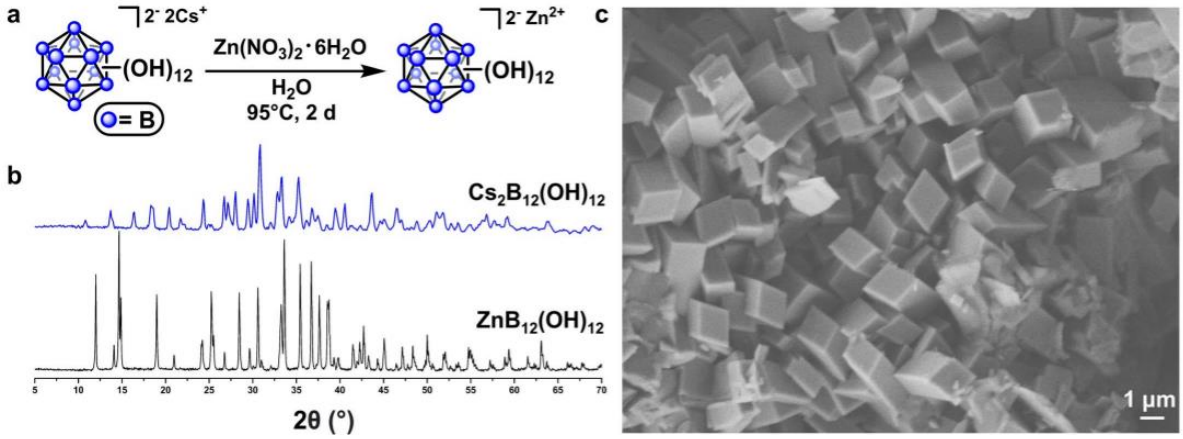

Figure 7.1. (a) Synthesis conditions to perform cation exchange on perhydroxylated dodecaborate. (b) PXRD pattern of as-synthesized boron cluster before (blue) and after cation exchange (black) from cesium to zinc. (c) SEM image of as-synthesized $ZnB_{12}(OH)_{12}$, showcasing the high degree of crystallinity and uniformity.

7.4.2 XRD Characterization

As discussed in the experimental section, XRD refinement was particularly useful in elucidating the structural features of this material (Figure 7.2). Structure determination was aided by the use of TOPAS, which allowed the identification of a monoclinic *C2/m* space group. The presence of solvent molecules in the crystal structure was omitted from these refinement procedures. Density measurements on the powder in a pycnometer confirmed that the experimental density of 2.27 g/cm^3 was close to the predicted density of 2.10 g/cm^3. The final structure was determined to be monoclinic but pseudo-tetragonal, with β close to 90° and α and c close in length. From these refinement methods, we determined the structure consists of each Zn(II) ion coordinating to three clusters by four bonding interactions (Figure 7.2c). Each Zn(II) ion is chemically equivalent, and is bound in a bidentate fashion by two -OH groups on one cluster, with bond lengths of 2.486 Å and 2.799 Å, and bound in a monodentate fashion by hydroxyl moieties on two additional clusters, with equivalent bond lengths of 2.092 Å. Large void spaces adjacent to the metal sites in the crystal structure are attributed to coordinated solvent molecules which were excluded from the refinement procedure. Considering the preference of Zn(II) for a six-coordinate environment in aqueous solution,[64-66] we suspect the presence of two H_2O molecules coordinated to each Zn(II) ion. However, the mass loss observed by TGA upon thermal activation more closely agrees with three H_2O molecules per $ZnB_{12}(OH)_{12}$ unit, therefore we suspect the presence of a third unbound H2O molecule located elsewhere in the crystal lattice. The higher-than-expected experimental density of 2.27 g/cm^3, as compared to the predicted density of 2.10 g/cm^3, further supports

this conclusion. We then set out to determine if these solvent molecules can be removed, and how that would affect the material properties.

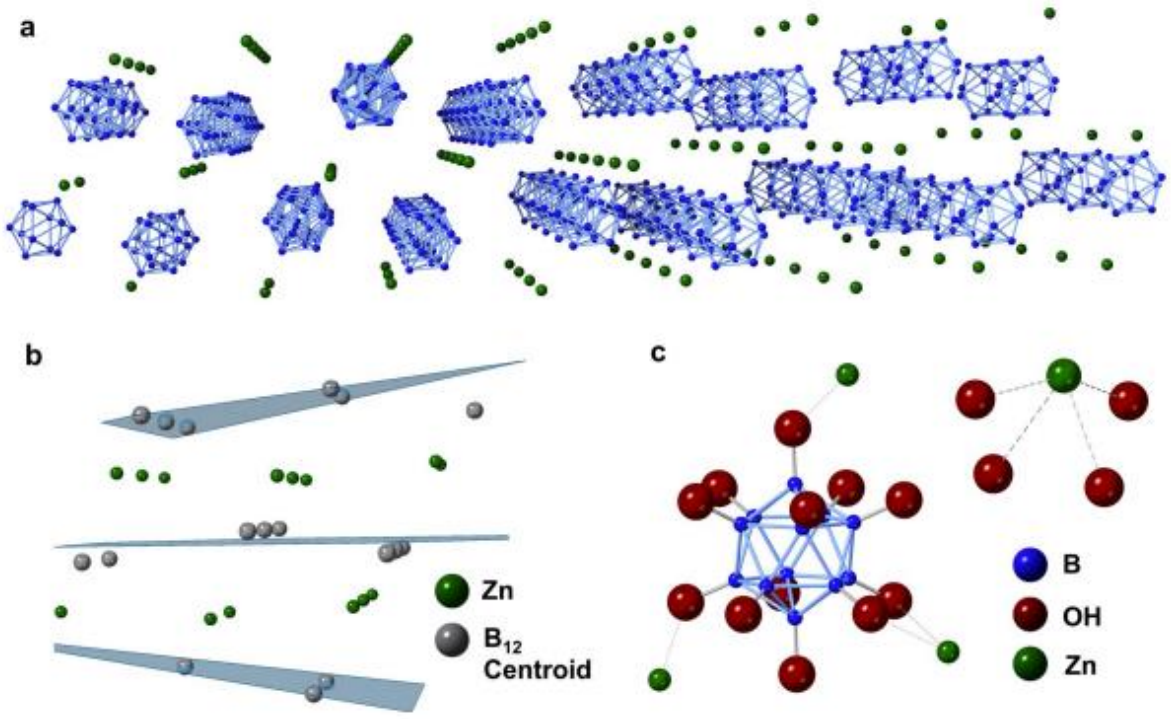

Figure 7.2. (a) Perspective view of the channels of zinc ions within the $[B_{12}(OH)_{12}]^{2-}$ framework; (-OH groups omitted for clarity). (b) Alternating planes of boron clusters and Zn(II) ions, in which each boron cluster is depicted by a simplified centroid. (c) Coordination environment around a single [B12(OH)12]2- cluster (left), and around a single Zn(II) ion (right); (solvent molecules omitted for clarity).

7.4.3 Activation

While the effect of activation is not readily apparent by SEM, it is more noticeable by XRD, FTIR, TGA (Figure 7.3), and solid-state NMR (Figure 7.4 and 7.5). The XRD pattern of the activated material is strikingly different from that of the as-synthesized material (Figure 7.3b). Despite having fewer total peaks, there appears to be a number of peaks which are retained upon activation, albeit significantly broadened and shifted, consistent with the changes in XRD patterns seen by Jorgensen et al. for various alkali metal $[B_{12}(OH)_{12}]^{2-}$ compounds upon thermal activation.[16] While further characterization and refinement methods would be needed to elucidate the exact structure of the activated material, we hypothesize that the loss of various peaks in the low 2Θ region (10-15°) could be due to a contraction of the unit cell, where upon the removal of coordinated water molecules, proximate boron clusters move in to fill the vacant coordination sites on the Zn(II) ions. This is consistent with the solid-state NMR characterization (see below), where the proportion of hydroxyl groups coordinating the Zn(II) ions seems to increase upon thermal activation. This is also observable by FTIR (Figure 7.3c), where the two peaks at 1207 cm^{-1} and 1127 cm^{-1}, and their small shoulders, in the as-synthesized material merge into one broadened peak at 1169 cm-1 in the IR spectrum of the activated material. The peak at 1207 cm1 is assigned to a B—B stretch associated with a "breathing/pulsation" of the icosahedral cage,[21,67-69] while the peak at 1127 cm^{-1} could be due to either a B—B cage vibration or a B—O vibrational mode. Similarly, the shouldering on either side of the peak at 726 cm^{-1} in the as-synthesized material disappears upon activation to give one peak at 718 cm^{-1}. This peak is also associated with the B—B breathing mode. Additionally, the loss of the small peaks between 3400 cm^{-}1 and 3550 cm^{-1} is attributed to the removal of coordinated water upon activation. The activation of this

material is further observable by TGA (Figure 7.3d), which shows a mass loss of approximately 12% between 200-250°C, which we attribute to the loss of three water molecules per $ZnB_{12}(OH)_{12}$ unit. The effects of activation are most obvious, however, upon examination of the solid-state NMR spectra.

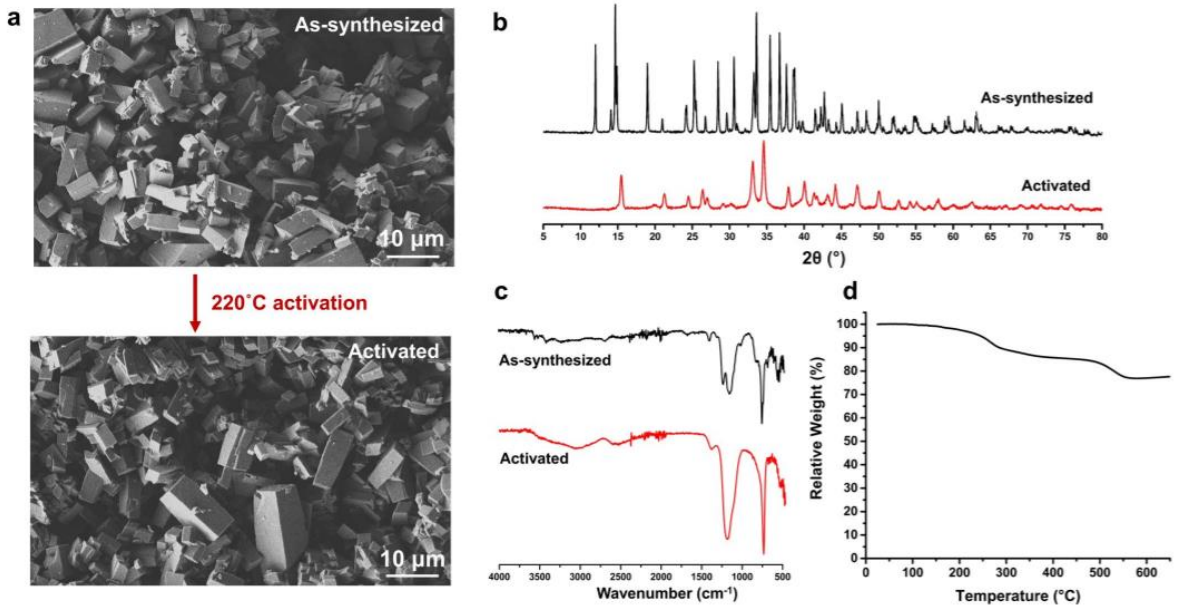

Figure 7.3. (a) SEM images of $ZnB_{12}(OH)_{12}$ as-synthesized (top) and after activation (bottom) at 220°C under vacuum. (b) PXRD patterns before (black) and after (red) activation. (c) FTIR of as-synthesized (black) and activated (red) material (d) TGA of as-synthesized $ZnB_{12}(OH)_{12}$.

7.4.4 NMR Characterization

Solid-state NMR analyses show that the presence of Zn(II) cations influence the local environments of the hydrogen and boron atoms within the cluster, though to differing extents,

according to their nanoscale proximities and interactions. This is evident in Figure 7.4a, where the Hahn-echo ^{1}H MAS NMR spectrum shown along the right vertical axis exhibits a broad distribution of ^{1}H intensity, which represents a continuous distribution of hydrogen moieties. ^{1}H signals at higher frequencies (higher chemical shifts) arise from moieties that are relatively deshielded, consistent with their nanoscale proximities to electronegative species, e.g., the electron-withdrawing Zn(II) ions. By comparison, ^{1}H signals at lower frequencies (lower chemical shifts) manifest more shielded environments and are expected to be more distant from the zinc cations. These different ^{1}H moieties are shown to be unambiguously associated with the Zn-boron clusters by the 2D ^{11}B{^{1}H} heteronuclear correlation (HETCOR) NMR spectrum in Figure 7.4a of activated Zn(II)-boron clusters. In this experiment, ^{1}H nuclei are excited by a radiofrequency pulse, allowed to evolve during an incremented evolution period, after which polarization is transferred via ^{1}H-^{11}B dipole-dipole couplings to nearby (1 nm) ^{11}B atoms, and the ^{11}B polarization subsequently detected. A double Fourier transform of the ^{11}B and ^{1}H time-domain signals yields a contour-plot 2D frequency map of correlated ^{11}B and ^{1}H signals that manifests pairs of nuclear spins that are in nanoscale proximity to one another. Specifically, the intensity distribution in the 2D ^{11}B{^{1}H} spectrum in Figure 7.4a shows a predominant ^{11}B signal at -17 ppm, which is associated with hydroxylated 3D-aromatic boron clusters, as previously established.[19] In conjunction with the high resolution 2D NMR, DFT modeling of local shielding environments of the different ^{1}H moieties (see Supporting Information, Figure S7.3) aids the assignment of the 2D-resolved signals. Interestingly, for the activated material the increased resolution provided by 2D NMR reveals that there are at least two types of ^{1}H nuclei, which are characterized by isotropic chemical shifts centered at 8.0 ppm (highlighted blue) and 3.0 ppm (mauve) and are attributed to moieties that are closer

to or more distant from the Zn(II) ions, respectively. Unresolved shoulders of these ^{1}H signals near 10.3 ppm (green) and 1.5 ppm (purple) indicate a broad distribution of local hydroxyl environments, which are discussed in more detail below. In addition, a distinct shoulder is notably present in the ^{11}B dimension at -23 ppm, which is displaced to lower frequency and correlated principally with the ^{1}H signal at 8.0 ppm (blue), consistent with the proximity of these moieties to the electron-withdrawing Zn(II) ions. The shielding of these ^{11}B nuclei is consistent with the electron density visualized by Mulliken charges on the geometry-optimized model system (Figure S7.1) of the Supporting Information, which suggests that the well-established, delocalized, 3D-aromatic character of the boron cluster compensates for the low electron density (deshielding) of ^{1}H nuclei on the hydroxyl groups that interact most strongly with the Zn(II) ions by increasing the local electron density on proximate boron atoms.

The enhanced resolution of the 2D NMR spectra enables the positions and linewidths of the two ^{11}B signals to be determined for use in deconvoluting the approximately quantitative 1D ^{11}B MAS spectrum of the relative boron populations in Figure 7.4b, yielding relative integrated intensities of 83% (red) and 17% (grey) for the signals at -17 ppm and -23 ppm, respectively. This corresponds to a 5:1 ratio, which indicates a unique chemical environment for 2 boron atoms in the cluster and a separate environment for the other 10 boron atoms. DFT calculations indicate that the electron density (as visualized via Mulliken charges) on the two boron atoms whose -OH groups are involved in a bidentate Zn(II)-binding motif (Figure 7.2c) is significantly higher than the other ten boron atoms on the cluster, which includes those involved in monodentate interactions and those not involved in a binding interaction. These two distinct chemical environments on the cluster account for the relative 2:10 ratio of boron

atoms derived from integration of the 1D ^{11}B MAS NMR spectrum. Overall, however, the chemical shifts of the boron atoms in the cluster seem to be only moderately affected by the Zn(II)-hydroxyl binding interactions.

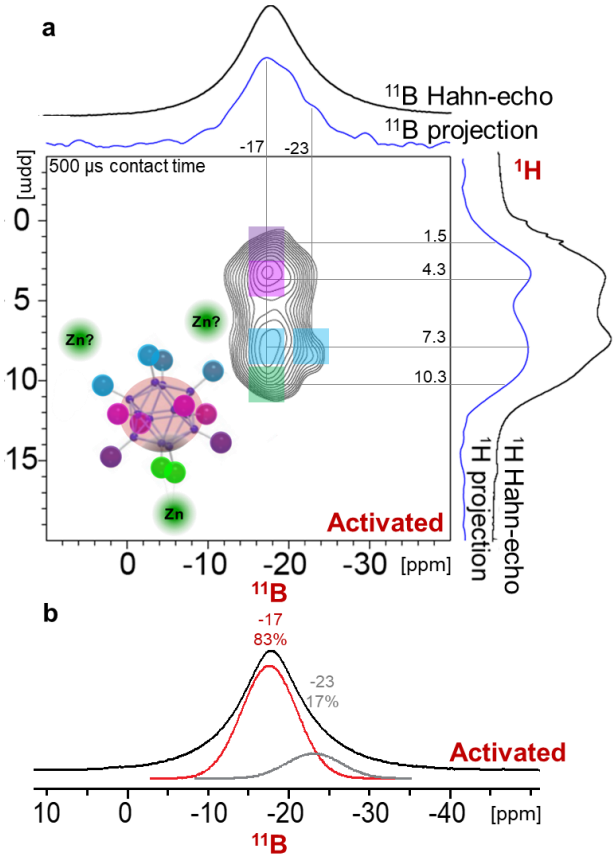

Figure 7.**4.** (a) Solid-state 2D ^{11}B{^{1}H} HETCOR NMR spectrum of the activated Zn-boron cluster material acquired at 18.8 T, 298 K, 25 kHz MAS and with a short 0.5 ms contact time. Different regions of correlated intensity are marked by colored squares that correspond to ^{1}H nuclei in different local environments that are dipole-dipole-coupled to ^{11}B nuclei in the clusters. A schematic diagram is shown of a single Zn^{2+}-boron cluster with hydroxylated vertices that are colored according to their local environments, consistent with the 2D

spectrum. (b) 1D Hahn-echo ^{11}B MAS NMR spectrum acquired under the same conditions as (a), with two partially resolved signals that are deconvolved based on their positions and widths in the 2D spectrum, which are attributed to boron atoms in different cluster environments as indicated by the red or grey shading.

The hydroxyl moieties, however, experience a much richer range of interactions with the Zn(II) cations and with each other. In particular, the spatial proximities of the different types of ^{1}H moieties can be probed by 2D ^{1}H{^{1}H} double-quantum–single-quantum (DQ-SQ) correlation NMR analyses, which resolve pairs of dipole-dipole-coupled ^{1}H nuclei according to their correlated isotropic chemical shifts. In a 2D ^{1}H{^{1}H} DQ-SQ spectrum, signal intensity in the double-quantum dimension (vertical axis) corresponds to the sum of the isotropic chemical shifts (horizontal axis) of dipole-dipole-coupled ^{1}H-^{1}H spin pairs. Consequently, intensity along the double-diagonal line corresponds to dipolar-coupled ^{1}H nuclei in moieties with identical isotropic chemical shifts (and thus in the same local environments), while intensity that is displaced off the double-diagonal corresponds to coupled ^{1}H spins in different environments that are within nanoscale proximity to each other. For example, the 2D ^{1}H{^{1}H} DQ-SQ correlation spectrum in Figure 7.5a of the as-synthesized hydroxylated Zn-boron cluster material shows an intensity maximum along the double-diagonal centered at 8 ppm (green dot), which is associated with pairs of dipole-dipole-coupled hydroxyl groups that are in similar environments. The intensity maximum along the double-diagonal centered at 6 ppm (orange dot) is attributed to structural water[10] (which is significantly reduced in intensity in Figure 7.5b, consistent with the loss of such water after activation at 220 ^{o}C). Strong off-double-diagonal intensity is also observed at 16.5 ppm in the double-quantum dimension and

at 10.5 ppm and 6 ppm (green squares) in the single-quantum dimension, consistent with the nanoscale proximity of hydroxyl groups nearest the Zn(II) ions and those next-distant on the boron-clusters. Similarly, strong off-double-diagonal intensity at 14.5 ppm and 10.5 ppm in the DQ dimension are correlated with pairs of ^{1}H SQ signals at 10.5 ppm and 4 ppm (blue squares), and at 8 ppm and 2.5 ppm (purple squares), respectively, each manifesting dipole-dipole-coupled ^{1}H nuclei in hydroxyl moieties of the boron clusters that are increasingly distant from the Zn(II) ions. Additionally, strong off-diagonal intensity at 12 ppm in the DQ dimension is associated with correlated ^{1}H SQ signals centered at 8 ppm and 4 ppm (orange squares), which manifests interactions between structural water and the hydroxyl moieties of the boron clusters. It is interesting to note the absence of correlated intensity along the double-diagonal at 21 ppm in the DQ dimension and at 10.5 ppm in the SQ dimension, which establishes that the moieties associated with these high-frequency signals are isolated from each other. Importantly, the improved resolution afforded by 2D ^{1}H{^{1}H} DQ-SQ NMR analysis enables the positions and linewidths of the otherwise broad and poorly resolved signals in the 1D Hahn-echo ^{1}H MAS NMR spectrum of Figure 7.5b of the as-synthesized Zn^{2+}-boron cluster material to be confidently deconvolved. Integration of the deconvoluted ^{1}H signals yields estimates of the relative populations of the different hydroxyl moieties, specifically 12%, 19%, 25%, and 19% for the signals at 10.5 ppm, 8 ppm, 4 ppm, and 2.5 ppm, respectively, and 25% associated with the signal at 6 ppm from structural water, the latter of which is consistent with the presence of two water molecules per boron cluster. Discounting the contribution from such structural water, the relative populations of the remaining boron-associated hydroxyl groups occur in approximate ratios of 2:3:4:3 for the ^{1}H signals at 10.5, 8, 4, and 2.5 ppm, respectively, which are consistent with the expected

stoichiometry of 12 hydroxyl moieties terminating each icosahedral boron cluster. This ratio appears to reflect a distribution of zinc-water-boron cluster interactions that are consistent with the presence of two icosahedral boron cluster motifs with 12 terminating hydroxyl moieties in different ratios of 2:4:4:2 and 2:2:4:4 for the respective ^{1}H signals. DFT electron density calculations (Figure S7.3) provide estimates of the relative extent of shielding of each hydrogen atom in the hydroxyl moieties, which allows confident assignment of the 2D-resolved isotropic chemical shifts to their local structural environments. A schematic diagram in Figure 7.5b shows the two types of hydroxyl-terminated boron clusters near intercalated Zn(II) ions and water molecules, with the colors of the different hydroxyl H atoms corresponding to those associated with the resolved ^{1}H signals in the 2D NMR spectrum of Figure 7.5a.

Upon post-synthetic activation at 220^{o}C under vacuum, structural water molecules are lost and the $ZnB_{12}(OH)_{12}$ clusters undergo atomic-scale structural changes that are manifested by the 2D $^{1}H\{^{1}H\}$ DQ-SQ NMR spectrum in Figure 7.5c. Similar intensity maxima at 10.3 ppm, 7.3 ppm, and at approximately 4.3 ppm are observed in the SQ dimension of the 2D spectrum (blue and grey squares), as observed for the as-synthesized material (Figure 7.5a). However, there are several notable differences, including a substantial reduction in intensity at 6 ppm in the SQ dimension which is consistent with the significant reduction of structural water that occurs during the activation treatment and is corroborated by separate thermal gravimetric analyses. In addition, new correlated intensity is observed at high frequency along the double-diagonal line at 20.6 ppm in the DQ dimension and at 10.3 ppm in the SQ dimension (black dot), which establishes the nanoscale proximity of these moieties that were previously isolated (Figure 7.5a).

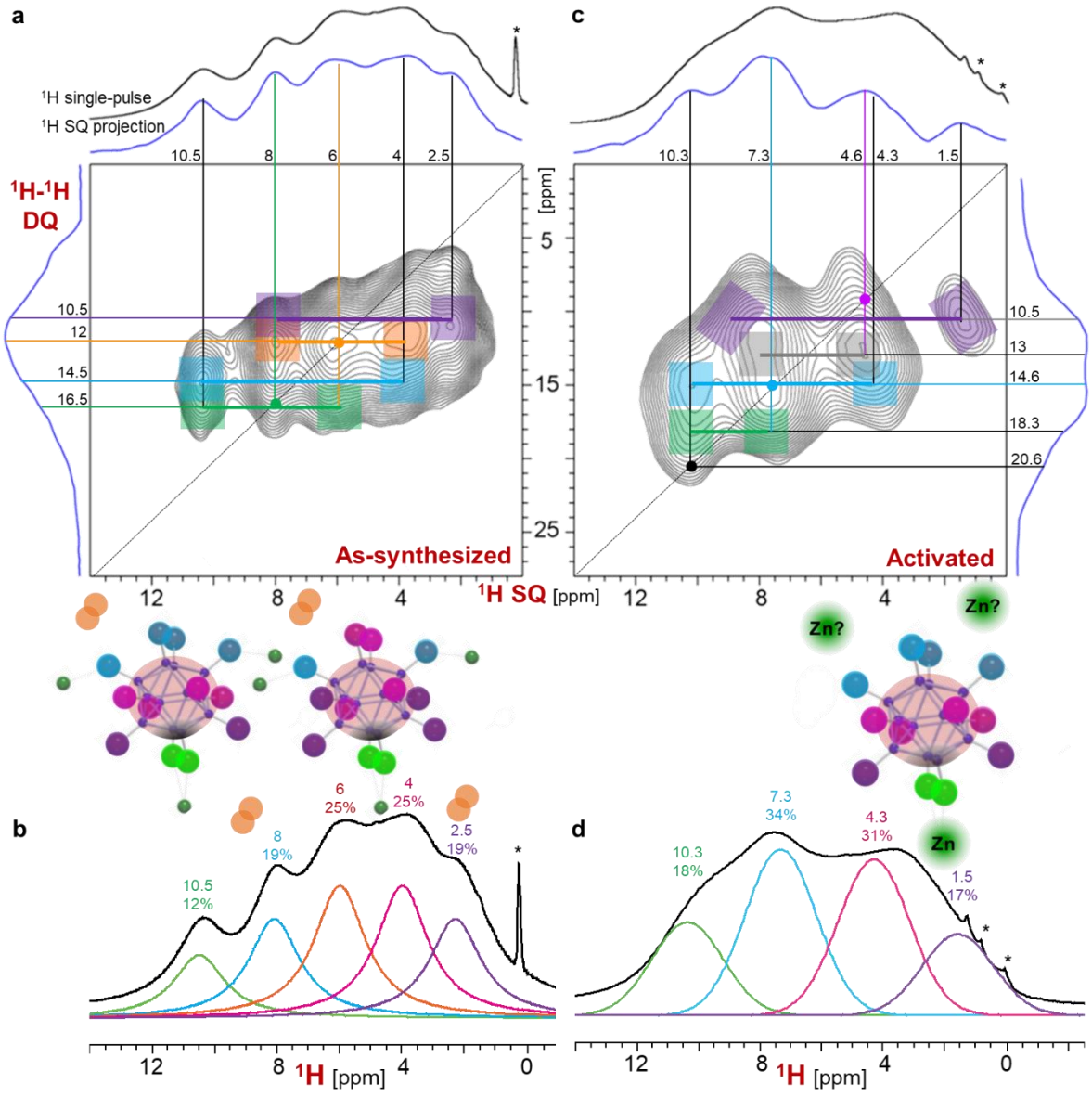

Figure 7.5. Solid-state (a,c) 2D ^{1}H{^{1}H} double-quantum/single-quantum correlation NMR spectra, (b,d) quantitative 1D Hahn-echo ^{1}H MAS NMR spectra of as-synthesized (a,b) or activated (c,d) boron clusters. The NMR spectra were acquired at 18.8 T, 298 K, and 25 kHz MAS. The colored regions at local intensity maxima along the dotted line highlight correlated isotropic chemical shifts arising from proximate (1 nm) dipole-dipole-coupled ^{1}H-^{1}H moieties. Signal assignments and widths in the 2D spectra were used to deconvolve and

integrate the partially resolved signals in the 1D spectra in (b,d). Schematic diagrams of Zn-boron clusters are shown with the Zn(II) ions (dark green), boron atoms (black), and OH groups colored according to their deconvoluted signal assignments. The asterisks denote impurity species.

Correlated intensity is furthermore observed for these high-frequency signals at 18.3 ppm in the DQ dimension with ^{1}H SQ signals at 10.3 ppm and approximately 8 ppm, manifesting closer proximities of hydroxyl moieties near the Zn^{2+} cations after activation. Finally, a large change is also observed in the low-frequency ^{1}H signals, which exhibit a well resolved ^{1}H SQ signal at 1.5 ppm that is correlated to a broad distribution of intensity at approximately 9 ppm (purple rectangles, 10.5 ppm DQ). Compared to the as-synthesized material, no intensity maximum is observed at 6 ppm in Figure 7.5b, consistent with the loss of structural water in the activated Zn-boron material. Integration of the deconvoluted ^{1}H signals in Figure 7.5d, yields estimates of the relative populations of the different hydroxyl moieties. The ^{1}H signals at 10.3 ppm, 7.3 ppm, 4.3 ppm, and 1.5 ppm account for approximately 18%, 34%, 31%, and 17% of the hydrogen atom environments, respectively. Based on these relative integrated ^{1}H signal intensities, the different hydroxyl moieties are established to be present in ratios of 2:4:4:2, consistent with the expected stoichiometry of the 12 terminating-hydroxyl moieties on the icosahedral boron clusters. There is a general increase in the integrated intensities of the ^{1}H signals that are displaced to higher frequency; for example, ^{1}H signals with chemical shifts greater to or equal 7.3 ppm have relative intensities that increase from 5/12 to 6/12 upon activation of the Zn-boron clusters. This is due, in part, to the removal of structural water

molecules, which leads to stronger interactions between the Zn(II) ions and terminating-hydroxyl groups on the boron clusters. The schematic diagram in Figure 7.5d shows for the activated material shows a hydroxyl-terminated boron cluster near intercalated Zn(II) ions, with the colors of the different hydroxyl H atoms corresponding to those associated with the resolved ^{1}H signals in the 2D NMR spectrum of Figure 7.5c and relative populations that are consistent with the ^{1}H ratios established by Figure 7.5d. Thus, the enhanced signal resolution and atomic-scale insights provided by the 1D and 2D solid-state NMR analysis yield detailed information about the interactions of the Zn(II) ions and hydroxyl groups terminating the boron clusters, along with atomic-scale differences between the as-synthesized and activated cluster materials.

7.5 Conclusions

A divalent Zn(II) dodecahydroxy-closo-dodecaborate coordination polymer was synthesized and thoroughly characterized via a variety of methods. The removal of solvent molecules from the crystal lattice was rigorously studied, providing key atomic insights into the changes in chemical environment of the boron cluster. Increased atomic level understandings were elucidated from solid state 1D and 2D NMR analyses of the as-synthesized and activated materials. Subtle changes in the electronic environment of both the boron atoms comprising the cluster and the -OH moieties on the cluster were investigated. The location of each Zn(II) ion and their binding modes (monodentate or bidentate) were revealed to have significant effects on the relative shielding of ^{11}B and ^{1}H nuclei, as evident by thorough analyses of the solid-state NMR spectra. Furthermore, 2D ^{1}H{^{1}H} double-

quantum/single-quantum correlation NMR spectra were correlated with quantitative 1D Hahn-echo ^{1}H MAS NMR spectra, suggesting that $[B_{12}(OH)_{12}]^{2-}$ may contain hemilabile -OH moieties, which can switch from monodentate to bidentate interactions with Zn(II) ions to fill vacant coordination sites generated on the metal ion upon the removal of coordinated water molecules. This analysis represents a valuable contribution to the field of coordination polymers, in which solid-state NMR is becoming recognized as a powerful tool for the elucidation of atomic-level structure.[71-80] Overall, the increased multi-scale characterizations and understandings provided here for the first time in these types of materials will pave the way for further studies into coordination polymers, especially those composed of dodecaborate building blocks.

7.6 Relevant Supplementary Information

Density Functional Theory Calculations

Calculations were performed using SCM ADF software. XYZ coordinates for $[B_{12}(OH)_{12}]^{2-}$ determined by refinement of the powder pattern were imported, and the structure was subsequently modified within the software to create a monodentate, bidentate, and fully bound cluster (two monodentate and one bidentate). To reduce the computational complexity, Zn(II) ions were replaced by electron-withdrawing $-CF_3$ or $-CF_2$ groups for the monodentate and bidentate interactions, respectively. Geometry pre-optimizations were performed, followed by full geometry optimizations at the GGA:PBE-D3(BJ) theory level with a DZP basis set and scalar relativistic effects considered. Electron densities were approximated by visualizing the Mulliken charges from the optimized geometries.

Full Structure Model

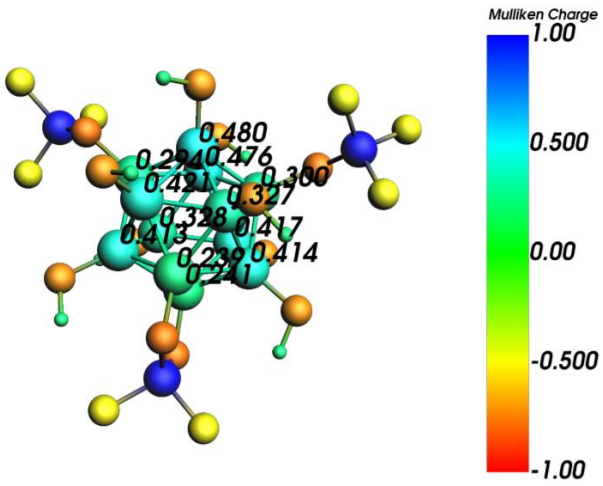

Figure S7.1. Mulliken charges on boron atoms for full structure model

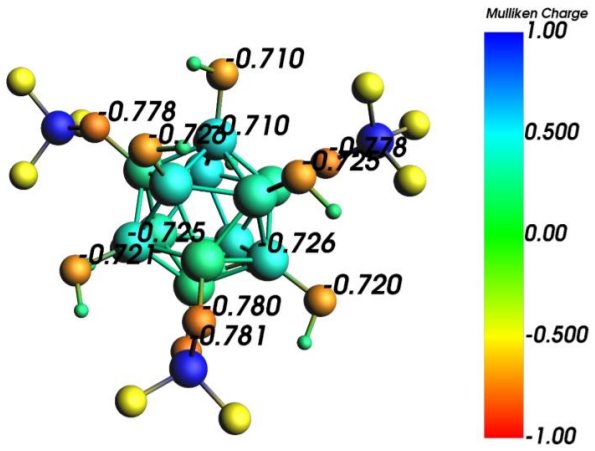

Figure S7.2. Mulliken charges on oxygen atoms for full structure model

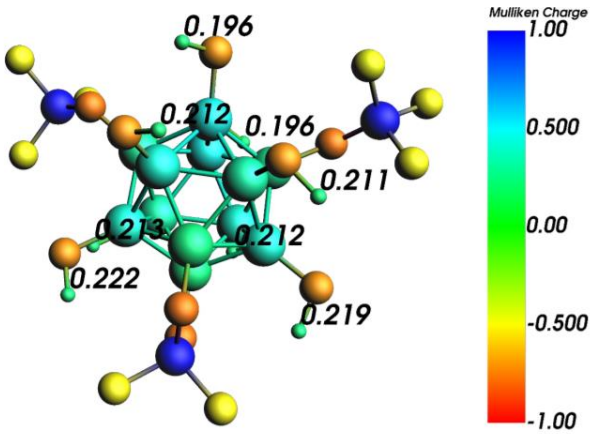

Figure S7.3. Mulliken charges on hydrogen atoms for full structure model

Atomic Coordinates for $ZnB_{12}(OH)_{12}$ unit cell (F replacing -OH)

The powder pattern was indexed using the EXPO2014 software with the N-TREOR09 indexing algorithm to obtain a unit cell with *P*–1 symmetry. This unit cell was put into TOPAS, along with the diffraction data, and a Pawley fit was performed to obtain refined cell, background, profile (peak shape), and sample displacement parameters. Note that coordinated

solvent molecules which are present in the as-synthesized material were omitted for all of the XRD refinement procedures. These parameters were fixed and information about the atoms was imported into TOPAS. The boron clusters were fixed in shape as rigid bodies with the -OH groups replaced by - F atoms for simplicity because they have the same X-ray scattering power. The clusters were allowed to rotate and translate, as well as the zinc ions. A simulated annealing algorithm was implemented in TOPAS which varied the atom positions in order to minimize the least squared error from the XRD pattern. When the cell parameters were also allowed to vary the cell relaxed into monoclinic symmetry. FINDSYM was used on the resulting structure to obtain the new space group, which was monoclinic *C2/m*. Simulated annealing was performed on the new monoclinic structure to obtain the best fit to the XRD pattern. Finally, a Rietveld refinement was performed in order to obtain atomic displacement parameters and statistical information about the quality of the fit.

Figure S7.4. CIF of $ZnB_{12}F_{12}$, determined through refinement of the powder pattern of as-synthesized $ZnB_{12}(OH)_{12}$

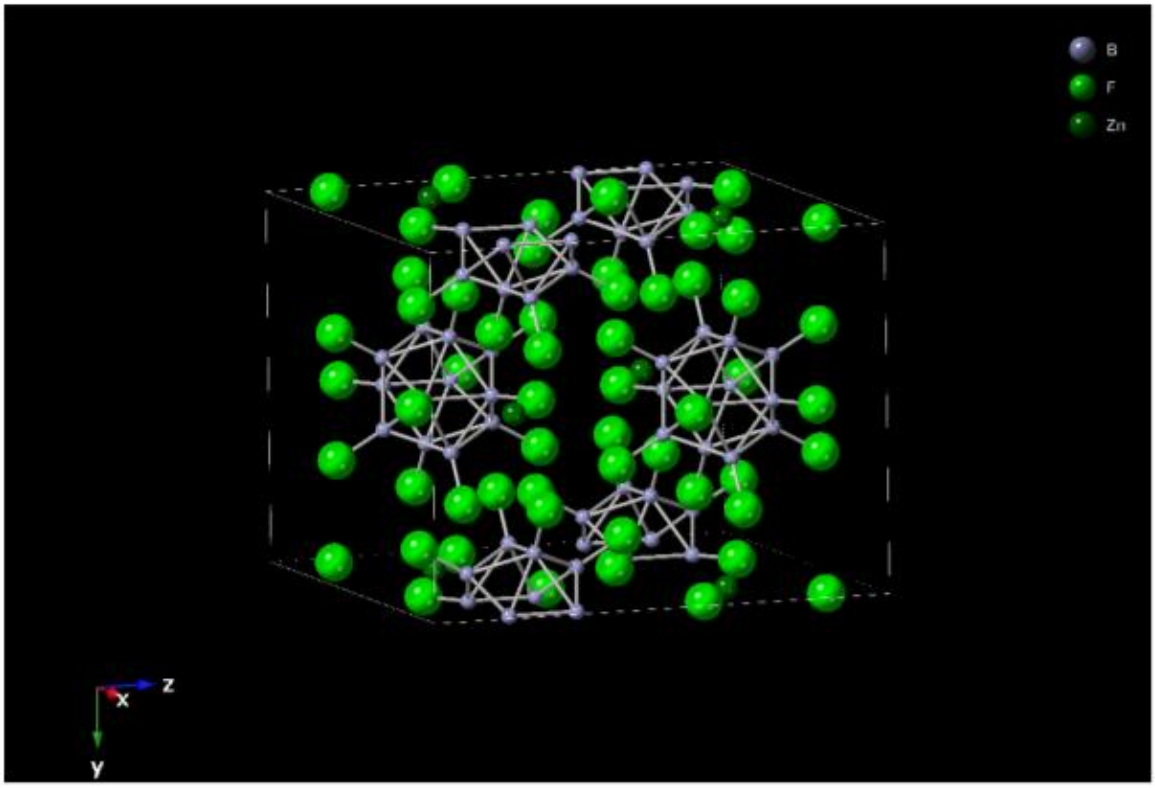

7.7 References

1. S. R. Batten, S. M. Neville and D. R. Turner, Coordination Polymers: Design, Analysis and Application, 2008.
2. A.-C. Stoica, M. Damoc, M.-F. Zaltariov, C. Racles and M. Cazacu, React. Funct. Polym., 2021, 168, 105039.
3. E. Fernandez-Bartolome, A. Martinez-Martinez, E. ResinesUrien, L. Piñeiro-Lopez and J. S. Costa, Coordination Chemistry Reviews, 2022, 452, 214281.
4. A. M. Spokoyny, Pure and Applied Chemistry, 2013, 85, 903.
5. M. F. Hawthorne and A. Pushechnikov, Pure and Applied Chemistry, 2012, 84, 2279-2288.
6. B. P. Dash, R. Satapathy, J. A. Maguire and N. S. Hosmane, New Journal of Chemistry, 2011, 35, 1955-1972.
7. B. R. S. Hansen, M. Paskevicius, H.-W. Li, E. Akiba and T. R. Jensen, Coordination Chemistry Reviews, 2016, 323, 60-70.
8. F. Cheng and F. Jäkle, Polymer Chemistry, 2011, 2, 2122-2132.
9. R. Núñez, I. Romero, F. Teixidor and C. Viñas, Chemical Society Reviews, 2016, 45, 5147-5173.
10. A. N. Alexandrova, A. I. Boldyrev, H.-J. Zhai and L.-S. Wang, Coordination Chemistry Reviews, 2006, 250, 2811-2866.
11. N. Das, P. J. Stang, A. M. Arif and C. F. Campana, The Journal of Organic Chemistry, 2005, 70, 10440-10446.
12. O. K. Farha, A. M. Spokoyny, K. L. Mulfort, S. Galli, J. T. Hupp and C. A. Mirkin, Small, 2009, 5, 1727-1731.

13. O. K. Farha, A. M. Spokoyny, K. L. Mulfort, M. F. Hawthorne, C. A. Mirkin and J. T. Hupp, Journal of the American Chemical Society, 2007, 129, 12680-12681.

14. L. Gan, A. Chidambaram, P. G. Fonquernie, M. E. Light, D. Choquesillo-Lazarte, H. Huang, E. Solano, J. Fraile, C. Viñas, F. Teixidor, J. A. R. Navarro, K. C. Stylianou and J. G. Planas, Journal of the American Chemical Society, 2020, 142, 8299-8311.

15. L. Gan, P. G. Fonquernie, M. E. Light, G. Norjmaa, G. Ujaque, D. Choquesillo-Lazarte, J. Fraile, F. Teixidor, C. Viñas and J. G. Planas, Molecules, 2019, 24.

16. M. Jørgensen, S. R. H. Jensen, T. D. Humphries, M. R. Rowles, M. V. Sofianos, C. E. Buckley, T. R. Jensen and M. Paskevicius, The Journal of Physical Chemistry C, 2020, 124, 11340-11349.

17. H. Jude, H. Disteldorf, S. Fischer, T. Wedge, A. M. Hawkridge, A. M. Arif, M. F. Hawthorne, D. C. Muddiman and P. J. Stang, Journal of the American Chemical Society, 2005, 127, 12131-12139.

18. D. Jung, M. Muni, G. Marin, R. Ramachandran, M. F. ElKady, T. Balandin, R. B. Kaner and A. M. Spokoyny, Journal of Materials Chemistry A, 2020, 8, 18015-18023.

19. D. Jung, L. M. A. Saleh, Z. J. Berkson, M. F. El-Kady, J. Y. Hwang, N. Mohamed, A. I. Wixtrom, E. Titarenko, Y. Shao, K. McCarthy, J. Guo, I. B. Martini, S. Kraemer, E. C. Wegener, P. Saint-Cricq, B. Ruehle, R. R. Langeslay, M. Delferro, J. L. Brosmer, C. H. Hendon, M. Gallagher-Jones, J. Rodriguez, K. W. Chapman, J. T. Miller, X. Duan, R. B. Kaner, J. I. Zink, B. F. Chmelka and A. M. Spokoyny, Nature Materials, 2018, 17, 341-348.

20. D. Nguyen, Institut für Anorganische Chemie der Universität Stuttgart, 2009.

21. T. Peymann, C. B. Knobler and M. F. Hawthorne, Inorg. Chem., 2000, 39, 1163-1170.

22. T. Peymann, C. B. Knobler, S. I. Khan and M. F. Hawthorne, Journal of the American Chemical Society, 2001, 123, 2182-2185.

23. S. Rodríguez-Hermida, M. Y. Tsang, C. Vignatti, K. C. Stylianou, V. Guillerm, J. Pérez-Carvajal, F. Teixidor, C. Viñas, D. Choquesillo-Lazarte, C. Verdugo-Escamilla, I Peral, J. Juanhuix, A. Verdaguer, I. Imaz, D. Maspoch and J. Giner Planas, Angewandte Chemie International Edition, 2016, 55, 16049-16053.

24. T. Scholköpf, Institut für Anorganische Chemie der Universität Stuttgart, 2011.

25. A. M. Spokoyny, D. Kim, A. Sumrein and C. A. Mirkin, Chemical Society Reviews, 2009, 38, 1218-1227.

26. F. Tan, A. López-Periago, M. E. Light, J. Cirera, E. Ruiz, A. Borrás, F. Teixidor, C. Viñas, C. Domingo and J. G. Planas, Advanced Materials, 2018, 30, 1800726.

27. M. Y. Tsang, S. Rodríguez-Hermida, K. C. Stylianou, F. Tan, D. Negi, F. Teixidor, C. Viñas, D. Choquesillo-Lazarte, C. Verdugo-Escamilla, M. Guerrero, J. Sort, J. Juanhuix, D. Maspoch and J. Giner Planas, Crystal Growth & Design, 2017, 17, 846-857.

28. N. Van, I. Tiritiris, R. F. Winter, B. Sarkar, P. Singh, C. Duboc, A. Muñoz-Castro, R. Arratia-Pérez, W. Kaim and T. Schleid, Chemistry – A European Journal, 2010, 16, 11242-11245.

29. T. J. Wedge, A. Herzog, R. Huertas, M. W. Lee, C. B. Knobler and M. F. Hawthorne, Organometallics, 2004, 23, 482-489.

30. Y. Zhang, L. Yang, L. Wang, S. Duttwyler and H. Xing, Angewandte Chemie International Edition, 2019, 58, 8145-8150.

31. Z. Zheng, C. B. Knobler, M. D. Mortimer, G. Kong and M. F. Hawthorne, Inorg. Chem., 1996, 35, 1235-1243.

32. A. R. Pitochelli and F. M. Hawthorne, Journal of the American Chemical Society, 1960, 82, 3228-3229.

33. I. Sivaev, V. Bregadze and S. Sjöberg, Collection of Czechoslovak Chemical Communications, 2002, 67.

34. E. L. Muetterties, J. H. Balthis, Y. T. Chia, W. H. Knoth and H. C. Miller, Inorg. Chem., 1964, 3, 444-451.

35. W. H. Knoth, H. C. Miller, J. C. Sauer, J. H. Balthis, Y. T. Chia and E. L. Muetterties, Inorg. Chem., 1964, 3, 159-167.

36. K. A. Solntsev, A. M. Mebel, N. A. Votinova, N. T. Kuznetsov and O. P. Charkin, Koordinatsionnaya Khimiya, 1992, 18, 340-364.

37. S. V. Ivanov, S. M. Miller, O. P. Anderson, K. A. Solntsev and S. H. Strauss, Journal of the American Chemical Society, 2003, 125, 4694-4695.

38. C. Knapp and C. Schulz, Chemical Communications, 2009, DOI: 10.1039/B908970E, 4991-4993.

39. V. Geis, K. Guttsche, C. Knapp, H. Scherer and R. Uzun, Dalton Transactions, 2009, DOI: 10.1039/B821030F, 2687-2694.

40. E. Bukovsky, S. Fiedler, D. V. Peryshkov, A. A. Popov and S. Strauss, European Journal of Inorganic Chemistry, 2012, 2012, 208-212.

41. D. V. Peryshkov, A. A. Popov and S. H. Strauss, Journal of the American Chemical Society, 2010, 132, 13902-13913.

42. D. V. Peryshkov, E. V. Bukovsky, M. R. Lacroix, H. Wu, W. Zhou, W. M. Jones, M. Lozinšek, T. C. Folsom, D. L. Heyliger, T. J. Udovic and S. H. Strauss, Inorg. Chem., 2017, 56, 12023-12041.

43. I. Krossing and I. Raabe, Angewandte Chemie International Edition, 2004, 43, 2066-2090.

44. C. Jenne, M. Keßler and J. Warneke, Chemistry – A European Journal, 2015, 21, 5887-5891.

45. D. V. Peryshkov and S. Strauss, Journal of Fluorine Chemistry, 2010, 131, 1252-1256.

46. D. V. Peryshkov, E. V. Bukovsky, T. C. Folsom and S. H. Strauss, Polyhedron, 2013, 58, 197-205.

47. M. Malischewski, D. V. Peryshkov, E. V. Bukovsky, K. Seppelt and S. H. Strauss, Inorg. Chem., 2016, 55, 12254- 12262.

48. B. R. S. Hansen, M. Paskevicius, M. Jørgensen and T. R. Jensen, Chemistry of Materials, 2017, 29, 3423-3430.

49. E. V. Bukovsky, D. V. Peryshkov, H. Wu, W. Zhou, W. S. Tang, W. M. Jones, V. Stavila, T. J. Udovic and S. H. Strauss, Inorg. Chem., 2017, 56, 4369-4379.

50. M. Kirchmann and L. Wesemann, Dalton Transactions, 2008, DOI: 10.1039/B715305H, 444-446.

51. E. A. Malinina, V. V. Avdeeva, L. V. Goeva and N. T. Kuznetsov, Russian Journal of Inorganic Chemistry, 2010, 55, 2148-2202.

52. Y. Zhang, Y. Sun, F. Lin, J. Liu and S. Duttwyler, Angewandte Chemie International Edition, 2016, 55, 15609-15614.

53. Y. Zhang, T. Wang, L. Wang, Y. Sun, F. Lin, J. Liu and S. Duttwyler, Chemistry – A European Journal, 2018, 24, 15812-15817.

54. T. Peymann, A. Herzog, C. B. Knobler and M. F. Hawthorne, Angewandte Chemie International Edition, 1999, 38, 1061-1064.

55. S. E. Korolenko, V. V. Avdeeva, E. A. Malinina and N. T. Kuznetsov, Russian Journal of Inorganic Chemistry, 2021, 66, 1350-1373.

56. S. J. R. Prabakar, K. J. Rao and C. N. R. Rao, Proceedings of the Royal Society of London. A. Mathematical and Physical Sciences, 1990, 429, 1 - 15.

57. K. R. Thurber and R. Tycko, Journal of magnetic resonance (San Diego, Calif. : 1997), 2009, 196, 84-87.

58. J. P. Yesinowski, H. D. Ladouceur, A. P. Purdy and J. B. Miller, J. Chem. Phys., 2010, 133, 234509.

59. M. Weingarth and M. Baldus, in Illustrated Medical Biochemistry, Jaypee Brothers Medical Publishers Ltd., 2005, ch. 1.

60. M. H. Levitt, Spin Dynamics: Basics of Nuclear Magnetic Resonance, John Wiley & Sons, 2 edn., 2008.

61. I. Schnell and H. W. Spiess, J Magn Reson, 2001, 151, 153-227.

62. M. Feike, D. E. Demco, R. Graf, J. Gottwald, S. Hafner and H. W. Spiess, Journal of Magnetic Resonance, Series A, 1996, 122, 214-221.

63. K. Saalwächter, F. Lange, K. Matyjaszewski, C. F. Huang and R. Graf, J Magn Reson, 2011, 212, 204-215.

64. M. Dudev, J. Wang, T. Dudev and C. Lim, The Journal of Physical Chemistry B, 2006, 110, 1889-1895.

65. Y. Marcus, Chemical Reviews, 1988, 88, 1475-1498.

66. H. Ohtaki and T. Radnai, Chemical Reviews, 1993, 93, 1157- 1204.

67. T. Peymann, C. B. Knobler, S. I. Khan and M. F. Hawthorne, Inorg. Chem., 2001, 40, 1291-1294.

68. E. L. Muetterties, R. E. Merrifield, H. C. Miller, W. H. Knoth, Jr. and J. R. Downing, J Am Chem Soc, 1962, 84, 2506.

69. L. A. Leites, Chemical Reviews, 1992, 92, 279-323.

70. B. Grünberg, T. Emmler, E. Gedat, I. Shenderovich, G. H. Findenegg, H. H. Limbach and G. Buntkowsky, Chemistry, 2004, 10, 5689-5696.

71. P. M. Aguiar, M. J. Katz, D. B. Leznoff and S. Kroeker, Physical Chemistry Chemical Physics, 2009, 11, 6925-6934.

72. H. A. Habib, A. Hoffmann, H. A. Höppe and C. Janiak, Dalton Transactions, 2009, DOI: 10.1039/B812670D, 1742-1751.

73. H. A. Habib, A. Hoffmann, H. A. Höppe, G. Steinfeld and C. Janiak, Inorg. Chem., 2009, 48, 2166-2180.

74. S. D. Jones, H. Nguyen, P. M. Richardson, Y.-Q. Chen, K. E. Wyckoff, C. J. Hawker, R. J. Clément, G. H. Fredrickson and R. A. Segalman, ACS Central Science, 2022, DOI: 10.1021/acscentsci.1c01260.

75. M. J. Katz, P. M. Aguiar, R. J. Batchelor, A. A. Bokov, Z.-G. Ye, S. Kroeker and D. B. Leznoff, Journal of the American Chemical Society, 2006, 128, 3669-3676.

76. A. V. Kuttatheyil, D. Lässig, J. Lincke, M. Kobalz, M. Baias, K. König, J. Hofmann, H. Krautscheid, C. J. Pickard, J. Haase and M. Bertmer, Inorg. Chem., 2013, 52, 4431-4442.

77. H. H. Lee, J. B. Lee, Y. Park, K. H. Park, M. S. Okyay, D.-S. Shin, S. Kim, J. Park, N. Park, B.-K. An, Y. S. Jung, H.-W. Lee, K. T. Lee and S. Y. Hong, ACS Applied Materials & Interfaces, 2018, 10, 22110-22118.

78. L. Ouyang, P. M. Aguiar, R. J. Batchelor, S. Kroeker and D. B. Leznoff, Chemical Communications, 2006, DOI: 10.1039/B512430A, 744-746.

79. L. Rodríguez-Cid, E. C. Sañudo, A. M. López-Periago, A. González-Campo, N. Aliaga-Alcalde and C. Domingo, Crystal Growth & Design, 2020, 20, 6555-6564.

80. J. J. Vittal, Coordination Chemistry Reviews, 2007, 251, 1781-1795.

8. Electron donor-acceptor small molecule thin films as active layers in solar cells

8.1 Motivation and project goals

Electronically active carbon materials may be the key to making large-scale energy conversion and storage devices with lower environmental impact than current industrial precious-metal and silicon-based materials. For example, one the diverse applications of electronically active carbon materials is in the solar cell, where solar energy is converted into electrical energy via the photoelectric effect. An alternative to current synthesis-extensive and expensive silicon based solar energy conversion devices, organic small molecule active layers can be a solution processable (printable), inexpensive alternative.[1] Although active layer small molecules combinations are being furiously developed throughout the field, not much is known about the composition-structure-function relationships of the electron donors/acceptor molecules that make up the active layer. A key characteristic of these types of materials is that they exhibit macroscopic conductivity due to their carbon-based structures, enabling electron transport and utilization. The broad objective of my thesis project is to measure and correlate atomic-level composition and structural properties of electronically active carbon materials with their desirable electrocatalytic, energy capture/storage, or water purification properties. Thus, the correlation of intra- and inter-molecular interactions with electrochemical performance of a solar cell, leads to improved understanding of local optoelectronic environments and their relation in increased solar cell activity.

8.2 Background, challenges, and approach

Donor-acceptor conjugated polymers/small molecule thin films, which are used in the fabrication of organic bulk heterojunction (BHJ) solar cells, are an inexpensive, solution-processable (printable), scalable alternative to current silicon-based solar cells and semiconductors.[1,2] In organic BHJ solar cells, thin films are generally grown on substrates by spin casting the solution-processable organic materials, which upon absorbing light, convert light energy into electrical energy via the photoelectric effect. When a photon promotes an electron from the highest occupied molecular orbital (HOMO) to the lowest unoccupied molecular orbital (LUMO) an electron-hole pair is formed inducing a charge difference, and charge migration occurs through the conjugated backbones.[3] Our hypothesis was that the efficiency of charge carrier properties of organic conjugated polymers depends on their local backbone and sidechain structures and conformations.

The active layer of these devices are comprised of electron donating and accepting molecules, which when cast phase segregate to nanoscale, bicontinuous domains that enable the formation of electron-hole pairs necessary for electrical charge production.[3] In the past, fullerene based PCBM molecules have been employed as the electron acceptor. However, the high fabrication cost and synthesis requirements of the molecule present concerns for production scale-up.[2,3] ITIC non-fullerene molecules were identified to be a scalable and more highly performing alternative electron acceptor.

My goal for this project was to characterize the atomic level interactions between the acceptor materials and the polymer backbone donors. A variety of techniques are routinely employed to probe the crystalline structure of the materials. However, the various extents of ordered and disordered regions, present challenges to characterization. Additionally, previous

work has found similar materials to be ~50% amorphous, regions not typically detected by conventional characterization techniques. NMR however, is sensitive to the atomic scale environments necessary to investigate small molecule polymer backbone interactions and does not rely on the long-range order.[4–7] Signal intensities present in the blend films, not present in the neat films indicate interfaces between backbone and acceptor regions. Thus, NMR spectroscopy was used to probe the atomic-level environments of both the crystalline and amorphous regions of the active layers of the conjugated polymer thin films.

This chapter is adapted from a manuscript accepted by *Solar RRL*. Above I outlined the project in terms of my (NMR specific) motivation, approach, and contribution. Below is the manuscript that includes my work along with the work of many others. This work is also included in Chapter 3 of the thesis of first author Benjamin R. Luginbuhl, titled *Towards a Fundamental Understanding of the Device Physics of Organic Solar Cells*.

Paper title: Low voltage-loss organic solar cells light the way for efficient semitransparent photovoltaics

Journal: *Solar RRL* **2022,** 2200135.

Authors: Benjamin R. Luginbuhl, Seo-Jin Ko, Niva A. Ran, Huawei Hu, Shona M. Becwar, Akchheta Karki, Martin Seifrid, Takashi Okubo, Ming Wang, Harald W. Ade, Bradley F. Chmelka, G. N. Manjunatha Reddy, Guillermo C. Bazan, and Thuc-Quyen Nguyen

8.3 Abstract

Organic solar cells that are transparent to visible light are highly desirable for applications such as window treatments or solar greenhouse panels. A key challenge is to simultaneously transmit most photons between 400 and 700 nm while retaining a high short-circuit current and power conversion efficiency (PCE). Here, we report organic bulk heterojunction (BHJ) solar cells consisting of a donor polymer (PM2) and the non-fullerene acceptor ITIC-Th have achieved a PCE of 9.3%, and the BHJ thin films exhibited an average visible transmittance over 40%. This value is achieved primarily due to a very high open-circuit voltage (V_{OC}) of 0.93 V, which represents a voltage loss of only 0.50 V relative to the material optical band gap, E_{opt}. In PM2:$PC_{61}BM$ devices, this voltage loss increases to 0.62 V (V_{OC} = 0.82 V). We find that this difference in V_{OC} is due to higher non-radiative recombination in the fullerene-based solar cell, suggesting that non-fullerene acceptors may lead to better performance in semi-transparent devices. The optoelectronic properties associated with PM2:ITIC-Th and PM2:$PC_{61}BM$ blends are further corroborated by different morphological features and local structures at the donor-acceptor interfaces characterized by atomic force microscopy, X-ray scattering, and solid-state NMR spectroscopy techniques.

8.4 Introduction

Traditionally, solar cells have been employed on roof-tops, where the solar cell panels utilize otherwise unused space. However, silicon solar cells are opaque, thick, heavy and rigid, and therefore are not suitable for applications that require semitransparency such as glass walls, windows, and roofs and greenhouses.[1] Consequently, there is a need to develop new solar cell materials for such applications. Organic solar cells typically consist of thin (below 300 nm), light weight, and flexible active layers, which opens many possibilities for applications where traditional silicon solar cells are not suitable. Further, due to the tunability of the active layer components, materials can be designed with selective absorption/transmission bands. Thus, organic solar cells can be used for passive energy production from previously unused areas, such as glass windows, while still transmitting visible light.

A major challenge for semi-transparent solar cells is the trade-off between power conversion efficiency (PCE) and transparency. The PCE is directly related to the short-circuit current (J_{SC}), open-circuit voltage (V_{OC}), and the fill factor (FF). The J_{SC} describes the current the solar cell can produce, and it is directly proportional to the number of photons absorbed. It follows therefore that a semitransparent solar cell will not have a J_{SC} as high as a solar cell capable of absorbing all incident photons. However, while the J_{SC} of a semitransparent solar cell may suffer, if we can maximize the V_{OC} and FF, the overall PCE may still be sufficiently high for practical applications. Furthermore, with a custom semiconductor band gap design, it is possible to choose which regions of the light spectrum will be absorbed, and therefore to fabricate solar cells with appealing colors, or that transmit wavelengths needed for other purposes such as photosynthesis in plants.[2]

While the field of organic photovoltaics (OPV) has seen continuous improvements in the J_{SC} and the FF, the V_{OC} has remained limited due to various losses.[3–8] As a first approximation, the maximum V_{OC} that a solar cell can achieve is determined by the optical band gap of the device, E_{opt}, which is given by the lowest energy singlet exciton of either the donor (E_{D*}) or acceptor material (E_{A*}), which is designated as S_1.[9] The difference in energy between S_1 and qV_{OC} is the total energy loss in the solar cell between absorption and charge collection. Since efficient OPV devices require a blend of two materials with offset energy levels to split excitons, some of the energy of the absorbed photons will be lost during the charge transfer process.[3,5] The frontier orbital overlap between the highest occupied molecular orbital of the donor ($HOMO_D$) and the lowest unoccupied molecular orbital of the acceptor ($LUMO_A$) forms a new electronic state at the donor/acceptor interface, known as the charge transfer (CT) state.[3,4,10,11] The energy of the CT state, E_{CT} determines the effective band gap in OPV materials, and thus energetic difference between the S_1 and E_{CT} can be attributed to energetic losses due to charge transfer.[3] E_{CT} correlates linearly with the $V_{OC,}$ and as recombination pathways are shut off (as $T \rightarrow 0$ K), E_{CT} and V_{OC} have been shown to converge.[12,13] The quantity $E_{CT} - qV_{OC}$ therefore reflects the energy losses due to charge recombination after charge transfer. A detailed balance analysis of solar cell devices concludes that some amount of radiative charge recombination is thermodynamically unavoidable,[14] however, OPV devices are characterized by large losses due to non-radiative recombination as well. Thus, $E_{CT} - qV_{OC}$ can be further separated into radiative losses and non-radiative losses. To maximize $V_{OC,}$ we must minimize charge transfer losses ($S_1 - E_{CT}$) as well as the recombination losses from $E_{CT} - qV_{OC}$.

Until recently, there were very few high-efficiency OPVs with $S_1 - E_{CT}$ lower than 0.6 eV. In the last several years, however, a number of reports have been published which highlight systems with high performance and low voltage losses.[7,15–21] These OPV blends include polymer-fullerene blends,[7,22] blends with non-fullerene acceptors,[15,18,21,23,24] as well as a ternary system.[25,26] However, despite the offset losses, the aforementioned blends have significant absorption through the visible range, with the exception of PIPCP:$PC_{61}BM$.[7,27]

In this report, we correlate the performance properties and multiscale structures of bulk heterojunction (BHJ) solar cell devices made from the narrow band gap donor polymer PM2 mixed with the non-fullerene acceptor, ITIC-Th.[21,28–31] PM2:ITIC-Th devices are able to achieve a PCE of 9.3% with V_{OC} of 0.93 V, and a remarkably low V_{OC} loss from the singlet exciton energy of the lower band gap component, in this case the donor, of 0.50 eV.[32] In contrast, PM2:$PC_{61}BM$ devices achieve a PCE of 7.5% with a V_{OC} of 0.82 V (E_{loss} = 0.62 eV). In viewing this difference as a function of the acceptor, we provide a thorough characterization of the morphology, long-range order, and short-range structures and interactions at different length scales using photo-conducting atomic force microscopy (pc-AFM), wide-angle X-ray scattering, and solid-state (ss)NMR spectroscopy techniques. These results were compared and correlated with the differences in the device physics such as voltage losses between the two blends, external quantum efficiency, energetic order, and recombination dynamics. Finally, we emphasize that by reducing voltage losses, it is possible to obtain high-performance despite the limited absorption in semitransparent solar cells.

8.5 Results and Discussion

Figure 8.1a shows the chemical structures of the conjugated polymer donor PM2, the fullerene acceptor $PC_{61}BM$, and the non-fullerene acceptor ITIC-Th. The PM2 polymer with a molecular weight Mn = 83 kDa and a polydispersity index $Đ$ = 2.0 was used.[24] Their respective ionization potentials and electron affinities are shown schematically in **Figure 8.1b**. The ionization potentials were determined using ultraviolet photoelectron spectroscopy (UPS) and the electron affinities were estimated by adding the optical band gap to these values.[33,34] The normalized absorption spectra of PM2:$PC_{61}BM$ and PM2:ITIC-Th blends are shown in **Figure 8.1c**. The PM2:ITIC-Th blends show a lower absorption for wavelengths < 550 nm compared to PM2:$PC_{61}BM$, mostly due to differences in the absorption properties of $PC_{61}BM$ *vs.* ITIC-Th (see **Figure S8.2**). In particular, the PM2:ITIC-Th blend is an excellent material for greenhouse applications, with high transmissivity between 400 and 520 nm wavelengths.[35]

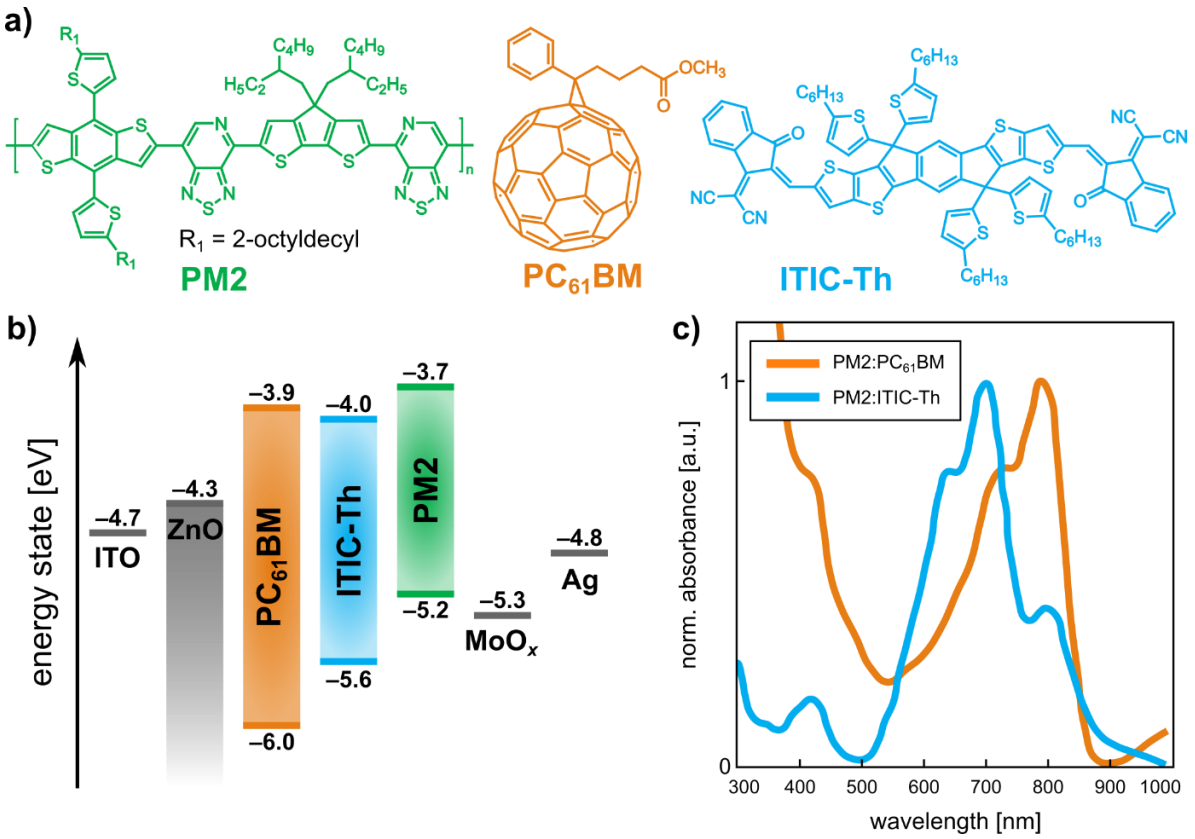

Figure 8.1. a) Chemical structures of PM2, $PC_{61}BM$ and ITIC-Th, b) energy states of the materials used in this study, and c) normalized absorption spectra of PM2:$PC_{61}BM$ and PM2:ITIC-Th blends.

8.5.1 Solar Cell Performance and Voltage Loss Analysis

The 1 sun (AM1.5G, 100 mW cm^{-2}) *J-V* characteristics and photovoltaic external quantum efficiency (EQE_{PV}) spectra of representative inverted architecture devices of each blend are shown in **Figure 8.2** and tabulated in **Table 8.1**. Detailed performance metrics for each blend and their optimizations are shown in **Table S8.1**. The optimized conditions for PM2:$PC_{61}BM$ devices were reported previously,[7,27,36] while the optimization of PM2:ITIC-Th blends is

detailed in **Figure S8.1** in the Supporting Information. Despite their relatively lower absorption between 300–550 nm, PM2:ITIC-Th solar cells show increased photovoltaic performance compared to PM2:$PC_{61}BM$, mainly due to a higher J_{SC} (16.35 mA/cm^2 *vs.* 13.76 mA/cm^2) and V_{OC} (0.93 V *vs.* 0.82 V). We will explore the reasons for this increase in performance below.

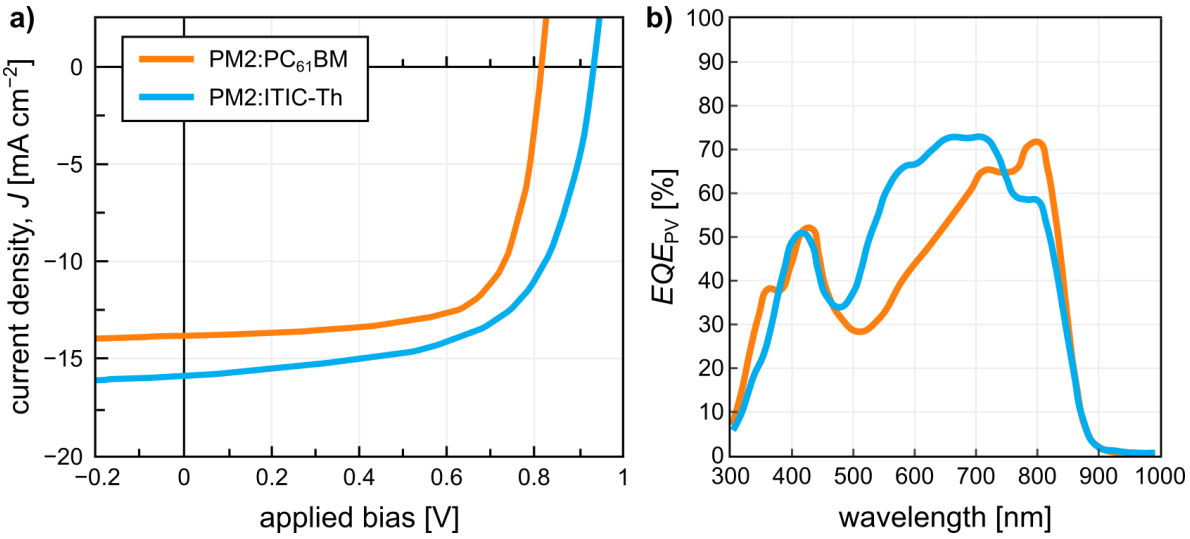

Figure 8.2. a) Current-density *vs.* voltage curves for example PM2:$PC_{61}BM$ and PM2:ITIC-Th solar cells. b) External quantum efficiency spectra for the same devices.

Table 8.1. Photovoltaic performance metrics for representative PM2:$PC_{61}BM$ and PM2:ITIC-Th devices under 1 sun illumination.

blend	V_{OC} **[V]**	J_{SC} **[mA cm^{-2}]**	**FF [%]**	**PCE [%]**
PM2:$PC_{61}BM$	0.822 (0.817 ± 0.003)	13.76 (13.78 ± 0.67)	66.4 (63.4 ± 2)	7.51 (7.17 ± 0.27)
PM2:ITIC-Th	0.926 (0.907 ± 0.019)	16.35 (16.60 ± 0.05)	61.6 (60.5 ± 2)	9.33 (9.15 ± 0.12)

The band gaps of organic semiconductors can be approximated by adding their optical gaps, which are roughly determined from the absorption onsets shown in **Figure S8.2**, to the ionization potential energy levels (measured *via* UPS). By this approximation, the energetic offsets for electron transfer, *i.e.*, the difference in electron affinities between the donor and acceptor ($EA_D - EA_A$), for PM2:$PC_{61}BM$ and PM2:ITIC-Th are 200 meV and 300 meV, respectively. These relatively low offsets suggest that the energy losses due to charge-transfer will be low, which correlates well with the high V_{OC} in both systems. To further understand the differences in V_{OC} between the PM2:$PC_{61}BM$ and PM2:ITIC-Th devices, the energy losses due to generation, radiative recombination, and non-radiative recombination were quantified. First, the energy difference between the first excited singlet state, S_1, and the energy of the CT state for each blend was measured using a combination of absorption spectroscopy, the EQE_{PV} spectra, and the electroluminescence (*EL*) spectra following the procedures detailed by Vandewal *et al.* and reported previously.[3,9,36,37] By fitting the optical absorption spectra (shown in **Figure S8.2d-f**), S_1 was determined to be 1.44 and 1.43 eV for PM2:$PC_{61}BM$ and PM2:ITIC-Th, respectively. To obtain a more accurate picture of the low-energy absorption behavior associated with direct excitation of CT states, the reciprocity relationship between emission and absorption (**Equation S8.1**) was used to calculate the shape of the low-energy absorption (calculated EQE, thicker dashed lines in **Figure 8.3a,b**). Then, E_{CT} was determined by simultaneously fitting the reduced EL and EQE spectra to **Equations S8.2 and S8.3** (detailed in the Supporting Information).[9,13] From these equations (dotted lines in **Figure 8.3a,b**), E_{CT} was determined to be 1.38 eV for both PM2:$PC_{61}BM$ and PM2:ITIC-Th blends.

Thus, the losses due to charge transfer are approximately the same for both blends, between 50 – 60 mV.

Table 8.2. S_1 and E_{CT} energy levels and fitting parameters from **Equations S8.2** and **S8.3** for PM2:$PC_{61}BM$ and PM2:ITIC-Th solar cells.

blend	S_1 **[eV]**	E_{CT} **[eV]**	f **[meV^2]**	λ **[meV]**
PM2:$PC_{61}BM$	1.44	1.38 ± 0.008	0.30 ± 0.09	110 ± 4
PM2:ITIC-Th	1.43	1.38 ± 0.002	0.30 ± 0.04	100 ± 5

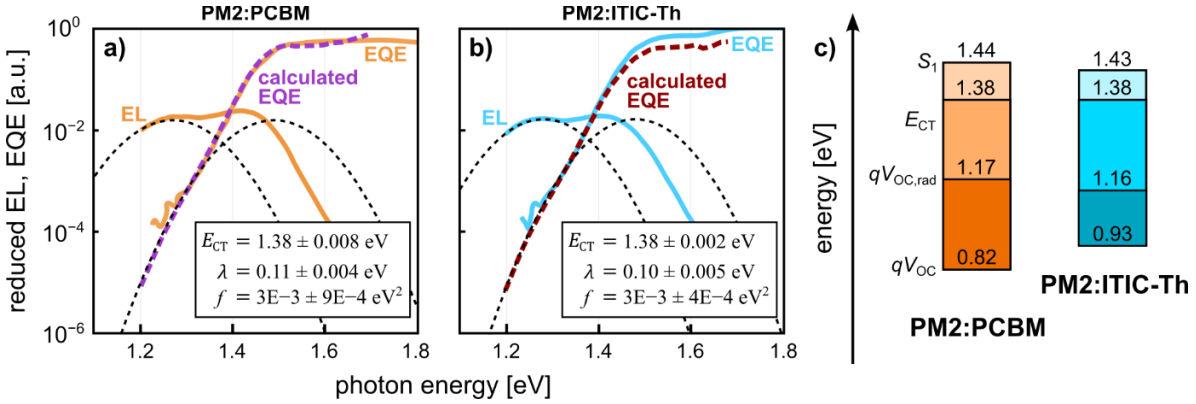

Figure 8.3. Determining the energy of the charge transfer state in a) PM2:$PC_{61}BM$ and b) PM2:ITIC-Th solar cells from their reduced electroluminescence and external quantum efficiency spectra. The dashed black lines are simultaneous fits using **Equations 8.2** and **8.3**. c) Schematic representations of the voltage losses in each blend material.

Next, the voltage losses due to radiative and non-radiative recombination were determined and compared.[38-40] The overall losses to the open-circuit voltage in a solar cell can be broken down as follows:

$$\Delta V_{\mathrm{OC}} = \frac{E_{\mathrm{CT}}}{q} - \Delta V_{\mathrm{rad}} - \Delta V_{\mathrm{nr}} \tag{8.1}$$

where ΔV_{rad} and ΔV_{nr} are the voltage losses due to only radiative and non-radiative recombination, respectively. ΔV_{rad} can be calculated using the following **Equation**:[36]

$$\Delta V_{\mathrm{rad}} = \frac{k_{\mathrm{B}}T}{q} \ln\left(\frac{J_{\mathrm{SC}} h^3 c^2}{f q 2\pi (E_{\mathrm{CT}} - \lambda)}\right) \tag{8.2}$$

where q is the elementary charge, k_{B} Boltzmann constant, T is the temperature, J_{SC} is the short-circuit current density measured under 1 sun illumination, h is Planck's constant, c is the speed of light in a vacuum, and f and λ are the fitting parameters shown in **Table 8.2**. Solving **Equation 8.2** for each blend reveals that the losses due to radiative recombination are 217 ± 7 mV and 213 ± 3 mV for PM2:$PC_{61}BM$ and PM2:ITIC-Th devices, respectively. Hence, the differences in the V_{OC} for these two blends are due primarily to losses from non-radiative recombination, with PM2:$PC_{61}BM$ devices losing 350 mV and PM2:ITIC-Th devices losing 230 mV. Each of these losses are summarized in **Figure 8.3c**.

This result can be further verified by directly measuring the electroluminescence quantum efficiency (EQE_{EL}), as shown in **Equation 8.3**:[41]

$$\Delta V_{\mathrm{nr}} = \frac{k_{\mathrm{B}}T}{q} \ln(EQE_{\mathrm{EL}}^{-1}) \tag{8.3}$$

EQE_{EL} is defined as the ratio of emitted photons to injected electrons (or holes), and it can be measured by driving the solar cell in forward bias and counting the emitted photons with a calibrated photodiode. The measured EQE_{EL} values were 3×10^{-7} and 2×10^{-5} for PM2:$PC_{61}BM$ and PM2:ITIC-Th, respectively, corresponding to non-radiative voltage losses

of approximately 390 and 280 mV, which agree reasonably well with the values obtained from **Equation 8.2**.

8.5.2 Morphology Characterization

Next, to understand the differences in performance between the PM2:$PC_{61}BM$ and PM2:ITIC-Th devices, we characterized these photovoltaic blends at micrometer to sub-nanometer length scales using different analytical techniques. Photo-conductive atomic force microscopy (pc-AFM) and grazing-incidence wide-angle X-ray scattering (GIWAXS) measurements were carried out to understand the surface and bulk morphologies and long-range order, and the local structures and intermolecular interactions were elucidated by using 1D and 2D solid-state NMR spectroscopy. In pc-AFM, the surface morphology of the semiconductor film was imaged in contact mode while collecting simultaneously a photocurrent image of the same area under white light illumination. By changing the bias between the AFM tip and the film, data about the *p*- and *n*-type domains at the film surface can be collected. Scans of both PM2:$PC_{61}BM$ and PM2:ITIC-Th blends revealed smooth surface topographies, with root-mean-square roughnesses of 1.8 nm and 1.2 nm, respectively, as shown in **Figure 8.4a,c**. Both blends show conductive networks. PM2:ITIC-Th films also show a higher photocurrent at 0V biases, which supports the observed differences in J_{SC} between PM2:ITIC-Th and PM2:$PC_{61}BM$ devices (**Figure 8.4b,d**).[42]

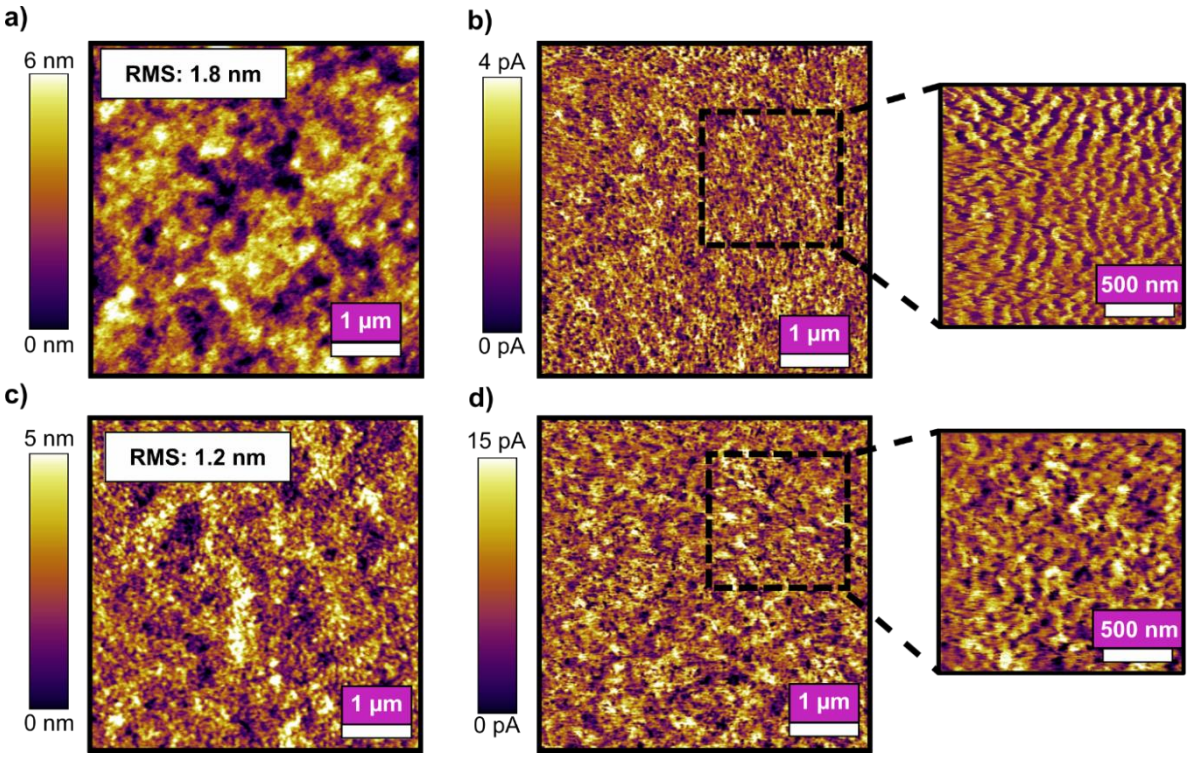

Figure 8.4. Contact mode topography AFM images (5.0 µm × 5.0 µm) of a) PM2:$PC_{61}BM$ and c) PM2:ITIC-Th blend films. Corresponding photocurrent images collected under white illumination with no applied bias for b) PM2:$PC_{61}BM$ and d) PM2:ITIC-Th.

Having analyzed the surface morphologies of PM2:ITIC-Th and PM2:$PC_{61}BM$ blends, we next studied molecular orientation and packing characteristics of these films by using GIWAXS measurements and analyses. The two-dimensional (2D) GIWAXS patterns of pristine PM2, ITIC-Th, PM2:$PC_{61}BM$ and PM2:ITIC-Th blend films under optimized-solvent conditions are shown in **Figure S8.4** (Supporting Information), and the corresponding in-plane (q_{xy}) and out-of-plane (q_z) line-cut profiles are presented in **Figure S8.5**. The PM2:ITIC-Th film shows a strong reflection at larger q_z values (attributed to scattering from π–π stacked moieties),[43] suggesting the presence of ordered crystallites with a face-on orientation with

respect to the substrate. These crystallites have an average π–π stacking distance of 3.53 Å. In comparison, PM2:$PC_{61}BM$ films show a weaker π–π stacking signal and larger spacing of 3.78 Å, as well as having no preferred crystallite orientation. The smaller π–π spacing and a larger fraction of face-on orientations in the PM2:ITIC-Th film may result in efficient vertical charge transport and extraction, and hence explain the higher J_{SC} in the device and higher photocurrent in pc-AFM.[8,44]

To estimate the degree of phase separation and domain purity in blends of PM2:ITIC-Th and PM2:$PC_{61}BM$, resonant soft X-ray scattering was performed on thin films of each optimized blend (**Figure S8.6**, **Table S8.3**). From these data, it was found that PM2:$PC_{61}BM$ blends have a higher purity and a smaller long period of 44.8 nm compared to that of PM2:ITIC-Th blends with 69.8 nm. Since the domain size can be roughly estimated as half of the long period, the PM2:$PC_{61}BM$ blends show smaller domains than that of PM2:ITIC-Th (~22.4 nm vs. ~34.9 nm). This suggests that ITIC-Th forms both more mixed domains and larger domains overall, which could lead to favorable charge generation and extraction.[45–47]

Solid-state organization and intermolecular interactions in organic semiconductors and their blends can be characterized by magic-angle spinning (MAS) NMR spectroscopy.[32, 48–55] We examined the local environments of ^{1}H and ^{13}C atoms and through-space ^{1}H-^{13}C proximities in pristine PM2, ITIC-Th and $PC_{61}BM$ materials, and in PM2:$PC_{61}BM$ and PM2:ITIC-Th blend films. While the one-dimensional (1D) ^{1}H direct-excitation MAS NMR spectra of these materials exhibit severely overlapped signals (Supporting Information, **Figure S8.7**), 1D $^{13}C\{^{1}H\}$ cross-polarization (CP)-MAS NMR spectra provide significantly enhanced resolution (Supporting Information, **Figure S8.8**) enabling distinct aliphatic and aromatic ^{13}C moieties to be resolved and identified. Notably, enhanced resolution associated

with the 2D $^{13}C\{^{1}H\}$ heteronuclear correlation (HETCOR) experiments facilitates the assignment and analysis of chemical shifts associated with different ^{1}H and ^{13}C moieties by distributing the signals into two frequency dimensions. By analyzing the 2D HETCOR spectra of neat donor and acceptor compounds and blends, through-space ^{1}H-^{13}C proximities at sub-nanometer to nanometer distances can be obtained and compared for the PM2:ITIC-Th and PM2:$PC_{61}BM$ BHJ blends. **Figure 8.5** compares the 2D $^{13}C\{^{1}H\}$ HETCOR NMR spectra of the blends together with the 1D $^{13}C\{^{1}H\}$ CP-MAS spectra of neat compounds and blends. Similar 2D $^{13}C\{^{1}H\}$ HETCOR NMR spectra of neat donor polymer and acceptor materials are shown in **Figure S8.9** of the Supporting Information. Aliphatic and aromatic ^{1}H and ^{13}C signals associated with PM2, ITIC-Th, $PC_{61}BM$ molecules are labeled according to the same color schemes as depicted in their schematic structural diagrams. In **Figure 8.5a**, the 2D $^{13}C\{^{1}H\}$ HETCOR spectrum of the PM2: $PC_{61}BM$ blend exhibits correlated ^{13}C signal intensity at 14 ppm and 23 ppm with ^{1}H signals at 1.2 ppm and in the range of 1.5-2.0 ppm, respectively, which correspond to $–CH_3$ and $–CH_2$ groups in the aliphatic side chains of PM2. In addition, the ^{13}C signal at 54 ppm correlated with the ^{1}H signal at ~3 ppm is due to methoxy groups of $PC_{61}BM$ molecules, and a plausible overlapping contribution from the quaternity carbon atom next to the phenyl ring. Of particular interest are the 2D correlation peaks between the ^{13}C signals associated with the PM2 sidechains at 30-32 ppm and the ^{1}H signals at 2.3 ppm from the $PC_{61}BM$ sidechains (red arrow) and between the ^{13}C signals at 34-36 ppm from $PC_{61}BM$ sidechains and ^{1}H signals at 1.2 ppm associated with the PM2 sidechains, which establish unambiguously the nanoscale proximities of the donor and acceptor moieties. In addition, the correlated 2D signals at 30 ppm in the ^{13}C dimension and at 6-8 ppm in the ^{1}H dimension associated with the aliphatic and aromatic moieties, respectively, of neat PM2

(**Figure S8.9a**, Supporting Information), were not observed in the 2D $^{13}C\{^{1}H\}$ HETCOR spectrum of the PM2:$PC_{61}BM$ blend (in dashed rectangles) acquired under identical conditions. This further corroborates the intercalation of $PC_{61}BM$ molecules into the sidechain regions of PM2 donor polymer. These results are consistent with previous ssNMR studies of polymer-fullerene blends (*e.g.*, PBTTT-C_{16}:$PC_{61}BM$) that indicate the $PC_{61}BM$ molecules can intercalate between the alkyl sidechains of the donor polymers and disrupt their lamellar stacking interactions.[50,56,57] To further validate these results, we analyzed and compared the aromatic spectral regions of neat materials (PM2 in turquoise and $PC_{61}BM$ in red) and their BHJ blend (black) shown in **Figure 8.5b**. 2D ^{13}C intensity in the range of 120-130 ppm is correlated with ^{1}H signals between 1-2 ppm (turquoise) corresponding to aromatic and sidechain moieties, respectively, was only detected in the neat PM2 donor polymer, and not in the PM2:$PC_{61}BM$ blend (black spectrum). Collectively, the 2D NMR analyses provide direct evidence that $PC_{61}BM$ is intercalated with PM2 and disrupts the backbone-sidechain interactions of the PM2 polymer.

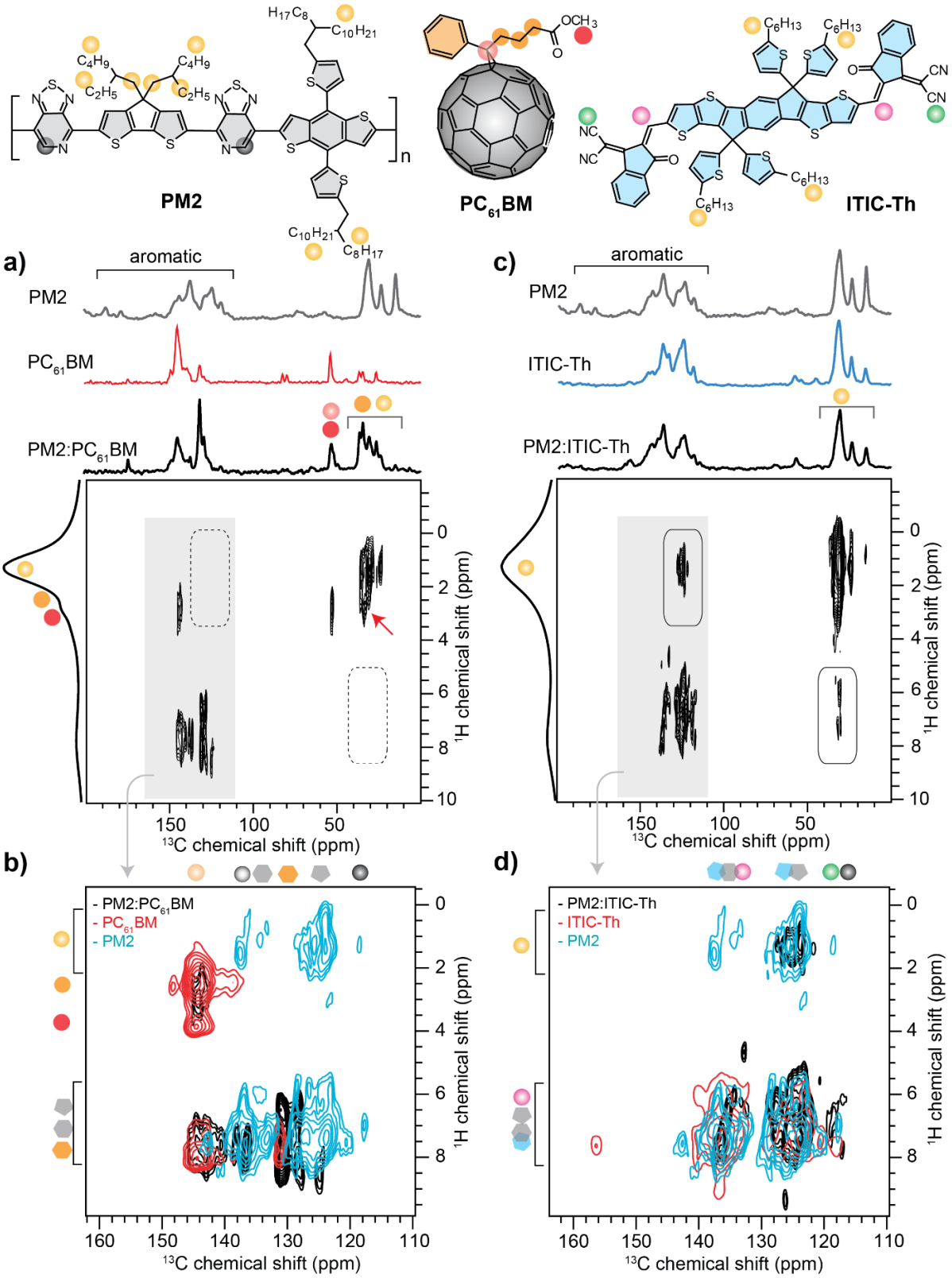
PM2
PC61BM
ITIC-Th
a)
aromatic
PM2
PC61BM
PM2:PC61BM
c)
aromatic
PM2
ITIC-Th
PM2:ITIC-Th
1H chemical shift (ppm)
13C chemical shift (ppm)
b)
- PM2:PC61BM
- PC61BM
- PM2
d)
- PM2:ITIC-Th
- ITIC-Th
- PM2

Figure 8.5. Solid-state 2D $^{13}C\{^{1}H\}$ heteronuclear correlation NMR spectra of (a,b) PM2:$PC_{61}BM$ and (c,d) PM2:ITIC-Th blends acquired at 11.7 T (Larmor frequencies of ^{1}H and ^{13}C were, 500.2 MHz and 125.8 MHz, respectively) at 12.5 kHz MAS, 298 K, and with a 4 ms CP contact time. Expanded aromatic regions of spectra of neat compounds and blends are shown in b) PM2:$PC_{61}BM$ and d) PM2:ITIC-Th. 2D signals corresponding to aromatic and aliphatic sites of donor-acceptor moieties are color coded, as depicted in the schematic structural diagrams. For comparison, 1D $^{13}C\{^{1}H\}$ CP-MAS spectra of neat compounds and blends are shown along the top horizontal axes and 1D direct-excitation ^{1}H MAS spectra of the blends are shown along the vertical axes, respectively, of a) and c).

In contrast to the PM2:$PC_{61}BM$ system, the 2D $^{13}C\{^{1}H\}$ HETCOR spectrum of the PM2:ITIC-Th blend (**Figure 8.5c**) shows several different 2D intensity correlations that are attributed to different inter- and intramolecular interactions. Notably, with ^{1}H signals at 1.2 ppm and in the range of 1.5-2.0 ppm, respectively, correlated ^{13}C signal intensity at 23 ppm is observed with ^{1}H signals at 6.0 and 7.5 ppm (rectangle), which are attributed to predominantly inter-molecular through-space interactions between the–CH_2 moieties of the aliphatic PM2 sidechains and aromatic protons of the PM2 backbones. This suggests that the addition of ITIC-Th into PM2 polymers does not substantially modify the morphology of the latter, indicating a phase separation between PM2 and ITIC-Th domains, which is crucially important for charge separation and extraction.[32] In addition, the ^{13}C signals in the range 122-128 ppm are correlated with ^{1}H signals in the range 1-2 ppm (dashed rectangle), which further establishes the through-space nanoscale proximities of the aromatic backbones and

sidechains of the PM2 polymer. It is noteworthy that similar 2D intensity correlations corresponding to such aromatic-sidechain interactions were not detected for the neat ITIC-Th material (Supporting Information, **Figure S8.9c**) or for the PM2:$PC_{61}BM$ blend (**Figure 8.5a**). Likewise, the comparisons shown in **Figure 8.5d** of the aromatic regions of the 2D HETCOR spectra acquired under identical conditions for neat PM2 (turquoise), neat ITIC-Th (red), and the PM2:ITIC-Th blend (black) provide more detailed evidence of the nanoscale aromatic-sidechain interaction detected in neat PM2 and in the PM2:ITIC-Th, but not in neat ITIC-Th or the PM2:$PC_{61}BM$ blend. Although overlapping intensity even in the 2D spectra limits analyses of specific inter-molecular interactions between the PM2 and ITIC-Th moieties, key differences are nevertheless observed in the 2D intensity distributions that are observed in **Figure 8.5b,d** for correlated ^{13}C signals in the range 138-142 ppm with the ^{1}H signals at 1-2, and 6-8 ppm for the neat PM2 donor, neat fullerene $PC_{61}BM$ and non-fullerene ITIC-Th acceptors, and their blends. These suggest that there are specific differences occur in the local structures and intermolecular interactions in the blends, compared to the neat compounds. Overall, the 2D ssNMR spectroscopy analyses provide detailed nanoscale insights on the different inter-molecular interactions that occur in the PM2:$PC_{61}BM$ and PM2:ITIC-Th blends and contribute to molecular-level understanding of the differences in morphological features and optoelectronic properties of the blend discussed above. We note that the phase separation and intermolecular interactions studied by solid-state NMR techniques are complementary to that of long-range probes such as X-ray scattering and AFM techniques, thus a combination of these techniques provide a comprehensive analysis of the BHJ morphology.

8.5.3 Energetic Order

The determination of the low energetic offset ($S_1 - E_{CT} \approx 0.05$-$0.06$ eV) for both blends emphasizes that PM2:$PC_{61}BM$ and PM2:ITIC-Th exhibit high performances, despite apparently low driving forces for charge separation. It still remains to be understood why certain blend systems have high photovoltaic efficiencies despite small energetic offsets, while other systems are not able to generate photocurrent with the same offsets. One hypothesis to explain these observations may be related to the energetic order, with highly ordered systems requiring only a very small energetic offset to generate photocurrent.[58] Additionally, energetic disorder has been associated with higher recombination losses.[59,60] Therefore, we characterized the energetic order in PM2:$PC_{61}BM$ and PM2:ITIC-Th to understand if this was related to the observed difference in recombination behavior.

The energetic order in the two blend systems was measured by using both the Urbach energy (E_U) and band-bending measurements with a Kelvin probe. E_U is a measure of the energetic order of the tail states within the band gap of a material (or blend, in this case).[61] In systems such as PM2:$PC_{61}BM$ and PM2:ITIC-Th, it is possible to calculate the E_U from the low energy tail of the EQE_{PV} spectrum using the **Equation 8.4**:

$$\alpha(E,T) \propto exp\left[\frac{E-E_{onset}(E,T)}{E_U(T)}\right] \tag{8.4}$$

where α is the sub-gap absorption and E_{onset} is the energy of the onset of the tail. It should be noted that EQE_{PV} is a measurement of both the absorption and charge generation/extraction, thus it can only be used to calculate the Urbach energy for states which generate photocurrent.[5, 44, 45] The Urbach energy is approximately 25 meV for both PM2:$PC_{61}BM$ and

PM2:ITIC-Th, indicating high energetic order of the tail states (**Figure 8.6a,c**), compared to Urbach energies of the order of 40 meV for other common BHJ blends.[62]

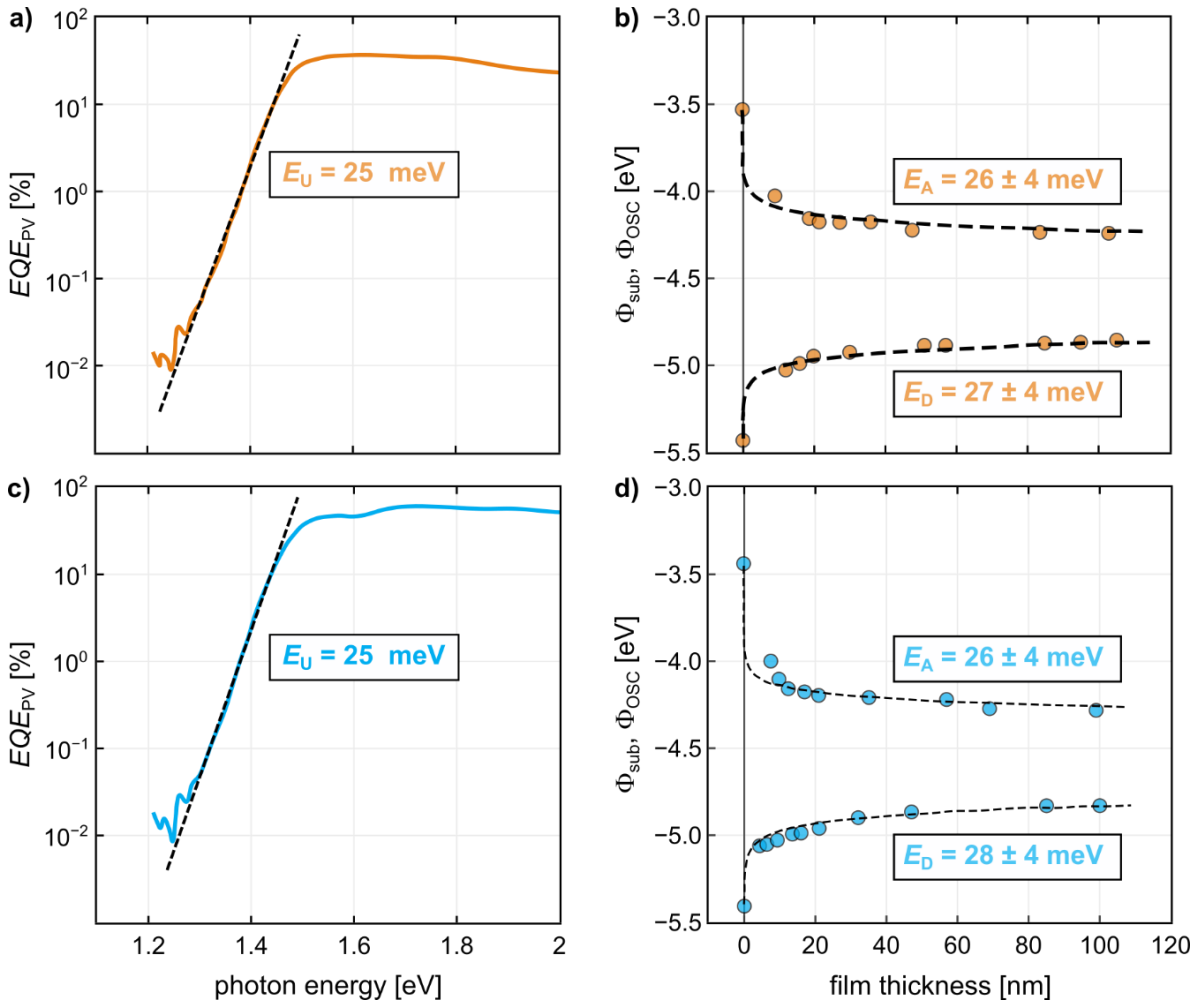

Figure 8.6. a) EQE spectrum and the fitted lines to **Equation 8.4** for PM2:$PC_{61}BM$ devices and b) band bending profiles of PM2:$PC_{61}BM$ films measured from Kelvin probe. The dashed lines are fitted data to **Equation 8.5**. c) and d) are the same data for PM2:ITIC-Th.

Another measure of the electronic order of the tail states can be obtained using Kelvin probe measurements. The Kelvin probe is a surface technique that measures the contact potential difference between a calibrated tip and a film of interest, from which the work function or Fermi level of the sample can be extracted.[55,63] Due to charge diffusion from ohmic contacts into a thin semiconductor layer, the HOMO and LUMO energy states exhibit band bending, which manifests as a shift in the measured Fermi level as a function of film thickness. The degree of band bending is related to the width of the density of states (DOS) manifold, and thus to the energetic disorder in the film. The work function of the electrode material will dictate if the Kelvin probe is measuring band bending in the $HOMO_D$ (high work function electrode) or $LUMO_A$ (low work function electrode). This method has been demonstrated on a number of polymers and small molecules, both for neat materials and blends.[55,64,65] When the active layer is cast onto a high work function electrode, band bending occurs due to the transfer of holes from the electrode into the HOMO of the semiconductor; similarly when the active layer is cast on a low work function electrode, band bending results from electron transfer into the LUMO. Using the relationship between band bending and film thickness from the model of charge transfer into an exponential DOS, the energetic disorder of the tail states can be extracted from an analytical expression relating the thickness of the semiconductor film, d, to the measured contact potential difference, $\phi(d)$:

$$d = \sqrt{\frac{2E_t \varepsilon_r \varepsilon_0}{q^2 N_t}} \exp\left(\frac{|\phi(d)|}{2E_t}\right) \times \arccos\left[\exp\left(\frac{-|\phi(d)|}{2E_t}\right)\right] \tag{8.5}$$

In **Equation 8.5**, the shape of the DOS tail is represented by an exponential function with E_t being a disorder parameter representing the characteristic length scale of the exponential function. Further, ε_0 is the vacuum permittivity, ε_r is the relative permittivity, q is the elementary charge, N_t is the maximum value of the DOS, d is the film thickness, and $\phi(d)$ =

$V(d) - V(0)$ is the measured contact potential difference between the bare electrode ($V(0)$) and the film at thickness d ($V(d)$).

PM2:$PC_{61}BM$ and PM2:ITIC-Th films were spun on glass/ITO/Al and glass/ITO/PEDOT:PSS-coated substrates to measure the disorder in the $LUMO_A$ and $HOMO_D$, respectively. All measurements show the work function of the blend changing with film thickness, shown in **Figure 8.6c,d**, indicating that the Fermi level of the blend is not pinned to the work function of the electrode material, thus the fits to **Equation 8.5** are measuring the band bending in the semiconductors. Due to thermal fluctuations, the minimum disorder parameter we expect to measure at room temperature is $k_BT \approx 26$ meV. We find that the exponential disorder, E_t, associated with band bending is low for the $HOMO_D$ and $LUMO_A$ for both PM2:$PC_{61}BM$ and PM2:ITIC-Th, at about 26 - 28 meV for all cases. These measurements are in good agreement with the Urbach energies, again indicating that PM2:$PC_{61}BM$ and PM2:ITIC-Th have high energetic order in their tail states. However, as is evident from the energy loss analysis above, while high energetic order may be necessary for charge generation, it is not necessarily sufficient to reduce recombination losses to the V_{OC} and the J_{SC}.

8.5.4 Transparency and Performance

Finally, to demonstrate the potential of PM2:ITIC-Th in semi-transparent solar cells, we fabricated PM2:ITIC-Th devices with thicknesses ranging from 55-135 nm to modulate the transparency. **Figure 8.7a** shows percentage transmittance of PM2:ITIC-Th devices at various active layer thicknesses without an anode electrode, and **Figure 8.7b** shows 4 different film

thicknesses cast on glass/ITO/ZnO substrates placed over black lettering to illustrate visually the differences in transparency. The optimal device performance of 9.3% PCE corresponds to a film thickness of 85 nm. **Figure 8.7c** shows the effect of film thickness on the PCE, transmittance, and the reflectance. Reducing the film thickness to 55 nm decreases the PCE to 7.8% and increasing to 135 nm decreases the PCE to 8.2%. It is noteworthy that the PM2:ITIC-Th solar cells are still able to achieve 7.8% PCE with an active layer only 55 nm thick. The average transmittance for wavelengths 370-740 nm changes linearly with film thickness, from 53% to 31% for 55 and 135 nm. The full transmittance curves for the different thicknesses are shown in **Figure 8.7a**, which highlights that PM2:ITIC-Th primarily absorbs from 550-850 nm, while it is mostly transparent for the remainder of the spectrum. The transparency/reflectance values reported in **Figure 8.7** are for the active layer alone without the top metal contact. For fully semi-transparent solar cells, it is necessary to develop transparent top contacts with efficient charge collection properties. Nonetheless, here we demonstrate the possibility of controlling the transparency of the active layer with materials that do not absorb significantly below 550 nm while still achieving high PCE values and low V_{OC} losses.

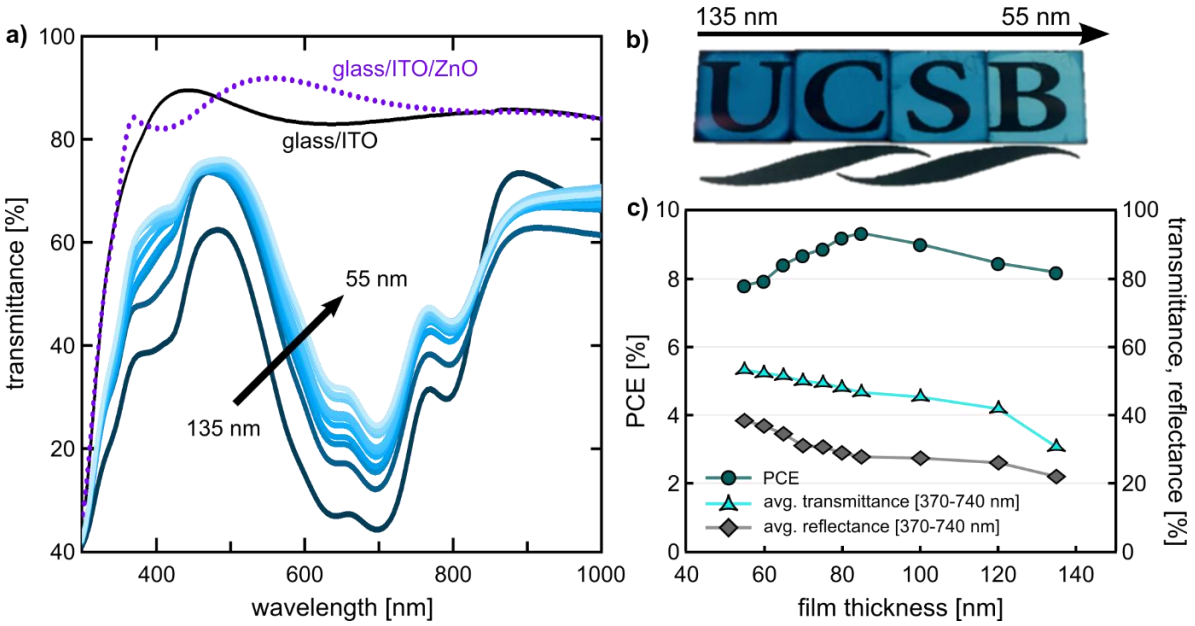

Figure 8.7. Modulating transparency with film thickness. a) Transmittance of PM2:ITIC-Th devices without an anode electrode at various active layer thicknesses. b) A photograph of PM2:ITIC-Th devices without an anode electrode with various active layer thicknesses. c) PCE, reflectance, and transmittance as a function of active layer thickness for PM2:ITIC-Th devices.

8.6 Conclusions

In summary, we have demonstrated the use of PM2:ITIC-Th as a model system for semi-transparent solar cells. In single junction solar cells, PM2:ITIC-Th blends achieve higher V_{OC} and J_{SC} values compared to similar devices with the traditional fullerene acceptor $PC_{61}BM$. The difference between PM2:$PC_{61}BM$ and PM2:ITIC-Th devices is first analyzed from the perspective of energetic losses that lead to the lower observed V_{OC} in the former. Notably, both blends have nearly identical S_1 and E_{CT} values of ~1.43 eV and 1.38 eV, respectively, indicating that the losses due to charge generation are similar in both cases. Further, the energetic losses from radiative recombination ($E_{CT} - qV_{OC,rad}$) are nearly identical in both blends, with each loss being approximately 125 meV. Thus, the difference in V_{OC} is attributed solely to non-radiative recombination losses, with PM2:$PC_{61}BM$ devices losing 120 meV more than the PM2:ITIC-Th devices. These values are in accord with other recent examples of solar cell blends that perform well despite the low energetic driving force for charge generation.

The performance differences were then characterized over a range of length scales by measuring the morphological and structural differences between the two blends. From X-ray scattering analyses, it was found that both materials show similar nanostructures and spacing parameters, although the PM2:ITIC-Th blends showed a higher degree of phase separation between the donor and acceptor domains. The interactions between the donor and acceptor moieties were further characterized by 2D NMR spectroscopy, which provided detailed molecular-level evidence of significantly different intermolecular interactions between the PM2 conjugated polymer donor and the two acceptors. Specifically, differences in the extents of acceptor intercalation into the polymer donor and their local separation into phase-separated

domains in account for the different opto-electronic properties of the PM2:ITIC-Th and PM2:$PC_{61}BM$ blends. The ssNMR results indeed establish the molecular origins for the different optoelectronic properties, which are due to the different degrees of D-A intermix and local domain separation for the PM2:ITIC-Th and PM2:$PC_{61}BM$ blends, consistently with the recent ssNMR studies of organic semiconductors and BHJ blends.[66-69]

Next, the relative degrees of energetic order of the CT states in the blends were analyzed. Previous work has suggested that many systems which obtain high photovoltaic performance despite low energetic offsets achieve this via highly ordered domains, which facilitate both charge generation and transport. Indeed, both the Urbach energy and band-bending measurements of both blends indicate highly ordered sub-gap states. However, despite the similarity in their order parameters, PM2:$PC_{61}BM$ devices suffer from larger energy losses due to non-radiative recombination, suggesting an intrinsic loss mechanism in fullerene-based devices, which is also consistent with previous reports.[16]

This study summarizes several aspects that are expected to be crucial in the design BHJ morphologies for semi-transparent solar cell applications. First, reduced absorption in the visible spectrum naturally leads to smaller photocurrents. Additionally, if the absorption is tuned to only the NIR region of the solar emission spectrum to produce a fully optically transparent solar cell, it is necessary to use narrow band gap donor and acceptor molecules, which introduces yet another limitation to the maximum possible V_{OC} due to a reduction in the maximum possible E_{CT} values. It is therefore most important to understand and reduce the losses to the V_{OC} to achieve high performing semitransparent or transparent solar cells. To improve upon the blend reported here, PM2:ITIC-Th, it may be favorable to develop an acceptor material with an even lower band gap, such that the absorption between 500-700 nm

is further reduced. For example, the $HOMO_A$ of ITIC-Th may be increased from −5.66 eV to around −5.4 eV to reduce the band gap of the acceptor (and thus shift the absorption spectrum further into the red and NIR), while maintaining some energetic offset between $HOMO_D$ and $HOMO_A$.

Finally, the efficiency of the PM2:ITIC-Th devices is characterized as a function of visible transparency and active layer thickness. The data show that the high performance is maintained across a range of transparencies, with ultra-thin films of only 55 nm achieving more than 7% PCE. This result places these devices among the highest-performing semitransparent OPVs reported to date, and suggests that further optimization of the energetic losses could lead to even higher performance.

8.7 Relevant Materials and Methods

Solid-state NMR spectroscopy

Spin-coated PM2, ITIC-Th, $PC_{61}BM$ materials and PM2:ITIC-Th and PM2:$PC_{61}BM$ blends were collected from glass substrates and packed into 4 mm (outer diameter) zirconia MAS rotors. All 1D ^{1}H, ^{13}C CP-MAS and 2D $^{13}C\{^{1}H\}$ solid-state NMR correlation experiments were carried out at room temperature and 11.7 Tesla on a Bruker AVANCE II spectrometer operating at Larmor frequencies of 500.2 MHz and 125.8 MHz for ^{1}H and ^{13}C, respectively, using a 4 mm H-X probehead. The nutation frequency of ^{1}H was 100 kHz, corresponding to 90° pulse duration of 2.5 μs. Direct-excitation ^{1}H MAS NMR experiments were carried out by co-adding 32 transients with a recycle delay of 4 s. The MAS frequency

was 10 kHz. 1D $^{13}C\{^{1}H\}$ CP-MAS and 2D HETCOR spectra were acquired with CP contact times of 0.1 and 2 ms, each by co-adding 2048 transients with a ^{1}H recycle delay of 4 s, corresponding to an experimental time of 2.3 h. The MAS frequency was 12.5 kHz. Heteronuclear decoupling was applied during the detection of ^{13}C dimension using a SPINAL-64 sequence. In the case of 2D $^{13}C\{^{1}H\}$ HETCOR experiments, the indirect ^{1}H dimension was acquired with 48 t_1 increments, each with 128 co-added transients, corresponding to a total experimental time of 7 h with a recycle delay of 4 s. High-power homonuclear decoupling was applied during the acquisition of the indirect ^{1}H dimension using a eDUMBO decoupling sequence,[73] and heteronuclear decoupling was applied during the detection of ^{13}C dimension using a two-pulse-phase-modulation (TPPM) sequence.[74] The vertical ^{1}H dimension was scaled by 1.6, which is consistent with a frequency scaling factor of 0.6 associated with the eDUMBO decoupling sequence. The ^{1}H and ^{13}C experimental shifts were calibrated with respect to neat TMS using adamantane as an external reference (higher ppm ^{13}C resonance, 38.5 ppm, and the ^{1}H resonance, 1.85 ppm).

8.8 References

[1] C. J. Traverse, R. Pandey, M. C. Barr, R. R. Lunt, *Nat. Energy* **2017**, *2*, 849.

[2] M. E. Deroche, J. M. Briantais, *Photochem. Photobiol.* **1973**, *19*, 233.

[3] K. Vandewal, A. Gadisa, W. D. Oosterbaan, S. Bertho, F. Banishoeib, I. Van Severen, L. Lutsen, T. J. Cleij, D. Vanderzande, J. V. Manca, *Adv. Funct. Mater.* **2008**, *18*, 2064.

[4] D. Veldman, S. C. J. Meskers, R. A. J. Janssen, *Adv. Funct. Mater.* **2009**, *19*, 1939.

[5] T. M. Burke, S. Sweetnam, K. Vandewal, M. D. McGehee, *Adv. Energy Mater.* **2015**, *5*, 1500123.

[6] S. D. Collins, C. M. Proctor, N. A. Ran, T.-Q. Nguyen, *Adv. Energy Mater.* **2016**, *6*, 1501721.

[7] N. A. Ran, J. A. Love, C. J. Takacs, A. Sadhanala, J. K. Beavers, S. D. Collins, Y. Huang, M. Wang, R. H. Friend, G. C. Bazan, T.-Q. Nguyen, *Adv. Mater.* **2016**, *28*, 1482.

[8] N. A. Ran, S. Roland, J. A. Love, V. Savikhin, C. J. Takacs, Y.-T. Fu, H. Li, V. Coropceanu, X. Liu, J.-L. Brédas, G. C. Bazan, M. F. Toney, D. Neher, T.-Q. Nguyen, *Nat. Commun.* **2017**, *8*, 79.

[9] K. Vandewal, J. Benduhn, V. C. Nikolis, *Sustain. Energy Fuels* **2018**, *2*, 538.

[10] T. M. Clarke, J. R. Durrant, *Chem. Rev.* **2010**, *110*, 6736.

[11] M. Stolterfoht, B. Philippa, S. Shoaee, H. Jin, W. Jiang, R. D. White, P. L. Burn, P. Meredith, A. Pivrikas, *J. Phys. Chem. C* **2015**, *119*, 26866.

[12] U. Hörmann, J. Kraus, M. Gruber, C. Schuhmair, T. Linderl, S. Grob, S. Kapfinger, K. Klein, M. Stutzman, H. J. Krenner, W. Brütting, *Phys. Rev. B* **2013**, *88*, 235307.

[13] K. Vandewal, K. Tvingstedt, A. Gadisa, O. Inganäs, J. V. Manca, *Phys. Rev. B* **2010**, *81*, 125204.

[14] W. Shockley, H. J. Queisser, *J. Appl. Phys.* **1961**, *32*, 510.

[15] Y. Li, X. Liu, F.-P. Wu, Y. Zhou, Z.-Q. Jiang, B. Song, Y. Xia, Z.-G. Zhang, F. Gao, O. Inganäs, Y. Li, L.-S. Liao, *J. Mater. Chem. A* **2016**, *4*, 5890.

[16] J. Benduhn, K. Tvingstedt, F. Piersimoni, S. Ullbrich, Y. Fan, M. Tropiano, K. A. McGarry, O. Zeika, M. K. Riede, C. J. Douglas, S. Barlow, S. R. Marder, D. Neher, D. Spoltore, K. Vandewal, *Nat. Energy* **2017**, *2*, 17053.

[17] Y. Li, J.-D. Lin, X. Che, Y. Qu, F. Liu, L.-S. Liao, S. R. Forrest, *J. Am. Chem. Soc.* **2017**, *139*, 17114.

[18] A. Mishra, M. L. Keshtov, A. Looser, R. Singhal, M. Stolte, F. Würthner, P. Bäuerle, G. D. Sharma, *J. Mater. Chem. A* **2017**, *5*, 14887.

[19] J.-M. Park, D. W. Kim, H. Y. Chung, J. E. Kwon, S. H. Hong, T.-L. Choi, S. Y. Park, *J. Mater. Chem. A* **2017**, *5*, 16681.

[20] H. Yao, Y. Cui, R. Yu, B. Gao, H. Zhang, J. Hou, *Angew. Chem. Int. Ed.* **2017**, *56*, 3045.

[21] Z. Zhang, W. Liu, T. Rehman, H.-X. Ju, J. Mai, X. Lu, M. Shi, J. Zhu, C.-Z. Li, H. Chen, *J. Mater. Chem. A* **2017**, *5*, 9649.

[22] K. Kawashima, Y. Tamai, H. Ohkita, I. Osaka, K. Takimiya, *Nat. Commun.* **2015**, *6*, 10085.

[23] D. Baran, T. Kirchartz, S. Wheeler, S. Dimitrov, M. Abdelsamie, J. Gorman, R. S. Ashraf, S. Holliday, A. Wadsworth, N. Gasparini, P. Kaienburg, H. Yan, A. Amassian, C. J. Brabec, J. R. Durrant, I. McCulloch, *Energy Environ. Sci.* **2016**, *9*, 3783.

[24] Y. Li, L. Zhong, B. Gautam, H.-J. Bin, J.-D. Lin, F.-P. Wu, Z. Zhang, Z.-Q. Jiang, Z.-G. Zhang, K. Gundogdu, Y. Li, L.-S. Liao, *Energy Environ. Sci.* **2017**, *10*, 1610.

[25] C. Wang, W. Zhang, X. Meng, J. Bergqvist, X. Liu, Z. Genene, X. Xu, A. Yartsev, O. Inganäs, W. Ma, E. Wang, M. Fahlman, *Adv. Energy Mater.* **2017**, *7*, 1700390.

[26] W. Zhao, D. Qian, S. Zhang, S. Li, O. Inganäs, F. Gao, J. Hou, *Adv. Mater.* **2016**, *28*, 4734.

[27] M. Wang, H. Wang, M. Ford, J. Yuan, C.-K. Mai, S. Fronk, G. C. Bazan, *J. Mater. Chem. A* **2016**, *4*, 15232.

[28] Y. Lin, F. Zhao, Q. He, L. Huo, Y. Wu, T. C. Parker, W. Ma, Y. Sun, C. Wang, D. Zhu, A. J. Heeger, S. R. Marder, X. Zhan, *J. Am. Chem. Soc.* **2016**, *138*, 4955.

[29] T. Liu, X. Pan, X. Meng, Y. Liu, D. Wei, W. Ma, L. Huo, X. Sun, T. H. Lee, M. Huang, H. Choi, J. Y. Kim, W. C. H. Choy, Y. Sun, *Adv. Mater.* **2017**, *29*, 1604251.

[30] Y. Liu, S. Chen, G. Zhang, P. C. Y. Chow, H. Yan, *J. Mater. Chem. A* **2017**, *5*, 15017.

[31] F. Zhao, S. Dai, Y. Wu, Q. Zhang, J. Wang, L. Jiang, Q. Ling, Z. Wei, W. Ma, W. You, C. Wang, X. Zhan, *Adv. Mater.* **2017**, *29*, 1700144.

[32] A. Karki, J. Vollbrecht, A. J. Gillett, S. S. Xiao, Y. Yang, Z. Peng, N. Schopp, A. L. Dixon, S. Yoon, M. Schrock, H. Ade, G. N. M. Reddy, R. H. Friend, T.-Q. Nguyen, *Energy Environ. Sci.* **2020**, *13*, 3679.

[33] C. B. Nielsen, S. Holliday, H.-Y. Chen, S. J. Cryer, I. McCulloch, *Acc. Chem. Res.* **2015**, *48*, 2803.

[34] W. Chen, Q. Zhang, *J. Mater. Chem. C* **2017**, *5*, 1275.

[35] H. Lodish, A. Berk, L. Zipursky, P. Matsudaira, D. Baltimore, J. Darnell, *Molecular Cell Biology*, Freeman, New York, NY, **2002**.

[36] K. D. Rosenthal, M. P. Hughes, B. R. Luginbuhl, N. A. Ran, A. Karki, S. Ko, H. Hu, M. Wang, H. Ade, T. Nguyen, *Adv. Energy Mater.* **2019**, *9*, 1901077.

[37] A. Karki, In-Depth Understanding of Loss Mechanisms in High Performing Polymer:Non-Fullerene Acceptor Bulk-Heterojunction Organic Solar CellsI, PhD, University of California, Santa Barbara, **2020**.

[38] U. Rau, *Phys. Rev. B* **2007**, *76*, 085303.

[39] X.-D. Dang, A. B. Tamayo, J. Seo, C. V. Hoven, B. Walker, T.-Q. Nguyen, *Adv. Funct. Mater.* **2010**, *20*, 3314.

[40] A. Mahmood, J. Wang, *Sol. RRL* **2020**, *4*, 2000337.

[41] T. L. Nguyen, H. Choi, S.-J. Ko, M. A. Uddin, B. Walker, S. Yum, J.-E. Jeong, M. H. Yun, T. J. Shin, S. Hwang, J. Y. Kim, H. Y. Woo, *Energy Env. Sci* **2014**, *7*, 3040.

[42] I. Angunawela, L. Ye, H. Bin, Z.-G. Zhang, A. Gadisa, Y. Li, H. Ade, *Mater. Chem. Front.* **2019**, *3*, 137.

[43] Z. Du, M. Mainville, J. Vollbrecht, A. L. Dixon, N. Schopp, M. Schrock, Z. Peng, J. Huang, S. Chae, H. Ade, M. Leclerc, G. N. M. Reddy, T.-Q. Nguyen, *Sol. Rapid Res. Lett.* **2021**, 2100213.

[44] L. Ye, H. Hu, M. Ghasemi, T. Wang, B. A. Collins, J.-H. Kim, K. Jiang, J. H. Carpenter, H. Li, Z. Li, T. McAfee, J. Zhao, X. Chen, J. L. Y. Lai, T. Ma, J.-L. Bredas, H. Yan, H. Ade, *Nat. Mater.* **2018**, *17*, 253.

[45] A. Melnyk, M. J. N. Junk, M. D. McGehee, B. F. Chmelka, M. R. Hansen, D. Andrienko, *J. Phys. Chem. Lett.* **2017**, *8*, 4155.

[46] S. R. Chaudhari, J. M. Griffin, K. Broch, A. Lesage, V. Lemaur, D. Dudenko, Y. Olivier, H. Sirringhaus, L. Emsley, C. P. Grey, *Chem. Sci.* **2017**, *8*, 3126.

[47] M. Seifrid, G. N. M. Reddy, B. F. Chmelka, G. C. Bazan, *Nat. Rev. Mater.* **2020**, *5*, 910.

[48] M. R. Hansen, R. Graf, H. W. Spiess, *Chem. Rev.* **2016**, *116*, 1272.

[49] M. T. Seifrid, G. N. M. Reddy, C. Zhou, B. F. Chmelka, G. C. Bazan, *J. Am. Chem. Soc.* **2019**, *141*, 5078.

[50] C. K. Lo, B. R. Gautam, P. Selter, Z. Zheng, S. D. Oosterhout, I. Constantinou, R. Knitsch, R. M. W. Wolfe, X. Yi, J.-L. Brédas, F. So, M. F. Toney, V. Coropceanu, M. R. Hansen, K. Gundogdu, J. R. Reynolds, *Chem. Mater.* **2018**, *30*, 2995.

[51] A. Karki, J. Vollbrecht, A. L. Dixon, N. Schopp, M. Schrock, G. N. M. Reddy, T. Nguyen, *Adv. Mater.* **2019**, *31*, 1903868.

[52] A. Karki, G. A. H. Wetzelaer, G. N. M. Reddy, V. Nádaždy, M. Seifrid, F. Schauer, G. C. Bazan, B. F. Chmelka, P. W. M. Blom, T. Nguyen, *Adv. Funct. Mater.* **2019**, *29*, 1901109.

[53] N. C. Miller, E. Cho, M. J. N. Junk, R. Gysel, C. Risko, D. Kim, S. Sweetnam, C. E. Miller, L. J. Richter, R. J. Kline, M. Heeney, I. McCulloch, A. Amassian, D. Acevedo-Feliz, C. Knox, M. R. Hansen, D. Dudenko, B. F. Chmelka, M. F. Toney, J.-L. Brédas, M. D. McGehee, *Adv. Mater.* **2012**, *24*, 6071.

[54] K. R. Graham, C. Cabanetos, J. P. Jahnke, M. N. Idso, A. El Labban, G. O. Ngongang Ndjawa, T. Heumueller, K. Vandewal, A. Salleo, B. F. Chmelka, A. Amassian, P. M. Beaujuge, M. D. McGehee, *J. Am. Chem. Soc.* **2014**, *136*, 9608.

[55] S. M. Menke, A. Cheminal, P. Conaghan, N. A. Ran, N. C. Greehnam, G. C. Bazan, T.-Q. Nguyen, A. Rao, R. H. Friend, *Nat. Commun.* **2018**, *9*, 277.

[56] S. R. Cowan, A. Roy, A. J. Heeger, *Phys. Rev. B* **2010**, *82*, 245207.

[57] T. Kirchartz, B. E. Pieters, J. Kirkpatrick, U. Rau, J. Nelson, *Phys. Rev. B* **2011**, *83*, 115209.

[58] B. R. Weinberger, C. B. Roxlo, S. Etemad, G. L. Baker, J. Orenstein, *Phys. Rev. Lett.* **1984**, *53*, 86.

[59] D. Venkateshvaran, M. Nikolka, A. Sadhanala, V. Lemaur, M. Zelazny, M. Kepa, M. Hurhangee, A. J. Kronemeijer, V. Pecunia, I. Nasrallah, I. Romanov, K. Broch, I. McCulloch, D. Emin, Y. Olivier, J. Cornil, D. Beljonne, H. Sirringhaus, *Nature* **2014**, *515*, 384.

[60] Lord Kelvin, *Lond. Edinb. Dublin Philos. Mag. J. Sci.* **1898**, *46*, 82.

[61] S. D. Collins, C. M. Proctor, N. A. Ran, T.-Q. Nguyen, *Adv. Energy Mater.* **2015**, 1501721.

[62] I. Lange, J. C. Blakesley, J. Frisch, A. Vollmer, N. Koch, D. Neher, *Phys. Rev. Lett.* **2011**, *106*, 216402.

[63] Y. Sun, J. H. Seo, C. J. Takacs, J. Seifter, A. J. Heeger, *Adv. Mater.* **2011**, *23*, 1679.

[64] S. Suzuki, C. Bower, Y. Watanabe, O. Zhou, *Appl. Phys. Lett.* **2000**, *76*, 4007.

[65] X. Cui, M. Freitag, R. Martel, L. Brus, P. Avouris, *Nano Lett.* **2003**, *3*, 783.

[66] B. Elena, G. de Paëpe, L. Emsley, *Chem. Phys. Lett.* **2004**, *398*, 532.

[67] B. M. Fung, A. K. Khitrin, K. Ermolaev, *J. Magn. Reson.* **2000**, *142*, 97.

8.9 Supporting Information

8.9.1 Device parameter optimization and J-V curves of photovoltaic blends

Table S8.1. Summary of device parameters for PM2:$PC_{61}BM$ and PM2:ITIC-Th solar cells.

BHJ blend	**Blend ratio**	J_{SC} **[mA cm^{-2}]**	V_{OC} **[V]**	***FF***	**PCE [%]**
PM2:ITIC-Th	1.0:1.0	16.69 (16.16 ± 0.49)	0.903 (0.888 ± 0.002)	0.536 (0.552 ± 0.01)	8.08 (7.92 ± 0.10)
	1.0:1.5	16.35 (16.60 ± 0.05)	0.926 (0.907 ± 0.019)	0.616 (0.605 ± 0.02)	9.33 (9.15 ± 0.12)
	1.0:3.0	14.30 (14.03 ± 0.19)	0.879 (0.885 ± 0.012)	0.599 (0.591 ± 0.01)	7.53 (7.18 ± 0.30)
PM2:$PC_{61}BM$	1:1[a)]	13.9	0.79	0.65	7.21
	1:2	13.76 (13.78 ± 0.67)	0.822 (0.817 ± 0.003)	0.664 (0.634 ± 0.02)	7.51 (7.17 ± 0.27)

[a)] The optimization of the 1:1 ratio PM2:$PC_{61}BM$ blend was shown in a previous publication from the Nguyen group.[1]

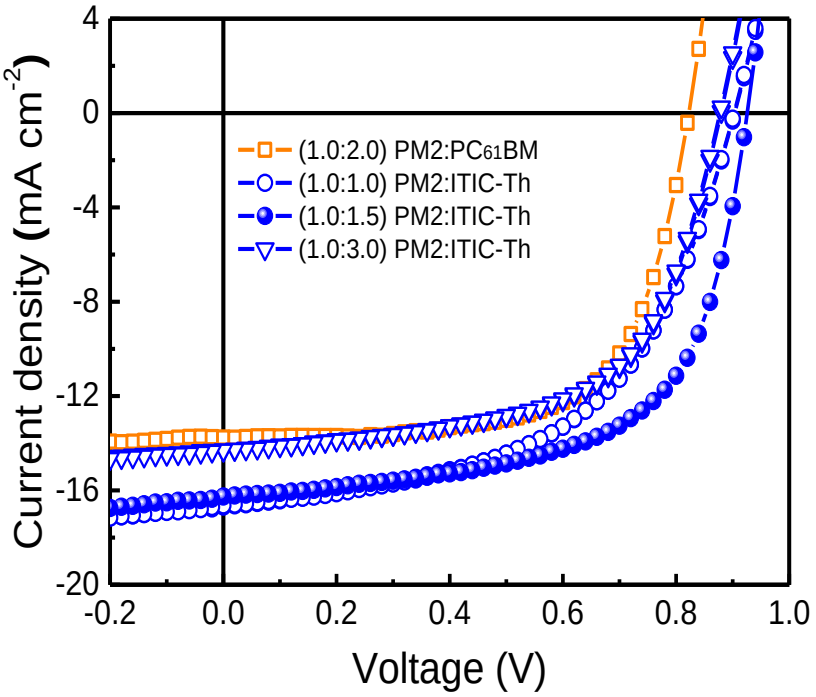

Figure S8.1. *J-V* characteristics of optimized PM2:$PC_{61}BM$ and PM2:ITIC-Th devices with varying donor:acceptor weight ratios.

8.9.2. Optical absorption spectroscopy of neat compounds and photovoltaic blends

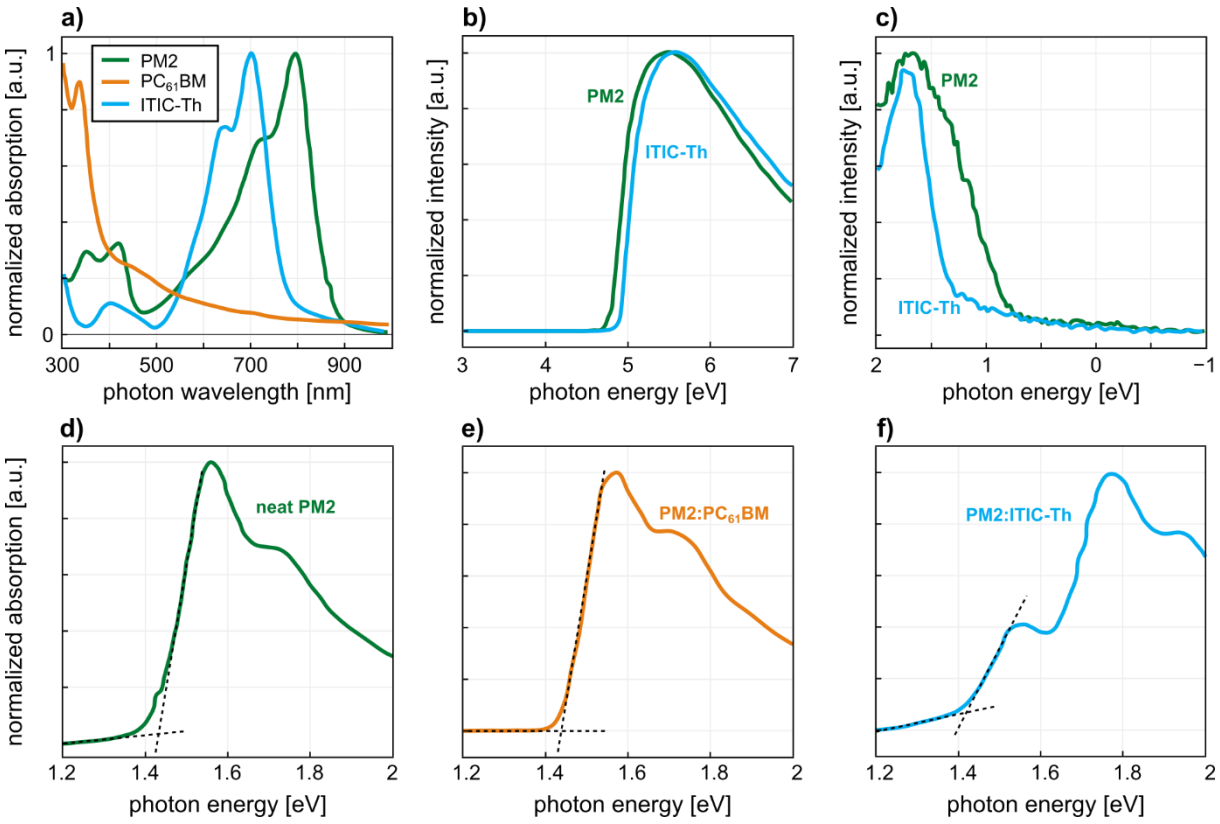

Figure S8.2. Normalized absorption spectra of a) neat PM2, $PC_{61}BM$, and ITIC-Th films. UPS spectra at b) kinetic energy (secondary electron cutoff) and c) binding energy (valence band region) of PM2 and ITIC-Th films. d-f) optical band gap determination for neat PM2, PM2:$PC_{61}BM$, and PM2:ITIC-Th films, respectively. E_{opt} is determined by the intersection of the dashed lines.

8.9.3. Electroluminescence spectra of neat compounds and photovoltaic blends

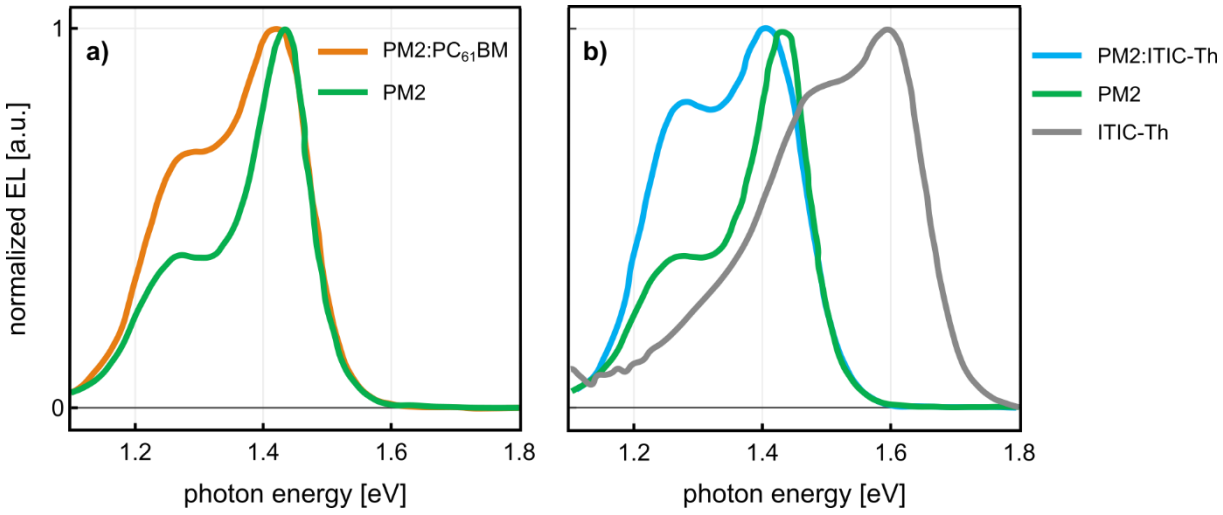

Figure S8.3. Normalized electroluminescence spectra for a) PM2:$PC_{61}BM$ and PM2; and b) PM2:ITIC-Th, PM2, and ITIC-Th.

8.9.4. Energy loss analysis

The reciprocity relationship between absorption and emission can be used to calculate the low energy absorption profile from the measured electroluminescence spectrum (*EL*):

$$EQE_{\mathrm{calc}}(E) \propto EL(E)^{-2} \exp\left(\frac{E}{k_{\mathrm{B}}T}\right) \qquad \text{(S8.1)}$$

where E is the photon energy, k_{B} is Boltzmann's constant, and T is the absolute temperature.[2,3]

The mean energy of the CT state, E_{CT}, in a photovoltaic cell can be found by simultaneous fitting of the reduced *EQE* and *EL* spectra:

$$E \cdot EQE_{\mathrm{PV}}(E) = \frac{f}{\sqrt{4\pi\lambda k_{\mathrm{B}}T}} \exp\left(\frac{-(E_{\mathrm{CT}}+\lambda-E)^2}{4\lambda k_{\mathrm{B}}T}\right) \quad \text{(S8.2)}$$

$$EL(E)/E = \frac{f}{\sqrt{4\pi\lambda k_{\mathrm{B}}T}} \exp\left(\frac{-(E_{\mathrm{CT}}-\lambda-E)^2}{4\lambda k_{\mathrm{B}}T}\right) \quad \text{(S8.3)}$$

where f is a prefactor related to the density of CT states and the electronic coupling between the ground and excited CT states (E_{CT} and $E_{\mathrm{CT}*}$), and λ is the reorganization energy associated with the electron transfer reaction.[4,5]

8.9.5. Wide-angle X-ray scattering images of neat compounds and photovoltaic blends

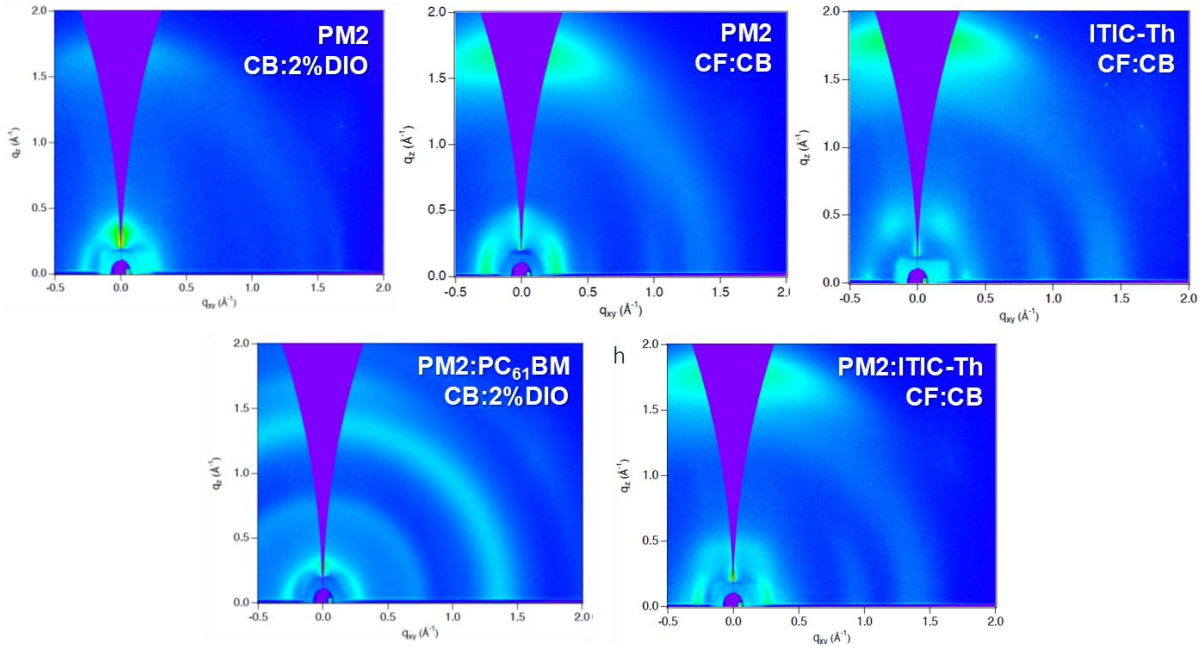

Figure S8.4. Grazing-incidence wide-angle X-ray scattering (2D-GIWAXS) images of neat films of PM2 and ITIC-Th and blend films of PM2:PC61BM and PM2:ITIC-Th prepared with the optimized preprocessing conditions.

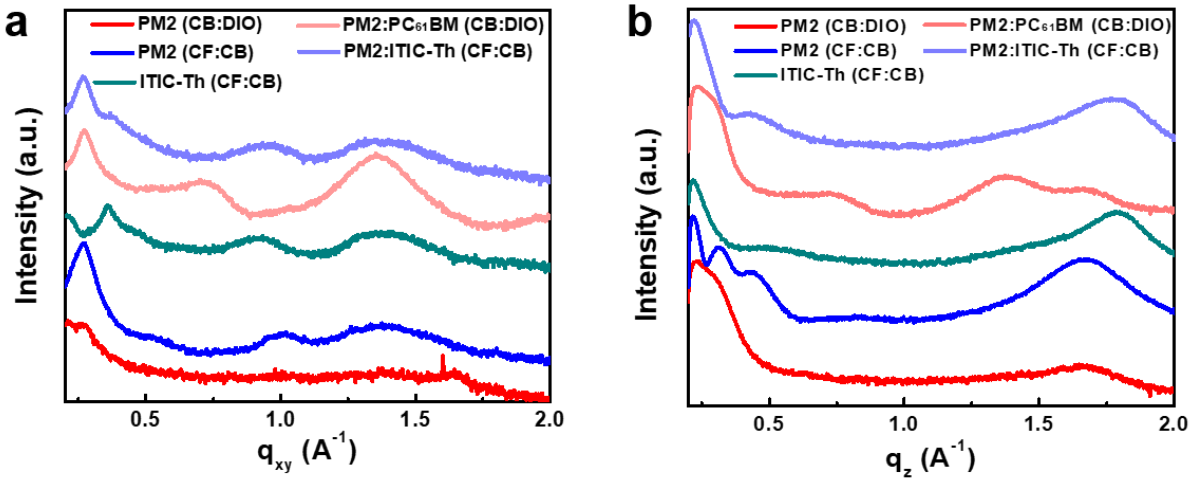

Figure S8.5. In-plane (a) and out-of-plane (b) GIWAXS line-cut data for pristine PM2, ITIC-Th and blends of PM2:$PC_{61}BM$ and PM2:ITIC-Th.

Table S8.2. Packing parameters derived from GIWAXS measurements.

Films	Polymers	Crystallographic parameters				
		Axis	π–π stack [$Å^{-1}$]	d-spacing [Å]	Lamellar stacking [$Å^{-1}$]	d-spacing [Å]
Pristine	PM2 (CB:2%DIO)	q_{xy}	1.66	3.78	0.27	23.67
		q_z	1.66	3.78	-	-
	PM2 (CF:CB)	q_{xy}	-	-	0.27	23.38
		q_z	1.68	3.75	0.32	19.87
	ITIC-Th (CF:CB)	q_{xy}	-	-	0.27	23.38
		q_z	1.8	3.49	0.32	19.87
Blend	PM2:$PC_{61}BM$ (CB:2%DIO)	q_{xy}	-	-	0.28	22.68
		q_z	1.66	3.78	-	-
	PM2:ITIC-Th (CF:CB)	q_{xy}	-	-	0.27	22.62
		q_z	1.78	3.53	-	-

8.9.6. Resonant soft X-ray scattering of photovoltaics blends

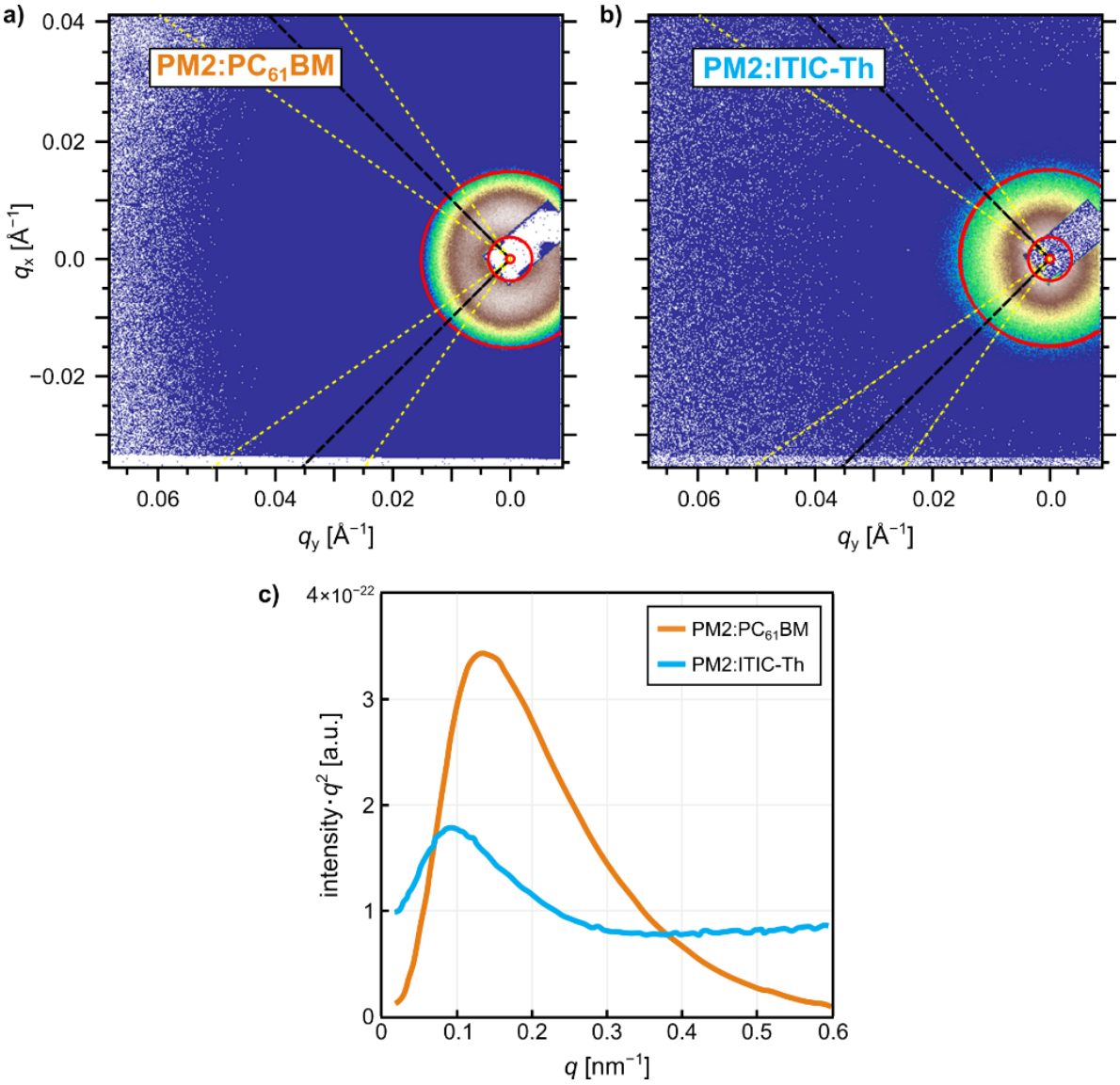

Figure S8.6. Resonant soft X-ray scattering (RSoXS) images of a) PM2:$PC_{61}BM$ and b) PM2:ITIC-Th films, and c) profiles of the blends. The length scales based on the peak positions are 44.8 and 69.8 nm for PM2:$PC_{61}BM$ and PM2:ITIC-Th, respectively.

Table S8.3. Domain purity and size obtained from RSoXS analysis shown in Figure S6b.

Device	ISI	Relative Purity	Peak	Long-period (Domain Spacing)
PM2:$PC_{61}BM$	2.24E-22	1	0.14	44.8 nm
PM2:ITIC-Th	1.76E-22	0.89	0.09	69.8 nm

8.9.7. Solid-state NMR spectral analysis of neat compounds and blends

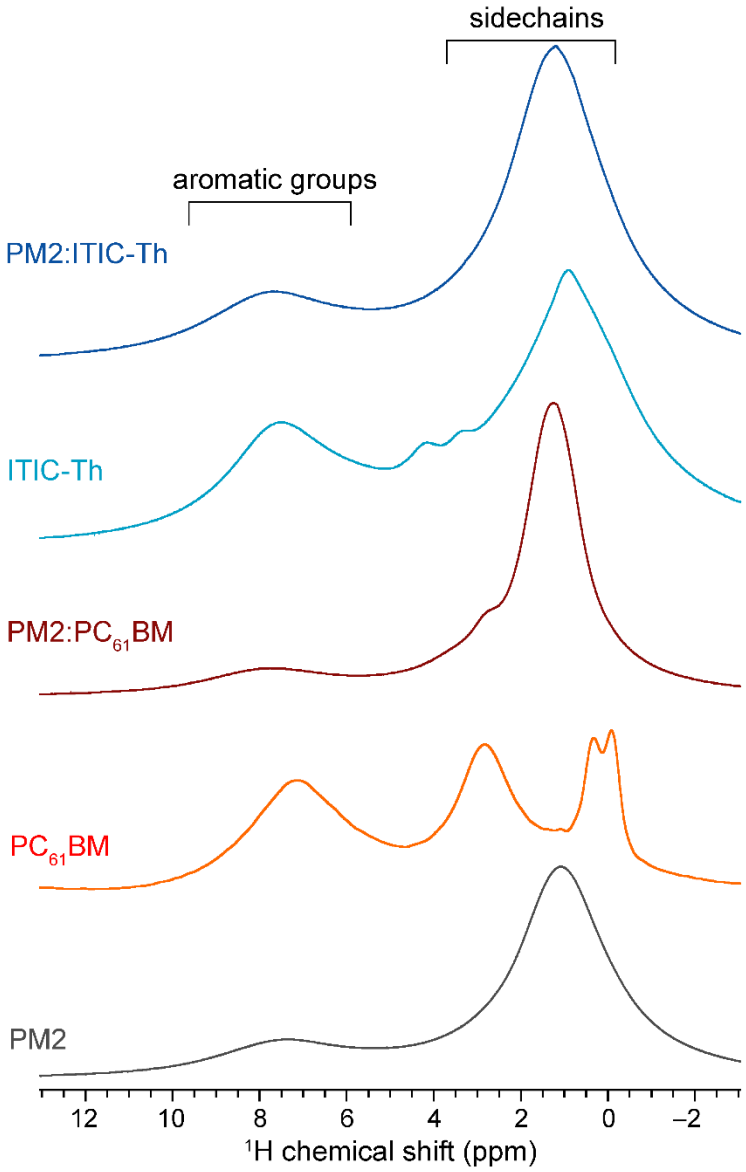

Figure S8.7. Comparison of solid-state 1D ^{1}H NMR spectra of neat PM2 polymer, ITIC-Th and $PC_{61}BM$ acceptors, and their blends acquired at 11.7 T (1H, 500.2 MHz), 12.5 kHz MAS and 298 K.

Figure S8.8 compares 1D $^{13}C\{^{1}H\}$ CP-MAS NMR spectra of neat PM2, ITIC-Th, $PC_{61}BM$ and their blends, which allows the ^{13}C signals corresponding to different aromatic groups in PM2:ITIC-Th and PM2:$PC_{61}BM$ blends to be distinguished and identified. A 1D $^{13}C\{^{1}H\}$ CP-MAS CP experiment involves a simultaneous excitation of ^{1}H and ^{13}C nuclei to obtain $^{1}H \rightarrow {}^{13}C$ polarization transfer, which enhances the signal intensities of the latter. In the case of neat PM2 material, well-resolved ^{13}C signals in the aliphatic region at 14 and 23 ppm are assigned to terminal methyl and methylene end groups, and a broad distribution of partially resolved signals in the range of 23-35 ppm to methylene groups in the branched sidechains. In the aromatic region of the PM2 and ITIC-Th molecules, the ^{13}C signals associated with the protonated carbon atom adjacent to pyridyl nitrogen (~123 ppm) and protonated carbon atoms in thiophene and benzodithiophene (124-130 ppm) and quaternary carbon atoms (130-146 ppm) are distinguished and identified. In comparison, the aromatic ^{13}C signals in the $^{13}C\{^{1}H\}$ CP-MAS spectrum of $PC_{61}BM$ molecules were based on previous assignments reported in the literature.[6–8]

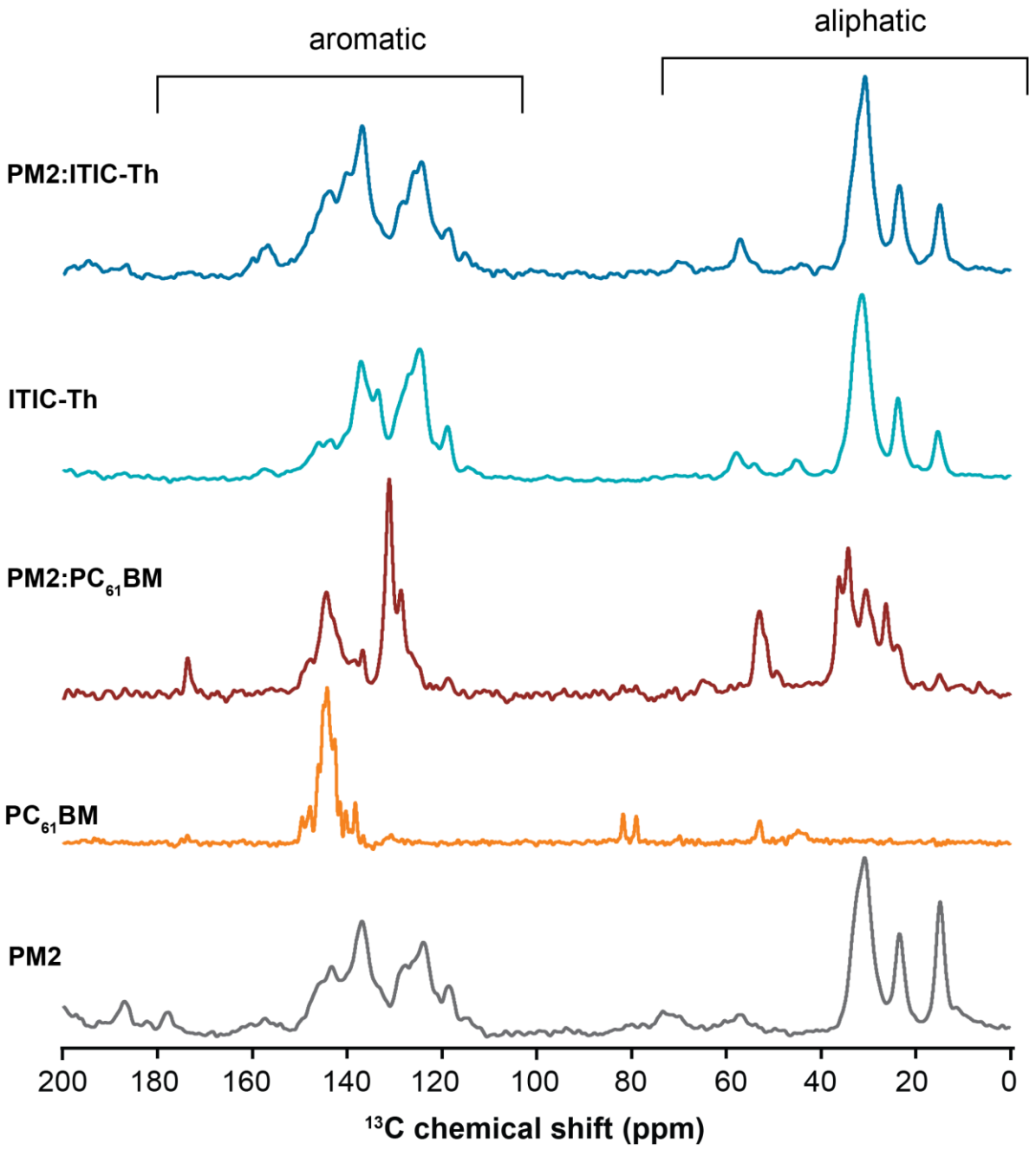

Figure S8.8. Comparison of solid-state 1D $^{13}C\{^{1}H\}$ CP-MAS NMR spectra of PM2 polymer, ITIC-Th and $PC_{61}BM$ acceptors, and their blends acquired at 11.7 T (Larmor frequencies of ^{1}H and ^{13}C were 500.2 and 125.8 MHz, respectively), 298 K with 8 kHz MAS.

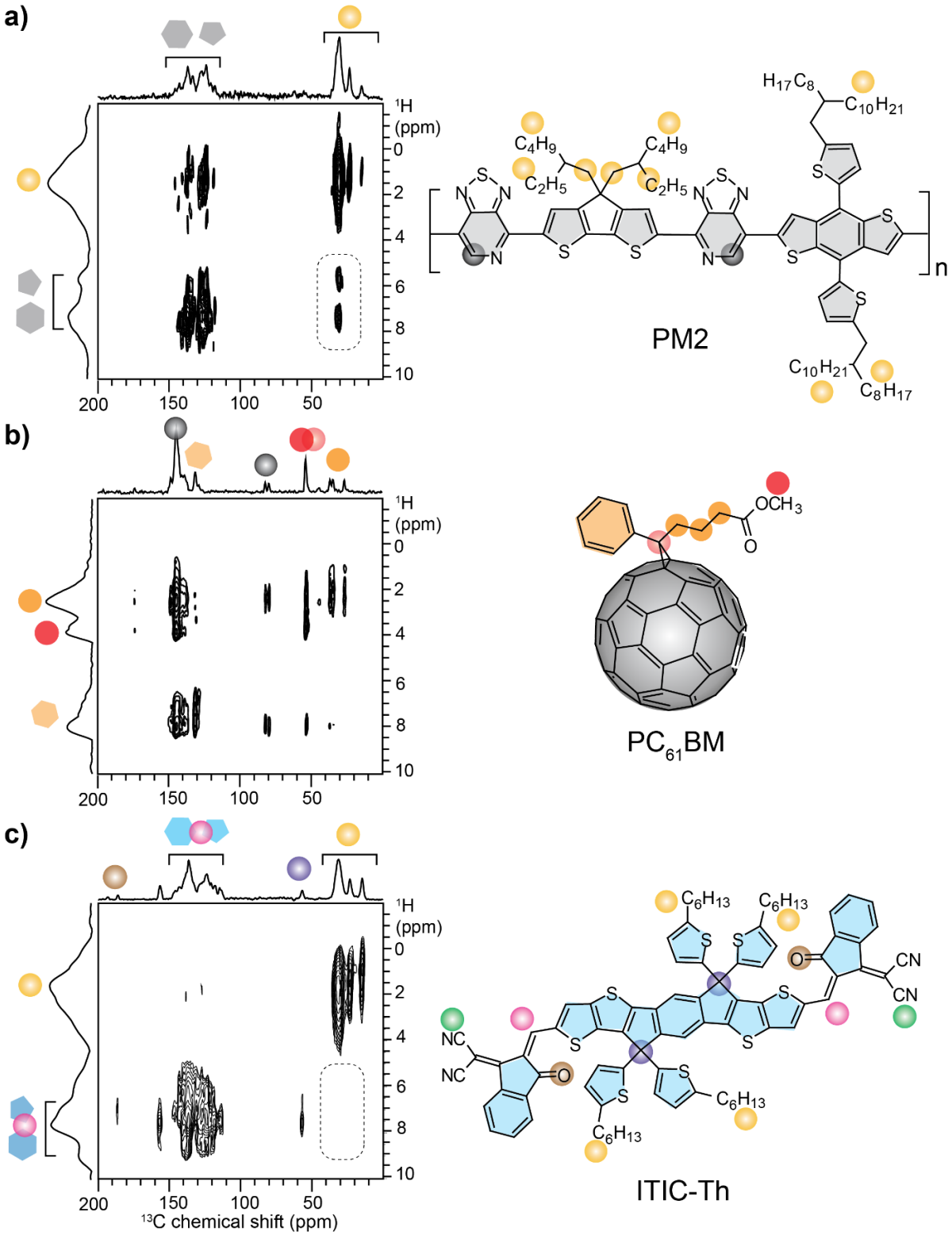

Figure S8.9. Comparison of solid-state 2D ^{13}C{^{1}H} HETCOR spectra of neat a) PM2 donor, b), PC$_{61}$BM and c) ITIC-Th acceptors acquired at 11.7 T (Larmor frequencies of ^{1}H and ^{13}C

were 500.2 and 125.8 MHz, respectively), 298 K, and at 12.5 kHz MAS with a 4 ms CP contact time. ^{1}H and ^{13}C signals are color coded as depicted in the schematic structural diagrams.

8.9.8 Supporting References

[1] M. Wang, H. Wang, M. Ford, J. Yuan, C.-K. Mai, S. Fronk, G. C. Bazan, *J. Mater. Chem. A* **2016**, *4*, 15232.

[2] U. Rau, *Phys. Rev. B* **2007**, *76*, 085303.

[3] A. Karki, G. A. H. Wetzelaer, G. N. M. Reddy, V. Nádaždy, M. Seifrid, F. Schauer, G. C. Bazan, B. F. Chmelka, P. W. M. Blom, T. Nguyen, *Adv. Funct. Mater.* **2019**, *29*, 1901109.

[4] K. Vandewal, J. Benduhn, V. C. Nikolis, *Sustain. Energy Fuels* **2018**, *2*, 538.

[5] K. Vandewal, K. Tvingstedt, A. Gadisa, O. Inganäs, J. V. Manca, *Phys. Rev. B* **2010**, *81*, 125204.

[6] R. Mens, S. Chambon, S. Bertho, G. Reggers, B. Ruttens, J. D'Haen, J. Manca, R. Carleer, D. Vanderzande, P. Adriaensens, *Magn. Reson. Chem.* **2011**, *49*, 242.

[7] S. Chambon, R. Mens, K. Vandewal, E. Clodic, M. Scharber, L. Lutsen, J. Gelan, J. Manca, D. Vanderzande, P. Adriaensens, *Sol. Energy Mater. Sol. Cells* **2012**, *96*, 210.

[8] F. Martini, S. Borsacchi, S. Spera, C. Carbonera, A. Cominetti, M. Geppi, *J. Phys. Chem. C* **2013**, *117*, 131.

9. Electrochemical Oxidative Fluorination of an Oxide Perovskite

This chapter is adapted from a published paper. I was responsible for the solid-state NMR experiments, analyses, and discussion shown in this paper. The specific goal for the NMR work was to understand and quantify F environments in ReO_3F_x materials, and how they differ with location in charge/discharge cycle, as well as with F content. Like the other materials discussed in this dissertation, the properties that enables their desirable electrochemical performance significantly overlap with the properties that make their characterization challenging. Thus, these materials are conductive, which cause signal broadening and challenges with bulk magnetic susceptibility. Our approach was to use solid state NMR to identify, characterize, and quantify the differences in the environments that occur with changes in charge/discharge cycle location (and thus F content) on a local atomic scale. This was achieved with fast MAS ^{19}F NMR, used to suppress the significant background signal experienced when measuring these types of materials, especially with the ^{19}F nuclei, in combination with DFT chemical shift predictions and relaxation resolved experiments. Solid-state ^{19}F MAS NMR allowed for the direct detection and resolution of signals from fluoride species in different local environments. The multitude of signals clearly showed that the fluoride species in the electrode are inhomogeneously distributed in diverse local environments and corroborate with the analyses of the PDF data.

Paper: *Chem. Mater.* 2021, 33, 5757−5768

DOI: 10.1021/acs.chemmater.1c01594

Authors: Nicholas H. Bashian, Mateusz Zuba, Ahamed Irshad, Shona M. Becwar, Julija Vinckeviciute, Warda Rahim, Kent J. Griffith, Eric T. McClure, Joseph K. Papp, Bryan D. McCloskey, David O. Scanlon, Bradley F. Chmelka, Anton Van der Ven, Sri R. Narayan, Louis F. J. Piper,* and Brent C. Melot*

9.1 Abstract

We report on the electrochemical fluorination of the A-site vacant perovskite ReO_3 using high-temperature solid-state cells as well as room-temperature liquid electrolytes. Using galvanostatic oxidation and electrochemical impedance spectroscopy, we find that ReO_3 can be oxidized by approximately 0.5 equiv of electrons when in contact with fluoride-rich electrolytes. Results from our density functional theory calculations clearly rule out the most intuitive mechanism for charge compensation, whereby F-ions would simply insert onto the A-site of the perovskite structure. *Operando* X-ray diffraction, neutron total scattering measurements, X-ray spectroscopy, and solid-state ^{19}F NMR with magic-angle spinning were, therefore, used to explore the mechanism by which fluoride ions react with the ReO_3 electrode during oxidation. Taken together, our results indicate that a complex structural transformation occurs following fluorination to stabilize the resulting material. While we find that this process of fluorinating ReO_3 appears to be only partially reversible, this work demonstrates a practical electrolyte and cell design that can be used to evaluate the mobility of small anions like

fluoride that is robust at room temperature and opens new opportunities for exploring the electrochemical fluorination of many new materials.

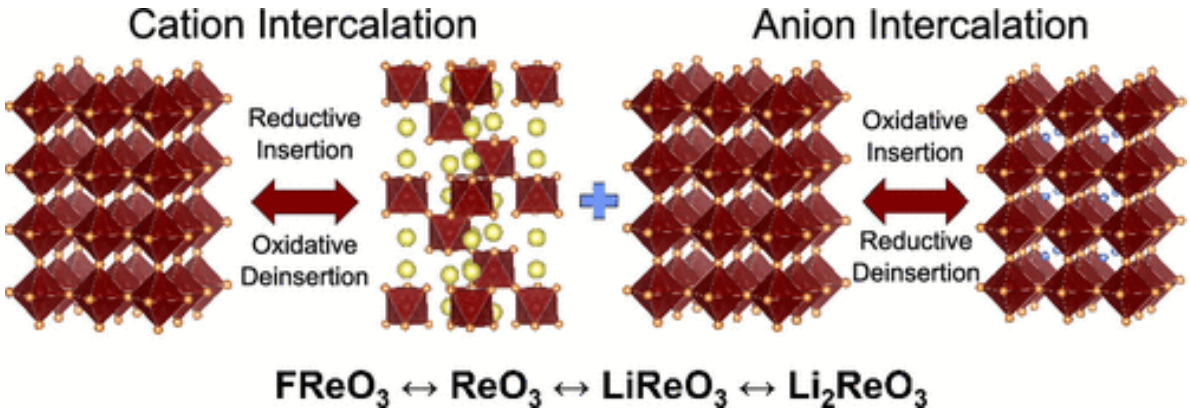

9.2 Introduction

The ability to topotactically control the insertion of ions into crystalline hosts is critical to a range of technologies, including energy storage, electrochromic displays, superconductivity, and catalysis.[1–3] While research on cationic intercalation chemistry has flourished,[4] anionic intercalation has largely been overlooked, with most work in the area focused on bulky polyanionic groups inserted into layered materials.[5] Given their substantially larger radius and negative charge polarity, anions require drastically different conditions from cations to promote fast ionic mobility.[6] The earliest work on anion insertion chemistry was performed by Schafhaeutl and then built upon by Rüdorff and Hofmann when they showed that SO_4^{2-} could intercalate between the sheets of graphite in the presence of a chemical oxidant.[7,8] Electrochemical intercalation into crystalline graphite was not achieved until the early 1980s using slow cyclic voltammetry to drive the ionic diffusion of species such as ClO_4^-, SO_4^{2-}, and BF_4^-.[9,10] Mallouk and Bartlett later described the chemical insertion of fluoride in graphite

using HF, identifying the formation of bifluoride $C_{12}HF_2$.[11] Carlin then built on this work to develop a symmetric graphite cell that intercalated bulky ions like imidazolium at the cathode and $AlCl_4^-$ at the anode to create one of the first embodiments of a dual-ion battery.[12]

While the intercalation chemistry of bulky polyanionic groups has received some attention,[13,14] the electrochemistry of smaller species like fluoride has been mostly limited toconversion-based systems where a reversible chemical transformation is used.[15−17] A critical challenge facing these systems is that they rely almost exclusively on solid-state fluoride conductors, like Ba-doped LaF_3,[18−20] sandwiched between metal and metal−fluoride electrodes.[21,22] Fichtner and coworkers, for example, have demonstrated a F-ion battery consisting of a CuF_2 cathode cycled against a film of La metal, which results in the reduction of the cathode to Cu metal and a conversion to LaF_3 on the anode side.[23] More recently, Clemens and co-workers have leveraged all-solid-state cells, showing some success with intercalating fluoride into La_2CoO_4, though the poor conductivity of the LaF_3 solid electrolyte required operating cells at 170 °C.[24,25] This was very recently followed by the work of Banerjee et al. who demonstrated chemical insertion and removal of fluoride from $FeSb_2O_4$ at room temperature using chemical redox methods.[26]

The high operating temperature of these solids precludes their use in any practical devices, which would require a fluoride electrolyte with high mobility at room temperature. Christe and others reported one of the earliest advances toward such an electrolyte when they reported that quaternary ammonium salts can stabilize free fluoride in tetrahydrofuran (THF).[27,28] More recently, Davis et al. showed that salts of *N*,*N*,*N*-trimethyl-*N*-neopentylammonium fluoride (Np1F) dissolved in fluoroether solvents could facilitate the stable cycling of CuF_2@LaF_3 core−shell nanoparticles as conversion cathodes.[29] This seminal work represented some of the

first tangible evidence that electrochemical energy storage can leverage anions like fluoride in similar ways to lithium.

Drawing inspiration from this extensive work in the literature, we sought to explore the fundamental structural requirements that facilitate fluoride-ion mobility in the solid state. Our recent work with ReO_3, in which we studied the fundamental structural distortions that occur during lithiation,[30] offered a natural starting material for these studies given that the A-site vacancy within perovskite provides an obvious interstitial where the fluoride could intercalate. The ability to simultaneously leverage cation and anion insertion within a single phase could provide an exciting breakthrough for increasing capacity limits. Furthermore, ReO_3 is intrinsically metallic, which removes the need for carbon coating and drastically simplifies the interpretation of spectroscopic data.

In this contribution, we demonstrate the first observation of electrochemical fluorination of an oxide host from a liquid fluoride electrolyte at room temperature. We find that the negative charge and larger ionic radii of F^- demand a vastly different mechanism for intercalation compared to that observed during Li insertion. Using complementary spectroscopic and structural tools, combined with *operando* electrochemical characterization, we show that incorporation of fluoride into the ReO_3 electrode during cycling creates a highly unstable phase that rapidly decomposes following oxidation. While this decomposition prevents reversible cycling, it also provides insight into a completely new mechanism for fluoride intercalation under relatively mild and tunable electrochemical conditions and how changing the host composition could stabilize F-ions on the A-site.

9.3 NMR Methods

Solid-State ^{19}F NMR Spectroscopy

Solid-state ^{19}F MAS NMR spectra were acquired on a Bruker AVANCE-III Ultrashield Plus 800 NMR spectrometer using a narrow-bore 18.8 T superconducting magnet and operating at a Larmor frequency of 752.980 MHz for ^{19}F. Experiments were conducted using a 1.3 mm double-resonance H/FX magic-angle spinning (MAS) probe head. For the solid-state NMR measurements, the conductive F_xReO_3 powders were mixed with KBr powder in a roughly 1:5 ratio by mass to reduce effects of eddy currents on the spinning samples. Samples were prepared in a glovebox and spun in nitrogen, as they are air-sensitive. KBr also served as an internal temperature probe for accurate determination of the sample temperature under the different measurement conditions.[58,59] One-dimensional (1D) ^{19}F Hahn-echo MAS spectra were acquired at 23 kHz MAS unless otherwise specified, at 298 K, and using a 90°−τ−180°−τ pulse sequence with rotor-synchronized τ delay times of one rotor period and 90° radio frequency (rf) pulses of 3.5 μs with a pulse power of 40 W. The ^{19}F spin−lattice (T_1) relaxation times were measured using a saturation recovery pulse sequence with a Hahn-echo detection (Figure S9.12, Supporting Information). Isotropic ^{19}F NMR chemical shifts were referenced to $CFCl_3$ using PTFE (−122 ppm) as a secondary standard.

Computational Thermodynamic Stability and Prediction of ^{19}F NMR Chemical Shifts

The CASM software package[60−62] was used to explore the phase stability of topotactic F insertion into perovskite ReO_3 by enumerating different F-vacancy orderings over the empty A-sites of ReO_3. The energies of these configurations were calculated with DFT Perdew−Burke−Ernzerhof (PBE) using the Vienna *ab initio* simulation package (VASP) plane-wave code, and[63−66] the generalized gradient approximation of Perdew, Burke, and

Ernzerhof (GGA-PBE) was used for the correlation and exchange potentials with a 17 × 17 × 17 *k*-point mesh used for all structures (i.e., ReO_3 and ReO_3F). Additionally, several configurations that allowed for a redistribution of Re or mixing between O and intercalated fluoride ions were considered. ^{19}F NMR shielding tensors for various structural models were calculated using the fully periodic gauge including projector-augmented wave (GIPAW) method[67–69] following a similar approach to Griffin and co-workers.[70] In brief, a linear relationship between the calculated chemical shifts for several reference compounds was correlated to their experimentally observed values and fitted to establish the relationship $\delta_{iso}^{exp} = k(\delta_{iso}^{calc}\delta_{ref})$, where k = 0.68 and δ_{ref} = 160 from the fits, as shown in Table T9.2 and Figure S9.10, SI. This expression was then used to predict the experimentally observed chemical shift of the models considered in this work.

9.4 Results and Discussion

ReO_3 was chosen as a model electrode compound to investigate the fundamentals of fluoride intercalation for several reasons, including the high degree of covalency in bonding, the existence of vacancies to accommodate ions, and its inherent metallic character. ReO_3 crystallizes in the $Pm\bar{3}m$ space group (#221) and possesses a perovskite-like structure composed of highly symmetric corner-sharing ReO_6 octahedra in a perfectly cubic arrangement with an empty A-site that creates large three-dimensional channels for ionic diffusion,[31] as shown in Figure 9.1a. While cation insertion has been demonstrated previously, the close-packed oxygen network (Figure 9.1b) makes anion transport pathways less obvious.

The synthesis of ReO_3, described in the Experimental Methods section, yields highly uniform and crystalline nanoparticles between 20 and 50 ns in diameter. ReO_3 is one of the few metallic oxides, exhibiting a conductivity on the order of 10–5 S/cm,[32] making it an excellent model battery electrode because it is possible to prepare test cells without conductive

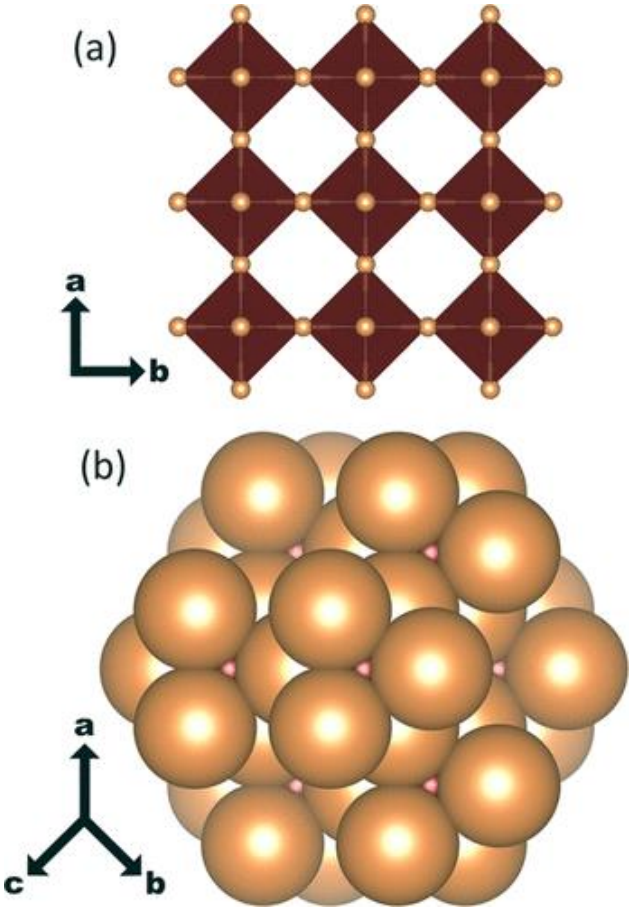

Figure 9.1. (a) Structure of ReO_3 with orange oxygen spheres and maroon rhenium-centered octahedra, shown along [001]. (b) Structure of ReO_3 is displayed along the [111] using the ionic radii of Re and O, emphasizing the tight packing of anions.

carbon additives, which would complicate many spectroscopic measurements. Additionally, using test electrodes composed entirely of ReO_3 removes any potential side reactions related to carbon or binder additives, an important consideration in new cell design.

In an attempt to insert fluoride into ReO_3, F-ion half-cells were assembled using a Cu-metal combined counter and reference electrode and an organic liquid fluoride electrolyte, as described in the Experimental Methods. Glass fiber separators soaked in an electrolyte of tetra-*n*-butylammonium fluoride (TBAF) dissolved in tetrahydrofuran (THF) served as the source of free fluoride ions between the working and counter electrodes. TBAF was chosen for its relative stability and wide electrochemical window as well as a reasonable fluoride-ion conductivity. As shown in Figure 9.2a, the oxidation reaction produces a smooth voltage curve with a smooth sloping region followed by a sharper voltage increase until approximately $F_{0.6}ReO_3$. While the use of Cu metal provides a consistent reference potential, it cannot be further reduced, which raised questions about the nature of the counter-reaction occurring at the cathode. To better understand this counter-reaction, differential electrochemical mass spectrometry (DEMS[33]) measurements were employed to monitor any evolution of gas in situ during the cycling at both the anode and cathode. Several gases were monitored during oxidation, including O_2, F_2, and CO_2 (shown in Figure S9.8, SI), but as seen in Figure 9.2b, the only gas that was observed to evolve in substantial quantities was H_2, which persisted throughout the plateau during charging and roughly corresponds to a $2e–/H_2$ process (see Figure S9.9, SI). Therefore, the reductive counter-reaction is found to be associated with a hydrogen evolution reaction (HER) from an attack of the THF or TBAF salt. The lack of oxygen release from ReO_3 throughout the measurement is notable given that the quasi-reference potentials observed scale to be far in excess of 4 V vs Li^+/Li. This suggests that there

is unlikely to be very much decomposition of the ReO_3 particles through the release of lattice oxygen in the manner previously reported for other metal oxides.[34,35] This high-voltage stability is most likely associated with the covalent character of the material—the strong hybridization between the metal and oxygen orbitals makes it very difficult to strip oxygen out of the lattice.

To validate the liquid-phase electrochemistry, all-solid-state cells were prepared using a Ba-doped LaF_3 electrolyte to eliminate solvent decomposition and only allow for redox reactions involving the transport of fluoride ions. Given the slow fluoride conductivity of the solid electrolyte, it was necessary to heat the cells to 150 °C during cycling to facilitate facile ion transport in the solid electrolyte. As the H2 evolution reaction observed in the liquid electrolyte half-cells in Figure 9.2b is not possible in the solid state, a CuF_2 counter electrode was chosen as a reductive fluoride source. A similar voltage profile was observed during charging of the solid-state cells as that of the liquid cells; however, the sluggish nature of F-ion transport in the solid state led to a high cell resistance in the solid-state cells, which were tested. Therefore, galvanostatic intermittent titration (GITT) measurements were used to examine the equilibrium voltage of the reaction.[36] GITT measurements were also performed on cells with a liquid electrolyte allowing for direct comparison to the electrochemistry performed in solid-state cells. As shown in Figure 9.3, a similar voltage relaxation profile was observed in both solid state and liquid cells, suggesting a very similar oxidative reaction at the ReO_3 electrode for both cell designs.

Electrochemical impedance spectroscopy (EIS) studies on the solid electrolyte cell were also used to monitor variations in the charge-transfer and mass transfer resistances at different levels of oxidation. The Nyquist plot in Figure S9.7a shows a depressed semicircle in the high-

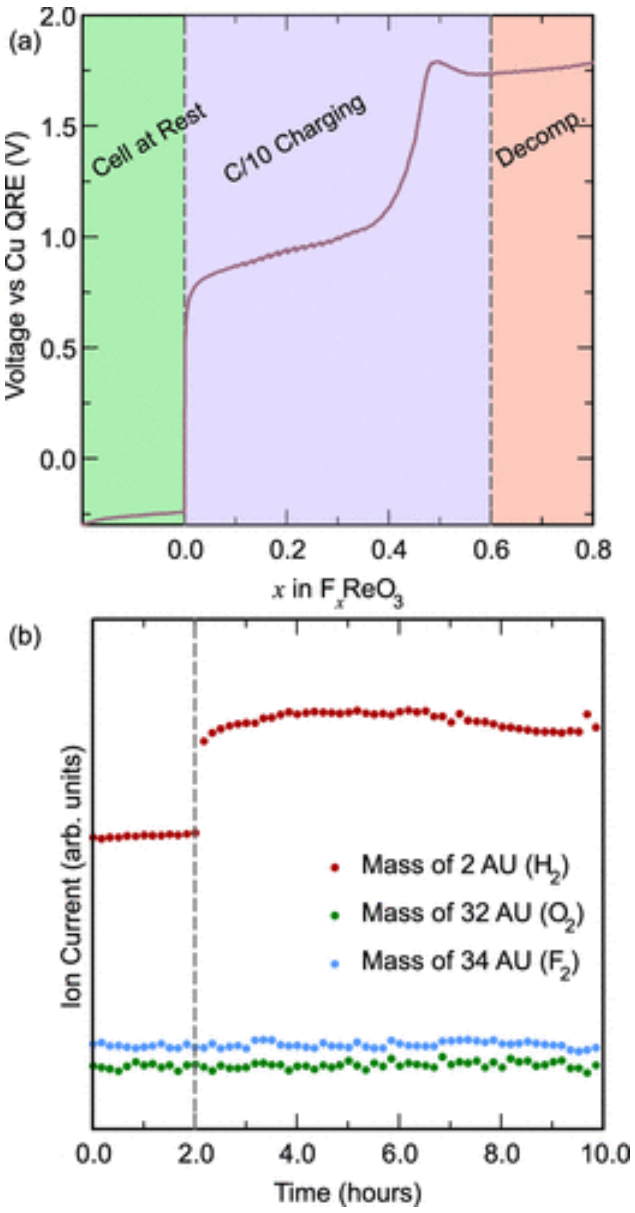

Figure 9.2. (a) Galvanostatic charge curve of a fluoride-ion half-cell during mass spectrometry measurements with a ReO_3 working electrode and Cu metal counter and reference electrodes. (b) Differential electrochemical mass spectrometry identified H_2 evolution in fluoride-ion battery half-cells; however, no O_2 or F_2 generation was seen.

frequency region characteristic of charge-transfer resistance (R_{ct}) in parallel with the interfacial double-layer capacitance (C_{dl}). The values of R_{ct} do not change significantly until x = 0.5, and a small increase of 2−3 Ω is noticed thereafter. The increase in R_{ct} occurs concurrently with the transition from the initial sloping voltage to a higher voltage plateau. In the low-frequency region of the impedance spectrum, the impedance increases steadily with decreasing frequency with a phase angle of approximately 45° suggesting a diffusion-limited process. Considering the diffusion length and the thickness of the sample, this section of the

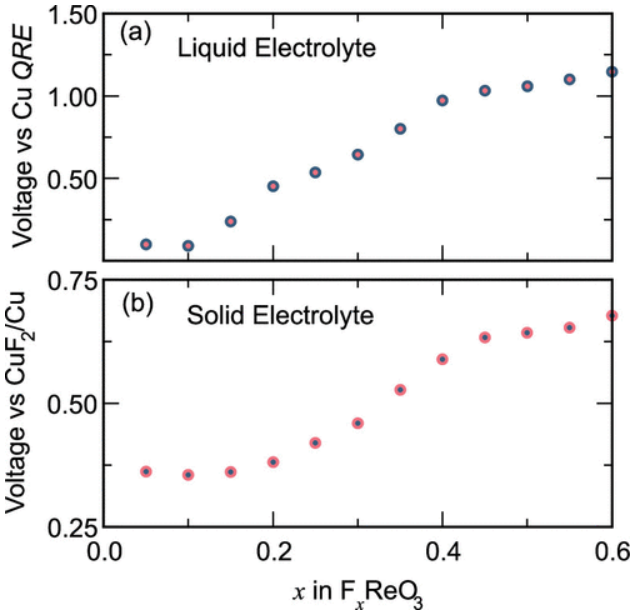

Figure 9.3. Galvanostatic intermittent titration measurements in (a) liquid electrolyte cells prepared with the TBAF electrolyte show similar open-circuit voltage traces when compared to (b) voltage traces from all-solid-state cells cycled at 150 °C. Note that differences in the nature of the counter electrode and operating temperatures explain the offsets in the voltage windows.

impedance spectrum can be modeled with the semi-infinite linear diffusion boundary conditions, as described in the Impedance Spectroscopy section, SI. A decrease in *D* is observed with an increasing state of charge (which nominally corresponds to an increasing degree of fluorination), as shown in Table T9.1, suggesting that changes to the material during charging hinder fluoride transport.

Having validated that the oxidative currents were indeed associated with a reaction at the ReO_3 electrode and were not simply electrolyte decomposition, we turned to developing a mechanistic understanding of how fluoride intercalation could occur within the structure of ReO_3. *Operando* X-ray diffraction (XRD) patterns were collected during oxidation until an equivalent current for one fluoride per formula unit had been passed. As seen in Figure 9.4a,b, the (111) reflection continuously shifts very slightly to higher angles, indicating a small contraction of the unit cell during charging but no new peaks evolve nor do any of the existing peaks split to suggest changes in the cubic symmetry of the lattice. Beyond a nominal fluoride content of roughly 0.6, the intensity of diffraction patterns begins to significantly decrease, indicating the onset of decomposition, as illustrated in Figure S9.5, SI. We note, however, that immediately after exposure to the TBAF electrolyte, and prior to cycling, several low-intensity peaks appear in data obtained at the synchrotron (further demonstrated in Figure S9.3, SI). These peaks cannot be seen with laboratory X-ray sources and do not change position or intensity at any point during the cycling (see Figure S9.4, SI) and are therefore believed to be associated with an electrochemically inert contaminant associated with the electrolyte solution

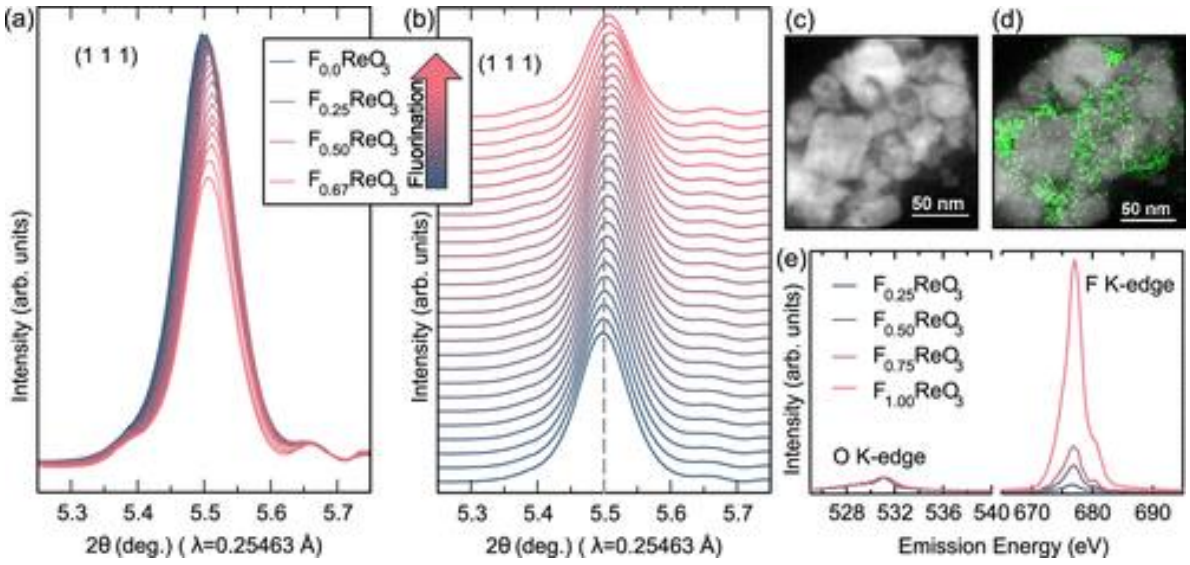

Figure 9.4. (a) *Operando* synchrotron X-ray powder diffraction (SXRD) captured at various states of charge during the fluorination of ReO_3. A loss of diffracted intensity is observed during charging. (b) The (111) reflection is highlighted to demonstrate the slight shift to higher 2θ values in conjunction with a loss of diffracted intensity at higher states of charge. (c) Transmission electron microscopy (TEM) images of the fluorinated ReO_3 show that the cubic particle morphology is maintained, while (d) electron energy loss spectroscopy (EELS) spectra show a F-rich shell on the particles. (e) X-ray emission spectroscopy (XES) of F_xReO_3 at various states of charge shows an increase in the F signal due to fluoride intercalation. Note that the compositions listed reflect the nominal state-of-charge.

While the extremely minor changes seen in the diffraction patterns initially seem puzzling, a careful look at the cubic structure shows that placing fluoride ions onto the vacant Asite would not break any of the symmetry elements within the parent perovskite (see Figure S9.6, SI), which is consistent with the absence of any new diffraction peaks. In parallel, *ex situ*

electron microscopy and electron energy loss spectroscopy (EELS) mapping were used to monitor the particle morphology and distribution of fluoride in the electrode after charging. As shown in Figure 9.4c, the particles maintain their cubic morphology with signs of crystallinity, suggesting that the ReO_3 does not dissolve or directly extrude any secondary phases during oxidation. EELS measurements, shown in Figure 9.4d, show an uneven fluoride distribution throughout the particles with fluoride-rich regions near the surfaces. Nevertheless, there is no evidence that the morphology of the ReO_3 nanoparticles alters during cycling, which rules out a dissolution−precipitation-style reaction. Furthermore, the fluoride persists on the particles even after washing the *ex situ* samples thoroughly to remove any residual electrolyte.

Ex situ X-ray emission spectroscopy (XES) was also collected on similarly washed samples to more directly track the fluoride content of the oxidized electrodes. The greater penetration depth allows for sensitivity to bulk fluoride rather than simply probing species isolated to the surface. By comparing the intensity of the spectra from the O 2p orbitals to the F 1s orbitals, relative changes in the bulk fluoride content are clearly seen. As shown in Figure 9.4e, the intensity of the peak at approximately 677 eV, associated with the F 1s orbitals from bulk fluoride species, grows with increasing state of charge, while that of the O 2p peak at 531 eV remains constant. As demonstrated by the DEMS measurements in Figure 9.2b, there is no reason to believe that O_2 is released from the lattice during oxidation; thus, the variation in the F peak corresponds to an increase in the fluoride content throughout the ReO_3 electrode during charge. In contrast, the states associated with the lattice oxygen of ReO_3 stay relatively constant but do show some restructuring due to changes in the chemical environment of the materials, which will be discussed in greater detail later. Taking these results together, it seems

clear that the fluoride reacts with the ReO_3, but it is not immediately clear whether the fluoride intercalates into the structure or if there is a more nuanced transformation that is missed by the *operando* X-ray diffraction experiments.

To assess the thermodynamics of various reaction mechanisms on the insertion of F into ReO_3, first-principles density functional theory (DFT) calculations were performed. We first explored topotactic insertion by enumerating different F-vacancy orderings over the A-sites of ReO_3. Figure 9.6a shows the calculated formation energies of these orderings at a variety of concentrations using the perovskite forms of ReO_3 and fully fluorinated $FReO_3$ as the reference states. The formation energies are very slightly negative, indicating that F-vacancy ordering over the A-sites might be expected at low temperatures, while a solid solution will emerge at elevated temperatures provided the ReO_3 perovskite host remains intact.

An alternative to topotactic insertion would be a reconstructive or conversion reaction mechanism,[37] whereby a completely new crystal structure emerges during oxidation. A survey of the Inorganic Crystal Structure Database[38] shows the existence of a monoclinic form of ReO_3F, where the structure consists of edge-sharing chains of octahedrally coordinated ReO_4F_2 units with two fluoride ions sitting along common edges of the polyhedra (see Figure S9.14, SI).[39] In the following, we distinguish the intercalated phase from this one by writing the compositions as $FxReO_3$ or mono-ReO_3F, respectively. The energy of this compound is predicted to be more than 2 eV lower per formula unit than that of the fully intercalated perovskite form of F_xReO_3, which points to the existence of an enormous thermodynamic driving force for a reconstructive transformation.

Given that the crystal structure of the mono-ReO_3F form is very different from that of the perovskite form of ReO_3, it may not be kinetically accessible at room temperature. We,

therefore, decided to begin exploring other hypothetical structures that may be more readily accessed during F− insertion into ReO_3 (see the models illustrated in Figure 9.5). One such structure can be obtained by inserting F in the vacant A-sites, followed by a coordinated migration of Re cations from their octahedral sites to a newly created tetrahedral interstitial, referred to as F_xReO_3−1F. This hopping of the cations was considered for several different compositions of fluoride but was repeatedly found to be higher in energy than when there is no migration of Re out of the octahedral sites. Similarly, geometric relaxations of the structures also indicated that the forces on the atoms can be fully minimized by distorting Re out of the center of the octahedra toward one of the triangular faces of the octahedra to create

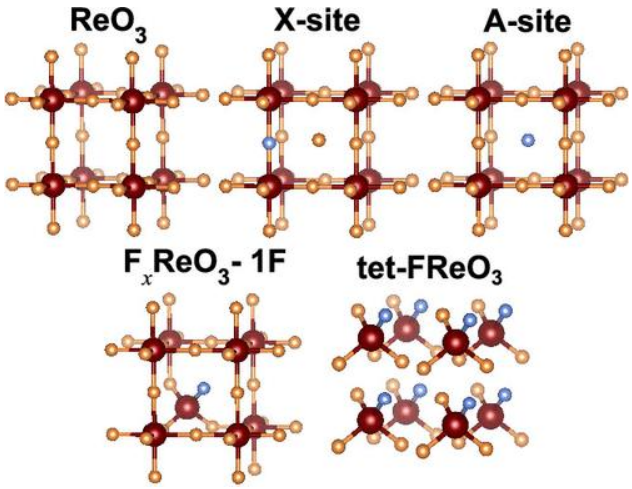

Figure 9.5. Various models for the fluorination of ReO_3 that are considered throughout the text with Re shown in red, oxygen in orange, and fluorine in blue. The tet-$FReO_3$ model, where all of the Re ions migrate to the tetrahedral positions, can be considered an end member to the $FxReO_3$−1F.

a highly distorted seven-coordinate environment, referred to as sevencoordinate ReO_3F (see Figure S9.13, SI). This too was found to be far less favorable than F-ions sitting in the empty cages of the cubic form of ReO_3.

Interestingly, however, we find that when all of the A-sites are filled by fluoride and all of the Re ions simultaneously migrate into the tetrahedral interstitials, as illustrated in Figure S9.16, this structure is significantly lower in energy than that with fluoride only on the A-site, considered as intermediate compositions. This phase, referred to as tet-$FReO_3$, is best viewed as a molecular crystal with covalently bonded ReO_3F tetrahedra that are loosely held together by weaker van der Waals forces. In this work, we have considered the polar form of the structure where the apical F-ions on each tetrahedron point in the same direction, but, in reality, the tetrahedra are likely to be far more disordered, which we have not considered here at all.

These calculations clearly suggest that if fluoride-intercalated ReO_3 were actually to be obtained, there would be a very strong driving force for it to transform into either the monoReO_3 polymorph reported in the material project or, while not as likely, the form with all of the Re migrated to tetrahedral interstitials (Figure S9.16, SI). At small values of x, *i.e.*, less than $F_{0.5}ReO_3$, the energy to form the phase with Re moved into the newly formed tetrahedral interstitial is actually higher than that of simply placing F-ions on the A-site.

This suggests that a reconstructive reaction could occur through a two-phase mechanism, and, indeed, an application of the common tangent construction to all of the formation energies of structures that are kinetically accessible predicts a two-phase coexistence between ReO_3 and tet-$FReO_3$, as shown by the dashed gray line in Figure 9.6a. This partitioning into two

phases could be expected to result in a core−shell geometry, in which the new tet-$FReO_3$ phase forms on the surface and grows inward, consuming the original ReO_3 core, which appears

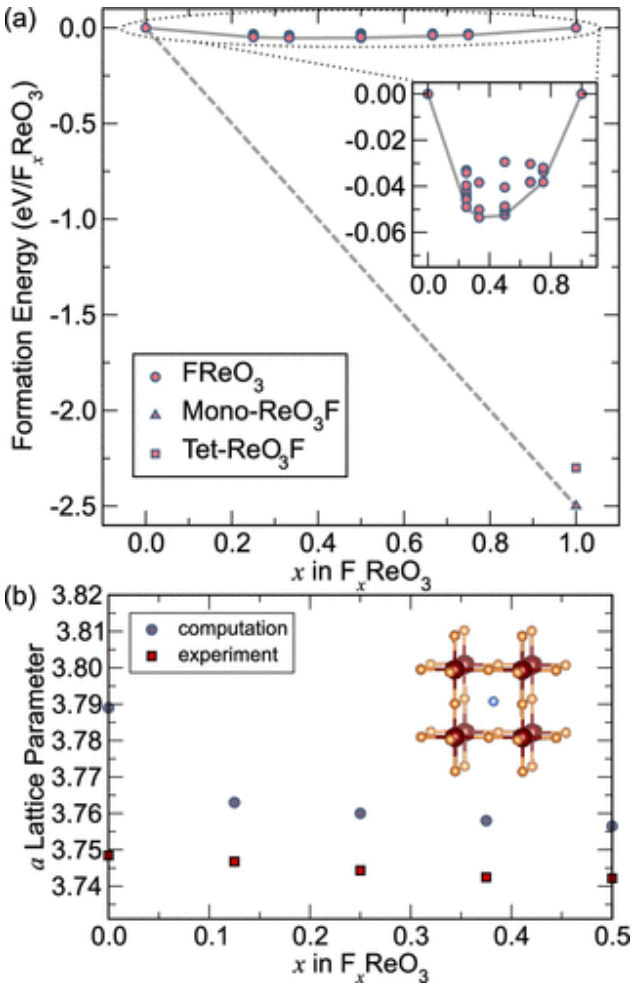

Figure 9.6. (a) Computed Hull diagram indicates that tetrahedral Re is energetically favorable upon fluoride intercalation, while the inset shows a small energetic minima for the insertion of F to the A-site. (b) Calculated a lattice parameter (filled blue circles) for $FReO_3$ indicates a unit cell contraction, similar to that seen in the *operando* XRD measurements (filled red squares).

consistent with the EELS maps but, in principle, should have been observable in the *operando* diffraction patterns if the shell were fully crystalline. However, given that the mono-ReO_3F is more stable than even tet-$FReO_3$, it is difficult to know exactly what phase the F-rich shell seen in EELS is composed of.

For this, we turned to structural tools that were more sensitive to the local environments within the material such as neutron total scattering to generate pair distribution function (PDF). Starting with the top panel of Figure S9.18, the *ex situ* neutron total scattering experiments for the pristine ReO_3 are clearly well described by the long-range average cubic structure, whereas the significantly changed scattering from a washed sample of $F_{0.6}ReO_3$ is shown in the bottom portion of the same figure. The first two peaks at 1.88 and 2.67 Å in the pristine phase can be assigned to the Re−O and O−O nearest neighbors, respectively, which, after oxidation, evolve into a complex mixture of peaks that makes precisely modeling the pattern exceptionally challenging. To aid in deconvoluting the contributions at each distance, the bottom panel of Figure S9.18 shows the calculated PDF adapted from the F_xReO_3−1F model discussed earlier, as described in the Neutron Pair Distribution Function Analysis section of the Supporting Information. For example, the first shell of distances at 1.88 Å splits into two distinct contributions that can be attributed to three short Re−O distances and one slightly longer Re−F bond within the newly created tetrahedra in the model. Furthermore, the peak at 3.75 Å, associated with Re−Re distances, is seen to split as Re migrates from its starting position and the O−O peak (2.67 Å) evolves into multiple peaks as new O−O and O−F environments are created. We also note that contributions from short C−H and C−C distances had to be included to account for all of the changes in the oxidized sample. These

organic species are believed to be associated with a decomposition product created during the electrolyte decomposition at the counter electrode discussed earlier.

While the new distances in the PDF might initially appear to support the migration of Re into the tetrahedral interstitials, the predicted lattice parameters for such a hop suggest that the unit cell should expand during such a transformation. In contrast, the *operando* diffraction data showed a contraction of the lattice (see Figure 9.6b), which would seem to imply that if such a hop were to occur, it would need to be in an uncorrelated fashion that exhibits no long-range periodic order to the new tetrahedral sites. Alternatively, this may also suggest that a Re environment resembling the tetrahedral or sevencoordinate models described previously might exist at the surface of the particles rather than as a completely separate new phase (see Figures S9.19−S9.22, SI).

To clarify the ambiguity of the PDF data, solid-state ^{19}F magic-angle spinning (MAS) NMR spectroscopy was used as a complementary probe of the local composition and structure of the intercalated fluoride ions. While the PDF results yield insights on locally averaged structural distortions within the bulk material, ^{19}F MAS NMR allows for the direct detection and resolution of signals from fluoride species in different local environments. As shown in Figure S9.11 of the Supporting Information, the one-dimensional (1D) ^{19}F MAS NMR spectra for bulk $F_{0.2}ReO_3$, $F_{0.4}ReO_3$, and $F_{0.6}ReO_3$ produced as a result of oxidative insertion during partial charge exhibit a complicated distribution of ^{19}F intensity over the frequency range of −100 to −250 ppm. Interestingly, several distinct and relatively narrow (∼5−10 ppm, full width at half-maximum) ^{19}F signals are observed at isotropic chemical shifts of −137, −142, −151, −158, −170, −175, −190, −220, and −251 ppm, which manifest fluorine species in well-defined local environments. The signals at −135 and −124 ppm are associated with a ^{19}F

spin−lattice relaxation time, T_1, of 4.0 s (Table T9.3 and Figure S9.12, Supporting Information), which is consistent with fluoride in a diamagnetic perovskite environment.[40,41] Interestingly, all of the other signals correspond to much shorter ^{19}F T_1 values of 0.3−0.4 s (Table T9.3), consistent with fluoride environments that are influenced by conducting or donor electrons.[40–42] It is also noted that the $F_{0.4}ReO_3$ sample exhibits several signals that are displaced to lower frequencies at chemical shifts of −175, −220, and −251 ppm, which may be associated with the state of maximum fluorination prior to decomposition. DFT calculations of several structural models selected from the phase diagram for fluoride intercalation into ReO_3 predict an isotropic ^{19}F chemical shift of −141 ppm for mono-ReO_3F, very near the values of several of the measured signals. By comparison, the calculations predict the isotropic chemical shift of a model structure with seven-coordinate distorted octahedra to be near −73 ppm and of tet-$FReO_3$ to be near −11 ppm, neither of which are experimentally observed (Figure S9.11). The multiple signals clearly show that the fluoride species in the electrode are inhomogeneously distributed in diverse local environments and corroborate the challenges to the analyses of the PDF data.

In a final attempt to reconcile the experimental results with computational models, X-ray spectroscopy was performed on the oxygen and fluorine K-edges for pristine and oxidized samples and compared with simulation based on the various structural permutations discussed previously. The O K-edge emission and absorption spectra reflect the bulk occupied and unoccupied O 2p partial density of states near the Fermi level. The oxygen K-edge, shown in Figure 9.7b, evolves significantly after cycling, which clearly indicates a change in the electronic structure of ReO_3 during oxidation. While the pristine material (blue) shows a large absorption peak at −2 eV associated with O 2p Re 5d bonding orbitals, these states are

suppressed upon charging (pink), reflecting electron density being extracted from the material. The emergence of a new peak at 9 eV indicates a change in the local oxygen environment during oxidation. The presence of F^- near very electrophilic Re^{6+} is expected to draw electron density from the O 2p states to higher binding energies.

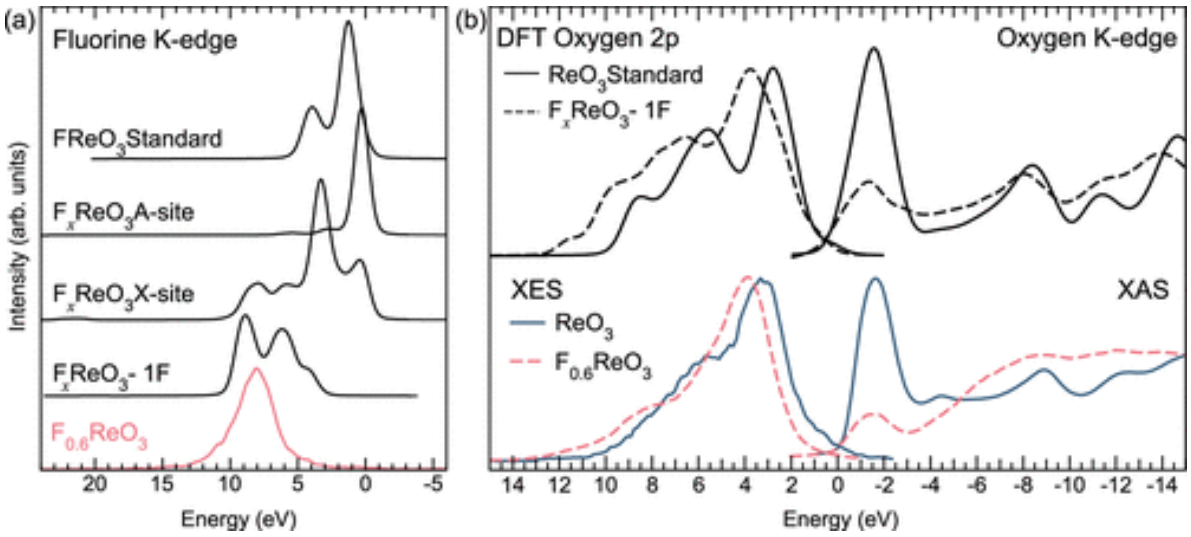

Figure 9.7. (a) Calculated X-ray emission spectra of the F K-edge are shown in black, while the measured spectra of ReO_3 are shown in orange and $F_{0.6}ReO_3$ is shown in blue. The energy shift of the measured spectra agrees well with the model of Re migration to the tetrahedral site. (b) Calculated and measured O K-edge X-ray emission and absorption spectra agree for both pristine and fluorinated ReO_3 using the proposed structural model.

As shown in Figure 9.7a,b, DFT calculations were used to model the expected O K-edge absorption and emission in both ReO_3 and $FReO_3$, using the structural models previously described, where Re migrates to one of the tetrahedral sites in $FReO_3$. Additional models are

provided in Figures S9.13−S9.16, SI. Curiously, the only model that captures the shape and energy shifts of the measured O 2p partial density of states is where a small number of tetrahedral sites are created, rather than the phase that was predicted to be more thermodynamically favored, i.e., where all of the Re jump to the tetrahedra (see Figure S9.16, SI). The relative change in intensity between X-ray absorption peaks at −2 and −9 eV, representing a change in O bonding environments as ReO_3 is fluorinated, is matched by the DFT calculations, as is the shape and energy shift of the main emission features observed. The fluorescent nature of O K-edge XES suggests that the spectral changes from the electrochemical reaction must not be limited to a surface reaction, but instead some change to the bulk ReO_3 electronic structure must also occur. A closer look at the geometrically relaxed model containing a small number of tetrahedral Re shows a slight off-centering within the octahedral cages and some rotational disorder that likely explains the changes seen in the spectra.

Calculations of the fluorine K-edge for each model are shown as black traces in Figure 9.7a. As seen, the measured XES spectra of $F_{0.6}ReO_3$ also agree well with the model where Re migrates to stabilize the intercalated F-ions. While challenges with alignment of the F K-edge led to broadening of the measured signal and prevented distinct peaks from being resolved, the strong agreement between the calculated and measured energy shifts further supports the presence of some tetrahedral species within the oxidized electrode.

Finally, hard X-ray photoelectron spectroscopy (HAXPES) measurements were performed on the Re 4f, O 2p, and F 1s orbitals of pristine and fluorinated ReO_3 and used to track changes in the oxidation state of the various species during oxidative charging. As mentioned, the highly covalent bonding of ReO_3 delocalizes electrons over both oxygen and

Re states, which leads to partial changes in the Re oxidation state during charging. This can be seen in Figure S9.17, where the Re 4f photoemission was measured during various states of charge. The doublet peaks at 43 and 46 eV are diagnostic of Re^{6+}, while a similar doublet at 46 and 48 eV is attributed to Re^{7+}. During oxidative charging, the formation of a shoulder at 48 eV is observed as Re is partially oxidized. However, owing to the strong covalency, no evidence for a fully ionic description of Re^{7+} species was detected.

Taking all of the experimental and computational results together, there is clear evidence that F^- ions have incorporated into ReO_3 during oxidative charging, but the precise mechanism remains ambiguous. *Operando* X-ray diffraction data shows a clear lattice contraction that agrees closely with the trends predicted for the models containing intercalated F-ions on the A-site of the ReO_3 cage. Yet, this A-site model is predicted to be unstable compared to less densely packed polymorphs, and the *ex situ* material characterization suggests that the fluoride in the oxidized materials is most likely associated with those more stable tetrahedral tet-ReO_3F species or a decomposition to the structurally distinct monoReO_3F phase. This leads us to conclude that this discrepancy is likely due to changes in the material once it is removed from the electrochemical cell. Note that the *operando* diffraction experiments are collected from start to finish in approximately 5 h, with each pattern being collected in a matter of seconds. Hence, the most likely explanation for the discrepancy between the various characterization tools is that F-ions intercalate onto the A-site of the perovskite host but quickly begin to decompose to the more thermodynamically favored phases over time.

It is curious that the best agreement between the *ex situ* experimental data and the computation is found for the model containing a dilute number of Re that have jumped to tetrahedral sites. We suggest two possibilities to explain this observation. Either a shell of

tetrahedrally coordinated Re forms as a decomposition product on the surface of the particles and the model we have considered is effectively capturing important interfacial effects or the correlated migration of Re into the tetrahedra environments is kinetically challenging and eventually results in some of the tetrahedral species trapped within the octahedral network even though they are thermodynamically disfavored. It is also possible that the final decomposition product contains some aspects of the dilute tetrahedral Re model, but the model fails to precisely capture all of the structural nuances. While we have gone to great lengths to evaluate as many possible forms of the intercalated structure, it is very likely that there are a vast number of alternate ways the perovskite lattice may be able to distort through octahedral tilting or cation migration. We therefore believe there is ample evidence to conclude that F- ions have incorporated into ReO_3 during oxidation despite being unable to definitively assign a unique structural model to the resulting material. Further exploration using the thermodynamic modeling with a greatly expanded phase space along with additional *operando* local probes would be helpful in this regard but falls outside the scope of the present study.

While the incorporation of fluoride ions into structures as dense as perovskite may initially seem too energetically demanding, several studies have shown the possibility to intercalate fluoride perovskite derivatives using aggressive chemical oxidants.[43–46] Other works have investigated the formation of interstitial fluoride species within similar $Sr_3Ru_2O_7$ species, in which layers of fluoride are formed and result in correlated rotations of the RuO_6 octahedra.[47] Crucially, fluorination of the parent oxide was performed at a low reaction temperature of 220−300 °C, demonstrating the relative ease of fluoride intercalation into this oxide.

It is also known that halide ions are very mobile within the perovskite structures, with studies of $CH_3NH_3PbI_3$ showing that this migration occurs easily under an applied bias.[48,49] These reactions are typically limited by halide diffusion through the structure *via* interstitials or vacancies but can proceed quite quickly. In fact, Walsh and Stranks have clearly shown that both the cationic and anionic sublattices in perovskites are mobile and the activation barrier for defect migration is relatively low, which is in good agreement with that observed here.[50]

9.5 Conclusions

In summary, we have presented, for the first time, the oxidative fluorination of the dense oxide ReO_3 using electrochemical cells and a liquid electrolyte at room temperature. We find that electrons are removed from the strongly hybridized Re−O orbitals at the Fermi level resulting in partial oxidation of both Re and O, with charge compensation occurring via the incorporation of fluoride ions into the electrode composition. The introduction of fluoride results in complex structural changes as some Re appear to migrate from the octahedral sites to newly formed tetrahedral sites, as evidenced by changes in the X-ray absorption spectroscopy (XAS) and XES spectra, SXRD patterns, and neutron PDF scattering. While DFT calculations clearly show that the intercalated forms of $FReO_3$ we have considered are strongly disfavored by thermodynamics, more exhaustive explorations of the phase space are necessary to fully understand whether more complex tilting/alterations of the initial octahedral network may serve to stabilize these phases. Fluoride intercalation at ambient conditions would represent a paradigm shift compared to traditional Li-ion battery technologies and

offers a window into a broad new avenue for developing methods for higher storage capacity if cationic and anionic intercalation can be successfully and sequentially achieved within single-phase materials.

9.6 References

(1) Whittingham, M. S. Lithium Batteries and Cathode Materials. Chem. Rev. 2004, 104, 4271−4302.

(2) Mortimer, R. J. Electrochromic materials. Chem. Soc. Rev. 1997, 26, 147.

(3) Rives, V.; del Arco, M.; Martín, C. Intercalation of drugs in layered double hydroxides and their controlled release: A review. Appl. Clay Sci. 2014, 88−89, 239−269.

(4) Manthiram, A. A reflection on lithium-ion battery cathode chemistry. Nat. Commun. 2020, 11, No. 1550.

(5) Gamble, F. R.; Osiecki, J. H.; Cais, M.; Pisharody, R.; DiSalvo, F. J.; Geballe, T. H. Intercalation Complexes of Lewis Bases and Layered Sulfides: A Large Class of New Superconductors. Science 1971, 174, 493−497.

(6) West, W. C.; Whitacre, J. F.; Leifer, N.; Greenbaum, S.; Smart, M.; Bugga, R.; Blanco, M.; Narayanan, S. R. Reversible Intercalation of Fluoride-Anion Receptor Complexes in Graphite. J. Electrochem. Soc. 2007, 154, A929.

(7) Schafhaeutl, C. Ueber die Verbindungen des Kohlenstoffes mit Silicium, Eisen und anderen Metallen, welche die verschiedenen Gallungen von Roheisen, Stahl und Schmiedeeisen bilden. J. Prakt. Chem. 1840, 21, 129−157.

(8) Rüdorff, W.; Hofmann, U. Über Graphitsalze. Z. Anorg. Allg. Chem. 1938, 238, 1−50.

(9) Beck, F.; Junge, H.; Krohn, H. Graphite intercalation compounds as positive electrodes in galvanic cells. Electrochim. Acta 1981, 26, 799−809.

(10) Beltrop, K.; Meister, P.; Klein, S.; Heckmann, A.; Grünebaum, M.; Wiemhöfer, H.-D.; Winter, M.; Placke, T. Does Size really Matter? New Insights into the Intercalation

Behavior of Anions into a Graphite-Based Positive Electrode for Dual-Ion Batteries. Electrochim.

Acta 2016, 209, 44−55.

(11) Mallouk, T.; Bartlett, N. Reversible intercalation of graphite by fluorine: a new bifluoride, C12HF2, and graphite fluorides, C_xF (5 > x> 2). J. Chem. Soc., Chem. Commun. 1983, 103.

(12) Carlin, R. T.; et al. Dual Intercalating Molten Electrolyte Batteries. J. Electrochem. Soc. 1994, 141, L73.

(13) Deunf, É.; Jiménez, P.; Guyomard, D.; Dolhem, F.; Poizot, P. A dual−ion battery using diamino−rubicene as anion−inserting positive electrode material. Electrochem. Commun. 2016, 72, 64−68.

(14) Seel, J. A.; Dahn, J. R. Electrochemical Intercalation of PF_6 into Graphite. J. Electrochem. Soc. 2000, 147, 892.

(15) Schoonman, J. A Solid-State Galvanic Cell with FluorideConducting Electrolytes. J. Electrochem. Soc. 1976, 123, 1772−1775.

(16) Gschwind, F.; Rodriguez-Garcia, G.; Sandbeck, D. J. S.; Gross, A.; Weil, M.; Fichtner, M.; Hörmann, N. Fluoride ion batteries: Theoretical performance, safety, toxicity, and a combinatorial screening of new electrodes. J. Fluorine Chem. 2016, 182, 76−90.

(17) Grenier, A.; Porras-Gutierrez, A.-G.; Groult, H.; Beyer, K. A.; Borkiewicz, O. J.; Chapman, K. W.; Dambournet, D. Electrochemical reactions in fluoride-ion batteries: mechanistic insights from pair distribution function analysis. J. Mater. Chem. A 2017, 5, 15700− 15705.

(18) Schoonman, J.; Oversluizen, G.; Wapenaar, K. Solid electrolyte properties of LaF_3. Solid State Ionics 1980, 1, 211−221.

(19) Roos, A.; Aalders, A.; Schoonman, J.; Arts, A.; de Wijn, H. Electrical conduction and ^{19}F NMR of solid solutions $La_{1-x}Ba_xF_{3-x}$. Solid State Ionics 1983, 9−10, 571−574.

(20) Breuer, S.; Gombotz, M.; Pregartner, V.; Hanzu, I.; Wilkening, M. Heterogeneous F anion transport, local dynamics and electrochemical stability of nanocrystalline $La_{1-x}BaF_3$. Energy Storage Mater. 2019, 16, 481−490.

(21) Reddy, M. A.; Fichtner, M. Batteries based on fluoride shuttle. J. Mater. Chem. 2011, 21, 17059.

(22) Rongeat, C.; Reddy, M. A.; Diemant, T.; Behm, R. J.; Fichtner, M. Development of new anode composite materials for fluoride ion batteries. J. Mater. Chem. A 2014, 2, 20861−20872.

(23) Thieu, D. T.; Fawey, M. H.; Bhatia, H.; Diemant, T.; Chakravadhanula, V. S. K.; Behm, R. J.; Kübel, C.; Fichtner, M. CuF_2 as Reversible Cathode for Fluoride Ion Batteries. Adv. Funct. Mater. 2017, 27, No. 1701051.

(24) Nowroozi, M. A.; Ivlev, S.; Rohrer, J.; Clemens, O. La_2CoO_4: a new intercalation based cathode material for fluoride ion batteries with improved cycling stability. J. Mater. Chem. A 2018, 6, 4658− 4669.

(25) Nowroozi, M.; Clemens, O. Insights on the Behavior of Conversion-Based Anode Materials for Fluoride Ion Batteries by Testing against an Intercalation-Based Reference Cathode. ACS Appl. Energy Mater. 2018, 1, 6626−6637.

(26) Zaheer, W.; Andrews, J. L.; Parija, A.; Hyler, F. P.; Jaye, C.; Weiland, C.; Yu, Y.-S.; Shapiro, D. A.; Fischer, D. A.; Guo, J.; Velázquez, J. M.; Banerjee, S. Reversible

Room-Temperature Fluoride-Ion Insertion in a Tunnel-Structured Transition Metal Oxide Host. ACS Energy Lett. 2020, 2520−2526.

(27) Christe, K. O.; Wilson, W. W.; Wilson, R. D.; Bau, R.; Feng, J. A. Syntheses, properties, and structures of anhydrous tetramethylammonium fluoride and its 1:1 adduct with trans-3-amino-2- butenenitrile. J. Am. Chem. Soc. 1990, 112, 7619−7625.

(28) Sharma, R. K.; Fry, J. L. Instability of anhydrous tetra-nalkylammonium fluorides. J. Org. Chem. 1983, 48, 2112−2114.

(29) Davis, V. K.; et al. Room-temperature cycling of metal fluoride electrodes: Liquid electrolytes for high-energy fluoride ion cells. Science 2018, 362, 1144−1148.

(30) Bashian, N. H.; Zhou, S.; Zuba, M.; Ganose, A. M.; Stiles, J. W.; Ee, A.; Ashby, D. S.; Scanlon, D. O.; Piper, L. F. J.; Dunn, B.; Melot, B. C. Correlated Polyhedral Rotations in the Absence of Polarons during Electrochemical Insertion of Lithium in ReO_3. ACS Energy Lett. 2018, 3, 2513−2519.

(31) Meisel, K. Rheniumtrioxyd. III. Mitteilung. Ü ber die Kristallstruktur des Rheniumtrioxyds. Z. Anorg. Allg. Chem. 1932, 207, 121−128.

(32) Ferretti, A.; Rogers, D. B.; Goodenough, J. B. The relation of the electrical conductivity in single crystals of rhenium trioxide to the conductivities of Sr_2MgReO_6 and Na_xWO_3. J. Phys. Chem. Solids 1965, 26, 2007−2011.

(33) Baltruschat, H. Differential electrochemical mass spectrometry. J. Am. Soc. Mass Spectrom. 2004, 15, 1693−1706.

(34) Tran, N.; Croguennec, L.; Menetrier, M.; Weill, F.; Biensan, P.; Jordy, C.; Delmas, C. Mechanisms Associated with the “Plateau” Observed at High Voltage for the

Overlithiated $Li_{1.12}(Ni_{0.425}Mn_{0.425}Co_{0.15})_{0.88}O_2$ System. Chem. Mater. 2008, 20, 4815−4825.

(35) Armstrong, A. R.; Holzapfel, M.; Novák, P.; Johnson, C. S.; Kang, S.-H.; Thackeray, M. M.; Bruce, P. G. Demonstrating Oxygen Loss and Associated Structural Reorganization in the Lithium Battery Cathode $Li[Ni_{0.2}Li_{0.2}Mn_{0.6}]O_2$. J. Am. Chem. Soc. 2006, 128, 8694− 8698.

(36) Weppner, W.; Huggins, R. A. Determination of the Kinetic Parameters of Mixed-Conducting Electrodes and Application to the System Li_3Sb. J. Electrochem. Soc. 1977, 124, 1569−1578.

(37) Van der Ven, A.; Deng, Z.; Banerjee, S.; Ong, S. P. Rechargeable Alkali-Ion Battery Materials: Theory and Computation. Chem. Rev. 2020, 120, 6977−7019.

(38) Zagorac, D.; Müller, H.; Ruehl, S.; Zagorac, J.; Rehme, S. Recent developments in the Inorganic Crystal Structure Database: theoretical crystal structure data and related features. J. Appl. Crystallogr. 2019, 52, 918.

(39) Supeł, J.; Marx, R.; Seppelt, K. Preparation and Structure of Rhenium Fluoride Trioxide ReO_3F, and the Polymorphism of Rhenium Trifluoride Dioxide, ReO_2F_3. Z. Anorg. Allg. Chem. 2005, 631, 2979−2986.

(40) Ruiz-Preciado, M. A.; Kubicki, D. J.; Hofstetter, A.; McGovern, L.; Futscher, M. H.; Ummadisingu, A.; Gershoni-Poranne, R.; Zakeeruddin, S. M.; Ehrler, B.; Emsley, L.; Milic, J. V.; Grätzel, M.́ Supramolecular Modulation of Hybrid Perovskite Solar Cells via Bifunctional Halogen Bonding Revealed by Two-Dimensional ^{19}F Solid-State NMR Spectroscopy. J. Am. Chem. Soc. 2020, 142, 1645− 1654.

(41) Cho, S. H.; Ghosh, S.; Berkson, Z. J.; Hachtel, J. A.; Shi, J.; Zhao, X.; Reimnitz, L. C.; Dahlman, C. J.; Ho, Y.; Yang, A.; Liu, Y.; Idrobo, J.-C.; Chmelka, B. F.; Milliron, D. J. Syntheses of Colloidal F:In_2O_3 Cubes: Fluorine-Induced Faceting and Infrared Plasmonic Response. Chem. Mater. 2019, 31, 2661−2676.

(42) Yesinowski, J. P.; Berkson, Z. J.; Cadars, S.; Purdy, A. P.; Chmelka, B. F. Spatially correlated distributions of local metallic properties in bulk and nanocrystalline GaN. Phys. Rev. B 2017, 95. DOI: 10.1103/PhysRevB.95.235201.

(43) Greaves, C.; Francesconi, M. G. Fluorine insertion in inorganic materials. Curr. Opin. Solid State Mater. Sci 1998, 3, 132−136.

(44) Greaves, C.; Kissick, J. L.; Francesconi, M. G.; Aikens, L. D.; Gillie, L. J. Synthetic strategies for new inorganic oxide fluorides and oxide sulfates. J. Mater. Chem. 1999, 9, 111−116.

(45) McCabe, E. E.; Greaves, C. Fluorine insertion reactions into pre-formed metal oxides. J. Fluorine Chem. 2007, 128, 448−458.

(46) Case, G. S.; Hector, A. L.; Levason, W.; Needs, R. L.; Thomas, M. F.; Weller, M. T. Syntheses, powder neutron diffraction structures and Mössbauer studies of some complex iron oxyfluorides: $Sr_3Fe_2O_6F_{0.87}$, Sr_2FeO_3F and $Ba_2InFeO_5F_{0.68}$. J. Mater. Chem. 1999, 9, 2821−2827.

(47) Li, R. K.; Greaves, C. Double-layered ruthenate $Sr_3Ru2O_7F_2$ formed by fluorine insertion into $Sr_3Ru_2O_7$. Phys. Rev. B 2000, 62, 3811−3815.

(48) Pellet, N.; Teuscher, J.; Maier, J.; Grätzel, M. Transforming Hybrid Organic Inorganic Perovskites by Rapid Halide Exchange. Chem. Mater. 2015, 27, 2181−2188.

(49) Elmelund, T.; Scheidt, R. A.; Seger, B.; Kamat, P. V. Bidirectional Halide Ion Exchange in Paired Lead Halide Perovskite Films with Thermal Activation. ACS Energy Lett. 2019, 4, 1961−1969.

(50) Walsh, A.; Stranks, S. D. Taking Control of Ion Transport in Halide Perovskite Solar Cells. ACS Energy Lett. 2018, 3, 1983−1990.

(51) Chong, Y. Y.; Fan, W. Y. Facile Synthesis of Single Crystalline Rhenium (VI) Trioxide Nanocubes with High Catalytic Efficiency for Photodegradation of Methyl Orange. J. Colloid Interface Sci. 2013, 397, 18−23.

(52) Neuefeind, J.; Feygenson, M.; Carruth, J.; Hoffmann, R.; Chipley, K. K. The Nanoscale Ordered Materials Diffractometer NOMAD at the Spallation Neutron Source SNS. Nucl. Instrum. Methods Phys. Res., Sect. B 2012, 287, 68−75.

(53) Borkiewicz, O. J.; Shyam, B.; Wiaderek, K. M.; Kurtz, C.; Chupas, P. J.; Chapman, K. W. The AMPIX electrochemical cell: a versatile apparatus for in situ X-ray scattering and spectroscopic measurements. J. Appl. Crystallogr. 2012, 45, 1261−1269.

(54) Toby, B. H.; Dreele, R. B. V. GSAS-II: the genesis of a modern open-source all purpose crystallography software package. J. Appl. Crystallogr. 2013, 46, 544−549.

(55) Rongeat, C.; Reddy, M. A.; Witter, R.; Fichtner, M. Solid Electrolytes for Fluoride Ion Batteries: Ionic Conductivity in Polycrystalline Tysonite-Type Fluorides. ACS Appl. Mater. Interfaces 2014, 6, 2103−2110.

(56) McCloskey, B. D.; Valery, A.; Luntz, A. C.; Gowda, S. R.; Wallraff, G. M.; Garcia, J. M.; Mori, T.; Krupp, L. E. Combining Accurate O_2 and Li_2O_2 Assays to Separate

Discharge and Charge Stability Limitations in Nonaqueous Li−O_2 Batteries. J. Phys. Chem. C 2013, 4, 2989−2993.

(57) McCloskey, B. D.; Scheffler, R.; Speidel, A.; Bethune, D. S.; Shelby, R. M.; Luntz, A. C. On the Efficacy of Electrocatalysis in Nonaqueous Li−O_2 Batteries. J. Am. Chem. Soc. 2011, 133, 18038− 18041.

(58) Yesinowski, J. P.; Ladouceur, H. D.; Purdy, A. P.; Miller, J. B. Electrical and ionic conductivity effects on magic-angle spinning nuclear magnetic resonance parameters of CuI. J. Chem. Phys. 2010, 133, No. 234509.

(59) Thurber, K. R.; Tycko, R. Measurement of sample temperatures under magic-angle spinning from the chemical shift and spin-lattice relaxation rate of ^{79}Br in KBr powder. J. Magn. Reson. 2009, 196, 84− 87.

(60) Thomas, J. C.; Van der Ven, A. Finite-temperature properties of strongly anharmonic and mechanically unstable crystal phases from first principles. Phys. Rev. B: Condens. Matter Mater. Phys. 2013, 88, No. 214111.

(61) Puchala, B.; Van der Ven, A. Thermodynamics of the Zr-O system from first-principles calculations. Phys. Rev. B: Condens. Matter Mater. Phys. 2013, 88, No. 094108.

(62) Van der Ven, A.; Thomas, J. C.; Puchala, B.; Natarajan, A. R. First-principles statistical mechanics of multicomponent crystals. Annu. Rev. Mater. Res. 2018, 48, 27−55.

(63) Kresse, G.; Hafner, J. Ab initio molecular dynamics for liquid metals. Phys. Rev. B: Condens. Matter Mater. Phys. 1993, 47, 558.

(64) Kresse, G.; Hafner, J. Ab initio molecular-dynamics simulation of the liquid-metal-amorphous-semiconductor transition in germanium. Phys. Rev. B: Condens. Matter Mater. Phys. 1994, 49, 14251.

(65) Kresse, G.; Furthmüller, J. Efficiency of ab-initio total energy calculations for metals and semiconductors using a plane-wave basis set. Comput. Mater. Sci. 1996, 6, 15−50.

(66) Kresse, G.; Furthmüller, J. Efficient iterative schemes for ab initio total-energy calculations using a plane-wave basis set. Phys. Rev. B: Condens. Matter Mater. Phys. 1996, 54, 11169.

(67) Monkhorst, H. J.; Pack, J. D. Special points for Brillouin-zone integrations. Phys. Rev. B 1976, 13, 5188−5192.

(68) Vanderbilt, D. Soft self-consistent pseudopotentials in a generalized eigenvalue formalism. Phys. Rev. B 1990, 41, 7892−7895.

(69) Pickard, C. J.; Mauri, F. All-electron magnetic response with pseudopotentials: NMR chemical shifts. Phys. Rev. B 2001, 63, No. 245101.

(70) Griffin, J. M.; Yates, J. R.; Berry, A. J.; Wimperis, S.; Ashbrook, S. E. High-Resolution ^{19}F MAS NMR Spectroscopy: Structural Disorder and UnusualJCouplings in a Fluorinated Hydroxy-Silicate. J. Am. Chem. Soc. 2010, 132, 15651−15660.

(71) Schwarz, K.; Blaha, P. Solid state calculations using WIEN2k. Comput. Mater. Sci. 2003, 28, 259−273.

(72) Blaha, P.; Schwarz, K.; Tran, F.; Laskowski, R.; Madsen, G. K. H.; Marks, L. D. WIEN2k: An APW + lo program for calculating the properties of solids. J. Chem. Phys. 2020, 152, No. 074101.

(73) McCulloch, D.; Lau, D.; Nicholls, R.; Perkins, J. The near edge structure of cubic boron nitride. Micron 2012, 43, 43−48.

(74) Hébert, C.; Luitz, J.; Schattschneider, P. Improvement of energy loss near edge structure calculation using Wien2k. Micron 2003, 34, 219−225.

(75) Luitz, J.; Maier, M.; Hébert, C.; Schattschneider, P.; Blaha, P.; Schwarz, K.; Jouffrey, B. Partial core hole screening in the Cu L3 edge. Eur. Phys. J. B 2001, 21, 363−367.

9.7 Supporting Information

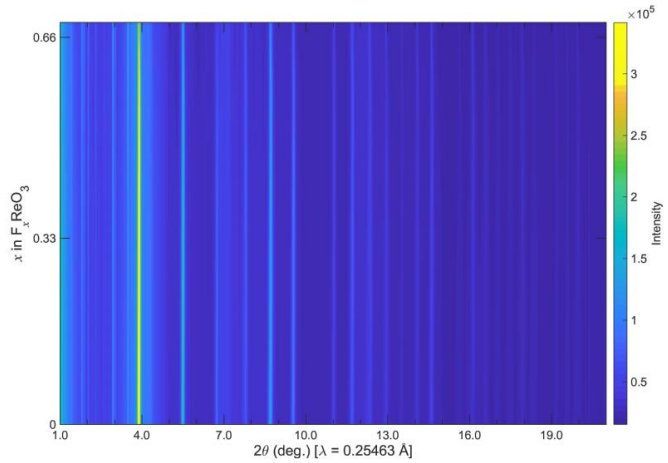

Figure S9.1. A heatmap of the operando synchrotron X-ray diffraction collected during the oxidative fluorination of ReO_3 displays diffracted intensity as a function of color. No new peaks are seen to form throughout the electrochemical charging process and reflections associated with cubic ReO_3 are maintained. We note a reduction in peak intensity beginning at higher states of charge.

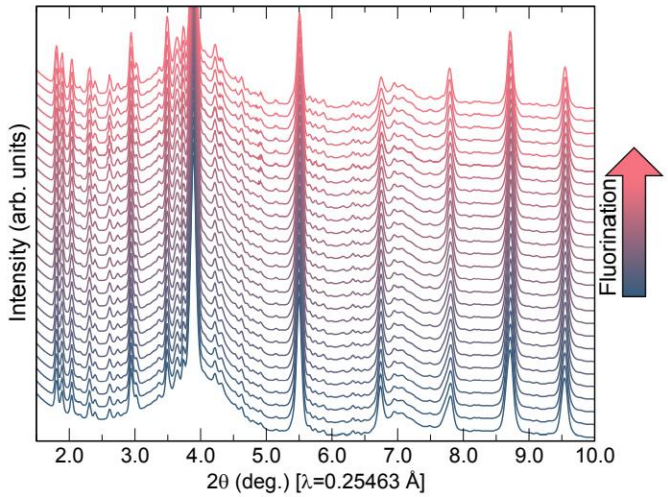

Figure S9.2. Operando synchrotron X-ray diffraction shows no new peak formation throughout the charging process of F_xReO_3, however we note the formation of a series of low angle peaks due to electrolyte decomposition. The spacing between each pattern is approximately 0.025 equivalent units of fluoride.

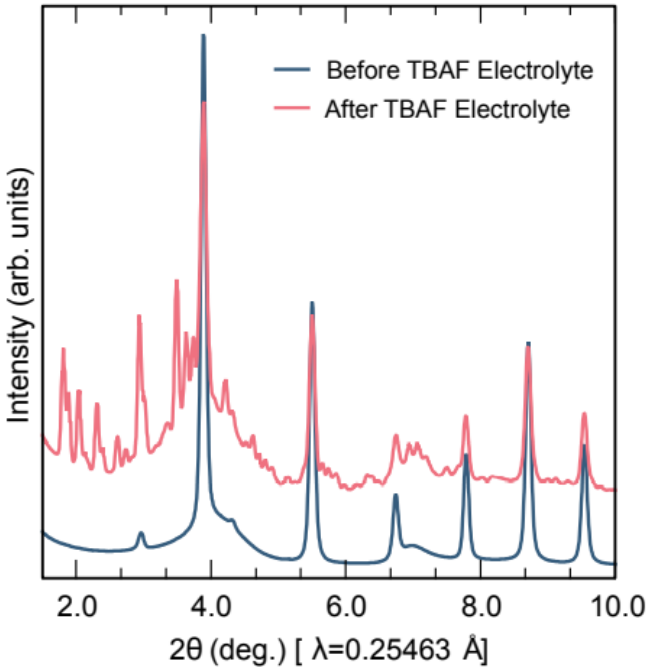

Figure S9.3. Upon the application of TBAF to ReO_3 electrodes, a series of additional XRD peaks are seen to form, associated with the decomposition of TBAF electrolyte. The XRD pattern shown in blue was collected on a ReO_3 electrode which was placed in a fully assembled AMPIX cell without any electrolyte. Once the electrolyte was added, a pattern (pink) was again collected prior to electrochemical measurement which showed the formation of a series of low-angle diffraction peaks.

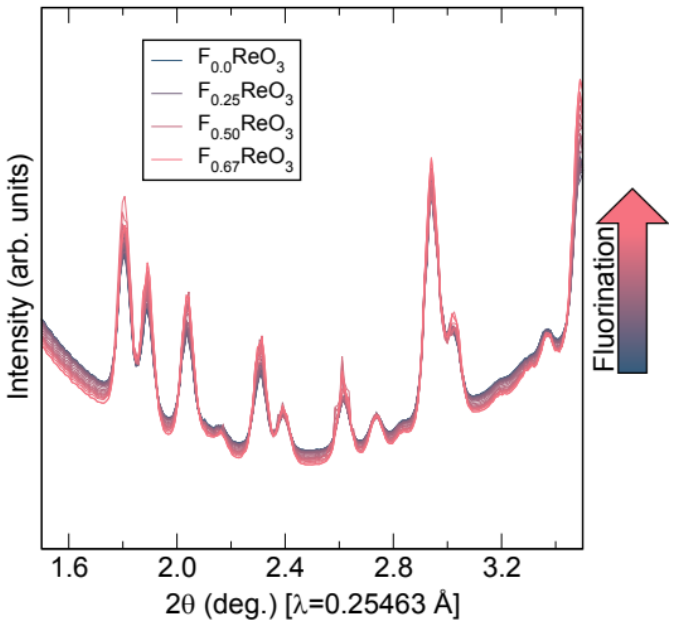

Figure S9.4. A series of low angle peaks form due to electrolyte decomposition in the operando X-ray diffraction experiments. None of the peaks observed at low angles are associated with cubic ReO_3. These peaks persist throughout the electrochemical charging process but do not vary in intensity or location. The spacing between each pattern is approximately 0.025 equivalent units of fluoride.

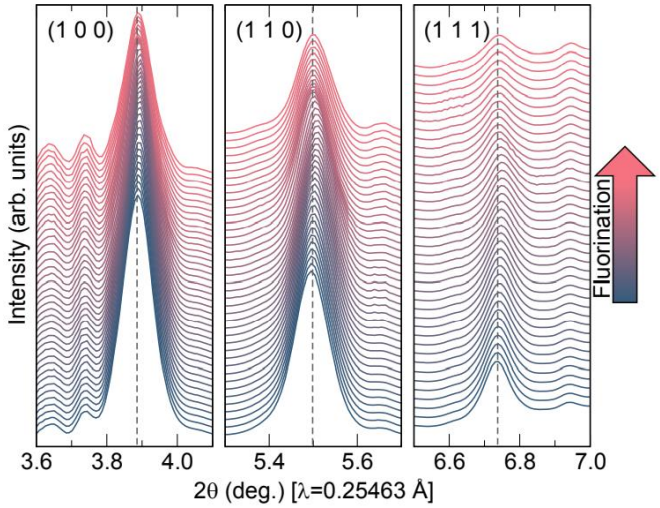

Figure S9.5. Throughout the initial oxidative fluorination process, diffraction peaks associated with ReO_3 steadily shift to higher angles, indicating a contraction of the unit cell. At high states of charge this abruptly reverses and the peaks of ReO_3 are seen to shift to lower angles, suggesting a decomposition of the material back to the original phase.

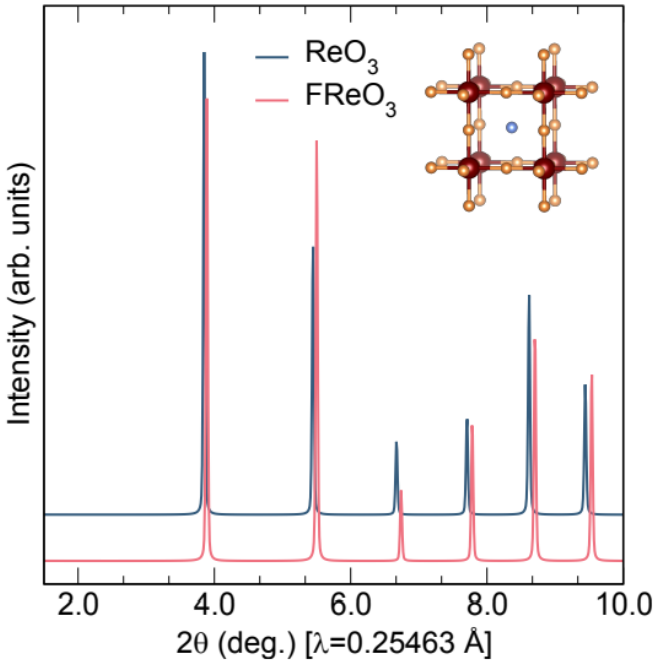

Figure S9.6. Comparison of simulated X-ray diffraction patterns of ReO_3 and $FReO_3$ in which F sits in the central A-site vacancy (see inset). The insertion of fluoride on the A-site does not produce any additional diffraction peaks, merely a slight contraction of the unit cell.

Impedance Spectroscopy

The slope of the real part of impedance vs ω, plotted in S.I. Figure S9.7(b), gives the Warburg factor (σ) that is inversely related to the diffusion coefficient (D), by the following equation where R is the gas constant, T is the absolute temperature, A is the surface area of the electrode, F is the Faraday constant, and C is the molar concentration of F− ions in the active material.

$$D = \frac{R^2T^2}{2A^2n^2F^4C^2\sigma^2} \tag{9.1}$$

The calculated value of D at x = 0.2 is 1.75 × 10–^{16} cm^{2}s^{-1} which is in close agreement with the reported values of 3 × 10^{-15} cm^{2}s^{-1} for fluoride ion diffusion in oxyfluoride materials. 1 The D values drop to 2.5 × 10^{-18} cm^{2}s^{-1} and 5.7 × 10^{-19} cm^{2}s^{-1} at x = 0.4 and x = 0.5 respectively, as shown in S.I. Table T9.1, indicative of change in the mechanism for the oxidative process around this point, and is consistent between the liquid and solid-state cells.

Table T9.1. Calculated fluoride diffusion coefficients for various states of charge of F_xReO_3.

x in F_xReO_3	Diffusion Coefficient (D) cm^2 s^{-1}
0.2	1.75×10^{-16}
0.4	2.5×10^{-18}
0.5	5.7×10^{-19}

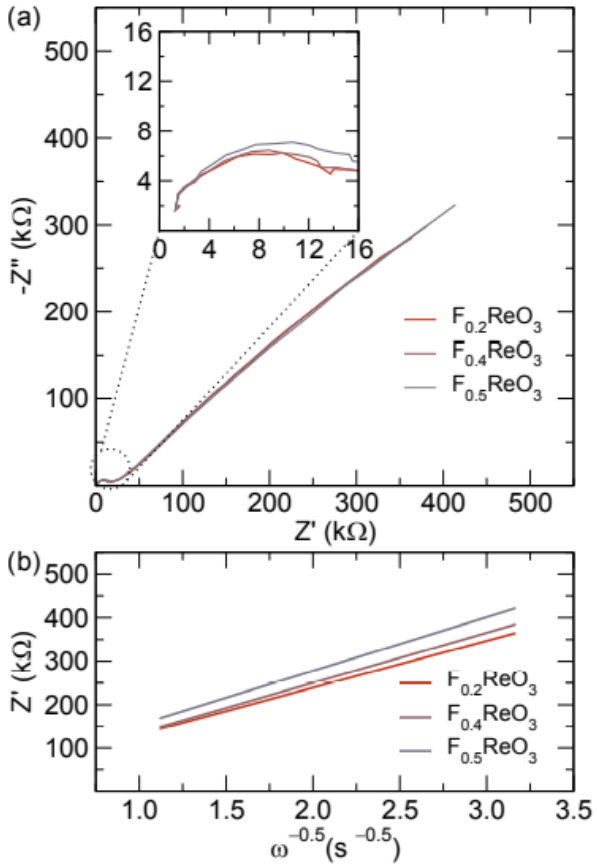

Figure S9.7. (a): Electrochemical impedance spectroscopy on all solid state cells demonstrate variations in the charge transfer resistance at different states of charge. As seen in the inset, the resistance rises slightly during fluorination. (b): Diffusion coefficients at different state of charge were calculated from the slope of a plot of $\omega^{-0.5}$ vs Z'.

Differential Electrochemical Mass Spectrometry

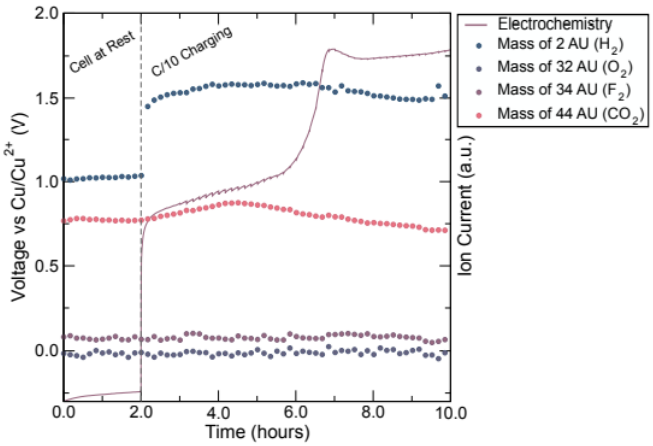

Figure S9.8. Differential electrochemical mass spectrometry identified H_2 evolution in fluoride ion battery half cells as well as the minor formation of CO_2 during the initial charge curve, due to electrolyte decomposition.

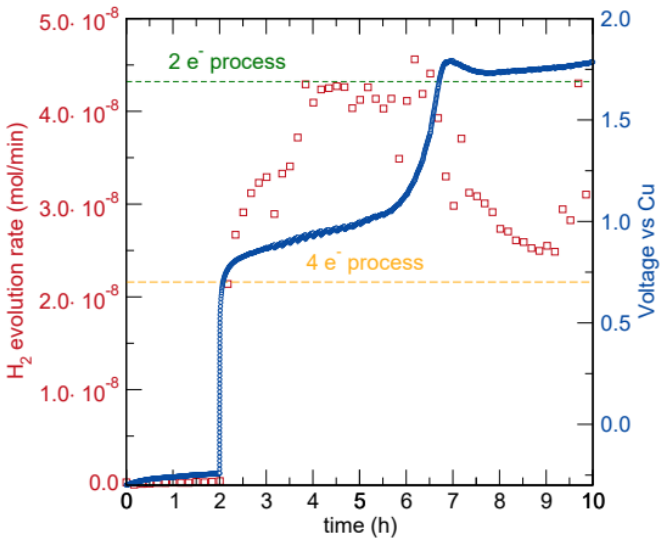

Figure S9.9. Quantitative differential electrochemical mass spectrometry showing the molar concentration of H_2 evolved during cycling. The four electron process at the higher voltage plateau of reflective of parasitic attack of the electrolyte at high voltages.

Solid State ^{19}F NMR

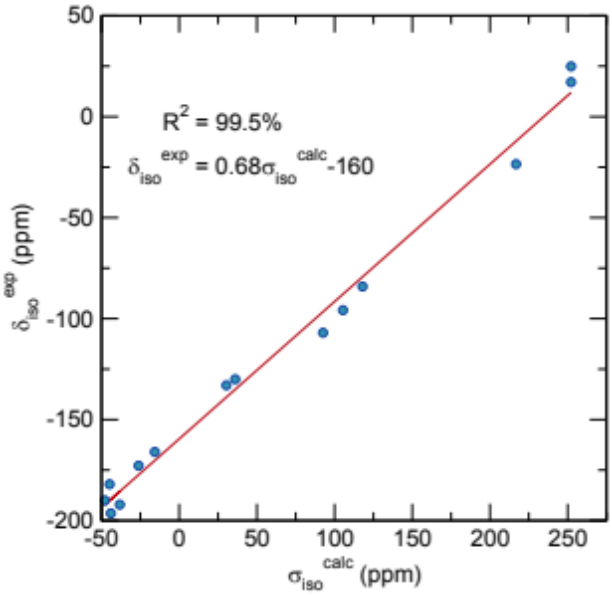

Figure S9.10. A plot of isotropic shieldings, δ_{iso}^{calc} vs δ_{iso}^{exp} for several fluorine-containing compounds was fit and the expression was used to scale calculated ^{19}F chemical shifts for comparison with experimental data.

Table T9.2: Calculated ^{19}F isotropic shieldings, δ_{iso}^{calc}, scaled calculated isotropic chemical shifts, $\delta_{iso}^{calc,\ scaled}$, and experimental ^{19}F chemical shifts, δ_{iso}^{exp}, for several fluorine-containing compounds. Experimental values taken from Griffen et al. and the references therein.

Compounds	site	δ_{iso}^{exp} (ppm)	σ_{iso}^{calc} (ppm)	$\delta_{iso}^{calc,scaled}$ (ppm)
AlF_3	a	-172.8	-26.1	-177.3
CaF_2	a	-107	92.6	-96.6
CdF_2	a	-192.1	-38.2	-185.6
HgF_2	a	-196.4	-44.0	-189.4
Hg_2F_2	a	-95.8	105.4	-87.9
$KF\text{-}2H_2O$	a	-133	30.4	-138.9
LaF_3	a	-23.5	216.8	-12.1
	b	24.9	252.2	11.9
	c	17.1	252.2	11.9
$Na_5Al_3F_{14}$	a	-190	-48.0	-192.2
	b	-166	-15.7	-170.2
	c	-182	-44.8	-190.0
SrF_2	a	-84.1	118.0	-79.3
KF	a	-130	36.0	-135.0
LiF	a	-204	-4.8	-162.8
NaF	a	-221	-83.4	-216.2
PbF_2	a	-20.5	190.9	-29.7
	b	-57.7	190.9	-29.7

Table T9.3: Spin-lattice relaxation times associated with the different resolved ^{19}F signals of $F_{0.2}ReO_3$, measured at 18.8 T, 23 kHz MAS, and 298 K from solid-state ^{19}F Hahn-echo saturation recovery MAS NMR spectra.

Chemical Shift (ppm)	Relaxation Time (sec)
-124	4.0
-135	4.0
-137	0.3
-142	0.3
-158	0.4
-190	0.4

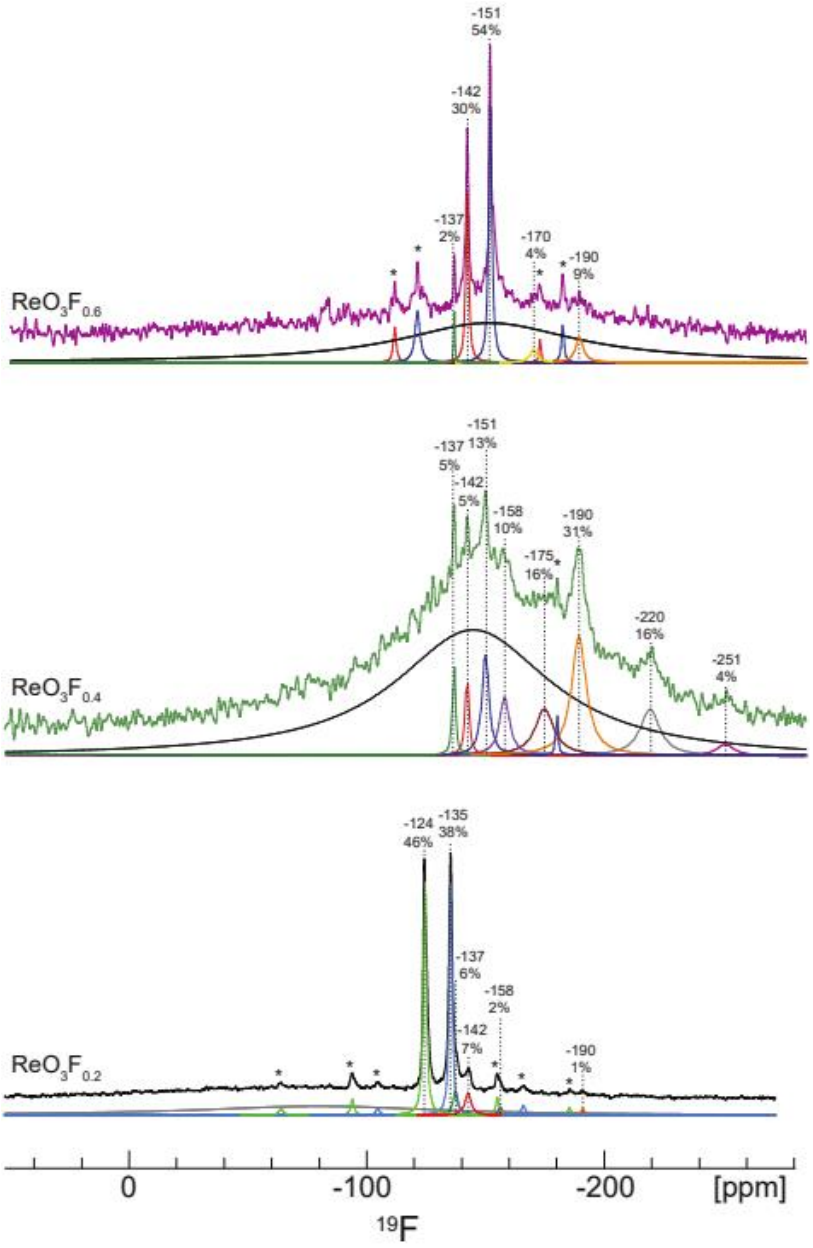

Figure S9.11. Solid-state 1D ^{19}F echo MAS NMR spectra acquired at 18.8 T, 298 K, 23 kHz MAS, with a recycle delay of 23 sec and 7000 scans for F_xReO_3 diluted 1:5 by mass with KBr. Partially resolved signals are observed at isotropic ^{19}F chemical shifts which change in intensity and position as the F-content of the materials increases, indicating the changes in local environments that occur with increased loading. All of the materials have isotropic ^{19}F chemical shifts of -137, -142, -151, and -190 ppm. Only the $F_{0.2}ReO_3$ material has additional

^{19}F shifts at -124 and -135 ppm, which are slow relaxing, corroborating that the $F_{0.2}ReO_3$ material remains in a relatively a well-ordered perovskite environment (see Figure S9.12). The $F_{0.4}ReO_3$ material has additional more negative (upfield) chemical shifts of -158, -220, and -251 ppm that may be associated with the state of maximum fluorination prior to decomposition. Finally, only the $F_{0.6}ReO_3$ material has an additional chemical shift of -170 ppm. (*) indicate a spinning sideband.

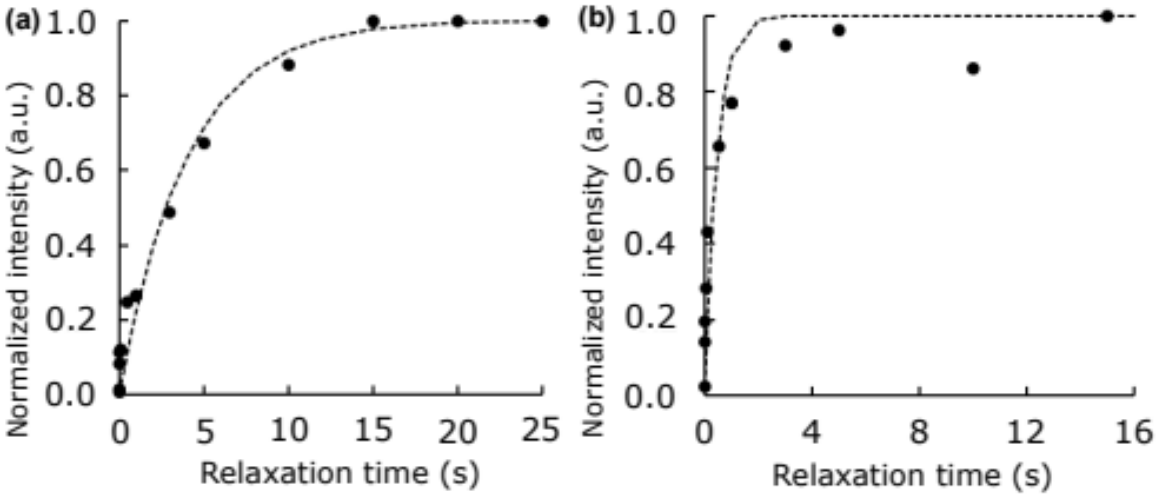

Figure S9.12. Solid-state ^{19}F Hahn-echo MAS NMR saturation-recovery data for $F_{0.2}ReO_3$. Normalized integrated ^{19}F signal intensity is plotted as functions of the τ delay time for signals with isotropic chemical shifts of (a) -135 and -124 ppm, corresponding to a spin-lattice relaxation time T_1 of 4.0 s, and (b) -151 ppm, corresponding to a T_1 value of 0.3 s; the latter is representative of the other signals at -137, -142, -158, and -190. The solid-state ^{19}F Hahn-echo NMR spectra were acquired for $F_{0.2}ReO_3$ diluted 1:5 by mass with KBr, and acquired at 18.8 T, 23 kHz, and 298 K.

X-ray Emission and X-ray Absorption Spectroscopy

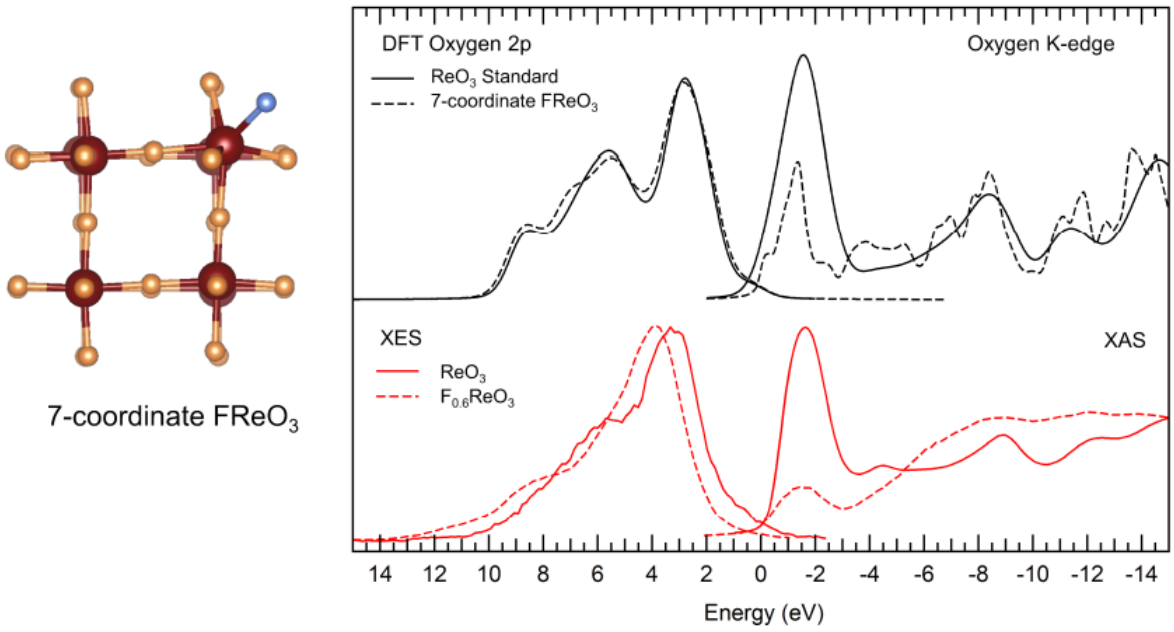

Figure S9.13. Experimental data (red) compared to simulated X-ray emission and absorption patterns for 7-coordinate $FReO_3$ formed when Re migrates towards the face of an ReO_6 octahedra to form seven coordinate ReO_6F unit.

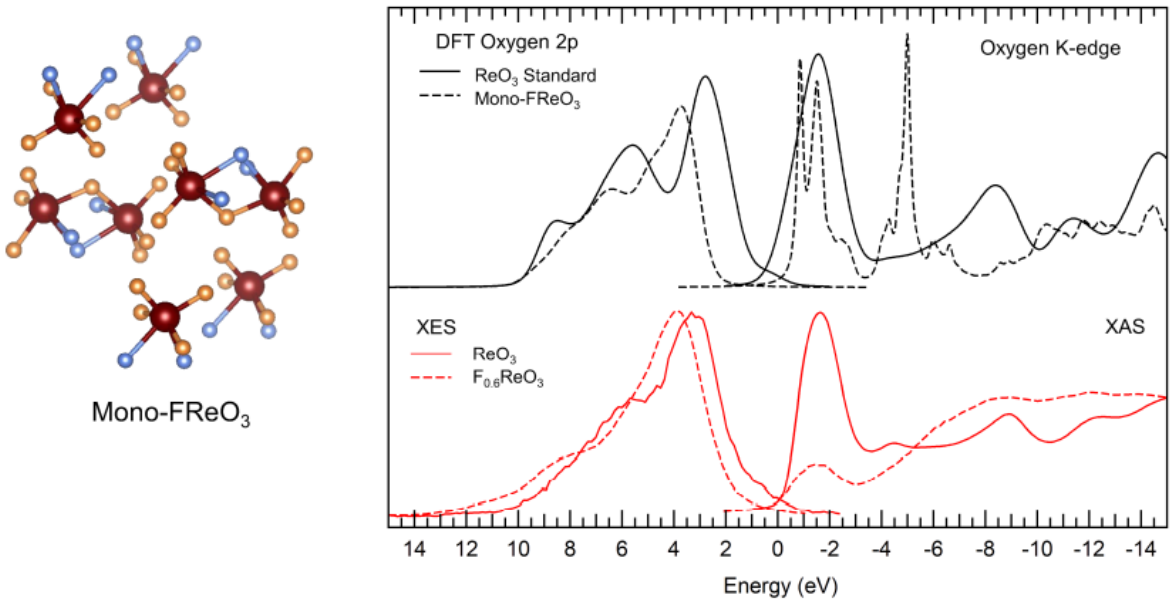

Figure S9.14. Experimental data (red) compared to simulated X-ray emission and absorption patterns for mono-ReO_3F, the structure identified by edge sharing octahedral units.

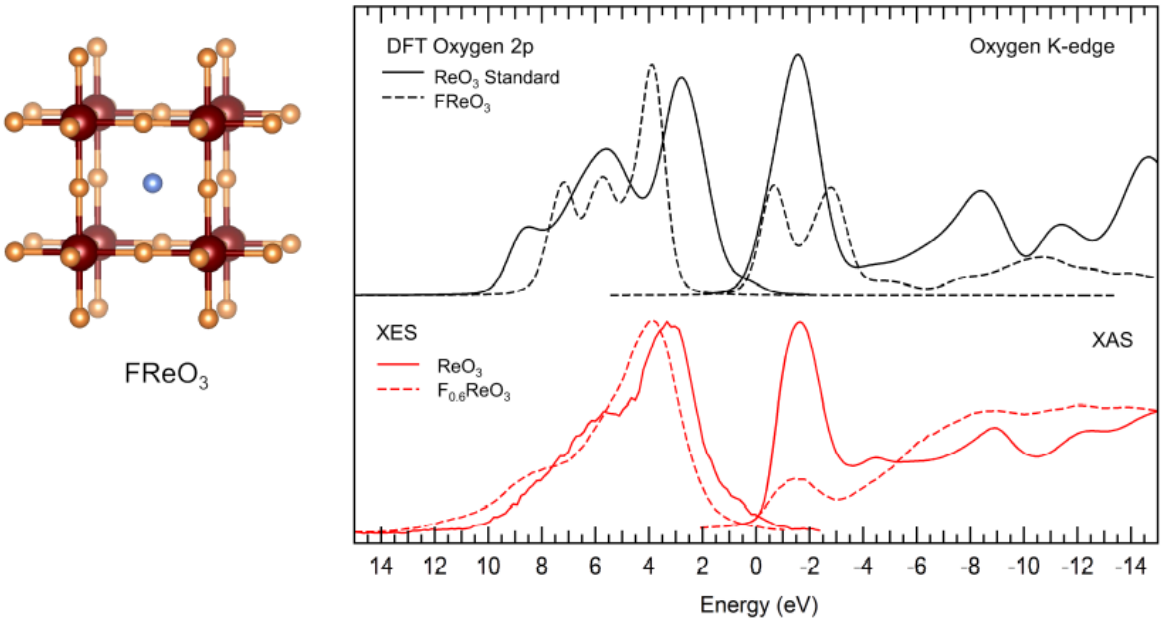

Figure S9.15. Experimental data (red) compared to simulated X-ray emission and absorption patterns for $FReO_3$ in which F occupies the perovskite A site and O moves to the X site.

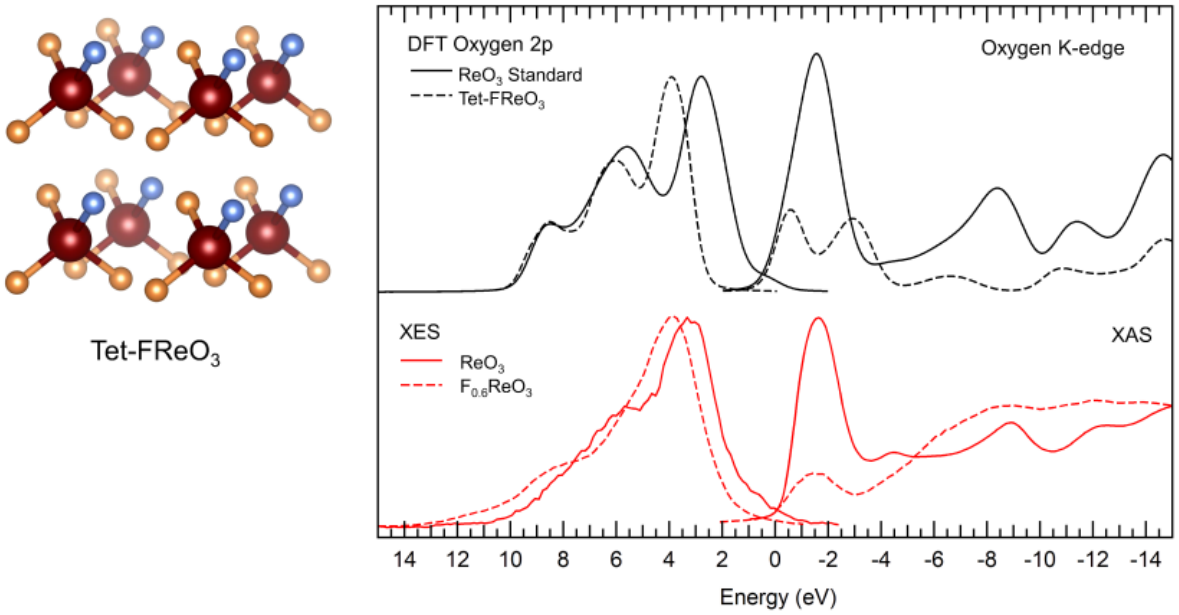

Figure S9.16. Experimental data (red) compared to simulated X-ray emission and absorption patterns for tet-ReO_3 model in which all Re atoms migrate to a tetrahedral configuration.

Hard X-ray Photoelectron Spectroscopy

HAXPES measurements were used to track the Re oxidation state in samples of F_xReO_3 at various states of charge.

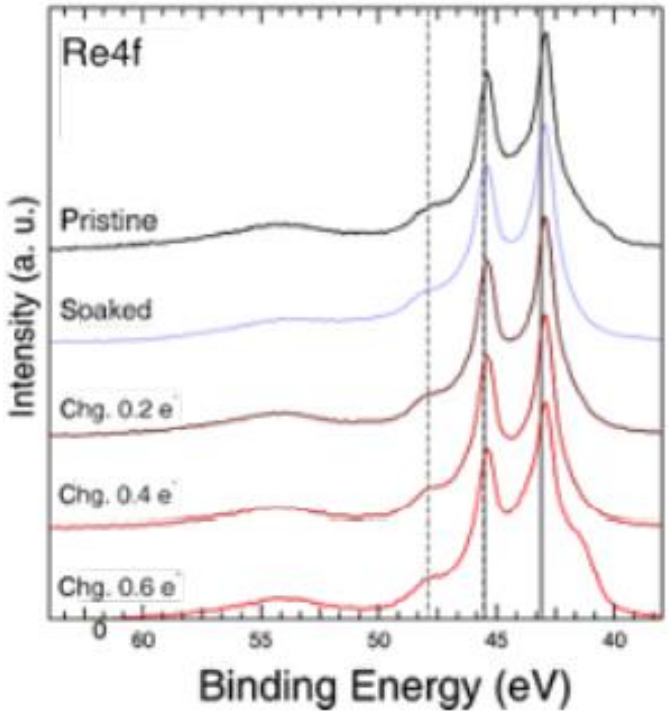

Figure S9.17. The Re 4f photoemission was used in order to track changes in the Re oxidation state during fluorination. A doublet at 43 and 46 eV is indicative of Re^{6+}, while a doublet at 46 and 48 eV is characteristic of Re^{7+}. Charging is seen to result in the growth of the peak at 48 eV, indicating partial oxidation of Re in F_xReO_3.

Neutron Pair Distribution Function Analysis

Several different structural motifs were explored to account for the changes observed in the neutron pair distribution function (NPDF) upon fluoride insertion. As can be seen in Figure S9.18, the data for pristine ReO_3 is in excellent agreement with the structural model. The pattern for $F_{0.}6ReO_3$ is significantly more complicated, and attempts to fit the data have been unsuccessful. Instead, we have calculated the patterns for different structural models and compared them to the raw data. In this example, the atom–atom pair interactions were calculated from a hypothetical cell generated by making a 2 × 2 × 2 supercell of ReO_3, inserting fluoride to half of the perovskite A-sites (approx. $F_{0.6}$), and translating half of the rhenium atoms from octahedral sites toward the inserted fluorides, thus generating tetrahedral ReO3F coordination sites. As can be seen, this correctly models the most significant features of the NPDF—such as the splitting of the first Re–X coordination sphere (1.87 Å to 1.73 and 1.90 Å)—but does not adequately capture the splitting observed in the X–X nearest neighbor distances around 2.47 and 2.68 Å. Figures S9.19–S9.22 show several different structural motifs explored to try to explain the structural changes that occurred upon fluoride insertion. Several can be assigned to the features observed in the data, but none can completely account for the complete pattern.

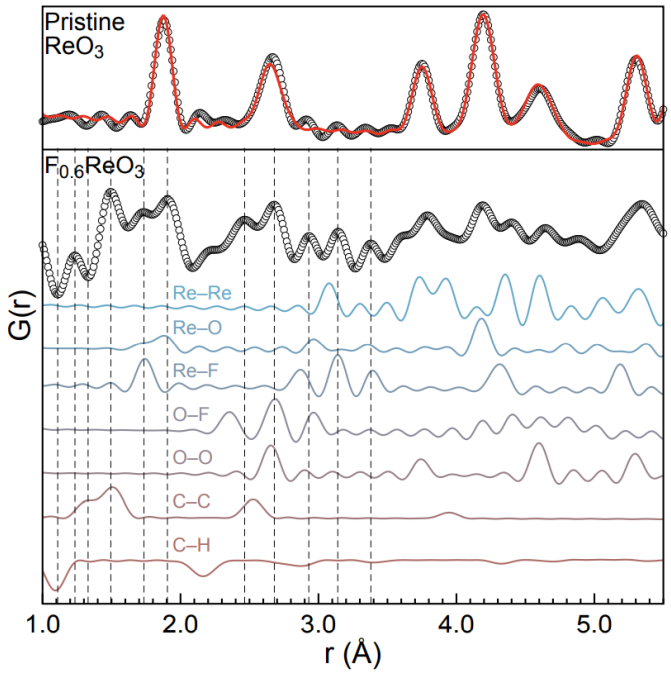

Figure S9.18. Fit of NPDF data for pristine ReO_3 and comparisons of different calculated atom–atom pair interactions with $F_{0.6}ReO_3$. Note that the peaks below 1.7 Å are believed to be associated with adsorbed electrolyte on the surface or organic compounds produced from parasitic electrolyte decomposition.

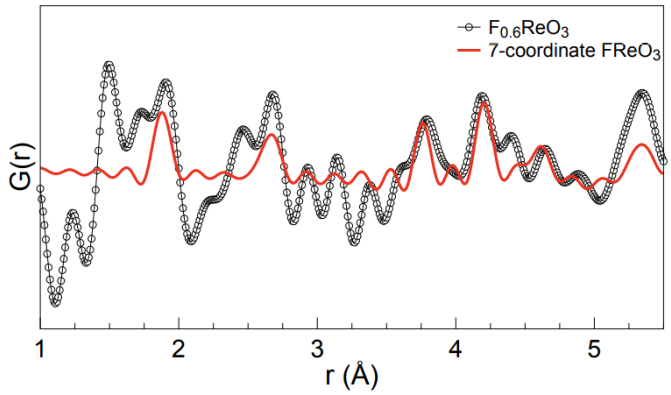

Figure S9.19. Comparison of observed data (black dots) for $F_{0.6}ReO_3$ versus the seven coordinate model.

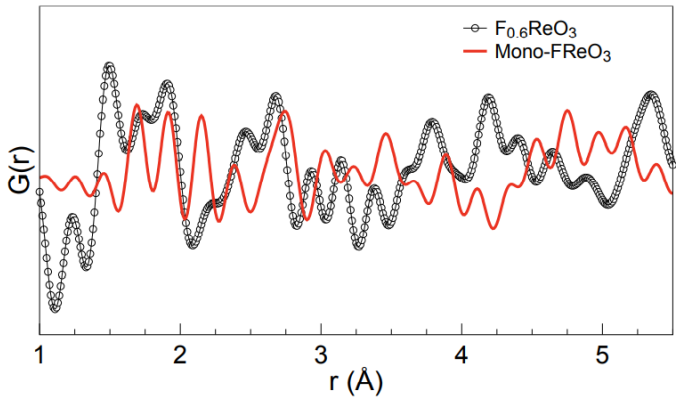

Figure S9.20. Comparison of observed data (black dots) for $F_{0.6}ReO_3$ versus the Mono-ReO_3F model.

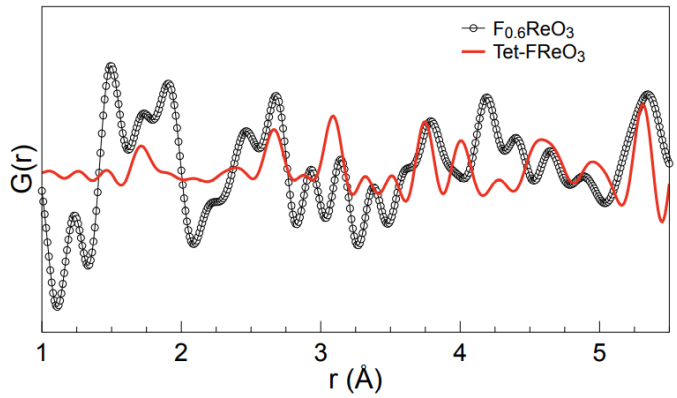

Figure S9.21. Comparison of observed data (black dots) for $F_{0.6}ReO_3$ versus the tetrahedral only ReO_3F model.

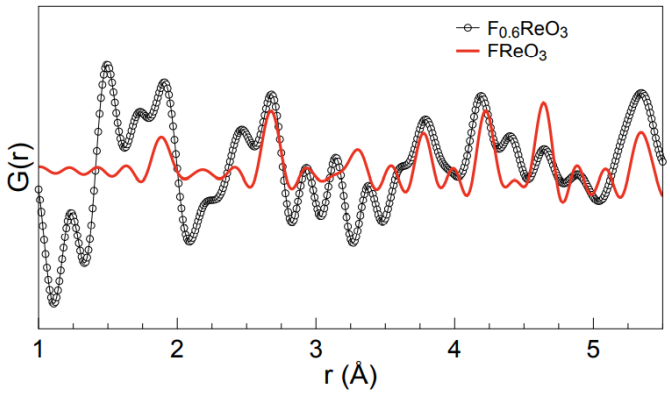

Figure S9.22. Comparison of observed data (black dots) for $F_{0.6}ReO_3$ versus the $FReO_3$ model (fluoride at the perovskite A-site).

Supporting Information References

(1) Katayama, T.; Chikamatsu, A.; Hirose, Y.; Takagi, R.; Kamisaka, H.; Fukumura, T.; Hasegawa, T. Topotactic fluorination of strontium iron oxide thin films using polyvinylidene fluoride. *J. Mater. Chem.* C **2014**, 2, 5350– 5356.

(2) Griffin, J. M.; Yates, J. R.; Berry, A. J.; Wimperis, S.; Ashbrook, S. E. High-Resolution 19F MAS NMR Spectroscopy: Structural Disorder and Unusual J Couplings in a Fluorinated Hydroxy-Silicate. *J. Am. Chem. Soc.* **2010**, 132, 15651–15660.

10. Conclusions

The overarching objective of these studies has been to improve understanding and viability of alternative energy conversion and storage materials. While this is a vast field, a few specific systems have been discussed in this dissertation, which are united by a few common themes. The first theme, being that the all the different types of materials discussed are comprised of extended networks with non-stoichiometric compositions. This leads to the second theme, in that the various material systems consist of complicated heterogenous distributions of ordered and disordered structural features which we sought to understand in an effort to improve the viability of such materials for large scale energy conversion and storage applications. And the third theme being that in all of the systems studied, atomic-level structures are important to electron transport and electrochemical activity. These themes are studied and discussed for each of the types of material systems in this dissertation, which include: (1) boron clusters for solid-state redox, (2) conductive polymers in semi-transparent organic solar cells, (3) perovskites undergoing fluoride ion intercalation, and (4) the main system discussed throughout the dissertation which is mesoporous n-carbons: oxygen & sulfur reduction. Because this work is so diverse, I have made conclusions and suggestions for future directions that I think will have a meaningful impact to the field, in each specific chapter. While my work has made a lot of progress correlating characterizations and understandings of complicated heterogenous ordered and disordered materials with electrochemical

performance properties, I feel that I have opened the door for a lot more questions to be answered in new and interesting ways. Specially, allowing for more strategic synthesis and optimization strategies than have been typically employed in the past. Thus, there are a lot of direction that this work can be taken in.

Appendix A. Understanding the eutectic melt and pyrolysis steps of the N-carbon synthesis, and the important role of the Zn^{2+} ion on the N moiety formation

A.1 Understanding eutectic melt chemistry with in situ and ex situ NMR techniques

The electrochemical performance of the mesoporous Fe,N-containing carbon material has been optimized by pyrolysis temperature, non-precious-metal types and concentration, and templating material. All of these steps follow the initial reaction occurring in the eutectic melt step which has not been thoroughly investigated. To understand the qualities of the synthesized materials which enable favorable electrochemical properties, I am interested in the atomic level reactions taking place during the low temperature eutectic melt step. Interestingly, I have found that while both of the reagents are stable solids at room temperature, given sufficient time the cyclohexanehexone-urea reagents will react, indicating the reactions taking place must be kinetically driven. Urea thermolysis, or the decomposition of urea at 363 K is known to produce an isocyanate intermediate,[1] which is highly reactive with ketones, amines, alcohols, and other urea.[2–4] Additionally, zinc chloride (part of the salt-template) has been found to catalyze the decomposition of urea into isocyanate.[4] I hypothesize that during the eutectic melt step, urea decomposes into a variety of products including isocyanate, which then reacts with the cyclohexanehexone to form a multitude of H,C,N-

containing intermediates. Therefore, my approach has been to investigate how melt temperature and catalyst inclusion affect the extent of urea decomposition during the eutectic melt step, the intermediate product compositions, final heteroatom environments formed, and electrochemical performance.

The goal is to identify the reactions occurring and intermediate products being formed during the eutectic melt step of the synthesis, which I intend to correlate with improved electrochemical performance. In the Chmelka lab, we have the unique capability of both performing synthesis and characterization by advanced solid-state NMR techniques. To investigate the reactions and correlation to performance of the eutectic melt, I proposed to combine synthesis, NMR characterization, and electrochemical testing techniques. To study the effects of urea decomposition on electrochemical activity, I propose to vary the eutectic melt time/temperature and zinc chloride inclusion during synthesis and measure the resulting electrochemical activity. To probe the reactions occurring during the eutectic melt, I propose and have some results from *in-situ* NMR characterization. With this technique, reactants are inserted into the NMR rotor, then into the magnet being held at reaction temperature, emulating reaction conditions while spectra are acquired. Single pulse ^{15}N, ^{13}C, and ^{1}H NMR spectra can then be acquired as a function of reaction time. Changes in both the chemical shift and intensities of the signals provide useful information about the reaction processes, kinetics, and eventual products. Additionally, to probe through bond and through space interactions between nuclei once the synthesis is complete, 2D NMR including $^{1}H\{^{13}C\}$ and $^{1}H\{^{15}N\}$ spectra will help to identify the extent of reactant interaction. If this type of experiment is repeated at multiple temperatures, it may even be possible to extract thermodynamic information.

Initial experiments have shown that both the ^{1}H and ^{15}N single-pulse spectra chemical shifts and signal intensities change as a function of reaction time at 80˚C, as can be seen in **Figure A.1**. Initial time and 250 min ^{1}H and ^{15}N MAS NMR spectra were acquired at 80˚C to the technique, attempting to emulate slow eutectic melt conditions and demonstrate the ability of in-situ NMR characterization techniques to detect changes in chemical bonding environments as a function of reaction time. These initial experiments were used to successfully prove the concept, but the experiments will be repeated for the ^{15}N, ^{13}C, and ^{1}H species at the synthesis eutectic melt temperature of 363 K where I expect to see more aggressive urea decomposition. Preliminary signal assignments have been made based on literature. In order to confidently assign signals, I suggest 2D $^{1}H\{^{13}C\}$ and $^{1}H\{^{15}N\}$ NMR experiments be conducted on each reactant and post-in-situ heated material. To compare initial spectra of the eutectic melt with pure reactant species, I suggest acquiring ^{15}N, ^{13}C, and ^{1}H single pulse NMR spectra of each reactant. Single-pulse experiments are quantitative, so suggest analyzing the data by compiling the integrated intensities as a function of reaction time (concentration as a function of time). With all of this information I expect that we will be able to elucidate the types of reactions that are occurring during the eutectic melt step, and possibly kinetic information valuable to the optimization of the initial synthesis step, which has been ignored until now.

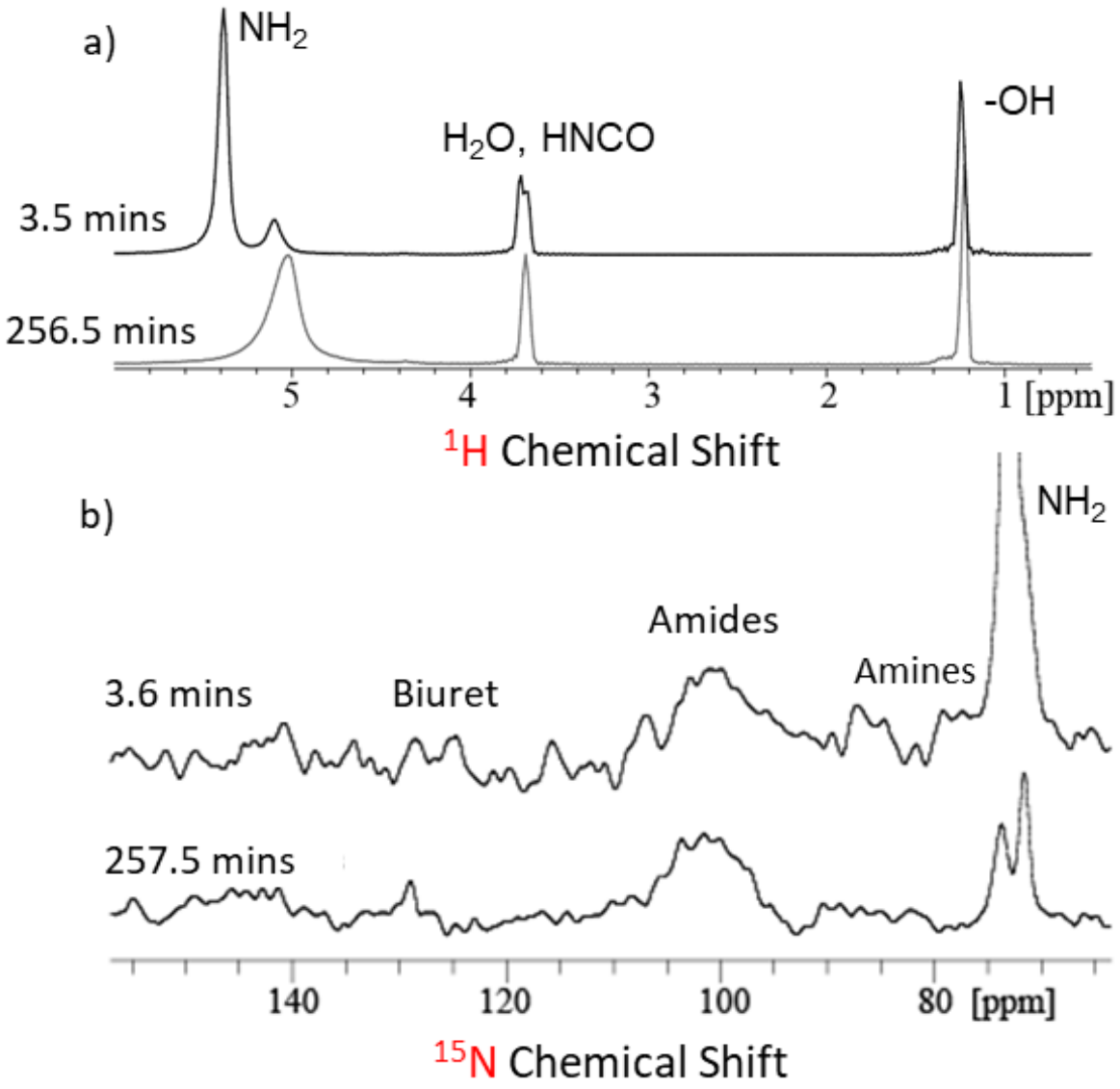

Figure A.1. In-situ eutectic melt NMR characterization. Single-pulse (a) ^{1}H and (b) ^{15}N NMR spectra of cyclohexanehexone and ^{15}N,^{13}C-enriched urea combined in an NMR rotor and inserted into the magnet being held at 80˚C were taken as a function of reaction time, or time from insertion into magnet. The spectra were acquired on the 11.7 T magnet at 10 kHz MAS.

A.2 Roles of divalent cations on eutectic syntheses and electrocatalytic reduction activity of mesoporous Fe,N-carbon materials

While previous chapters have established the superior performance of the salt-templated materials over their silica-templated counterparts due to their ability to encourage the formation of specific heteroatom environments. It would be very interesting and impactful to the field to understand the interactions that occur between the template and material during synthesis, which enable formation of desirable surface species. Some previous work done by my predecessor lead us to the tentative conclusions that (1) the formation of desirable N-moieties in Fe,N-carbon materials can be adjusted by varying ratio of divalent (e.g., Zn^{2+}) and monovalent (e.g., Na^{+}) ions of the mesopore salt-template, and (2) that the low temperature eutectic of salt-template correlates with formation of desirable Fe,N- and N-moieties resulting in increased reduction activities. I propose synthesizing N-carbon materials with varied eutectic and pyrolysis temperatures and times, measuring their reduction performance, and correlating that with the relative fractions of N-moieties formed as determined by quantitative solid-state ^{15}N NMR (Chapter 3 Figure 3.2c,d). This would allow for direct comparison of the N-moieties and distributions to the low temperature eutectic melt and pyrolysis time and temperature synthesis conditions.

Along the same lines, compared to silica-templating, salt-templating of the N-carbons is shown to increase both the oxygen- and sulfur-reduction performances by increasing the fraction of isolated pyridinic N moieties formed. We hypothesize that the differences in N environment distributions are caused by the differences in carbon-template interactions that occur during the high temperature pyrolysis step of the reaction, as the silica template is only

expected to have weak non-ionic interactions with the graphitizing carbons, but the salt template is expected to have strong electrostatic interactions, specifically between the Zn ion and N. Correlating a varied $NaCl/ZnCl_2$ ratio with the oxygen reduction properties has been done (Chapter 3 Figure S3.5). However, understanding the reactions that occur during pyrolysis to promote the formation of the desirable environments would be very interesting and a valuable contribution to the field. I suggest solid-state ^{67}Zn and ^{23}Na NMR studies at a high magnetic field of the salt-templated material, post-pyrolysis and pre-washing, so that the template materials are still in the graphitized N-carbon. Correlating this data for materials synthesized at a variety of $NaCl/ZnCl_2$ ratios with the types and distributions of N-moieties formed and with reduction performance should elucidate the types of environments formed during pyrolysis that result in higher insolated pyridinic N environments and higher reduction performances. This is discussed in the future work sections of Ch 3 and 5.

Additionally, I think that it is important to determine if the desirable affects achieved by the presence of the Zn^{2+} ions during N-carbon synthesis are specific to the Zn^{2+} ion, or if any divalent ions will achieve the same results. To investigate this, I suggest synthesizing and testing the performance of materials with a variety of divalent ions (e.g., Ni^{2+}, Cu^{2+}, Co^{2+}, Fe^{2+}) in the salt-template. It seems that the presence of the n ion is key to the development of specific N moieties that result in better reduction performance. The unique access that the Chmelka lab provides us with a feedback loop between synthesis, material performance, and advanced materials characterizations such as the NMR experiments suggested above. Thus, I believe that the Chmelka group is the ideal group to conduct the experiments suggested above, and I believe that they will be uniquely interesting and impactful to the fields of various reduction synthesis and environmentally responsible energy sources.

A.3 Future directions

In the sections above I discuss the experiments that I proposed and completed some work on. Going forward, I think that it will be very important not only to understand the reaction discussed above, but how the templating agent affects that eutectic melt as well. To do this I suggest similar experiments to those outlined above, but incorporating the template into the study of the eutectic melt. Specifically, comparing the *in situ* ^{1}H, ^{15}N, and ^{13}C NMR of silica- and salt-templating (or varied salt template ratios) synthesis steps would be very insightful.

A.4 References

1. Bernhard, A. M., Peitz, D., Elsener, M., Wokaun, A. & Kröcher, O. Applied Catalysis B : Environmental Hydrolysis and thermolysis of urea and its decomposition byproducts biuret , cyanuric acid and melamine over anatase TiO 2. *"Applied Catal. B, Environ.* **115**–**116**, 129–137 (2012).
2. Kawasaki, A. & Ogata, Y. Kinetics of the formation of biuret from urea in 2-methoxyethanol. *Tetrahedron* **21**, 2893–2898 (1965).
3. Sharmin, E. & Zafar, F. Polyurethane: An Introduction. *Intech Open* 4–15 (2012). doi:10.5772/32009
4. Hoover, F. W., Stevenson, H. B. & Rothrock, H. S. Chemistry of Isocyanic Acid. I. Reactions of Isocyanic Acid with Carbonyl Compounds. *J. Org. Chem.* **28**, 1825–1830 (1963).